

EBS Model Development and Evaluation Report

(FCRD-UFD-2013-000312)

Fuel Cycle Research & Development

***Prepared for
U.S. Department of Energy
Used Fuel Disposition Campaign***

***Carlos F. Jové Colón, Jeffrey A. Greathouse, Stephanie
Teich-McGoldrick, Randall T. Cygan, Philippe F. Weck,
Glen A. Hansen, Louise J. Criscenti (SNL)***

***Florie A. Caporuscio, Michael Cheshire,
Michael S. Rearick, Mary K. McCarney (LANL)***

***Harris R. Greenberg, Thomas J. Wolery, Mark
Sutton, Mavrik Zavarin, Annie B. Kersting, James
D. Begg, James A. Blink, Thomas A. Buscheck,
Ana Benedicto-Cordoba, Pihong Zhao (LLNL)***

***Jonny Rutqvist, Carl I. Steefel, Jens Birkholzer,
Hui-Hai Liu, James A. Davis, Ruth Tinnacher, Ian
Bourg, Liange Zheng, Victor Vilarrasa (LBNL)***



***September 27th, 2013
SAND2013 - 8512 P***

DISCLAIMER

This information was prepared as an account of work sponsored by an agency of the U.S. Government. Neither the U.S. Government nor any agency thereof, nor any of their employees, makes any warranty, expressed or implied, or assumes any legal liability or responsibility for the accuracy, completeness, or usefulness, of any information, apparatus, product, or process disclosed, or represents that its use would not infringe privately owned rights. References herein to any specific commercial product, process, or service by trade name, trade mark, manufacturer, or otherwise, does not necessarily constitute or imply its endorsement, recommendation, or favoring by the U.S. Government or any agency thereof. The views and opinions of authors expressed herein do not necessarily state or reflect those of the U.S. Government or any agency thereof.

Prepared by:

Sandia National Laboratories

Albuquerque, New Mexico 87185

Sandia National Laboratories is a multi-program laboratory managed and operated by Sandia Corporation, a wholly owned subsidiary of Lockheed Martin Corporation, for the U.S. Department of Energy's National Nuclear Security Administration under contract DE-AC04-94AL85000.



**U.S. DEPARTMENT OF
ENERGY**



Sandia National Laboratories

APPENDIX E
FCT DOCUMENT COVER SHEET ¹

Name/Title of Deliverable/Milestone/Revision No. EBS Model Development and Evaluation Report (M2FT-13SN0806061)

Work Package Title and Number DR Generic Engineered Barrier System Evaluations – SNL, FT-13SN080606

Work Package WBS Number 1.02.08.06

Responsible Work Package Manager Carlos F. Jove Colon 
(Name/Signature)

Date Submitted: 09/27/2013

Quality Rigor Level for Deliverable/Milestone ²	<input checked="" type="checkbox"/> QRL-3	<input type="checkbox"/> QRL-2	<input type="checkbox"/> QRL-1 Nuclear Data	<input type="checkbox"/> Lab/Participant QA Program (no additional FCT QA requirements)
--	---	--------------------------------	--	--

This deliverable was prepared in accordance with Sandia National Laboratories
(Participant/National Laboratory Name)

QA program which meets the requirements of
 DOE Order 414.1 NQA-1-2000 Other

This Deliverable was subjected to:

- | | |
|---|--|
| <input type="checkbox"/> Technical Review | <input type="checkbox"/> Peer Review |
| Technical Review (TR) | Peer Review (PR) |
| Review Documentation Provided | Review Documentation Provided |
| <input type="checkbox"/> Signed TR Report or, | <input type="checkbox"/> Signed PR Report or, |
| <input type="checkbox"/> Signed TR Concurrence Sheet or, | <input type="checkbox"/> Signed PR Concurrence Sheet or, |
| <input checked="" type="checkbox"/> Signature of TR Reviewer(s) below | <input type="checkbox"/> Signature of PR Reviewer(s) below |

Name and Signature of Reviewers
Yifeng Wang 

NOTE 1: Appendix E should be filled out and submitted with the deliverable. Or, if the PICS:NE system permits, completely enter all applicable information in the PICS:NE Deliverable Form. The requirement is to ensure that all applicable information is entered either in the PICS:NE system or by using the FCT Document Cover Sheet.

NOTE 2: In some cases there may be a milestone where an item is being fabricated, maintenance is being performed on a facility, or a document is being issued through a formal document control process where it specifically calls out a formal review of the document. In these cases, documentation (e.g., inspection report, maintenance request, work planning package documentation or the documented review of the issued document through the document control process) of the completion of the activity, along with the Document Cover Sheet, is sufficient to demonstrate achieving the milestone. If QRL 1, 2, or 3 is not assigned, then the Lab / Participant QA Program (no additional FCT QA requirements) box must be checked, and the work is understood to be performed and any deliverable developed in conformance with the respective National Laboratory / Participant, DOE or NNSA-approved QA Program.

ACKNOWLEDGEMENTS

The authors acknowledge our gratitude to Yifeng Wang (SNL), Ernest Hardin (SNL), Peter Swift (SNL), Kevin McMahon (SNL), Davis Sassani (SNL), Victor G. Figueroa (SNL), Carlos Lopez (SNL), William Spezialetti (DOE NE-53), Prasad Nair (DOE NE-53), Mark Tynan (DOE NE-53), and Tim Gunther (DOE NE-53) for their helpful discussions on various topics covered in this report.

SUMMARY

Engineered Barrier Systems (EBS) model evaluation and development is fundamental to the design and analysis of disposal concepts for generic repository systems within the Used Fuel Disposition R&D Campaign. This analysis is key to the advancement of design concept recommendations for the different host media under consideration. The use of high-fidelity modeling tools and methods along with an experimental program provides the much needed framework to analyze, for example, coupled processes of multilayered EBS plus the intricacies of thermal anisotropies in the host rock media and fluid-mineral interactions. Engineering analysis and trade-off studies of disposal concepts requires a comprehensive evaluation of thermal constraints for the analysis of thermal loads (DSEF, Albany), its effect on temperature-driven coupled processes (chemical, mechanical, transport), and optimization of the EBS configuration within the repository layout. Furthermore, experimental work on clay barrier interactions is needed to accurately resolve issues important to EBS performance such as phase stability relations, sorption and transport properties, and material degradation in response to elevated temperatures (i.e., well above 100°C). Therefore, experimental programs are crucial to the study of the extent and state of *sacrificial zones* based on the thermal effects on the clay backfill chemical and mechanical properties. This provides the scientific basis to the development of the thermal criteria governing barrier performance within the safety case. All these aspects of EBS analysis and tool development are crucial to site screening evaluation activities targeting different geologic disposal media.

This report centers on progress made on modeling and experimental approaches to analyze physical and chemical interactions affecting clay barrier performance. It also provides new advances made in these areas in support of EBS engineering and scientific R&D objectives:

- Develop theoretical, experimental, and testing methodologies to gauge key processes central to barrier performance in response to variants in generic disposal and nuclear fuel cycle options.
- Advance robust and agile computational strategies that allow, to the extent possible, integration and cross-fertilization of information between models to be utilized in EBS performance assessment.
- Reconcile modeling results with experimental data (when possible) to verify and validate simulation approaches.

An example of model cross-fertilization is the use of atomistic simulations of clay to obtain high temperature diffusion rates of chemical species and analysis of swelling phenomena that could inform or be integrated with other models (see parts II and VIII of this report). Another example is the retrieval of high temperature thermodynamic data for the salt solid anhydrite using *ab initio* (first principles) atomistic simulations. Strong agreement is found between the results obtained by this approach and handbook data and could potentially fill information gaps (e.g., high temperature extrapolations) in thermodynamic databases (parts IV and V).

The results obtained from these modeling methodologies can be integrated with coupled THMC, thermodynamic or even GDSM/ADSM PA models through either bounding constraints on input parameter data or directly used these data in a model. One example is the coupling proposed for the Fuel Degradation Model (FDM) with system-level and sub-system level process models as part of the EBS Used Fuel Degradation activity. The PA system models such as ADSM are also conceptualized to accept process level information from key EBS process models such as diffusion rates, thermal effects, and radionuclide source term data. This information is generated from EBS process and sub-process level models to analyze coupled phenomena such as THMC, reactive diffusion, and FDM affecting the source term behavior and barrier performance. Therefore, system- and process-level couplings are anticipated in model integration activities (see part I). However, further development of integration strategies and schemes are needed to fulfill the requirements posed by these multi-level couplings.

The EBS processes evaluated in this report include sorption and transport of radionuclides, THMC behavior of clay barriers, atomistic simulations of barrier materials, and clay/metal interactions with fluids at high temperatures. The major accomplishments of various tasks encompassing these DOE multi-laboratory (SNL, LBNL, LANL, LLNL) activities within this UFD campaign are organized into eight parts. Engagements in international activities such as DECOVALEX will be documented in a separate milestone report. Planned work for continuing research activities in FY14 are given at the end of each part:

- (Part I) **Engineered Barrier System (EBS) Optimization Analysis**: An overview of the importance of THMC processes to barrier performance for the thermal analysis of a multi-barrier EBS design concept using DSEF was given in Jové Colón et al. (2012). In this report, an example of repository design optimization (RDO) based on 2-D and 3-D thermal analysis modeling was conducted using the FEM code Albany interfaced with high performance computational (HPC) tools for geometry meshing, uncertainty quantification (UQ) and optimization, and domain discretization. Coupling the Albany thermal analysis with the DAKOTA optimization tool provides a robust and yet flexible platform for the analysis optimal barrier thermal properties at various scales which is key to the evaluation of the extent of *sacrificial barriers* in the composite EBS together with the analysis of disposal design concepts. This information is to be integrated with other scientific knowledge obtained from research activities such as thermal constraints on clay phase stability and the coupled THMC behavior at elevated temperatures. Minimization of an objective function in the optimization analysis also illustrates the need for robust tools such as DAKOTA to resolve the global minima in systems with complex material heterogeneities and geometries.
- (Part II) **Investigation of Reactive Transport and Coupled THM Processes in EBS (FY13)**. This part documents progress made in two R&D focus areas:
 - Modeling of THMC processes within bentonite and the interaction between the EBS and a clay disposal formation in the near field by implementation of the dual-structure approach and the expansive Barcelona Basic Model (BExM). Such an extension of the BBM provides for a description of dual-structure behavior of expansive soils, including dependency of swelling strains and swelling pressures on the initial state and on the stress path, strain accumulation upon suction cycles, as well as secondary swelling.

- Reactive-diffusive transport modeling approaches for radionuclide migration in bentonite. This modeling is performed by applying a combination of microcontinuum scale models based on the Poisson-Boltzmann and Poisson-Nernst-Planck equations. This allows for elucidation of the coupling between electric double layer (EDL) phenomena and molecular diffusion in clay nanopores. This work also leverages progress made on MD modeling of ion diffusion in clay nanopores. Using these approaches, uranium transport through the compacted bentonite is modeled using the Mean Electrostatic Model, with rigorous treatment of overlapping EDL.
- Experimental investigations were conducted to study U(VI) sorption onto clay and implications to reactive diffusive transport in bentonite. This research encompassed a detailed theoretical analysis of the potential impacts of solution chemistry on uranium diffusion and clay (surface) characteristics. Furthermore, uranium(VI)-montmorillonite batch sorption equilibrium experiments were performed to characterize uranium sorption as a function of chemical solution conditions, and to provide data sets for the development of a surface complexation model. Lastly, lab-scale diffusion experiments were designed and the reactive diffusive transport of calcium and U(VI) were evaluated experimentally in predictive model calculations.

(Part III) **Update on Experimental Activities on Buffer/Backfill Interactions at elevated Pressure and Temperature:** This part presents progress made in experimental activities evaluating high temperature interactions with bentonite clay and the resulting alteration to other phases. The results of these experiments (performed at 150 – 160 bars at temperatures up to 300°C for five to six weeks) can be summarized as follows:

- The pH, K^+ , and Ca^{2+} concentrations dropped, while $SiO_{2(aq)}$, Na^+ , and SO_4^{2-} concentrations increased throughout the experiments.
- The alkali and alkaline earth metals aqueous concentrations appear to be buffered via the montmorillonite and clinoptilolite exchange reactions.
- Illite or illite/smectite mixed-layer formation is significantly retarded in the closed system due to Na^+ and $SiO_{2(aq)}$ accumulation and limited K^+ supply.
- Precursor clinoptilolite underwent extensive dissolution during the six week, 300°C experiments subsequently producing a high-silicon analcime in addition to authigenic silica phases.
- Analcime and feldspar formation partially sequesters aqueous Al^{3+} , thereby potentially inhibiting illitization. Associated with the zeolite alteration is a ~ 17 % volume decrease (assuming quartz formation) that translates into ~ 2% volume loss in the bulk bentonite.
- Pyrite decomposition is first observed at ~210 °C, generating available $H_2S_{(aq,g)}$ that reacts with metal plates or evolves as a gas. The copper rapidly degrades in the presence of $H_2S_{(aq,g)}$, resulting in the formation of a chalcocite crust on the copper.

- A layer of Fe-saponite (or rarely, chlorite) forms at the steel bentonite interface, potentially acting as a passivating agent to retard further metal corrosion.
- **(Part IV) Thermodynamic Database (TDB): Recommendations and Guidelines on Future TDB Development:**
 - Progress made on TDB development with recommendation on how to proceed towards the development of a comprehensive TDB effort allowing for transparency, ease of usage, validation/verification, and potential for model expansion.
 - Guidelines for TDB development consistent with OECD-NEA procedures to ensure consistency in the retrieval and derivation of thermodynamic data, traceability, multi-faceted benchmarking strategies with interbational collaborators, and open dissemination.
- **(Part V) Thermodynamic Modeling: Clay Hydration, Ion Exchange, and First Principles Calculations of Mineral Thermodynamic Properties at Elevated Temperatures:** Progress made on the application of thermodynamic methods to represent non-ideal solid solutions (Margules type) and computation of chemical equilibrium using a Gibbs energy minimization (GEM) in the Cantera code suite to model:
 - Clay hydration (swelling) as a function of relative humidity (RH)
 - Na-Ca cation exchange in clay.

In addition, a thermodynamically-based pseudo-steady state kinetic approach to surface complexation using Cantera code suite has been developed. Lastly, the use of *ab initio* (first-principles) methods (without the need for any experimental input) to

- Calculate missing thermodynamic data for minerals relevant to disposal in salt media. The system treated in this part of the report is defined by crystalline anhydrite (CaSO_4), bischofite ($\text{MgCl}_2 \cdot 6\text{H}_2\text{O}$) and polyhalite ($\text{K}_2\text{SO}_4 \cdot \text{MgSO}_4 \cdot 2\text{CaSO}_4 \cdot 2\text{H}_2\text{O}$).
- Provide an independent assessment of existing experimental thermodynamic data and resolve contradictions in existing calorimetric data.
- Validate our computational approach using high-quality calorimetric data.

This approach can be seen as a fast, inexpensive, and systematic way to obtain thermodynamic parameters at elevated temperature conditions where experimental data is largely lacking or difficult to obtain. It is also a powerful tool to improve the design of new experiments and complementing existing experimental data.

- (Part VI) **Molecular Dynamic (MD) Study on the Swelling Properties of Montmorillonite and Beidellite Clays**: This MD study investigates:
 - Swelling phenomena influenced by temperature ($T = 298\text{ K}$ and 425 K), cation species, and charge location of smectite clays (Na^+ - Cs^+ - Ca^{2+} - Mg^{2+} - montmorillonite and beidellite).
 - Generation of water adsorption isotherms at 300 K using Grand Canonical Monte Carlo (GCMC) MD simulations.
 - Interrogate the above-mentioned MD simulation results with the considered clay compositions to elucidate the thermodynamics of clay swelling. Furthermore, make comparisons to the thermodynamic values extracted from existing experimental data.

- (Part VII) **Disposal Systems Evaluation Framework (DSEF) (Version 3.0 User Manual)**: The Disposal Systems Evaluation Framework (DSEF) has become a key tool to formalize and facilitate the development and documentation of repository conceptual design options for a range of waste forms, geologic environments, repository design concepts, and repository operating modes. DSEF has been instrumental in the high-level thermal analysis of various disposal concepts. This part of the report provides extensive documentation on the usage of DSEF knowledge management system with a broad library of thermal analysis cases for various disposal concepts. This version has the capability to assess cost analysis based on repository design, licensing, construction, maintenance, and other cost-based and/or performance-based items.

- (Part VIII) **Np(V) Sorption and Diffusion on Montmorillonite Clay**: This research activity is focused on quantifying Np(V) sorption to and diffusion through montmorillonite clay which is the primary mineralogic component of proposed bentonite backfill material in certain nuclear waste repository scenarios. This activity integrates experimental and modeling aspect of Np(V) sorption on the basis of cation exchange modeling in clay and development of a non-electrostatic model (NEM) for surface complexation based on various sets of existing data. The methodology for Np(V) clay diffusion experiments in FY13 is described along with results on the characterization of U(VI) diffusion through compacted MX-80 bentonite cores. The latter is the product of a seven year experiment providing a unique opportunity to evaluate U diffusion profiles. This is an international collaboration between LLNL and the Helmholtz Zentrum Dresden Rossendorf in Germany. This part also discusses the RES³T thermodynamic sorption database and its use in sorption modeling.

TABLE OF CONTENTS

AKNOWLEDGEMENTS.....	2
SUMMARY	3
ACRONYMS.....	25

(Part I) Engineered Barrier System (EBS) Optimization Analysis

1. Engineered Barrier System (EBS) Optimization Analysis.....	29
1.1 Introduction.....	29
1.2 Conceptual Integration with System-Level and Sub-System Level Process Models	30
1.2.1 Thermal Analysis for Multi-Layered EBS: 2-D and 3-D FEM Approach.....	32
1.3 Plans for FY14.....	39
1.4 References.....	41

(Part II) Investigation of Reactive Transport and Coupled THM Processes in EBS (FY13)

1. Introduction	44
2. Modeling Coupled THMC Processes in the EBS.....	44
2.1 Implementation and testing of a Dual-Structure Bentonite Model into TOUGH-FLAC	46
2.1.1 The dual-structure approach and Barcelona Expansive Model.....	46
2.1.2 Implementation of BExM into TOUGH-FLAC.....	53
2.1.3 Testing and verification of implementation	54
2.2 Linking dual-structure model to chemistry and testing.....	58
2.3 Summary	61
3. Modeling Reactive Diffusive Transport.....	62
3.1 Mean Electrostatic Model for Diffusive Transport in the EBS.....	65
3.1.1 Derivation from Poisson-Boltzmann Equation	65
3.1.2 Dynamic Calculation of Electrical Double Layer Thickness.....	68
3.1.3 Testing of EDL Model using the DR-A Experiment at Mont Terri, Switzerland	70
3.1.4 Development of a CrunchEDL-Comsol Coupling for Flow and Transport in Charged Porous Media.....	73
3.2 Molecular scale predictions of diffusion in the EBS.....	74

3.2.1	Temperature Dependence of Water and Solute Diffusion in the EBS	74
3.2.2	Methodology	77
3.2.3	Results and Discussion.....	78
3.2.4	Summary	89
4.	Experimental Studies on Reactive Diffusive Transport	89
4.1	Background	90
4.1.1	Relevance.....	90
4.1.2	Effects of Chemical Solution Conditions on U(VI) Diffusion Coefficients	91
4.1.3	Influence of Solution Chemistry on Clay (Surface) Properties.....	94
4.2	Materials and Methods.....	97
4.2.1	Overview of Materials	97
4.2.2	Batch Sorption Equilibrium Experiments	98
4.2.3	Modeling Setup for Surface Complexation Models.....	98
4.2.4	Design of Diffusion Cell and Clay Packing Device.....	99
4.2.5	Clay Pretreatment Specific to Diffusion Experiments	102
4.2.6	Diffusion Experiment: Calcium Bromide Diffusion in Na-Montmorillonite	102
4.2.7	Predictive Modeling of Uranium(VI) Diffusion in Lab-Scale Experiments.....	104
4.3	Results and Discussion.....	107
4.3.1	Batch sorption equilibrium experiments and surface complexation modeling	107
4.3.2	Calcium Bromide Diffusion in Na-Montmorillonite	113
4.3.3	Predictive Modeling of Uranium(VI) Diffusion in Lab-Scale Experiments.....	121
4.4	Summary	125
5.	Overall Summary.....	125
5.1	THMC Process Modeling in Bentonite.....	125
5.2	Modeling Reactive-Diffusive Transport in Bentonite.....	126
5.3	Experimental Study on Reactive-Diffusive Transport	128
6.	References	130

(Part III) Update on Experimental Activities on Buffer/Backfill Interactions at elevated Pressure and Temperature

2.	Introduction	143
3.	Methods	144
4.	Results	148

5.	Discussion.....	175
6.	Potential EBS mineralogic/petrologic effects on geological repository - Conclusions.....	181
7.	FY14 Experimental program.....	182
8.	References	184

(Part IV) Thermodynamic Database (TDB): Recommendations and Guidelines on Future TDB Development

1.	Thermodynamic Data: Progress	190
2.	Recommendations for Future Database Development	194
3.	Outline for Guidelines on Thermodynamic Database (TDB) Development and Programmatic goals.....	195
4.	References	206

(Part V) Thermodynamic Modeling: Clay Hydration, Ion Exchange, and First Principles Calculations of Mineral Thermodynamic Properties at Elevated Temperatures

1.	Thermodynamic Modeling of Smectitic Clay Hydration: Na-Ca-Mg-K-Al-Si-H ₂ O System.....	214
2.	Thermodynamic Modeling Using the Cantera Code Suite.....	215
2.1	Modeling Approach and Discussion	215
3.	Generating Thermodynamic Data for Geochemical and Used Fuel Degradation Models: A First-Principles Study of Salt Minerals	226
3.1	Background	226
3.2	Computational Methods.....	228
3.3	Results and Discussion.....	230
3.4	Conclusions.....	238
3.5	Planned FY14 Work on Thermodynamic Modeling.....	238
4.	References	239

(Part VI) Molecular Dynamic (MD) Study on the Swelling Properties of Montmorillonite and Beidellite Clays

1.	Introduction	247
2.	Model and Method	247

2.1	GCMC Simulations Methodology	249
3.	Results and Discussion	250
3.1	Swelling Curves	250
3.2	Potential Energies	252
3.3	Temperature Effects	254
3.4	Interlayer Molecular Structure	255
4.	Comparing energetic information from molecular simulations and experimental adsorption data for montmorillonite swelling	261
4.1	Solid Solution Model	261
4.2	Energies Derived from Molecular Simulation	262
4.3	Approach and Results	262
4.4	Summary	267
5.	References	268

(part VII) Disposal Systems Evaluation Framework (DSEF) Version 3.0 User Manual

1.	Overview	273
2.	Information Flow	274
3.	Finding Your Way Around – the NAVIGATION, README, LISTS and REV HISTORY Worksheets	276
4.	Getting Started – Working with the DSEF Workbook	279
5.	The Starting Point to Define an Analysis Case - the INPUTS Worksheet	281
6.	The INPUTS CHECKLIST Worksheet	291
7.	Reviewing Previous Analyses – the CASE LIBRARY and the THERMAL-INTERPOLATE Worksheets	292
8.	Getting a Quick Overview of the Latest Analysis – the RESULTS and the THERMAL-ANALYTICAL OUTPUT Worksheets	304
	The COST Worksheets	305
9.	The WASTE FORM Worksheet	314
10.	Defining Thermal Data Inputs and Outputs -the THERMAL Worksheets	317

11.	Finding and Comparing Material Properties - the MATERIALS Worksheets	320
12.	Placeholder worksheets for future development.....	322
13.	References	324

(Part VIII) **Np(V) Sorption and Diffusion on Montmorillonite Clay**

1	Introduction	326
1.1	Relevance of Np to Nuclear Waste Repositories	326
1.2	Np Reactive Transport	327
2	Development of a Np(V) Ion Exchange Model.....	329
2.1	Materials and Methods.....	329
2.2	Results and Discussion.....	332
2.2.1	Np(V) Speciation	332
2.2.2	Cation Composition of Batch Sorption Samples	332
2.2.3	Np(V) Experimental Sorption Data	333
2.2.5	Simulation of Np(V) Sorption to Montmorillonite	338
2.3	Summary	339
3	Development of a Np(V) Surface Complexation Model	340
3.1	Non-Electrostatic Surface Complexation Model Development	341
3.3	Np(V) on Silica	347
3.4	Np(V) on Aluminosilicates	349
3.5	Summary	351
4	Comprehensive Approaches to Developing Ion Exchange and Surface Complexation Models for Nuclear Waste Repository Conditions.....	352
5	Diffusion Cell Experiments	356
5.1	Materials and Methods.....	356
5.2	Characterization of Long-term Uranium Diffusion Experiments	357
6.	Planned FY14 Efforts	360
7.	References	361
	Appendix A.....	368
	Appendix B	369

Appendix C.....	1
Appendix D.....	18
Appendix E.....	22
Appendix F.....	47
Appendix G.....	56
Appendix H.....	59

TABLE OF FIGURES

(Part I) **Engineered Barrier System (EBS) Optimization Analysis**

Figure 1. EBS coupled process phenomena (center) and interrelations between process models from other domains.....	29
Figure 2. Performance assessment (PA) model/code framework for ADSM.....	30
Figure 3. Disposal system integrated process models.....	30
Figure 4. Information flow diagram showing the relationship of the Fuel Degradation Model (FDM) to the system-level model and sub-models (modules).	31
Figure 6. Schematic view of 2-D diagram of EBS along with meshed geometry for the Albany thermal problem.....	36
Figure 7. Schematic view of 3-D diagram of EBS along with meshed geometry for the Albany thermal problem.....	36
Figure 8. Computed temperature profile from the Albany code for a 2-D EBS geometry	37
Figure 9. Minimization path of descent for the optimization of thermal conductivities of barrier materials from the Albany-DAKOTA coupling	39

(Part II) **Investigation of Reactive Transport and Coupled THM Processes in EBS (FY13)**

Figure 2.1. Schematic representation of the two structural levels considered	46
Figure 2.2. Three-dimensional representation of the yield surface in the BBM.....	48
Figure 2.3. Microstructural and macrostructural elastoplastic responses in a double-structure model equivalent to the Barcelona Expansive Model.	49
Figure 2.4. Summary of micro–macropore interaction mechanisms.	50
Figure 2.5. Reference pressure and plastic flow direction	53
Figure 2.6. Strain evolution during suction cycles for a low confining pressure.....	55
Figure 2.7. Evolution of the interaction functions for a low confining pressure.	55
Figure 2.8. Evolution of the plastic strain due to the interaction between the microstructure and the macrostructure for a low confining pressure.	56
Figure 2.9. Void ratio evolution of the microstructure during suction changes for a low confining pressure.....	56
Figure 2.10. Void ratio evolution of the macrostructure during suction changes for a low confining pressure.....	56
Figure 2.12. Volumetric deformation upon suction cycles reported by Pousada (1984) in an oedometric test under a vertical stress of 0.1 MPa.	57
Figure 2.13. Volumetric deformation upon suction cycles mimicking the test of Pousada (1984).	58
Figure 2.14. Changes in water saturation in the middle of the sample	60
Figure 2.15. Changes in equivalent fraction of each cation in the middle of the sample when the sample is saturated with 1M CaCl ₂ solution.....	60

Figure 2.16. Changes in equivalent fraction of each cation in the middle of the sample when the sample is saturated with 1M NaCl solution.....	61
Figure 2.17. Volumetric deformation in the middle of the sample for the case with 1 M NaCl and CaCl ₂ solution.....	61
Figure 3.1. Schematic illustration of the Gouy-Chapman-Stern model of the solid-electrolyte interface, with the potential distribution $\psi(z)$ versus distance from the charged solid surface.....	66
Figure 3.2. Schematic representation of the potential distribution in a nanochannel with height h in direction z when the EDLs overlap (solid line), compared to the EDL potentials if the opposite wall is not present.....	68
Figure 3.3. Results of dynamic EDL porosity calculations after 5 days of diffusion. Left panel: A high ionic strength front ($I=0.45M$) diffuses front left to right through the domain that is initially lower ionic strength ($I=0.045M$)..	70
Figure 3.4. Stratigraphic section of the Jura Mountains in which the Mont Terri rock laboratory is located.....	70
Figure 3.5. Schematic of the experimental setup from the DI-A test, similar in concept to the DR-A test.....	72
Figure 3.6. Fit of borehole HTO concentration versus time using a capacity factor of 2.175. This is solved in radially symmetric cylindrical coordinates using CrunchEDL.	72
Figure 3.7. Anion concentration versus time in the borehole for the first DR-A test.....	73
Figure 3.8. Illustration of the coupling scheme between Comsol and CrunchEDL.....	74
Figure 3.9. D values of Na ⁺ (top) and water (bottom) as a function of inverse simulation cell size	80
Figure 3.10. Comparison of the shear viscosity of the SPC/E water model	80
Figure 3.11. Basal spacing d_{001} (open circles) and interlayer water density (filled circles) as a function of the number of water molecules per unit cell (UC) in a MD simulation.....	82
Figure 3.12. MD simulation snapshots showing the four different simulation cells that were used to study the 3W hydrate of montmorillonite.....	83
Figure 3.13. D values of Na ⁺ (top) and water (bottom) as a function of temperature and the mean inverse simulation cell size $1/L$	83
Figure 3.14. MD simulation snapshots showing the 1W, 2W, 3W and the 10W hydration states (with $d_{001} = 12.4, 15.6, 18.8, \text{ and } 40.7 \text{ \AA}$, respectively) at 298 K and the corresponding atomic density profiles along z-direction for Na ⁺ , H _{water} , O _{water} and montmorillonite.	85
Figure 3.15. Normalized self-diffusion coefficients of Na ⁺ (left) and water (right) as a function of clay layer rigidity and hydration state (1W, 2W, 3W, or 10W) at 298 K.....	86
Figure 3.16. Activation energy of diffusion of Na ⁺ and water in water-saturated Na-smectite, plotted as a function of dry bulk density	88
Figure 4.1. Expected gradients across the EBS.	91
Figure 4.2. Visualization of constrictivity and tortuosity.	93
Figure 4.3. Overview of chemical solution effects on clay (surface) characteristics and diffusion rates.....	95

Figure 4.4. Visualization of anion exclusion effects.....	96
Figure 4.5. Diffusion cell design.....	100
Figure 4.6. Design for clay packing device.	101
Figure 4.7. Diffusion cell and clay packing device.....	101
Figure 4.8. Schematic of setup for diffusion experiment.....	103
Figure 4.9. Schematic of diffusion cell, containing a clay packing sandwiched between two filter plates, used in ANADIFF simulations.....	104
Figure 4.10. U(VI) adsorption onto Na-montmorillonite at varying chemical solution conditions.....	109
Figure 4.11. K_d values for U(VI) sorption to Na-montmorillonite at varying chem. solution conditions.....	109
Figure 4.12. Total, measured Ca concentrations in solution for batch sorption equilibrium experiments.....	110
Figure 4.13. Aqueous speciation of a 1 micromolar U(VI) solution in 0.1 M NaCl in equilibrium with atmospheric CO ₂ (log CO ₂ = -3.5) as a function of pH.	111
Figure 4.14. Same as Figure 4.13. except solution now contains 2 mM Ca. Aqueous speciation of a 1 micromolar U(VI) solution in 0.1 M NaCl in equilibrium with atmospheric CO ₂ (log CO ₂ = -3.5) as a function of pH.	111
Figure 4.15. Modeling results for U(VI) sorption onto Na-montmorillonite over the whole pH range.	112
Figure 4.16. Detailed modeling results for U(VI) sorption onto Na-montmorillonite between pH values of 5.5 and 8.5.....	113
Figure 4.17. Results for monitoring of solution pH in low-concentration reservoir solutions during CaBr ₂ diffusion experiment.....	114
Figure 4.18. Results for monitoring of Ca and Br concentrations in high-concentration reservoir solution during CaBr ₂ diffusion experiment.....	114
Figure 4.19. Diffusive flux of Ca through pretreated Na-montmorillonite as a function of time in CaBr ₂ through-diffusion experiment at 1 mM CaBr ₂ , I=0.1 M NaCl and pH~7. Steady-state conditions are approximately reached at 32.97 days.....	117
Figure 4.20. Cumulative mass of Ca as a function of time in CaBr ₂ through-diffusion experiment in pretreated Na-montmorillonite at 1 mM CaBr ₂ , I=0.1 M NaCl and pH~7.....	117
Figure 4.21. Diffusive flux of Br through pretreated Na-montmorillonite as a function of time in CaBr ₂ through-diffusion experiment at 1 mM CaBr ₂ , I=0.1 M NaCl and pH~7.	118
Figure 4.22. Cumulative mass of Br as a function of time in CaBr ₂ through-diffusion experiment in pretreated Na-montmorillonite at 1 mM CaBr ₂ , I=0.1 M NaCl and pH~7.....	118
Figure 4.23. Diffusive flux of tritium through pretreated Na-montmorillonite as a function of time in CaBr ₂ through-diffusion experiment at I=0.1 M NaCl and pH~7.	119
Figure 4.24. Cumulative activity of tritium as a function of time in CaBr ₂ through-diffusion experiment in pretreated Na-montmorillonite at I=0.1 M NaCl and pH~7.	119
Figure 4.25. Simulated diffusion profiles: Total U(VI) concentration along a clay packing as a function of Total Inorganic Carbon (TIC) conc. and time.....	123

Figure 4.26. Simulated diffusion profiles: Total U(VI) concentrations along a clay packing as a function of solution pH and time.	123
Figure 4.27. Simulated relative U(VI) solution concentrations as a function of Total Inorganic Carbon (TIC) concentrations and pH after a 360-day experiment.	124

(Part III) Update on Experimental Activities on Buffer/Backfill Interactions at elevated Pressure and Temperature

Figure 1. Minerals associated with the Colony, WY bentonite	149
Figure 2. Oriented XRD patterns for the glycolated, < 2 μm fraction from the ramped thermal profile experiments with d-spacings labeled above each peak.	153
Figure 3. Post-reaction mineralogical characteristics from ramp heating experiments	154
Figure 4. Oriented XRD patterns for the glycolated, < 2 μm fraction from the isothermal, 300 °C thermal profile experiments	156
Figure 5. Post-reaction SEM images showing mineralogical characteristics from the isothermal 300 °C experiments	157
Figure 6. Analcime growth stages associated with a systematic Si/Al changes.	158
Figure 10. XRD patterns of the air-dried and ethylene glycol saturated corrosion products on the 304 SS plate used in the EBS-2 experiment.	163
Figure 11. XRD patterns of the air-dried and ethylene glycol saturated corrosion products on the 304 SS plate used in the EBS-5 experiment.	163
Figure 12. SEM image (plan view) of Fe-phyllsilicates (saponite and chlorite) using 304 SS as a growth substrate from both ramped (EBS-2) and isothermal, 300 °C (EBS-5) heating profiles.	164
Figure 13. SEM image of 304 SS cross-section showing Fe-saponite interface reaction products using steel surface as a growth substrate.	165
Figure 14. XRD patterns of the air-dried and ethylene glycol saturated interface reaction products on the 316 SS plate used in the EBS-3 experiment.	166
Figure 15. XRD patterns of the air-dried and ethylene glycol saturated interface reaction products on the 316 SS plate used in the EBS-10 experiment.	166
Figure 16. SEM image of Fe-saponite using 316 SS as a growth substrate from both ramped (EBS-3) and isothermal, 300 °C (EBS-10) heating profiles.	167
Figure 17. SEM image of 316 SS cross-section showing Fe-saponite/chlorite growth due to exfoliation corrosion from EBS-3.	168
Figure 18. XRD patterns of the air-dried and ethylene glycol saturated interface reaction products on the low-carbon steel plate used in the EBS-6 experiment	169
Figure 19. SEM image (plan view) of Fe-saponite growth on low-carbon steel from the ramped (EBS-6) heating experiment.	170
Figure 20. SEM image of low-carbon steel cross-section showing Fe-saponite reaction products using steel surface as a growth substrate	171

Figure 21. XRD plots of the 06l diffraction bands showing Fe-rich smectite and chlorite formed as a interface reaction product are trioctahedral.	172
Figure 22. XRD plots for corrosion products on the copper foils used in the ramped heating experiment (EBS-4).	173
Figure 23. XRD plots for corrosion products on the copper foils used in the six week, 300 °C heating experiment (EBS-11).	173
Figure 24. SEM image (plan view) of copper surface showing corroded copper surfaces and various interface reaction products from both ramped (EBS-4) and isothermal, 300 C (EBS-8) heating profiles.	174
Figure 25. Log aNa ⁺ /aH ⁺ and Log aSiO _{2(aq)} data from the a) 120 °C solution chemistries, b) 210 °C solution chemistries, and c) 300 °C solution chemistries plotted on a Na-H ₂ O-SiO ₂ phase diagram.	175
Figure 26. Log aK ⁺ /aH ⁺ and Log aSiO _{2(aq)} data from the 120 °C solution chemistries, 210 °C solution chemistries, and 300 °C solution chemistries plotted on a K-H ₂ O-SiO ₂ phase diagram.	176

(Part VI) Molecular Dynamic (MD) Study on the Swelling Properties of Montmorillonite and Beidellite Clays

Figure 2.1. Plot of the of the number of moles of H ₂ O (per O ₁₀ (OH) ₂) ($n_{H_2O,il}$) for the Na-smectite clay interlayer versus RH for adsorption/desorption experimental and computed isotherms using Cantera.	220
Figure 2.2. Plot of the of the number of moles of H ₂ O (per O ₁₀ (OH) ₂) ($n_{H_2O,il}$) for the K-smectite the clay interlayer versus RH for adsorption/desorption experimental and computed isotherms using Cantera.	220
Figure 2.3. Plot of the of the number of moles of H ₂ O (per O ₁₀ (OH) ₂) ($n_{H_2O,il}$) for the Ca-smectite the clay interlayer versus RH for adsorption/desorption experimental and computed isotherms using Cantera.	221
Figure 2.4. Plot of the of the number of moles of H ₂ O (per O ₁₀ (OH) ₂) ($n_{H_2O,il}$) for the Mg-smectite the clay interlayer versus RH for adsorption/desorption experimental and computed isotherms using Cantera.	221
Figure 2.5. Computed molar volumes for each of the beidellite compositions considered in this study. The depicted curves are solely based on the theoretical equilibrium isotherms.	222
Figure 2.7. Cantera structure of the thermodynamic implementation of a surface complexation model based on steady-state surface kinetics.	225
Figure 2.8. Cantera prediction of the surface charge profile for rutile (TiO ₂) as a function of pH. The shown experimental data was used to bound the thermodynamic parameter fitting of the surface species.	226
Figure 3.1. Schematic representation of the three-step computational approach used to calculate the thermal properties of crystalline systems using first-principles methods.	228

Figure 3.2. The crystal unit cells of anhydrite (CaSO_4 ; space group <i>Amma</i> , $Z = 4$), bischofite ($\text{MgCl}_2 \cdot 6\text{H}_2\text{O}$; space group <i>C2/m</i> , $Z = 2$) and polyhalite ($\text{K}_2\text{SO}_4 \cdot \text{MgSO}_4 \cdot 2\text{CaSO}_4 \cdot 2\text{H}_2\text{O}$; <i>P-1</i> , $Z = 1$) relaxed at the GGA/PBE level of theory.....	231
Figure 3.3. Thermal properties of anhydrite (per formula unit) calculated at the GGA/PBE level of theory.....	232
Figure 3.4. Thermal properties of bischofite (per formula unit) calculated at the GGA/PBE level of theory.....	233
Figure 3.5. Thermal properties of polyhalite (per formula unit) calculated at the GGA/PBE level of theory.....	234
Figure 3.6. Enthalpy function and Gibbs energy function per formula unit for anhydrite, bischofite, and polyhalite calculated at the GGA/PBE level of theory.....	237

(Part VI) Molecular Dynamic (MD) Study on the Swelling Properties of Montmorillonite and Beidellite Clays

Figure 1. A snapshot (<i>ac</i> plane) of the orthogonal Na-montmorillonite simulation supercell containing 210 water molecules in each of the five clay interlayers..	249
Figure 2: Montmorillonite swelling curves (left) and hydration energy as a function of water content at $T= 298 \text{ K}$ and 425 K	253
Figure 3: Beidellite swelling curves (left) and hydration energy (right) as a function of water content at $T= 298 \text{ K}$ and 425 K	254
Figure 4. Swelling curves for Na^+ - beidellite (left) and Na^+ - montmorillonite at $T= 298 \text{ k}$ and $T= 425 \text{ K}$	255
Figure 5. Density profiles for montmorillonite showing various interlayer cation species, water oxygens, water hydrogens, and clay surface oxygens.	256
Figure 6. Density profiles for beidellite showing various interlayer cation species, water oxygens, water hydrogens, and clay surface oxygens.....	257
Figure 7. Atomistic snapshots corresponding to the density profiles for a one-layer Na^+ -beidellite, two-layer Na^+ -beidellite, one-layer Na^+ -montmorillonite, and two-layer Na^+ -montmorillonite	258
Figure 8. Integral hydration energies as a function of water concentration in montmorillonite interlayers	263
Figure 9. Comparison of integral hydration energies for calcium and sodium. The calculated points derived from molecular simulation data using Method 2 with two different maximum water contents.....	264
Figure 10. Isotheric heat of adsorption calculated using method of Smith (1998).....	265
Figure 11. Immersion energies calculated using Eqn. (5).....	266

(part VII) Disposal Systems Evaluation Framework (DSEF) Version 3.0 User Manual

Figure 1- DSEF Input-Process-Output diagram.....	275
Figure 2 – Example of the information flow in DSEF.....	276

Figure 3 – Using the Excel tab navigation bar	277
Figure 4 – The two lists of worksheets in the NAVIGATION worksheet.....	278
Figure 5 – A drop-down list to select the waste form	280
Figure 6 – A spinner control to select the number of assemblies in a waste package	280
Figure 7 - An example of some of the cross-checks and cautions displayed in the INPUTS worksheet.....	282
Figure 8 - An example of one of the ways DSEF lets you use data from the case library, or override the data with user input	282
Figure 9 – Example of repository level cost input data with Carter/Hardin example case data	287
Figure 10 – Example of cost contingency input data.....	288
Figure 11 – Example of comparison of thermal results against thermal constraints from the RESULTS worksheet	289
Figure 12 – Example of parametric study input data from Step 13 on the INPUTS worksheet	290
Figure 13 - Example from a section of the inputs checklist.....	291
Figure 14 - The data fields used in the CASE LIBRARY	293
Figure 15 - The enclosed mode analysis case catalog.....	294
Figure 16 - The open mode analysis base case catalog.....	295
Figure 17 - The open mode sensitivity studies case catalog	296
Figure 18 - Case number catalog for repository layout and required ventilation trade studies in clay/shale (1 of 2)	297
Figure 19 - Case number catalog for repository layout and required ventilation trade studies in clay/shale (2 of 2)	298
Figure 20 - Case number catalog for scoping thermal analysis of alternative DPC disposal concepts in clay/shale (subset 1).....	299
Figure 21 - Case number catalog for scoping thermal analysis of alternative DPC disposal concepts in clay/shale (subset 2).....	300
Figure 22 - Side-by-side case comparison table	302
Figure 23 - The template for variable interpolation between relevant cases	303
Figure 24- Summary of waste package numbers for the 5 example cost cases	307
Figure 25- Summary of mined opening length and volume for the 5 example cost cases.....	307
Figure 26- Summary of shaft and ramp quantities for the 5 example cost cases	308
Figure 27– Cost example case 1 - crystalline (enclosed) repository drift panel detail summary.....	308
Figure 28– Cost summary table example as shown on the RESULTS worksheet	310
Figure 29– Cost summary table comparing Carter/Hardin Case 1 (Crystalline Enclosed) results with DSEF results.....	310
Figure 30– Cost summary table comparing Carter/Hardin Case 2 (Salt Enclosed) results with DSEF results	311

Figure 31– Cost summary table comparing Carter/Hardin Case 3 (Clay/Shale Enclosed) results with DSEF results	311
Figure 32– Cost summary table comparing Carter/Hardin Case 4 (Clay/Shale Open) results with DSEF results	312
Figure 33– Cost summary table comparing Carter/Hardin Case 5 (Sedimentary Open) results with DSEF results	312
Figure 34– Tables from the WASTE FORM worksheet	315
Figure 35- WASTE FORM worksheet – calculated waste form outer radius lookup table.....	316
Figure 36- Example of parametric study plots on the THERMAL-ANALYTICAL OUTPUT worksheet.....	318
Figure 37- Example transient output data plotted in the THERMAL-ANALYTICAL OUTPUT worksheet.....	318
Figure 38– Decay heat data built-in to the THERMAL-SOURCE worksheet	319
Figure 39- Examples of decay heat update caution and confirmation prompts	319
Figure 40 - The first step – selecting the materials data to plot	321
Figure 41- Example output of the materials data plotting macro.....	321
Figure 42 - Example of data structure in the MATERIALS-THERMAL PROPERTIES worksheet	321
Figure 43 - Example of data structure in the MATERIALS-TRANSPORT PROPERTIES worksheet.....	322

(part VIII) Np(V) Sorption and Diffusion on Montmorillonite Clay

Figure 1. Fraction of mean total annual dose attributed to different radionuclides for the nominal scenario projected by the TSPA-SR model.	326
Figure 2. Annual dose attributed to different radionuclides for the IMARC 8.0.....	327
Figure 3. Example of an elementary volume of compacted bentonite, estimates of the volume fractions of interlayer porosity versus free porosity and effects on diffusion	328
Figure 4. Example of diffuse-layer, outer-sphere, and inner-sphere interlayer adsorption processes. Each adsorption process may lead to unique diffusion rates.....	329
Figure 5. Cation composition of the electrolyte at the end of the experiment in the different system studied (Na, K, Ca and Mg-Montmorillonite) vs. Np loading in solution.....	333
Figure 6. Percent Np sorbed to montmorillonite plotted vs. log Np concentration in solution at pH 4.5 and ionic strengths of 0.001 M, 0.01 M and 0.1 M in monovalent systems (Na/K-montmorillonite in NaCl/KCl) and divalent systems (Ca/Mg-montmorillonite in CaCl ₂ /MgCl ₂).....	334
Figure 7. Experimental data (K_d) and model fit of Np(V) ion exchange (pH 4.5) on Na-montmorillonite, K-montmorillonite and Ca ²⁺ -montmorillonite.	338
Figure 8. Simulation of Np(V) ionic exchange on montmorillonite (2 g L ⁻¹) at pH 4.5 in pure electrolyte (NaCl, KCl, MgCl ₂ and CaCl ₂) for [Np] _{total} = 5 x 10 ⁻⁷ M.	339
Figure 9. Sorption of 10 ⁻¹⁴ mol/L Np(V) on colloidal alumina.....	344

Figure 10. Sorption of 10^{-14} mol/L Np(V) on colloidal alumina.....	345
Figure 11. Sorption of 10^{-14} mol/L Np(V) on colloidal alumina.....	345
Figure 12. Sorption of 6×10^{-6} mol/L Np(V) on colloidal alumina (175 m ² /g) and low surface area α -alumina (2.5 m ² /g)	346
Figure 13. Sorption of 10^{-6} mol/L Np(V) on low surface area α -Al ₂ O ₃ (two data sets)	347
Figure 14. Sorption of 1.9×10^{-7} (red) and 1.9×10^{-9} mol/L Np(V) on alumina	347
Figure 15. Sorption of 10^{-14} mol/L Np(V) on colloidal silica	348
Figure 16. Sorption of 10^{-7} mol/L Np(V) to 40 g/L and 80 g/L SiO ₂	348
Figure 17. Sorption of 10^{-6} mol/L Np(V) on 40 g/L SiO ₂ in air, 40 g/L SiO ₂ w/o CO ₂ , and 4 g/L fine grained SiO ₂ w/o CO ₂	349
Figure 18. Sorption of $\sim 9 \times 10^{-7}$ mol/L Np(V) on montmorillonite in air and w/o CO ₂	350
Figure 19. Sorption of 10^{-6} mol/L Np(V) on clinoptilolite with 4 g/L, I = 0.1, in air, 4 g/l, I = 0.1, w/o CO ₂ , 8 g/L, I = 0.01, in air, and 8 g/L, I = 0.01, w/o CO ₂	350
Figure 20. Diffusion cell with two ports on each side of the core to allow for continuous circulation of fluid on the upstream and downstream ends of the core.	356
Figure 21. Configuration of diffusion cell under heated aerobic conditions	357
Figure 22. U(IV) diffusion profiles in compacted MX-80 bentonite cores after 7 years of diffusion.....	359

LIST OF TABLES

(Part I) **Engineered Barrier System (EBS) Optimization Analysis**

Table 1. Input parameters for 2-D EBS geometry used in the Albany thermal problem.	37
Table 2. Initial and bounding values for the optimization of thermal conductivities of barrier materials.....	38

(Part II) **Investigation of Reactive Transport and Coupled THM Processes in EBS (FY13)**

Table 2.1. Parameters used to reproduce the suction cycles test of Pousada (1984).	58
Table 2.2. Parameters used to test the effect of chemistry on the swelling capacity of expansive clays.....	59
Table 3.1. Parameters for DR-A test.....	71
Table 3.2. Shear viscosity of water and self-diffusion coefficients of Na ⁺ and water in bulk liquid water. Predicted <i>D</i> values are shown for simulations with 512 water molecules (<i>D</i>), after correction for the finite-size effect (<i>D</i> _{0,s}), and after correction for both size and viscosity (<i>D</i> _{0,sv}). The subscript ‘exp’ denotes experimental values (Talekar, 1977; Holz et al., 2000).	81
Table 3.3. Two-dimensional self-diffusion coefficients of Na ⁺ and water in clay interlayer nanopores in systems with fully flexible clay sheets and five H ₂ O molecules per unit cell per hydrate layer.	87
Table 4.1. Effects of solution chemistry on diffusion coefficients	91
Table 4.2. Overview of variable model input parameters	107
Table 4.3. Constant model input parameters.....	107
Table 4.4. Summary of U(VI) adsorption data in batch sorption envelope experiments.....	110
Table 4.5. Overview of uranium(VI) surface reactions in surface complexation model	112
Table 4.6. Parameters determined in CaBr ₂ diffusion experiment.....	121

(Part III) **Update on Experimental Activities on Buffer/Backfill Interactions at elevated Pressure and Temperature**

Table 1. Synthetic groundwater chemistry used in each experiment.....	145
Table 2. Initial components and reaction conditions for EBS experiments. EBS-8 developed a leak during experiment.	146
Table 3. Bulk mineralogical composition (wt. %) of the starting bentonite and post-reaction samples.	150
Table 4. Chemical composition (XRF) of the starting bentonite and < 2 μm size fractions from post-reaction samples from each EBS experiment.	151
Table 5. Structural formula for post-reaction montmorillonites	152
Table 6. Bulk chemical composition from the 304 SS corrosion layer developed from the ramped heating cycle (EBS-2).....	161

Table 7. Bulk chemical composition (EMPA) from the low-carbon corrosion layer developed from the ramped heating cycle (EBS-6)	162
---	-----

(Part IV) Thermodynamic Database (TDB): Recommendations and Guidelines on Future TDB Development

Table 1. List of potential institutions and personnel with common interests in TDB development	201
Table 2. Example of a preliminary 3-year timeline for various TDB development activities	203

(Part V) Thermodynamic Modeling: Clay Hydration, Ion Exchange, and First Principles Calculations of Mineral Thermodynamic Properties at Elevated Temperatures

Table 3.1. Coefficients of the Haas-Fisher heat capacity polynomial $C_p(T)$ for anhydrite, bischofite and polyhalite. The range of validity of the fit is 290–800 K.	236
--	-----

(Part VI) Molecular Dynamic (MD) Study on the Swelling Properties of Montmorillonite and Beidellite Clays

Table 1. Values of interlayer spacing for montmorillonite and beidellite as a function of interlayer cation species. The interlayer spacing is given in angstroms, and the parenthetical values are the corresponding number of water molecules per clay unit cell for each state	252
Table 2. Maximum Loadings ($H_2O/u.c.$) from GCMC Simulations at d -spacings of 12.0 Å and 15.0 Å. ^a	259
Table 3. Comparison of RH at Maximum Loading from GCMC Simulations ^a with Water Content from MD Simulations ^b	260

(Part VIII) Np(V) Sorption and Diffusion on Montmorillonite Clay

Table 1. Reaction constants for Na, K, Ca, and Mg ion exchange on montmorillonite based on the Vanselow and Gaines-Thomas conventions	336
Table 2. Fitted ion exchange reaction constants for Np(V)	337
Table 3. Summary of reaction constants developed for Np(V) surface complexation to aluminosilicate minerals.	343
Table 4. Average non-electrostatic surface complexation model constants for Np(V) sorption to aluminosilicates.	351
Table 5. Surface complexation reaction constants extracted from the RES ³ T database for Np(V) sorption to aluminosilicate minerals	354
Table 6. Composition of porewaters in equilibrium with MX-80 bentonite at the three bulk densities examined in these experiments	358

ACRONYMS

1D	One Dimensional
2D, 2-D	Two Dimensional
3D, 2-D	Three Dimensional
ADSM	advanced disposal system modeling
BBM	Barcelona Basic Model
CEC	Cation Exchange Capacity
DECOVALEX	DEvelopment of COupled Models and their VALidation against EXperiments
DOE	Department of Energy
DOE-NE	Department of Energy, Office of Nuclear Energy
DOE-EM	Department of Energy, Office of Environmental Management
DOE-FE	Department of Energy, Office of Fossil Energy
DSEF	Disposal Systems Evaluation Framework
EBS	Engineered Barrier System
EC	European Community
EDL	Electric Double Layer
EDZ	Excavated Disturbed Zone
EoS	Equation of State
EDX	Energy dispersive X-ray spectroscopy
FCRD	Fuel Cycle Research and Development
FDM	Fuel Degradation Model
FEBEX	Full-scale Engineered Barriers Experiment
FEP	Features, Events, and Processes
GCMC	Grand Canonical Monte Carlo
GDSM	Generic Disposal System Model
GEM	Gibbs Energy Minimization
GWd	Gigawatt days
GWd/MT	Gigawatt (thermal) - days per Metric Ton
HKF	Helgeson-Kirkham-Flowers
HLW	High-Level nuclear Waste
HM	Heavy Metal
IAPWS	International Association for the Properties of Water and Steam

IGD-TP	Implementing Geological Disposal of Radioactive Waste Technology Platform
IUPAC	International Union of Pure and Applied Chemistry
JANAF	Join-Army-Navy-Air Force
LAMMPS	Large-scale Atomic/Molecular Massively Parallel Simulator
LANL	Los Alamos National Laboratory
LBNL	Lawrence Berkeley National Laboratory
LLNL	Lawrence Livermore National Laboratory
MD	Molecular Dynamics
MT	Metric Ton
NAGRA	National Cooperative for the Disposal of Radioactive Waste
NBS	Natural Barrier System
NE	DOE-Nuclear Energy
NEA	Nuclear Energy Agency
NIST	National Institute of Standard and Technology
NW	Nuclear Waste
OECD	Organization for Economic Co-operation and Development
PA	Performance Assessment
QA	Quality Assessment
QC	Quality Control
R&D	Research and Development
RDO	Repository Design Optimization
RH	Relative Humidity
SEM	Scanning Electron Microscopy
SIT	Specific Interaction Theory
SNL	Sandia National Laboratories
SRA	Strategic Research Agenda
TDB	Thermodynamic Database
TEM	Transmission Electron Microscopy
THM	Thermal-Hydrological-Mechanical
TIC	Total Inorganic Carbon
TM	Thermal-Mechanical

THMC	Thermal-Hydrological-Mechanical-Chemical
UFDC	Used Fuel Disposition Campaign
UOX	Uranium Oxide Fuel
UOX-40	UOX with 40-GWd/MTU burnup
UOX-60	UOX with 60-GWd/MTU burnup
URL	Underground Research Laboratory
VCS	Villars-Cruise-Smith
VBA	Visual Basic for Applications
V&V	Verification and Validation
WIPP	Waste Isolation Pilot Plant
WP	Waste Package
XRD	X-ray Diffraction

Engineered Barrier System (EBS) Optimization Analysis (Part I)

1. Engineered Barrier System (EBS) Optimization Analysis

1.1 Introduction

As discussed in Jové Colón et al. (2011) and Jové Colón et al. (2012), the analysis of Engineered Barrier System (EBS) design concepts is paramount to the safety evaluation and performance assessment (PA) of the repository post-closure period. These evaluations of the EBS are generic, that is, regardless of the geologic host media (e.g., salt, clay and crystalline rock) but focused on backfilled sub-surface repository concepts. Within this development and evaluation of generic EBS design concepts, the objectives of Repository Design Optimization (RDO) has been delineated in Jové Colón et al. (2012). It involves the agile (flexible and yet structured) analysis of EBS design configurations based on information from THMC coupled process models, site characterization and laboratory data, and a wide range of modeling and experimental activities analyzing processes at various scales. The results of these comprehensive modeling and experimental activities embody the contents of this report.

Jové Colón et al. (2012) described the general concepts of RDO which have been adopted in previous repository R&D programs and are mainly based on extensive site characterization information. The current strategy of RDO also relies on similar characterization of the host-rock media but focuses on THMC phenomena and related processes affecting EBS materials. Most of this information is currently under development through modeling activities or various types of laboratory- and field-scale investigations at underground research laboratories (URL). Figure 1 illustrates the type of processes and coupled interactions affecting the EBS in the repository lifetime.

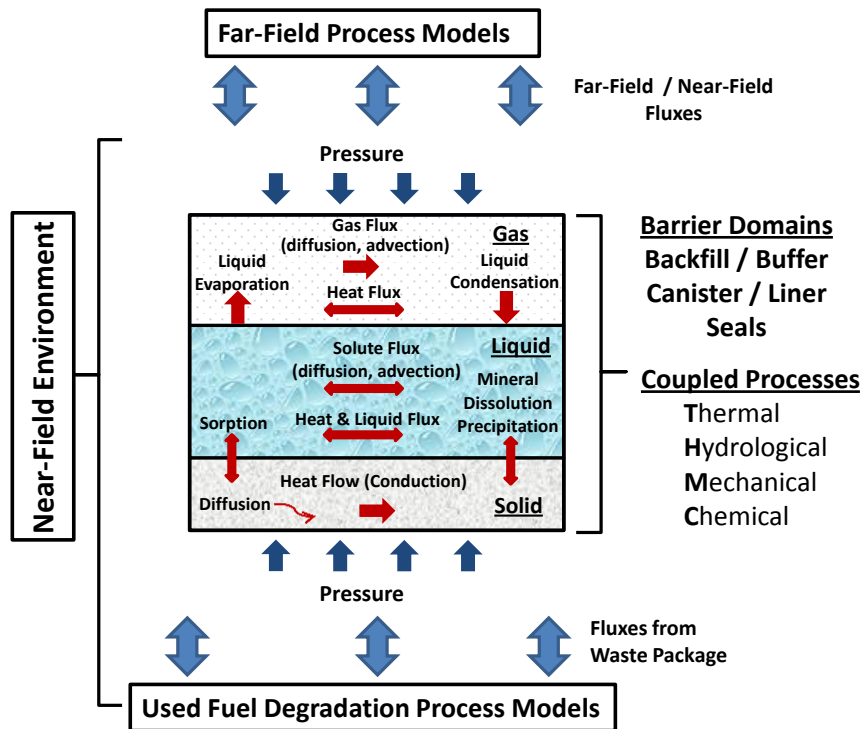


Figure 1. EBS coupled process phenomena (center) and interrelations between process models from other domains (modified after Olivella et al. 2011).

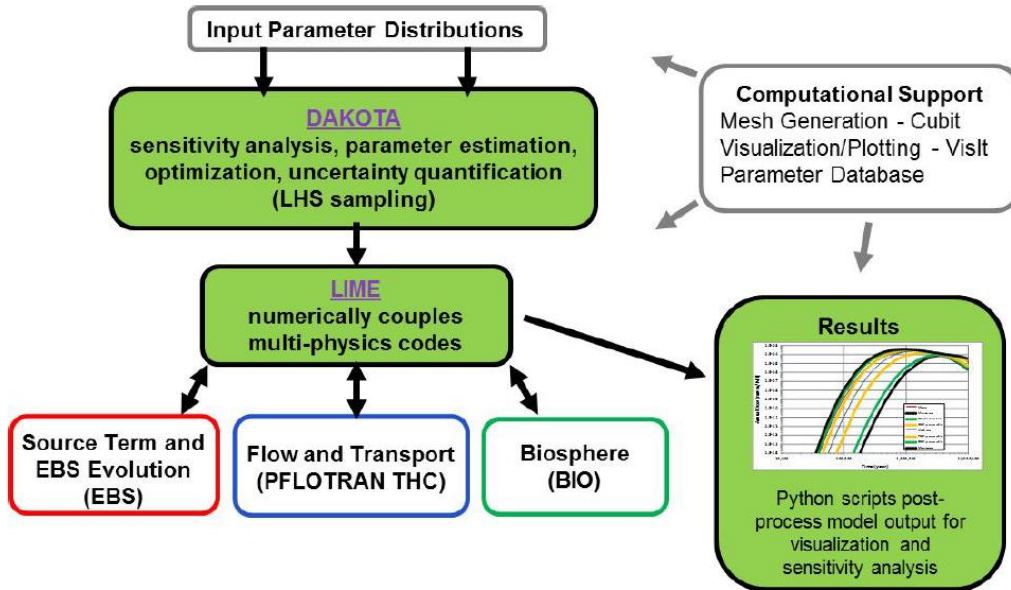


Figure 2. Performance assessment (PA) model/code framework for ADSM (Freeze et al. 2013).

1.2 Conceptual Integration with System-Level and Sub-System Level Process Models

The importance of all these EBS coupled processes can be also understood as part of the PA model integration structure in Generic Disposal System Modeling (GDSM) and Advanced Disposal System Modeling (ADSM) (Freeze et al., 2013). This is represented within the “Source Term and EBS Evolution” box in Figure 2. The PA model framework illustrates input feeds from various process model components such as the EBS as intended in a generic repository concept.

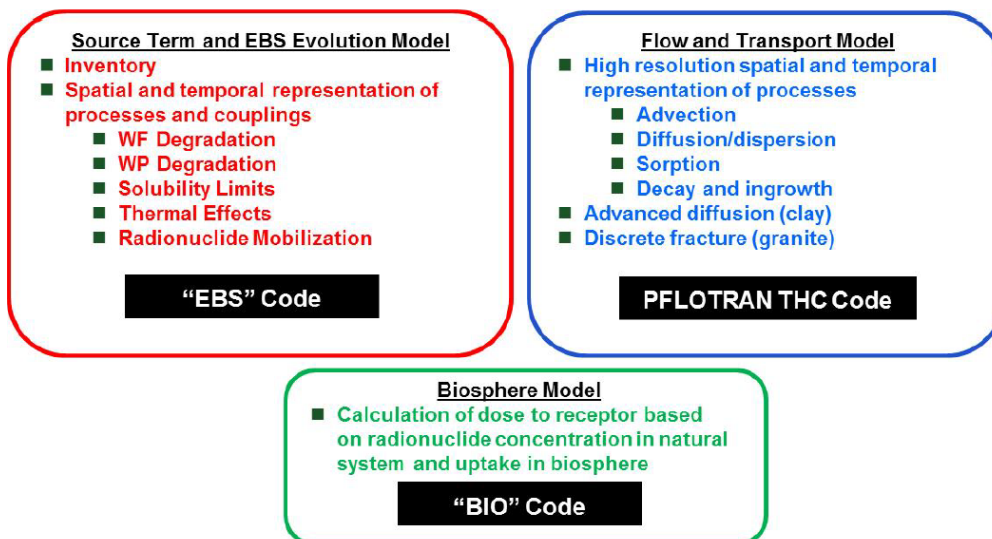


Figure 3. Disposal system integrated process models (Freeze et al. 2013).

Figure 3 illustrates a generalized breakdown of key processes within each of the main components of the PA framework depicted in Figure 2. Focusing on the coupled processes within the “EBS Code” box as part of this ADSM PA integration shows that these are consistent with the EBS coupled THMC and other phenomena affecting barrier performance assessed in this report. For example, thermal effects that drive barrier interactions such as waste package (WP) degradation and radionuclide mobilization controlled by reactive diffusion are addressed as part of EBS R&D. Furthermore, other PA inputs such as solubility limits are related to thermodynamic database development and associated geochemical modeling.

The integration of EBS process models with ADSM PA is so far envisioned in the form of coupling multiphysics with the LIME code for information passing. However, details of how these linkages will be built are still under consideration within the current state of PA development. It should be noted that integration of process models is also part of EBS R&D so integrated approaches are present at various level of the generic system modeling schemes. An example is given in Figure 4 for the couplings of the Fuel Degradation Model (FDM) with system-level and sub-system level process models as part of the EBS Used Fuel Degradation activity. Therefore, the “EBS Code” box in Figure 3 may be comprised of various code couplings.

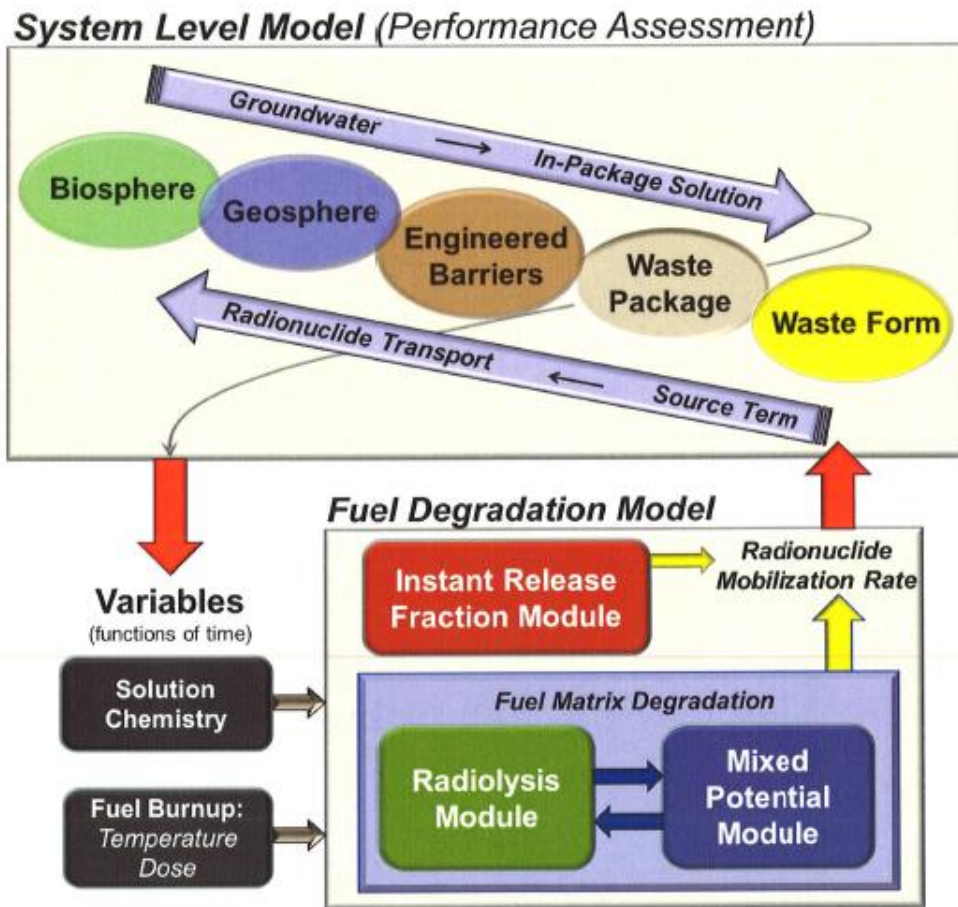


Figure 4. Information flow diagram showing the relationship of the Fuel Degradation Model (FDM) to the system-level model and sub-models (modules) (Jerden et al. 2013).

Process models and simulation methodologies to describe coupled phenomena in the EBS have advanced to a level that key pieces of information on the spatio-temporal evolution of the clay barrier (e.g., THM) can be evaluated. Also, thermodynamic modeling and database development to evaluate fluid-mineral interactions and constrains on solubility limits of radionuclides under specified environmental conditions (redox, ionic strength) can also be assessed. Therefore, some level of information passing between EBS to system-level PA models may be possible but further development of these multi-level coupling operations is needed.

It is also important to note that the aforementioned EBS processes closely map those outlined in the UFDC Disposal R&D Roadmap prioritization (Nutt et al., 2011) for THMC and related phenomena as discussed in Jové Colón et al. (2012). These are also consistent with The Strategic Research Agenda (SRA; www.igntp.eu) report (SRA, 2011) in Implementing Geological Disposal of Radioactive Waste Technology Platform (IGD-TP) advanced by the European Community (EC) framework programme.

1.2.1 Thermal Analysis for Multi-Layered EBS: 2-D and 3-D FEM Approach

Sacrificial Barrier and Thermal Alteration

Temperature is a key driver to many important chemo-mechanical processes affecting barrier materials. For example, thermally-induced phase transformations, dissolution/precipitation phenomena, and mechanical expansion can affect barrier performance through changes in mineralogy and porous properties (permeability and porosity). As discussed in Hardin et al. (2012), thermal responses to clay-based engineered and natural barrier materials including hydration phenomena are among the most influential processes impacting repository performance. Depending on the waste stream scenario, Hardin et al. (2012) considered seven nuclear waste types where four belong to spent fuel and three are high level waste (HLW). The important aspect of these waste inventories is that it can generate specific thermal loads that could ultimately determine the repository design. Thermal criteria for EBS materials have not been rigidly established except for the international consensus of a 100°C limit for clay-based barriers applicable to certain disposal concepts. The reason for such a temperature limit is to prevent degradation of the clay barrier whether by phase transformation to illite or silica cementation that could compromise swelling and sorption properties. It has been recognized that a thermal limit of 100°C is difficult to accommodate for many concepts seeking disposition of waste with high thermal loads. Examples of this are the Swiss concept described in NAGRA (2002) and the UFD analysis for the disposal of large capacity Dual Purpose Canisters (DPC) with elevated thermal loads (Hardin et al., 2012). Moreover, such thermal constraints need to be based on a sound scientific basis that to a large extent is lacking (Wersin et al., 2007). Similar constrains can be imposed on the host rock to prevent thermally-induced alteration. A notable exception is salt host rock where higher temperatures of up to 200°C have been proposed given its ductile properties and high thermal conductivities. There is ample agreement for relaxing thermal constrains in engineered and natural barriers allowing for adequate compliance with any future thermal limits imposed by the safety case. This also suggests that research on barrier thermal degradation is crucial to evaluation and establishment of any thermal criteria.

Another important issue in the evaluation of thermal limits is to analyze the extent of a *sacrificial barrier* for disposal of waste with high thermal loads. The sacrificial domain consists of barrier

material that has undergone extensive geochemical alteration as a result of exposure to high temperatures promoting the aforementioned processes. Again, it should be noted that the term *sacrificial* doesn't necessarily mean the complete destruction or compromise of the barrier isolation capacity at a particular location. Depending on the temperature at which the barrier material is exposed, the extent of the sacrificial barrier may be limited to regions adjacent to the waste package surface therefore sparing other (outwards) buffer layers from pervasive mineralogical changes. This assessment requires precise knowledge of the clay phase stability at elevated temperatures and the type of reaction products generated from these interactions. Conversion to other phases through heterogeneous chemical reactions could produce minerals that may not have the same mechanical properties as swelling clays. However, it could result in mineral assemblages (e.g., zeolites, mica, secondary clays) that could still perform satisfactorily as a chemical barrier (e.g., sorption). Further, it is known that clays can be stable at temperatures (see Part III) in excess of 150°C depending on the extent and type of interaction with reactive fluids. This allows for relaxation of thermal limits in the clay-based barrier materials allowing for disposal options that can accommodate the emplacement of larger capacity waste packages such as DPCs therefore reducing the repository footprint and cost. Such tradeoffs are necessary for the advancement of feasible repository design concepts that can permit safe long-term isolation of the waste inventory along with reduction of complex waste handling operations (repackaging) and the risks of worker dose exposure.

Thermal Modeling: 2-D and 3-D FEM Analysis Using Albany

Study of the thermal effects requires analysis of temperature profiles reaching from the waste canister surface toward the EBS outward boundaries in the near-field environment. In the case of multilayered EBS as discussed in Jové Colón et al. (2011), it's necessary to accurately capture the thermal anisotropies of EBS layered materials but also coupled these to the thermal responses of the heterogeneous structure and composition of the host rock at the repository scale. Moreover, the complex 3-D geometric arrangements of proposed disposal concepts, EBS designs of disposal galleries, and host rock structure can often result in asymmetrical configurations. The material composing these heterogeneous domains can have distinct thermal properties (e.g., thermal conductivities) and boundary conditions. Therefore, sophisticated finite element modeling (FEM) approaches are suitable to simulate heat transfer in highly heterogeneous 2-D and 3-D domains. The thermal optimization problem is formulated as an inverse thermal problem with target temperatures for specific interfaces of the EBS domain.

Inverse heat transport problems and related methodologies have advanced into an essential analysis to evaluate many thermophysical processes involving thermal simulation and engineering design (Alifanov, 1994; Vikhrenko, 2011). Inverse problems can become very problematic to assess when the domain of interest is composed of several materials with different thermal properties and intricate geometries. Although there are adequate analytical methods for solving heat conduction problems quite efficiently, these are mainly restricted to 2-D, simple geometries, and homogenous materials with known thermophysical properties. Analytical methods have been adopted in the DSEF implementation (Jové Colón et al., 2012) of thermal analysis and in the work of Choi and Choi (2008). As in the current analysis, the latter focuses on the issue of thermal performance of a double-layer clay barrier for heat generating waste for the Korean reference disposal system. Similar issues include dealing with prevention of clay material degradation, corrosion, spacing of disposal tunnels, and the cost analysis of the disposal

concept as determined by the thermal limit compliance. The goal of this type of analysis is to evaluate optimal thermal conductivities and geometric characteristics to minimize the peak temperatures at certain locations in the EBS. For example, enhancement of thermal conductivities can be accomplished the use of additives such as graphite or quartz to the clay barriers (Beziat et al., 1992; Geneste et al., 1990; Jobmann and Buntebarth, 2009; Westerman, 1979). Furthermore, graphite addition can have several advantages such as lowering bulk barrier permeability, significantly enhance thermal conductivity, and provide chemically reduced conditions (Beziat et al., 1992; Geneste et al., 1990).

The most common approach used in inverse heat transfer problems is the minimization of a least squares or residual formulation through iterative procedures (Vikhrenko, 2011). The optimization methodology for solving the inverse problem here is to analyze the computed temperatures at specific locations of the barrier interfaces by minimizing an objective function to attain a set of target temperatures. In this study we develop and test an optimization methodology for inverse thermal problems using the code DAKOTA (Design Analysis Kit for Optimization and Terascale Applications) (Adams et al., 2012) coupled with the multi-physics code Albany to determine the thermal spatio-temporal response on the multi-layered EBS. DAKOTA is an open source software package developed at Sandia National Laboratories that contains a large collection of algorithms for optimization, uncertainty quantification (UQ), and sensitivity analysis. The optimization methodology for the objective function minimization is based on a non-gradient method. Albany is a finite element code (FEM) based on the Agile Components vision built almost entirely from the functionality obtained in reusable libraries. The goal of the Agile Components strategy is to enable the rapid development of simulation code based on independent but yet interoperable components that are mature and quality tools. For example, Albany is highly integrated with computational libraries/tools such as those in the Sandia Trilinos Project (solvers) (Heroux and Willenbring, 2012), Sierra Toolkit (STK) libraries for meshing (Edwards et al., 2010), Sierra Encore for post-processing (Copps and Carnes, 2013), and the DAKOTA uncertainty quantification (UQ) and optimization toolkit (see Figure 5). For these reasons, the flexible and yet structured Albany multi-physics platform is used to conduct the thermal transport and optimization analysis. The analysis is done in 2-D but preliminary work is under way to extend it to 3-D comprising single and multiple waste packages emplaced within a disposal tunnel. The option of Albany using DSEF inputs is one of many when it comes to selecting an analysis tool. In this case, Albany has the capability of interfacing with a set of tools to conduct thermal analysis that includes a FEM mesh generator, visualization, post-processing, and a rich suite of numerical solvers (Figure 5). Moreover, Albany has the potential of extending thermal problems with coupled mechanical given its use as a large-scale application platform for multi-physics model development. For example, Albany has been used in modeling the mechanical performance of Zry4 δ -hydrides in cladding, under conditions of long-term storage of used fuel (Hansen et al., 2012). Albany has also been used in the simulation of strongly-coupled hydro-mechanical problems for fluid percolation through a porous solid (Sun et al., 2013).

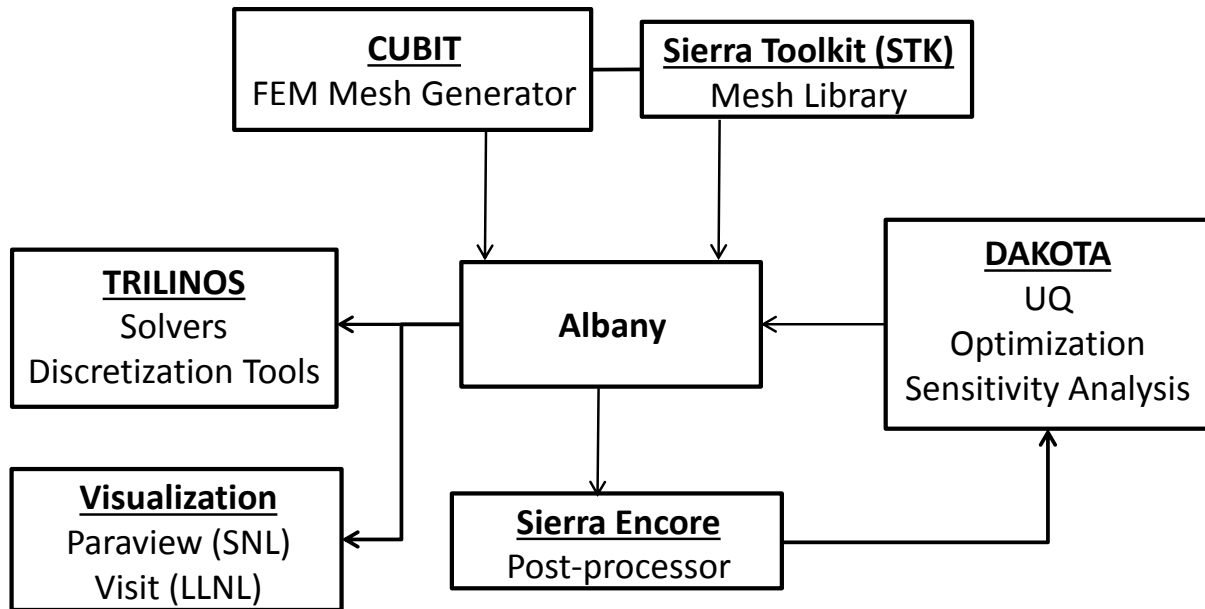


Figure 5. Generalized relational diagram showing Albany multiphysics code and other components such as Trilinos tools, Sierra toolkit (STK) libraries, and DAKOTA optimization toolkit.

Inputs such as waste package radius, thermal conductivities, and heat load were obtained from the Disposal System Evaluation Framework (DSEF) spreadsheet. In this example, a 12-assembly UOX fuel with a burnup rate of 40 GWd/MT is considered to represent the waste. The decay heat values were obtained from the DSEF (version 3.0) spreadsheet and converted to volumetric heat loads by normalizing the values according to the canister cylindrical volume with a radius of 0.53 meters and length of 5 meters. The time span for the volumetric heat loads extend up to 10,000 years. A period of 50 years for time out of the reactor is assumed. The double layer EBS configuration is depicted in Figures 6 and 7 where the latter described the adopted meshed geometry. It is composed of a waste canister, overpack, two clay buffer layers, and cement liner whose properties and geometric parameters are given in Table 1. Thermal conductivities are assumed to be constant with temperature. Future work aims at including temperature dependencies on thermal conductivities, particularly for mixed buffer materials. The geometry is based on a peak drift-wall radius of 2.25 meters and a constant temperature Dirichlet boundary condition of 313.15 K (40°C) at 10 meters away from the drift wall. Boundary conditions can be modified to test model sensitivities and/or optimize repository geometry. Figure 8 shows the computed temperatures as a function of distance from the waste package center for 100, 150, and 350 years. It should be noted that this exercise only describes a single waste package thermal behavior without any external heat contributions from the far-field or adjacent drifts with waste packages. The computed temperatures from the waste package overpack surface show the expected decrease towards the drift wall. However, heating sources in the far-field (i.e., waste packages from adjacent drifts or within the same tunnel) need to be accounted for as to have meaningful results with respect to accurate temperature predictions in the EBS. For example, DSEF thermal analytical modeling shows that drift spacing can have significant effects on the EBS thermal profile (see part VI). Still, the results show that for this simple case, a drift diameter of 4.5 meters with barrier materials (clay, cement) having moderate thermal conductivities will not likely result in near-field temperatures exceeding 150°C except

for a few hundred years. As expected, matching results are also obtained for the 3-D single drift example for distances of 10 and 50 meters for the rock boundary from the waste package center when testing for thermal sensitivities. Yet again, further analysis is needed to account for far-field thermal sources instead of a constant temperature boundary condition.

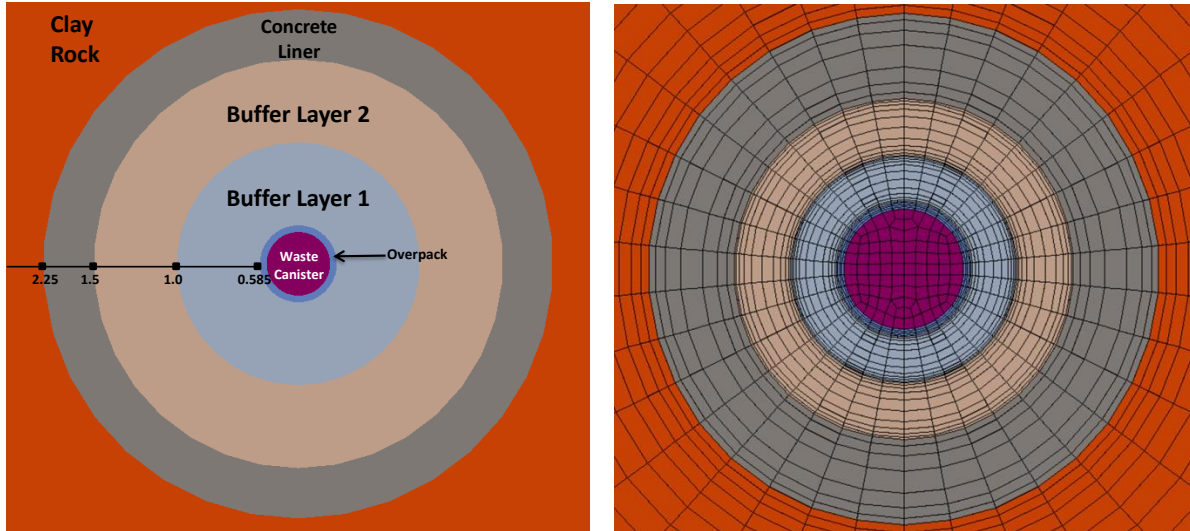


Figure 6. Schematic view of 2-D diagram of EBS(left panel) along with meshed geometry (right panel) for the Albany thermal problem. Values in the figure are radii distances from the center of the waste canister.

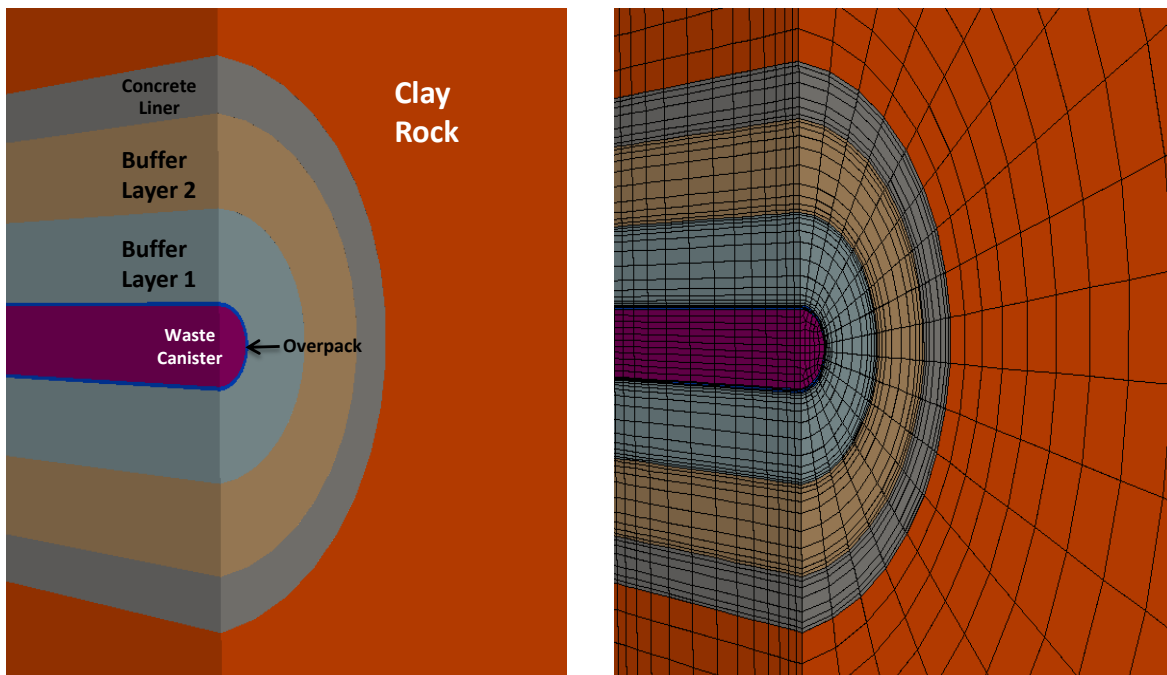


Figure 7. Schematic view of 3-D diagram of EBS (left panel) along with meshed geometry (right panel) for the Albany thermal problem.

Table 1. Input parameters for 2-D EBS geometry used in the Albany thermal problem.

Parameter	Value	Sources / Remarks
UOX Fuel burnup rate	40 GWd/MT	DSEF (version 3.0),
Thermal Conductivity: Waste package / overpack (steel)	46 W/m K	DSEF (version 3.0), Materials-Thermal Properties worksheet
Thermal Conductivity: Clay buffer layer 1	1.75 W/m K	Obtained from a range of values in DSEF (version 3.0)
Thermal Conductivity: Clay buffer layer 2	1.6 W/m K	Obtained from a range of values in DSEF (version 3.0)
Thermal Conductivity: Cement liner	1.7 W/m K	DSEF (version 3.0), Materials-Thermal Properties worksheet
Waste package outer radius	0.53 m	-
Overpack outer radius	0.585 m	-
Clay buffer layer 1 outer radius	1.0 m	-
Clay buffer layer 2 outer radius	1.5 m	-
Cement liner outer radius	2.25 m	Consistent with DSEF modeling of DPC
Boundary condition	Constant temperature of 40°C at 10 m in the far-field	-

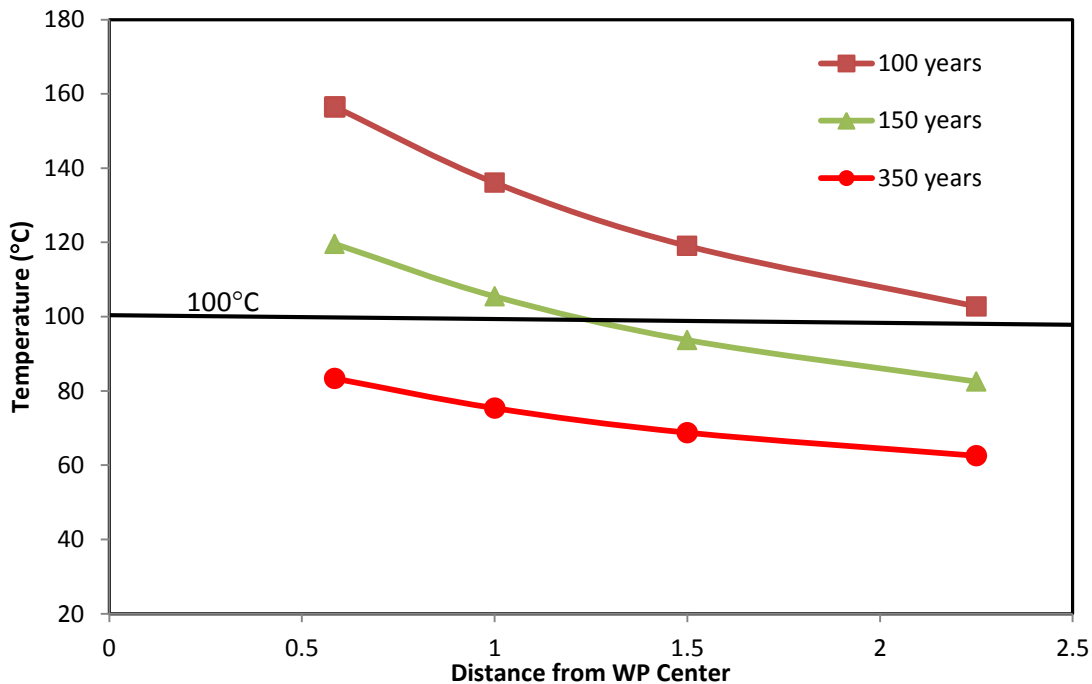


Figure 8. Computed temperature profile from the Albany code for a 2-D EBS geometry described in Figure 6. The 100°C temperature line is shown for reference.

Thermal Optimization Modeling: Albany-DAKOTA Coupling

The Albany-DAKOTA optimization was conducted to test the code coupling for the aforementioned simple 2-D thermal problem of a multi-layered EBS. The inverse analysis was conducted by minimizing an objective function using the coliny nongradient-based optimization method (SCOLIB library) in DAKOTA. The Albany-DAKOTA optimization realizations are based on the minimization of an objective function defined simply as a residual or the sum of squared differences between Albany code prediction ($T_{pred,t,i}$) and target ($T_{target,t,i}$) temperature values in the transient calculation at a given time t and location i across the sampling domain:

$$\min \sum (T_{pred,t,i} - T_{obs,t,i})^2 \quad (\text{Transient}) \quad (1)$$

Albany is externally coupled to DAKOTA through a Linux shell script to generate multiple iterations of the thermal computations in the optimization analysis by adjusting the thermal conductivity values of the three barrier materials. A more direct coupling to DAKOTA may be possible through Trilinos by using the TriKota wrapper. The objective functions (Eqn. 1) are coded in the DAKOTA simulation script along with post-processing routines like Sierra Encore to extract the needed data to compute the values to be minimized. Target temperatures correspond to 125°C at the overpack / waste package surface and a 100°C at the interface between clay barrier 1 and clay barrier 2 (see Figure 6). These target temperatures are operationally hypothetical since these would never be attained at the sampled time of 100 years given the decay heat loads and material thermal conductivities. Note that Eqn. (1) allows for sampling multiple times and locations for the domain of interest. The initial and bounding (maximum and minimum) values for the optimization of thermal conductivities of all barrier materials are listed in Table 2. To test the Albany-DAKOTA coupling, initial and bounding values for thermal conductivities were constrained to be relatively far from the target values to evaluate the minimization path of descent in the transient thermal simulations.

The sampling points for the optimization routine are 0.585 m (waste package surface) and 1.0 m at the interface between Buffer Layer 1 and Buffer Layer 2 as shown in Figure 6 (left panel). The main reason for sampling at these EBS interfaces is because of the rather elevated temperatures experienced at these locations that are conducive towards enhanced material alteration. Also, the choice of target temperatures above 100°C is experienced in these locations for a longer period of time. More locations can be sampled and accommodated straightforwardly within the objective function if needed. Figure 9 shows the results of the DAKOTA-Albany iteration runs showing two minimization paths of descent for local and global minima.

Table 2. Initial and bounding values for the optimization of thermal conductivities of barrier materials

Phase / Bounds	Buffer Layer 1 (W/m K)	Buffer Layer 2 (W/m K)	Cement Liner (W/m K)
Lower Bound	0.9	0.8	1.2
Initial	1.0	1.0	1.0
Upper Bound	2.0	1.7	2.2

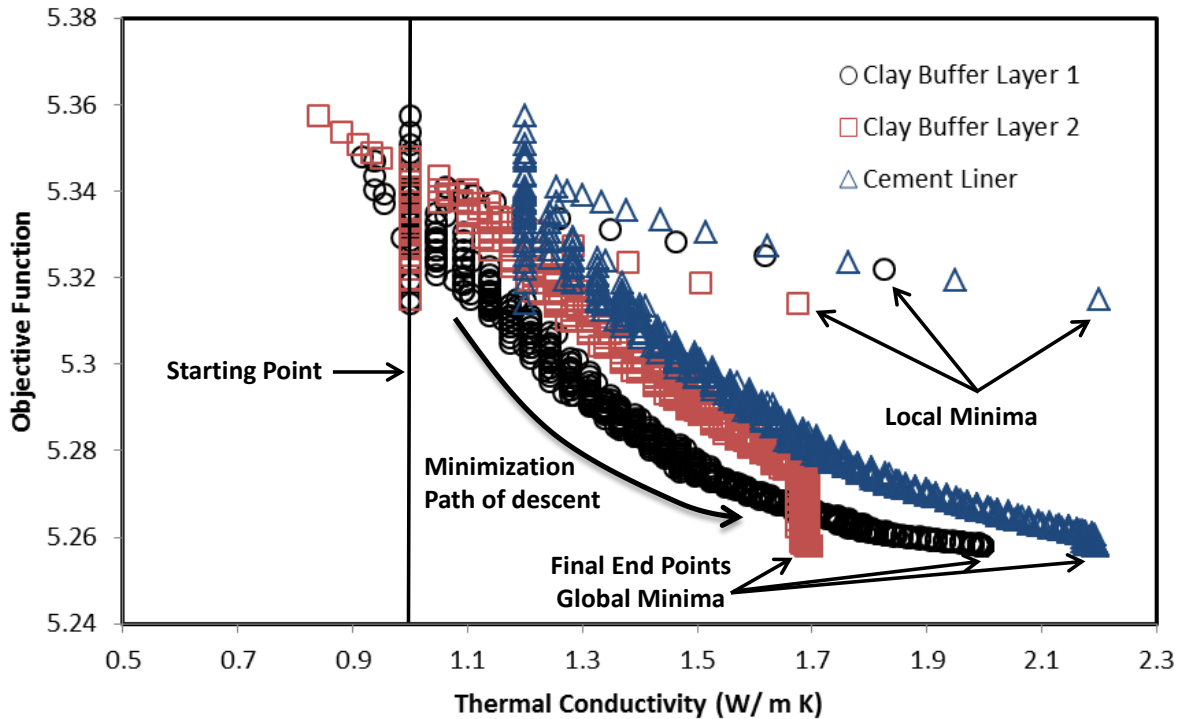


Figure 9. Minimization path of descent for the optimization of thermal conductivities of barrier materials from the Albany-DAKOTA coupling. The plot shows the obtained global minima and minimization path trends for local minima.

As expected, the minimization paths progressed towards the end points corresponding to the upper bounds of the thermal conductivities of these materials as defined in the DAKOTA runs. The local minimum for the cement liner coincides with its global minimum at the iteration end. However, there are some differences between the local and global minima for the buffer layer 1 and 2 even for this symmetric geometry and a small sampling set at a single time and location. This highlights the usefulness of non-gradient based optimizers to resolve global minima given that more intricate geometries and larger sampling spatio-temporal sets could lead to this type result.

1.3 Plans for FY14

The Albany FEM code and associated suite of tools offers the ideal template to analyze thermal effects for EBS disposal concepts and their complex geometries. Thermal anisotropies in multi-layered EBS and those present in the host rock can significantly influence the repository configuration and hence its footprint at the site. The expansion of this modeling approach in FY14 would allow the following:

- A 3-D representation of the disposal concept having multiple drifts and barrier materials. Waste package configurations and drift spacing along with other configurations can be investigated in 3-D using FEM approaches to accurately resolve thermal anisotropies at the repository scale.

- Analyze thermal responses from far-field sources that could influence repository design features, particularly in the cases of multiple disposal galleries as mentioned above.
- Implement temperature dependencies on the expression for thermal conductivity instead of using constant values. Optimization of EBS material properties, particularly for layered concepts, should evaluate role of additives in buffer materials to enhance thermal conductivities. Also, other dependencies such as porosity and saturation will also be considered.
- Utilize the DSEF thermal analysis and associated parameter database along with the FEM modeling to not only perform comparisons but also catalog results. DSEF has become a very valuable tool for high level analysis of generic disposal concepts and its structure conforms with the envisioning of an RDO tool to facilitate repository analysis.

1.4 References

- Adams, B. M., Dalbey, K. R., Eldred, M. S., Swiler, L. P., Bohnhoff, W. J., Eddy, J. P., Vigil, D. M., Hough, P. D., and Lefantzi, S., 2012, DAKOTA, A Multilevel Parallel Object-Oriented Framework for Design Optimization, Parameter Estimation, Uncertainty Quantification, and Sensitivity Analysis: Version 5.2+ User's Manual (SAND2010-2183): Sandia National Laboratories, SAND2010-2183.
- Alifanov, O. M., 1994, Inverse heat transfer problems, Berlin ; New York, Springer-Verlag, International series in heat and mass transfer, xii, 348 p. p.:
- Beziat, A., Dardaine, M., and Mouche, E., 1992, Measurements of the thermal conductivity of clay-sand and clay-graphite mixtures used as engineered barriers for high-level radioactive waste disposal: Applied Clay Science, v. 6, p. 245-263.
- Choi, H.-J., and Choi, J., 2008, Double-layered buffer to enhance the thermal performance in a high-level radioactive waste disposal system: Nuclear Engineering and Design, v. 238, p. 2820.
- Copps, K. D., and Carnes, B. R., 2013, SIERRA Verification Module: Encore User Guide – Version 4.2 (2013-3344): Sandia National Laboratories, 279 pp.
- Edwards, H. C., Williams, A. B., Sjaardema, G. D., Baur, D. G., and Cochran, W. K., 2010, SIERRA Toolkit Computational Mesh Conceptual Mode (SAND2010-1192): Albuquerque, NM, Sandia National Laboratories, 60 pp.
- Freeze, G., Gardner, P., Vaughn, P., Sevougian, S. D., Mariner, P., Mousseau, V., Performance Assessment Modeling of a Generic Salt Disposal System: Annotated Outline, DOE-NE Fuel Cycle R&D, FCRD-UFD-2013-000219, SAND2013-6183P, 21 pp.
- Geneste, P., Raynal, M., Atabek, R., Dardaine, M., and Oliver, J., 1990, Characterization of a French Clay Barrier and Outline of the Experimental Program: Engineering Geology, v. 28, no. 3-4, p. 443-454.
- Hansen, G. A., Ostien, J. T., and Chen, Q., 2012, NEAMS VLTS Project: Level 2 Milestone Summary, SAND2012-5808: Albuquerque, New Mexico, Sandia National Laboratories.
- Hardin, E., Hadgu, T., Clayton, D., Howard, R., Greenberg, H. R., Blink, J. A., Sharma, M., Sutton, M., Carter, J., Dupont, M., and Rodwell, P., 2012, Repository Reference Design Concepts and Thermal Load Management Analysis (FCRD-UFD-2012-000219): Sandia National Laboratories.
- Heroux, M. A., and Willenbring, J. M., 2012, A new overview of the Trilinos project: Scientific Programming, v. 20, no. 2, p. 83-88.
- Jerden, J., Frey, K. E., and Cruse, T., 2013, ANL Mixed Potential Model with Experimental Results; Implementation of Noble Metal Particle Catalysis Module, DOE-NE Fuel Cycle R&D, FCRD-UFD-2013-000305, 38 pp.
- Jobmann, M., and Buntebarth, G., 2009, Influence of graphite and quartz addition on the thermo-physical properties of bentonite for sealing heat-generating radioactive waste: Applied Clay Science, v. 44, no. 3-4, p. 206-210.

- Jové Colón, C. F., Caporuscio, F. A., Levy, S. S., Blink, J. A., Greenberg, H. R., Halsey, W. G., Fratoni, M., Sutton, M., Wolery, T. J., Rutqvist, J., Liu, H. H., Birkholzer, J., Steefel, C. I., and Galindez, J., 2011, Disposal Systems Evaluations and Tool Development - Engineered Barrier System (EBS) Evaluation, p. 1-192.
- Jové Colón, C. F., Greathouse, J. A., Teich-McGoldrick, S., Cygan, R. T., Hadgu, T., Bean, J. E., Martinez, M. J., Hopkins, P. L., Argüello, J. G., Hansen, F. D., Caporuscio, F. A., and Cheshire, M., et al., 2012, Evaluation of Generic EBS Design Concepts and Process Models: Implications to EBS Design Optimization (FCRD-USED-2012-000140): U.S. Department of Energy.
- NAGRA, 2002, Demonstration of disposal feasibility for spent fuel, vitrified high-level waste and long-lived intermediate-level waste: NAGRA (National Cooperative for the Disposal of Radioactive Waste).
- Nutt, M., Voegelé, M., Jové-Colón, C., Wang, Y., Howard, R., Blink, J., Liu, H.-H., Hardin, E., and Jenni, K., 2011, Used Fuel Disposition Campaign Disposal Research and Development Roadmap (Fuel Cycle Research and Development), Prepared for U.S. Department of Energy Used Fuel Disposition Campaign FCR&D-USED-2011-000065
- SRA, 2011, Implementing Geological Disposal of Radioactive Waste Technology Platform Strategic Research Agenda 2011 (IGD-TP), European Community (EC) Euratom framework programme, www.igdtp.eu, 63 pp.
- Sun, W.-C., Ostien, J., and Salinger, A. G., 2013, A stabilized assumed deformation gradient finite element formulation for strongly coupled poromechanical simulations at finite strain: *Int. J. Numer. Anal. Meth. Geomech.*, v. 37, no. 16, p. 2755-2788.
- Vikhrenko, V. S., 2011, Heat Conduction – Basic Research, Rijeka, Croatia, InTech, 392 p.:

**Investigation of Reactive Transport and Coupled THM
Processes in EBS: FY13
(Part II)**

1. Introduction

Geological repositories for disposal of high-level nuclear waste generally rely on a multibarrier system to isolate radioactive waste from the biosphere. The multi-barrier system typically consists of the natural barrier system (NBS), which includes the repository host rock and its surrounding subsurface environment, and the engineered barrier system (EBS). The EBS represents the man-made, engineered materials placed within a repository, including the waste form, waste canisters, buffer materials, backfill, and seals (OECD, 2003). The EBS plays a significant role in the containment and long-term retardation of radionuclide release.

During the lifespan of a geologic repository, the performance of the EBS is affected by complex thermal, hydrogeological, mechanical, chemical and biological processes, such as heat release due to radionuclide decay, multiphase flow (including gas release due to canister corrosion), swelling of buffer materials, radionuclide diffusive transport, waste dissolution, and chemical reactions. All these processes are related to each other. An in-depth understanding of these coupled processes is critical for the performance assessment (PA) of an EBS and the entire repository. Within the EBS work package of the Used Fuel Disposition (UFD) Campaign, LBNL's research is currently focused on two relevant areas, namely (1) the thermal-hydrological-mechanical-chemical (THMC) processes in buffer materials (bentonite), and (2) the diffusive transport in the EBS associated with clay host rock, with the long-term goal of developing a full understanding of (and verified modeling capabilities to simulate) the impact of coupled processes on radionuclide transport in different components of the EBS, as well as the interaction between the EBS components and the near-field host rock (e.g., clay/shale)—and how these processes affect radionuclide release.

LBNL's focus areas address key Features, Events and Processes (FEPs), which have been ranked in importance from medium to high, as listed in Tables 7 and 8 of the *Used Fuel Disposition Campaign Disposal Research and Development Roadmap* (FCR&D-USED-2011-000065 REV0) (Nutt, 2011). Specifically, they address FEP 2.2.01, Excavation Disturbed Zone (EDZ) for shale by investigating the effects of coupled processes on interactions between shale (clay) disposal formations and the EBS; FEP 2.1.04.01, Buffer/Backfill; FEPs 2.1.07.02, 03, 04, 09, Mechanical Processes; FEPs 2.1.08.03, 07, 08, Hydrologic Processes; and FEP 2.1.11.04, Thermal Processes, by studying coupled processes in the EBS; and FEPs 2.1.09.52, 53, 54, Chemical Processes—Transport, by investigating reactive-diffusive radionuclide transport in bentonite.

This report documents the progress that LBNL has made in its two R&D focus areas in FY13. Section 2 presents the modeling results of THMC processes within bentonite and the interaction between the EBS and a clay disposal formation in the near field. Section 3 documents the development of reactive-diffusive transport modeling approaches for radionuclide migration in bentonite. Section 4 reports on experimental studies of reactive diffusive transport of U(VI) in bentonite. Work activities in the remaining months of FY13 and proposed activities in FY14 are presented in Section 5.

2. Modeling Coupled THMC Processes in the EBS

The long-term chemical and mechanical stability of protective bentonite buffers and tunnel backfill is a key issue in the long-term performance of backfilled, multiple barrier nuclear waste repositories. For example, a certain swelling pressure should be maintained to keep the buffer

homogenous, to prevent canister sinking, to prevent the adverse effect of external rock shear movements, to limit colloid transport, and to prevent the buffer from being a preferred pathway of radionuclide transport. The long-term stability of the buffer is governed by coupled thermal-hydrological-mechanical and chemical (THMC) processes. These coupled THMC processes can be simulated by numerical modeling, e.g., by a coupling of LBNL's TOUGHREACT reactive transport simulator to a geomechanical code such as FLAC3D. However, this requires appropriate constitutive models describing couplings between the different processes.

In this section, we describe our ongoing work on developing and applications of such models for the analysis of EBS coupled processes. As part of the UFD Campaign, we have previously implemented the Barcelona Basic Model (BBM) into the TOUGH-FLAC simulator and we have conducted model simulations related to a generic repository involving a bentonite-backfilled repository tunnel hosted in a clay formation, with properties corresponding to the Opalinus Clay. We also recently coupled TOUGHREACT and FLAC3D for the modeling of coupled THMC processes in the EBS, using a simplified approach for the modeling of mechanical-chemical (MC) coupling in bentonite. This development and the results were summarized in a peer-reviewed journal article entitled "Modeling of Coupled Thermo-Hydro-Mechanical Processes with Links to Geochemistry Associated with Bentonite-Backfilled Repository Tunnels in Clay Formations", which was published online in *Rock Mechanics and Rock Engineering* in March 2013 (Rutqvist et al. 2013).

The THM modeling results summarized in the paper showed strong THM-driven interactions between the bentonite buffer and the low-permeability host rock. It was shown that the resaturation of the buffer is delayed as a result of the low rock permeability, and the fluid pressure in the host rock is strongly coupled with the temperature changes, which under certain circumstances could result in a significant increase in pore pressure. Moreover, using the BBM, the bentonite buffer was found to have a rather complex geomechanical behavior that eventually leads to a slightly non-uniform density distribution. Nevertheless, the simulation showed that the swelling of the buffer is functioning to provide an adequate increase in confining stress on the tunnel wall, leading to a stabilization of any failure that may occur during the tunnel excavation. Finally, we described the application of a possible approach for linking THM processes with chemistry, focusing on the evolution of primary and secondary swelling, in which the secondary swelling is caused by changes in ionic concentration, which in turn is evaluated using a transport simulation model. This is a simplified approach for modeling of the MC coupling related to bentonite swelling and we applied this approach for simulating the effects of salt concentration on the swelling stress.

In FY2013, we have made significant progress in the implementation and testing of a dual-structure model for expansive clay into TOUGH-FLAC, and we have made the first link of this model to reactive chemistry through TOUGHREACT-FLAC coupling. In a dual-structure model, the material consists of two structural levels: a microstructure in which the interactions occur at the particle level, and a macrostructure that accounts for the overall fabric arrangement of the material comprising aggregates and macropores (Figure 2.1) (Gens et al., 2006, Sánchez et al., 2005, Gens and Alonso, 1992). A dual-structure model has important features for modeling the mechanical behavior of a bentonite buffer, such as irreversible strain during suction cycles. However, most importantly, a dual-structure model provides the necessary link between chemistry and mechanics, enabling us to develop a fully coupled THMC model for the analysis of long-term EBS behavior. The dual-structure (or double-structure) model approach is

especially useful when trying to incorporate the effects of chemical variables on the mechanical behavior of expansive clays. Because they contain large amounts of active clay minerals, those materials are especially susceptible to changes in the geochemical environment. Thus, the double structure model can provide the link between mechanical and chemical processes modeling, which enables mechanistic modeling of processes important for long-term buffer stability, including effects of pore water salinity on swelling (loss of swelling), conversion of smectite to non-expansive mineral forms (loss of swelling), and swelling pressure vs exchangeable cations. We first linked chemistry to the bentonite mechanics through the dual-structure model using an approach suggested by Gens (2010), in which some of the parameters related to the swelling micro-structure depend on the concentration of each exchangeable cation, and demonstrated this approach by modeling a swelling experiment. Moreover, we are currently working on a second more rigorous approach, linking chemistry to mechanics through the micro-structure strain, where the micro-structural strain is calculated using diffuse-double layer theory.

2.1 Implementation and testing of a Dual-Structure Bentonite Model into TOUGH-FLAC

In this section, we present the development and implementation of a dual-structure material model of expansive clay into TOUGH-FLAC. We first present an overview of the basic equations in the dual-structure model following (in part) the developments by Alonso et al. (1999) and Sánchez et al. (2005). We then summarize the implementation of this model into TOUGH-FLAC.

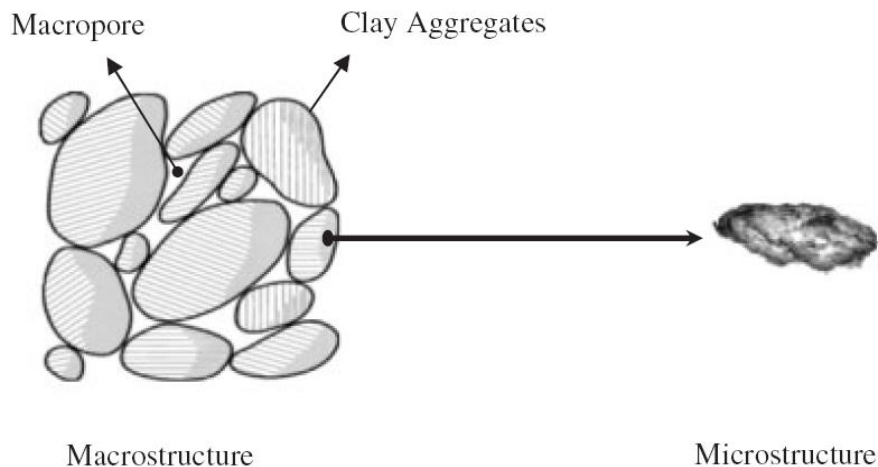


Figure 2.1. Schematic representation of the two structural levels considered (Sánchez et al., 2005).

2.1.1 The dual-structure approach and Barcelona Expansive Model

Sections 2.1.1 and 2.1.2 have been updated from the corresponding sections of last year's report (Rutqvist et al. 2012). These sections have been included here to explain the progress made in the implementation of the Barcelona Expansive Model (BExM) and because the information is

needed to understand the subsequent material that follows in Sections 2.1.3 and 2.2. Alonso et al. (1999), in their presentation of the BExM, provide a suitable mathematical formulation for implementation of a dual-structure model into TOUGH-FLAC. Sánchez et al. (2005) provide another comprehensive description and mathematical formulation in terms of generalized elastoplasticity and implementation into a finite element code. The implementation of the BExM into TOUGH-FLAC is done as an extension of the existing TOUGH-FLAC implementation of the BBM, adding the microstructural level. The BBM model can describe many typical features of unsaturated-soil mechanical behavior, including wetting-induced swelling or collapse strains, depending on the magnitude of applied stress, as well as the increase in shear strength and apparent preconsolidation stress with suction (Gens et al., 2006). The extension to dual-structure behavior enables modeling of more expansive soils, including dependency of swelling strains and swelling pressures on the initial state and on the stress path, strain accumulation upon suction cycles, as well as secondary swelling. It is believed that such behavioral features are mainly related to the existence of coupled chemo-hydro-mechanical phenomena between distinct levels of structure within the material (Alonso et al., 1999).

Conceptually, in a dual-structure model, as described by Alonso et al. (1999) and Sánchez et al. (2005), the total volume, V , of the material consists of the solid phase, V_s , the microstructural voids V_{vm} , and the macrostructure voids V_{vM} :

$$V = V_s + V_{vm} + V_{vM} = V_m + V_{vM} \quad (2.1)$$

with the total void ratio and porosity being the sum of microstructural and macrostructural components according to

$$e = \frac{V_v}{V_s} = \frac{V_{vM}}{V_s} + \frac{V_{vm}}{V_s} = e_M + e_m, \quad (2.2)$$

$$\phi = \frac{V_v}{V} = \frac{V_{vM}}{V} + \frac{V_{vm}}{V} = \phi_M + \phi_m. \quad (2.3)$$

The microstructure can swell to invade the macroporosity, depending on the mechanical confinement and load level. This is relevant when considering permeability changes during bentonite swelling, because fluid movement takes place through the macroporosity, which is not proportional to the total strain and deformation of the bentonite.

Macrostructural level

The macrostructural behavior is modeled based on the BBM, in which the mechanical behavior depends on a three-dimensional yield surface in p - q - s space (Figure 2.2), where p is net mean stress (i.e., total stress minus gas-phase pressure), q is deviatoric stress (or shear stress), and s is suction. The size of the elastic domain increases as suction increases. The rate of increase, represented by the loading-collapse (LC) curve, is one of the fundamental characteristics of the BBM (Gens et al., 2006).

The suction-dependent loading collapse (LC) yield surface (Figure 2.2) bounds the elastic region according to

$$f_{LC} = \frac{q^2}{g_y(\theta)^2} - \frac{M^2}{g_y(\theta=0)^2} (p + p_s)(p_0 - p) = 0 \quad (2.4)$$

where θ is the Lode's angle and the function $g_y(\theta)$ describes the shape of the yield surface in the deviatoric plane, M is the constant slope of the critical state line (Figure 2.2), whereas p_s represents the increase in cohesion with suction and the function

$$p_0 = p^c \left(\frac{p_0^*}{p^c} \right)^{[\lambda_{ps0} - \kappa_{ps0}] / [\lambda_{ps} - \kappa_{ps0}]} \quad (2.5)$$

is the net mean yield stress (or apparent pre-consolidation stress) at current suction, where p_0^* is the net mean yield stress (or pre-consolidation stress) at full saturation, where p^c is a reference stress, λ_{ps0} is a compressibility parameter in virgin soil states at zero suction, $\lambda_{ps} = \lambda_{ps0} [(1-r)\exp(-\xi s) + r]$ is a compressibility parameter in virgin soil states at suction s , r is a constant related to the maximum stiffness of the soil (for an infinite suction), ξ is a parameter that controls the rate of increase of soil stiffness with suction and κ_{ps0} is the elastic stiffness parameter for changes in net mean stress at zero suction.

The flow rule is given by

$$g_{LC} = \frac{\alpha_a q^2}{g_y(\theta)^2} - \frac{M^2}{g_y(\theta=0)^2} (p + p_s)(p_0 - p) \quad (2.6)$$

where α_a is a parameter that gives rise to the non-associative model, i.e., $g_{LC} \neq f_{LC}$.

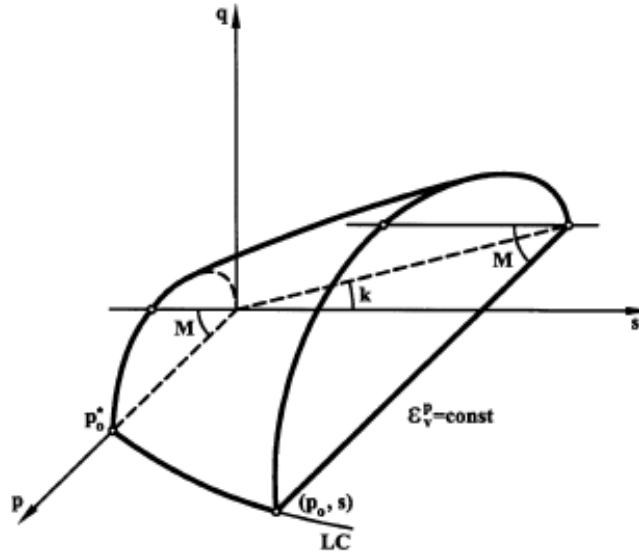


Figure 2.2. Three-dimensional representation of the yield surface in the BBM (Gens et al. 2006).

Microstructural level

In the BExM, the following assumptions are adopted related to microstructural behavior and its interaction with the macrostructure:

- The microstructure is mainly saturated and the effective stress concept holds.
- The microstructural behavior is elastic and volumetric.
- Mechanical, hydraulic, and chemical equilibrium exists between microstructure and macrostructure.
- Coupling between microstructure and macrostructure results in a possible buildup of macrostructural elastoplastic strains when elastic microstructural strains occur.

With these assumptions, the increment of volumetric microstructural strain increment $d\varepsilon_{vm}^e$ depends exclusively on the increment of mean effective stress $d\hat{p} = d(\bar{p} - p_l) = d(\bar{p} - p_g + p_g - p_l) = d(p + s)$, where \bar{p} is mean stress (or mean pressure), p_l is liquid phase pressure, p_g is gas phase pressure and s is suction. Therefore, a straight line $p + s = \text{constant}$ can be drawn around the current state of stress and suction along which no microstructural strain takes place. This line, called Neutral Line (NL), moves with the current stress state (C) and separates at each instant the zone of microstructural swelling from the zone of microstructural shrinkage in the $p-s$ plane (Figure 2.3).

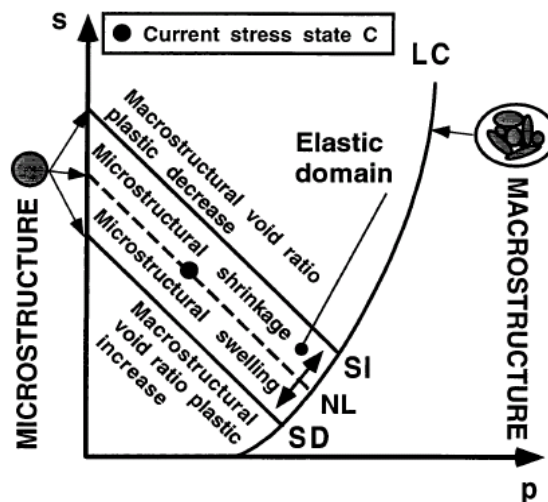


Figure 2.3. Microstructural and macrostructural elastoplastic responses in a double-structure model equivalent to the Barcelona Expansive Model.

Interaction between structural levels

Microstructural swelling affects the structural arrangement of the macrostructure, inducing an irreversible increase of the macroporosity. Reciprocally, microstructural shrinkage induces an irreversible decrease of the macroporosity. In BExM, the irreversible macrostructural

deformations induced by microstructural effects are considered proportional to the microstructural strain according to interaction functions with the general form:

$$d\varepsilon_{v\beta}^p = f d\varepsilon_{vm}^e \quad (2.7)$$

where $\varepsilon_{v\beta}^p$ is the macrostructural plastic strain arising from the interaction between both structures. Two interaction functions are defined; f_c for MC (microstructural contraction) path and f_s for MS (microstructural swelling) paths (Sánchez et al., 2005). Alonso et al. (1999) proposed the following possible interaction functions, in which case for isotropic loading, f_c (or f_I , corresponding to a drying process in which the soil shrinks) and f_s (or f_D , corresponding to a wetting process in which the soil swells) depend on the ratio p/p_o (Figure 2.4)

$$f_c = f_{c0} + f_{c1}(p/p_o)^{n_c} \text{ and } f_s = f_{s0} + f_{s1}(1-p/p_o)^{n_s}, \quad (2.8)$$

The ratio p/p_o is a measure of the distance from the current stress state to the yield locus for the macrostructure LC and has the same meaning as the overconsolidation ratio for an isotropically consolidated soil. A low p/p_o implies a dense packing of the material. It is expected that under such dense packing (dense macrostructure), the microstructural swelling strongly affects the global arrangement of clay aggregates, which becomes more open. This results in a softening of the macrostructure, which implies that the macrostructural yield surface LC shrinks. Under this condition, expansion accumulates upon suction cycles. On the other hand, a high p/p_o implies a looser macrostructure. Thus, the microstructural swelling produces an invasion of the macropores, which tends to close the macrostructure and compression accumulates upon suction cycles. In such a case, the elastic domain increases and LC expands (Alonso et al. 1999; Sánchez et al., 2005).

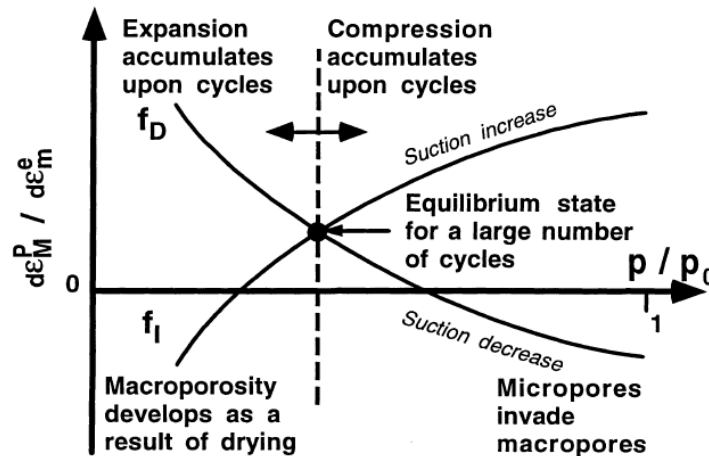


Figure 2.4. Summary of micro-macropore interaction mechanisms.

Elastic Strain

Equivalent to the BBM model, the macrostructural volumetric elastic strain increment for the BExM model is associated with changes in net mean stress dp and suction ds (Alonso et al., 1999)

$$d\varepsilon_{vM}^e = \frac{1}{K_M} dp + \frac{1}{K_s} ds \quad (2.9)$$

where K_M is the macrostructural bulk modulus and K_s is the modulus associated with suction strain. K_M and K_s are defined as

$$K_M = \frac{(1+e_M)p}{\kappa_{ps}(s)}, \quad (2.10)$$

$$K_s = \frac{(1+e_M)(s+p_{atm})}{\kappa_{sp}(p,s)} \quad (2.11)$$

where $\kappa_{ps} = \kappa_{ps0}(1+s\alpha_{ps})$ and κ_{sp} are compressibility parameters for changes in net mean stress and suction, respectively, and α_{ps} is an empirical parameter.

In BExM, the microstructural volumetric strain depends on the change in the microstructural effective stress

$$d\varepsilon_{vm}^e = \frac{1}{K_m} d\hat{p} \quad (2.12)$$

where K_m is the microstructural bulk modulus for change in mean effective stress. Alonso et al. (1999) define two alternative laws for the microstructural behavior through two alternative expressions for the microstructural modulus

$$K_m = \frac{(1+e_m)\hat{p}}{\kappa_m}, \quad (2.13)$$

$$K_m = \frac{e^{-\alpha_m \hat{p}}}{\beta_m}, \quad (2.14)$$

where κ_m , α_m and β_m are compressibility parameters.

The deviatoric elastic strain increment is defined as

$$d\varepsilon_q^e = \frac{1}{3G} dq \quad (2.15)$$

where G is the shear modulus and may be obtained using a constant Poisson's ratio ν in

$$G = \frac{3(1-2\nu)}{2(1+\nu)} K_M. \quad (2.16)$$

Thus, the equations for elastic mechanical strain indicate the dependency of bulk modulus on suction (and hence fluid saturation), which in a dry clay can be significantly stiffer than in a water-saturated clay.

Plastic Strain

Macrostructural plastic strain occurs by two possible mechanisms: either when the stress lies on the LC yield surface, or as a result of microstructural contraction/swelling (MC and MS path). The increment of plastic volumetric macrostructural strain is described as a result of microstructural contraction/swelling as

$$d\varepsilon_{v\beta}^p = f d\varepsilon_{vm}^e, \quad (2.17)$$

where $d\varepsilon_{v\beta}^p$ is the macrostructural plastic strain as a result of microstructural contraction/swelling (MC or MS path, respectively).

When the stress state lays on the LC yield surface, the plastic strains are obtained from the plastic flow rule

$$d\varepsilon_{vLC}^p = d\Lambda \frac{\partial g}{\partial p}, \quad (2.18)$$

$$d\varepsilon_{qLC}^p = d\Lambda \frac{\partial g}{\partial q}, \quad (2.19)$$

where $d\Lambda$ is the plastic multiplier obtained from the consistency condition $df_{LC} = 0$ (recall Eq. (2.4)).

The macrostructural plastic strain induced by microstructural volumetric strain is given by the flow rule at the image point on the LC yield surface. The coordinates of the image point (p^* , q^* , s^*) are given by (Alonso et al., 1999) (Figure 2.5)

$$p^* = \frac{\eta^2 k_s s - M^2 p_0}{\eta^2 - M^2}, \quad q^* = \eta(p + k_s s), \quad s^* = s \quad (2.20)$$

where $\eta = \frac{q}{p + k_s s}$.

The total plastic volumetric strain is the sum of both plastic mechanisms

$$d\varepsilon_v^p = d\varepsilon_{vLC}^p + d\varepsilon_{v\beta}^p. \quad (2.21)$$

Then the hardening variable of the macrostructure — the pre-consolidation pressure p_0^* — depends on the total plastic volumetric strain ε_v^p , which is the sum of the plastic strain induced by LC yielding (ε_{vLC}^p) and the plastic strain induced by microstructural strain impact on the macrostructure ($\varepsilon_{v\beta}^p$). That is,

$$\frac{dp_0^*}{p_0^*} = \frac{(1 + e_M)d\varepsilon_v^p}{\lambda_{p_s,0} - \kappa} \quad (2.22)$$

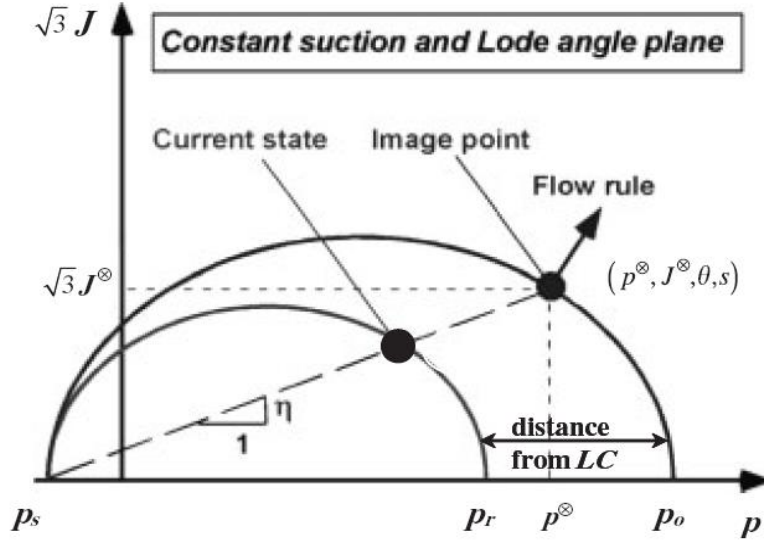


Figure 2.5. Reference pressure and plastic flow direction (Sánchez et al. 2005).

2.1.2 Implementation of BExM into TOUGH-FLAC

We implemented the BExM in FLAC^{3D}, by extending our previous implementation of the BBM to include the microstructure level and its interactions with the macrostructure. This is done using the User Defined constitutive Model (UDM) option in FLAC3D, including C++ coding and dynamic link libraries. Specifically, the following calculation items were added

- 1) Microstructural strain and effective stress
- 2) Macrostructural strain
- 3) Global elastic tensor depending on microscopic and macroscopic structural compliances
- 4) Micro/macrostructural interaction functions
- 5) Plastic macrostructural strain from structural interactions
- 6) Plastic corrections in the FLAC3D elastoplastic algorithm
- 7) Plastic hardening/softening factors

Implementation of the first five items is straightforward, whereas items 6 and 7 are related to the FLAC3D elastoplastic algorithm and involve calculation of the plastic multiplier $d\lambda$ associated with the elastic predictor-plastic corrector algorithm in FLAC3D. In this algorithm, current stress increments are guessed (by Hooke's law) and added to the stresses from the previous time step, and then corrected back to the yield surface if the calculated principal stresses violate the yield criterion. Using such an approach the current stress is calculated as

$$p = p_{est} + Kd\lambda c_a \quad (2.23a)$$

$$q = q_{est} + Kd\lambda c_b \quad (2.23b)$$

where p_{est} and q_{est} are the estimated stresses obtained in the previous step, plus the current incremental elastic estimates, and constants c_a and c_b are the components normal to the plastic potential calculated as (Rutqvist et al., 2011):

$$c_a = M^2(2p - p_c + p_s) \quad (2.24a)$$

$$c_b = \alpha_a 2q \quad (2.24b)$$

The value of the plastic multiplier $d\lambda$ is defined by substituting Equations (2.24a) and (2.24b) in Equation (2.4), requiring that the new stress point be located on the yield surface ($f_{LC}(q, p) = 0$). Then,

$$a(d\lambda)^2 + bd\lambda + c = 0 \quad (2.25)$$

where

$$a = (MKc_a)^2 + (3Gc_b)^2 \quad (2.26a)$$

$$b = -\left[Kc_a c_a^e + \frac{3}{\alpha_a} Gc_b c_b^e \right] \quad (2.26b)$$

$$c = f(q_{est}, p_{est}) \quad (2.26c)$$

Finally, FLAC^{3D} evaluates new stresses p and q from Equations (2.23a) and (2.23b) using the expression for $d\lambda$ corresponding to the root of Equation (2.25) with the smallest magnitude (Rutqvist et al., 2011). In the case of microstructural contraction or swelling (i.e., MC or MS path), the components normal to the plastic potential are given by substituting p and q with p^* and q^* into (2.23a) and (2.23b). In the case of simultaneous *LC* yield and microstructural contraction or swelling, the stress state will be on the *LC* surface, and therefore $p = p^*$ and $q = q^*$, and Equations 2.23–2.26 are still valid.

Finally, at the end of each FLAC3D step, the hardening parameter, i.e., the pre-consolidation pressure p_0^* , the bulk modulus of both microstructure and macrostructure and the tangential bulk modulus, are updated based on the total plastic volumetric strain and stress state, and these are stored for use in the next step.

2.1.3 Testing and verification of implementation

Expansive clays show a non-reversible behavior when they undergo several wetting-drying cycles. This phenomenon cannot be reproduced with the BBM model, but the incorporation of the interactions between the microstructure and the macrostructure of an expansive soil allows accumulating plastic strain. To test our implementation of the BExM, we perform cyclic wetting-drying tests based on the ones presented by Alonso et al. (1999) and Sanchez et al. (2005).

First, we perform a cyclic wetting-drying test under a very low confining pressure (0.01 MPa). In this test example, the macrostructure is dense and expansion is expected to accumulate upon cycles because macroporosity will develop as a result of the interaction between the microstructure and the macrostructure. Figure 2.6 shows how expansion accumulates upon

suction cycles. Furthermore, the magnitude of the plastic strain decreases upon cycles, because the plastic strain that occurs during wetting and dryings tends towards equilibrium. This can be observed from the interaction functions (Figure 2.7). As the number of cycles increases, the interaction functions converge towards the equilibrium point (point *E* in Figure 2.7) and the accumulated expansion between two successive suction cycles decreases (Figure 2.8). Note that since the confining pressure is low, the ratio between the mean net stress and the apparent pre-consolidation stress is small, so suction cycles occur mainly on the left side of the equilibrium point *E*. This results in a net expansion of the soil sample. Therefore, after a cycle of wetting and drying, the plastic strain that occurs during wetting is higher than the one of drying (Figure 2.8). Since the soil expands during wetting, this gives rise to an overall expansion of the soil.

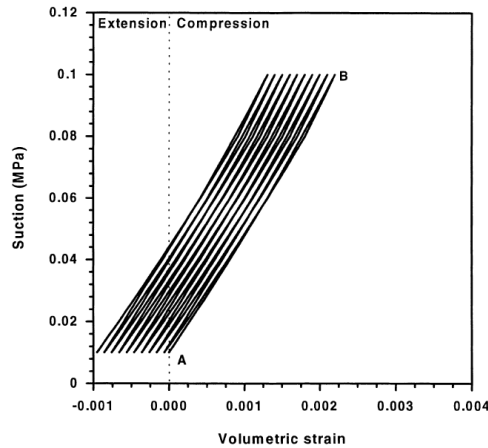


Figure 2.6. Strain evolution during suction cycles for a low confining pressure.

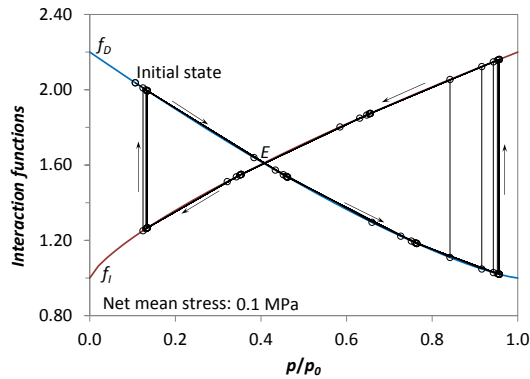


Figure 2.7. Evolution of the interaction functions for a low confining pressure.

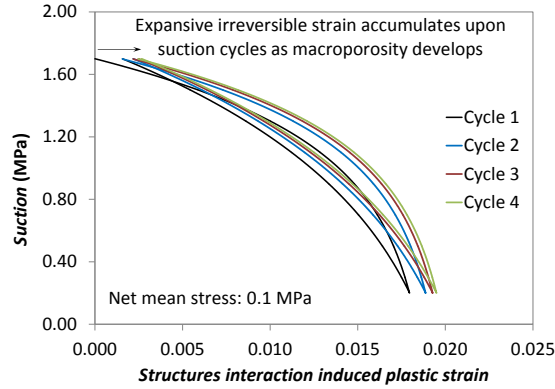


Figure 2.8. Evolution of the plastic strain due to the interaction between the microstructure and the macrostructure for a low confining pressure.

During suction cycles the microstructure behaves elastically (Figure 2.9). However, the macrostructure accumulates plastic strain, so its behavior is not reversible (Figure 2.10). Nevertheless, the expansion that accumulates upon each cycle decreases with number of cycles, so the macrostructure will eventually behave elastically.

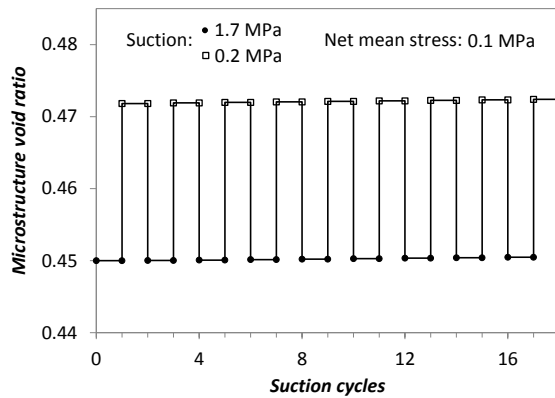


Figure 2.9. Void ratio evolution of the microstructure during suction changes for a low confining pressure.

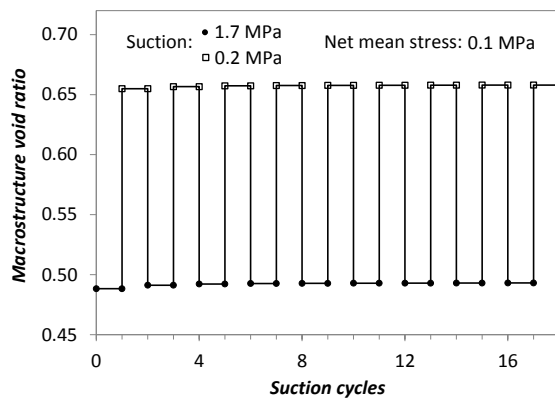


Figure 2.10. Void ratio evolution of the macrostructure during suction changes for a low confining pressure.

On the other hand, when the confining pressure is high the stress state is close to the LC yield surface and the macrostructure is relatively loose, so the microstructure will invade the macropores and compression will accumulate upon cycles (recall Figure 2.6). Figure 2.11 shows the strain evolution during suction cycles and how compression accumulates upon cycles. Note that in the first cycle the compression is much larger than in the other cycles. This is because the LC yield surface becomes active during the first wetting. In the following cycles, the LC yield surface does not become active. Similarly to the other case, the microstructure behaves elastically but the macrostructure does not.

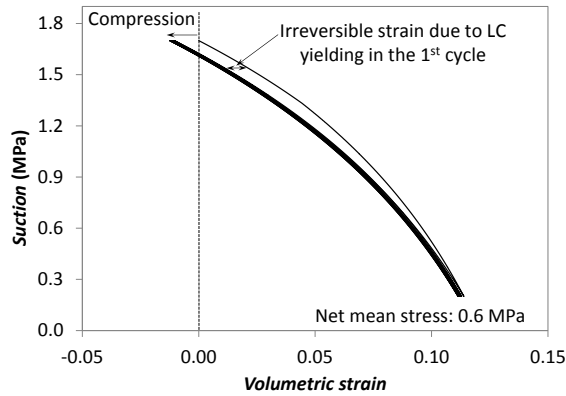


Figure 2.11. Strain evolution during suction cycles for a high confining pressure.

We show with these two opposite examples that the implementation of the BExM model in FLAC3D reproduces the behavior of expansive clays. We also calibrate our model to reproduce the results of a laboratory experiment made by Pousada (1984) (Figure 2.12). Our results are shown in Figure 2.13 and the values of the parameters used for this test are displayed in Table 2.1.

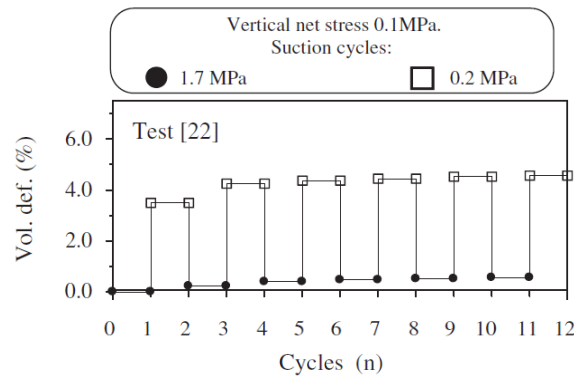


Figure 2.12. Volumetric deformation upon suction cycles reported by Pousada (1984) in an oedometric test under a vertical stress of 0.1 MPa.

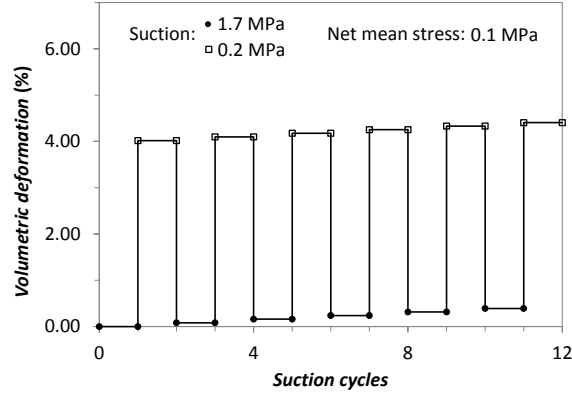


Figure 2.13. Volumetric deformation upon suction cycles mimicking the test of Pousada (1984).

Table 2.1. Parameters used to reproduce the suction cycles test of Pousada (1984).

Parameters defining the Barcelona Basic Model for macrostructural behavior

$$\kappa=0.01 \quad \kappa_s=0.0001 \quad \lambda(0)=0.065 \quad p^c \text{ (MPa)}=0.01 \quad r=0.96 \quad \xi \text{ (MPa}^{-1}\text{)}=0.2 \quad p_0^* \text{ (MPa)}=0.75$$

Parameters defining the law for microstructural behavior

$$\alpha_m \text{ (MPa}^{-1}\text{)}=0.8 \quad \beta_m \text{ (MPa}^{-1}\text{)}=0.01$$

Interaction functions between the microstructure and the macrostructure

$$f_c = 1.0 + 1.2(p/p_0)^{1.3} \quad f_s = 1.0 + 1.2(1 - p/p_0)^{0.7}$$

$$e_{micro}=0.45 \quad e_{macro}=0.55$$

2.2 Linking dual-structure model to chemistry and testing

The BExM can be linked to chemistry through the dependence of β_m (see Eq. 2.14) on exchangeable cation concentration as shown in the following equation (Gens, 2010):

$$\beta_m = \sum_i \beta_m^i x_i, \quad (2.27)$$

where x_i is the equivalent fraction of the exchangeable cation, i , ranging from 0 to 1, and β_m^i is the parameters that control the microstructure stiffness and defined for each of the exchangeable cation. If a rough analogy is made with diffuse double layer theory, β_m^i is proportional to the ionic hydrated radius and inversely proportional to its valence (Guimaraes et al., 2013). Typically we have $\beta_m^{Li} > \beta_m^{Na} > \beta_m^K$ and $\beta_m^{monovalent} > \beta_m^{bivalent}$. After implementing equation 2.27 in TOUGHREACT-FLAC, we compute a hypothetical case to illustrate the effect of changes in concentrations of exchangeable cations on the volumetric strain.

We model a sample of 2 cm³ discretized in 20 elements of 1 mm in the vertical direction. The properties of the expansive clay are summarized in Table 2.2. The experiment is performed under constant confining stress of 0.2 MPa. The sample has an initial water saturation degree of 0.5. The sample is wetted by injecting water through the bottom of the sample until the sample becomes practically saturated (water saturation degree of 0.98).

Table 2.2. Parameters used to test the effect of chemistry on the swelling capacity of expansive clays.

<i>Parameters defining the Barcelona Basic Model for macrostructural behavior</i>						
$\kappa=0.001$	$\kappa_s=0.0001$	$\lambda(0)=0.065$	p^c (MPa)=0.01	$r=0.96$	ξ (MPa ⁻¹)=0.2	p_0^* (MPa)=7.5
<i>Parameters defining the law for microstructural behavior</i>						
α_m (MPa ⁻¹)=0.8		β_m (MPa ⁻¹)=variable				
<i>Interaction functions between the microstructure and the macrostructure</i>						
$f_c = 1.0 + 1.2(p/p_0)^{1.3}$		$f_s = 1.0 + 1.2(1 - p/p_0)^{0.7}$				
$e_{micro}=0.45$		$e_{macro}=0.55$				
<i>Permeability of the sample</i>						
$k=5 \cdot 10^{-18} \text{ m}^2$						
<i>Van Genuchten retention curve</i>						
P_0 (MPa)=0.11		$\lambda=0.19$		$S_{lr}=0.1$		

The initial pore water composition is assumed to be the same as FEBEX bentonite (Fernandez et al., 2001). We model two scenarios here. In the first one the sample is saturated with 1 M NaCl solution, and in the second case the sample is saturated with 1M CaCl₂ solution. The model runs for 3 days and it takes about 1.5 days to fully saturate the sample (Figure 2.14). Initially exchangeable Ca (X_Ca) is the dominant exchangeable cation that accounts for about 90% of total sites. When the sample is hydrated with 1 M CaCl₂ solution, equivalent fraction of exchangeable Ca continues to increase over the course of hydration because the incoming aqueous Ca exchange with other cation from the exchangeable sites (Figure 2.15). If we hydrate the sample with 1 M NaCl, as shown in Figure 2.16, the exchangeable Na (X_Na) eventually dominates the exchangeable sites by taking over about 80% of the equivalent fraction. Based on the fact that β_m^i is proportional to the ionic hydrated radius and inversely proportional to its valence (Guimaraes et al., 2013), we can roughly estimate β_m^i using the following equation:

$$\beta_m^i = \kappa r^i / v^i, \quad (2.28)$$

where κ is a constant that has to be calibrated and r^i is hydrated radii of the cation and v^i is the valence of the cation. The hydrated radius for Na, K, Ca and Mg are 7.9, 5.3, 9.6 and 10.8 Å,

respectively (Mitchell and Soga, 2005). For this case we use a κ of $3.24 \times 10^{-4} \text{ \AA}^{-1} \text{ MPa}^{-1}$ and the calculated β_m for the case with NaCl solution at the end of saturation is $2.45 \times 10^{-3} \text{ MPa}^{-1}$ and that for the case with CaCl_2 solution is $1.6 \times 10^{-3} \text{ MPa}^{-1}$. Using these β_m , we calculate the volumetric strain (Figure 2.17). Model results show that NaCl solution leads to a volumetric strain that is 47% higher than a CaCl_2 solution, which is qualitatively consistent laboratory test results (e.g. Di Maio, 1996).

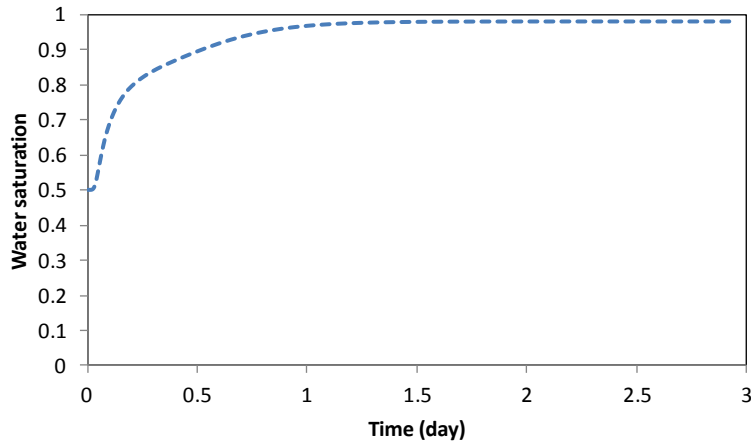


Figure 2.14. Changes in water saturation in the middle of the sample (sample is hydrated from the bottom).

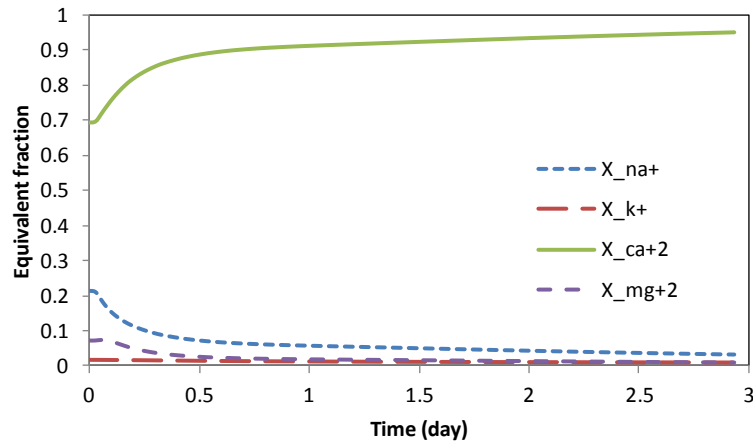


Figure 2.15. Changes in equivalent fraction of each cation in the middle of the sample when the sample is saturated with 1M CaCl_2 solution.

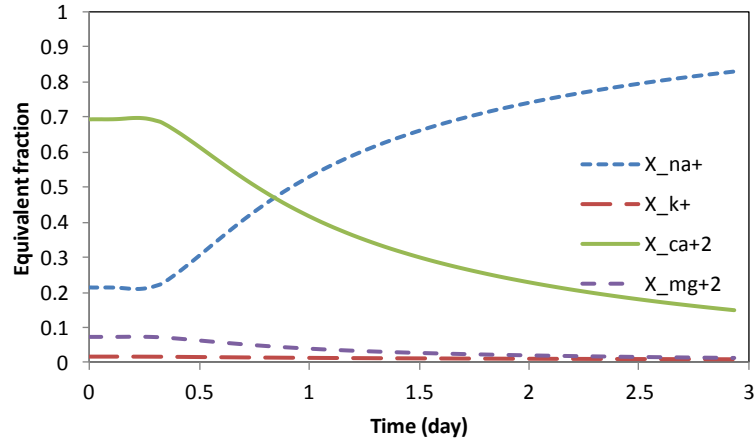


Figure 2.16. Changes in equivalent fraction of each cation in the middle of the sample when the sample is saturated with 1M NaCl solution.

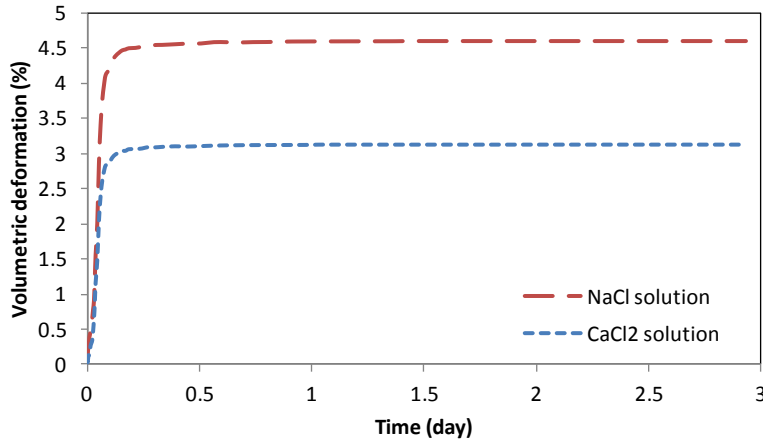


Figure 2.17. Volumetric deformation in the middle of the sample for the case with 1 M NaCl and CaCl₂ solution.

Although the modeling exercise presented here demonstrates the modeling capability of TOUGHREACT-FLAC that accounts for the effect of exchangeable cations, our confidence level will be increased if we can validate our model with laboratory data. However, those published laboratory tests (e.g. Di Maio, 1996; Wakim et al., 2009) typically lack detailed characterization of the geochemical parameters such as mineralogical and aqueous composition, which makes it difficult to find a suitable laboratory test.

2.3 Summary

We are developing and applying coupled THMC models for the analysis of EBS coupled processes in bentonite-backfilled repositories. We based this development on the extension of the Barcelona Basic Model to a dual-structure model for expansive clay, such as bentonite. We have implemented of the dual-structure model into TOUGH-FLAC and we have tested the model against literature data from experiments and independent models, although more testing is

underway. We have also successfully linked the dual-structure model to chemistry in a rational approach suggested by Gens (2010), enabling the analysis of the effects of exchangeable cations on swelling strain. We are currently working on a more rigorous approach in linking the dual-structure model with the diffuse double layer theory for the coupling between chemistry and mechanics, resulting in a more complete coupled THMC model for the analysis of various THMC processes relevant to the long-term EBS behavior and stability.

3. Modeling Reactive Diffusive Transport

Engineered clay barriers have remarkable macroscale properties, such as high swelling pressure (Gonçalvès et al., 2007), very low permeability (Mammar et al., 2001), semi-permeable membrane properties (Malusis et al., 2003), and a strong coupling between geochemical, mechanical, and osmotic properties (Malusis and Shackelford, 2004; Gonçalvès et al., 2007). These properties are thought to arise from the distinct geochemical, transport, and mechanical properties of the interlayer nanopores of swelling clay minerals, such as Na-montmorillonite and other smectites (Gonçalvès et al., 2007).

In compacted smectite-rich media, most of the pore space is located in clay interlayer nanopores with the width of a few statistical water monolayers (Kozaki et al., 2001; Bourg et al., 2006). The complex microstructure of these clay barriers (Cebula et al., 1979; Melkior et al., 2009) can be approximated with a conceptual model in which all pores are identical planar pores between parallel negatively-charged smectite surfaces. With this model, the width of the interlayer pores can be derived from the dry bulk density of the smectite, and properties such as the anion exclusion volume or the swelling pressure of the clay barrier can be predicted by solving the Poisson-Boltzmann equation in the space between the parallel, negatively charged clay particles (Gonçalvès et al., 2007; Tachi et al., 2010). Solving the Poisson-Boltzmann equation, however, is not a minor exercise when carried out in the context of a general multicomponent framework. In addition, it requires a fine discretization to capture the chemical and electrostatic gradients in the vicinity of the charged clay surfaces. This is why we are also pursuing a mean electrostatic approach, which makes it easier to consider larger length scales for transport (e.g., Tournassat and Appelo, 2011). The Poisson-Boltzmann approach, or even the Mean Electrostatic (or Donnan equilibrium) approach that is based on it, potentially provides a more mechanistic treatment of swelling pressure and anion exclusion than is possible with the largely empirical approaches employed by Gens (2010) and Guimarães et al (2013).

Microstructural investigations of compacted smectite-rich media reveal the existence of *crystalline hydrates* (known as the 1-, 2-, and 3-layer hydrates, in which the interlayer nanopore contains one, two, or three statistical water monolayers) at dry bulk densities where the average pore size is much larger than the width of the largest crystalline hydrate (Kozaki et al., 2001; Holmboe et al., 2012). These studies show that compacted smectite contains at least two types of pores: (1) crystalline hydrate nanopores with a width of 0.3, 0.6, or 0.9 nm (the 1-, 2-, and 3-layer hydrates); and (2) a population of larger, poorly characterized pores. Models that account for this “bimodal” distribution of pore widths (Bourg et al., 2006; Ichikawa et al., 2004; Tournassat and Appelo, 2011) provide useful insights into the diffusion of water and cations in the EBS. The power of these models arises from the fact that they can harness the extensive knowledge base that exists on the behavior of water and ions in the crystalline hydrate nanopores, from experimental (Sposito and Prost, 1982; González Sánchez et al., 2009; Ferrage

et al., 2011; Marry et al., 2011) and molecular modeling studies (Sposito et al., 1999; Rotenberg et al., 2007a; Kosakowski et al., 2008; Bourg and Sposito, 2010; Churakov and Gimmi, 2011).

Several key properties of the EBS, however, such as anion diffusion and water advection, are likely to be determined by the largest pores in the compacted clay system rather than by the crystalline interlayer nanopores. The “bimodal” models of smectite clay barriers listed above either assumed that the water in the large pores is similar to bulk liquid water (Bourg et al., 2006, 2007, 2008; Bourg and Sposito, 2010) or they artificially assigned a width to these large pores [or equivalently, a value to the ratio of the number of crystalline hydrate nanopores to larger pores (Ichikawa et al., 2004; Tournassat and Appelo, 2011)]. Obviously, neither approach is satisfactory for predicting anion diffusion or water flow in the EBS. In the present project, we are developing a new model of diffusion in the EBS based on the knowledge that in conditions relevant to the EBS, Na-smectite has only four stable swelling states. These states are the 1-, 2-, 3-layer crystalline hydrates, with d -spacings $d_{001} = 12.4, 15.4, 18.4$ (Norris, 1954; Holmboe et al., 2012), and the smallest possible “osmotic hydrate” with an average reported d -spacing of $32.7 \pm 2.4 \text{ \AA}$ (Foster et al., 1955; Zhang and Low, 1989; Wilson et al., 2004). We hypothesize that compacted water-saturated Na-smectite can be approximated, at any dry bulk density, as a mixture of (at most) two swelling states. For a smectite consisting of a single swelling state with a basal spacing d_{001} , the dry bulk density ρ_b is given by the simple relation:

$$\rho_b = \frac{\rho_s d_s}{d_{001}} \quad (3.1)$$

where $d_s = 9.4 \pm 0.1 \text{ \AA}$ and $\rho_s = 2.84 \pm 0.04 \text{ kg dm}^{-3}$ are the thickness and density of a smectite lamellum. We expect, therefore, that Na-smectite at $\rho_b = 0.82 \pm 0.06 \text{ kg dm}^{-3}$ consists entirely (with minor deviations due to imperfect stacking of clay particles) of the smallest osmotic hydrate (with $d_{\text{osmotic}} = 32.7 \pm 2.4 \text{ \AA}$), whereas at $\rho_b = 1.45 \pm 0.05 \text{ kg dm}^{-3}$, it consists entirely of the 3-layer hydrate (with $d_{3\text{-layer}} = 18.4 \pm 0.5 \text{ \AA}$). At intermediate values of ρ_b , Na-smectite must consist of a mixture of the smallest osmotic hydrate and the largest crystalline hydrate as shown by the XRD results of Holmboe et al. (2012). The fraction of clay interlayers that form the osmotic hydrate (X_{osmotic}) can be determined from the relation:

$$\rho_b = X_{\text{osmotic}} \left(\frac{\rho_s d_s}{d_{\text{osmotic}}} \right) + (1 - X_{\text{osmotic}}) \left(\frac{\rho_s d_s}{d_{3\text{-layer}}} \right) \quad (3.2)$$

According to the simple conceptual model proposed above, in the range of dry bulk densities of interest in EBS applications, no assumptions need to be made regarding the size of the largest pores in any compacted water-saturated Na-smectite sample. The pores in the system consist of a mixture of the 3-layer hydrate and the smallest osmotic hydrate, and the relative proportion of the two types of pores varies with the dry bulk density ρ_b .

The simple conceptual model proposed above suggests that EBS performance (ion diffusion, water flow, semi-permeable membrane properties, swelling pressure) depends on the properties of the smallest osmotic hydrate (with $d_{001} = 32.7 \pm 2.4 \text{ \AA}$) and the largest crystalline hydrates (the 3-layer hydrate with $d_{001} = 18.4 \pm 0.5 \text{ \AA}$, and possibly also the 2-layer hydrate at very high degrees of compaction). The two types of pores have significantly different properties: for example, the crystalline hydrates are so narrow that the behavior of water and ions is dominated by short-range interactions with the clay surface, whereas the osmotic hydrate is sufficiently large that long-range, mean-field interactions in the so-called electrical double layer (EDL) play an important role (Tournassat et al., 2009; Bourg and Sposito, 2011b).

In this subtask, we describe the development of our conceptual model and its application to the self-diffusion of water and “hard” acids and bases (alkali metals, chloride). To develop our model, we apply a combination of microcontinuum scale models based on the Poisson-Boltzmann and Poisson-Nernst-Planck equations, to elucidate the coupling between EDL phenomena and molecular diffusion in clay nanopores, and molecular dynamics (MD) simulations, to gain insight into the influence of short-range intermolecular interactions on diffusion in clay nanopores. Our conceptual model will be broadened in the future to describe other phenomena that are discussed in this report, such as coupled THM processes (Section 2) or the diffusion of UO_2^{2+} (Section 4). Specifically, we propose to use the Poisson-Boltzmann equation, and the Mean Electrostatic Model based on it, to develop mechanistic descriptions of clay swelling pressure. Rather than being empirically based on cation exchange capacity which incorporates both inner sphere and outer sphere sorption, as well as EDL ions, this will consider the overlap of electrical double layers in the context of Stern layer (inner sphere) sorption. As an application to UO_2^{2+} diffusion, we will simulate uranium transport through the compacted bentonite using the Mean Electrostatic Model, with rigorous treatment of overlapping EDL where appropriate.

During the first part of FY13, we focused primarily on the following aspects:

- First, we used micro-continuum scale simulations as described in section 3.1 to investigate the effects of ionic strength on the electrical double layer thickness, and thus on the EDL porosity that is available for diffusive transport. When the bentonite is highly compacted, the EDL porosity may make up the major portion of the porosity available for transport (i.e., bulk water is mostly not present). A dynamic model for EDL thickness was developed and implemented within a general purpose multicomponent reactive transport framework (i.e., one that can consider the full range of aqueous and surface complexation). The simulations demonstrate that ionic strength effects may partly reverse the effects of clay swelling. The model was then validated against a tracer test carried out in the Opalinus Clay, where it was able to capture the transport behavior of both uncharged non-reactive species (HTO) and anionic species (bromide and chloride). In addition, the reaction portion of CrunchEDL is being coupled to Comsol, which will make it possible to consider both pore scale electrostatic effects on diffusion and flow (including non-Darcian flow), as well as larger scale porous media behavior at the repository scale.
- Second, we used MD simulations to predict the temperature-dependence of diffusion of water and Na^+ in clay nanopores in the temperature range from $T = 278$ to 353 K. This area of inquiry was selected for two reasons: (1) because temperature in the EBS may range from roughly 283 to 368 K (JNC, 2000; SKB, 2009), whereas most data on diffusion in clay barriers were obtained at or near 298 K; and (2) because the temperature dependence of diffusion (expressed as an activation energy of diffusion E_a) is a *macroscopic scale* property that directly reflects—if tortuosity and other features that determine the geometric factor of the porous medium are invariant with T —the potential energy landscape explored by the diffusing species at the *pore scale*. Therefore, macroscopic measurements of E_a , when compared with pore-scale predictions of E_a obtained by MD simulation, yield direct information on the predominant diffusion pathway of the species of interest (e.g., does the species diffuse preferentially in the crystalline hydrate or in the osmotic hydrate?). This research is described in Section 3.2

During the remainder of FY13, we plan to focus on the following activities: (1) we plan to begin simulations of the UO_2^{2+} diffusion experiments conducted by Davis and Tinnacher (Section 4); (2) we plan to complete our MD simulation study of the temperature dependence of diffusion in clay nanopores by studying the behavior of Cs^+ , Sr^{2+} , Ca^{2+} , Cl^- , and UO_2^{2+} ; and (3) we plan to carry out a joint microcontinuum scale and MD simulation study of anion exclusion, the structure of the EDL, and water and ion diffusion in the smallest osmotic hydrate of Na-smectite as a function of ionic strength. These planned activities are described in section 3.3.

3.1 Mean Electrostatic Model for Diffusive Transport in the EBS

3.1.1 Derivation from Poisson-Boltzmann Equation

A rigorous model for the structure of the electrical double layer (EDL) can be derived from the combination of several equations, including the Poisson equation describing the distribution of electrical potential, ψ , in water

$$\nabla^2 \psi = -\frac{\rho_z}{\varepsilon}, \quad (3.3)$$

where ε is the permittivity and ρ_z is the volumetric charge density given by

$$\rho_z = e \sum_i z_i C_i^{EDL}. \quad (3.4)$$

In Eq. (3.4), e is the elementary charge of the electron and z_i is the valence of the ion. The Boltzmann distribution gives an expression for the concentration, $C_i^{EDL}(z)$, in the electrical double layer as a function of distance from the charge solid surface, z ,

$$C_i^{EDL}(z) = C_i \exp\left(\frac{-z_i e \psi(z)}{k_B T}\right), \quad (3.5)$$

where C_i is here the concentration in the bulk solution, k_B is the Boltzmann constant, and T is the absolute temperature. Combining Eq. (3.5) with the Poisson equation (Eq. (3.3)) yields the Poisson-Boltzmann equation (Schoch et al., 2008)

$$\nabla^2 \psi = \frac{-e}{\varepsilon} \sum_i z_i C_i \exp\left(\frac{-z_i e \psi(z)}{k_B T}\right) \quad (3.6)$$

which can be solved exactly for various simple formulations (e.g., the Gouy-Chapman model, which assumes a symmetric electrolyte).

Integrating the Poisson-Boltzmann equation over nanometer length scales from charged mineral surfaces, however, was not practical in the present version of CrunchEDL because of the desire to consider larger length scales, so an alternative approach based on a Donnan Equilibrium model (Wersin et al., 2004; Leroy and Revil, 2004; Appelo et al., 2007; Leroy et al., 2007; Appelo et al., 2008; Birgersson and Karnland, 2009; Tournassat and Appelo, 2011) is used. The electrical double layer is conceptualized as consisting of two parallel layers of charge, one being the surface charge associated with direct sorption at the mineral surface (the Stern layer, typically divided into an inner and outer Helmholtz layer), and the second being the diffuse layer charge, a swarm of counterbalancing ions (Figure 3.1).

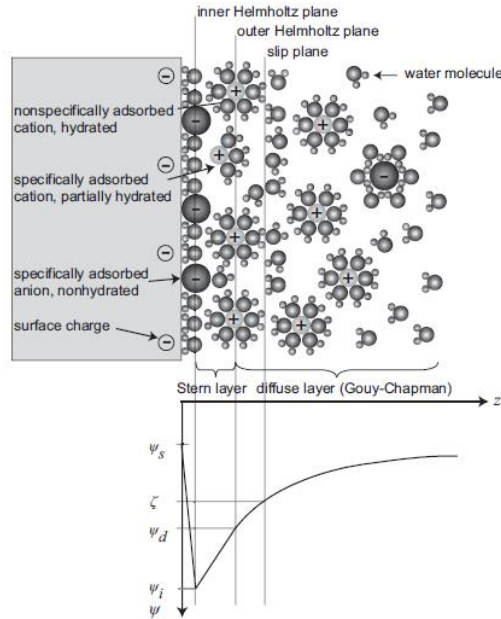


Figure 3.1. Schematic illustration of the Gouy-Chapman-Stern model of the solid-electrolyte interface, with the potential distribution $\psi(z)$ versus distance from the charged solid surface. The solid is illustrated with a negative surface potential ψ_s , described by three layers in solution. The inner Helmholtz plane layer ψ_i consists of nonhydrated co-ions and counterions (inner sphere complexes), whereas the outer Helmholtz plane layer ψ_d is built up of only hydrated counterions (outer sphere complexes). The diffuse layer is defined beyond the outer Helmholtz plane (from Schoch et al., 2008).

In the approach taken in CrunchEDL, the chemical potentials of the species in the diffuse layer and the bulk solution are equated. Writing equations for the chemical potentials of the species i in the bulk solution (or macroporosity) (superscript “B”) and electrical double layer (superscript “EDL”) respectively, we have

$$\begin{aligned}\mu_i^B &= \mu_i^{B,0} + k_B T \ln a_i^B \\ \mu_i^{EDL} &= \mu_i^{EDL,0} + k_B T \ln a_i^{EDL} + q_i \psi_m\end{aligned}\quad (3.7)$$

where the superscript 0 (first term on the right-hand side) refers to the chemical potential at the reference state, a_i are the species activities, q_i is the charge of an ion (the elementary charge of a particle, e , multiplied by the valence of the ion, z_i), k_B is the Boltzmann constant, and ψ_m is the mean electrical potential in the electrical double layer. The condition of Donnan Equilibrium implies that

$$\begin{aligned}\mu_i^{EDL} &= \mu_i^B \\ \mu_i^{EDL,0} &= \mu_i^{B,0}\end{aligned}\quad (3.8)$$

Combining Eqs. (3.5), (3.7), and (3.8) and assuming that the activity coefficients for the diffuse layer and bulk solution are the same gives the Boltzmann distribution for the ion activities in the electrical double layer, C_i^{EDL} :

$$C_i^{EDL} = C_i^B \exp\left(\frac{-z_i e \psi_m}{k_B T}\right). \quad (3.9)$$

The diffuse layer charge balances the charge within the Stern layer, Q^{SL} , which may consist in CrunchEDL of either a fixed mineral charge due to vacancies in the mineral structure (as in the case of classical ion exchange), or of fixed mineral charge modified by inner sphere and outer sphere complexes developed within the Stern layer calculated with a surface complexation model:

$$\phi^{EDL} \sum_i z_i C_i^{EDL} = Q^{SL} \quad (3.10)$$

where ϕ^{DL} is the volume (or porosity) of the electrical double layer. The left-hand side of Eq. (3.10) gives a volumetric charge density in units of charge equivalents per unit volume porous medium. The surface charge is given by

$$Q^{SL} = \sum_k^{N_s} z_k \Gamma_k \quad (3.11)$$

where Γ_k is the concentration in units of moles sorbed species per unit volume porous medium and z_k is the valence of the surface complex. In the CrunchEDL approach, therefore, one new equation is introduced (Eq. (3.10)), with one new unknown, the mean electrostatic potential of the diffuse layer, ψ_m . Note that in this formulation, the concentrations of the ions in the diffuse layer are dependent (or secondary) species that are calculated algebraically from the knowledge of the bulk solution composition and the mean electrostatic potential. A kinetic treatment of the diffuse layer ions would require that they be considered as primary unknowns.

Several approaches are available for calculating the fixed or Stern layer charge that is balanced by an electrical double layer. Even if the full Poisson-Boltzmann (PB) equation is used, special consideration needs to be given to the charge present in the Stern layer, a feature not always seen in the simpler implementations of the Poisson-Boltzmann equation. The starting point is the fixed mineral charge, which is normally given by the cation exchange capacity. If no Stern layer sorption occurred, the fixed mineral charge would provide a Dirichlet boundary condition for the electrostatic potential, ψ_f , at the solid surface,

$$\psi(0) = \psi_f. \quad (3.12)$$

In the case of no Stern layer sorption, therefore, the PB equation can be integrated across the entire thickness z of the electrical double layer. In the case where the charged bentonite particles are bordered by bulk water, this would be the point in space where the local solution becomes electroneutral (where the electrostatic potential goes to zero). In the case of overlapping double layers, as considered by Goncalves et al (2007) and Schoch et al (2008), this would be the midpoint between the two charged clay (or solid) surfaces. In the case of overlapping double

layers, the boundary condition at the midpoint is that the derivative of the electrical potential goes to zero (Figure 3.2)

$$\left[\frac{\partial \psi}{\partial z} \right]_{z=1/2h} = 0 \quad (3.13)$$

where h is the distance between the two charged solid (clay) surfaces. In the case where Stern layer sorption is not present, the fixed mineral charge (or CEC) is used in CrunchEDL as the charge to be balanced. Where protonation or other cation sorption reactions within the Stern layer also take place, changes in pH and cation concentration will result in changes in the surface charge to be balanced by the EDL. These are treated in CrunchEDL with a surface complexation model, with the EDL charge then calculated from the modified surface charge according to Eqs. (3.10) and (3.11). The surface complexation model can be either electrostatic (with Coulombic corrections to the Gibbs free energy, as in Dzombak and Morel, 1990) or non-electrostatic, in which case the energy associated with charging the mineral surface is captured directly in the equilibrium constant. Note that in the case of overlapping double layers, the conventional Coulombic corrections to the surface complexation constants that are proposed in Dzombak and Morel (1990) are not correct, as discussed by Goncalves et al (2007), since these are based on the assumption of an electrically neutral solution bordering the clay (or in terms of the electrostatic potential, an infinite half-space).

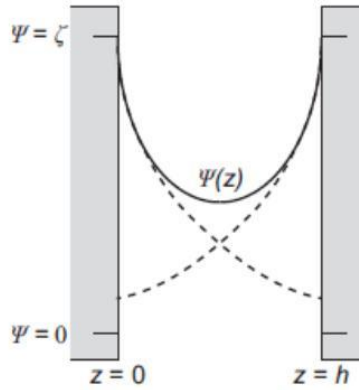


Figure 3.2. Schematic representation of the potential distribution in a nanochannel with height h in direction z when the EDLs overlap (solid line), compared to the EDL potentials if the opposite wall is not present (dashed line). From Schoch et al. (2008).

3.1.2 Dynamic Calculation of Electrical Double Layer Thickness

CrunchEDL also now includes a dynamic calculation of the electrical double layer porosity, ϕ^{EDL} , based on the diffuse layer thickness as a function of ionic strength according to

$$\phi^{EDL} = A_{clay} \lambda_{DL} D_L = A_{clay} \lambda_{DL} \frac{\beta_{DL}}{\sqrt{I}} \quad (3.14)$$

where D_L is the Debye length, λ_{DL} gives the multiples of the Debye length used in calculating the electrical double layer porosity (as in the approach of Tournassat and Appelo, 2011), β_{DL} is a temperature-dependent factor ($= 2.15 \times 10^{-10}$ meters at 25°C), I is the ionic strength of the bulk

solution, and A_{clay} is the surface area of the charged mineral surfaces (normally clays). The Debye length provides an approximate measure of the width of the electrical double layer, although in their Donnan or mean electrostatic model, Tournassat and Appelo (2011) included as many as five Debye lengths to describe the EDL porosity.

Previously we have presented results in which the ionic strength is constant over the domain. It is also possible, however, to consider transient cases in which a salinity front propagates through the domain, changing the Debye length and thus the diffuse layer porosity dynamically. Note that in this case, the EDL thickness and thus the transport properties of the compacted bentonite are modified by the changing ionic strength. The effect is different from the swelling behaviour described in Section 2, and may in fact work in the opposite way.

In the CrunchEDL approach in which solute mass is tracked in both the bulk porosity and the diffuse layer (EDL) porosity, this gives an accumulation term (neglecting liquid saturation) of

$$\frac{\partial [\phi^B C_i^B + \phi^{EDL} C_i^{EDL}]}{\partial t} = \frac{\partial \left[\phi^B C_i^B + \left(\frac{A_{clay} \lambda_{DL} \beta_{DL}}{\sqrt{I}} \right) C_i^{EDL} \right]}{\partial t}. \quad (3.15)$$

In this case, the bulk porosity is treated as a constant, or at least as separately determined or fixed. Since the total porosity then can increase or decrease as the EDL thickness changes, special considerations need to be made to conserve mass in the system. Alternatively, it is preferred to treat the total porosity (bulk and EDL) as constant, in which case the bulk and EDL porosities would be updated according to:

$$\frac{\partial \left[(\phi^{Tot} - \phi^{EDL}) C_i^B + \phi^{EDL} C_i^{EDL} \right]}{\partial t} \quad (3.16)$$

where ϕ^{Tot} is the total porosity = $\phi^B + \phi^{EDL}$.

The processes represented by Eqs. (3.15) and (3.16) are captured in a test problem in which a higher ionic strength solution (0.45M) propagates through a 10 cm long column of compacted bentonite that initially has a lower ionic strength (0.045M). In Figure 3.3, the total porosity is fixed at 4%, while the EDL porosity is predicted to change from 3.11% at the lower ionic strength to 0.98% at the higher ionic strength after 5 days of diffusion in the case where a single Debye length in Eq. (3.15) is used to describe the EDL porosity. As a result of the changes in the EDL thickness (and porosity), the bulk porosity changes according to Eq. (3.16) from 0.89% to 3.02% as the salinity front diffuses through the domain. The simulation was carried out by applying Dirichlet and no-flux boundary conditions at the left and right boundaries, respectively. The decrease in the EDL thickness as a result of the salinity front (here considered purely in terms of ionic strength, rather than the specific hydration properties of the cations) results in an increase in the bulk porosity, which should normally increase transport rates for all ions, but particularly for the anions that are either partially excluded or forced to follow more tortuous diffusion paths than would be the case for either cations or uncharged species.

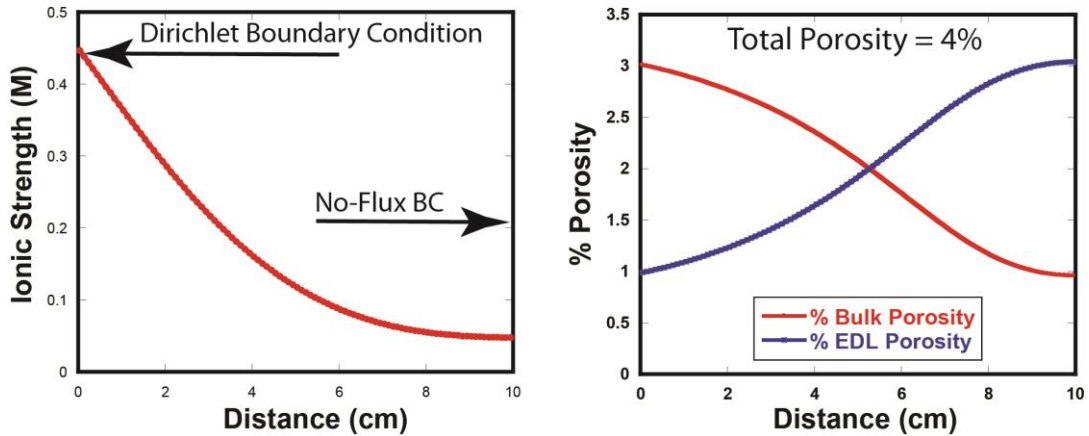


Figure 3.3. Results of dynamic EDL porosity calculations after 5 days of diffusion. Left panel: A high ionic strength front ($I=0.45M$) diffuses front left to right through the domain that is initially lower ionic strength ($I=0.045M$). The left boundary is a Dirichlet boundary condition, while the right boundary is no-flux. Right panel: Spatial profiles for bulk porosity and EDL porosity for the case of a constant total porosity of 4%.

3.1.3 Testing of EDL Model using the DR-A Experiment at Mont Terri, Switzerland

To test the EDL transport model developed and described here, we have used it to simulate non-reactive and reactive transport processes in the DR-A experiment at Mont Terri in Switzerland. While the Mont Terri site consists of Opalinus Clay, a primarily marly claystone with differing proportions of sand and carbonates. The Opalinus Clay is about 180 million years old. The stratigraphic section in which the Mont Terri site is located is shown in Figure 3.4. The Opalinus Clay is characterized by a very low permeability, which makes diffusion the dominant mode of solute transport (in this respect, similar to compacted bentonite under normal conditions).

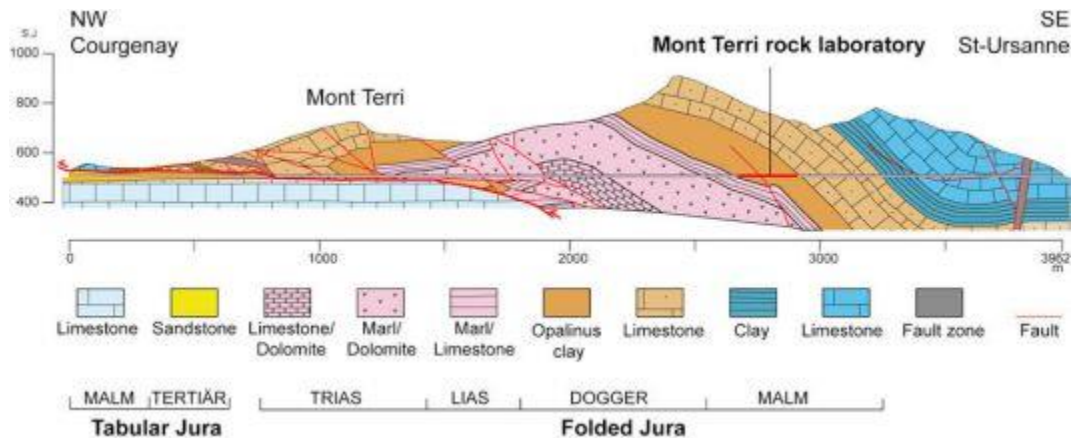


Figure 3.4. Stratigraphic section of the Jura Mountains in which the Mont Terri rock laboratory is located.

The DR-A test to date has consisted of a single borehole drilled in the Opalinus Clay that contains a constant ionic strength cocktail and anions, cations, and non-reactive tracers like

tritium (HTO). An experiment in which the ionic strength is varied is underway now and will be the subject of modeling and simulation to be carried out in the next phase. Figure 3.5 shows the experimental setup used for the earlier DI-A test at Mont Terri. The key point is that there is a volume of cocktail in excess of the actual cylindrical volume through which solutes diffuse into the Opalinus Clay. This is treated in CrunchEDL by defining a capacity factor, α ($= 2.175$), that represents the additional volume needed to accommodate the extra solution volume (11.2 L) available to the actual borehole volume. Doing so and solving in radially symmetric cylindrical coordinates produces the fit of the actual HTO (tritium) data (Figure 3.6).

Table 3.1. Parameters for DR-A test

Length of injection interval	104 cm
Length of filter screen	67 cm
Volume of circulation system	11.2 L
Borehole diameter	76 mm
Filter, outer diameter	70 mm
Filter, inner diameter	62 mm
Filter, porosity	45%
Gap between filter and borehole wall	3 mm
Central tube, outer diameter	61 mm
Dip of bedding	32.5°
Porosity of Opalinus Clay	15%

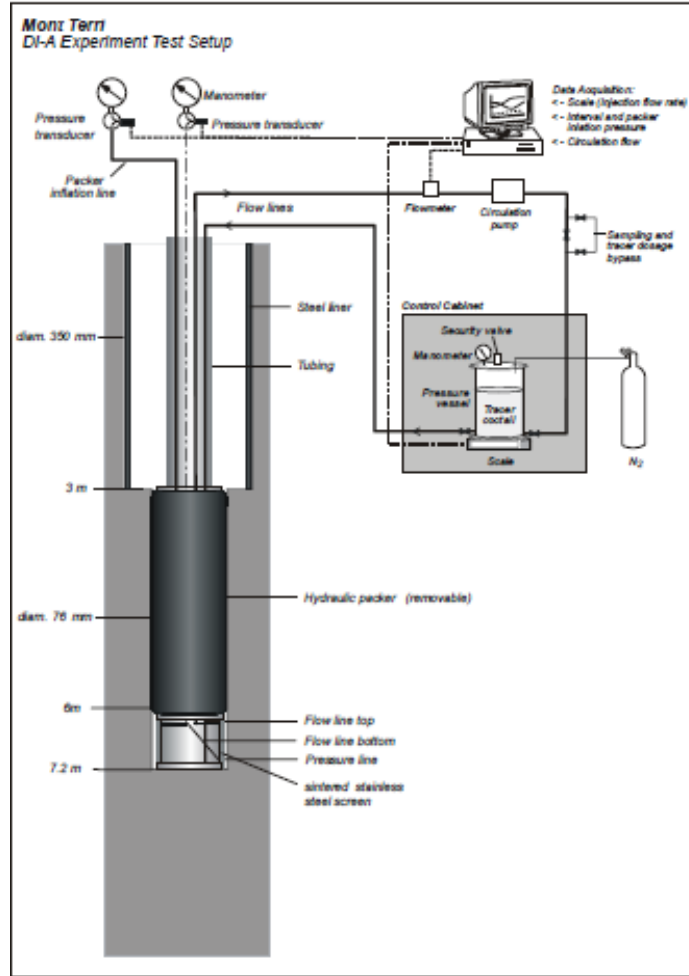


Figure 3.5. Schematic of the experimental setup from the DI-A test, similar in concept to the DR-A test.

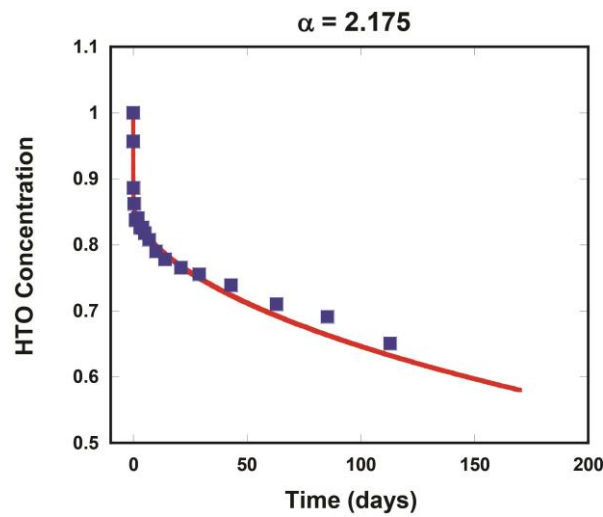


Figure 3.6. Fit of borehole HTO concentration versus time using a capacity factor of 2.175. This is solved in radially symmetric cylindrical coordinates using CrunchEDL.

The same system is then solved for the time evolution of the anions iodide and bromide in the borehole using a diffusion coefficient of $10^{-6} \text{ cm}^2/\text{s}$ (an order of magnitude slower than the cations and HTO) for the anions in the EDL and one Debye length to define the EDL porosity (Figure 3.7). This is carried out assuming Stern layer sorption, with 20% of the rock made up of illite with $5 \times 10^{-7} \text{ sites}/\text{m}^2$ having a specific surface area of $200 \text{ m}^2/\text{g}$. Note the slower decrease in concentration of the anions relative the HTO in the borehole as a result of anion exclusion in the Opalinus Clay.

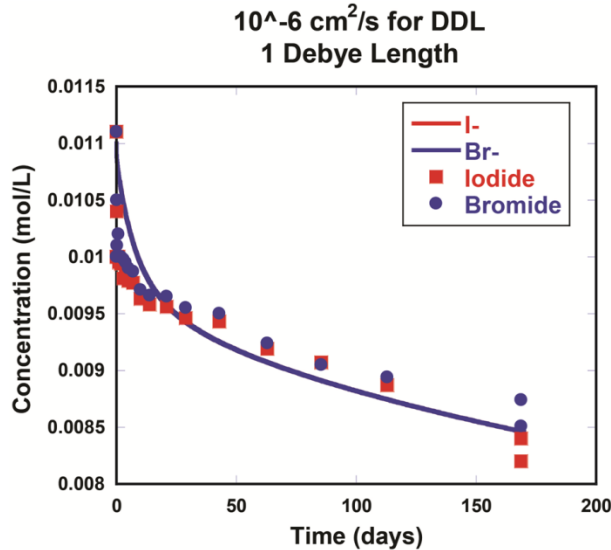


Figure 3.7. Anion concentration versus time in the borehole for the first DR-A test.

3.1.4 Development of a CrunchEDL-Comsol Coupling for Flow and Transport in Charged Porous Media

Now under development is a new coupling of the reaction portion of CrunchEDL with the general purpose flow and transport code Comsol. While CrunchEDL can handle transport through porous media, it is not as well suited to handle pore scale flow and transport, or Navier-Stokes flow in general. The Comsol coupling offers the ability to include Navier-Stokes or Darcian flow, while still solving the full Nernst-Planck equation (as CrunchEDL does). Figure 3.8 shows a schematic of the coupling procedure between Comsol and CrunchEDL. Followed by an initialization (including initial and boundary condition speciation), the primary exchange between the two routines are the total concentrations, the individual species concentrations when the full Nernst-Planck equation is desired, and the charge density. Total concentrations in the bulk and EDL porosity are tracked and transported separately.

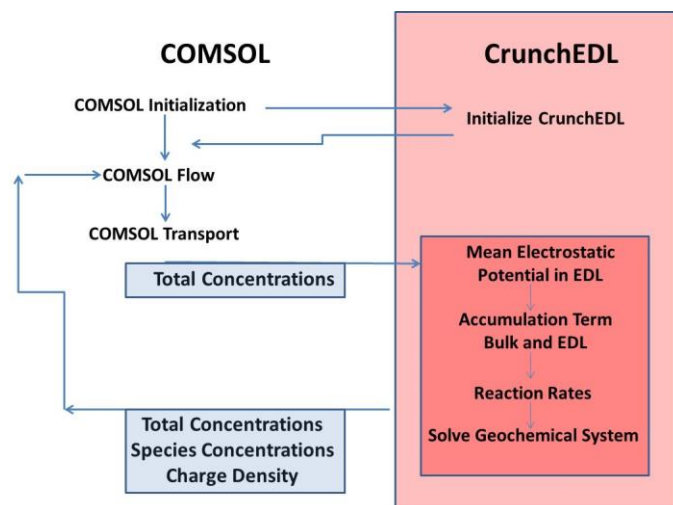


Figure 3.8. Illustration of the coupling scheme between Comsol and CrunchEDL.

3.2 Molecular scale predictions of diffusion in the EBS

3.2.1 Temperature Dependence of Water and Solute Diffusion in the EBS

As noted above, predicting the long-term performance of engineered and natural clay barriers near high-level radioactive waste (HLRW) repositories requires a fundamental understanding of the rates of molecular diffusion in these barriers. The diffusion of water and ions in water-saturated compacted clay barriers has, therefore, been extensively characterized, though mostly at ambient temperatures (Molera and Eriksen, 2002; Molera et al., 2003; Nakashima, 2003; Sato, 2003; Wang et al., 2005; Melkior et al., 2009; Tachi et al., 2010; Glaus et al., 2011; Tanaka et al., 2011; Holmboe et al., 2011).

Because of the large heat flux generated by high-level radioactive waste, the design of HLRW repositories requires knowledge of the self-diffusion coefficients (D) of water and solutes in compacted bentonite over a broad range of temperatures (roughly 283 to 368 K—JNC, 2000; SKB, 2009). The temperature dependence of diffusion (expressed as the activation energy of diffusion E_a through the Arrhenius relation $D \propto \exp(-E_a/RT)$, where R is the ideal gas constant and T is absolute temperature) also is of interest, because it is a *macroscopic scale* property that directly reflects—if tortuosity and other features that determine the geometric factor of the porous medium are invariant with T —the potential energy landscape explored by the diffusing species at the *pore scale*.

The vast majority of measurements of solute E_a values in compacted bentonite were reported by Kozaki and co-workers (Kozaki et al., 1996, 1997, 1998, 1999, 2001, 2005, 2008, 2010; Liu et al., 2003) from diffusion experiments with centimeter scale samples of compacted water-saturated montmorillonite, a common type of smectite. These experiments probed a range of temperatures ($T = 278$ to 323 K), dry bulk densities ($\rho_b = 0.7$ to 1.8 kg dm⁻³), solutes (Na, Cs, Sr, Cl), ionic strengths ($I = 0$ to 0.5 mol dm⁻³ NaCl), and type of counterion (Na-, Ca-, and mixed Na/Ca-montmorillonite). The results showed that solute E_a values have a particularly strong dependence on dry bulk density. In the case of Na⁺ self-diffusion in Na-montmorillonite, according to Kozaki et al. (2005), E_a equals $\sim 18.5 \pm 1.5$ kJ mol⁻¹ (consistent with the value in

bulk liquid water) at low dry bulk densities ($\rho_b \leq 0.8 \text{ kg dm}^{-3}$), $\sim 15.5 \pm 1.5 \text{ kJ mol}^{-1}$ at intermediate dry bulk densities ($\rho_b = 0.9 \text{ to } 1.2 \text{ kg dm}^{-3}$), and $\sim 25 \pm 2 \text{ kJ mol}^{-1}$ at high dry bulk densities ($\rho_b \geq 1.6 \text{ kg dm}^{-3}$).

In the case of water diffusion, E_a values in water-saturated smectite have been studied by a number of research groups using both macroscopic scale diffusion experiments (Nakazawa et al., 1999; Nakashima, 2000; Suzuki et al., 2004; Gonzalez-Sánchez et al., 2009) and quasi-inelastic neutron scattering (QENS) experiments (Gonzalez-Sánchez et al., 2009; Marry et al., 2011). These studies yielded conflicting results, with two groups (Nakazawa et al., 1999; Nakashima, 2000) reporting E_a values of 15 to 19 kJ mol^{-1} [near the value for bulk liquid water, $17.4 \pm 0.2 \text{ kJ mol}^{-1}$ in the temperature range 278-353K (Holz et al., 2000)] and three groups (Suzuki et al., 2004; Gonzalez-Sánchez et al., 2009; Marry et al., 2011) reporting E_a values of 19 to 23 kJ mol^{-1} in overlapping ranges of dry bulk density.

Molecular dynamics (MD) simulations are routinely used to gain insight into the molecular scale basis of water and solute diffusion in nanoporous materials, including clay interlayers (Sposito et al., 1999; Marry and Turq, 2003; Malikova et al., 2004a,b, 2005; Rotenberg et al., 2007a,b; Kosakowski et al., 2008; Marry et al., 2008, 2011; Mazo et al., 2008; Tournassat et al., 2009; Bourg and Sposito, 2010, 2011a,b; Botan et al., 2011; Pitman and van Duin, 2012). For example, molecular simulations helped reveal that most cations (with the notable exception of the weakly solvated cations K^+ , Rb^+ , and Cs^+) adsorb on smectite surfaces primarily as outer-sphere surface complexes (Sposito et al., 1999; Bourg and Sposito, 2011a); that ion adsorption on smectite basal surfaces is roughly consistent with the well known triple layer model (Tournassat et al., 2009; Bourg and Sposito, 2011b); and that the primary diffusion pathway of cations in compacted bentonite is through smectite interlayer nanopores (Rotenberg et al., 2007a; Bourg and Sposito, 2010). In principle, this type of simulation can readily predict the T -dependence of water and solute diffusion in clay interlayer nanopores. At present, however, only a handful of MD simulation studies have investigated diffusion in hydrated clay systems at non-ambient temperatures (Malikova et al., 2004a,b; Mazo et al., 2008; Marry et al., 2011; Pitman and van Duin, 2012). This scarcity results from a combination of methodological difficulties, as noted below.

The first difficulty in predicting E_a from MD simulations of clay interlayer nanopores is that simulation results can be highly sensitive to the choice of interatomic potential parameters (the main input of these simulations). Most interatomic potential models are parameterized to describe the properties of a system of interest at a specific temperature, and they sometimes fare poorly when used to simulate the same system at different temperatures (Vega et al., 2005). In the case of clay-water systems, the CLAYFF model, when used in combination with the SPC/E water model, has been successfully tested against the properties of interlayer water at 298 K (Cygan et al., 2004; Bourg and Sposito, 2010; Ferrage et al., 2011). This set of interatomic potential parameters remains almost entirely untested with regard to its ability to accurately predict the properties of clay-water systems at temperatures far beyond ambient conditions—with the exception of a study by Marry et al. (2011) that showed that it predicts the T -dependence of water diffusion in the one-layer hydrate of Na-hectorite more accurately than the widely used clay model of Skipper and coworkers (Skipper et al., 1991, 1995).

A second difficulty is that the D values of fluids and solutes obtained by MD simulation are influenced by the periodic boundary conditions of the simulation cell. This well-known artifact

originates from the viscous coupling between the particles and their neighboring image particles, resulting in a reduced D value. In simulations of bulk liquids in a cubic simulation cell of length L , this effect is inversely proportional to the simulation cell size according to the theoretical relation (Placzek et al., 1951; Yeh and Hummer, 2004a,b; Zeebe, 2011):

$$D_s = D_{\text{PBC}} + \frac{k_B T \xi}{6\pi\eta L} \quad (3.17)$$

where D_s is the size-corrected diffusion coefficient, D_{PBC} is the diffusion coefficient predicted using periodic boundary conditions, k_B is Boltzmann's constant, $\xi \approx 2.837297$ is the so-called self-term for a cubic lattice, and η is the viscosity of the medium. The finite-size correction (the last term in Eq. (3.17)) has the same temperature dependence as the ratio $T/\eta(T)$. Therefore, the T -dependence of D_s is not *a priori* equal to the T -dependence of D_{PBC} . For bulk fluids, MD simulation results (i.e., D_{PBC} values) can be converted to D_s values using Eq. (3.17) if the viscosity of the fluid is known. In hydrated clay systems (or in any other heterogeneous system), however, the applicability of Eq. (3.17) is unknown. Therefore, accurate predictions of E_a in clay interlayer nanopores require carrying out multiple simulations of the system of interest with a range of simulation cell sizes, for each temperature of interest. To our knowledge, this has never been carried out for a hydrated clay or any other nanoporous system.

A third difficulty is that the influence of temperature on the initial hydration and swelling of smectite particles is not well characterized. At ambient conditions, stacked smectite layers have stable hydration states in which the interlayer nanopores contain zero, one, two, or three (or, for some smectites, four) statistical monolayers of water molecules (designated hereafter as 0W, 1W, 2W, etc.) with experimental basal spacings d_{001} of 9.5 to 10.1 Å (0W), 12.0 to 12.7 Å (1W), 15.0 to 15.7 Å (2W), 18 to 19 Å (3W) and 21.4 to 22 Å (4W) (Norrish, 1954; Kozaki et al., 1998; Saiyouri et al., 2004; Ferrage et al., 2007, 2011; Svensson and Hansen, 2010; Holmboe et al., 2012). The range of reported values results from the fact that the water content per unit cell depends on the type of smectite (in particular, the magnitude of the negative structural charge and its origin from isomorphic substitutions in either the octahedral or the tetrahedral sheets) and the type of counterion. The values reported above were obtained at ambient temperatures, and their temperature dependence (which may influence the temperature dependence of D) is not known.

A fourth and final significant difficulty in predicting E_a is that the E_a values of interlayer water predicted by MD simulation are sensitive to the vibrational motions of clay structural atoms. Most previous MD simulations of hydrated clay systems treated the clay particles as rigid entities (i.e., the vibrational motion of clay atoms were prevented). Several authors have advocated the use of fully flexible clay lamellae (Kalinichev et al., 2000; Cygan et al., 2004), but data comparing simulations with rigid and flexible clay particles (and testing the results against experimental data) have not previously reported, to our knowledge.

To address the difficulties listed above, we performed a systematic analysis of the sensitivity of the D and E_a values of Na^+ and water in the interlayer nanopores of Na-montmorillonite to key methodological choices—the size of the simulated system (1285 to 61680 atoms), the internal degrees of freedom of the clay particles (from fully rigid to fully flexible)—for a range of temperatures ($T = 278$ to 353 K) and swelling states (1W, 2W, 3W, and 10W; with basal spacings of 12.4 to 40 Å). We focused particularly on the 2W and 3W hydration states, as X-ray diffraction (XRD) results show that in the KBS-3 concept (the reference concept for Sweden's

HLLRW repository), the montmorillonite particles in the engineered bentonite barrier form a mixture of the 2W ($d_{001} \sim 15.6 \text{ \AA}$) and 3W ($d_{001} \sim 18.9 \text{ \AA}$) states in proportions of 35–40% and 60–65% (Holmboe et al., 2012). To keep the size of this study reasonable, we used a single set of interatomic interaction parameters (the SPC/E water model, the CLAYFF force field) that have been found in several studies to accurately predict experimental data on the structure and dynamics of water and ions in smectite interlayer nanopores (Cygan et al., 2004; Bourg and Sposito, 2010; Ferrage et al., 2011; Marry et al., 2011). To test the accuracy of our MD simulation methodology and gain insight into the molecular scale basis of previously reported E_a values, we compared our MD simulation predictions with experimental results on the E_a values of Na^+ and water in compacted water-saturated Na-smectite.

3.2.2 Methodology

All MD simulations were carried out with the code LAMMPS (Plimpton, 1995). Interatomic interactions were modeled with the SPC/E water model (Berendsen et al., 1987) (treated as rigid using the SHAKE algorithm—Ryckaert et al., 1977), the Joung-Cheatham model of the Na^+ ion (Joung and Cheatham, 2008), and the CLAYFF force field (Cygan et al., 2004). CLAYFF assigns partial charges and van der Waals parameters to each atom type in the clay structure, along with a single physical bond stretch parameter for the structural O-H groups. Smectite particles are periodically layered two-dimensional aluminium phyllosilicates, consisting of an octahedrally coordinated metal-oxide sheet sandwiched between two tetrahedrally coordinated silicate sheets. Smectite particles hold a net negative structural charge because of isomorphic substitution by elements of lower valence in the tetrahedral and octahedral sheets. The smectite modeled in this study was a generic Wyoming type Na-montmorillonite with the unit cell formula $\text{Na}_{0.66}[\text{Al}_{3.33}\text{Mg}_{0.66}][\text{Si}_8]\text{O}_{20}[\text{OH}]_4$ having isomorphic substitutions of Al^{3+} by Mg^{2+} in the octahedral sheet. The montmorillonite lattice structure was based on a triclinic pyrophyllite structure taken from the literature (Bickmore et al., 2003) and was subjected to semi-random isomorphic substitutions, outlawing the simultaneous substitutions of neighboring octahedral sites sharing a OH group. Unless otherwise stated, the periodically replicated simulation cells enclosed two unique montmorillonite layers, each consisting of 45 unit cells (9×5 unit cells, extending ~ 46.6 and $\sim 45.9 \text{ \AA}$ in the lateral x and y directions, respectively) with Na^+ counterions and different amounts of water molecules in the interlayer nanopores. Production runs were carried out in the NVT ensemble (i.e., at fixed composition, volume, and temperature) at 278, 298, 323, and 353 K for a minimum of 5 ns. The production runs were preceded by 0.5 ns of simulation in the NPT ensemble (i.e., at fixed composition, pressure, and temperature) at 1 bar, to relax the montmorillonite layers and interlayers in the x, y , and z directions, and 1 ns simulation in the NVT ensemble to fully equilibrate the system. Electrostatic and dispersion interactions beyond a cut-off of 12 \AA were computed by Ewald summation. To avoid translational drift of the montmorillonite layers (Teppen et al., 1997; Cygan et al., 2004), the simulations in the NVT ensemble were performed by independently fixing the center of mass of the montmorillonite layers. For the simulations in the NP_zT ensemble (see, for instance, Figure 3.11), the center of mass was only occasionally fixed in the lateral directions and only for water contents corresponding to $> 2W$. For lower water contents, lateral translation of the clay sheets was prevented by the high transverse shear moduli of the 1W and 2W state, which have been estimated to be 20 and 2–4 GPa, respectively (Mazo et al., 2008).

Self-diffusion coefficients (D) were calculated from the slope of the mean square displacement $\langle l^2 \rangle$ using the well-known Einstein relation:

$$D = \frac{1}{2n} \lim_{\tau \rightarrow \infty} \frac{d\langle l^2 \rangle}{d\tau} \quad (3.18)$$

The infinite time limit in Eq. (3.18) was approximated by using probe time scales of $\tau = 150$ to 250 ps. The D values from the hydrated montmorillonite systems were calculated using $n = 2$, thus describing the two-dimensional diffusion in the interlayer nanopores. Error bars were estimated at the 95% confidence level, in most cases from five block-averaged values. Size-corrected diffusion coefficient D_s were obtained by extrapolating D versus inverse system size L^{-1} to $1/L = 0$. In the case of bulk liquid water, the Stokes-Einstein Brownian diffusion model (which predicts that $D \propto \eta^{-1}$) was used to estimate a “viscosity-corrected” D_s value (D_{sv}):

$$D_{sv} = D_s \frac{\eta_{\text{SPC/E}}}{\eta_{\text{exp}}} \quad (3.19)$$

where $\eta_{\text{SPC/E}}$ and η_{exp} are the simulated and measured viscosities of bulk liquid water.

From the D_s values obtained at the different temperatures, activation energies of diffusion (E_a) were calculated based on the slope of the linearized Arrhenius equation, using the standard error in the slope to calculate the 95 % confidence interval.

$$\ln D = \ln D_0 - E_a/RT \quad (3.20)$$

In order to account for the fact that our interatomic potential parameters underestimated E_a in bulk liquid water by a factor ΔE_a , we calculated a corrected value E_a^* with the relation:

$$E_a^* = E_a + \Delta E_a \quad (3.21)$$

The same correction would have resulted, equivalently, by multiplying all D_s values in clay interlayers by the ratio of the diffusion coefficients of the species of interest in real water *versus* SPC/E water ($D_{0,\text{exp}}/D_{0,s}$) at the temperature of interest.

The shear viscosity of SPC/E water was obtained from a separate set of simulations of 512 water molecules in the *NVT* ensemble at each corresponding temperature, by applying the standard Green-Kubo relations on the auto-correlation function of the stress tensor elements:

$$\eta = \frac{1}{5} \sum_{\alpha,\beta} \lim_{t \rightarrow \infty} \frac{V}{k_B T} \int_0^t \langle p_{\alpha\beta}(t) p_{\alpha\beta}(0) \rangle dt \quad (3.22)$$

where $p_{\alpha\beta}$ are the five anisotropic components of the stress tensor, i.e., the off-diagonal elements p_{xy} , p_{xz} , p_{yz} and the differences between the diagonal elements $(p_{xx}-p_{yy})/2$ and $(p_{yy}-p_{zz})/2$ (Yeh and Hummer, 2004a; Chen et al., 2009; Medina et al., 2011; Tazi et al., 2012). The stress tensor elements were recorded every 2 fs for 10 ns. By comparing different relaxation times for the autocorrelation function (from 1 to 10 ps) and the uncertainties in the block-averaged viscosities at the 95% confidence level, the suitable integration times (t) were found to be, with increasing temperature, 8, 5, 3, and 2 ps, respectively.

3.2.3 Results and Discussion

3.2.3.1 Diffusion in bulk liquid water

In order to establish the influence of clay particles on the D and E_a values of water and sodium, we first determined the ability of our MD simulation methodology to predict water and Na^+ diffusion in bulk liquid water. Figure 3.9 shows the D values of water and Na^+ in bulk liquid

water (calculated with Eq. (3.18)) as a function of the reciprocal simulation cell size (L^{-1}) for systems containing 512, 2778, or 22224 water molecules. For each temperature, the solid line shows the linear regression of the plotted data, whereas the dashed line is the best fit obtained with Eq. (3.17) using the viscosity η of SPC/E water (Figure 3.10). By comparing the slope of this extrapolated line with the slope obtained from Eq. (3.17), we find that in the case of Na^+ , Eq. (3.17) correctly predicts the size dependence of D . In the case of water (where the D values are much more precisely known because of the larger number of water molecules than Na^+ ions in our simulations), Eq. (3.17) predicts the correct size dependence at ambient temperature (298 K). At lower temperatures, the size dependence predicted by Eq. (3.17) is slightly too small; at higher temperatures, it is too large.

For each temperature, a size-corrected $D_{0,s}$ value was obtained by extrapolating the D versus L^{-1} data in Figure 3.9 to infinite size using linear regression. As shown in Table 3.2, the resulting $D_{0,s}$ values underestimate the E_a values of water and Na^+ in bulk liquid water by $\Delta E_a = 2.8 \pm 0.6$ and 0.7 ± 0.3 kJ/mol, respectively. To determine whether this effect can be explained by the fact that the SPC/E model underestimates the T -dependence of η , we used a relation based on the Stokes-Einstein model of Brownian diffusion (Eq. 3.19) to calculate a “viscosity-corrected” diffusion coefficient $D_{0,sv}$. Our results show that viscosity alone cannot fully explain the disagreement between predicted and measured E_a values.

Our results on the viscosity of SPC/E water are consistent with previously reported data (Medina et al., 2011). The slight difference with the results of Medina et al. (2011) may arise from the fact that we did not set the density of the SPC/E water to the experimental water density. This was necessary because we did not impose the density of water in the simulations of hydrated montmorillonite. As seen in Figure 3.10, the SPC/E water model overestimates the density of liquid water by up to 1.8%.

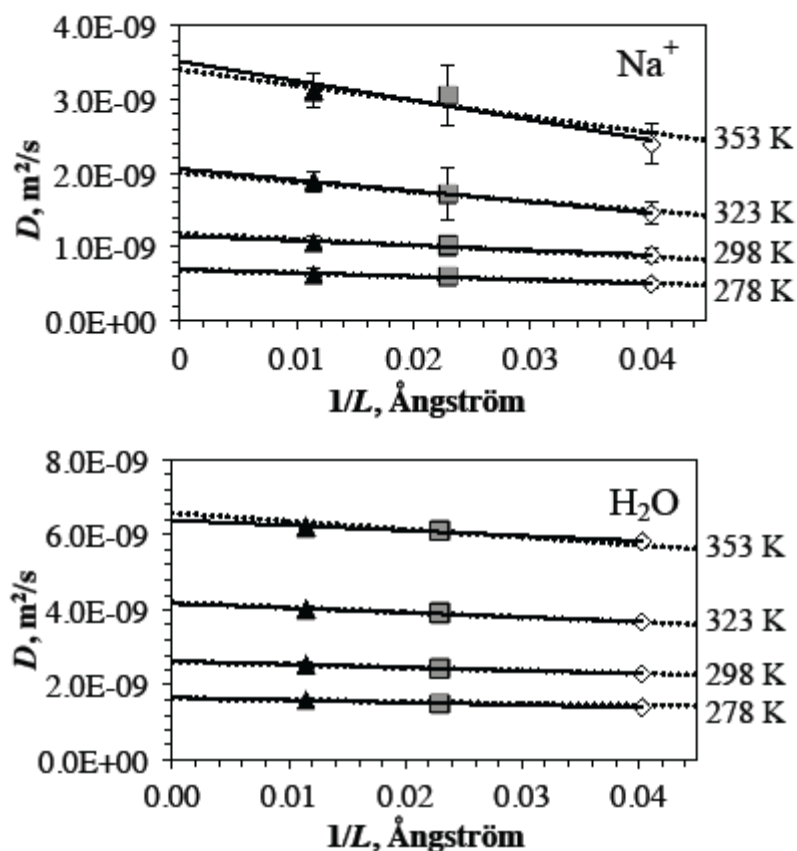


Figure 3.9. D values of Na^+ (top) and water (bottom) as a function of inverse simulation cell size (for simulations with 512, 8334, or 22224 water molecules) at different temperatures. The size-corrected diffusion coefficient $D_{0,s}$ is determined by linear regression (black line) to $1/L = 0$. The dashed line shows the best fit obtained with Eq. (3.17) using the viscosity of SPC/E water.

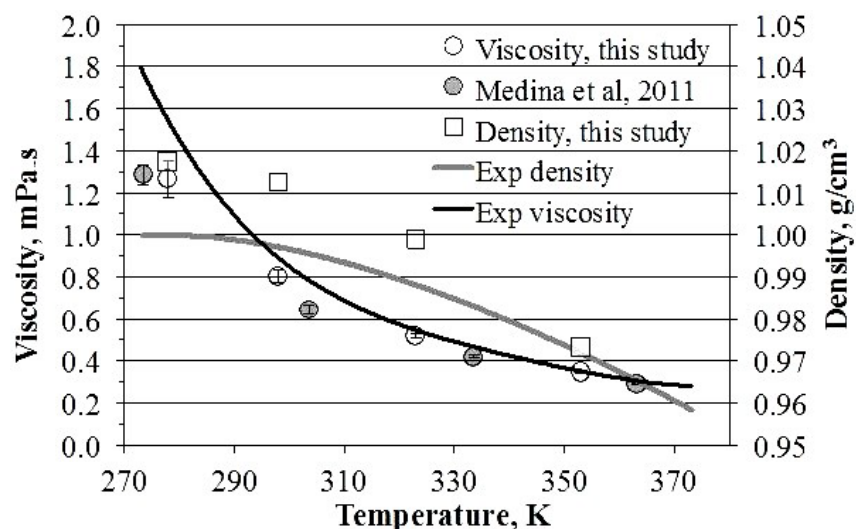


Figure 3.10. Comparison of the shear viscosity of the SPC/E water model, from this study (white circles) and from Medina et al. (2011) (gray circles), with the experimental viscosity of water (Lide, 2012) (black line). Right hand axis indicates our simulated (white squares) and the experimental (gray line) water density, respectively.

Table 3.2. Shear viscosity of water and self-diffusion coefficients of Na^+ and water in bulk liquid water. Predicted D values are shown for simulations with 512 water molecules (D), after correction for the finite-size effect ($D_{0,s}$), and after correction for both size and viscosity ($D_{0,sv}$). The subscript ‘exp’ denotes experimental values (Talekar, 1977; Holz et al., 2000).

T [K]	Viscosity [mPa.s]		Na^+ [10^{-9} .m ² /s]				H_2O [10^{-9} .m ² /s]			
	$\eta_{SPC/E}$	η_{exp}	D (24Å)	$D_{0,s}$	$D_{0,sv}$	$D_{0,exp}$	D (24Å)	$D_{0,s}$	$D_{0,sv}$	$D_{0,exp}$
278	1.266±0.087	1.514	0.50±0.06	0.69±0.03	0.56±0.02	0.752	1.40±0.01	1.66±0.02	1.39±0.02	1.303
298	0.804±0.031	0.891	0.88±0.10	1.15±0.04	1.03±0.03	1.335	2.29±0.01	2.63±0.01	2.37±0.01	2.299
323	0.520±0.008	0.548	1.45±0.15	2.06±0.01	1.95±0.01	2.314	3.68±0.04	4.17±0.04	3.96±0.04	3.956
353	0.345±0.006	0.355	2.39±0.27	3.51±0.24	3.41±0.24	3.859	5.83±0.06	6.39±0.06	6.21±0.04	6.557

3.2.3.2 Basal spacing and water content of clay nanopores

As noted in the introduction, the basal spacing and water content of smectite are not precisely known. For example, previous MD simulation studies of smectite interlayer nanopores used either 4 (Kosakowski et al., 2008), 4.5 (Marry and Turq, 2003; Malikova et al., 2005), or 5 (Bourg and Sposito, 2010) water molecules per unit cell per hydration layer. Our tests with 4, 5, or 6 water molecules per unit cell per hydrate layer (not shown) indicated that the D values of interlayer water and Na^+ are highly sensitive to the water content of the interlayer: an increase in water content from 4 to 5 or from 5 to 6 water molecules per unit cell and hydration layer caused the D values of interlayer water and Na^+ to increase by on average 15–20%, decreasing with increasing temperature. A small but significant decrease in the E_a of diffusion was also found (not shown) as well as a substantial increase in d_{001} with increasing water content. Our tests also showed that the unit cell volume of Na-montmorillonite increases slightly in the temperature range from 273 to 353 K, primarily because of the T -dependence of the d -spacing: from 273 to 353 K, d_{001} increased by about 1 Å (as shown by the black crosses in Figure 3.3 in the case of systems with 12, 15, or 18 water molecules per unit cell), whereas the unit cell area ab increased by only 0.1 Å².

The comparison between experimental (Holmboe et al., 2012) and simulated d_{001} data in Figure 3.11 shows that each statistical water monolayer contains about 5 water molecules per montmorillonite unit cell. This finding is supported by the fact that the density of interlayer water (calculated from the d_{001} value, the effective montmorillonite layer thickness, and the unit cell area), when plotted as a function of water content, oscillates with a periodicity of almost exactly 5 water molecules per unit cell (Figure 3.11). The effective montmorillonite thickness (9.25 Å) was obtained by extrapolating the slope of d_{001} in the linear regime at high water contents to the fully dehydrated state. Interestingly, the unit cell area increased by about 1% with decreasing water content. The density maxima of interlayer water (Figure 3.11) are consistent with the density of bulk liquid water shown in Figure 3.9. Similar simulations with other types of smectites (not shown) indicate that this is not always the case for the 1W state.

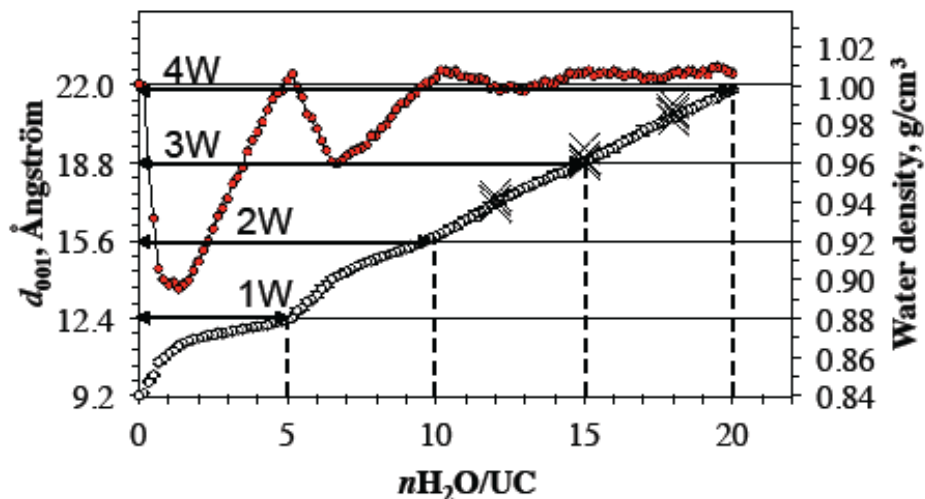


Figure 3.11. Basal spacing d_{001} (open circles) and interlayer water density (filled circles) as a function of the number of water molecules per unit cell (UC) in a MD simulation where the number of water molecules was slowly decreased by removing one water molecule every 40 ps (NP_zT ensemble). Experimental data on the d_{001} -values of the 1W, 2W, 3W, and 4W hydrate states of montmorillonite (Holmboe et al., 2012) are shown as black horizontal arrows. The precision of predicted d_{001} values is roughly 0.1 Å. Black crosses show the d_{001} values predicted from NP_zT ensemble simulations with 12, 15, or 18 water molecules per unit cell at $T = 278$ to 353 K.

3.2.3.3 Simulation cell size dependence of D in MD simulations of clay nanopores

In order to determine the size dependence of D in MD simulations of montmorillonite nanopores, a set of simulations of the 2W and 3W hydration states was conducted using nearly cubical simulation cells, with simulation cell sizes ranging from 24.3 to 86 Å (1285 to 61680 atoms; Figure 3.12). Interestingly, and contrary to the behavior observed in simulations of bulk liquid water (Figure 3.9), the D values of Na^+ and water in clay nanopores had no significant size dependence. This is illustrated in Figure 3.13 in the case of the 3W hydration state for $T = 273$ to 353 K. Similar results were obtained for the 2W hydration state, as well as for the 3W hydration state using fully rigid clay layers (not shown). A few of the datasets on D vs. $1/L$ (for instance for water at 353K in Figure 3.13) could be consistent with a size dependence of D , but the absence of a consistent trend between simulations at different temperatures or with different pore sizes indicates that this is likely caused by the use of different individual montmorillonite layers, each having a different configuration of isomorphic substitutions. According to Eq. (3.17), the invariance of D with $1/L$ indicates that the effective viscosity of the clay-water system is much higher than that of bulk liquid water or, equivalently, that viscous interactions in the clay-water system are much more short-ranged than in bulk liquid water. The absence of a size dependence of D in our simulations of the 2W and 3W hydration states would likely also be observed in simulations of the 1W hydration state. Simulations of larger pores (such as the 10W hydrate) may have a system size dependence intermediate between that observed in the 3W hydrate and in bulk liquid water. Hereafter, we use systems with two clay layers (90 unit cells) to probe the 1W, 2W, and 3W hydration state, and a system with one clay layer (45 unit cells) to probe the 10W hydration state (Figure 3.14).

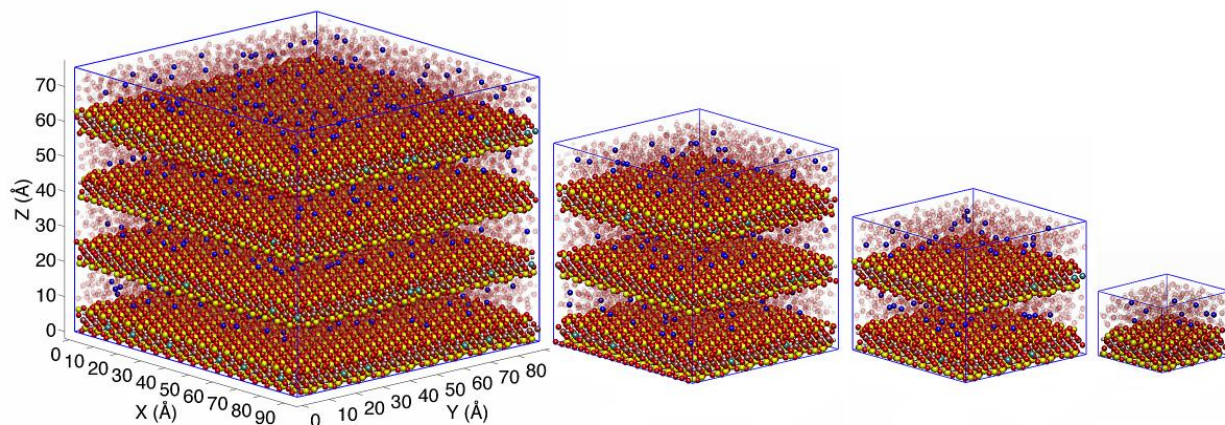


Figure 3.12. MD simulation snapshots showing the four different simulation cells that were used to study the 3W hydrate of montmorillonite. From left to right, the systems contained 61680, 16962, 7710 and 1285 atoms corresponding to $(18 \times 10 \times 4)$, $(11 \times 6 \times 3)$, $(9 \times 5 \times 2)$, and $(5 \times 3 \times 1)$ unit cells in the $(a \times b \times c)$ directions, respectively.

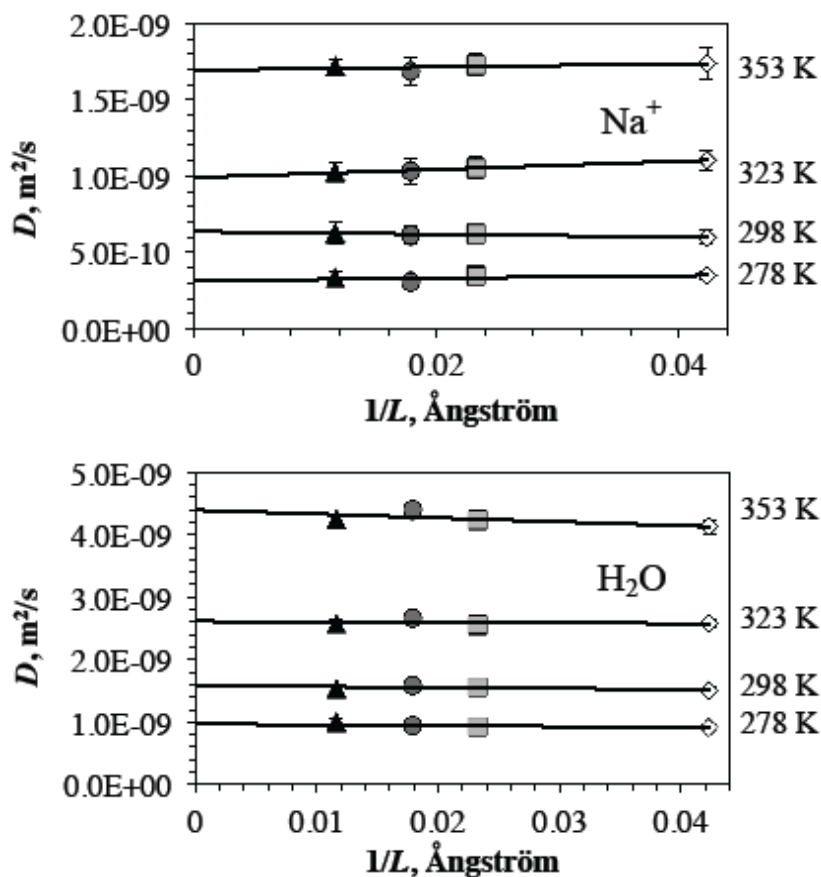


Figure 3.13. D values of Na^+ (top) and water (bottom) as a function of temperature and the mean inverse simulation cell size $1/L$.

3.2.3.4 Influence of clay layer rigidity

In order to investigate the influence of the vibrational motions of clay atoms on the structure and dynamics of interlayer water and solutes, simulations were carried out with clay layers that were either fully rigid, fully flexible, or semi-flexible. For the last state, either all atoms in the clay layer were kept fixed except the hydroxyl hydrogens (“flex O-H”), or vice versa (“rigid O-H”). Our results show that clay-layer rigidity has no significant influence on the one-dimensional atomic density profiles of interlayer species along the direction normal to the clay surfaces (representative density profiles are shown in Figure 3.14 in the case of the fully flexible systems) or on the coordination of interlayer species. In all systems having rigid or semi-flexible clay layers, small and localized irregularities were found in two-dimensional density maps displaying the preferential locations of water oxygen and hydrogen atoms above the clay siloxane surface. These artifacts stem from the fact that we carried out all equilibration runs using fully flexible clay particles, as described in Section 3.2.2, which unavoidably resulted in small irregularities in the coordinates of structural clay atoms in the production runs that used rigid or semi-flexible structures. To determine the influence of this effect on the D values of interlayer species, we conducted a comparative set of simulations of the 3W hydration state equilibrated in two different ways, using either our default methodology or an optimized clay structure for the production run, in which the positions of all structural clay atoms were fixed to their median positions during the final 100 ps of the equilibration run. The second equilibration method yielded two-dimensional density maps with no localized irregularities. This second equilibration method yielded one-dimensional density profiles in the direction normal to the clay surface that were slightly narrower than those obtained with the default methodology, indicating that structural disorder arising from the vibrational motions of structural clay atoms causes a slight broadening of the density distribution features of nanopore species. The differences in the D values of Na^+ and water obtained with the two methods of equilibration were found to be small and often insignificant, especially for the systems simulated with a fully rigid clay layer.

The normalized $D/D_{0,s}$ values of Na^+ and water for the same systems at the different degrees of clay-layer rigidity are shown in Figure 3.15. For all hydration states and temperatures investigated, simulations with fully flexible clay structures consistently resulted in higher D values for both Na^+ and water in the interlayer nanopores compared to simulations with fully rigid clay particles, regardless of equilibration method. For the two types of systems with semi-flexible clay layers, the D values of Na^+ and water were indifferent from each other and intermediate between the D values obtained with fully rigid or fully flexible clay structures. This reveals that the influence of clay flexibility arises roughly equally from the motions of structural H atoms and from the motions of all other atoms.

The influence of clay vibrational motions on interlayer D values increases sharply as water content decreases, demonstrating the short-ranged nature of this effect. For instance, for the 1W hydration state, the D value of Na^+ in contact with a fully flexible clay particle was higher by a factor of four compared to the corresponding value in contact with a fully rigid clay particle. For the 3W hydration state, the difference was approximately 25%, and for the 10W hydration state, no significant difference was detected. These findings demonstrate the importance of using a flexible clay structure when studying diffusion in clay nanopores. Although no significant effect was found at the highest hydration state for Na^+ or water, this may not be true for other types of counter-ions that predominantly form inner-sphere surface complexes, such as K^+ or Cs^+ .

Table 3.3 summarizes the D values of Na^+ and water for each hydration state and temperature modeled with fully flexible clay layers (along with the ratio $D_{0,\text{exp}}/D_{0,\text{s}}$ for each species at each temperature). These pore scale diffusion coefficients are not directly equivalent to the “apparent” diffusion coefficient obtained from macroscopic scale diffusion experiments (Marry and Turq, 2003; Kosakowski et al., 2008; Bourg and Sposito, 2010). This is because our MD simulations inherently cannot describe pore-network-scale geometric effects such as tortuosity and pore connectivity. Nevertheless, macroscopic scale diffusion coefficients can in principle be estimated from our predicted pore scale diffusion coefficients if the relevant microstructural parameters are known (Marry et al., 2003; Gonzalez-Sánchez et al., 2009; Bourg and Sposito, 2010; Churakov and Gimmi, 2011).

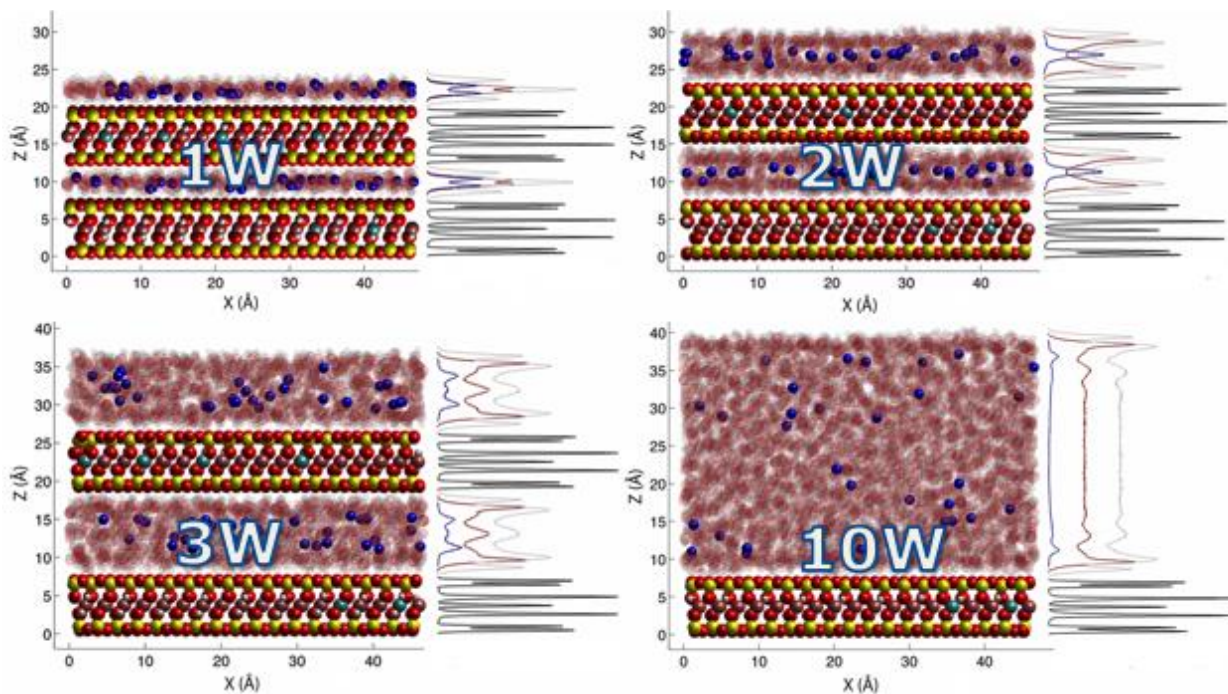


Figure 3.14. MD simulation snapshots showing the 1W, 2W, 3W and the 10W hydration states (with $d_{001} = 12.4, 15.6, 18.8,$ and 40.7 \AA , respectively) at 298 K and the corresponding atomic density profiles along z -direction for Na^+ (blue), H_{water} (light gray), O_{water} (red) and montmorillonite (black).

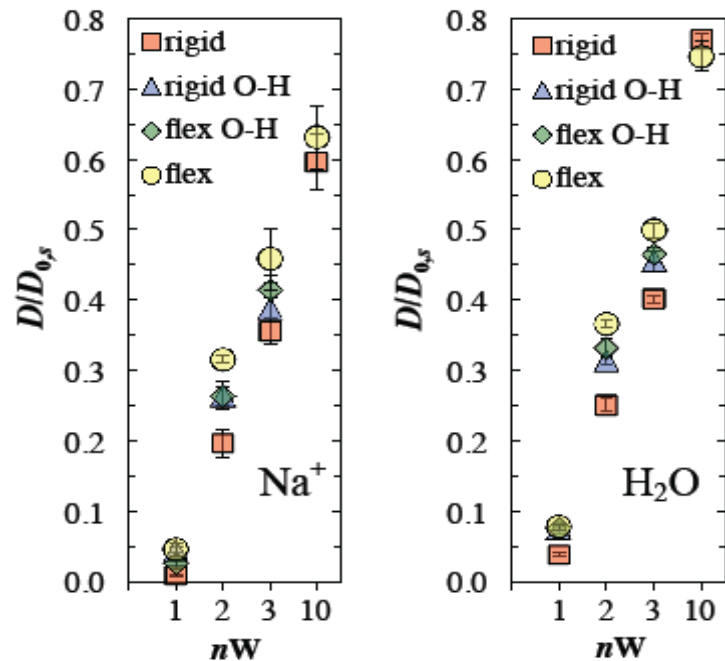


Figure 3.15. Normalized self-diffusion coefficients of Na^+ (left) and water (right) as a function of clay layer rigidity and hydration state (1W, 2W, 3W, or 10W) at 298 K. The normalization of D was made with regard to the corresponding size corrected $D_{0,s}$ value from Table 3.2. The clay layer rigidity was varied from fully rigid (red squares) to fully flexible (yellow circles). In the two semi-flexible states, either all structural clay atoms were kept fixed except the bonded hydroxyl hydrogen (green diamonds) or vice versa (blue triangles).

Table 3.3. Two-dimensional self-diffusion coefficients of Na^+ and water in clay interlayer nanopores in systems with fully flexible clay sheets and five H_2O molecules per unit cell per hydrate layer. The last column shows the correction factor that can be applied to account for the discrepancy between measured and predicted diffusion coefficients in bulk liquid water. The last row shows the E_a values of Na^+ and water in the clay interlayer nanopores at different hydration states, corrected for the difference in E_a values between bulk liquid SPC/E water and real water.

$D_{\text{Na}} (10^{-9} \text{ m}^2/\text{s})$					
T (K)	1W	2W	3W	10W	$D_{0,\text{exp}}/D_{0,\text{s}}$
278	0.025±0.003	0.15±0.01	0.28±0.03	0.44±0.04	1.085
298	0.053±0.010	0.36±0.01	0.53±0.05	0.77±0.15	1.165
323	0.109±0.022	0.65±0.07	0.79±0.11	1.29±0.15	1.126
353	0.217±0.017	1.13±0.14	1.43±0.10	1.90±0.20	1.099
E_a^* (kJ/mol)	24.3±1.1	22.0±1.0	18.0±0.8	16.7±1.1	
$D_{\text{H}_2\text{O}} (10^{-9} \text{ m}^2/\text{s})$					
T (K)	1W	2W	3W	10W	$D_{0,\text{exp}}/D_{0,\text{s}}$
278	0.113±0.006	0.47±0.01	0.75±0.02	1.15±0.03	0.783
298	0.205±0.011	0.96±0.01	1.31±0.03	1.91±0.02	0.873
323	0.385±0.021	1.68±0.06	2.19±0.07	3.19±0.04	0.949
353	0.789±0.048	2.82±0.15	3.63±0.02	5.09±0.08	1.030
E_a^* (kJ/mol)	23.7±0.4	22.1±0.6	19.9±0.3	19.0±0.3	

3.2.3.5 Comparison with measured E_a values in compacted Na-montmorillonite

As noted in the introduction, most interatomic potentials used in MD simulations were parameterized to describe the system of interest at a specific temperature, and they sometimes fare poorly when applied at very different temperatures. To account for this, we report E_a values that were calculated from our MD simulations of clay interlayer nanopores, then corrected for the difference (ΔE_a) between measured and predicted E_a values in bulk liquid water (Table 3.3). Based on the experimental results of Talekar (1977) and Holz et al. (2000) ($E_a = 18.4 \pm 0.3$ and 17.4 ± 0.2 kJ/mol for Na^+ and water in the temperature range of our study), we used $\Delta E_a = 0.7 \pm 0.3$ and 2.8 ± 0.6 kJ/mol for Na^+ and water, respectively.

In Figure 3.16, we compare our predicted E_a values with macroscopic and pore scale experimental data on E_a in water-saturated Na-smectite. Most experimental values were reported as a function of the dry bulk density (ρ_b) of the porous medium. Therefore, we used recent XRD data to estimate the range of ρ_b values in which water-saturated smectite forms the 1W, 2W, 3W, or ~10W hydrates. As shown in Figure 3.16, our MD simulation predictions are consistent with most experimental results. In the case of Na^+ , our predicted E_a values are equal to or slightly lower than the experimental results of Kozaki et al. (2005). In the case of H_2O , our predicted E_a

values are consistent with the results of Marry et al. (2011) and Suzuki et al. (2004), and with half of the data reported by Nakazawa et al. (1999), while being ~ 2 to 3 kJ mol^{-1} higher than the results of Gonzalez-Sánchez et al. (2009) and Nakashima (2000). Our results predict a $\sim 6 \text{ kJ mol}^{-1}$ increase in the E_a values of Na^+ and water with increasing clay-water ratio (from bulk liquid water to the 1W hydrate). Finally, our results show that Na^+ has a higher E_a value in the so-called *crystalline hydrates* (1W, 2W, 3W states) and a lower value in the *osmotic hydrates* (such as the 10W state) than in bulk liquid water, as hypothesized by Kozaki et al. (2005).

The different studies compiled in Figure 3.16 are not perfectly equivalent, because they used different smectite minerals with small differences in the magnitude and distribution of their negative structural charge. As noted in Section 3.2.2, the smectite used in this study was a Wyoming-type montmorillonite with a structural charge of -0.66 e per unit cell arising exclusively from isomorphous substitutions in the octahedral layer. The smectite used by Kozaki et al. (2005), for example, was the Kunipia-F montmorillonite (a reference montmorillonite of the Japanese radioactive waste management program), which has a larger negative structural charge (-0.84 e per unit cell) and has isomorphous substitutions in both the octahedral and tetrahedral layers. Our preliminary results modeling a generic Kunipia-F type montmorillonite with the methodology developed in this study suggest that the additional negative structural charge in the tetrahedral sheet results in a significant degree of inner-sphere surface complexation of interlayer Na^+ ions, which may lead to higher E_a values. This matter will be the investigated during the end of FY13.

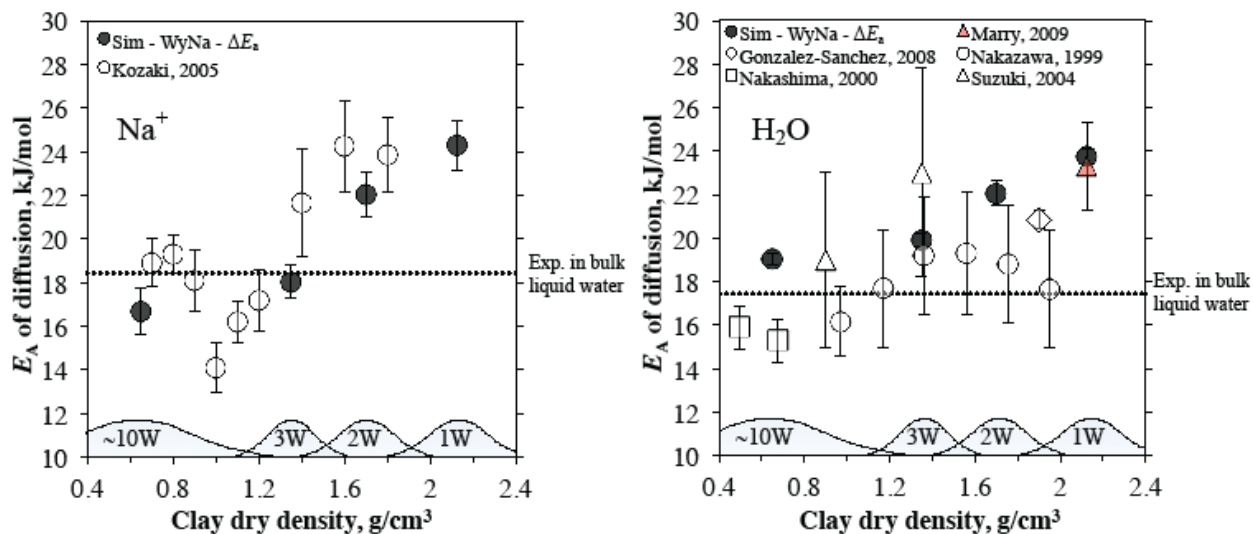


Figure 3.16. Activation energy of diffusion of Na^+ and water in water-saturated Na-smectite, plotted as a function of dry bulk density. Our MD simulation results are shown as black circles. Other symbols represent macroscopic (white symbols) or pore scale (red symbols) experimental results. Error bars represent the standard error in the slope of the linearized Arrhenius plot. Dashed horizontal lines indicate the measured E_a values of diffusion of Na^+ and water in bulk liquid water (Talekar, 1977; Holz et al., 2000). Approximate regions of predominance of each hydration state (shown schematically in the lower part of each figure) were estimated from X-ray diffraction data (Holmboe et al., 2012).

3.2.4 Summary

Using a new capability for a dynamic electrical double layer (EDL) thickness, we simulated the effects of the diffusive propagation of a ionic strength front on EDL porosity and transport. The simulations demonstrate that the changes in EDL thickness as a function of ionic strength may in fact have an opposite effect to that resulting from clay swelling. In addition, we were able to implement the Mean Electrostatic Model for the EDL with and without Stern layer sorption. A full treatment of these layers is more complicated in the context of the Poisson-Boltzmann equation and will be the focus of much of the work for the remainder of FY13. The ionic strength dependent EDL model was then used to simulate anion and uncharged species out-diffusion from a borehole in the DR-A experiment at the Mont Terri experimental facility in Switzerland. The key accomplishment was the ability to capture both behaviors (uncharged and charged species) with the same model. In addition, we completed much of the necessary software changes needed to couple the reaction portion of CrunchEDL with the general purpose PDE simulator Comsol. This will provide the basis for both pore scale electrostatic flow and transport, as well as larger repository scale simulations.

We determined the influence of water content, temperature, simulation cell size, and clay-layer flexibility on MD simulation predictions of Na^+ and water diffusion in the montmorillonite interlayer nanopores. Our simulations led to the development of a robust MD simulation methodology that correctly predicts the temperature dependence of Na^+ and water diffusion in bulk liquid water and in the interlayer nanopores of hydrated montmorillonite. Our results show that MD simulations can help to extrapolate existing diffusion measurements to the high temperatures that occur in the near field of high-level radioactive waste repositories, while also providing molecular scale insights into the predominant diffusion pathways of water and solutes in the EBS. In particular, our results support the view that the predominant diffusion pathway of Na^+ in compacted water-saturated bentonite shifts from the osmotic hydrate to the crystalline (3- and 2-layer) hydrates with increasing dry bulk density.

4. Experimental Studies on Reactive Diffusive Transport

The long-term management of nuclear waste repositories requires reliable predictions of uranium(VI) diffusion through waste containment barriers, such as compacted bentonite. Uranium diffusion coefficients can be affected by metal solution speciation and chemical solution conditions, such as pH and inorganic ligand concentrations, as well as a variety of metal-mineral surface interactions. Furthermore, specifically for clays, metal diffusion processes are influenced by: (1) the electrical charge of the diffusing solute, (2) the degree of compaction, and (3) the electrical double layer structure at the clay/water interface. Most currently available uranium diffusion models do not specifically include the expected changes in metal diffusion rates due to these variations. However, we believe that a “de-coupling” of parameters and processes is necessary to ensure an accurate prediction of apparent diffusion rates under the chemical gradients expected within engineered barrier systems.

In order to achieve this goal, we first completed a detailed theoretical analysis of the potential impacts of solution chemistry on various types of uranium diffusion coefficients and clay (surface) characteristics. In addition, uranium(VI)-montmorillonite batch sorption equilibrium experiments were performed to characterize uranium sorption as a function of chemical solution conditions, and to provide data sets for the development of a surface complexation model. Last,

lab-scale diffusion experiments were designed, and the reactive diffusive transport of calcium (an important element driving uranium solution speciation) and uranium(VI) were evaluated experimentally and/or in predictive model calculations.

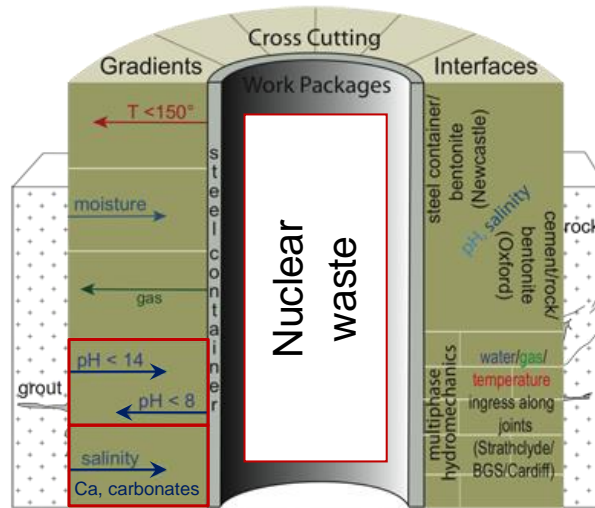
4.1 Background

4.1.1 Relevance

The long-term management of nuclear waste repositories requires reliable predictions of contaminant transport in the subsurface at chemical conditions varying over time and space. This includes an evaluation of radionuclide mobility through waste containment barriers in engineered barrier systems (EBS) close to the source term. Compacted bentonite has been proposed as a backfill material in EBS because of its low permeability (Pusch, 1992; Bourg, et al., 2003; Kim et al., 1993) and strong sorptive properties (Eriksen et al., 1999; Ochs et al., 2001). The limited permeability of bentonite is at least partially the result of its low porosity and the swelling of Na-montmorillonite, its major component, in water. Due to these characteristics, the transport of contaminants through bentonite layers is expected to be limited and dominated by diffusion (Ochs et al., 2001; Madsen, 1998; Bourg et al., 2007).

However, the state of knowledge with respect to diffusion-driven flux shows that there are large differences in diffusion behavior between various radionuclides, e.g., between halides (^{36}Cl , ^{129}I) and actinides ($^{238,235}\text{U}$, ^{237}Np , ^{232}Th). The differing behaviors are a result of the two major processes that have important effects on macroscopic diffusive transport, i.e., molecular diffusion and sorption. Hence, laboratory sorption and diffusion studies are an important component for the design of waste containment barriers (Shackelford, 1991) and the calibration of diffusion-based transport models. As the basis of nuclear fuel, uranium is one of the primary elements to be considered in environmental risk assessments for nuclear waste repositories, with U(VI) representing its most mobile oxidation state. Therefore, a fundamental understanding of uranium(VI) diffusion through bentonite is essential.

In current models for radionuclide diffusion through bentonite in an EBS, the apparent and effective diffusion coefficients are linked through a K_d value, a sorption partitioning coefficient (or another type of sorption isotherm). This parameter is often believed to be a constant value for a particular radionuclide and solid-phase sample. In the case of U(VI), however, this is unlikely to be true because of the very high sensitivity of the K_d value to pH, as well as bicarbonate and calcium concentrations. By extension to the aqueous chemistry of other actinides, we can expect the K_d values of Np, Am, and Pu to also be sensitive to pH and bicarbonate concentrations. It should be noted that waste forms, and possibly concrete in the vicinity of an EBS, are likely to create gradients in these chemical variables (pH, HCO_3^- , Ca^{2+}) within the EBS (Figure 4.1). Therefore, it is important to develop conceptual models that can describe U(VI) diffusion as a function of chemical solution conditions. Specifically, predictive models need to independently take into account the effects of chemical solution conditions on (1) molecular diffusion, (2) metal sorption reactions and (3) clay surface properties.



http://www.eng.ox.ac.uk/about-us/jobs/fp/THMC.png/image_preview

Figure 4.1. Expected gradients across the EBS.

4.1.2 Effects of Chemical Solution Conditions on U(VI) Diffusion Coefficients

In the following, we present our theoretical analysis of the potential impacts of solution chemistry on various types of uranium diffusion coefficients and clay (surface) characteristics (Tinnacher and Davis, 2013). First, we will provide an overview of various types of diffusion coefficients and discuss the influence of chemical solution conditions on these parameters as they are relevant for U(VI) diffusion (Table 4.1). We will begin with the simplest case, molecular diffusion in a liquid, and then increase the level of complexity, taking into account more and more effects of the porous media. It is important to note that, along this discussion from simple to more complex coefficients, the impacts of chemical solution conditions on diffusion coefficients are additive.

Table 4.1. Effects of solution chemistry on diffusion coefficients

Diffusion coefficient	Equation	Diffusion in	Impact of solution chemistry on
Molecular diffusion coefficient	$D_0 = \frac{k_B T}{6\pi\eta R_0}$	Dilute aqueous solution	<ul style="list-style-type: none"> Molecular size of solute species (R_0) Solute concentration
Pore diffusion coefficient	$D_p = \frac{\delta}{\tau^2} D_0$	Pore water	<ul style="list-style-type: none"> Clay constrictivity (δ) Clay tortuosity (τ^2)
Effective diffusion coefficient	$D_e = \epsilon D_p$	Overall porous media	Diffusion-accessible porosity (ϵ), e.g. for anions
Apparent diffusion coefficient	$D_a = \frac{D_e}{\epsilon + \rho K_d}$	Overall porous media including sorption	Sorption behavior (K_d) due to changes in: <ul style="list-style-type: none"> Solution speciation Main sorption processes

Molecular diffusion is defined as solute transport resulting from the random thermal motion of molecules in solution (Selim and Amacher, 1997). In liquids, the Stokes-Einstein equation is the

most common basis for the estimation of diffusion coefficients in free aqueous solution, also known as molecular diffusion coefficients (D_0) (Cussler, 1997):

$$D_0 = \frac{k_B T}{f} = \frac{k_B T}{6\pi\mu R_0} \quad (4.1)$$

where f is the friction coefficient of the solute, k_B is Boltzmann's constant, T is temperature, μ is the solvent viscosity, and R_0 is the solute radius.

Molecular diffusion coefficients typically vary with solute concentration, and decrease with increasing solute radii. If the solute of interest is hydrated or solvated in any way, then the "diffusion-relevant" radius is represented by the solute-solvent complex, and not the solute itself (Cussler, 1997). For uranium, changes in chemical solution speciation and U(VI) complexation with inorganic ligands, such as carbonates, can change the molecular size of aqueous species, as well as their hydration properties and the water exchange kinetics with the hydration sphere (Kerisit and Liu, 2010). Current results from potential-based molecular dynamics simulations suggest that these changes lead to differences in molecular diffusion coefficients for various U(VI) solution species, e.g., UO_2^{2+} and $\text{UO}_2(\text{CO}_3)_3^{4-}$ (Kerisit and Liu, 2010). However, molecular diffusion rates of the fastest and slowest U(VI) species vary by less than a factor of 2, which will lead to only minor changes in overall U(VI) diffusion rates in porous media relative to other effects associated with metal-solid interactions.

In porous media, migrating solutes experience tortuous pathways and potentially changing diffusion volumes over increased transport distances. This is taken into account with the pore diffusion coefficient (D_p), which is defined as

$$D_p = \frac{\delta}{\tau^2} D_0 \quad (4.2)$$

The constructivity factor (δ) is a measure of the diffusion volume along the diffusion pathway (Figure 4.2), with $\delta < 1$ for decreasing and $\delta > 1$ for increasing volumes along the pathway. For saturated bentonite, the diffusion volume and clay porosity are typically assumed to be constant throughout the sample, resulting in $\delta = 1$ (Holmboe, 2009). The tortuosity (τ^2) is a dimensionless, geometric parameter, or a 'winding factor' (≥ 1) (Holmboe, 2009), representing the average length of diffusion paths linking the system boundaries relative to the distance ∂x (Figure 4.2). As described in detail below, τ^2 is a function of various (chemical) system conditions that can influence clay characteristics. Hence, overall, the pore diffusion coefficient (D_p) is subject to all chemical changes affecting molecular diffusion and clay tortuosity.

Further increasing the degree of complexity, the effective diffusion coefficient (D_e) represents a measure of the diffusive flux within the porous media while taking into account the porosity (ε) of the media.

$$D_e = \varepsilon D_p \quad (4.3)$$

Hence, according to Fick's first law of diffusion, the diffusive flux (J) of a solute under steady-state conditions is described by

$$J = -D_e \frac{\partial C}{\partial x} \quad (4.4)$$

In clays, chemical solution conditions can change the diffusion-accessible porosity, e.g. for anions, as described in further detail below. Therefore, overall chemical solution conditions can affect effective diffusion coefficients owing to their impact on molecular diffusion coefficients and clay properties, such as τ^2 and ε .

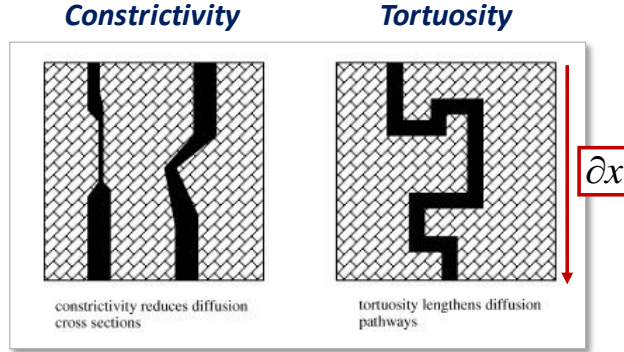


Figure 4.2. Visualization of constrictivity and tortuosity (Van Loon and Soler, 2004).

Last, for reactive solutes, such as uranium, metal interactions with the mineral surface in the pore environment have to be expected over the course of diffusion-dominated metal transport. As a result, some researchers have proposed the use of some form of an apparent diffusion coefficient (Maes et al., 2002; Tokunaga et al., 2004), which further extends the effective diffusion coefficient to directly include metal sorption or ion exchange reactions. The apparent diffusion coefficient (D_a) represents the overall macroscopic diffusion rate, and is included in Fick's second law of diffusion describing the solute concentration change in a (porous) volume element under transient conditions.

$$\frac{\partial C}{\partial t} = D_a \frac{\partial^2 C}{\partial x^2} \quad (4.5)$$

Apparent and effective diffusion coefficients are linked through the rock capacity factor (α) with

$$D_a = \frac{D_e}{\alpha} \quad (4.6)$$

where α is defined as

$$\alpha = \varepsilon + \rho K_d \quad (4.7)$$

In Eq. 4.7, ρ represents the dry bulk density of the mineral and K_d the sorption distribution coefficient. For non-sorbing species, K_d is equal to zero, and the rock capacity factor equals clay porosity. For sorbing solutes, the K_d value represents the slope of a linear sorption isotherm; however, non-linear isotherms can also be incorporated into apparent diffusion coefficients (Bai et al., 2009).

Chemical solution conditions and metal speciation are known to affect uranium sorption behavior and K_d values in clays (Bradbury and Bayens, 2011; Fox et al., 2006; Davis et al., 2004). Hence, in addition to the effects discussed for effective diffusion coefficients above, D_a

is also impacted by chemical effects on U(VI) sorption parameters. Furthermore, Muurinen (1990) reported changes in apparent diffusion coefficients due to differences in uranium speciation, and argued that different species appear to follow different diffusion mechanisms.

While U(VI)-clay interactions are important to consider, their direct incorporation into diffusion coefficients in the form of K_d values or non-linear sorption isotherms appears problematic for a variety of reasons. First, the overall values of apparent diffusion coefficients become inherently dependent and sensitive to the correct values of α . As a result, it becomes meaningless to report values of apparent diffusion coefficients of reactive solutes without a characterization of their sorption characteristics (Shackelford, 1991). Second, sorption isotherms are inherently dependent on the sorption characteristics of the solid phase, and the concentrations and chemical solution speciation of the solute. While they provide good estimates for specific system conditions, they do not allow for any predictions of contaminant transport under conditions changing over time and space. For example, the application of linear sorption isotherms for the simulation of uranium diffusion in London clay is very limited (Brown et al., 1991). Uranium retardation was shown to be highly dependent on uranium solution concentrations, which varied substantially over space, even in a small, well-controlled lab system (9 mm clay sample, pH=8).

Therefore, an independent treatment of sorption terms and diffusion mass transfer appears to be a better approach. However, at this point, this strategy has been applied less frequently (Bai et al., 2009; Liu et al., 2010).

4.1.3 Influence of Solution Chemistry on Clay (Surface) Properties

Chemical solution conditions can affect the structural properties of clays, in terms of diffusion-accessible porosity and clay tortuosity, the dominant pathways of solute diffusion, as well as the reactive surface sites available and relevant for U(VI) sorption and ion exchange reactions (Figure 4.3). More specifically, diffusion processes are known to be influenced by: (1) the electrical charge of the diffusing solute, (2) the degree of compaction, and (3) the electrical double layer structure at the clay-water interface. In the following, we will briefly discuss these interactions in the context of montmorillonite and bentonite (Tinnacher and Davis, 2013).

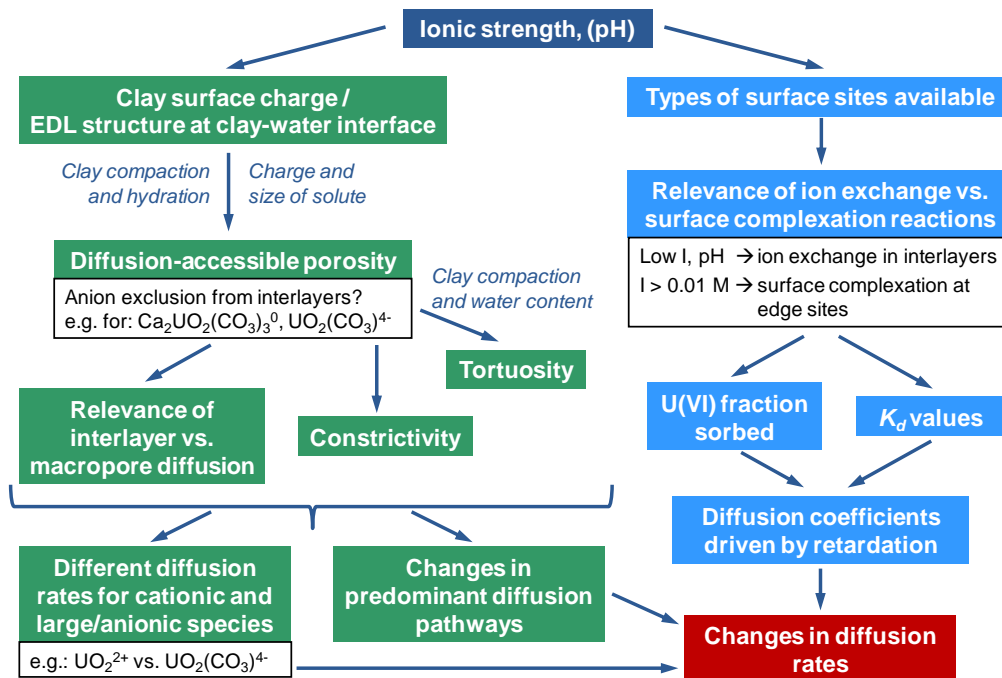


Figure 4.3. Overview of chemical solution effects on clay (surface) characteristics and diffusion rates.

In bentonite, the majority of the connected porosity is associated with the clay mineral fraction, which primarily consists of montmorillonite, a negatively-charged smectite. Montmorillonite particles are composed of stacks of smectite layers, which create interlayer spaces within individual clay particles. Hence, compacted smectite will have two porosities (Bourg et al., 2003): (1) large pores between clay particles, where diffusion is relatively unaffected by the clay surface, and (2) very thin interlayer pores, where diffusion is affected by surface charge and ionic strength. As diffusion is expected to take place differently in these two volumes (Bourg et al., 2003), this essentially creates two “small-scale diffusion pathways”, where each may become dominant under different system conditions.

For instance, in compacted bentonite, smectites will be primarily present in the one- and two-layer hydrate form (i.e., one to two statistical monolayers of water in each interlayer). In addition, pore sizes can be so small that electric double layers balancing the charge of the bentonite may overlap (Bourg et al., 2003; Kerisit and Liu, 2009; Bourg, et al., 2006; Leroy et al., 2006). Under these conditions, anions have limited or no access to the interlayer (Figure 4.4) and can only diffuse through the macropore environments between clay particles. However, neutral and cationic solutes can, in principle, diffuse through the clay interlayers.

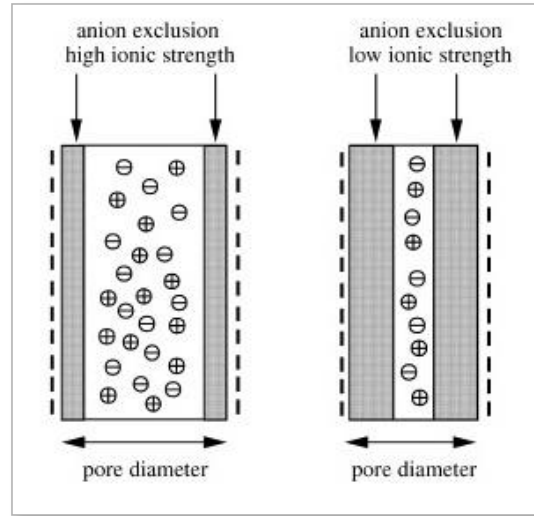


Figure 4.4. Visualization of anion exclusion effects (Van Loon & Soler, 2004).

On the other hand, at zero or minor degrees of compaction, anionic or larger neutral species may be able to enter the interlayer space in three-layer hydrate smectite particles. Furthermore, the influence of electrical double layers and background ionic strength might be expected to play greater roles under these conditions.

For uranium in the EBS, predominant U(VI) species may be either neutral or anionic depending on chemical solution conditions (Tinnacher and Davis, 2013). Anionic U(VI) species may not enter the interlayer when bentonite is compacted; perhaps even the neutral $\text{Ca}_2\text{UO}_2(\text{CO}_3)_3^0$ will not be able to enter because of steric hindrance. Thus, U(VI) diffusion into interlayer pores of compacted bentonite may be controlled by the supply of cationic U(VI) species, which may be found at low concentrations relative to other species. The diffusion of other U(VI) species will be limited to macropores between clay particles. As a result, different diffusion rates have to be expected for uranium as a function of the specific, molecular charge of individual species, e.g., UO_2^{2+} and $\text{UO}_2(\text{CO}_3)_3^{4-}$. In fact, Muurinen (1990) reported first indications of anion-exclusion effects for uranium in bentonite, and changes in effective diffusion coefficients due to variations in uranium speciation.

Moving on to another clay characteristic, tortuosity (τ^2) is in principal a dimensionless, geometric parameter. In practice, however, it is likely to depend on water content (Selim and Amacher, 1997), as well as clay compaction (dry density) and the ionic strength conditions in the pore-water (Van Loon et al., 2007).

Last, chemical solution effects on uranium speciation and clay surface properties will influence the fraction of sorbed U(VI), and hence, changes in metal diffusion coefficients driven by retardation. In addition, they will determine the dominant U(VI) sorption mechanism onto montmorillonite in terms of ion exchange or surface complexation. For instance, at low ionic strengths and mildly acidic pH, ion exchange within the interlayer space is expected to drive overall sorption. At ionic strengths greater than 0.01 M, surface complexation at edge sites predominates. Thus, even without strong compaction, solution conditions may still influence the “diffusion-accessible” porosity for U(VI).

4.2 Materials and Methods

During this past fiscal year, our experimental efforts were focused primarily on two main areas: (1) U(VI) batch sorption equilibrium experiments with Na-montmorillonite, and (2) diffusion studies in Na-montmorillonite. The data sets of previously performed equilibrium sorption experiments were further extended to include an evaluation of the effects of calcium on uranium(VI) sorption behavior. This is motivated by the relevance of Ca for U(VI) solution speciation and the formation of ternary U-Ca-carbonato solution complexes in the circumneutral pH-range. All data sets were then used for the development of a U(VI)-Na-montmorillonite surface complexation model.

The implementation of diffusion experiments entailed the design of a diffusion cell and clay packing device that would allow experiments over a wide range of chemical solution conditions, including corrosive conditions at low pH and high ionic strength. In addition, because of the significantly higher solid-solution ratio in diffusion experiments compared to sorption studies, diffusion experiments also required an improved pretreatment procedure for the standardized Source Clay (Na-montmorillonite, SWy-2, Clay Minerals Society) to further minimize Ca impurities and the “uncontrolled” release of Ca from the solid phase. Motivated by the relevance of Ca for U(VI) solution speciation and the limited availability of Ca diffusion constants in pure montmorillonite in the literature (Kozaki et al., 2001), we performed a calcium bromide diffusion experiment in pretreated Na-montmorillonite. Finally, given the long duration of diffusion experiments, we simulated U(VI) diffusion behavior in lab-scale experiments in predictive models using the code ANADIFF (Eriksen et al., 1999; Eriksen and Jansson, 1996). These modeling results illustrate the relevance of chemical solution conditions for U(VI) diffusion rates, and are the basis for experimental planning and the selection of appropriate chemical solution conditions in U(VI) diffusion experiments.

A detailed description of materials and the setup for batch sorption equilibrium experiments has been provided in last year’s report (Rutqvist et al., 2012; Section 5.2); hence, only a short summary will follow with respect to these subject areas.

4.2.1 Overview of Materials

All acids, bases and salt solutions used in experiments were of TraceSelect grade (Sigma Aldrich) in order to minimize calcium background concentrations. Uranium(VI) solutions contained ^{238}U from a 1.299 mM uranyl nitrate stock solution (provided by David Singer and Wayne Lukens at Lawrence Berkeley National Laboratory), and were analyzed by ICP-MS (Perkin-Elmer SCIEX ICP-Mass Spectrometer ELAN DRC II).

A commercially available, well-characterized, standardized Source Clay (Na-montmorillonite, SWy-2, Clay Minerals Society) was selected for experimental study. This material is known to contain considerable impurities of quartz (8%) and feldspars (16%) as well as calcite (Costanzo and Guggenheim, 2001; Chipera and Bish, 2001; Mermut and Cano, 2001). Hence, purification procedures were applied with the goal to effectively remove mineral impurities while preserving the original clay characteristics as much as possible. The pretreatment method described in last year’s report was sufficient to decrease Ca release from Na-montmorillonite in batch sorption equilibrium experiments (0.5 g/L montmorillonite) to Ca concentrations that were low enough to avoid any influences on U(VI) solution speciation (5-30 μM Ca concentrations found in sorption experiments versus millimolar Ca concentrations required for changes in U(VI) solution speciation at $\text{U(VI)}_{\text{Tot}} = 10^{-6}$ M). However, due to the substantially higher clay concentration in

diffusion studies (e.g., ~1 g/mL=1000 g/L), this procedure needed further improvement to prevent any unintended Ca release in these experiments.

4.2.2 Batch Sorption Equilibrium Experiments

All batch sorption experiments were set up at room temperature (22.5°C-23.5°C), with a nominal total U(VI) concentration of 10^{-6} M, a Na-montmorillonite concentration of 0.5 g/L, and a total ionic strength of 0.1 M NaCl. The main steps of the experiments included: (1) the pre-equilibration of Na-montmorillonite with a background electrolyte solution at the specified pH and chemical solution conditions, (2) U(VI) sorption equilibration with the mineral phase, (3) sampling and analysis of supernatant fractions after removal of the solid phase by centrifugation, and (4) a correction for U(VI) wall sorption effects based on an acid-wash procedure.

Experimental results for batch sorption envelope experiments are reported in terms of distribution coefficients (K_d values) and fractions of U(VI) sorbed. Distribution coefficients, with units of L/kg, represent the ratio of sorbed (e.g., in mol/kg) over dissolved (e.g., in mol/L) U concentrations after sorption over 48.5 hours. Sorbed U(VI) fractions were calculated based on concentration differences between (solid-free) standards and (solid-containing) samples.

4.2.3 Modeling Setup for Surface Complexation Models

In this report we present the results of a preliminary surface complexation model (SCM) to evaluate our ability to describe and predict the variations in uranium(VI) K_d values for sorption on montmorillonite as a function of solution conditions. We expect to refine this preliminary model further and produce the final SCM by the end of FY13. A review of the current status of U(VI) surface complexation modeling for montmorillonite was provided in last year's annual report (Rutqvist et al., 2012).

To use an SCM to describe the U(VI) sorption data, one must initially choose the electrical double layer (EDL) model that is part of the conceptual model of the SCM. In this case, we have chosen the triple layer model (TLM) because of the likely need to use EDL charge distribution terms in the final SCM to match the surface species with surface spectroscopy (Arai et al., 2006). Charge distribution terms cannot be used in simpler EDL models such as the diffuse double layer model.

Because we have not yet performed acid-base titrations of our specific montmorillonite sample to evaluate surface charge as a function of pH, we have employed the TLM developed for montmorillonite by McKinley et al. (1995), including the use of the same parameter values (see Table 4.5). Following the conceptual approach for the SCM of McKinley et al., we assume that UO_2^{2+} cations can exchange with other cations in the interlayer region of the montmorillonite, and that surface complexes can form on the edge sites of montmorillonite sheets. Furthermore, the same BET surface area of the SWy-1 montmorillonite used by McKinley et al. (1995), 31 m²/g, has been included in our model as well. The edge surface area of montmorillonite has been estimated as 19.2 m²/g (Duc et al., 2005) and this value was used in the EDL model.

In order to apply an EDL and SCM from the literature, one must ensure that the site densities and ion exchange capacities are self-consistent (Davis et al., 2004). We have used the same cation exchange capacity (0.74 mmoles/g) and site densities for silanol and aluminol surface ligands (18.6 and 16.8 μmoles/g, respectively) as were used in the modeling by McKinley et al. (1995). In addition, we have used the same values of inner and outer layer capacitance (1.2 and

0.2 Farads/m², respectively) that were used by McKinley et al. (1995) and Zachara and Smith (1994).

The program FITEQL 4.0 (Herbelin and Westall, 1999) was used to fit U(VI) cation exchange and surface complexation constants to describe the U(VI) sorption data in the CO₂-free experimental system. For this preliminary model, surface complexation of U(VI) was assumed to occur only at aluminol sites. In addition, the constants obtained from that fit were then used in to predict U(VI) sorption at other experimental conditions. The refinement of the model during the remainder of FY13 will include the fitting of our own EDL parameters and additional U(VI) surface species as needed to fit the underpredictions of U(VI) sorption at other solution conditions.

4.2.4 Design of Diffusion Cell and Clay Packing Device

A detailed description of all considerations and steps for the design of the diffusion cell and clay packing device goes beyond the scope of this report. However, we will summarize the most important points in the following.

Research groups in Europe (e.g., Royal Institute of Technology, Sweden and Paul Scherrer Institute, Switzerland) have gained considerable experience with diffusion cells in through-diffusion experiments over the past years, but have also reported difficulties with specific components, such as the metal filters (e.g., Glaus et al., 2008). In these designs, a diffusion cell consists of the following main components: (1) a “ring-like” cell containing the clay packing, (2) two metal filters holding the clay packing in place, and (3) two end pieces that allow for a homogeneous delivery of solutions over the metal filters, with solution flow in parallel to the filters. These end pieces are then connected to tubings that deliver the solutions of interest from two different reservoirs, the high-concentration and the low-concentration reservoirs.

We have decided to largely follow these designs (Figs. 4.5–4.7), which has the additional benefit of allowing for a direct comparison of our diffusion results with existing data in the literature. However, given the expected long time frames for uranium(VI) diffusion experiments, and our goal to characterize U(VI) diffusion behavior over a broad range of chemical solution conditions, including corrosive conditions at low pH and high ionic strength, the following additional design considerations were taken into account. With regards to the diffusion cell:

- Materials for the diffusion cell (PEEK) and the metal filters (Hastelloy C276, Mott Corporation) were selected to ensure (1) resistance to corrosion, (2) resilience to clay swelling pressures, (3) minimal swelling of the (plastic) material itself to ensure a constant volume of the clay packing, and (4) low machining costs.
- Dimensions for the “ring-like” cell containing the clay packing ($D_i=2.54$ cm, $L=1$ cm) were chosen in order to:
 - Minimize wall effects during reactive, diffusive transport and to
 - Ensure sufficient amounts of clay material for the slicing of the clay packing with an abrasion technique at the end of U(VI) diffusion experiments (with $D_i=2.54$ cm and the use of a U-233 tracer, we anticipate layer thicknesses as low as 20 μm).
- Hastelloy C276 was selected as material for the filters (Mott Corporation) to prevent the formation of fractures in the filter media caused by clay swelling during experiments, and

to allow for rigorous cleaning of filters in between experiments (acid/base washes under oxidizing and reducing conditions, sonication).

- The porosity of the metal filters (10 μm) was chosen to decrease the potential trapping of clay particles in the filter media. The length of the clay packing (1 cm) and the filter thickness (0.16 cm) were selected to minimize the effects of potentially changing filter diffusivities on experimentally determined U(VI) diffusion coefficients based on mathematical considerations (Glaus et al., 2008).

In addition, a clay packing device was designed based on the following requirements:

- Reproducible packing of clay directly into the “ring-like” component of the diffusion cell.
- The possibility of quantifying the pressures applied during clay packing.

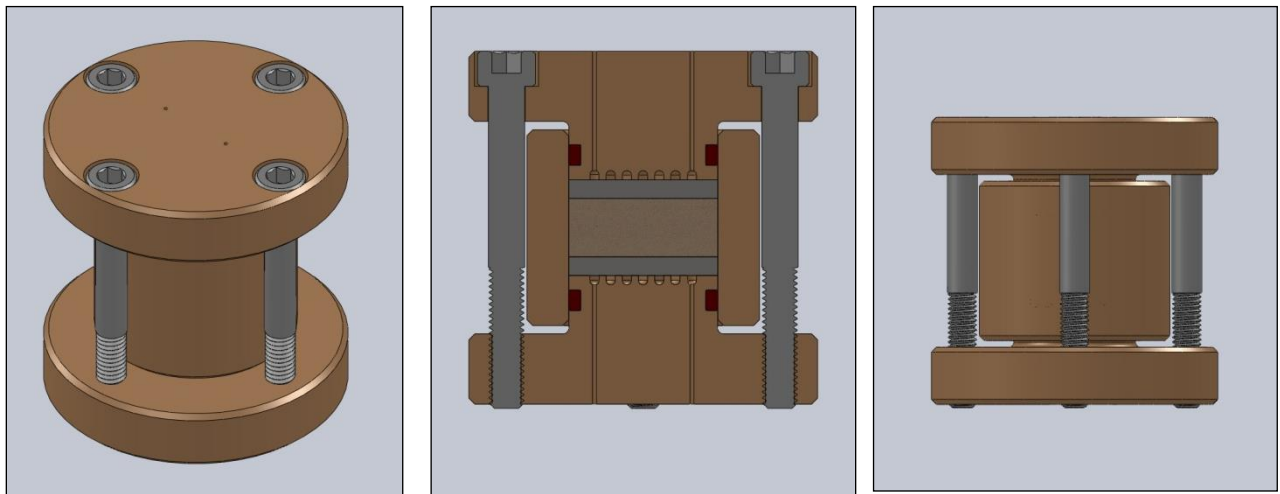


Figure 4.5. Diffusion cell design.

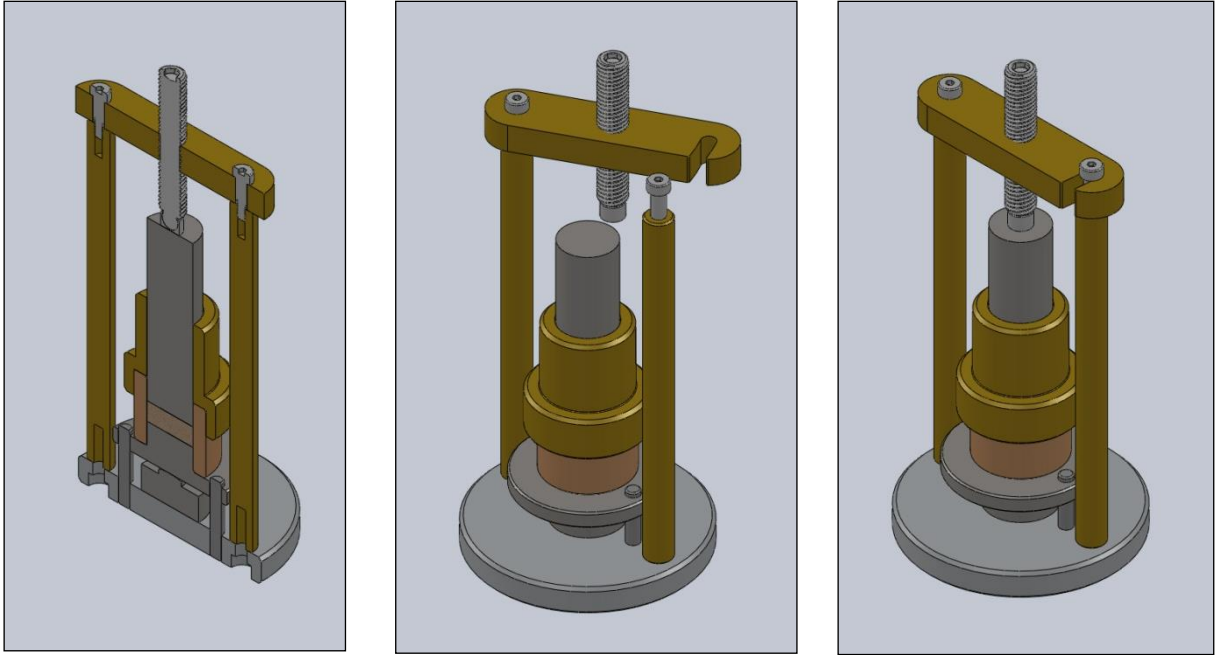


Figure 4.6. Design for clay packing device.

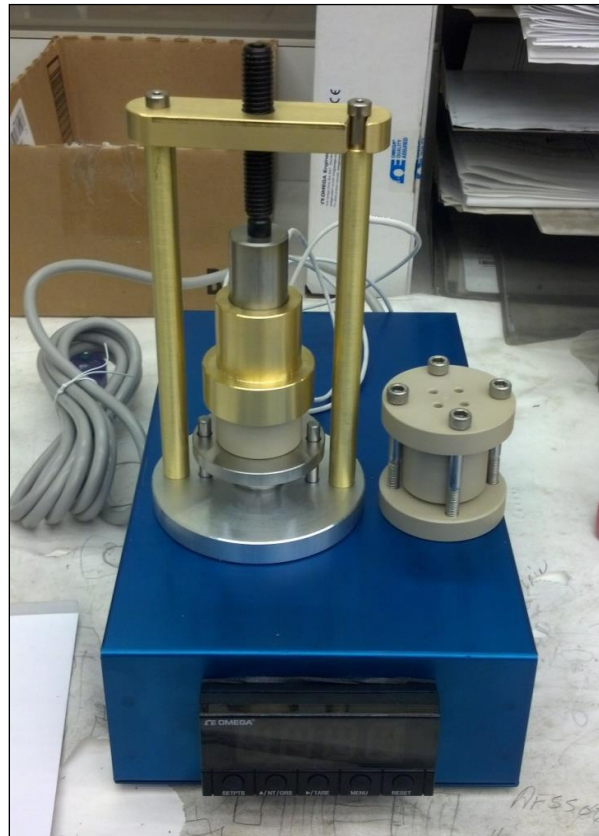


Figure 4.7. Diffusion cell and clay packing device.

4.2.5 Clay Pretreatment Specific to Diffusion Experiments

In last year's report (Rutqvist et al., 2012), we reported a pretreatment procedure for Na-montmorillonite (SWy-2, Clay Minerals Society), which included the following steps: (1) the removal of calcite impurities using a sodium acetate/acetic acid solution, (2) transforming the clay into its sodium form by equilibration with a Na-salt solution, (3) the removal of excess Na-salts from suspended clay, (4) the separation of quartz and feldspar impurities from clay particles by centrifugation and (5) oven-drying of the clay mineral phase. Pretreatment steps were performed using dialysis membranes, since this allows us to efficiently “up-scale” this setup for the purification of larger mineral quantities. To further improve the purification method for the use of Na-montmorillonite in diffusion experiments, the procedure was repeated with the following modifications:

- The number of extraction steps with sodium acetate/acetic acid solutions was increased from 4 to 6 steps.
- Clay equilibration in the Na-salt solution (1 M NaCl) was repeated 5 instead of 4 times.
- Clay centrifugation steps were performed 2–3 times, depending on the purity of the material based on visual evaluation, instead of only once.

4.2.6 Diffusion Experiment: Calcium Bromide Diffusion in Na-Montmorillonite

Calcium was selected for a diffusion experiment in Na-montmorillonite due to its relevance for U(VI) solution speciation and sorption behavior. Furthermore, impurities of calcium minerals have to be expected in engineered barrier systems, both in the bentonite buffer as well as the bordering cement-based layer. Hence, a calcium concentration gradient (Figure 4.1) and the diffusive transport of Ca within barrier systems seem very likely. At this point, only a few diffusion studies have been performed for Ca in bentonite (Mazzieri et al., 2010; Shackelford and Lee, 2003); data for Ca diffusion in Na-montmorillonite are even scarcer (Kozaki, 2001). However, these data will be very relevant for interpreting uranium(VI) diffusion behavior in Na-montmorillonite at varying Ca concentrations. Furthermore, using calcium bromide as a salt allowed us to study the diffusion behavior of a fairly non-reactive anion (bromine) in a sodium chloride background electrolyte solution.

The experimental setup for diffusion experiments consists of the diffusion cell containing the clay packing, the high-concentration and low-concentration reservoirs, the tubings and fittings connecting the reservoirs with the diffusion cell, and a peristaltic pump (Figure 4.8). All solutions used in the experiment were repeatedly adjusted to pH 7 using small volumes of acid/base solutions (TraceSelect grade NaOH and HCl) prior to their contact with the mineral phase.

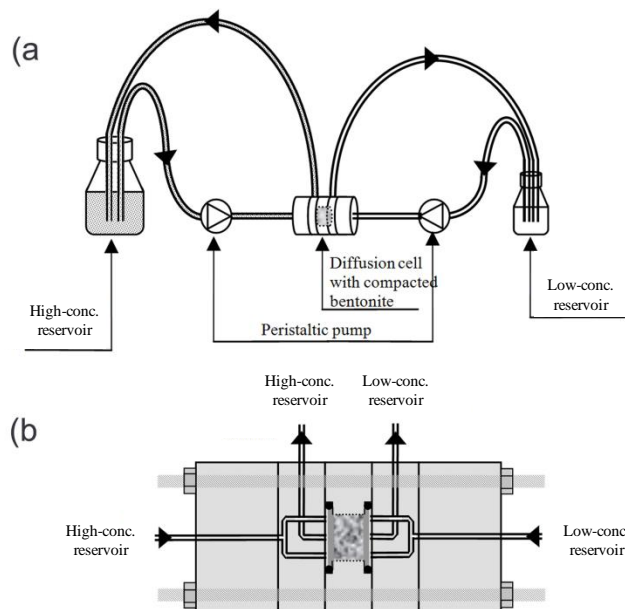


Figure 4.8. Schematic of setup for diffusion experiment (Courtesy of M. Holmboe; modified).

At the beginning of the experiment, a known weight of dry, pretreated Na-montmorillonite is packed into the “ring-like” component of the diffusion cell to give the desired dry density ($\sim 1.0 \text{ g/cm}^3$) in the given volume of the cell. Then, the high-concentration (200 mL) and the low-concentration (20 mL) reservoirs are filled with background electrolyte solution (0.1 M NaCl, pH=7), and the clay is saturated with electrolyte by circulating the solutions through the cell with a peristaltic pump (0.7 mL/min) for about 4 ½ weeks.

After clay saturation, the solution in the high-concentration reservoir is exchanged for a background electrolyte containing 1 mM CaBr_2 , and the solution in the low-concentration reservoir is replaced with a 20 mL aliquot of fresh, CaBr_2 -free electrolyte. Over the following weeks, the circulation of solutions through the diffusion cell is continued at the same flow rate. However, CaBr_2 -free background electrolyte solutions in the low concentration reservoir are continuously exchanged by replacing reservoir vials. This provides a constant concentration gradient between high- and low-concentration reservoirs, which is defined as less than 2% of the CaBr_2 concentration in the high-concentration reservoir found in the low-concentration reservoir. The collected low-concentration reservoir vials are weighed to correct for volume losses due to evaporation, sampled for Ca and Br analysis by ICP-MS, and their solution pH values are recorded. Furthermore, small volumes (1.5 mL) of the high-concentration reservoir solution are repeatedly sampled for Ca and Br analysis by ICP-MS, in order to monitor solute concentrations and the concentration gradient over the course of the experiment. This procedure is continued until the diffusive fluxes for both Ca and Br, have reached steady-state conditions, and a series of data points have been collected at steady state. The latter is a requirement for the mathematical determination of diffusion coefficients for Ca and Br based on experimental results (see Section 4.3. “Results and Discussion” for details below).

After reaching steady-state conditions for Ca and Br diffusion, the solution in the high-concentration reservoir is replaced with a CaBr_2 -free background electrolyte solution containing approximately 1000 Bq/mL (27 nCi/mL) of tritiated water (HTO). Again, low-concentration

$$J = -A\varepsilon_f D_{a,f} \frac{\partial C_1}{\partial x} \quad (4.8)$$

where J is the diffusive flux through the inlet filter ($-F < x < 0$, see Figure 4.9), A the cross-sectional area of the diffusion cell, ε_f the filter porosity, $D_{a,f}$ the *apparent* diffusion coefficient in the filter, C_1 the solute concentration in the filter and x distance. In this equation (Eq. 4.8), applicable to non-sorbing solutes, the “*effective*” diffusion coefficient in the filter ($D_{e,f}$) is the product of the apparent diffusion coefficient and the filter porosity ($D_{e,f} = D_{a,f} \varepsilon_f$).

In contrast, for diffusion through the clay packing, the code explicitly allows for solute interactions with the clay mineral, based on a linear sorption distribution coefficient (K_d value), resulting in

$$J = -A\varepsilon_c D_{a,c} \frac{\varepsilon_c + \rho K_d}{\varepsilon_c} \frac{\partial C_2}{\partial x} \quad (4.9)$$

where ε_c is the clay porosity, $D_{a,c}$ the apparent diffusion coefficient of the solute in clay, ρ the dry (bulk) density, and C_2 the solute concentration in the clay pore solution. The capacity (retardation) factor R is related to the K_d value by

$$R = \frac{\varepsilon_c + \rho K_d}{\varepsilon_c} \quad (4.10)$$

Hence, the expression ($\varepsilon_c D_{a,c} R$) is equivalent to the effective diffusion coefficient in clay ($D_{e,c}$) for sorbing solutes.

4.2.7.2 Modeling Setup

ANADIFF is used to predict U(VI) diffusion through Na-montmorillonite in lab-scale experiments as a function of pH and Total Inorganic Carbon (TIC) concentrations in solution (Table 4.2). In these simulations, we combine our own experimental data with values from the literature.

For U(VI), an assumption of negligible solute-filter interactions may not be universally valid, especially if fine clay particles become trapped in the filter media (Glaus et al., 2008). Hence, U(VI)-filter interactions were implicitly included in our simulations as described in the following, while assuming that these interactions can vary with chemical conditions. In the first step, the dominant U(VI) solution species was determined individually for each set of chemical solution conditions to be simulated (Table 4.2), based on our previous results from speciation modeling with existing thermodynamic data (NEA database (Guillaumont et al., 2003); data not reported). Then, U(VI) diffusion coefficients in free aqueous solution (D_0) were estimated for these species using literature values from molecular dynamics simulations (Kerisit and Liu, 2010). Finally, the *effective* uranium diffusivities in the filter media ($D_{e,f}$) were computed by taking into account that solute diffusion coefficients are typically 10-times smaller in filters than in free aqueous solution (Glaus et al., 2008). However, since ANADIFF only allows for a direct input of *apparent* but not *effective* filter diffusion coefficients, we “tricked” the code by entering the calculated effective diffusion coefficient as an apparent diffusion coefficient with an “artificial” filter porosity of 1.

For the simulation of U(VI) diffusion through the clay sample, model input parameters were based on results from our U(VI)-Na-montmorillonite batch sorption experiments (Table 4.2),

performed at room temperature, and literature values for uranium diffusion coefficients in clay (Korichi et al., 2010). At this point, we assumed that uranium(VI) diffusion coefficients in Na-montmorillonite are estimated best by using published, experimentally determined U(VI) diffusion coefficients in clay (Korichi et al., 2010), rather than performing calculations with simulated values for molecular U(VI) diffusion coefficients. In general, extreme caution has to be exercised when transferring diffusion coefficients for reactive solutes between studies (Shackelford and Daniel, 1991), especially to avoid confusion between effective and apparent coefficients. In addition, it is useful to clearly state the underlying assumptions when applying published diffusion coefficients to new systems. In this case, we assumed that, for a given dry (bulk) density, the clay sample used in the study by Korichi et al. (from Maghna, Algeria) has similar tortuosity and porosity values as our pretreated Na-montmorillonite (SWy-2 from Wyoming, USA; Clay Minerals Society). This assumption is supported by fairly comparable U(VI) sorption parameters for both clays. Furthermore, we assumed that the dimensions of Korichi's diffusion cell were selected in such a way that filter effects on the experimentally determined U(VI) diffusion coefficients are negligible.

Based on these assumptions, we could back-calculate the U(VI) pore diffusion coefficient ($D_{p,c}$) based on the reported values for the apparent U(VI) diffusion coefficient ($D_{a,c}$) and the U(VI) K_d value determined at the same chemical solution conditions (pH=7.2, I=0.1 M NaNO₃, C₀=20 mg/L U(VI), dry density $\rho = 1.4 \text{ g/cm}^3$, porosity $\varepsilon_c = 0.512$, tortuosity=4.6, K_d value=1905 L/kg).

$$D_{p,c} = D_{a,c} \frac{\varepsilon_c + \rho K_d}{\varepsilon_c} \quad (4.11)$$

Then, this value of $D_{p,c}$ ($D_{p,c} = 4.12 \times 10^{-8} \text{ m}^2/\text{sec}$) was used to compute values of apparent U(VI) diffusion coefficients in clay for the individual chemical solution conditions to be simulated (Eq. 4.11), as by definition $D_{p,c}$ is independent of chemical solution conditions. In this calculation, we used U(VI) K_d values determined in our batch sorption experiments under variable chemical conditions (Table 4.2), and clay porosity and bulk density values reported by Korichi et al. (Table 4.3).

Overall, for the simulation of U(VI) diffusion over changing chemical solution conditions, we varied the following model input parameters: (1) the apparent U(VI) diffusion coefficients in the filter media, (2) the apparent U(VI) diffusion coefficients in the clay packing, and (3) the U(VI) K_d values for U(VI) sorption onto clay. An overview of input parameters that remained constant during all model runs is provided in Table 4.3.

Table 4.2. Overview of variable model input parameters

Sim.	pH	CO ₂	TIC	Dominant U(VI) species	D_0 ¹⁾	$D_{e,f}$	$D_{a,f}$ ²⁾	$D_{a,c}$	K_d
()	()	()	(mol/L)	()	(m ² /sec)	(m ² /sec)	(m ² /sec)	(m ² /sec)	(L/kg)
<i>Variable TIC, comparable pH conditions (pH~7.3)</i>									
1	7.29	'CO ₂ -free'	4.76E-05	(UO ₂) ₂ CO ₃ (OH) ₃ ⁻	6.10E-10	6.10E-11	2.03E-10	8.60E-13	17,528
2	7.35	Atm. CO ₂	3.52E-04	(UO ₂) ₂ CO ₃ (OH) ₃ ⁻	6.10E-10	6.10E-11	2.03E-10	3.99E-12	3,780
3	7.24	1% CO ₂	2.39E-03	UO ₂ (CO ₃) ₂ ²⁻	5.52E-10	5.52E-11	1.84E-10	2.94E-11	512
<i>Variable pH, comparable TIC concentrations (TIC~2E-05 mol/L, atmospheric CO₂)</i>									
4	3.95	Atm. CO ₂	1.10E-05	UO ₂ ²⁺	7.66E-10	7.66E-11	2.55E-10	7.88E-11	191
5	4.40	Atm. CO ₂	9.45E-06	UO ₂ ²⁺	7.66E-10	7.66E-11	2.55E-10	3.47E-11	434
6	5.12	Atm. CO ₂	2.18E-05	UO ₂ ²⁺	7.66E-10	7.66E-11	2.55E-10	7.83E-12	1,925
7	5.63	Atm. CO ₂	2.88E-05	UO ₂ (OH) ⁺	7.66E-10	7.66E-11	2.55E-10	2.59E-12	5,820
8	6.12	Atm. CO ₂	5.12E-05	UO ₂ (OH) ⁺	7.66E-10	7.66E-11	2.55E-10	9.06E-13	16,624

¹⁾ From Kerisit and Liu, 2010 and Kerisit, personal communication; ²⁾ Assuming a filter porosity of 0.3 (-)

Table 4.3. Constant model input parameters

	Parameter	Value (units)
Filters	Thickness	0.155 (cm) ¹⁾
	Porosity	0.3 (-) ^{1,2)}
	Cross-sectional area	5.11 (cm ²) ¹⁾
Clay packing	Length	1.1 (cm) ¹⁾
	Porosity	0.512 (-) ³⁾
	Dry density	1.4 (g/cm ³) ³⁾
	Cross-sectional area	5.11 (cm ²) ¹⁾
Solutions	Conc. in source reservoir	10 ⁻⁶ (M)
	Conc. in receiving reservoir	0 (M)
Experiment	Time of interest	360 (days)

¹⁾ Van Loon et al., 2003.

²⁾ Entered as porosity of 1 in ANADIFF (see text).

³⁾ Korichi et al., 2010.

4.3 Results and Discussion

4.3.1 Batch sorption equilibrium experiments and surface complexation modeling

4.3.1.1 Experimental Results

In batch sorption equilibrium experiments, we evaluated the effects of CO₂(g) (atmospheric CO₂ (~ 0.039% CO₂), CO₂-free atmosphere and ~1% CO₂) and dissolved calcium (2 mM CaCl₂) on

U(VI) sorption behavior to Na-montmorillonite. It is important to note here that CO₂ levels of ~1% are not uncommon in natural systems and probably represent a “low end” value of CO₂ concentrations in disturbed environments. An overview of all experimental data sets in terms of percent U(VI) sorbed (Figure 4.10; Table 4.4) and U(VI) log K_d values (Figure 4.11; Table 4.4) is provided below. Error bars represent 95% confidence intervals of analytical errors. These data sets were the basis for the development of a U(VI)-montmorillonite surface complexation model.

A detailed discussion of the impacts of CO₂ has been provided in Rutqvist et al. (2012). Briefly, under atmospheric CO₂ conditions, U(VI)-montmorillonite distribution coefficients vary over three orders of magnitude as a function of pH. At low pH, U(VI) sorption is assumed to be limited due to its competition with protons for the same reactive surface/ion exchange sites (Stumm, 1992). At high pH, low uranium sorption is attributed to increasing carbonate concentrations, leading to weakly sorbing or non-sorbing aqueous U(VI)-carbonato complexes (Davis et al., 2004; Hsi and Langmuir, 1985). In CO₂-free systems, the shape of the U(VI) batch sorption envelope is different compared to the atmospheric CO₂ system. In the low-pH region, U(VI) sorption characteristics remain similar with comparable K_d values in the pH range from 4 to 6. Above pH 7, however, U(VI) sorption is much stronger in the absence of CO₂. The increase in U(VI) sorption at high pH values is attributed to the lack of aqueous U(VI)-carbonato complexes in the N₂(g) environment. The effect of carbonato solution complexes on U(VI) sorption characteristics is also demonstrated by U(VI) sorption results for the system with elevated CO₂ concentrations (~1% CO₂ atmosphere). In this case, the shape of the sorption envelope is similar to the one determined under atmospheric carbon dioxide conditions. However, U(VI) sorption decreased at pH values greater than 5.8.

Overall, a variation in CO₂(g) and TIC concentrations in solution has substantial impact on the fraction of U(VI) sorbed (Figure 4.10) and causes changes in U(VI) K_d values over several orders of magnitude (Figure 4.11). As a result, changes in inorganic carbon concentrations can lead to variations in U(VI) mobility over several orders of magnitude.

Comparing the data sets for U(VI) sorption under atmospheric CO₂ conditions in the presence of 2 mM CaCl₂ and Ca background concentrations (Figure 4.12), we find that the data sets only diverge for pH values greater than ~7.4. In this higher pH region, U(VI) solution speciation changes due to the presence of 2 mM Ca, which leads to the formation of ternary Ca-U-carbonato complexes (Figs. 4.13 and 4.14). This shift in U(VI) speciation further causes a decrease in the fraction of U(VI) sorbed onto Na-montmorillonite. For instance, at pH~8, the U(VI) K_d value is lowered by approximately half an order of magnitude.

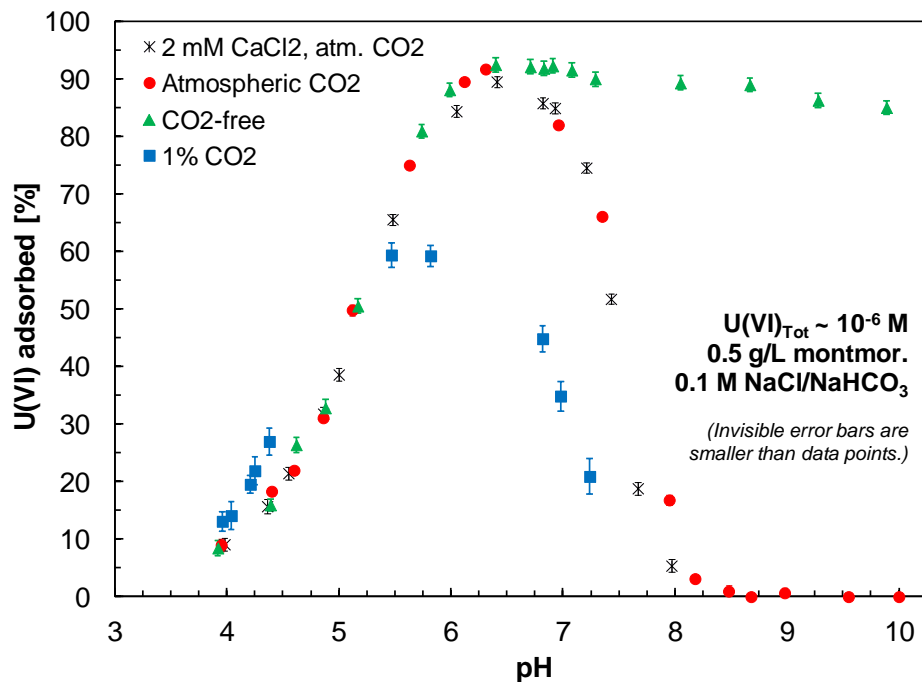


Figure 4.10. U(VI) adsorption onto Na-montmorillonite at varying chemical solution conditions.

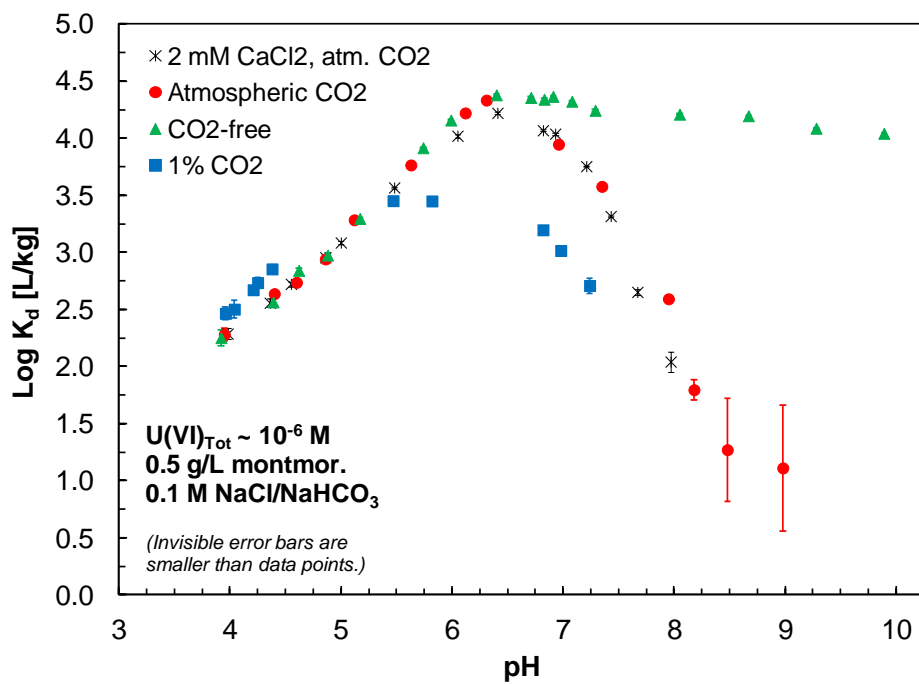


Figure 4.11. K_d values for U(VI) sorption to Na-montmorillonite at varying chem. solution conditions.

Table 4.4. Summary of U(VI) adsorption data in batch sorption envelope experiments

Atmospheric CO ₂ , Ca-free				CO ₂ -free atmosphere, Ca-free				~1% CO ₂ atmosphere, Ca-free				Atmospheric CO ₂ , 2 mM Ca			
pH	U(VI) sorbed	Kd	log Kd	pH	U(VI) sorbed	Kd	log Kd	pH	U(VI) sorbed	Kd	log Kd	pH	U(VI) sorbed	Kd	log Kd
[]	[%]	[L/kg]	[L/kg]	[]	[%]	[L/kg]	[L/kg]	[]	[%]	[L/kg]	[L/kg]	[]	[%]	[L/kg]	[L/kg]
3.95	8.98	191	2.28	3.92	8.46	179	2.25	3.96	13.10	292	2.47	3.98	9.11	194	2.29
4.40	18.33	434	2.64	4.39	15.96	367	2.57	4.04	14.09	318	2.50	4.36	15.73	361	2.56
4.60	21.98	545	2.74	4.62	26.42	695	2.84	4.21	19.53	470	2.67	4.55	21.47	529	2.72
4.86	31.10	874	2.94	4.88	32.83	946	2.98	4.25	21.89	543	2.73	4.86	31.82	904	2.96
5.12	49.86	1,925	3.28	5.17	50.54	1,978	3.30	4.38	26.99	715	2.85	5.00	38.62	1,218	3.09
5.63	75.04	5,820	3.76	5.74	80.98	8,239	3.92	5.47	59.41	2,833	3.45	5.48	65.63	3,697	3.57
6.12	89.57	16,624	4.22	5.99	88.15	14,403	4.16	5.82	59.27	2,817	3.45	6.05	84.41	10,484	4.02
6.31	91.75	21,533	4.33	6.40	92.52	23,945	4.38	6.82	44.86	1,575	3.20	6.41	89.58	16,635	4.22
6.96	82.05	8,845	3.95	6.71	92.15	22,712	4.36	6.98	34.88	1,037	3.02	6.82	85.83	11,728	4.07
7.35	66.13	3,780	3.58	6.83	91.89	21,917	4.34	7.24	20.91	512	2.71	6.93	84.97	10,943	4.04
7.95	16.82	391	2.59	6.91	92.30	23,211	4.37	n/a	n/a	n/a	n/a	7.21	74.59	5,683	3.75
8.18	3.13	63	1.80	7.08	91.58	21,049	4.32	n/a	n/a	n/a	n/a	7.43	51.77	2,078	3.32
8.48	0.95	19	1.27	7.29	90.06	17,528	4.24	n/a	n/a	n/a	n/a	7.67	18.84	449	2.65
8.68	n.d.	n/a	n/a	8.05	89.33	16,212	4.21	n/a	n/a	n/a	n/a	7.97	5.39	110	2.04
8.98	0.66	13	1.11	8.67	89.03	15,703	4.20	n/a	n/a	n/a	n/a	n/a	n/a	n/a	n/a
9.55	n.d.	n/a	n/a	9.28	86.32	12,216	4.09	n/a	n/a	n/a	n/a	n/a	n/a	n/a	n/a
10.00	n.d.	n/a	n/a	9.89	85.07	11,027	4.04	n/a	n/a	n/a	n/a	n/a	n/a	n/a	n/a

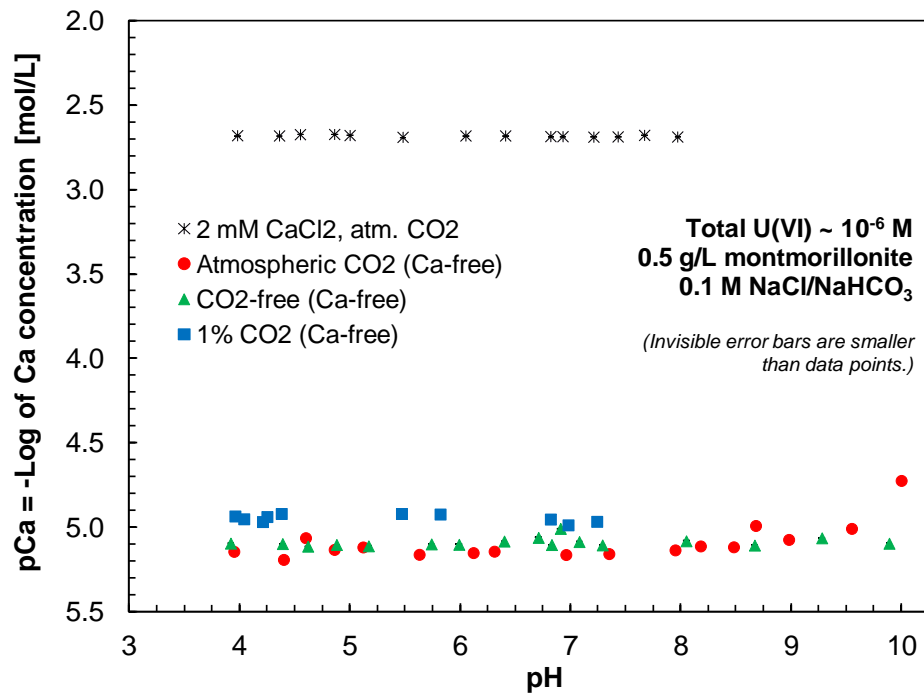


Figure 4.12. Total, measured Ca concentrations in solution for batch sorption equilibrium experiments.

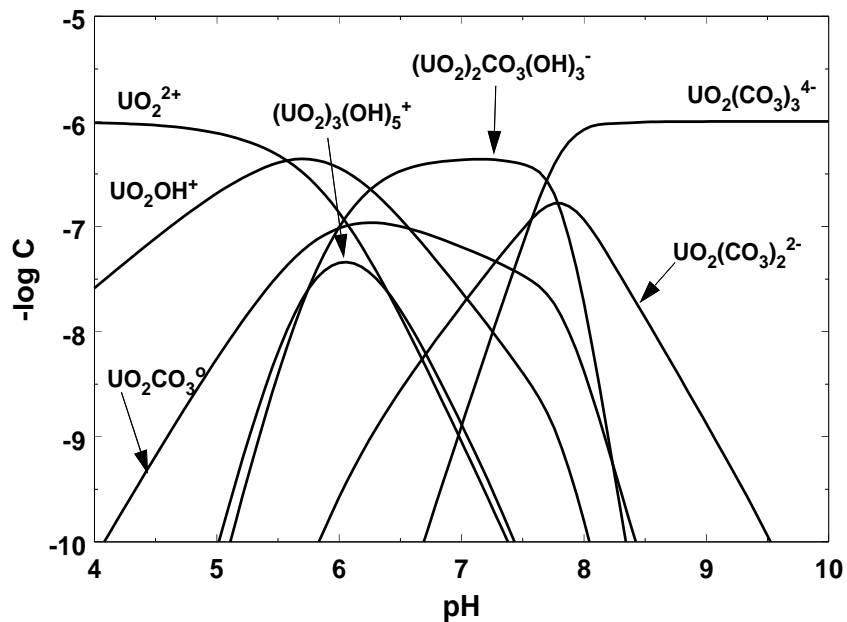


Figure 4.13. Aqueous speciation of a 1 micromolar U(VI) solution in 0.1 M NaCl in equilibrium with atmospheric CO_2 ($\log \text{CO}_2 = -3.5$) as a function of pH. Vertical axis is the negative log of the concentration of each U(VI) species.

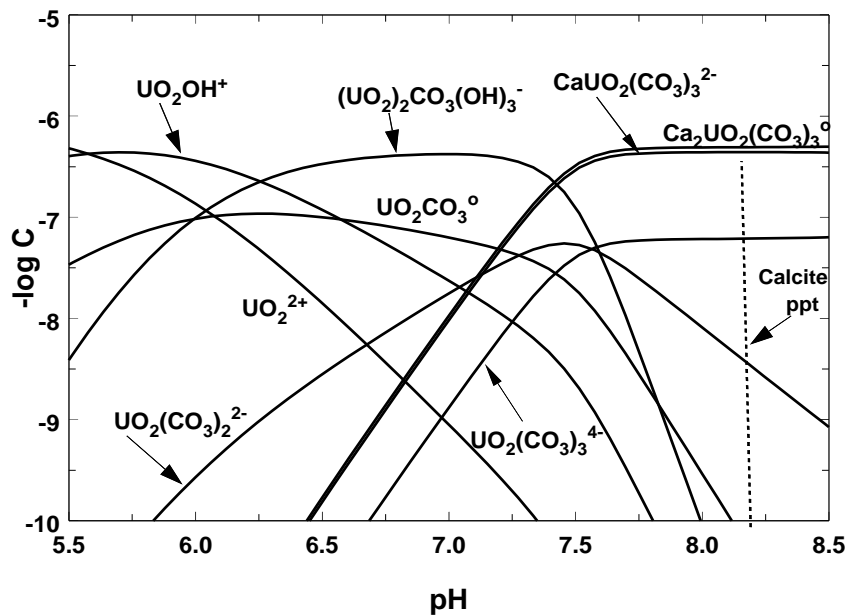


Figure 4.14. Same as Figure 4.13. except solution now contains 2 mM Ca. Aqueous speciation of a 1 micromolar U(VI) solution in 0.1 M NaCl in equilibrium with atmospheric CO_2 ($\log \text{CO}_2 = -3.5$) as a function of pH. Vertical axis is the negative log of the concentration of each U(VI) species.

4.3.1.2 Modeling Results

In our preliminary modeling approach, we used only one of the four U(VI) sorption data sets for the fitting of model parameters, namely U(VI) sorption data determined in the CO₂-free (and Ca-free) system. Uranium(VI) sorption trends in the remaining three systems (1% CO₂, Ca-free; atmospheric CO₂, Ca-free; and atmospheric CO₂, 2 mM Ca) were then *predicted*, based on fitted values of surface complexation and ion exchange constants (Table 4.5) and the known changes in U(VI) solution speciation, which were calculated using published thermodynamic data (Guillaumont et al., 2003; Dong and Brooks, 2008).

Table 4.5. Overview of uranium(VI) surface reactions in surface complexation model

Species	Reaction	Log K (I = 0)
UO ₂ X ₂	UO ₂ ²⁺ + 2NaX = UO ₂ X ₂ + 2Na ⁺	7.99
AlO ₂ UO ₂	Al(OH) ₂ + UO ₂ ²⁺ = AlO ₂ UO ₂ + 2H ⁺	-1.50
AlO ₂ UO ₂ OH	Al(OH) ₂ + UO ₂ ²⁺ = AlO ₂ UO ₂ OH + H ⁺	-10.34

Model predictions are able to capture very well the general changes in U(VI) sorption behavior as a function of varying chemical solution conditions (Figure 4.15). Ion exchange was more important than surface complexation only below pH 4 at this Na concentration (0.1 M). Hence, these results demonstrate the strong capability of surface complexation models to *predict* contaminant sorption behavior for various chemical solution conditions, which is possible due to their strong link to solution chemistry and metal solution speciation. In comparison, radionuclide transport models with constant K_d values do not have the same predictive capabilities, unless they are linked to surface complexation models in some manner, e.g., through expressions for “smart” K_d values.

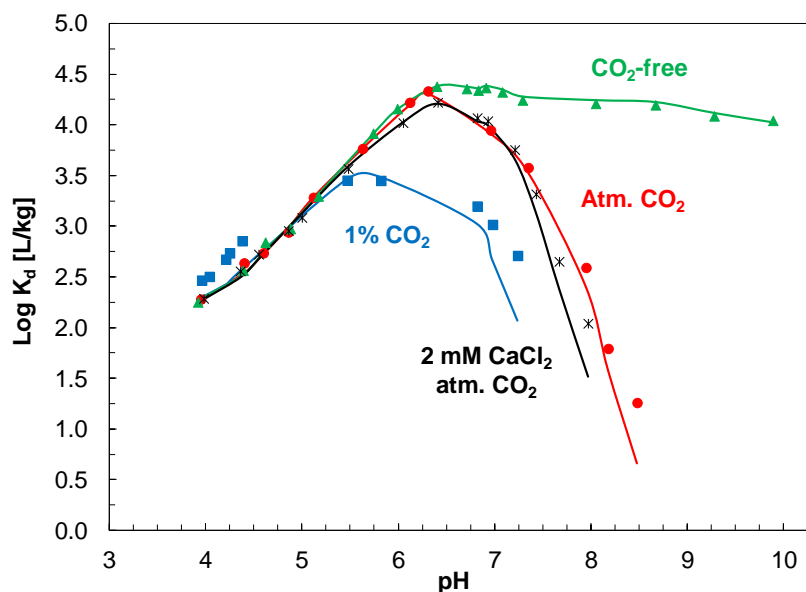


Figure 4.15. Modeling results for U(VI) sorption onto Na-montmorillonite over the whole pH range.

A more detailed comparison of the modeling results with the experimental data in the circumneutral pH range reveals two interesting features (Figure 4.16). First, at pH > 5.8, the model underpredicts U(VI) sorption in the 1% CO₂ system. This suggests that the formation of ternary U(VI)-carbonato surface complexes, which has not been included in this model at this point, may be relevant under these conditions. Second, while the model is able to capture the differences in U(VI) sorption in the presence and absence of Ca at pH values greater than ~7.4, it also predicts a larger decrease in U(VI) sorption for the 2 mM Ca system than the experimental data. A few additional experiments are needed in order to fully clarify both points, e.g., at higher CO₂ and Ca concentrations and varying ionic strength conditions.

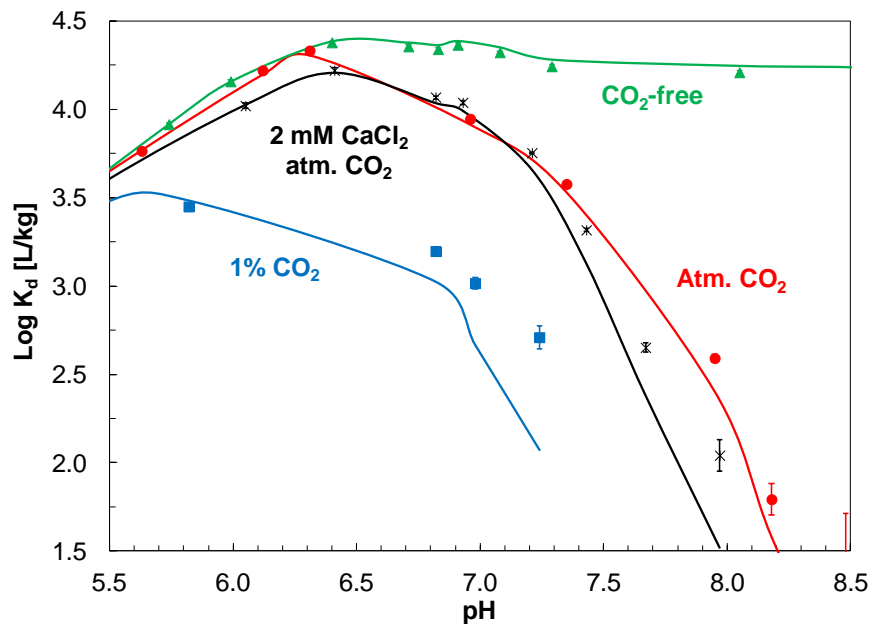


Figure 4.16. Detailed modeling results for U(VI) sorption onto Na-montmorillonite between pH values of 5.5 and 8.5.

4.3.2 Calcium Bromide Diffusion in Na-Montmorillonite

4.3.2.1 Experimental Results

After the collection of low-concentration reservoir solutions for the individual time points in the CaBr₂ diffusion experiment, solution pH was measured in each sample vial. Based on our results (Figure 4.17), the pH in these solutions continuously shifted from pH 7 to slightly lower values, most likely due to solution contact with the clay mineral phase.

Over the course of the experiment, the high-concentration reservoir (200 mL) was repeatedly sampled for small volume fractions (1.5 mL) in order to monitor Ca and Br concentrations by ICP-MS (Figure 4.18), while minimizing the loss of solution from the reservoir. Our analytical results show fairly constant total concentrations of Ca and Br in this reservoir. Furthermore, Ca and Br concentrations measured in low-concentration reservoir samples only exceeded 2% of their respective concentrations in the high-concentration reservoir for three data points. Hence, we can conclude that our assumption of a constant concentration gradient between high- and low-concentration reservoirs is generally justified, which is an important mathematical

requirement for the application of the selected analytical solution of the diffusion equation (see details below).

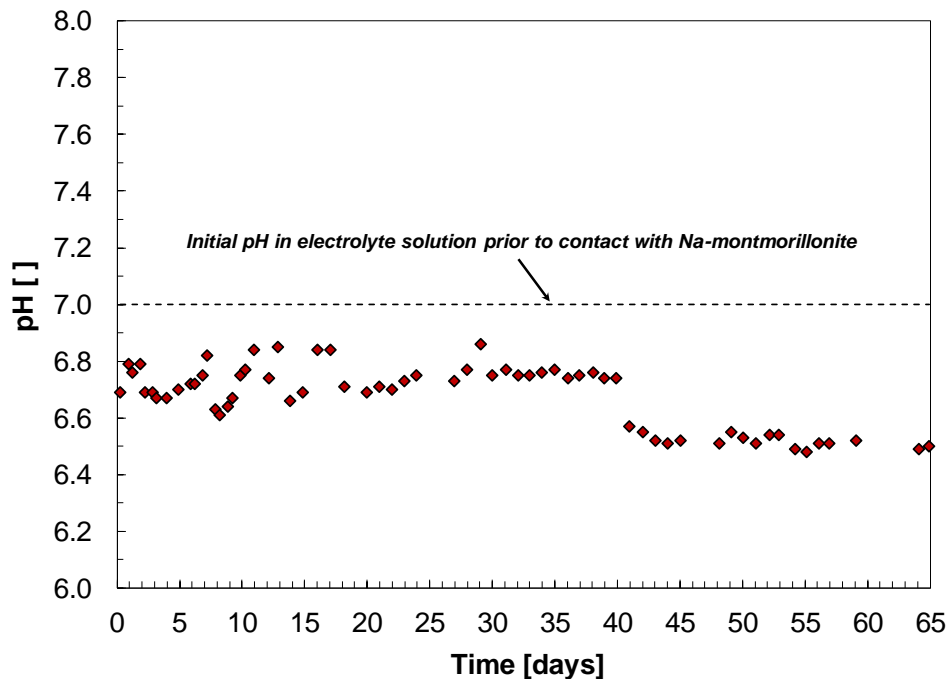


Figure 4.17. Results for monitoring of solution pH in low-concentration reservoir solutions during CaBr_2 diffusion experiment.

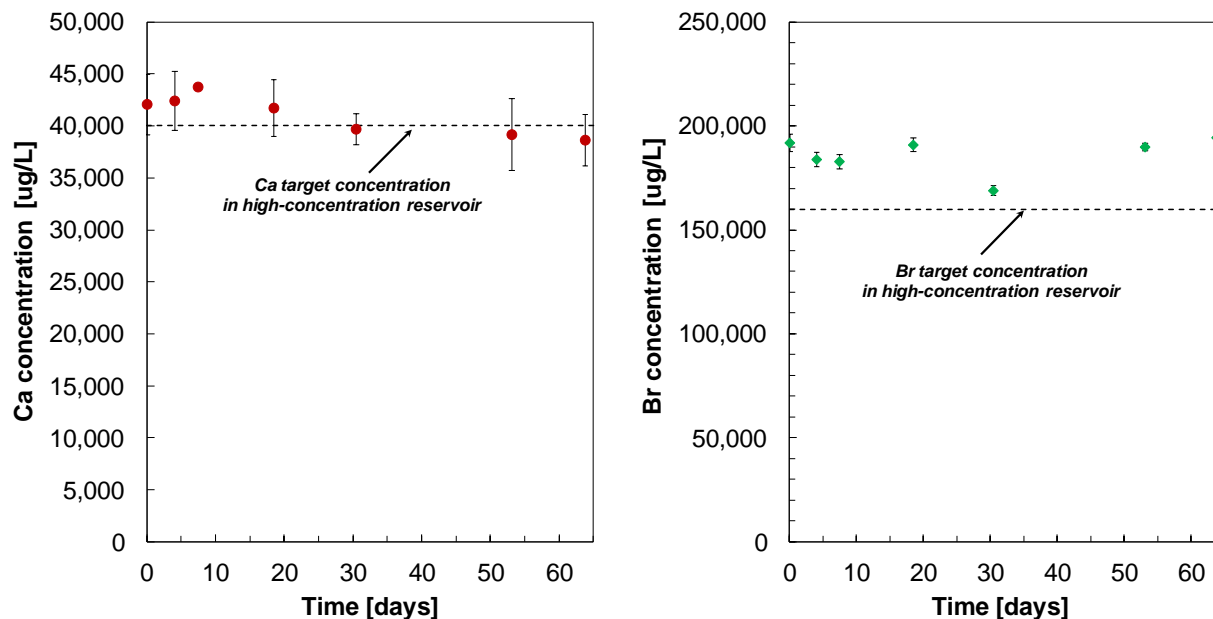


Figure 4.18. Results for monitoring of Ca and Br concentrations in high-concentration reservoir solution during CaBr_2 diffusion experiment. Error bars for Ca data represent standard deviations of replicate ICP-MS analysis of the same samples; error bars for Br data are standard deviations for replicate injections during ICP-MS analysis of the same samples.

In through-diffusion experiments, the solute concentrations or activities measured in the low-concentration reservoir solutions over time are typically used to compute the diffusive flux and cumulative mass of solutes based on the following equations (Van Loon et al., 2003; Van Loon and Soler, 2004). Following these data interpretation steps, measured Ca and Br concentrations and tritium activities were first corrected for their background values found in the background electrolyte solution. The net concentrations or activities for the individual time-point samples were then used to calculate the total concentration or activity that is diffused through the diffusion cell during each time interval Δt_i .

For tritium activity measurements, determined in terms of counts per minute (cpm) on the liquid scintillation counter (LSC), the net diffused activity ($N_{diff}^{\Delta t_i}$) per time step (Δt_i) was calculated for the *first* time step ($\Delta t_i = \Delta t_1$ and $N_S^{\Delta t_i} = N_S^{\Delta t_1}$) as

$$N_{diff}^{\Delta t_i} = \frac{N_S^{\Delta t_i}}{V_{count}} V_{sample} + \frac{N_S^{\Delta t_i}}{V_{count}} V_{dead} \quad (4.12)$$

where $N_S^{\Delta t_i}$ represents the net counts in each sample fraction after background subtraction, V_{count} the volume fraction of the low-concentration reservoir sample that is counted on the LSC (mL), V_{sample} the exact volume in the low-concentration reservoir determined by weighing (mL), and V_{dead} the dead volume ($V_{dead}=1.3869$ mL) on the low-concentration reservoir side of the diffusion setup, including the volumes in tubings, the grooves in the end plate and the metal filter pore space (all determined by weighing).

For all *later* time points, the net diffused activity per time step was computed with the following expression, which now also corrects for the activity left in the dead volume of the cell from the previous time step:

$$N_{diff}^{\Delta t_i} = \frac{N_S^{\Delta t_i}}{V_{count}} V_{sample} + \frac{N_S^{\Delta t_i}}{V_{count}} V_{dead} - \frac{N_S^{\Delta t_{i-1}}}{V_{count}} V_{dead} \quad (4.13)$$

Now, the activity (in units of nanoCi) diffused through the clay packing in the diffusion cell during each time step can be expressed as follows, while taking into account the tritium counting efficiency of the LSC ($E=0.3911$) and the conversion from disintegrations per minute (dpm) to nanoCi (1 nCi=2220 dpm):

$$A_{diff}^{\Delta t_i} = \frac{N_{diff}^{\Delta t_i}}{E \times 2220} \quad (4.14)$$

Hence, the total diffused activity (or cumulative activity) up to time point t_n (in nCi) is then given by

$$A_{diff}^{t_n} = \sum_{i=1}^n A_{diff}^{\Delta t_i} \quad (4.15)$$

and the average diffusive flux (nCi/(cm² hr)) per time step as

$$J^i = \frac{A_{diff}^{\Delta t_i}}{S \Delta t_i} \quad (4.16)$$

where S is the cross-sectional area of the clay packing (cm²).

For the data interpretation of Ca and Br concentration measurements, the same general procedure is followed, but in concentration and mass units. Hence, the net diffused mass ($m_{diff}^{\Delta t_i}$) per time step (Δt_i) is computed for the *first* time step as

$$m_{diff}^{\Delta t_i} = \frac{c_S^{\Delta t_i}}{1000} V_{sample} + \frac{c_S^{\Delta t_i}}{1000} V_{dead} \quad (4.17)$$

where $c_S^{\Delta t_i}$ is the net concentration of Ca or Br ($\mu\text{g/L}$) measured by ICP-MS analysis. For all *other* timepoints,

$$m_{diff}^{\Delta t_i} = \frac{c_S^{\Delta t_i}}{1000} V_{sample} + \frac{c_S^{\Delta t_i}}{1000} V_{dead} - \frac{c_S^{\Delta t_{i-1}}}{1000} V_{dead} \quad (4.18)$$

Furthermore, the total diffused mass (or cumulative mass) up to time point t_n (in μg) is then given by

$$m_{diff}^{t_n} = \sum_{i=1}^n m_{diff}^{\Delta t_i} \quad (4.19)$$

The average diffusive flux (in $\mu\text{g}/(\text{cm}^2 \text{ hr})$) per time step is calculated as

$$J^i = \frac{m_{diff}^{\Delta t_i}}{S \Delta t_i} \quad (4.20)$$

The experimental results for the diffusive flux and cumulative mass/activity plots for Ca, Br, and tritium (^3H) are given in the following figures 4.19 to 4.24. For Ca, the time-frame needed to reach steady-state conditions in our Na-montmorillonite diffusion experiment (~ 33 days) agrees well with previously published data for calcium diffusion in bentonite (31 days (Mazzieri et al., 2010) or 35 days (Shackelford and Lee, 2003)).

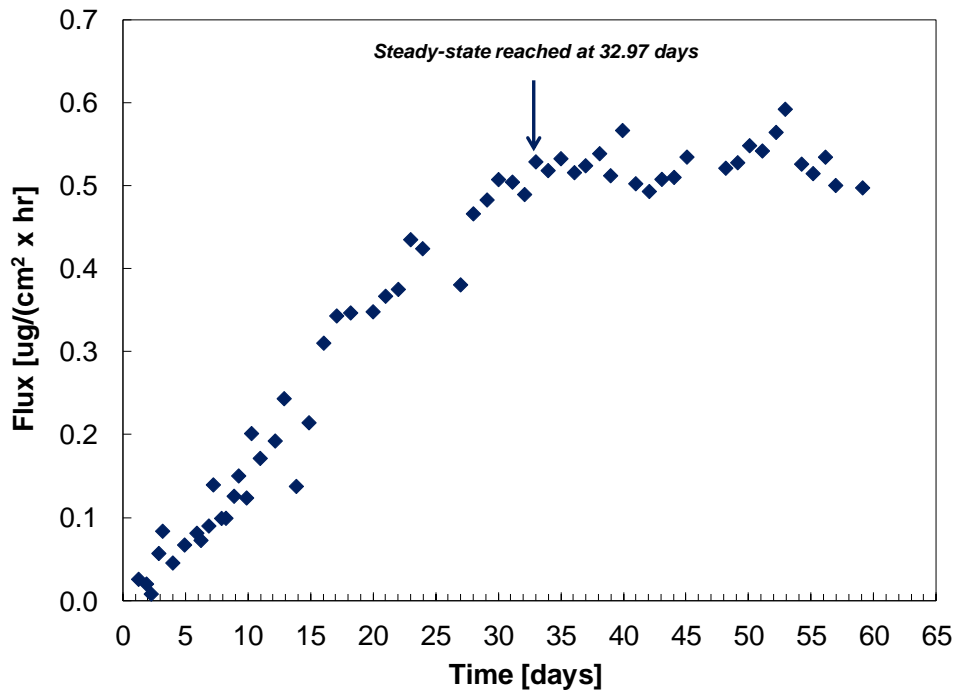


Figure 4.19. Diffusive flux of Ca through pretreated Na-montmorillonite as a function of time in CaBr₂ through-diffusion experiment at 1 mM CaBr₂, I=0.1 M NaCl and pH~7. Steady-state conditions are approximately reached at 32.97 days.

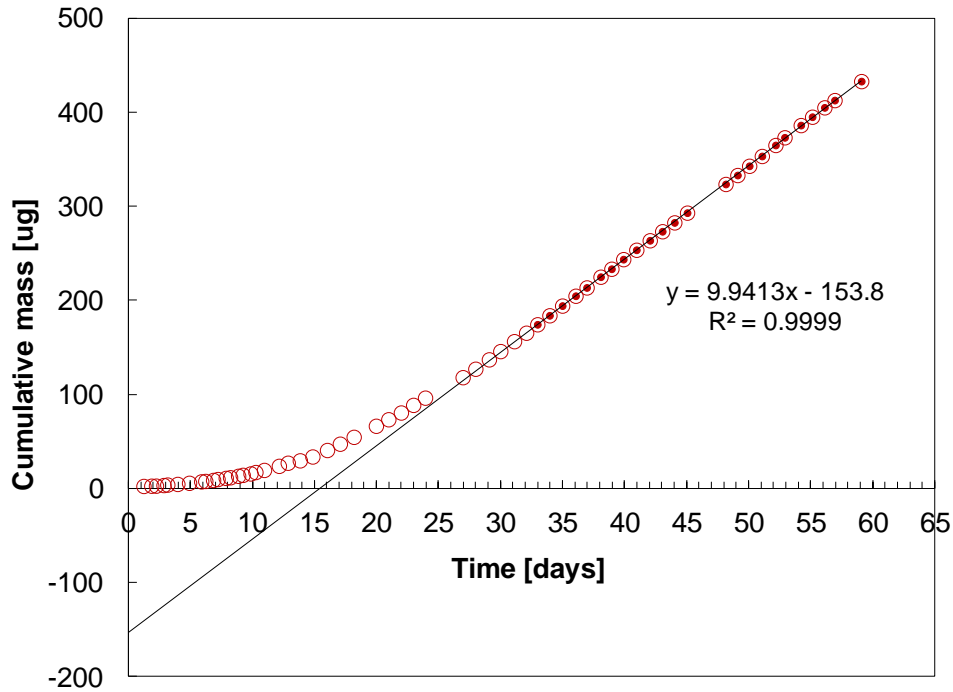


Figure 4.20. Cumulative mass of Ca as a function of time in CaBr₂ through-diffusion experiment in pretreated Na-montmorillonite at 1 mM CaBr₂, I=0.1 M NaCl and pH~7. Data points shown as dots are assumed to be under steady-state conditions and are used for the fitting of the asymptote to calculate diffusion parameters (see text for details).

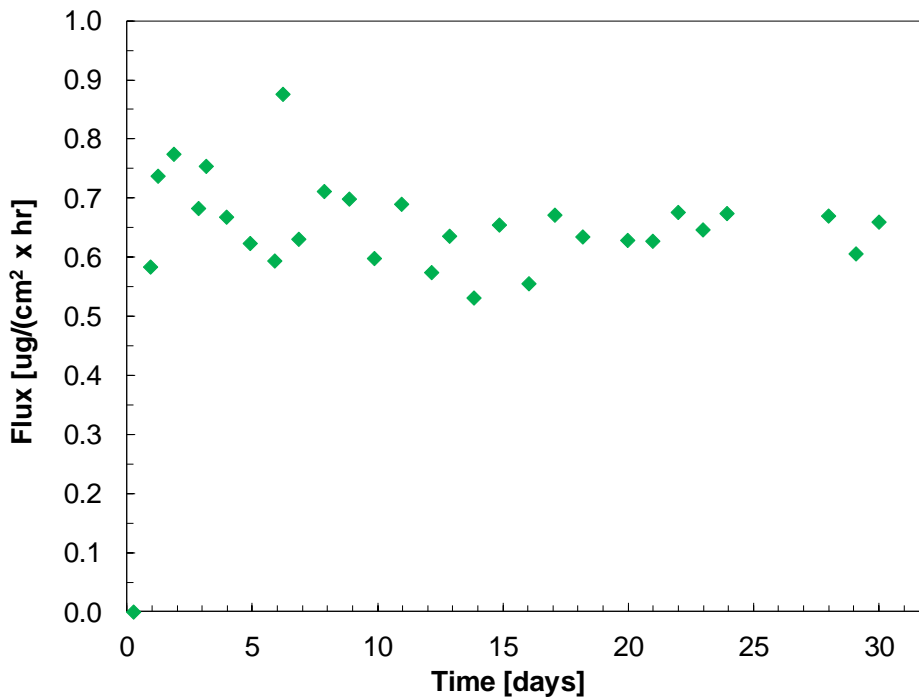


Figure 4.21. Diffusive flux of Br through pretreated Na-montmorillonite as a function of time in CaBr_2 through-diffusion experiment at 1 mM CaBr_2 , $I=0.1$ M NaCl and $\text{pH}\sim 7$. Steady-state conditions are most likely reached after a few days.

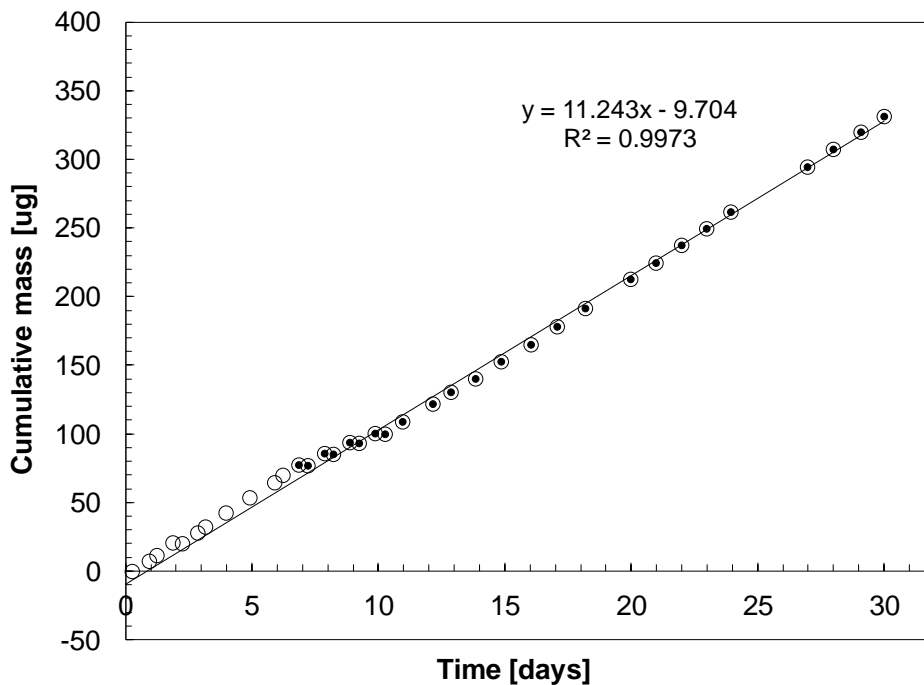


Figure 4.22. Cumulative mass of Br as a function of time in CaBr_2 through-diffusion experiment in pretreated Na-montmorillonite at 1 mM CaBr_2 , $I=0.1$ M NaCl and $\text{pH}\sim 7$. Data points shown as dots are assumed to be under steady-state conditions and are used for the fitting of the asymptote to calculate diffusion parameters (see text for details).

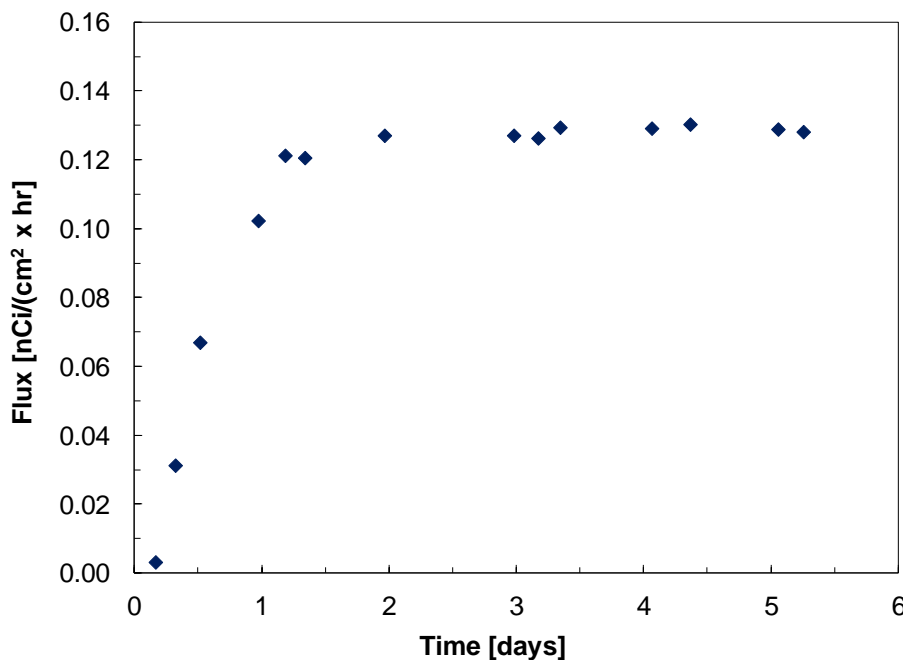


Figure 4.23. Diffusive flux of tritium through pretreated Na-montmorillonite as a function of time in CaBr₂ through-diffusion experiment at I=0.1 M NaCl and pH~7. Steady-state conditions are most likely reached after 1-2 days.

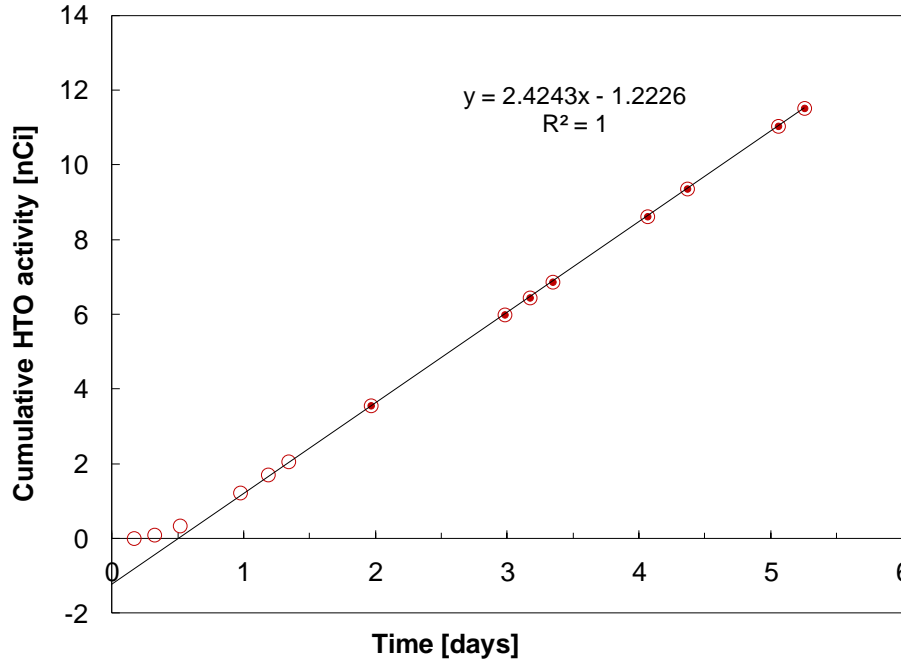


Figure 4.24. Cumulative activity of tritium as a function of time in CaBr₂ through-diffusion experiment in pretreated Na-montmorillonite at I=0.1 M NaCl and pH~7. Data points shown as dots are assumed to be under steady-state conditions and are used for the fitting of the asymptote to calculate diffusion parameters (see text for details). Tracer experiment is currently still ongoing in order to collect a larger number of data points under steady state conditions.

4.3.2.2 Mathematical Background for Data Interpretation

In the following, we provide a brief overview of the mathematical background for the interpretation of diffusion data; additional detail is given elsewhere (van Loon et al., 2003; Van Loon and Soler, 2004). For one-dimensional diffusion through a clay packing with a diffusion length of L , the diffusive flux (J) can be calculated based on Fick's first law:

$$J = -D_e \frac{\partial c}{\partial x} \quad (4.21)$$

where D_e represents the effective diffusion coefficient, c the solute concentration, and x the distance along the diffusion cell. The concentration change within the system is described by Fick's second law of diffusion:

$$\frac{\partial c}{\partial t} = D_a \frac{\partial^2 c}{\partial x^2} \quad (4.22)$$

where the apparent diffusion coefficient (D_a) is linked to the effective diffusion coefficient through the rock capacity value (α):

$$D_a = \frac{D_e}{\alpha} \quad (4.23)$$

For through-diffusion experiments, the concentration gradient in the clay packing along the diffusion length (x) is assumed to be linear under steady-state conditions. Hence, the analytical solution to the through-diffusion problem is found by solving Fick's second law (Eq. 4.22) with the following initial and boundary conditions:

$$\begin{aligned} c(x,t) &= 0 & t &= 0 \\ c(0,t) &= C_0 & x &= 0 \\ c(L,t) &= 0 & x &= L \end{aligned}$$

and by taking into account that the diffusive flux at the end of the clay packing ($x = L$) is equal to

$$J(L,t) = -D_e \left. \frac{\partial c}{\partial x} \right|_{x=L} \quad (4.24)$$

The general analytical solution (Crank, 1975; Jakob et al., 1999) gives the cumulative mass (or activity) diffused through the clay packing in the diffusion cell as a function of time. In terms of cumulative or total diffused mass, it can be expressed as

$$m_{diff}^t = c(L,t) \cdot V_{sample} = S \cdot L \cdot C_0 \left(\frac{D_e}{L^2} t - \frac{\alpha}{6} - \frac{2\alpha}{\pi^2} \sum_{n=1}^{\infty} \frac{(-1)^n}{n^2} \exp\left(-\frac{D_e n^2 \pi^2 t}{L^2 \alpha}\right) \right) \quad (4.25)$$

in terms of cumulative activity, it is equal to

$$A_{diff}^t = S \cdot L \cdot A_0 \left(\frac{D_e}{L^2} t - \frac{\alpha}{6} - \frac{2\alpha}{\pi^2} \sum_{n=1}^{\infty} \frac{(-1)^n}{n^2} \exp\left(-\frac{D_e n^2 \pi^2 t}{L^2 \alpha}\right) \right) \quad (4.26)$$

However, under steady-state conditions (with $t \rightarrow \infty$) the analytical solution can be simplified to

$$m_{diff}^t = \frac{SC_0 D_e}{L} t - \frac{SLC_0 \alpha}{6} \quad (4.27)$$

for concentration units, and analogously to

$$A_{diff}^t = \frac{SA_0 D_e}{L} t - \frac{SLA_0 \alpha}{6} \quad (4.28)$$

for activity units. As a result, the slopes of cumulative mass and activity curves are equal to

$$a = \frac{SC_0 D_e}{L} \quad a = \frac{SA_0 D_e}{L} \quad (4.29)$$

and the intercepts of their asymptotes to

$$-b = \frac{SLC_0 \alpha}{6} \quad -b = \frac{SLA_0 \alpha}{6} \quad (4.30)$$

After fitting the asymptotes to the experimental data for cumulative mass and activity plots, these equations (Eq. 4.29 and 4.30) can be further used to calculate the effective diffusion coefficient of the solute (D_e) as well as the rock capacity factor (α), e.g., for concentration units,

$$D_e = a \frac{L}{SC_0} \quad \alpha = -\frac{6b}{SLC_0} \quad (4.31)$$

Furthermore, based on Eq. (4.23), the determined effective diffusion coefficient and rock capacity factor can now be used to compute the apparent diffusion coefficient (D_a) for the individual solutes.

In general, the rock capacity factor is defined as

$$\alpha = \varepsilon + \rho \cdot K_d \quad (4.32)$$

and includes the diffusion-accessible porosity (ε), the dry bulk density of the mineral (ρ), and the sorption distribution coefficient (K_d). For non-reactive tracers, such as tritiated water, the sorption distribution coefficient is equal to zero, and the calculated rock capacity factor can be directly used to determine the diffusion-accessible porosity in the clay packing. Then, this porosity value can be applied to compute the K_d values for sorbing solutes in the diffusion experiment based on Eq. 4.32. This is of particular interest, as the differences in solid concentrations between batch sorption equilibrium experiments and diffusion studies may affect the values of distribution coefficients determined in each type of experiment.

The results of our data interpretation are summarized in Table 4.6. In the calculation of sorption distribution coefficients, a value of 0.784 (g/cm³) was used for the dry bulk density, which was determined based on the clay mass weighed into the diffusion cell and the known volume of the cell. A second determination of the exact clay mass will follow at the end of the diffusion experiment in order to minimize the experimental error associated with the computed parameters.

Table 4.6. Parameters determined in CaBr₂ diffusion experiment

	Ca	Br	HTO
Effective diffusion coefficient, D_e [cm ² /hr]	6.41E-03	1.60E-03	2.43E-03
Rock capacity factor, α []	5.71E+01	7.96E-04	7.05E-01
Apparent diffusion coefficient, D_a [cm ² /hr]	1.12E-04	2.01E+00	3.44E-03
K_d [cm ³ /g]=[L/kg]	71.99	-0.90	0

4.3.3 Predictive Modeling of Uranium(VI) Diffusion in Lab-Scale Experiments

In Figures 4.25 and 4.26, we depict simulated U(VI) diffusion profiles as a function of chemical solution conditions and time. These profiles represent *total* metal concentrations (sorbed and dissolved U(VI)) plotted over the total length of the diffusion cell. The positions of the inlet and outlet filters are high-lighted by two blue-shaded areas on the left and right hand-side of each figure. The initial U(VI) solution concentration of 10⁻⁶ mol/L in the high-concentration reservoir is equivalent to 1 mM U(VI)/m³. Hence, similar U(VI) concentration ranges found in the metal filter close to the high-concentration reservoir are not easily visible in these figures due to the scaling selected for the y-axis.

Based on these results, both the total concentration of U(VI) found in the clay packing as well as the overall shape of the diffusion profiles are strongly influenced by chemical solution conditions. For TIC, low inorganic carbon concentrations lead to high total U(VI) concentrations and steep slopes of diffusion profiles. In contrast, high TIC concentrations result in low total

U(VI) concentrations and relatively flat profiles. For pH variations ranging from pH=4 to pH=6.1, we observe higher total U(VI) concentrations and steeper slopes of diffusion profiles with increasing pH. These trends are directly linked to U(VI) sorption behavior and the U(VI) K_d values specified for individual solution conditions. Large U(VI) K_d values lead to high concentrations of sorbed and hence total U(VI), especially within short distances from the inlet filter. This, in turn, creates steeper slopes for diffusion profiles.

In addition, U(VI) sorption affinities affect the distribution of total U(VI) over the length of the diffusion cell as a function of time. High U(VI) K_d values limit metal mobility through the clay packing at the beginning of the experiment. For instance, after 36 days, U(VI) is only transported about 0.6 cm into the diffusion cell setup in the “CO₂-free” system ($K_d=17,528$ L/kg), while it migrates through the entire clay packing under 1% CO₂ conditions ($K_d=512$ L/kg). Independent of the chemical solution conditions, we see an increase in total and sorbed U(VI) with each time step simulated over 360 days. This further implies that none of these systems becomes limited in mineral surface sites for U(VI)-clay interactions over time.

In Figure 4.27, we show relative U(VI) solution concentrations plotted over the length of the diffusion cell setup at the end of the simulated diffusion experiment (360 days). These are solution concentrations of U(VI) that are found in the pores of the clay packing or the filter media. Again, chemical solution conditions and U(VI) sorption affinities have large impacts on U(VI) solution concentrations and metal mobility. Systems with high U(VI) K_d values (e.g., “CO₂-free” system at pH=7.3) show higher concentrations of sorbed U(VI), which results in lower U(VI) solution concentrations in the clay pores. On the other hand, systems with low K_d values (e.g., pH=4, 4.4 and 5.1 at atmospheric CO₂) are characterized by higher U(VI) solution concentrations in the clay packing.

Overall, we conclude that chemical solution conditions and U(VI) speciation may have significant impacts on metal diffusion through clays in engineered barriers systems. However, these simulations are based on simplified conceptual models due to the limitations of the code ANADIFF. They can only account for changes in U(VI) sorption behavior (K_d values), but not the impacts of chemical solution conditions on clay (surface) characteristics (see Section 4.1.3 for details), potentially leading to indirect effects on U(VI) diffusion behavior, e.g., due to anion exclusion effects. Hence, there is a strong need to consider these parameters in further experimental investigations and predictive transport models.

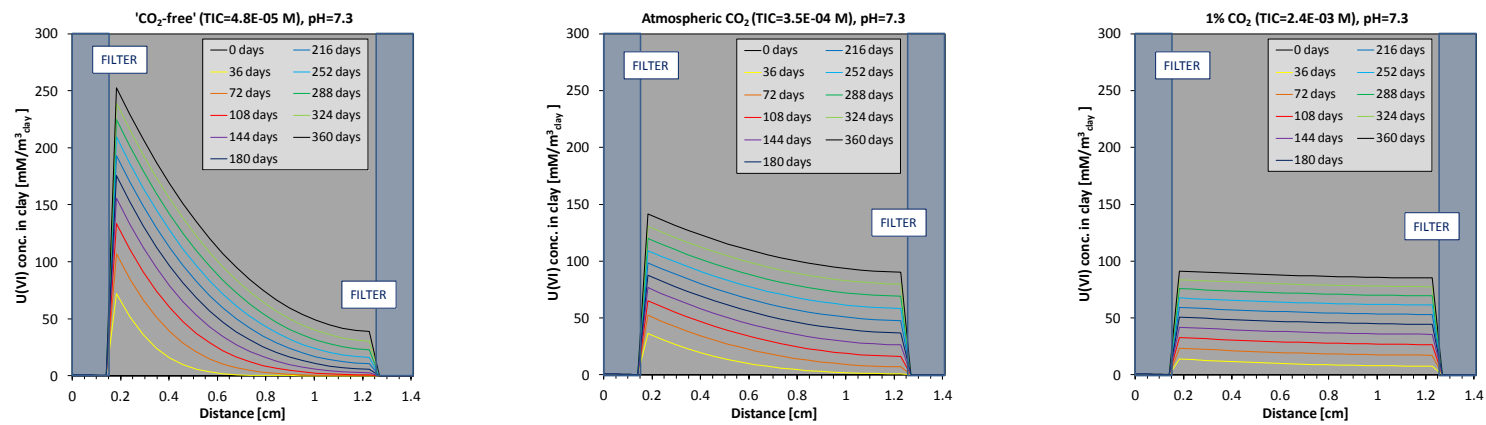


Figure 4.25. Simulated diffusion profiles: Total U(VI) conc. along a clay packing as a function of Total Inorganic Carbon (TIC) conc. and time.

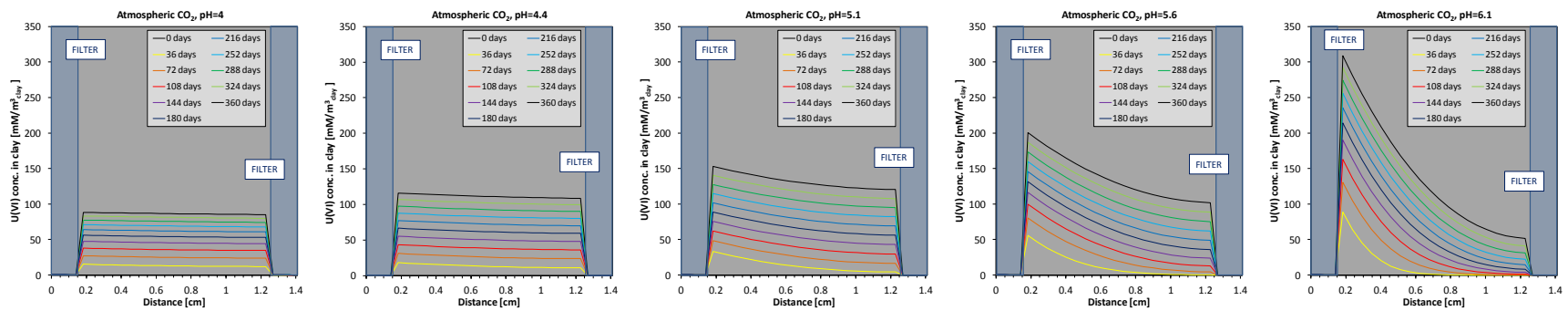


Figure 4.26. Simulated diffusion profiles: Total U(VI) concentrations along a clay packing as a function of solution pH and time.

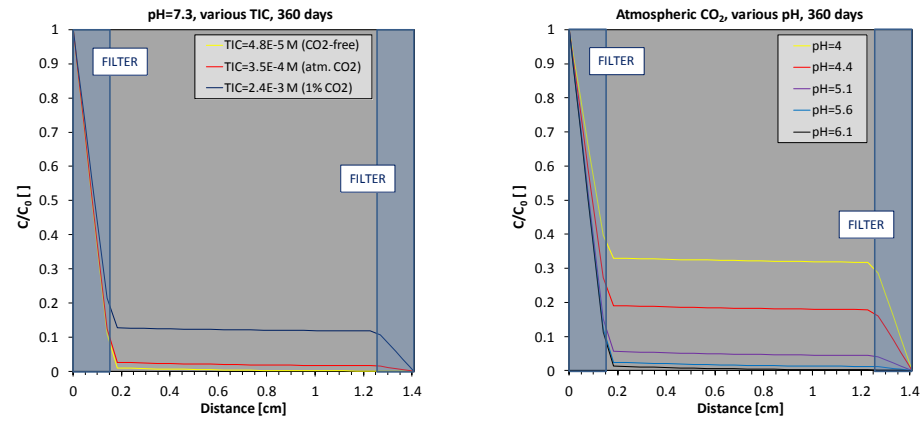


Figure 4.27. Simulated relative U(VI) solution concentrations as a function of Total Inorganic Carbon (TIC) concentrations and pH after a 360-day experiment.

4.4 Summary

From our theoretical analysis of the effects of chemical solution conditions on uranium(VI) diffusion coefficients and clay (surface) properties, we concluded that solution chemistry can literally affect *all types* of U(VI) diffusion coefficients, from the molecular diffusion coefficient in solution to the apparent diffusion coefficient in porous media.

In batch sorption equilibrium experiments, we demonstrated the influence of chemical solution conditions, in terms of pH, total inorganic carbon (TIC) and calcium concentrations, on U(VI) sorption behavior. As a result, U(VI) K_d values can vary over several orders of magnitude, which will lead to a change in U(VI) mobility to the same degree.

The surface complexation model we developed describes U(VI) sorption onto Na-montmorillonite based on two types of U(VI) sorption processes, ion exchange and two surface complexation reactions. During model development, only one data set of U(VI) sorption data (CO₂- and Ca-free system) was used for the fitting of model parameters. The model was then applied to *predict* uranium sorption behavior at all other experimental conditions varying in CO₂ and calcium concentrations. A slight underprediction of U(VI) sorption was noted in the presence of CO₂ and calcium, and a refinement of the model is now in progress.

Furthermore, we designed and built a diffusion cell and clay packing device and demonstrated our ability to perform clay diffusion experiments over extended time-frames (4 ½ months). In the first diffusion experiment, we determined diffusion coefficients and sorption parameters for Ca, an important element driving U(VI) solution speciation, and Br at pH 7 and an ionic strength of 0.1 M NaCl.

With respect to uranium(VI) diffusion, we have simulated U(VI) diffusion profiles and relative U(VI) solution concentrations in lab-scale experiments in predictive calculations using the code ANADIFF. The modeling results facilitate the selection of appropriate chemical solution conditions in U(VI) diffusion experiments. Experimental U(VI) diffusion studies are currently ongoing.

Ultimately, all of these efforts will lead to a decrease in uncertainties in reactive transport models describing uranium diffusion in engineered barrier systems and clay formations.

5. Overall Summary

Bentonite and bentonite-sand mixtures have been found to have favorable properties for use as a backfill/buffer material for nuclear waste repositories. This report focuses on analyses of bentonite as a component of the EBS. Specific analyses presented here highlight progress made in areas of THMC coupled processes models, reactive transport models, and reactive transport experiments for bentonite. These research activities address key Features, Events and Processes (FEPs) with rankings from medium to high, as listed in Tables 7 and 8 of *Used Fuel Disposition Campaign Disposal Research and Development Roadmap* (FCR&D-USED-2011-000065 REV0) (Nutt, 2011).

5.1 THMC Process Modeling in Bentonite

We are developing and applying coupled THMC models for the analysis of EBS coupled processes in bentonite-backfilled repositories. This activity addresses FEPs 2.1.04.01,

Buffer/Backfill; FEPs 2.1.07.02, 03, 04, 09, Mechanical Processes; FEPs 2.1.08.03, 07, 08, Hydrologic Processes; and FEP 2.1.11.04, Thermal Processes, by studying coupled processes in the EBS. Our FY13 accomplishments for this activity include:

- Implementing and testing a dual-structure model for expansive clay (Barcelona Expansive Model (BExM)) into TOUGH-FLAC.
- Linking BExM to the concentration of exchangeable cations through TOUGHREACT-FLAC coupling and demonstrating the capability of modeling the effect of exchangeable cation on the swelling of clay through a generic case.

In the remaining months of FY13, we will

- Improve the numerical stability of the BExM in TOUGH-FLAC and further test it with more comprehensive examples.
- Validate the link of BExM to the concentration of exchangeable cations with published laboratory test.
- Initiate work on more rigorous approach to link chemistry to mechanics through using double-layer theory and BExM dual structure framework (see item 1 in FY14)

For FY14, we propose to

- Work on a more rigorous approach to link chemistry to mechanics through the micro-structure strain. Currently this model is only linked to exchangeable cations as suggested by Gens (2010). However, it is known that chemistry can affect mechanical behavior in clay through the change in pore water salinity, abundance of swelling clay and exchangeable cations. Next step is to develop more comprehensive links between chemistry and mechanics taking advantage of the framework provided by a dual-structure model implemented in TOUGHREACT-FLAC.
- Testing of double-structure THMC model using existing laboratory data, such as swelling pressure vs salinity, swelling pressure vs abundance of swelling clays (sand/bentonite mixtures ratio vs swelling pressure), Swelling pressure vs exchangeable cations
- Application of double-structure THMC model for mechanistic modeling of long-term bentonite-buffer stability in a generic repository emplacement tunnel
- Develop MC coupling relation to describe effects of cementation on mechanical properties of bentonite (transition from plastic to brittle)

5.2 Modeling Reactive-Diffusive Transport in Bentonite

The focus of this activity has been on developing rigorous and yet practically useful approaches to modeling diffusive process in bentonite. This activity addresses Features, Events and Processes (FEPs), FEPs 2.1.04.01, Buffer/Backfill; and FEPs 2.1.09.52, 53, 54, Chemical Processes—Transport by investigating reactive-diffusive radionuclide transport in bentonite. Our FY13 accomplishments include:

- Use of a new capability for a dynamic electrical double layer (EDL) thickness to simulate the effects of the diffusive propagation of a ionic strength front on EDL porosity and transport.
- Implementation of the Mean Electrostatic Model for the EDL with and without Stern layer sorption.
- Use of our ionic strength dependent EDL model to simulate anion and uncharged species out-diffusion from a borehole in the DR-A experiment at the Mont Terri experimental facility in Switzerland, with a single model capturing the behavior of both charged and uncharged species.
- Completion of most of the necessary software changes needed to couple the reaction portion of CrunchEDL with the general purpose PDE simulator Comsol.
- Development of a robust MD simulation methodology that correctly predicts the temperature dependence of Na^+ and water diffusion in bulk liquid water and in the interlayer nanopores of hydrated montmorillonite for a range of dry bulk densities.
- Demonstration that MD simulations can help to extrapolate existing diffusion measurements to the high temperatures that occur in the near-field of high-level radioactive waste repositories while also providing molecular scale insights into the predominant diffusion pathways of water and solutes in the EBS.

In FY14, we will:

- Simulate the Davis-Tinnacher Ca^{2+} and Mg^{2+} diffusion experiments (Section 4) using CrunchEDL, with consideration of both planar and edge site sorption and EDL effects.
- Calculate the swelling pressure and osmotic efficiency of compacted clays in the case of overlapping double layers using a full numerical treatment of the Mean Electrostatic Potential model. This will remove the requirement of treating only symmetric electrolytes.
- Implement a full multicomponent treatment of the Poisson-Boltzmann equation in 1D and 2D. The key challenge will be to accommodate the various sub-zones shown in Figure 3.1 as well as the case of overlapping EDLs (Figure 3.2).
- Continue the work to couple Comsol and CrunchEDL. This will allow us to simulate non-Darcian flow at low flow velocities and as affected by electrostatic effects, in addition to making it possible to carry out pore scale flow and transport simulations.
- Complete our investigations of the T -dependence of diffusion for a different type of smectite (Kunipia-F), different types of ions (Cs^+ , Sr^{2+} , Ca^{2+} , UO_2^{2+} , and Cl^-), and different populations of background cations (Na-, Ca-, or mixed Na/Ca-smectite). Our simulations of Ca^{2+} and UO_2^{2+} diffusion will inform the analysis of the Davis-Tinnacher diffusion experiments (Section 4).
- Carry out MD simulations of the smallest osmotic hydrate of Na-montmorillonite for a range of ionic strengths (0 to 0.4 M NaCl) in order to benchmark our Mean Electrostatic and Poisson-Boltzmann models of EDL phenomena (Section 3.1).

Develop a MD simulation methodology for predicting the swelling pressure of Na-montmorillonite as a function of pore size and solution chemistry.

5.3 Experimental Study on Reactive-Diffusive Transport

The major objective of this activity is to develop an improved understanding of radionuclide transport mechanisms and providing data sets for more accurately modeling the transport process in bentonite. This activity addresses Features, Events and Processes (FEPs), FEPs 2.1.04.01, Buffer/Backfill; and FEPs 2.1.09.52, 53, 54, Chemical Processes—Transport by investigating reactive-diffusive radionuclide transport in bentonite. In current models for radionuclide diffusion through bentonite in an engineered barrier, the apparent and effective diffusion coefficients are linked through the K_d value, which is often believed to be a constant value for a particular radionuclide. In the case of U(VI), this is less likely to be true, because of the very high sensitivity of the K_d value to pH, as well as bicarbonate and calcium concentrations. Our FY13 accomplishments for this activity include:

- Generated data sets of K_d values for uranium(VI) sorption onto Na-montmorillonite as a function of pH, TIC, and Ca concentrations.
- Developed a surface complexation model to describe the dependence of K_d values on chemical solution conditions.
- Published and presented a proceedings paper at the International High-Level Radioactive Waste Management Conference 2013 (Tinnacher and Davis, 2013), focusing on
 - Chemical solution effects on U(VI) diffusion coefficients and clay (surface) properties, and a
 - Simulation of uranium(VI) diffusion as a function of pH and TIC concentrations in lab-scale experiments.
- Designed and built a diffusion cell and clay packing device.
- Purified standardized montmorillonite (SWy-2) to minimize Ca release and to control chemical solution conditions in later diffusion experiments.
- Performed a calcium bromide diffusion experiment (1 mM CaBr₂, 0.1 M NaCl, pH~7) in pretreated Na-montmorillonite, and determined Ca and Br diffusion coefficients (total experimental time frame: 4.5 months). Uranium(VI) diffusion experiments are ongoing.

For FY14, we propose to:

- Organize the allocation of a heat-treated clay or bentonite sample from Florie Caporuscio's research group at Los Alamos National Laboratory (LANL).
- Further extend the data set for uranium(VI)-Na-montmorillonite K_d values to include varying chemical solution conditions (e.g., Ca and CO₂(g) concentrations, ionic strength), and if already available, heat-treated clay or bentonite samples from LANL.
- Refine the surface complexation model accordingly.
- Continue uranium(VI) diffusion studies in Na-montmorillonite at varying chemical solution conditions.
- Conduct uranium(VI) equilibrium sorption experiments with heat-treated clay or bentonite samples, when they become available.

- Conduct uranium(VI) diffusion experiments as a function of chemical solution conditions and, when available, with heat-treated clay or bentonite.
- Perform an analysis and comparison of uranium(VI) diffusion in pure montmorillonite and bentonite.
- Publish a journal paper on U(VI) sorption onto Na-montmorillonite: experimental results and surface complexation modeling.
- Publish a journal article on analysis of Ca and Br diffusion coefficients in montmorillonite.
- Publish a review-type journal paper on the effects of chemical solution conditions on U(VI) diffusion coefficients and clay (surface) properties.

6. References

- Alonso, E.E., Vaunat, J., Gens, A. Modelling the mechanical behavior of expansive clays. *Engineering Geology*, 54, 173-183 (1999).
- Appelo C.A.J., Vinsot A., Mettler S., Wechner S. Obtaining the porewater composition of a clay rock by modeling the in- and out-diffusion of anions and cations from an in-situ experiment. *J. Contam. Hydrol.*, 101, 67-76 (2008).
- Appelo C.A.J., Wersin P. Multicomponent diffusion modeling in clay systems with application to the diffusion of tritium, iodide, and sodium in Opalinus Clay. *Environ. Sci. Technol.*, 41, 5002-5007 (2007).
- Arai, Y., McBeath, M., Bargar, J.R., Joye, J., and Davis, J.A., Uranyl adsorption and surface speciation at the imogolite-water interface: Self-consistent spectroscopic and surface complexation models, *Geochimica et Cosmochimica Acta*, 2006, 70, 2492-2509.
- Bai, J.; Liu, C. X.; Ball, W. P., Study of Sorption-Retarded U(VI) Diffusion in Hanford Silt/Clay Material. *Environ. Sci. Technol.* 2009, 43, (20), 7706-7711.
- Berendsen H.J.C., Grigera J.R., Straatsma T.P. The missing term in effective pair potentials. *J. Phys. Chem.*, 91, 6269-6271 (1987).
- Bickmore B.R., Rosso K.M., Nagy K.L., Cygan R.T., Tadanier C.J. Ab initio determination of edge surface structures for dioctahedral 2:1 phyllosilicates: Implications for acid-base reactivity. *Clays Clay Miner.*, 51, 359-371 (2003).
- Birgersson M., Karnland O. Ion equilibrium between montmorillonite interlayer space and an external solution - Consequences for diffusional transport. *Geochim. Cosmochim. Acta*, 73, 1908-1923 (2009).
- Botan A., Rotenberg B., Marry V., Turq P., Noetinger B. Hydrodynamics in clay nanopores. *J. Phys. Chem. C*, 115, 16109-16115 (2011).
- Bourg I.C., Sposito G. Connecting the molecular scale to the continuum scale for diffusion processes in smectite-rich porous media. *Environ. Sci. Technol.*, 44, 2085-2091 (2010).
- Bourg I.C., Sposito G. Ion exchange phenomena. In: *Handbook of Soil Science*, 2nd ed., Sumner M.E., ed., CRC Press, Boca Raton, FL, Chap. 6 (2011a).
- Bourg I.C., Sposito G. Molecular dynamics simulations of the electrical double layer on smectite surfaces contacting concentrated mixed electrolyte (NaCl-CaCl₂) solutions. *J. Colloid Interface Sci.*, 360, 701-715 (2011b).

- Bourg I.C., Sposito G., Bourg A.C.M. Modeling the diffusion of Na⁺ in compacted water-saturated Na-bentonite as a function of pore water ionic strength. *Appl. Geochem.*, 23, 3635-3641 (2008).
- Bourg, I. C.; Bourg, A. C. M.; Sposito, G., Modeling diffusion and adsorption in compacted bentonite: a critical review. *J. Contam. Hydrol.* 2003, 61, (1-4), 293-302.
- Bourg, I. C.; Sposito, G.; Bourg, A. C. M., Modeling cation diffusion in compacted water-saturated sodium bentonite at low ionic strength. *Environ. Sci. Technol.* 2007, 41, (23), 8118-8122.
- Bourg, I. C.; Sposito, G.; Bourg, A. C. M., Tracer diffusion in compacted, water-saturated bentonite. *Clay Clay Min.* 2006, 54, (3), 363-374.
- Bradbury, M. H.; Baeyens, B., Predictive sorption modelling of Ni(II), Co(II), Eu(III), Th(IV) and U(VI) on MX-80 bentonite and Opalinus Clay: A "bottom-up" approach. *Appl. Clay Sci.* 2011, 52, (1-2), 27-33.
- Brown, P. L.; Haworth, A.; Sharland, S. M.; Tweed, C. J., Modeling studies of the sorption of radionuclides in the far field of a nuclear waste repository. *Radiochim. Acta* 1991, 52-3, 439-443.
- Cebula D.J., Thomas R.K., Middleton S., Ottewill R.H., White J.W. Neutron diffraction from clay-water systems. *Clays Clay Miner.*, 27, 39-52 (1979).
- Chen T., Smit B., Bell A.T. Are pressure fluctuation-based equilibrium methods really worse than nonequilibrium methods for calculating viscosities? *J. Chem. Phys.*, 131, 246101 (2009).
- Chipera, S.J., D.L. Bish, Baseline studies of the Clay Minerals Society source clays: Powder X-ray diffraction analysis, *Clays and Clay Minerals*, 49, 398-409 (2001).
- Churakov S.V., Gimmi T. Up-scaling of molecular diffusion coefficients in clays: A two-step approach. *J. Phys. Chem. C*, 115, 6703-6714 (2011).
- Costanzo, P.A., S. Guggenheim, Baseline studies of the Clay Minerals Society source clays: Preface, *Clays and Clay Minerals*, 49, 371-371 (2001).
- Crank, J., *The Mathematics of Diffusion*. Oxford Univ. Press, Oxford, 1975.
- Cussler, E. L., *Diffusion, mass transfer in fluid systems*. 2nd ed.; Cambridge University Press: Cambridge, UK, 1997.
- Cygan R.T., Liang J.J., Kalinichev A.G. Molecular models of hydroxide, oxyhydroxide, and clay phases and the development of a general force field. *J. Phys. Chem. B*, 108, 1255-1266 (2004).

- Davis, J. A.; Meece, D. E.; Kohler, M.; Curtis, G. P., Approaches to surface complexation modeling of uranium(VI) adsorption on aquifer sediments. *Geochim. Cosmochim. Acta* 2004, 68, (18), 3621-3641.
- Di Maio, C.. Exposure of bentonite to salt solution: osmotic and mechanical effects. *Geotechnique* 46, No. 4, 695-707, (1996).
- Dong, W. M.; Brooks, S. C., Formation of aqueous $MgUO_2(CO_3)_3^{2-}$ complex and uranium anion exchange mechanism onto an exchange resin. *Environmental Science & Technology* 2008, 42, (6), 1979-1983.
- Duc, M., Gaboriaud, F., and Thomas, F., Sensitivity of the acid-base properties of clays to the methods of preparation and measurement. 2. Evidence from continuous potentiometric titrations, *J. Colloid Interface Sci.*, 2005, 289, 148-156.
- Dzombak D.A., Morel F.M.M. *Surface Complexation Modeling: Hydrous Ferric Oxide*. J.W. Wiley, 416 p. (1990).
- engineering. *Geotechnique*, 60, 3-74 (2010).
- Eriksen, T. E.; Jansson, M. Diffusion of I-, Cs⁺ and Sr²⁺ in compacted bentonite - Anion exclusion and surface diffusion, SKB Technical Report 96-16; Royal Institute of Technology, Stockholm: 1996.
- Eriksen, T. E.; Jansson, M.; Molera, M., Sorption effects on cation diffusion in compacted bentonite. *Eng. Geol.* 1999, 54, (1-2), 231-236.
- Fernández, A., Cuevas, J., Rivas, P. Pore water chemistry of the FEBEX bentonite. *Mat. Res. Soc. Symp. Proc.* 663, 573-588, (2001).
- Ferrage E., Lanson B., Sakharov B.A., Geoffroy N., Jacquot E., Drits V.A. Investigation of dioctahedral smectite hydration properties by modeling of X-ray diffraction profiles: Influence of layer charge and charge location. *Amer. Mineral.*, 92, 1731-1743 (2007).
- Ferrage E., Sakharov B.A., Michot L.J., Delville A., Bauer A., Lanson B., Grangeon S., Frapper G., Jimenez-Ruiz M., Cuello G.J. Hydration properties and interlayer organization of water and ions in synthetic Na-smectite with tetrahedral layer charge. Part 2. Toward a precise coupling between molecular simulations and diffraction data. *J. Phys. Chem. C*, 115, 1867-1881 (2011).
- Foster W.R., Savins J.G., Waite J.M. Lattice expansion and rheological behavior relationships in water-montmorillonite systems. *Clays Clay Miner.*, 3, 296-316 (1955).
- Fox, P. M.; Davis, J. A.; Zachara, J. M., The effect of calcium on aqueous uranium(VI) speciation and adsorption to ferrihydrite and quartz. *Geochim. Cosmochim. Acta* 2006, 70, (6), 1379-1387.

- Gens A. Soil - environmental interactions in geotechnical engineering. *Geotechnique*, 60, 3-74 (2010).
- Gens, A, Alonso, E. A framework for the behaviour of unsaturated expansive clays. *Can. Geotech. J.* 29, 1013-1032 (1992).
- Gens, A., Sánchez, M., Sheng, D. On constitutive modelling of unsaturated soils. *Acta Geotechnica*, 1, 137-147 (2006).
- Glaus M.A., Frick S., Rossé R., van Loon L.R. Consistent interpretation of the results of through-, out-diffusion and tracer profile analysis for trace anion diffusion in compacted montmorillonite. *J. Contam. Hydrol.*, 123, 1-10 (2011).
- Glaus, M. A.; Rosse, R.; Van Loon, L. R.; Yaroshchuk, A. E., Tracer diffusion in sintered stainless steel filters: measurement of effective diffusion coefficients and implications for diffusion studies with compacted clays. *Clay Clay Min.* 2008, 56, (6), 677-685.
- Gonçalvès J., Rousseau-Gueutin P., Revil A. Introducing interacting diffuse layers in TLM calculations: A reappraisal of the influence of the pore size on the swelling pressure and the osmotic efficiency of compacted bentonites. *J. Colloid Interface Sci.*, 316, 92-99 (2007).
- González Sánchez F., Gimmi T., Jurányi F., Van Loon L., Diamond L.W. Linking the diffusion of water in compacted clays at two different time scales: Tracer through-diffusion and quasielastic neutron scattering. *Environ. Sci. Technol.*, 43, 3487-3493 (2009).
- Greathouse J.A., Feller S.E., McQuarrie D.A. The modified Gouy-Chapman theory: Comparisons between electrical double layer models of clay swelling. *Langmuir*, 10, 2125-2130.
- Guillaumont, R.; Fanghanel, T.; Fuger, J.; Grenthe, I.; Neck, V.; Palmer, D. A.; Rand, M. H., Update on the Chemical Thermodynamics of Uranium, Neptunium, Plutonium, Americium and Technetium. Elsevier: Amsterdam, 2003; Vol. 5.
- Guimarães L.D.N., Gens A., Sánchez M., Olivella S. A chemo-mechanical constitutive model accounting for cation exchange in expansive clays. *Geotechnique*, 63, 221-234 (2013).
- Herbelin, A. L. and Westall, J.C., FITEQL: A Computer Program for the Determination of Chemical Equilibrium Constants from Experimental Data, Version 4.0, Report 99-01, 1999, Chemistry Department, Oregon State University, Corvallis, Oregon.
- Holmboe M., Jonsson M., Wold S. Porosity investigation of compacted bentonite using XRD profile modeling. *J. Contam. Hydrol.*, 128, 19-32 (2012).
- Holmboe M., Norrfors K., Jonsson M., Wold S. Effect of γ -radiation on radionuclide retention in compacted bentonite. *Radiat. Phys. Chem.*, 80, 1371-1377 (2011).

- Holmboe, M. The bentonite barrier: Microstructural aspects on colloid filtration and radiation effects on bentonite colloid stability. KTH, Royal Institute of Technology, Stockholm, 2009.
- Holz M., Heil S.R., Sacco A. Temperature-dependent self-diffusion coefficients of water and six selected molecular liquids for calibration in accurate ¹H NMR PFG measurements. *Phys. Chem. Chem. Phys.*, 2, 4740-4742 (2000).
- Hsi, C.K.D., D. Langmuir, Adsorption of uranyl onto ferric oxyhydroxides: Application of the surface complexation site-binding model. *Geochim. Cosmochim. Acta* 1985, 49, 1931-1941.
- Ichikawa Y., Kawamura K., Fujii N., Kitayama K. Microstructure and micro/macro-diffusion behavior of tritium in bentonite. *Appl. Clay Sci.*, 26, 75-90 (2004).
- Jakob, A., Sarott, F.A., Spieler, P., 1999. Diffusion and Sorption on Hardened Cement Pastes. Experiments and Modelling Results. Paul Scherrer Institut Report 99-05.
- JNC (Japanese Nuclear Cycle Development Institute) H12 project to establish the scientific and technical basis for HLW disposal in Japan. JNC Technical Report JNC TN1410 2000-001 (2000).
- Joung I.S., Cheatham T.E., III. Determination of alkali and halide monovalent ion parameters for use in explicitly solvated biomolecular simulations. *J. Phys. Chem. B*, 112, 9020-9041 (2008).
- Kalinichev A.G.K., Kirkpatrick R.J.K., Cygan R.T. Molecular modeling of the structure and dynamics of the interlayer and surface species of mixed-metal layered hydroxides: Chloride and water in hydrocalumite (Friedel's salt). *Amer. Mineral.*, 85, 1046-1052 (2000).
- Kerisit, S.; Liu, C. X., Molecular simulation of the diffusion of uranyl carbonate species in aqueous solution. *Geochim. Cosmochim. Acta* 2010, 74, (17), 4937-4952.
- Kerisit, S.; Liu, C., Molecular Simulations of Water and Ion Diffusion in Nanosized Mineral Fractures. *Environ. Sci. Technol.* 2009, 43, (3), 777-782.
- Kim, H.-T.; Suk, T.-W.; Park, S.-H.; Lee, C.-S., Diffusivities for ions through compacted Na-bentonite with varying dry bulk density. *Waste Manage.* 1993, 13, (4), 303-308.
- Korichi, S.; Bensmaili, A.; Keddami, M., Reactive diffusion of uranium in compacted clay: Evaluation of diffusion coefficients by a kinetic approach. *Defect Diff. Forum* 2010, 297-301, 275-280.
- Kosakowski G., Churakov S.V., Thoenen T. Diffusion of Na and Cs in montmorillonite. *Clays Clay Miner.*, 56, 190-206 (2008).

- Kozaki T., Fujishima A., Saito N., Sato S., Ohashi H. Effects of dry density and exchangeable cations on the diffusion process of sodium ions in compacted montmorillonite. *Eng. Geol.*, 81, 246-254 (2005).
- Kozaki T., Fujishima A., Sato S., Ohashi H. Self-diffusion of sodium ions in compacted sodium montmorillonite. *Nucl. Technol.*, 121, 63-69 (1998).
- Kozaki T., Inada K., Sato S., Ohashi H. Diffusion mechanism of chloride ions in sodium montmorillonite. *J. Contam. Hydrol.*, 47, 159-170 (2001).
- Kozaki T., Liu J., Sato S. Diffusion mechanism of sodium ions in compacted montmorillonite under different NaCl concentration. *Phys. Chem. Earth A/B/C*, 33, 957-961 (2008).
- Kozaki T., Sato H., Fujishima A., Saito N., Sato S., Ohashi H. Effect of dry density on activation energy for diffusion of strontium in compacted sodium montmorillonite. *Mat. Res. Soc. Symp. Proc.*, 465, 893-900 (1997).
- Kozaki T., Sato H., Fujishima A., Sato S., Ohashi H. Activation energy for diffusion of cesium in compacted sodium montmorillonite. *J. Nucl. Sci. Technol.*, 33, 522-524 (1996).
- Kozaki T., Sato H., Sato S., Ohashi H. Diffusion mechanism of cesium ions in compacted montmorillonite. *Eng. Geol.*, 54, 223-240 (1999).
- Kozaki T., Sawaguchi T., Fujishima A., Sato S. Effect of exchangeable cations on apparent diffusion of Ca²⁺ ions in Na- and Ca-montmorillonite mixtures. *Phys. Chem. Earth A/B/C*, 35, 254-258 (2010).
- Kozaki, T.; Adachi, Y.; Inada, K.; Sato, S.; Ohashi, H. Diffusion behavior of Ca²⁺ ions in compacted Na-montmorillonite. In: *Scientific Basis for Nuclear Waste Management XXIV. Symposium, Sydney, NSW, Australia, 27-31 Aug. 2000* (Materials Research Society Proceedings Vol.663). Hart, K.P.; Lumpkin, G.R. (eds). p. 629-635, 2001.
- Leroy P., Revil A. A triple-layer model of the surface electrochemical properties of clay minerals. *J. Colloid Interface Sci.*, 270, 371-380 (2004).
- Leroy P., Revil A., Altmann S., Tournassat C. Modeling the composition of a pore water in a clay-rock geological formation (Callovo-Oxfordian, France). *Geochim. Cosmochim. Acta*, 71, 1087-1097 (2007).
- Leroy, P.; Revil, A.; Coelho, D., Diffusion of ionic species in bentonite. *J. Colloid Interf. Sci.* 2006, 296, (1), 248-255.
- Lide D.R. *CRC Handbook of Chemistry and Physics*. CRC Press (2012).
- Liu J., Kozaki T., Horiuchi Y., Sato S. Microstructure of montmorillonite/silica sand mixture and its effects on the diffusion of strontium ions. *Appl. Clay Sci.*, 23, 89-95 (2003).

- Liu, C.; Zhong, L.; Zachara, J. M., Uranium(VI) diffusion in low-permeability subsurface materials. *Radiochim. Acta* 2010, 98, (9-11), 719-726.
- Madsen, F. T., Clay mineralogical investigations related to nuclear waste disposal. *Clay Min.* 1998, 33, (1), 109-129.
- Maes, N.; Moors, H.; Wang, L.; Delecaut, G.; De Canniere, P.; Put, M., The use of electromigration as a qualitative technique to study the migration behaviour and speciation of uranium in the Boom Clay. *Radiochim. Acta* 2002, 90, (9-11), 741-746.
- Malikova N., Cadéne A., Marry V., Dubois E., Turq P., Zanotti J.-M., Longeville S. Diffusion of water in clays - Microscopic simulation and neutron scattering. *Chem. Phys.*, 317, 226-235 (2005).
- Malikova N., Marry V., Dufrêche J.-F., Simon C., Turq P., Giffaut E. Temperature effect in a montmorillonite clay at low hydration-microscopic simulation. *Mol. Phys.*, 102, 1965-1977 (2004a).
- Malikova N., Marry V., Dufrêche J.-F., Turq P. Na/Cs montmorillonite: Temperature activation of diffusion by simulation. *Curr. Opin. Colloid Interface Sci.*, 9, 124-127 (2004b).
- Malusis M.A., Shackelford C.D. Explicit and implicit coupling during solute transport through clay membrane barriers. *J. Contam. Hydrol.*, 72, 259-285 (2004).
- Malusis M.A., Shackelford C.D., Olsen H.W. Flow and transport through clay membrane barriers. *Eng. Geol.*, 70, 235-248 (2003).
- Mammar N., Rosanne M., Prunet-Foch B., Thovert J.-F., Tevissen E., Adler P.M. Transport properties of compact clays. I. Conductivity and permeability. *J. Colloid Interface Sci.*, 240, 498-508 (2001).
- Marry V., Dubois E., Malikova N., Durand-Vidal S., Longeville S., Breu J. Water dynamics in hectorite clays: Influence of temperature studied by coupling neutron spin echo and molecular dynamics. *Environ. Sci. Technol.*, 45, 2850-2855 (2011).
- Marry V., Rotenberg B., Turq P. Structure and dynamics of water at a clay surface from molecular dynamics simulation. *Phys. Chem. Chem. Phys.*, 10, 4802-4813 (2008).
- Marry V., Turq P. Microscopic simulations of interlayer structure and dynamics in bihydrated heteroionic montmorillonites. *J. Phys. Chem. B*, 107, 1832-1839 (2003).
- Mazo M.A., Manevitch L.I., Gusarova E.B., Berlin A.A., Balabaev N.K., Rutledge G.C. Molecular dynamics simulation of thermomechanical properties of montmorillonite crystal. II. Hydrated montmorillonite crystal. *J. Phys. Chem. C*, 112, 17056-17062 (2008).

- Mazzieri, F.; Di Emidio, G.; Van Impe, P.O., (Van Impe, Peter O.), Diffusion of Calcium Chloride in a Modified Bentonite: Impact on Osmotic Efficiency and Hydraulic Conductivity, *Clays and Clay Minerals*, 58, 351-363 (2010).
- McKinley, J.P., Zachara, J.M., Smith, S.C., and Turner, G.D., The influence of uranyl hydrolysis and multiple site-binding reactions on adsorption of U(VI) to montmorillonite, *Clays Clay Min.*, 1995, 43, 586-598.
- Medina J.S., Prosmi R., Villarreal P., Delgado-Barrio G., Winter G., Gonzalez B., Aleman J.V., Collado C. Molecular dynamics simulations of rigid and flexible water model: Temperature dependence of viscosity. *Chem. Phys.*, 388, 9-18 (2011).
- Melkior T., Gaucher E.C., Brouard C., Yahiaoui S., Thoby D., Clinard C., Ferrage E., Guyonnet D., Tournassat C., Coelho D. Na⁺ and HTO diffusion in compacted bentonite: effect of surface chemistry and related texture. *J. Hydrol.*, 370, 9-20 (2009).
- Mermut, A.R., A.F. Cano, Baseline studies of the Clay Minerals Society source clays: Layer-charge determination and characteristics of those minerals containing 2:1 layers, *Clays and Clay Minerals*, 49, 393-397 (2001).
- Mitchell, J. K. & Soga, K. (2005). *Fundamentals of soil behaviour*, 3rd edn. Hoboken, NJ, USA: Wiley.
- Molera M., Eriksen T. Diffusion of ²²Na⁺, ⁸⁵Sr²⁺, ¹³⁴Cs⁺ and ⁵⁷Co²⁺ in bentonite clay compacted to different densities: Experiments and modeling. *Radiochim. Acta*, 90, 753-760 (2002).
- Molera M., Eriksen T., Jansson M. Anion diffusion pathways in bentonite clay compacted to different dry densities. *Appl. Clay Sci.*, 23, 69-76 (2003).
- Muurinen, A., Diffusion of uranium in compacted sodium bentonite. *Eng. Geol.* 1990, 28, (3-4), 359-367.
- Nakashima T. Diffusivity measurement of heavy ions in Wyoming montmorillonite gels by X-ray computed tomography. *J. Contam. Hydrol.*, 61, 147-156 (2003).
- Nakazawa T., Takano M., Nobuhara A., Torikai Y., Sato S., Ohashi H. Activation energies of diffusion of tritium and electrical conduction. *Radioact. Waste Manag. Environ. Rem.*, 1999, 8-12 (1999).
- Norrish K. The swelling of montmorillonite. *Disc. Faraday Soc.* 18, 120 (1954).
- Nutt, M., Used Fuel Disposition Campaign Disposal Research and Development Roadmap (FCR&D-USED-2011-000065 REV0), U.S. DOE Used Fuel Disposition Campaign, 2011.

- Ochs, M.; Lothenbach, B.; Wanner, H.; Sato, H.; Yui, M., An integrated sorption-diffusion model for the calculation of consistent distribution and diffusion coefficients in compacted bentonite. *J. Contam. Hydrol.* 2001, 47, (2-4), 283-296.
- OECD, Engineering barrier systems and the safety of deep geological repositories (State-of-the-art Report), ISBN 92-64-18498-8, 2003.
- Parsegian V.A. Van der Waals forces: a handbook for biologists, chemists, engineers, and physicists. Cambridge University Press (2006).
- Pitman M.C., van Duin A.C.T. Dynamics of confined reactive water in smectite clay-zeolite composites. *J. Am. Chem. Soc.*, 134, 3042-3053 (2012).
- Placzek G., Nijboer B., Hove L. Effect of short wavelength interferences on neutron scattering by dense systems of heavy nuclei. *Phys. Rev.*, 82, 392-403 (1951).
- Plimpton S. Fast parallel algorithms for short-range molecular dynamics. *J. Comput. Phys.*, 117, 1-42 (1995).
- Pousada, P.E. Deformabilidad de arcillas expansivas bajo succión controlada. Ph. D. Thesis, Technical University of Madrid, Spain (1984).
- Pusch, R., Use of bentonite for isolation of radioactive-waste products. *Clay Min.* 1992, 27, (3), 353-361.
- Rotenberg B., Marry V., Vuilleumier R., Malikova N., Simon C., Turq P. Water and ions in clays: Unraveling the interlayer/micropore exchange using molecular dynamics. *Geochim. Cosmochim. Acta*, 71, 5089-5101 (2007a).
- Rotenberg B., Marry V., Dufrêche J.-F., Malikova N., Giffaut E., Turq P. Modelling water and ion diffusion in clays: A multiscale approach. *C.R. Chim.*, 10, 1108-1116 (2007b).
- Rutqvist, J., Ijiri, Y. Yamamoto, H. Implementation of the Barcelona Basic Model into TOUGH-FLAC for simulations of the geomechanical behavior of unsaturated soils. *Computers & Geosciences*, 37, 751-762 (2011).
- Rutqvist, J., Steefel, C., Davis, J., Bourg, I., Tinnacher, R., Galindez, J., Holmboe, M., Birkholzer, J., Liu, H.H. Investigation of Reactive Transport and Coupled THM Processes in EBS: FY12 Report, Lawrence Berkeley National Laboratory, DOE Used Fuel Disposition Campaign, FCRD-UFD-2012-000125. (2012).
- Rutqvist, J., Zheng, L., Chen, F., Liu, H.-H., Birkholzer, J. Modeling of Coupled Thermo-Hydro-Mechanical Processes with Links to Geochemistry Associated with Bentonite-Backfilled Repository Tunnels in Clay Formations. *Rock Mechanics and Rock Engineering*, (In Press, January 2013).

- Ryckaert J.-P., Ciccotti G., Berendsen H.J.C. Numerical integration of the Cartesian equations of motion of a system with constraints: Molecular dynamics of n-alkanes. *J. Comput. Phys.*, 23, 327-341 (1977).
- Safran S.A. Statistical thermodynamics of surfaces, interfaces, and membranes. Addison-Wesley, Reading, MA (1994).
- Saiyouri N., Tessier D., Hicher P.Y.Y. Experimental study of swelling in unsaturated compacted clays. *Clay Miner.*, 39, 469-479 (2004).
- Sánchez, M., Gens, A., Guimarães, L. do N., Olivella, S. A double structure generalized plasticity model for expansive materials. *Int. J. Numer. Anal. Meth. Geomech.*, 29, 751-787. (2005).
- Sato H. Fundamental study on the effect of an orientation of clay particles on diffusion pathway in compacted bentonite. *Appl. Clay Sci.*, 23, 51-60 (2003).
- Schoch R.B., Han J., Renaud P. Transport phenomena in nanofluidics. *Rev. Mod. Phys.*, 80, 840-883 (2008).
- Selim, H. M.; Amacher, M. C., Reactivity and transport of heavy metals in soils. CRC Press, Inc.: Boca Raton, 1997; p 201.
- Shackelford, C. D., Laboratory diffusion testing for waste disposal - a review. *J. Contam. Hydrol.* 1991, 7, (3), 177-218.
- Shackelford, C. D.; Daniel, D. E., Diffusion in saturated soil. I: Background. *J. Geotech. Eng.-ASCE* 1991, 117, (3), 467-484.
- Shackelford, C. D.; Lee, J.-M., The destructive role of diffusion on clay membrane behavior. *Clays and Clay Minerals*, 51, 186-196 (2003).
- SKB (Swedish Nuclear Fuel and Waste Management Co) Thermal dimensioning of the deep repository. SKB Technical Report TR-03-09 (2009).
- Skipper N.T., Chang F.-R.C., Sposito G. Monte Carlo simulation of interlayer molecular structure in swelling clay minerals. 1. Methodology. *Clays Clay Miner.*, 43, 285-293 (1995).
- Skipper N.T., Refson K., McConnell J.D.C. Computer simulation of interlayer water in 2:1 clays. *J. Chem. Phys.*, 94, 7434-7445 (1991).
- Sposito G., Prost R. Structure of water adsorbed on smectites. *Chem. Rev.*, 82, 553-573 (1982).
- Sposito G., Skipper N.T., Sutton R., Park S., Soper A.K., Greathouse J.A. Surface geochemistry of the clay minerals. *Proc. Natl. Acad. Sci. U.S.A.*, 96, 3358-3364 (1999).

- Stumm, W. *Chemistry of the Solid-Water Interface: Processes at the Mineral-Water Particle-Water Interface in Natural Systems*, John Wiley & Sons, 428 p., 1992.
- Suzuki S., Sato H., Ishidera T., Fujii N. Study on anisotropy of effective diffusion coefficient and activation energy for deuterated water in compacted sodium bentonite. *J. Contam. Hydrol.*, 68, 23-37 (2004).
- Svensson P.D., Hansen S. Freezing and thawing of montmorillonite - A time-resolved synchrotron X-ray diffraction study. *Appl. Clay Sci.*, 49, 127-134 (2010).
- Tachi Y., Nakazawa T., Ochs M., Yotsuji K., Suyama T., Seida Y., Yamada N., Yui M. Diffusion and sorption of neptunium(V) in compacted montmorillonite: Effects of carbonate and salinity. *Radiochim. Acta*, 98, 711-718 (2010).
- Talekar S.V. Temperature dependence of activation energies for self-diffusion of water and of alkali ions in aqueous electrolyte solutions. *Int. J. Quantum Chem. Biol. Symp.*, 4, 459-469 (1977).
- Tanaka S., Noda N., Sato S., Kozaki T., Sato H. Electrokinetic study of migration of anions, cations, and water in water-saturated compacted sodium montmorillonite. *J. Nucl. Sci. Technol.*, 48, 454-462 (2011).
- Tazi S., Botan A., Salanne M., Marry V., Turq P., Rotenberg B. Diffusion coefficient and shear viscosity of rigid water models. *J. Phys.: Condens. Matter*, 24, 284117 (2012).
- Teppen B.J., Rasmussen K., Bertsch P.M., Miller D.M., Schaefer L. Molecular dynamics modeling of clay minerals. 1. Gibbsite, kaolinite, pyrophyllite, and beidellite. *J. Phys. Chem. B*, 101, 1579-1587 (1997).
- Tinnacher, R. M., Davis, J. A. Effects of Chemical Solution Conditions on Uranium(VI) Diffusion in Clays, Proceedings to IHLRWM Conference, 2013.
- Tokunaga, T. K.; Wan, J. M.; Pena, J.; Sutton, S. R.; Newville, M., Hexavalent uranium diffusion into soils from concentrated acidic and alkaline solutions. *Environ. Sci. Technol.* 2004, 38, (11), 3056-3062.
- Tournassat C., Appelo C.A.J. Modelling approaches for anion-exclusion in compacted Na-bentonite. *Geochim. Cosmochim. Acta*, 75, 3698-3710 (2011).
- Tournassat C., Chapron Y., Leroy P., Bizi M., Boulahya F. Comparison of molecular dynamics simulations with Triple Layer and Modified Gouy-Chapman models in a 0.1 M NaCl-montmorillonite system. *J. Colloid Interface Sci.*, 339, 533-541 (2009).
- Van Loon, L. R.; Glaus, M. A.; Mueller, W., Anion exclusion effects in compacted bentonites: Towards a better understanding of anion diffusion. *Appl. Geochem.* 2007, 22, (11), 2536-2552.

- Van Loon, L. R.; Soler, J. M. Diffusion of HTO, $^{36}\text{Cl}^-$, $^{125}\text{I}^-$ and $^{22}\text{Na}^+$ in Opalinus Clay: Effect of Confining Pressure, Sample Orientation, Sample Depth and Temperature. Paul Scherrer Institut Report Nr. 04-03, 2004.
- Van Loon, L. R.; Soler, J. M.; Bradbury, M. H., Diffusion of HTO, $^{36}\text{Cl}^-$ and $^{125}\text{I}^-$ in Opalinus Clay samples from Mont Terri - Effect of confining pressure. *J. Contam. Hydrol.* 2003, 61, (1-4), 73-83.
- Vega C. Sanz E., Abascal J.L.F. The melting temperature of the most common models of water. *J. Chem. Phys.*, 122, 114507 (2005).
- Wakim, J., F. Hadj-Hassen and L. De Windt 2009. Effect of aqueous solution chemistry on the swelling and shrinkage of the Tournemire shale. *International Journal of Rock Mechanics and Mining Sciences* 46(8): 1378-1382.
- Wang X., Tan X., Chen C., Chen L. The concentration and pH dependent diffusion of ^{137}Cs in compacted bentonite using capillary method. *J. Nucl. Mater.*, 345, 184-191 (2005).
- Wersin P., Curti E. Appelo C.A.J. Modelling bentonite-water interactions at high solid/liquid ratios: swelling and diffuse double layer effects. *Applied Clay Sci.*, 26, 249-257 (2004).
- Wilson J., Cuadros J., Cressey G. An in situ time-resolved XRD-PSD investigation into Na-montmorillonite interlayer and particle rearrangement during dehydration. *Clays Clay Miner.*, 52, 180-191 (2004).
- Yeh I.C., Hummer G. System-size dependence of diffusion coefficients and viscosities from molecular dynamics simulations with periodic boundary conditions. *J. Phys. Chem. B*, 108, 15873-15879 (2004a).
- Yeh I.C., Hummer G. Diffusion and electrophoretic mobility of single-stranded RNA from molecular dynamics simulations. *Biophys. J.*, 86, 681-689 (2004b).
- Zachara, J.M. and Smith, S.C., Edge complexation reactions of cadmium on specimen and soil-derived smectite, *Soil Sci. Soc. Amer. J.*, 1994, 58, 762-769.
- Zeebe R.E. On the molecular diffusion coefficients of dissolved CO_2 , HCO_3^- , and CO_3^{2-} and their dependence on isotopic mass. *Geochim. Cosmochim. Acta*, 75, 2483-2498 (2011).
- Zhang Z.Z., Low P.F. Relation between the heat of initial water content of Li-, Na-, and K-montmorillonite. *J. Colloid Interface Sci.*, 133, 461-472 (1989).

**Update on Experimental Activities on Buffer/Backfill
Interactions at elevated Pressure and Temperature
(PART III)**

1. Introduction

The United States has initiated the Used Fuel Disposition campaign to evaluate various generic geological repositories for the permanent disposal of used nuclear fuel. The development and evaluation of engineered barrier system (EBS) design concepts and their potential interactions with the natural barrier or with other EBS interfaces are inherently important to the long-term (i.e., tens of thousands of years) safety and performance of geological repositories (Jove-Colon et al. 2011; Nutt et al. 2011). One of the more commonly proposed ideas for high-level nuclear waste repository is to surround waste canisters with bentonite in an underground repository (Pusch 1979; Meunier et al. 1998). There have been numerous investigations on the stability of bentonites under various repository conditions and in contact with various metals replicating possible canister compositions (Pusch 1979; Madsen 1998; Meunier et al. 1998; Guillaume et al. 2003; Wersin et al. 2007; Mosser-Ruck et al. 2010; Ferrage et al. 2011). However, there remain uncertainties regarding the long-term stability of bentonite EBS and corrosion products under potential repository conditions. The focus of this experimental work is to expand our understanding of the stability of bentonite barriers under different geochemical, mineralogical, and engineering conditions than what has been previously investigated. Alteration of smectite to other minerals (i.e., illite, illite/smectite, chlorite), steam-induced swelling loss, and interaction of smectite with metal waste canisters are some of the more prevalent concerns (Couture 1985; Wersin et al. 2007; Mosser-Ruck et al. 2010). Most previous investigations focused on cleaned, cation exchanged smectites. Jobmann and Buntebarth (2009) examined the effect of adding graphite or quartz sand to bentonite to enhance the thermo-physical properties of buffer materials. This report addresses the various authigenic minerals occurring within unprocessed Wyoming bentonite and clay/metal interface reactions during hydrothermal investigations replicating a high temperature repository-like environment. This is exemplified by the observed zeolite mineralogy alteration, metal-bentonite interface reactions, and illitization retardation under these experimental repository conditions which are key considerations for the evaluation of long-term barrier material stability in a used fuel repository environment.

The Used Fuel Disposition Campaign (UFDC) is presently investigating various generic repository options for disposal of used fuel. Of interest are the disposal of high heat load canisters (up to 300°C), which may allow for a reduced repository footprint. The focus of this experimental work is to increase our understanding on the stability of bentonite barriers under different geochemical and mineralogical conditions other than what has been previously investigated. Experiments were performed at 150 – 160 bars at temperatures up to 300°C for five to six weeks. Unprocessed Wyoming bentonite was saturated with a K-Ca-Na-Cl-rich water at a 9:1 water:rock ratio. Experiments contained various steel plates or Cu-foil and were buffered to low Eh conditions using magnetite and metallic iron. Other experiments for international EBS research included mixed buffers and a heated bentonite with 20 wt. % free moisture for LBNL. The mixed buffer experiments (bentonite-graphite, bentonite-quartz sand) were conducted to investigate potential mineralogic/petrologic changes to mixed buffer systems proposed by the German nuclear repository program. Reaction products associated with the international EBS research were characterized by LANL with thermal-mechanical properties to be characterized by LBNL.

The results of the current experimental work can be summarized as follows:

- The pH, K^+ , and Ca^{2+} concentrations dropped, while $SiO_{2(aq)}$, Na^+ , and SO_4^{2-} concentrations increased throughout the experiments.
- The alkali and alkaline earth metals aqueous concentrations appear to be buffered via the montmorillonite and clinoptilolite exchange reactions.
- Illite or illite/smectite mixed-layer formation is significantly retarded in the closed system due to Na^+ and $SiO_{2(aq)}$ accumulation and limited K^+ supply.
- Precursor clinoptilolite underwent extensive dissolution during the six week, 300°C experiments subsequently producing a high-silicon analcime in addition to authigenic silica phases.
- Analcime and feldspar formation partially sequesters aqueous Al^{3+} , thereby potentially inhibiting illitization. Associated with the zeolite alteration is a ~ 17 % volume decrease (assuming quartz formation) that translates into ~ 2% volume loss in the bulk bentonite.
- Pyrite decomposition is first observed at ~210 °C, generating available $H_2S_{(aq,g)}$ that reacts with metal plates or evolves as a gas. The copper rapidly degrades in the presence of $H_2S_{(aq,g)}$, resulting in the formation of a chalcocite crust on the copper.
- A layer of Fe-saponite (or rarely, chlorite) forms at the steel bentonite interface, potentially acting as a passivating agent to retard further metal corrosion.

2. Methods

Experimental setup

The bentonite used in this experimental work is mined from a reducing horizon in Colony, Wyoming. The bentonite was pulverized and sieved to < 3 mm and used with a free moisture of ~15.5 wt. %. The synthetic groundwater solution was chosen to replicate a deep groundwater composition (Table 1, Stripa sample V2 (69-4), Frape et al. 2003). The groundwater solution was prepared using reagent grade materials dissolved in double deionised water. KOH and HCl were added to adjust the initial solution pH. This solution was then filtered through a 0.45 µm filter and sparged with He before each experiment. The salt solution was added at a 9:1 water: bentonite ratio. Initial components for all experiments have been summarized in Table 2.

Table 1. Synthetic groundwater chemistry used in each experiment.

Species	mg/L
Ca ²⁺	89
Cl ⁻	1045
K ⁺	583
Na ⁺	167
Si	1
SO ₄ ²⁻	47
Sr ²⁺	0.05
TDS	1934
pH	8.59

The redox conditions for each system were buffered using a 1:1 mixture (by mass) of Fe₃O₄ and Fe⁰ added at 0.07 wt. % of the bentonite mass. Approximately 7 wt. % (of total mass) 304 stainless steel (NIST SRM 101g), 316 stainless steel (NIST SRM 160b), Cu-foil, and low-carbon steel (provided by Sandia National Laboratory) were added to the experiments to mimic the presence of a waste canister.

Reactants were loaded into either a flexible gold or titanium bag and fixed into a 500 mL Gasket Confined Closure reactor (Seyfried et al. 1987). Experiments were pressurized to 150 - 160 bar and were heated following two different temperature profiles: 1) 120 °C for 2 weeks, 210 °C for 2 weeks, and then 300 °C for 1 week and 2) isothermal at 300 °C for 6 weeks. Reaction liquids were extracted during the experiments and analyzed to investigate the aqueous geochemical evolution in relationship to mineralogical alterations. The sampled reaction liquids were split three-ways producing aliquots for unfiltered anion, unfiltered cation, and filtered (0.45 µm syringe filter) cation determination. All aliquots were stored in a 1 °C refrigerator until analysis.

Table 2. Initial components and reaction conditions for EBS experiments. EBS-8 developed a leak during experiment. This experiment was discarded and was repeated as EBS-11.

	Clay, g	Brine, g	pH	Fe ^o , g	Fe ₃ O ₄ , g	Accessory, g	EBS Component	Run temp, °C	Run time
EBS-1	7.4	79.0	8.59	0.257	0.252	na	na	25/100/200/300/25	4 weeks
EBS-2	7.2	62.0	8.59	0.251	0.253	4.980	304SS	25/100/200/300/25	4 weeks
EBS-3	6.790	59.4	7.56	0.255	0.261	4.245	316SS	25/100/200/300/25	5 weeks
EBS-4	16.207	145.0	7.56	0.574	0.579	9.753	Cu	25/100/200/300/25	5 weeks
EBS-5	15.770	135.9	6.73	0.505	0.505	11.189	304SS	300	6 weeks
EBS-6	12.109	104.2	9.48	0.424	0.424	8.375	Low-C Steel	25/100/200/300/25	5 weeks
EBS-7	14.627	157.9	6.69	0.589	0.586	3.656	Graphite	25/100/200/300/25	5 weeks
EBS-8	15.284	131.9	7.72	0.489	0.489	10.816	Cu	300	6 weeks
EBS-9	15.516	167.6	7.16	0.625	0.625	3.878	Quartz sand	25/100/200/300/25	5 weeks
EBS-10	21.105	182.3	6.36	0.675	0.675	14.937	316SS	300	6 weeks
EBS-11	15.039	129.8	6.74	0.481	0.481	10.643	Cu	300	6 weeks
EBS-12	208.5	41.7	6.74	na	Na	na	none	300	7 weeks

Mineral Analyses

X-ray diffraction (XRD) analyses of experimental materials determined mineral compositions. Each sample was ground with 20 wt. % corundum (Al_2O_3) for quantitative XRD analysis of the bulk rock (Chung 1974). XRD measurements were conducted with a Siemens D500 diffractometer using $\text{Cu-K}\alpha$ radiation. Data were collected from 2 to 70 $^\circ 2\theta$ with a 0.02 $^\circ 2\theta$ step-size and count times of 8 to 12 seconds per step. To better analyze the non-clay and clay fractions, the $< 2 \mu\text{m}$ particles were separated via sedimentation in DI H_2O . An aliquot of the $< 2 \mu\text{m}$ suspension was dropped on a zero-background quartz plate and dried. This oriented mount was X-rayed from 2 to 40 $^\circ 2\theta$ at 8 to 12 s per step. The oriented mount was then saturated with ethylene glycol in a 60 $^\circ\text{C}$ oven for 24 hours and XRD analysis was repeated. A portion of the $> 2 \mu\text{m}$ particles was ground with a mortar/pestle, deposited on a zero-background quartz plate, and X-rayed under the same parameters as the bulk powder material. The remaining $> 2 \mu\text{m}$ portion was used for electron microscopy. Mineral identification and unit-cell parameters analysis was performed using Jade[®] 7.5 X-ray data evaluation program with ICDD PDF-4 database. Quantitative phase analysis was performed using FULLPAT (Chipera and Bish 2002).

X-ray fluorescence (XRF) analysis of the experimental materials was performed using a Rigaku ZSX Primus II. Samples were mixed with Li-metaborate at 7:1 or 36:1 and fluxed at 1100 $^\circ\text{C}$ for 45 minutes. All reported values exceed three times the reported detection limits. A portion of the $< 2 \mu\text{m}$ fraction from the reaction products and starting bentonite was analyzed to determine the structural formulas. All other starting materials were analyzed without separation. Loss on ignition (LOI) was determined by heating the sample to 1000 $^\circ\text{C}$ for 30 minutes.

Electron microscopic analyses were performed using a FEI[™] Inspect F scanning electron microscope (SEM). All samples were Au-coated prior to SEM analysis. Imaging with the SEM was performed using a 5.0 kV accelerating voltage and 1.5 spot size. Energy dispersive X-ray spectroscopy (EDX) was performed at 30 kV and a 3.0 spot size.

Electron microprobe analyses were performed at the University of Oklahoma using a Cameca SX50 electron microprobe equipped with five wavelength-dispersive spectrometers and PGT PRISM 2000 energy-dispersive X-ray detector. Petrographic characterization was performed by backscattered electron imaging coupled with energy-dispersive X-ray analysis, using beam conditions of 20 kV acceleration and 20 nA sample current. Quantitative analysis was performed by wavelength-dispersive spectrometry using 20 kV accelerating voltage, 20 nA beam current, and 2 μm spot size. Matrix corrections employed the PAP algorithm (Pouchou and Pichoir 1985), with oxygen content calculated by stoichiometry. Counting times were 30 seconds on peak for all elements, yielding minimum levels of detection (calculated at 3- σ above mean background) in the range of 0.01 to 0.03 wt% of the oxides for all components except F (0.16 wt%). All standards for elements in the silicates were analyzed using 30 second count times on peak, using K-alpha emissions. The standards and oxide detection limits are presented in Appendix A. Sodium analyses for clinoptilolite are problematic due to sodium migration under an electron beam, whereas analcime shows no sodium migration (Broxton *et al.*, 1987). Zeolite structural formulae were calculated from data that have $\text{Al} + \text{Fe}/(\text{Na} + \text{K} + 2*(\text{Ca} + \text{Mg}))$ ratios within a range of 1.20 to 0.80. Microprobe results of select silicates are presented in Appendix B.

Aqueous geochemical analyses

Major cations and trace metals were analyzed via inductively coupled plasma-optical emission spectrometry (Perkin Elmer Optima 2100 DV) and inductively coupled plasma-mass spectrometry (Elan 6100) utilizing EPA methods 200.7 and 200.8. Ultra-high purity nitric acid was used in sample and calibration preparation prior to sample analysis. Internal standards (Sc, Ge, Bi, and In) were added to samples and standards to correct for matrix effects. Standard Reference Material (SRM) 1643e Trace Elements in Water was used to check the accuracy of the multi-element calibrations. Inorganic anion samples were analyzed by ion chromatography (IC) following EPA method 300 on a Dionex DX-600 system. Aqueous geochemical results are presented in Appendix C.

Reaction modeling and phase diagrams were calculated via The Geochemist's Workbench v.8.0.8 using a modified *thermo.dat* database. These thermodynamic databases were modified to incorporate various mineral compositions that are more consistent to what is found in these experiments (Neuhoff et al. 2004; Wilkin and Barnes 1998; Blanc and Vieillard 2010). Solution chemistry data (analyzed at room temperature) was adjusted to reflect the activities present at reaction temperatures. Temperature corrected data were plotted on phase diagrams to show the geochemical progression. Pressures for the GWB modeling were held at water saturation pressures.

3. Results

Bentonite Pre- and Post-Reaction Characteristics

The starting bentonite used in this experiment is a Na-montmorillonite with minor amounts of clinoptilolite, feldspars, biotite, cristobalite, quartz, and pyrite (Table 3). This material differs from the more commonly evaluated MX-80 bentonite by lacking calcite and gypsum, but contains significant amounts of clinoptilolite (Guillaume et al. 2004; Karnland 2010). The montmorillonite displays the typical foily or 'cornflake' morphology associate with smectite (Figure 1a). The bulk and < 2 μm bentonite compositions are listed in Table 4. Montmorillonite associated with this bentonite has a structural formula of $(\text{Na}_{.31}, \text{Ca}_{.04}, \text{K}_{.01})(\text{Al}_{1.53}, \text{Fe}_{.21}, \text{Mg}_{.18}, \text{Ti}_{.01})(\text{Si}_{3.98}, \text{Al}_{.02})\text{O}_{10}(\text{OH})_2$. Clinoptilolite in the bentonite appears to maintain the precursor volcanic shard morphology (Figure 1b) with a structural composition of $(\text{Na}_{4.30}, \text{Ca}_{0.39}, \text{K}_{0.14}, \text{Mg}_{0.20})(\text{Si}_{29.82}, \text{Al}_{6.28}, \text{Fe}_{0.03})\text{O}_{72} \cdot n\text{H}_2\text{O}$ ($n \sim 21$, based on stoichiometric clinoptilolite). Feldspars are primarily albitic plagioclases $(\text{Na}_{0.71}\text{Ca}_{0.19}\text{K}_{0.07}(\text{Si}_{2.80}\text{Al}_{1.21})\text{O}_8)$ and K-feldspars $(\text{K}_{0.66}\text{Na}_{0.29}\text{Ca}_{0.01}(\text{Si}_{2.97}\text{Al}_{1.05})\text{O}_8)$. The bentonite contains no more than 0.4 wt. % pyrite. There are two forms of pyrite in the starting bentonite: 1) framboidal pyrite from microbial activity (Figure 1c) and 2) cubic pyrite principally from abiotic processes (Figure 1d).

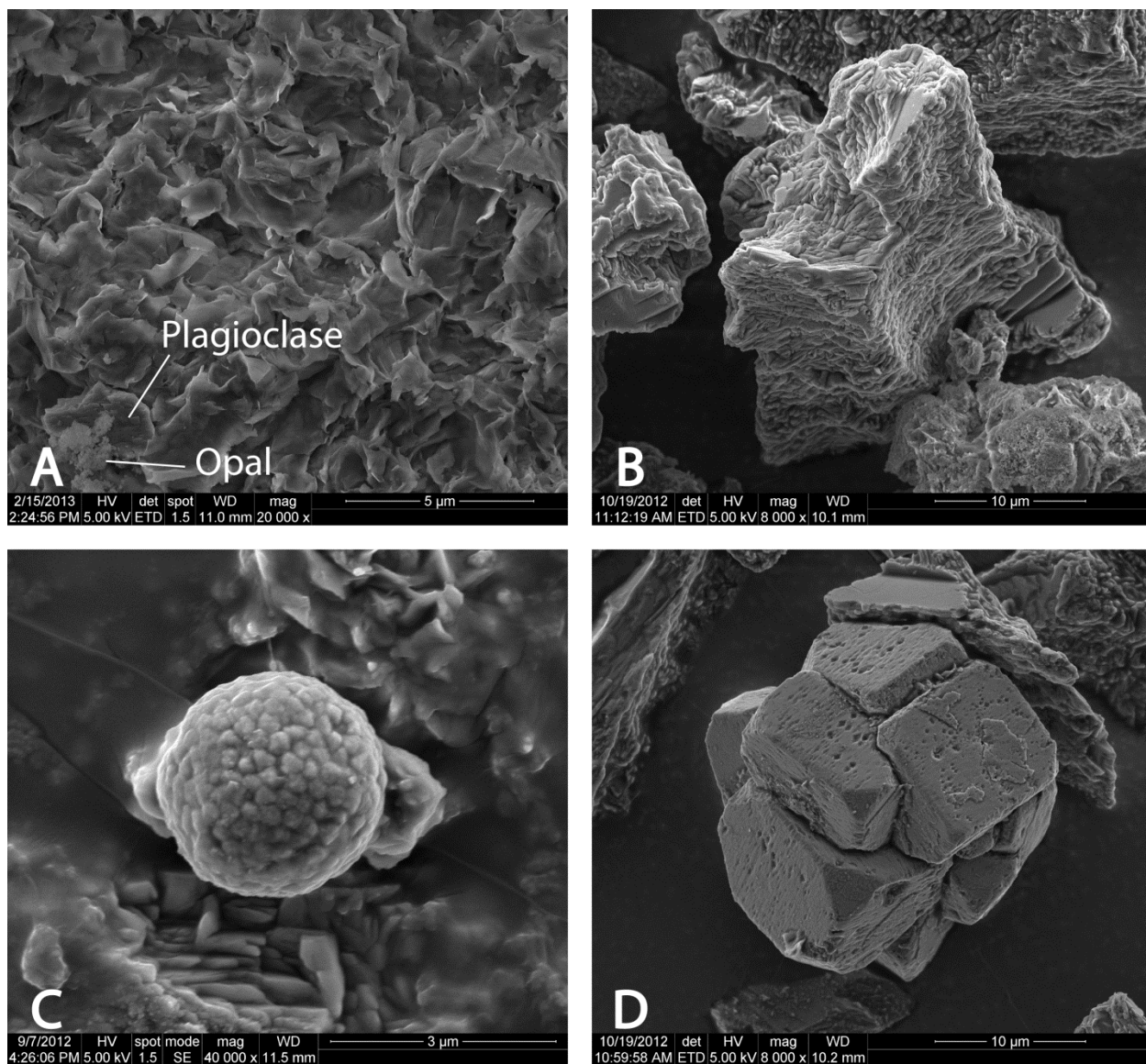


Figure 1. Minerals associated with the Colony, WY bentonite A) typical montmorillonite foily morphology with discrete plagioclase and possibly cristobalite/opal-C phases, B) tabular clinoptilolite replacing precursor volcanic shards, C) framboidal pyrite, and D) cubic pyrite.

Table 3. Bulk mineralogical composition (wt. %) of the starting bentonite and post-reaction samples. b.d.l. indicates below detection limits. “+” indicates present but is < 0.5 wt. %.

	Initial Bentonite	Ramped heating 120 to 300C							Isothermal 300C			
		EBS-1 --	EBS-2 304SS	EBS-3 316SS	EBS-4 Cu	EBS-6 LC Steel	EBS-7 graphite	EBS-9 quartz	EBS-5 304SS	EBS-10 316SS	EBS-11 Cu	EBS-12 20% H ₂ O
Montmorillonite	72	81	75	79	79	81	75	73	79	79	80	71
Quartz	1	2	1	2	1	2	3	16	2	3	2	3
Crist/Opal-C	2	2	3	2	1	4	1	2	4	2	2	10
Clinoptilolite	13	8	9	6	6	7	5	6	2	6	8	4
Analcime	b.d.l.	b.d.l.	b.d.l.	b.d.l.	b.d.l.	b.d.l.	b.d.l.	b.d.l.	3	1	1	1
Feldspar	9	6	9	8	9	4	3	3	7	8	7	10
Biotite	3	2	4	1	2	1	+	+	2	1	+	+
Pyrite	0.4	b.d.l.	b.d.l.	b.d.l.	b.d.l.	b.d.l.	b.d.l.	b.d.l.	b.d.l.	b.d.l.	b.d.l.	+
Magnetite	b.d.l.	b.d.l.	b.d.l.	2	1	+	+	1	1	b.d.l.	b.d.l.	b.d.l.
Graphite	b.d.l.	b.d.l.	b.d.l.	b.d.l.	b.d.l.	b.d.l.	12	b.d.l.	b.d.l.	b.d.l.	b.d.l.	b.d.l.
Halite	b.d.l.	b.d.l.	b.d.l.	b.d.l.	+	b.d.l.	b.d.l.	b.d.l.	+	b.d.l.	b.d.l.	b.d.l.

Table 4. Chemical composition (XRF) of the starting bentonite and < 2 μm size fractions from post-reaction samples from each EBS experiment. Oxides and loss on ignition (LOI) data are presented as wt.% and trace element data are presented as ppm. *Total iron is represented as Fe₂O₃. b.d.l. indicates below detection limits.

Metal fuse ratio	Bentonite bulk		Bentonite < 2 μm	Ramped heating 120 to 300 °C						Isothermal 300 °C				Detection Limits	
	n = 4 7:1	1 s 7:1		EBS-1 < 2 μm none 36:1	EBS-2 < 2 μm 304SS 36:1	EBS-3 < 2 μm 316SS 36:1	EBS-4 < 2 μm Cu 36:1	EBS-6 < 2 μm LC St. 36:1	EBS-7 < 2 μm gr 36:1	EBS-9 < 2 μm qtz 36:1	EBS-5 < 2 μm 304SS 36:1	EBS-10 < 2 μm 316SS 36:1	EBS-11 < 2 μm Cu 36:1		EBS-12 < 2 μm H ₂ O 36:1
Na ₂ O	2.85	0.025	2.57	2.35	2.10	2.22	2.40	2.23	2.30	2.54	2.39	2.16	2.60	2.58	0.163
MgO	1.64	0.023	1.96	2.04	2.00	1.91	1.87	1.84	1.85	1.89	1.92	1.75	1.81	1.98	0.0891
Al ₂ O ₃	19.5	0.038	20.9	20.6	20.5	20.6	20.1	19.8	19.6	20.0	20.9	19.7	19.5	20.9	0.0778
SiO ₂	61.9	0.116	63.3	62.3	63.2	62.5	62.2	63.6	61.0	61.2	62.8	59.9	63.0	61.1	0.293
P ₂ O ₅	0.044	0.002	b.d.l.	b.d.l.	b.d.l.	b.d.l.	b.d.l.	b.d.l.	0.012	0.010	b.d.l.	b.d.l.	b.d.l.	b.d.l.	0.0174
K ₂ O	0.572	0.005	0.174	0.700	0.660	0.684	0.702	0.982	0.160	0.182	0.193	0.399	0.345	0.147	0.0224
CaO	0.860	0.019	0.636	0.736	0.547	0.710	0.746	0.792	0.755	0.733	0.764	0.721	0.663	0.682	0.0298
TiO ₂	0.142	0.001	0.137	0.121	0.121	0.124	0.132	0.132	0.125	0.128	0.120	0.122	0.127	0.118	0.0344
MnO	0.013	0.001	b.d.l.	b.d.l.	0.015	0.021	0.024	0.018	0.022	0.030	0.021	0.020	0.017	0.013	0.0128
Fe ₂ O ₃	4.12	0.039	4.49	4.55	4.55	5.24	5.87	4.83	6.22	7.59	5.12	5.45	4.82	4.67	0.074
V	7	0.96	b.d.l.	b.d.l.	b.d.l.	b.d.l.	b.d.l.	b.d.l.	b.d.l.	b.d.l.	b.d.l.	b.d.l.	b.d.l.	b.d.l.	44
Cr	6	1.7	b.d.l.	b.d.l.	b.d.l.	b.d.l.	b.d.l.	b.d.l.	b.d.l.	b.d.l.	b.d.l.	b.d.l.	b.d.l.	b.d.l.	73
Co			b.d.l.	b.d.l.	b.d.l.	b.d.l.	b.d.l.	b.d.l.	b.d.l.	b.d.l.	b.d.l.	b.d.l.	b.d.l.	b.d.l.	69
Ni	5	0.82	41	46	56	48	33	47	53	42	35	35	41	53	26
Cu	7	2.5	54	61	252	94	119	45	63	73	55	66	193	62	27
Zn	96	16	b.d.l.	b.d.l.	b.d.l.	b.d.l.	58	b.d.l.	b.d.l.	b.d.l.	b.d.l.	34	75	40	26
Ge			b.d.l.	b.d.l.	b.d.l.	b.d.l.	b.d.l.	b.d.l.	b.d.l.	b.d.l.	b.d.l.	b.d.l.	b.d.l.	b.d.l.	47
As			b.d.l.	b.d.l.	b.d.l.	b.d.l.	b.d.l.	b.d.l.	b.d.l.	b.d.l.	b.d.l.	b.d.l.	b.d.l.	b.d.l.	71
Rb	18	0.82	b.d.l.	b.d.l.	b.d.l.	b.d.l.	b.d.l.	b.d.l.	b.d.l.	b.d.l.	b.d.l.	171	b.d.l.	b.d.l.	23
Sr	297	3.9	133	139	164	126	125	215	101	130	110	164	134	177	27
Zr	196	1.5	144	137	143	150	144	139	140	145	149	61	144	141	30
Ba	664	15.3	177	149	b.d.l.	b.d.l.	b.d.l.	230	b.d.l.	b.d.l.	b.d.l.	b.d.l.	b.d.l.	126	105
W			b.d.l.	b.d.l.	b.d.l.	b.d.l.	b.d.l.	b.d.l.	b.d.l.	b.d.l.	b.d.l.	b.d.l.	b.d.l.	b.d.l.	209
U			b.d.l.	b.d.l.	b.d.l.	b.d.l.	b.d.l.	b.d.l.	b.d.l.	b.d.l.	b.d.l.	b.d.l.	b.d.l.	b.d.l.	33
LOI	8.21		5.76	6.46	6.13	5.85	5.88	5.61	7.82	5.66	5.69	9.71	6.95	7.63	
total	99.99		99.98	99.91	99.88	99.90	99.97	99.90	99.90	100.00	99.95	99.98	99.89	99.88	

Ramped Thermal Profile.

There were no significant alterations to the montmorillonite away from the metal plates (> 1 mm from metal surface) during the ramped heating cycle. However, there were significant changes to the phyllosilicates due to metal interaction at the bentonite-metal interface producing Fe-rich phyllosilicates (i.e., Fe-saponite and chlorite) on steel surfaces and chalcocite on copper surfaces. The various reactions away from the bentonite-metal interface all showed similar mineralogical reactions indicating various metallic plates do not significantly influence the bulk bentonite (Table 3). The glycol saturated samples yielded d_{001} of 17 Å with higher order d_{00l} consistent with integer values of the d_{001} values (Figure 2). The XRD data suggests that neither illite nor illite-smectite was produced during the reactions. Additionally, there appears to be no major morphological changes to the montmorillonite (Figure 3a). The structural formulae (calculated from XRF analyses of < 2 µm size separates (Table 4)) of the post-reaction montmorillonites has been summarized in Table 5. All structural iron has been assumed to be in the ferric-state. However, the true nature of the montmorillonite's structural iron is unknown and most likely contains both ferric to ferrous iron. Clinoptilolite maintains a similar composition to the starting clinoptilolite, but has a slight K^+ and Ca^{2+} enrichment, $(Na_{3.17}, K_{0.65}, Ca_{0.73}, Mg_{0.09})(Si_{29.84}, Al_{6.36}, Fe_{0.03})O_{72} \cdot nH_2O$ (Appendix B).

Table 5. Structural formula for post-reaction montmorillonites. Calculated from XRF analyses of the < 2 µm size fractions.

Run Conditions	Run #	Metal Plate	Montmorillonite Structural Formulae
Initial Bentonite	Na	Na	$(Na_{3.1}, Ca_{0.4}, K_{0.1})(Al_{1.53}, Fe_{0.21}, Mg_{0.18}, Ti_{0.1})(Si_{3.98}, Al_{0.2})O_{10}(OH)_2$
Ramped, 120 to 300 °C 150 – 160 bar 5 weeks	EBS-1	None	$(Na_{2.9}, K_{0.6}, Ca_{0.5})(Al_{1.51}, Fe^{3+}_{0.22}, Mg_{0.19}, Ti_{0.1})(Si_{3.96}, Al_{0.4})O_{10}(OH)_2$
	EBS-2	304SS	$(Na_{2.6}, K_{0.4}, Ca_{0.5})(Al_{1.53}, Fe^{3+}_{0.22}, Mg_{0.19}, Ti_{0.1})(Si_{4.00})O_{10}(OH)_2$
	EBS-3	316SS	$(Na_{2.7}, K_{0.6}, Ca_{0.5})(Al_{1.50}, Fe^{3+}_{0.25}, Mg_{0.18}, Ti_{0.1})(Si_{3.96}, Al_{0.4})O_{10}(OH)_2$
	EBS-4	Copper	$(Na_{3.0}, K_{0.6}, Ca_{0.5})(Al_{1.46}, Fe^{3+}_{0.28}, Mg_{0.18}, Ti_{0.1})(Si_{3.95}, Al_{0.5})O_{10}(OH)_2$
	EBS-6	low C Steel	$(Na_{2.7}, K_{0.8}, Ca_{0.5})(Al_{1.47}, Fe^{3+}_{0.23}, Mg_{0.17}, Ti_{0.1})(Si_{4.02})O_{10}(OH)_2$
	EBS-7	Graphite	$(Na_{2.8}, K_{0.1}, Ca_{0.5})(Al_{1.31}, Fe^{3+}_{0.30}, Mg_{0.17}, Ti_{0.1})(Si_{3.85}, Al_{0.15})O_{10}(OH)_2$
	EBS-9	Quartz	$(Na_{3.1}, K_{0.2}, Ca_{0.5})(Al_{1.35}, Fe^{3+}_{0.36}, Mg_{0.18}, Ti_{0.1})(Si_{3.86}, Al_{0.14})O_{10}(OH)_2$
Isothermal, 300 °C 150 – 160 bar 6 weeks	EBS-5	304SS	$(Na_{3.1}, K_{0.2}, Ca_{0.5})(Al_{1.46}, Fe^{3+}_{0.26}, Mg_{0.19}, Ti_{0.1})(Si_{3.83}, Al_{0.17})O_{10}(OH)_2$
	EBS-10	316SS	$(Na_{2.8}, K_{0.3}, Ca_{0.5})(Al_{1.18}, Fe^{3+}_{0.27}, Mg_{0.17}, Ti_{0.1})(Si_{3.64}, Al_{0.36})O_{10}(OH)_2$
	EBS-11	Copper	$(Na_{3.3}, K_{0.3}, Ca_{0.5})(Al_{1.37}, Fe^{3+}_{0.24}, Mg_{0.18}, Ti_{0.1})(Si_{3.85}, Al_{0.15})O_{10}(OH)_2$

Odor of the aqueous samples and loss of pyrite in post-experiment samples suggests pyrite decomposition occurred during the experiments yielding $H_2S_{(aq,g)}$. Experiments containing stainless steel evolved $H_2S_{(g)}$ more readily due to limited interactions with steel surfaces. Experiments with copper plates did not evolve substantial $H_2S_{(g)}$ due to the formation of chalcocite (Cu_2S) on the copper surfaces.

SEM evidence suggests that minor authigenic plagioclase and K-feldspars are formed during these reactions (Figure 3c). Plagioclases are albitic with a structural composition of $(\text{Na}_{0.68}\text{Ca}_{0.26}\text{K}_{0.05})(\text{Al}_{1.25}\text{Si}_{2.75}\text{Fe}_{0.01})\text{O}_8$. K-feldspar has a structural composition of $(\text{K}_{.68}\text{Na}_{0.29}\text{Ca}_{0.01})(\text{Al}_{1.01}\text{Si}_{3.00})\text{O}_8$.

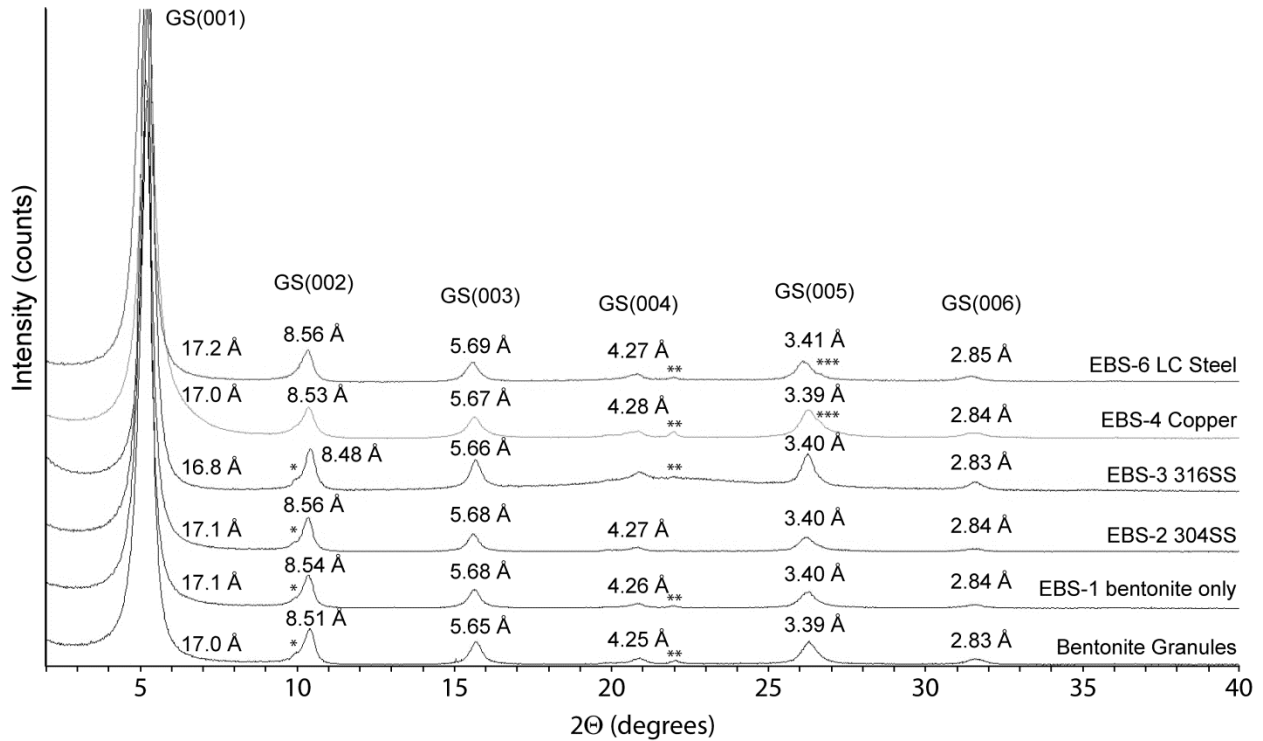


Figure 2. Oriented XRD patterns for the glycolated, $< 2 \mu\text{m}$ fraction from the ramped thermal profile experiments with d-spacings labeled above each peak. XRD results show no alteration of the montmorillonite to illite/smectite. Minor amounts of clinoptilolite (*), cristobalite/opal-C (**), and quartz (***) are also present in the $< 2 \mu\text{m}$ fraction.

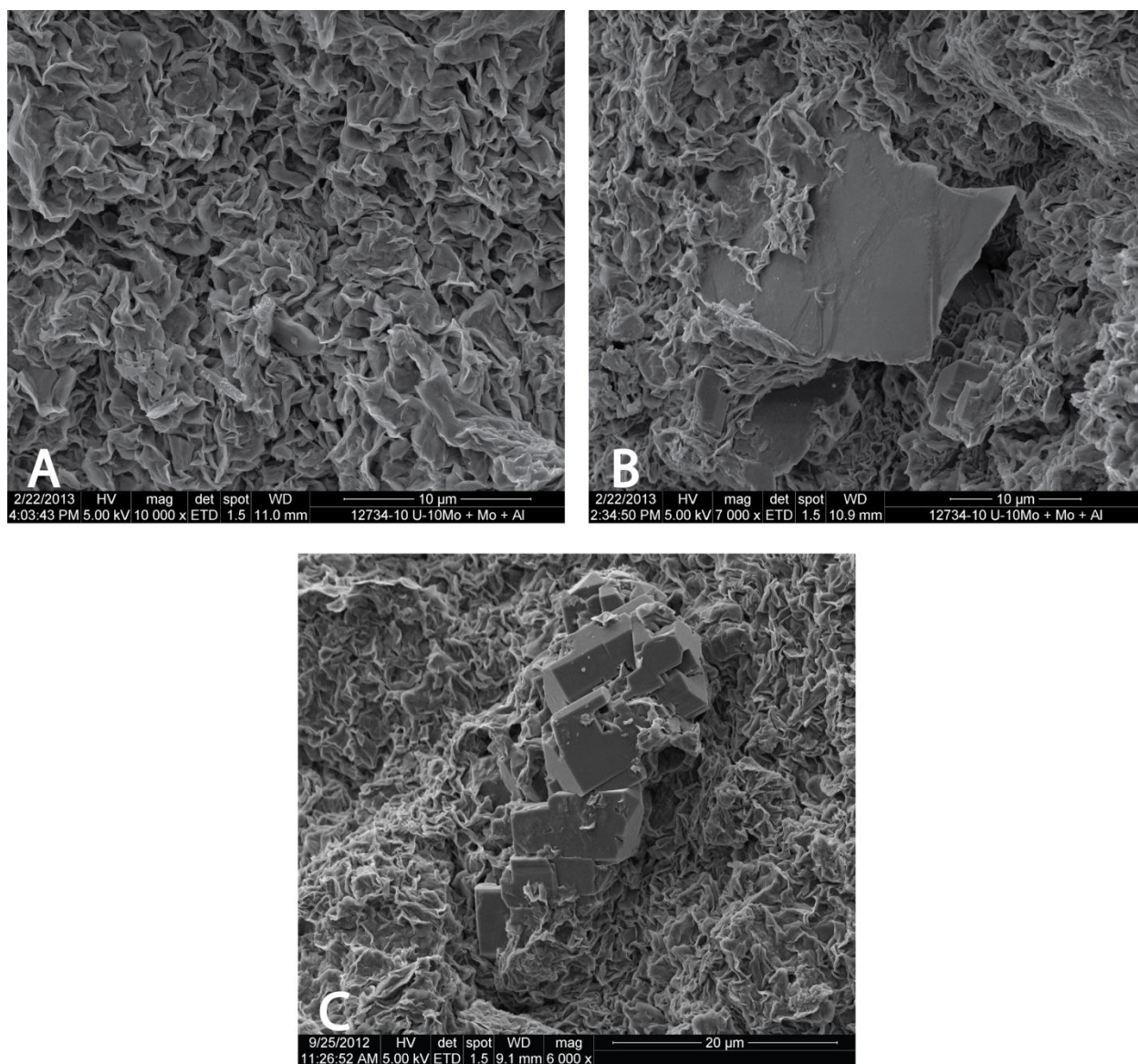


Figure 3. Post-reaction mineralogical characteristics from ramp heating experiments A) typical montmorillonite foily morphology from EBS-2, B) montmorillonite foily morphology with biotite and feldspars from EBS-2, and C) authigenic albitic plagioclase embedded in montmorillonite from EBS-1.

Isothermal, 300 °C Profile. Partial dissolution of the montmorillonite developed rough edges during the long-term, isothermal 300 °C experiments (Figure 5a). Structural formulas presented in Table 5 have been adjusted for SiO₂ contribution from 5 wt. % cristobalite/opal-C (indicated by XRD).

The glycol saturated samples yielded d_{001} of 17 Å with higher order $d_{00\ell}$ consistent with integer values of the d_{001} values (Figure 4), suggesting illite-smectite is not present. However, there does appear to be a minor 10 Å peak present in the < 2 μm fraction (Figure 4). Additionally, there possibly is a broadened peak superimposed over the 10 Å biotite peak associated with the > 2 μm samples. These broadened 10 Å peaks do not shift upon glycolation, suggesting an occurrence of

Odor of the aqueous samples and loss of pyrite in post-experiment samples suggests pyrite decomposition occurred during the experiments yielding $\text{H}_2\text{S}_{(\text{aq,g})}$. Experiments containing stainless steel evolved $\text{H}_2\text{S}_{(\text{g})}$ more readily, limiting interaction with steel surfaces. There is evidence of a 0.4 – 0.8 μm sulfur-rich layer (Figures 13 and 17) developed on outer surfaces of the steel plates. Experiments with Cu° plates did not evolve substantial $\text{H}_2\text{S}_{(\text{g})}$ due to the formation of chalcocite (Cu_2S) on the Cu surfaces.

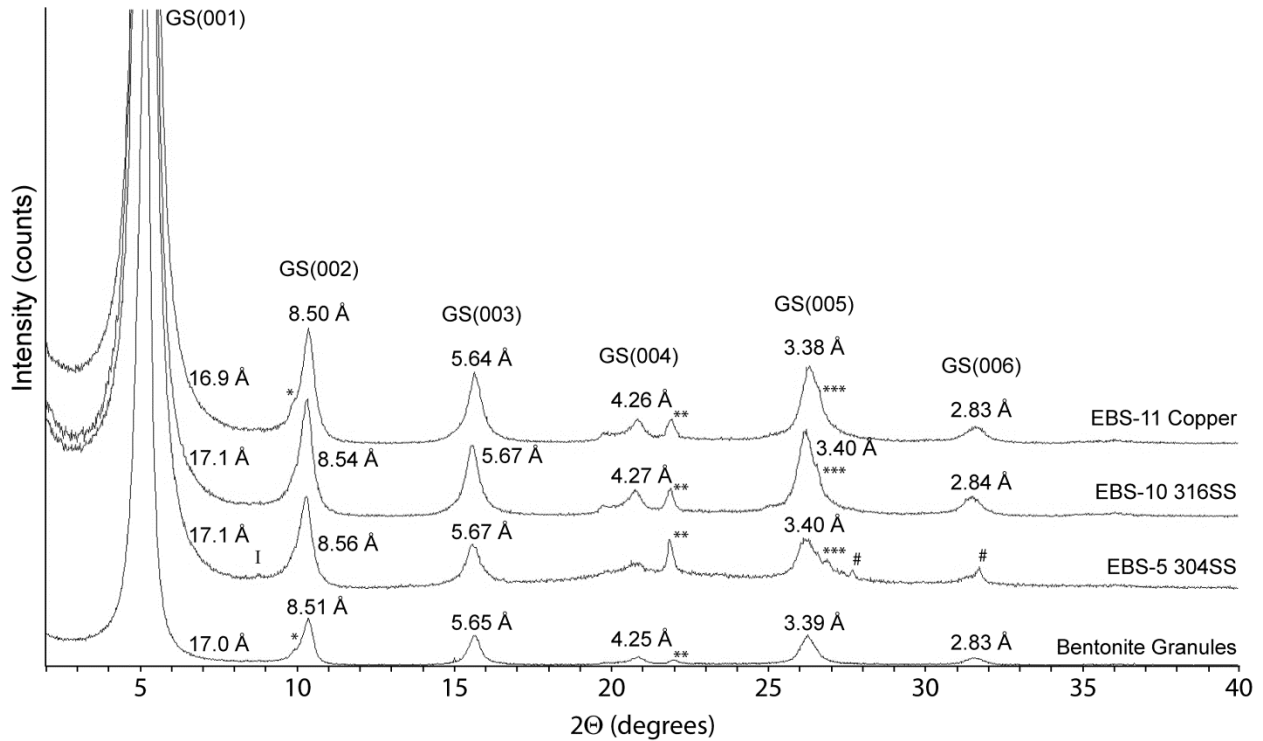


Figure 4. Oriented XRD patterns for the glycolated, $< 2 \mu\text{m}$ fraction from the isothermal, $300 \text{ }^\circ\text{C}$ thermal profile experiments. XRD results show no alteration of the montmorillonite to illite/smectite. A small, 10 \AA peak (possibly illite (I)) appears to be present in EBS-5 material. Minor amounts of clinoptilolite (*), cristobalite/opal-C (**), quartz (***), and halite (#) are also present in the $< 2 \mu\text{m}$ fraction.

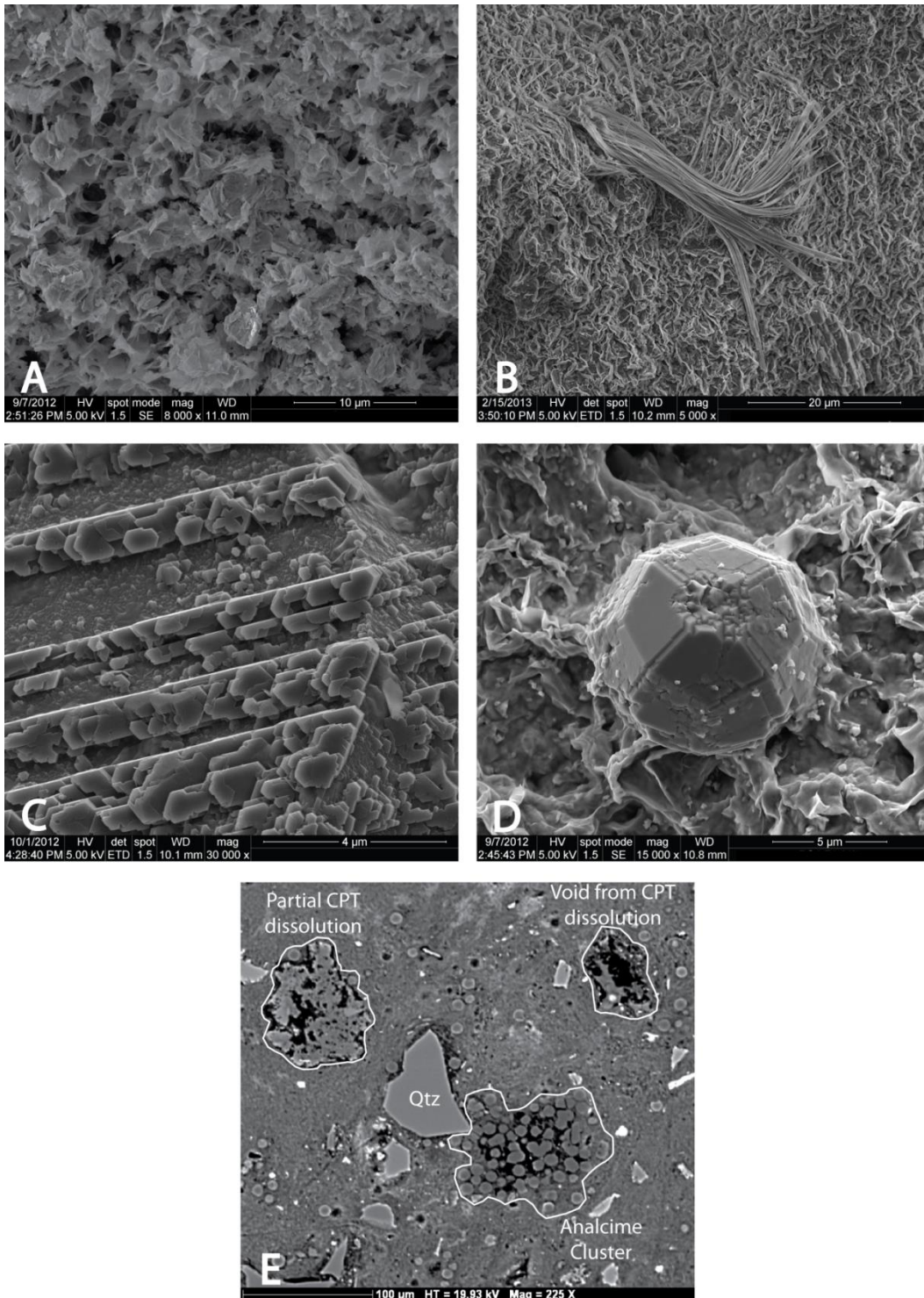


Figure 5. Post-reaction SEM images showing mineralogical characteristics from the isothermal 300 °C experiments including A) montmorillonite foils displaying partially deteriorated edges, B) bundle of authigenic fibrous illite, C) authigenic albitic plagioclase overgrowths showing possible polysynthetic twinning, D) subhedral analcime formed from the dissolution of clinoptilolite, and E) backscatter electron image showing discrete analcime crystals, various stages of clinoptilolite dissolution, and clinoptilolite replacement by analcime.

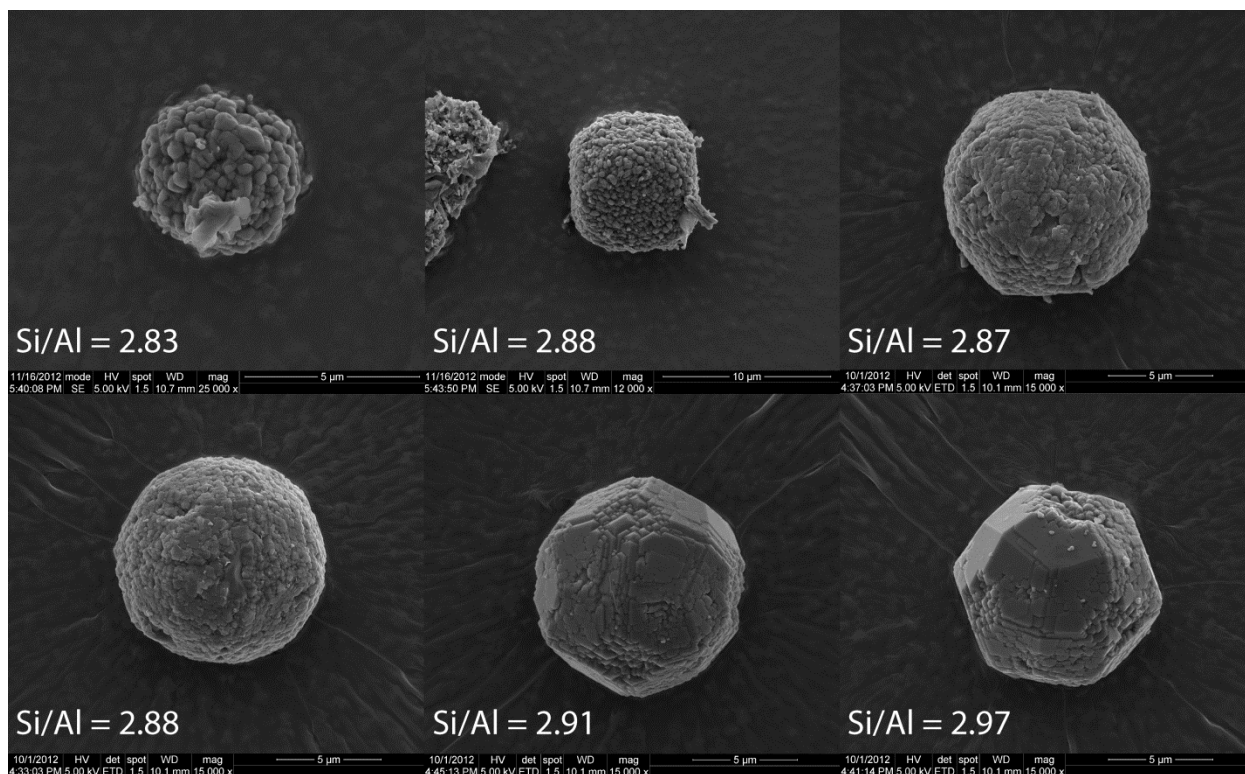


Figure 6. Analcime growth stages associated with a systematic Si/Al changes. Anhedral analcime formed initially as an agglomeration of nano-sized, spherical crystals followed by ripening of analcime nuclei to subhedral, trapezohedral analcime.

Aqueous geochemistry

Changes to the solution chemistry are fairly consistent between the different EBS experiments. There is an exchange of Na^+ for K^+ in the solution most likely controlled by the cation exchange capacity of both the Na-smectites and clinoptilolite (Figure 7a and 8a). This cation exchange yielded $\sim 451 \text{ mg/L Na}^+$ enrichment and $\sim 542 \text{ mg/L K}^+$ depletion in solution producing a K⁺ enriched montmorillonite. There is also a decline in the Ca^{2+} aqueous concentrations ($\sim 76 \text{ mg/L}$) during experiments mostly due to montmorillonite exchange.

Silica activity stays saturated with respect to cristobalite as the temperature increases (Figures 7b and 8b). Silica concentrations increase in increments closely following the temperature profile of the ramped heating cycle, indicating that silicate mineral dissolution is closely tied to the reaction temperature (Figure 7b). During the 300 °C experiments, silica (Si) concentrations rapidly increase to $\sim 500 \text{ mg/L}$ and remained fairly steady for the experiment duration. Partial smectite dissolution and clinoptilolite alteration are the most likely controls on the silica activity.

Sulfur evolution is complicated by the occurrence of multiple redox states and interaction with metal plates. Sulfur concentrations during the ramped experiments increased from $\sim 47 \text{ mg/L}$ to $\sim 125 \text{ mg/L}$ until reactions temperatures reached 300 °C, when sulfur values dropped to $\sim 46 \text{ mg/L}$ (Figure 9a). During the 300 °C experiments, sulfur concentrations steadily climbed to a

~191 mg/L. Aluminum concentrations tend to increase in increments closely following the temperature profile during the ramped heating cycle (Figure 9b). The changes in aluminum concentration are similar to the observed changes in the silica concentration. During the 300 °C experiments, aluminum concentrations rapidly increase to ~1.5 to 3.5 mg/L. After the initial increase the aluminum concentrations slowly decreased. The decrease is likely related to the crystallization of analcime, fibrous illite, and feldspars.

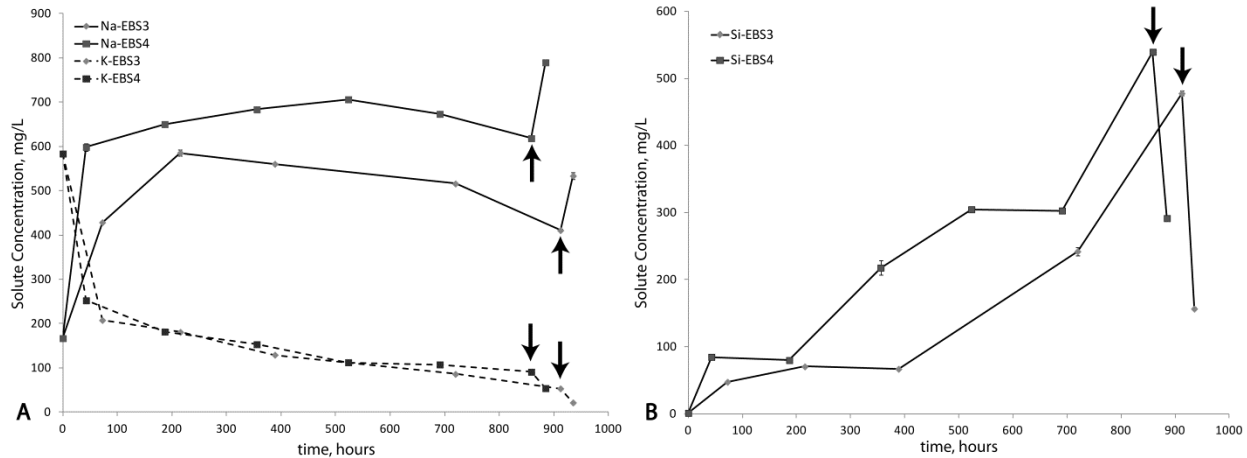


Figure 7. Plots of Na⁺, K⁺, and Si⁴⁺ concentrations through the ramped experiments (EBS-3 and EBS-4) showing evolution of solutes in contact with bentonite. Quenching experiment to room temperature (black arrows) significantly changes the solution chemistry. Note silica precipitation upon quenching.

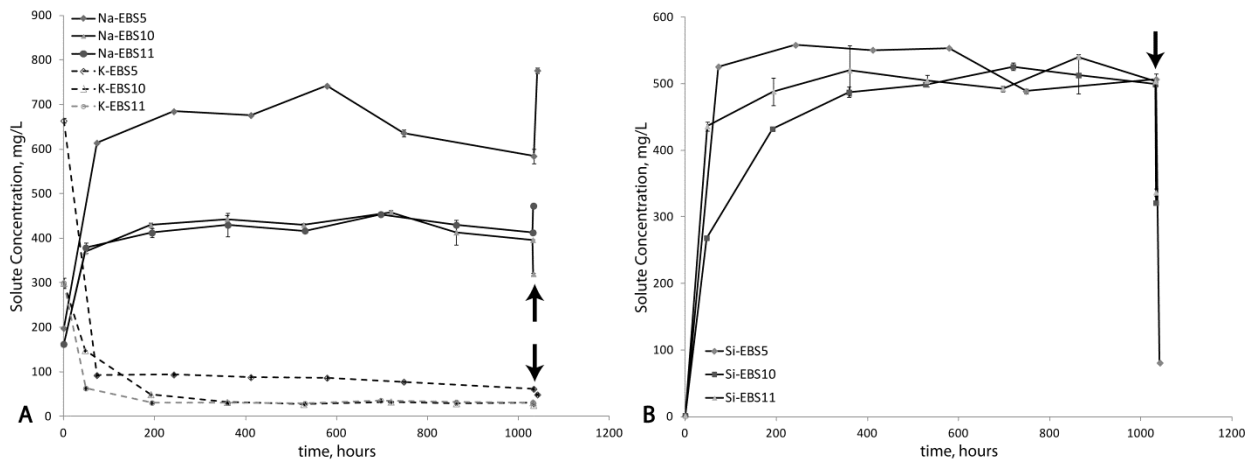


Figure 8. Plots of Na⁺, K⁺, and Si⁴⁺ concentrations through the isothermal 300 °C long-term experiments (EBS-5, EBS-10, and EBS-11) showing evolution of solutes in contact with bentonite. Quenching experiment to room temperature (black arrows) significantly changes the solution chemistry. Note silica precipitation upon quenching.

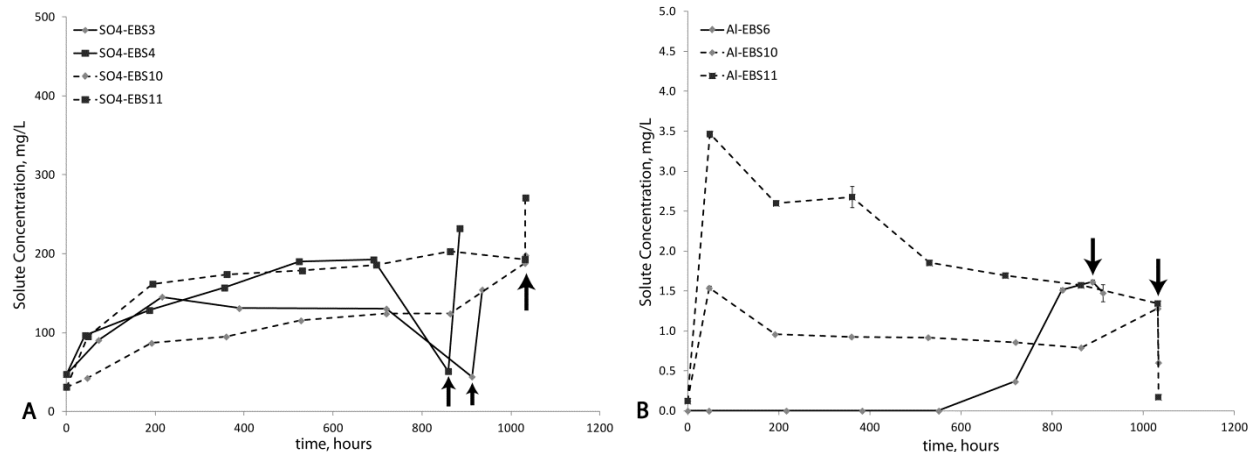


Figure 9. Sulfate (left) and aluminum (right) solution chemistry evolution during the ramped and isothermal experiments. Quenching experiment to room temperature (black arrows) significantly changes the solution chemistry.

Metal-Bentonite Interface

Steel reaction with bentonite

304 SS.

The initial 304 SS (NIST SRM 101g) is an iron alloy primarily with 18.46 wt.% Cr, 10.00 wt. % Ni, 1.08 wt. % Si, and 0.029 wt.% Cu. 304SS underwent uniform interface reaction during the ramped and isothermal, 300 °C experiments. Post-reaction 304 SS formed a layer of smectite and chlorite covering the surface of the steel plate (Figure 10). However, smectite was the only phyllosilicates associated with the reaction site products in the six week, 300 °C reaction (Figure 11). The primary type smectite associated with the steel surface appears to be an Fe-saponite. Smectite expands upon ethylene glycol saturation to 16.8 Å (with 002 at 8.35 Å) suggesting no significant amount of mixed-layering is present. Pentlandite ((Cu, Ni, Fe)-sulfide) appears to have formed sparingly in both 304 SS experiments along with an unknown fibrous material (Figure 12A and B). The smectite and chlorite morphologies tend to be fairly consistent producing a bladed to micaceous habit with a rose-like texture (Figure 12). The initial montmorillonite has a distinctly different foily morphology (Figure 12C) suggesting smectite associated with the 304SS is newly formed. The interface reaction products have thicknesses ranging from 9 to 44 μm with crystallites occurring perpendicular to 304SS substrate (Figures 12D and 13). There was no significant change in the interface layer thicknesses with increased reaction time at 300 °C. This is further evidenced by focused ion beam (FIB) and SEM analysis where milling or “carving” perpendicular to the sample surface reveals the fine-scale textural profile of the clay-metal interface. Supplemental Figures S1 and S2 in Appendix A show the vertical textural profile of the interface between metal and clay. It also shows an Fe-leached O-rich layer on the steel surface with a nearly constant thickness of ~1.5 – 2 microns. Chemical analyses of post-reaction 304SS and the smectite mantle indicates there was a slight Fe leaching from the 304SS forming a Cr-enriched steel outer layer and a Fe-rich smectite and chlorite coating (Figure 13). The reaction products do include varying degrees of Cr and Ni substitutions.

Accurate chemical formula for the interface reaction products are not possible due to the intimate mixing of multiple phases. The average bulk chemistry of the corrosion layer is provided in Table 6. Fe-rich phyllosilicates that formed on steel plates in the ramped experiments have two 06ℓ diffraction bands 1.536 and 1.523 Å (9.138 and 9.216 Å b-parameters), corresponding to trioctahedral chlorite and smectite (Figure 21). It is uncertain which minerals species correspond to the b-parameters as there is overlap in the unit-cell parameters between the Mg, Fe-saponites (9.120 (Mg²⁺) to 9.30 (Fe²⁺) Å) and chlorite (9.228 to 9.294 Å) species (Kohyama et al. 1973; Moore and Reynolds 1997). The Fe-smectite produced in the six week, 300 °C experiment has a 1.547 Å (9.282 Å b-parameters) 06ℓ diffraction band, consistent with Fe-saponite (Kohyama et al. 1973).

Table 6. Bulk chemical composition from the 304 SS corrosion layer developed from the ramped heating cycle (EBS-2)

	SiO ₂	Al ₂ O ₃	Cr ₂ O ₃	FeO*	MnO	MgO	NiO	CaO	Na ₂ O	K ₂ O	Total
EBS-2	33.47	13.14	1.25	31.03	0.38	1.98	1.26	1.31	1.60	0.62	86.04

316SS.

The initial 316 SS (NIST SRM 160b) is an iron alloy primarily with 18.37 wt. % Cr, 12.35 wt. % Ni, 2.26 wt. % Mo, 1.619 wt. % Mn, 0.5093 wt. % Si, and 0.175 wt. % Cu. 316 SS underwent exfoliation corrosion during the ramped and isothermal, 300 °C experiments. Post-reaction 316 SS formed smectite dominated interface reaction products with some chlorite covering the surface of the steel plate (Figure 14). However, smectite was the only phyllosilicates associated with interface reaction products in the six week, 300 °C reaction (Figure 15). The primary type smectite associated with the steel surface appears to be an Fe-saponite. Smectite expands to 16.8 Å (with 002 at 8.44 Å) upon ethylene glycol saturation suggesting no significant amount of mixed-layering is present. However, the six weeks, 300 °C smectite product expands to 16.3 Å (002 at 8.25 Å) upon ethylene glycol saturation indicating a possible decrease in swelling capacity. A pentlandite-like ((Cu, Ni, Fe)-sulfide) material appears to have also been formed in both 316 SS experiments along with what appears to be fibrous sulfides (Figure 16 A, B, and D). The smectite and chlorite morphologies tend to be fairly consistent producing a bladed to micaceous habit with a rose-like texture (Figure 16). The interface reaction products have thicknesses ranging from 20 to 40 μm with crystallites occurring perpendicular to 316 SS substrate (Figures 16 and 17). There was no significant change in the interface reaction layer thicknesses with increased reaction time at 300 °C. Chemical analyses of post-reaction 316 SS and mantling products indicates there was significant Fe leaching from the 316 SS forming a Cr-enriched steel outer layer up to 4 μm thick. The Cr-enriched layer also underwent oxidation and sulfidation producing a noticeable alteration zone (Figure 17). Smectite and chlorite coatings were enriched in iron most likely from the iron leached from the 316 SS (Figure 17). Fe-rich phyllosilicates that formed on steel plates in the ramped experiments have 06ℓ diffraction bands 1.535 (9.210 Å b-parameters), corresponding to a trioctahedral phyllosilicate (Figure 21; Kohyama et al. 1973; Moore and Reynolds 1997). It is uncertain which minerals species correspond to the b-parameters, however the b-parameter is probably related to an Fe-saponite due to a smectite dominance in the corrosion products. The Fe-smectite produced in the six week, 300 °C experiment has a fairly broad 1.54 Å (9.24 Å b-parameters) 06ℓ diffraction band, consistent with Fe-saponite (Kohyama et al. 1973).

Low-carbon steel.

The initial low-carbon steel contains 0.19 wt. % Cr, 0.16 wt. % Ni, 1.07 wt. % Mn, 0.24 wt. % Si, and 0.30 wt. % Cu. Low-carbon steel underwent pitting corrosion during the ramped and isothermal, 300 °C experiments. Post-reaction low-carbon steel developed a smectite coating the steel plate surfaces (Figures 18 and 19A). Unlike the 304SS and 316SS, there was no evidence of any chlorite phases present in the interface reaction product of the low-carbon steel. The primary type smectite associated with the steel surface appears to be an Fe-saponite. Smectite expands to 16.6 Å (with 002 at 8.32 Å) upon ethylene glycol saturation suggesting no significant amount of mixed-layering is present (Figure 18). Also, pyrrhotite (Fe_{1-x}S) platelets formed concurrently with the smectite phases as determined their spatial distribution (Figure 19C). Smectite morphology is varied between a honeycombed texture and rose-like texture with a bladed to micaceous habit (Figure 19B and D). In addition to the small scaled textures, there is an overlying botryoidal texture with the interface reaction products (Figure 19C). These interface reaction products have thicknesses ranging from 13 to 56 μm with additional $\sim 7 \mu\text{m}$ corrosion pits. The bladed to micaceous crystallites tend to occur with the longer dimensions perpendicular to the steel substrate (Figures 19 and 20). Chemical analyses of post-reaction low-carbon steel and interface reaction products indicate no chemical fractionation associated with the phase transformation process. Accurate chemical formula for the interface reaction products are not possible due to the intimate mixing of multiple phases. The average bulk chemistry of the interface reaction layer is provided in Table 7. There does appear to be oxidation and sulfidation associated with the surface (Figure 20). Smectite is enriched in iron most likely due to the iron dissolved from the steel (Figure 20). The Fe-rich smectite has 06 ℓ diffraction bands of 1.547 Å (9.264 Å b-parameters), corresponding to a trioctahedral smectite (Figure 21; Kohyama et al. 1973; Moore and Reynolds 1997).

Table 7. Bulk chemical composition (EMPA) from the low-carbon corrosion layer developed from the ramped heating cycle (EBS-6)

	SiO ₂	Al ₂ O ₃	Cr ₂ O ₃	FeO*	MnO	MgO	NiO	CaO	Na ₂ O	K ₂ O	Total
EBS-6	36.00	12.80	0.02	33.75	0.22	0.83	0.01	0.64	1.02	0.35	85.63

Copper reaction with bentonite

The initial copper foil appears to be 100% Cu (based on EDX analyses). The primary corrosion product for both types of experiments is chalcocite (Cu_2S) (Figures 22 and 23). Corrosion seems to take place with an initial dissolution of the copper developing dissolution features on the surface of the copper (Figure 24A). Chalcocite forms a hexagonal morphology ranging from discrete plates to completely coalesce patches on the copper surface (Figure 24A and C). Also, there are minor amounts of an unknown fibrous material associated with the copper surface (Figure 24B).

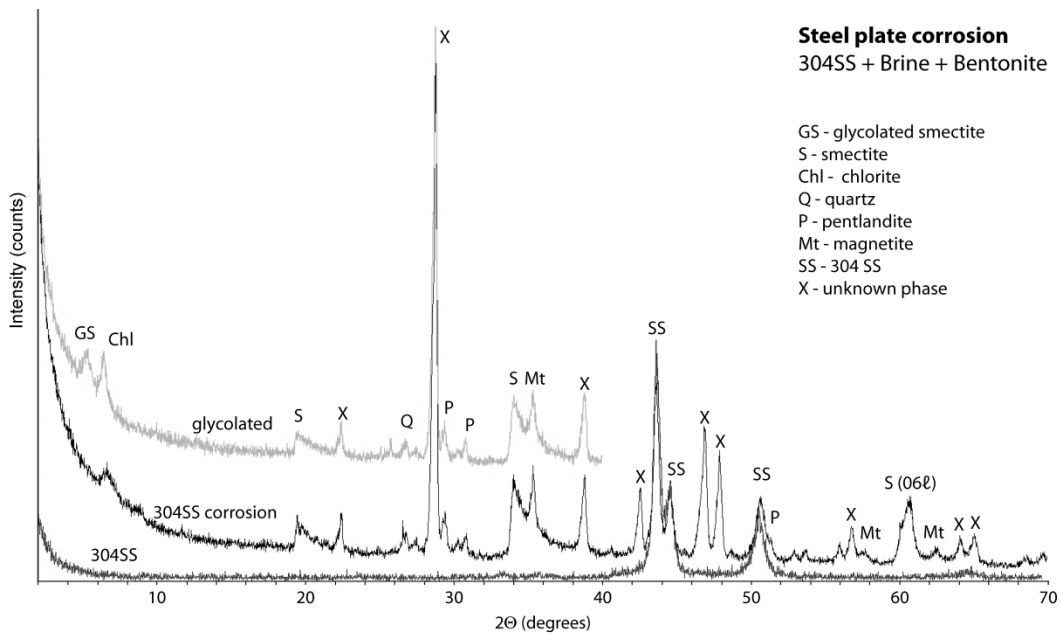


Figure 10. XRD patterns of the air-dried and ethylene glycol saturated corrosion products on the 304 SS plate used in the EBS-2 experiment. Smectite, chlorite, and a pentlandite-like material are the dominant interface reaction phases. Starting 304 SS XRD plot is also shown for comparison.

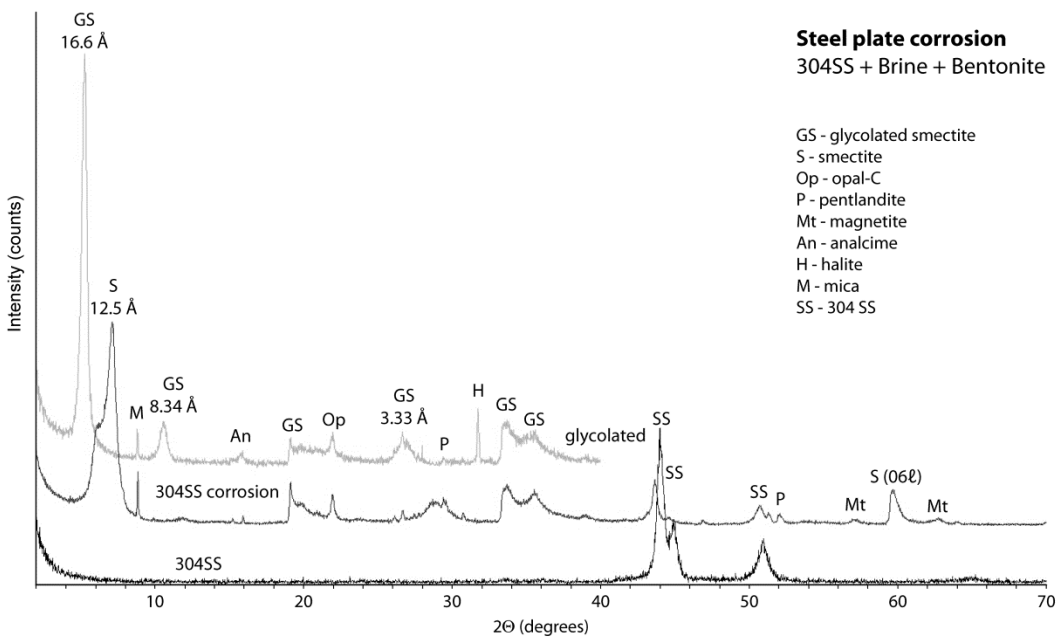


Figure 11. XRD patterns of the air-dried and ethylene glycol saturated corrosion products on the 304 SS plate used in the EBS-5 experiment. Smectite and a pentlandite-like material are the dominant interface reaction phases. Starting 304 SS XRD plot is also shown for comparison.

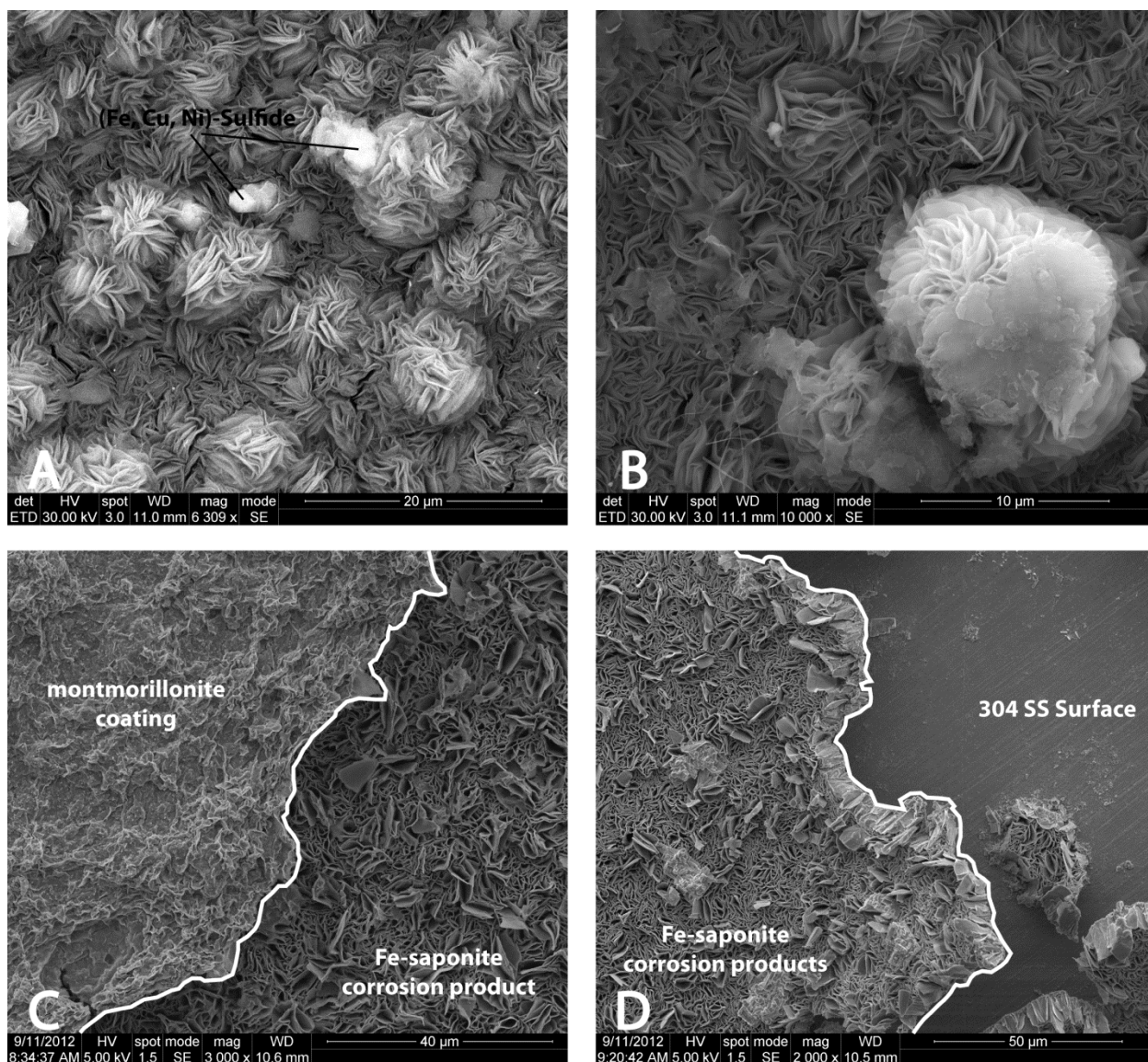


Figure 12. SEM image (plan view) of Fe-phyllsilicates (saponite and chlorite) using 304 SS as a growth substrate from both ramped (EBS-2) and isothermal, 300 °C (EBS-5) heating profiles. A) Fe-saponite and chlorite growths with later-stage pentlandite-like ((Fe, Cu, Ni)-sulfide) material from EBS-2. B) Unknown fibers overlaying rose-like Fe-saponite and chlorite interface reaction products from EBS-2. C) Montmorillonite coating on Fe-saponite showing the distinct morphology between the two smectites from EBS-5. D) Boundary between the Fe-saponite interface reaction product and 304 SS surface from EBS-5.

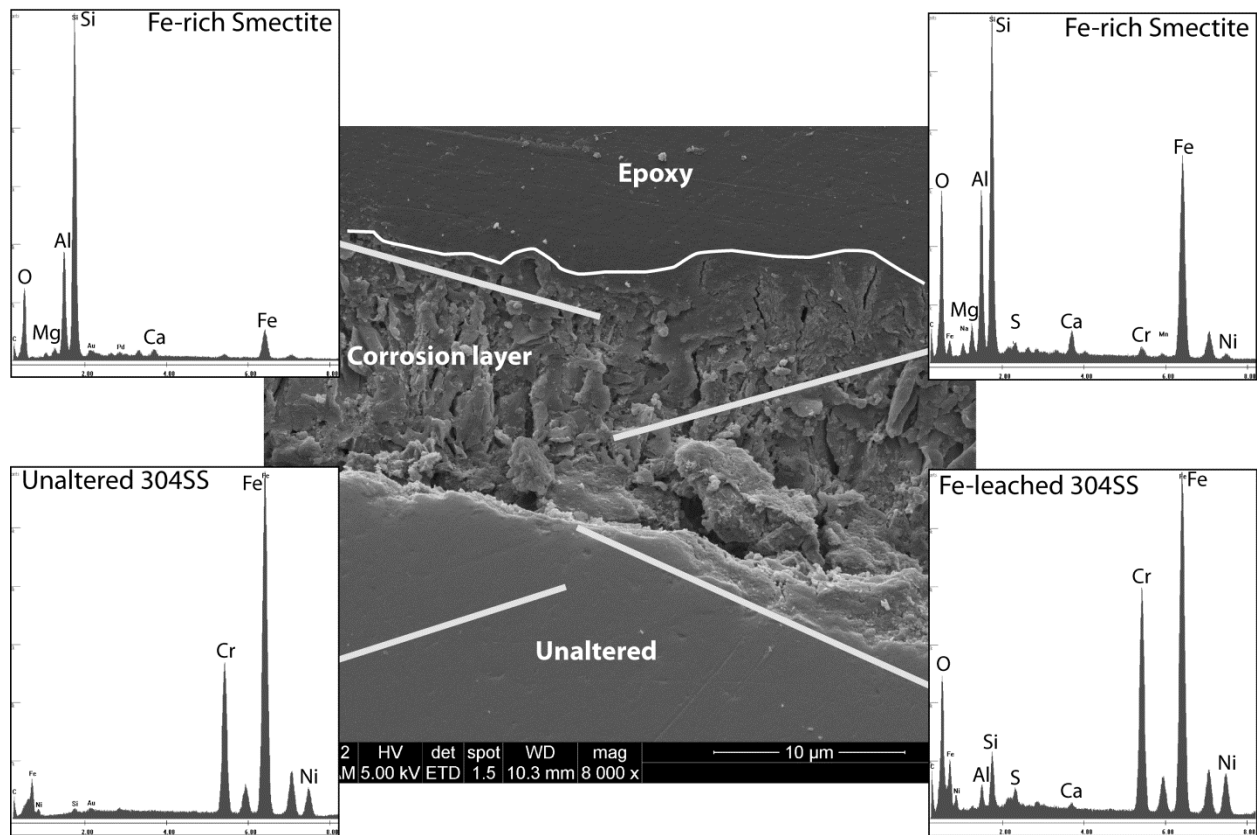


Figure 13. SEM image of 304 SS cross-section showing Fe-saponite interface reaction products using steel surface as a growth substrate. EDX analyses of post-reaction 304SS and interface reaction products indicates Fe is leached from the 304 SS forming a slightly Cr-enriched steel outer layer and an Fe-rich aluminosilicate (Fe-saponite/chlorite) coating. Uniform corrosion of the 304 SS does not appear to develop significant incongruent dissolution.

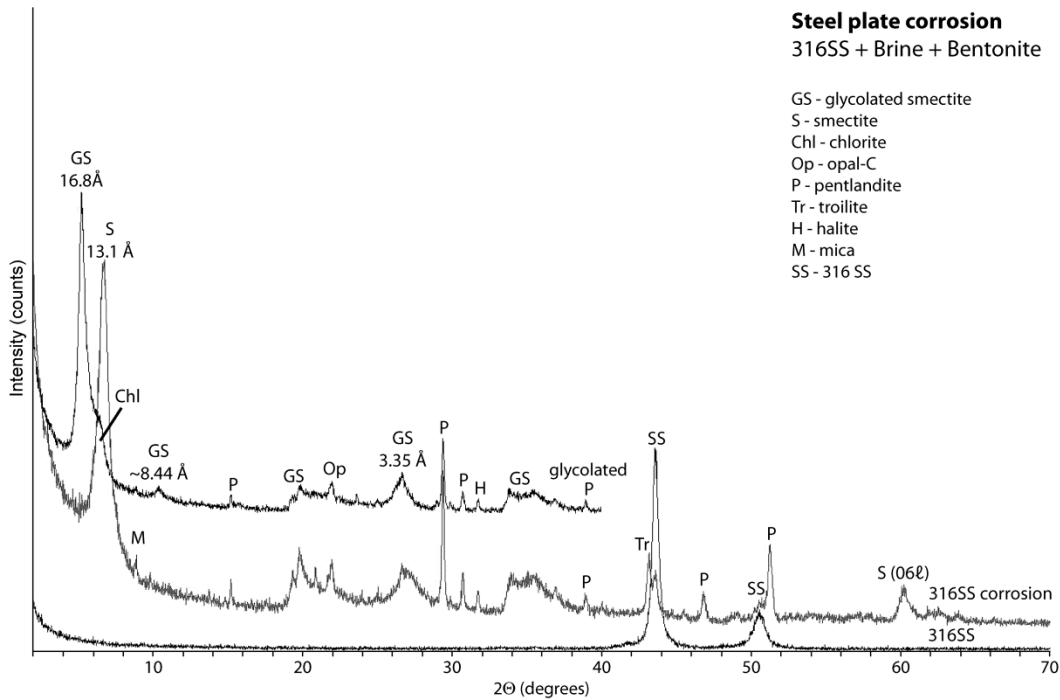


Figure 14. XRD patterns of the air-dried and ethylene glycol saturated interface reaction products on the 316 SS plate used in the EBS-3 experiment. Smectite, chlorite, and a pentlandite-like material are the dominant corrosion phases. Starting 316 SS XRD plot is also shown for comparison.

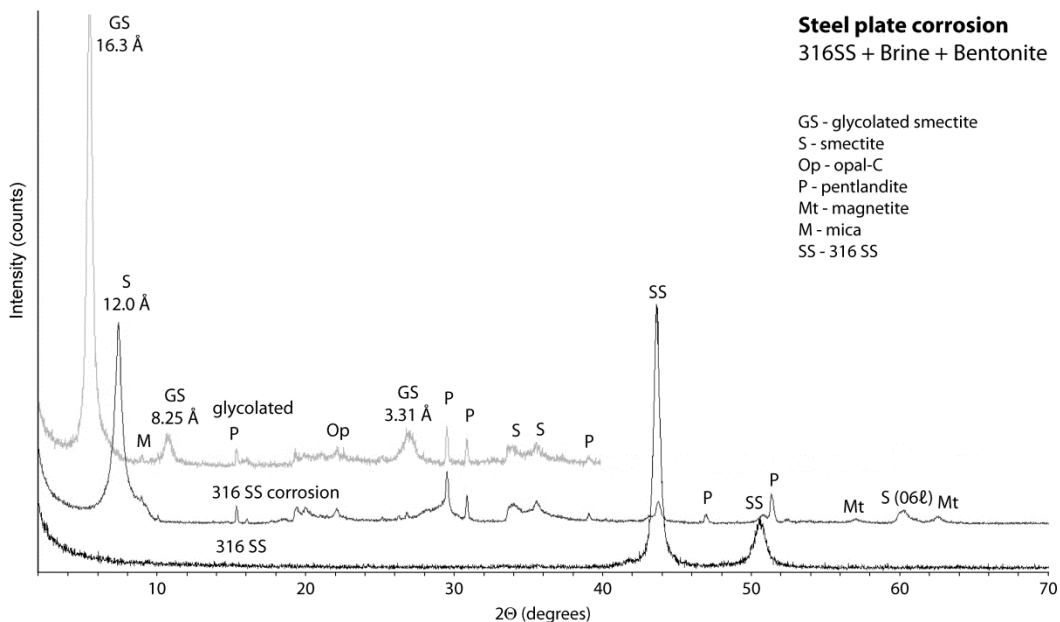


Figure 15. XRD patterns of the air-dried and ethylene glycol saturated interface reaction products on the 316 SS plate used in the EBS-10 experiment. Smectite and a pentlandite-like material are the dominant corrosion phases. Starting 316 SS XRD plot is also shown for comparison.

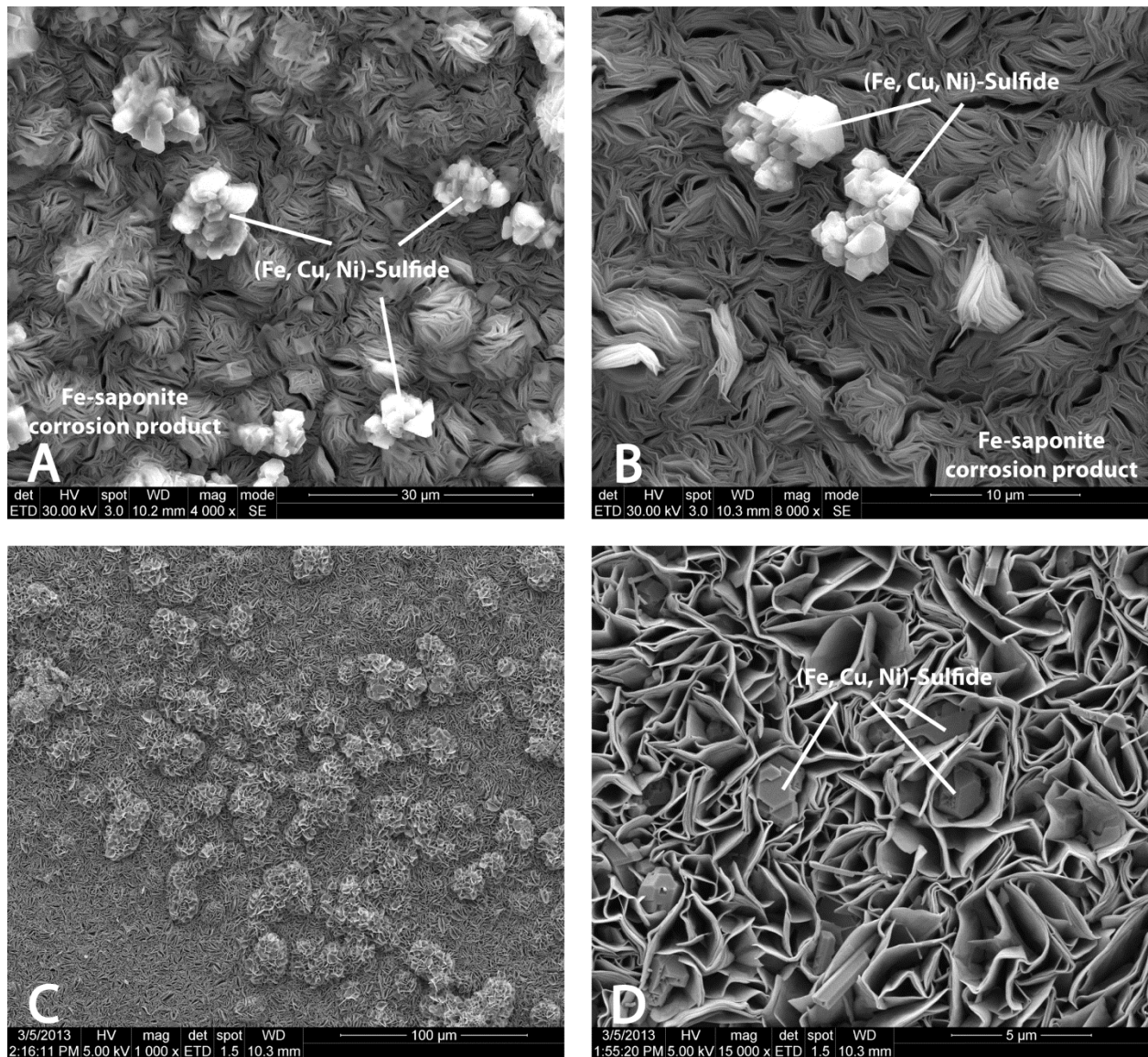


Figure 16. SEM image (plan view) of Fe-saponite using 316 SS as a growth substrate from both ramped (EBS-3) and isothermal, 300 °C (EBS-10) heating profiles. A) Dense growth of Fe-saponite and chlorite with late-stage pentlandite-like ((Fe, Cu, Ni)-sulfide) material from EBS-3. B) Close-up of pentlandite-like ((Fe, Cu, Ni)-sulfide) material on Fe-phyllsilicates from EBS-3. C) Honeycomb and rose-like textures associated with Fe-saponite interface reaction products from EBS-10. D) Fe-saponite rose-like texture with pentlandite-like materials occurring between Fe-saponite foils from EBS-10.

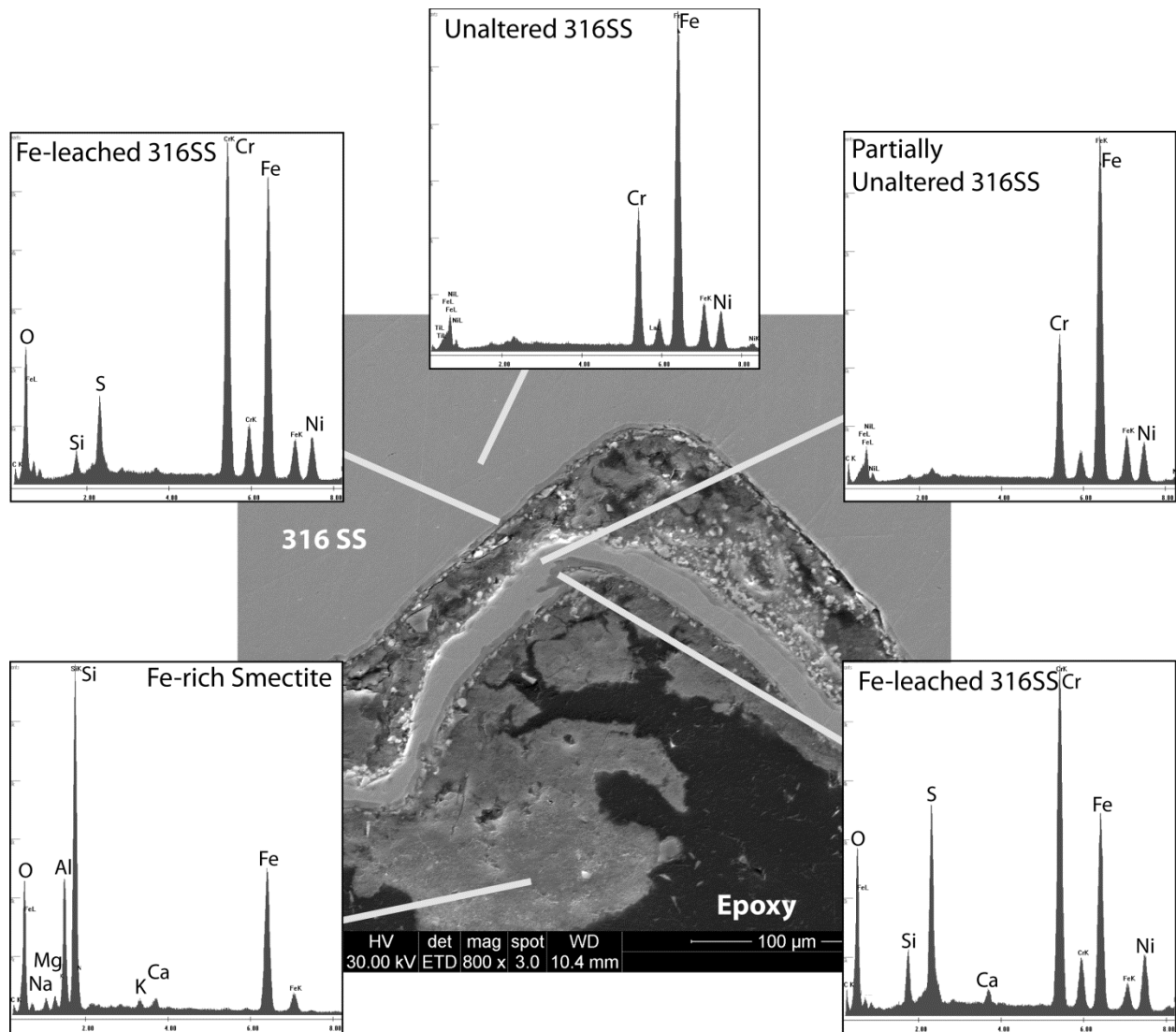


Figure 17. SEM image of 316 SS cross-section showing Fe-saponite/chlorite growth due to exfoliation corrosion from EBS-3. Chemical analyses of post-reaction 316 SS and interface reaction products indicates there was significant Fe leaching from the 316 SS forming a Cr-enriched steel outer layer up to 4 μm thick.

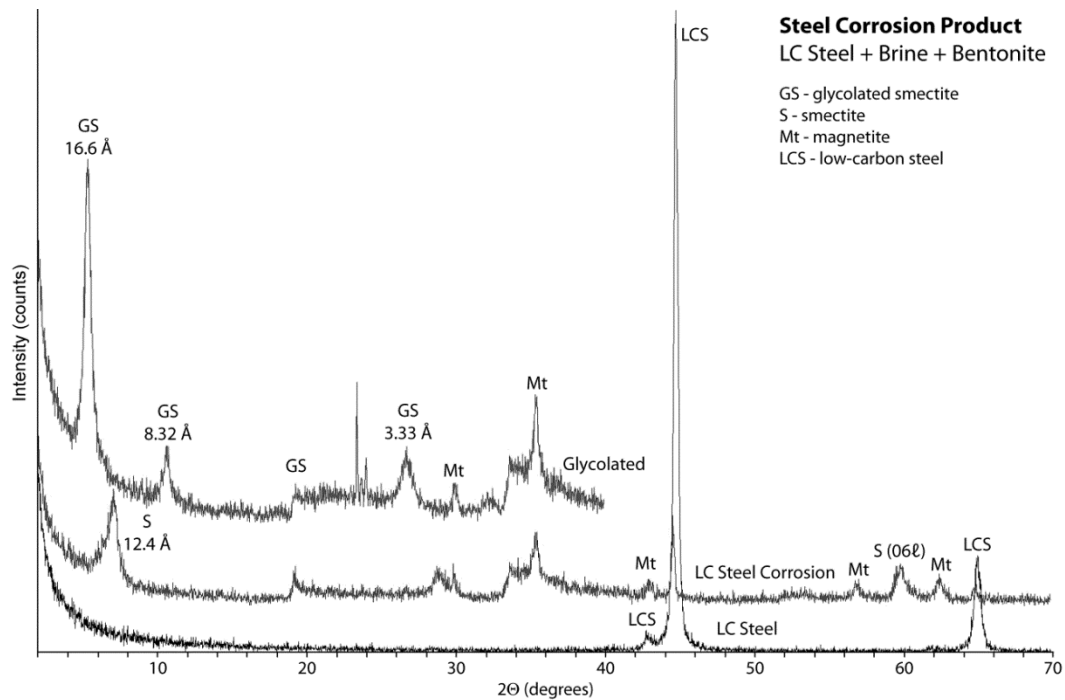


Figure 18. XRD patterns of the air-dried and ethylene glycol saturated interface reaction products on the low-carbon steel plate used in the EBS-6 experiment. Smectite is the dominant interface reaction phase. Magnetite is most likely from the starting magnetite materials used to control redox conditions. Initial low-carbon steel XRD plot is also shown for comparison.

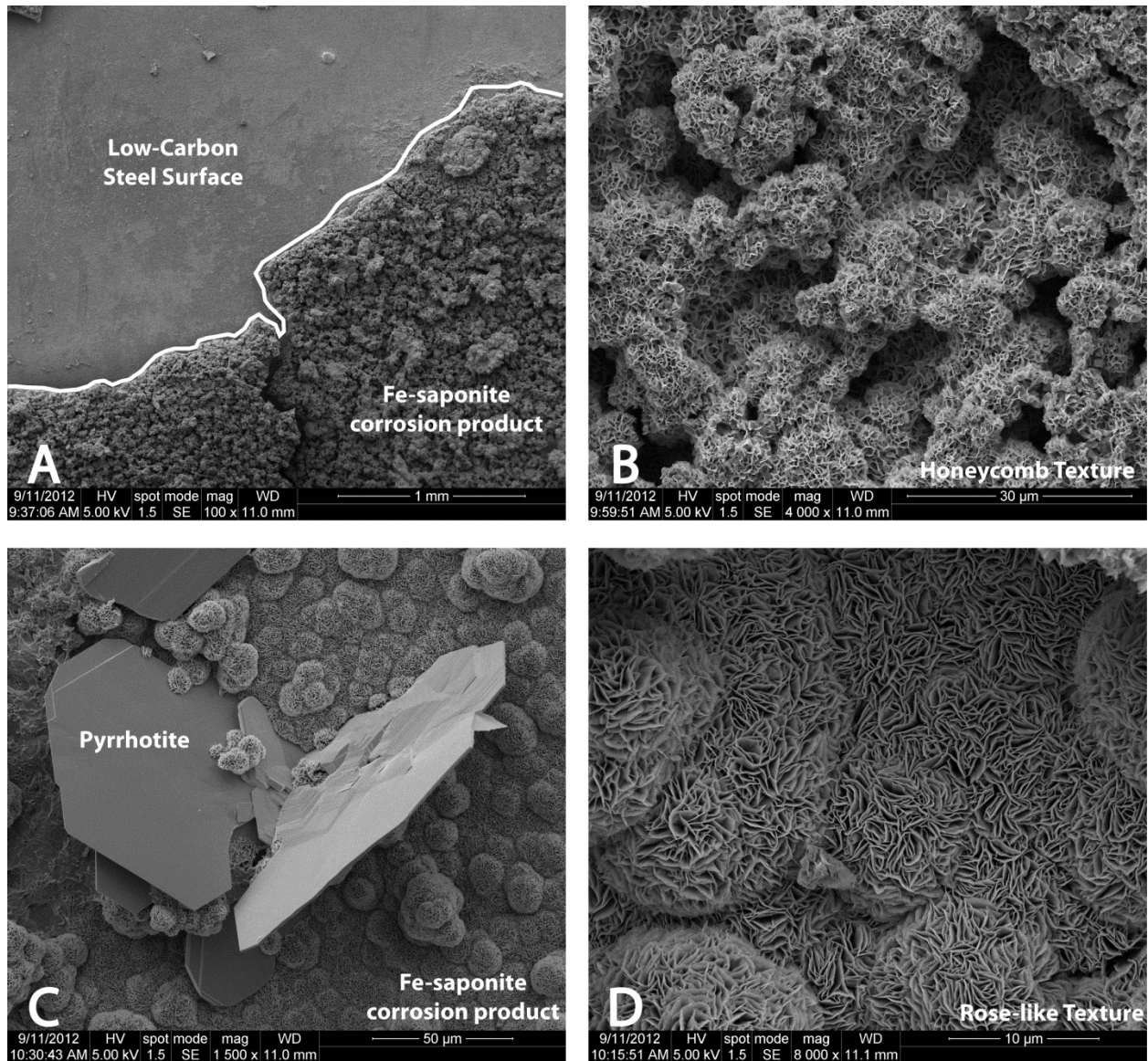


Figure 19. SEM image (plan view) of Fe-saponite growth on low-carbon steel from the ramped (EBS-6) heating experiment. A) Boundary between the Fe-saponite interface reaction product and low-carbon steel surface. B) Honeycombed Fe-saponite. C) Botryoidal Fe-saponite interface reaction product with pyrrhotite platelets from EBS-6. D) Rose-like texture of Fe-saponite.

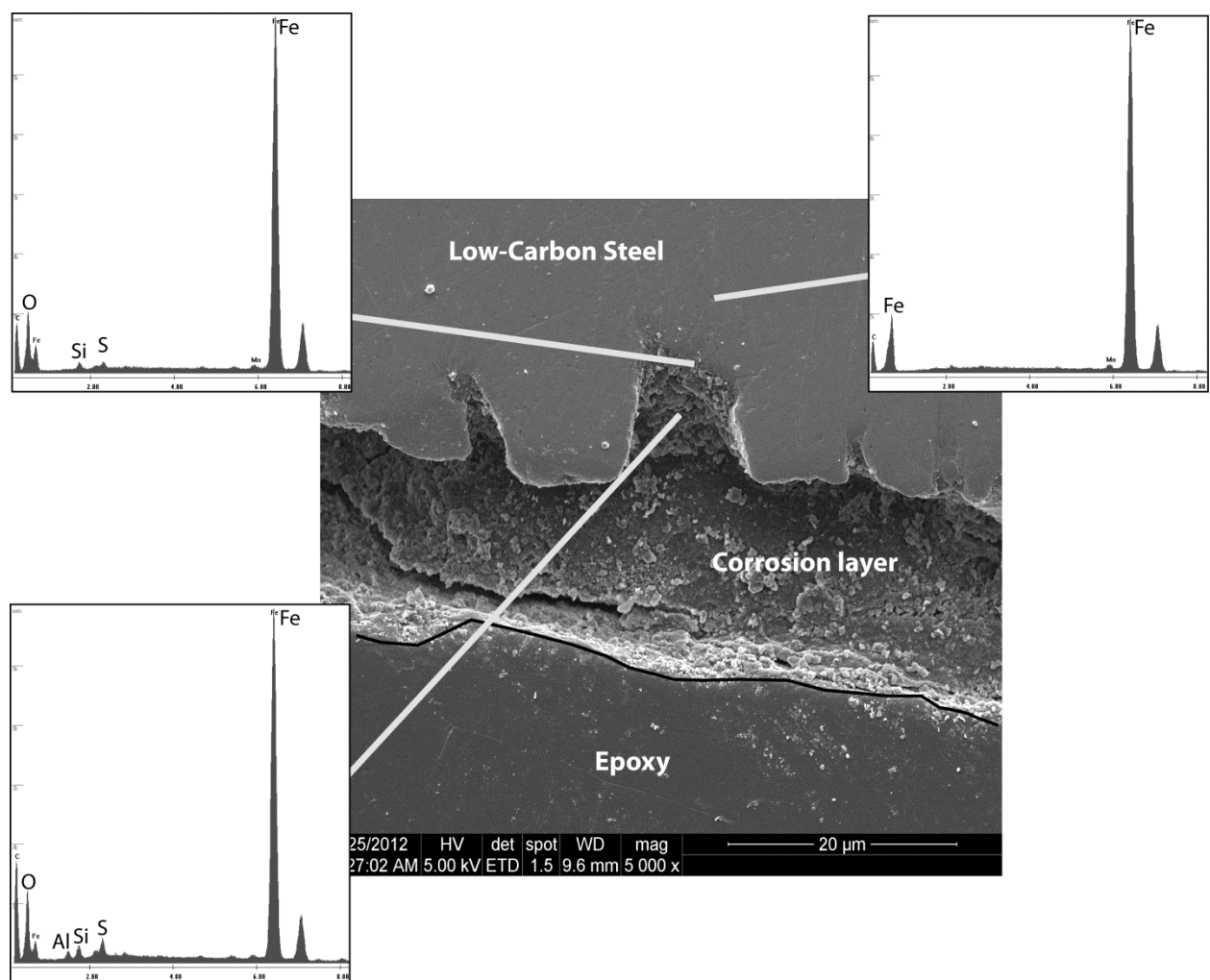


Figure 20. SEM image of low-carbon steel cross-section showing Fe-saponite reaction products using steel surface as a growth substrate. EDX analyses of post-reaction low-carbon steel and interface reaction surfaces show a slight oxidation and sulfidation of the surface (probably due to oxide and sulfide precipitates). EDX composition of the reaction product was not collected due to erosion of Fe-saponite during sample preparation. Extensive pitting corrosion of the low-carbon steel occurs during the ramped experiments (EBS-6).

06l-diffraction bands
sensitive to
b cell dimension

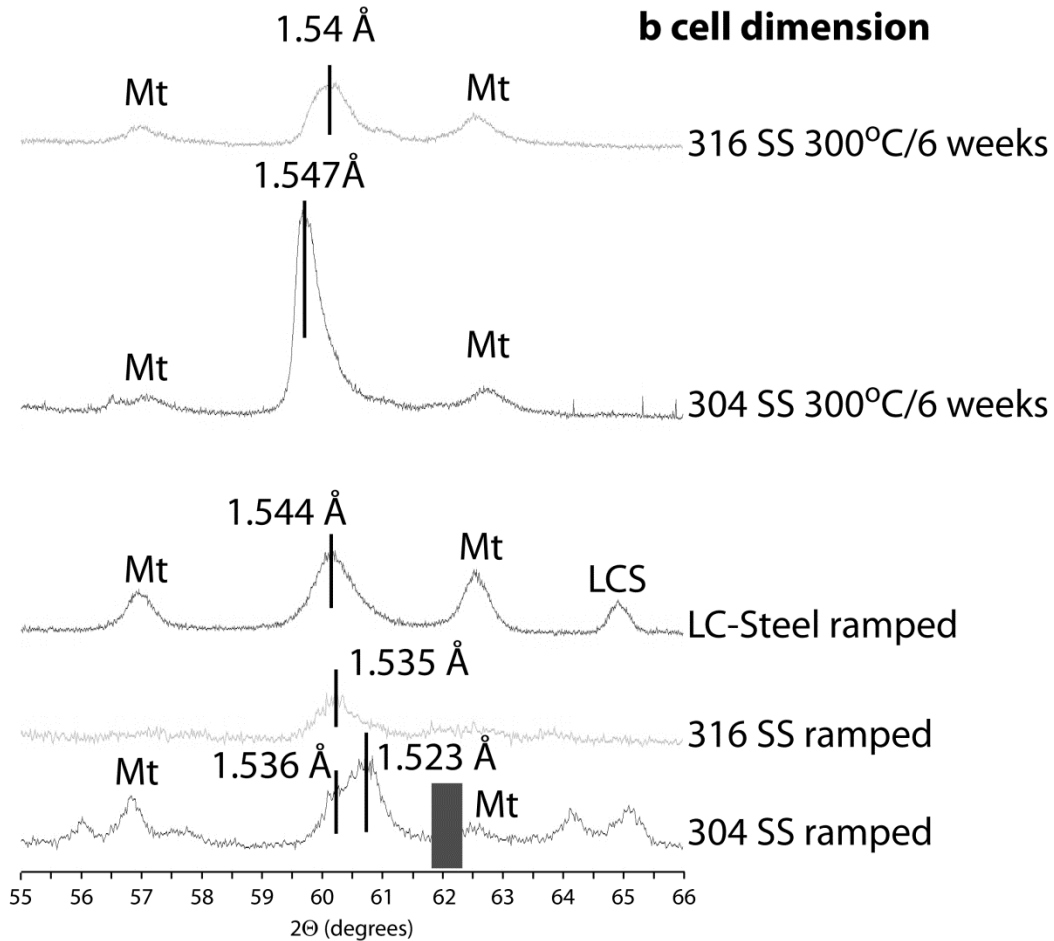


Figure 21. XRD plots of the 06l diffraction bands showing Fe-rich smectite and chlorite formed as a interface reaction product are trioctahedral. Montmorillonite (dioctahedral) typically has a 1.492 – 1.504 Å 06l band (black box). The smectite principally is a Fe-saponite with varying amounts of Ni and Cr substitutions. Contributions from magnetite (Mt) are probably from magnetite used in the initial experimental setup.

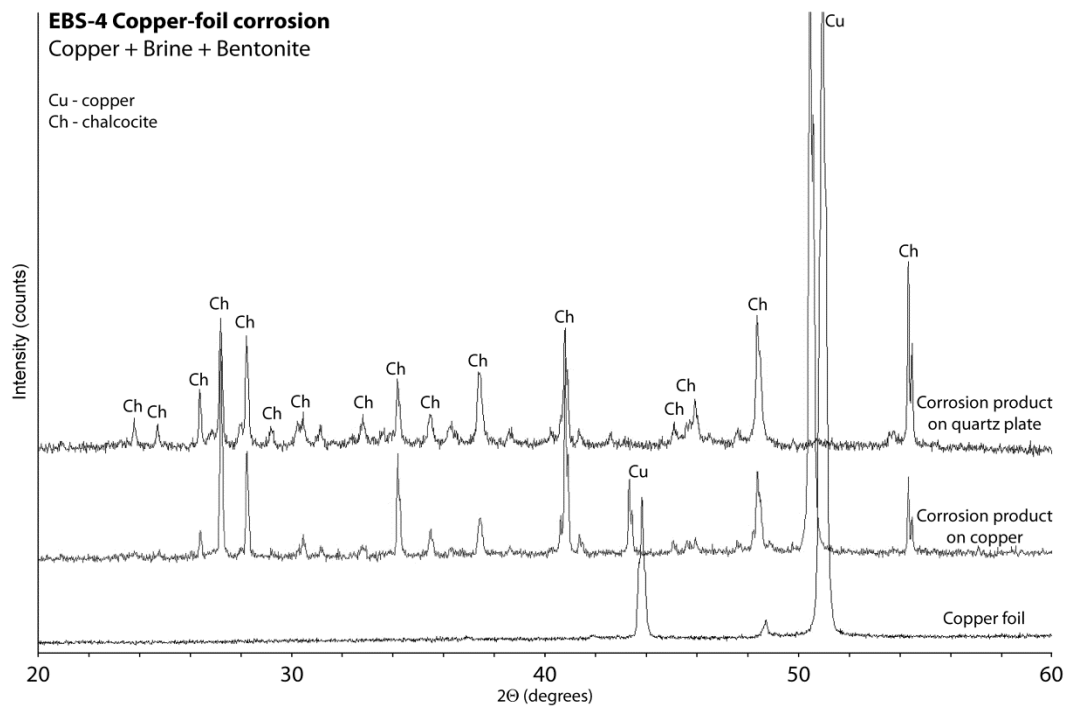


Figure 22. XRD plots for corrosion products on the copper foils used in the ramped heating experiment (EBS-4). Chalcocite (Cu_2S) is the principal corrosion phase.

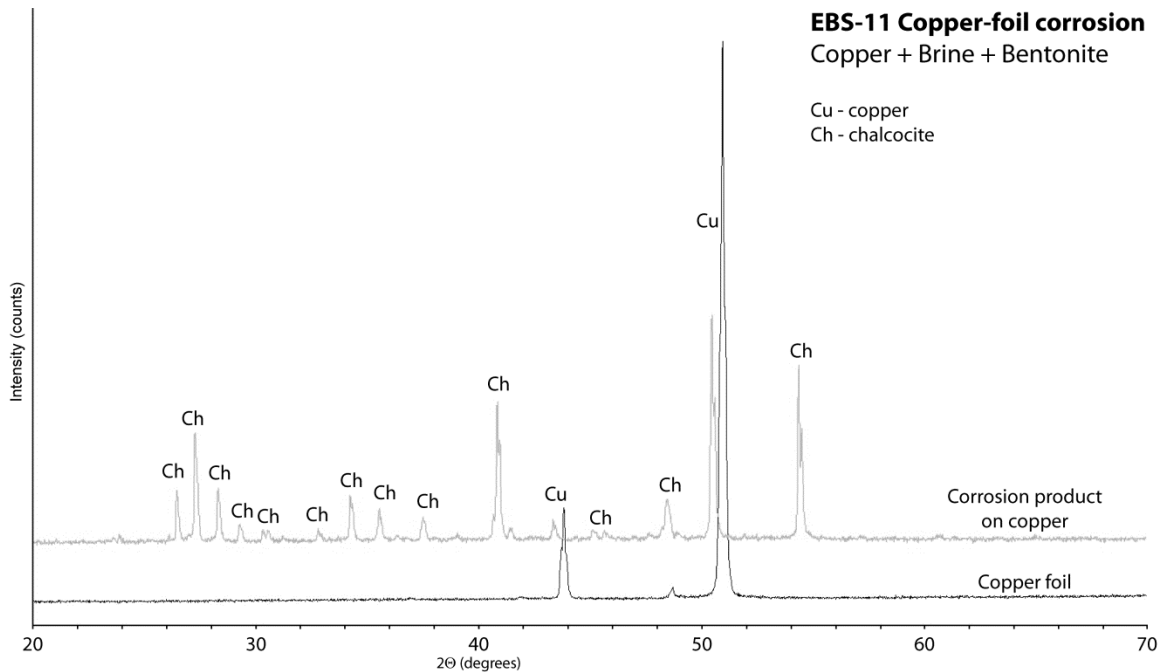


Figure 23. XRD plots for corrosion products on the copper foils used in the six week, 300 °C heating experiment (EBS-11). Chalcocite (Cu_2S) is the principal corrosion phase.

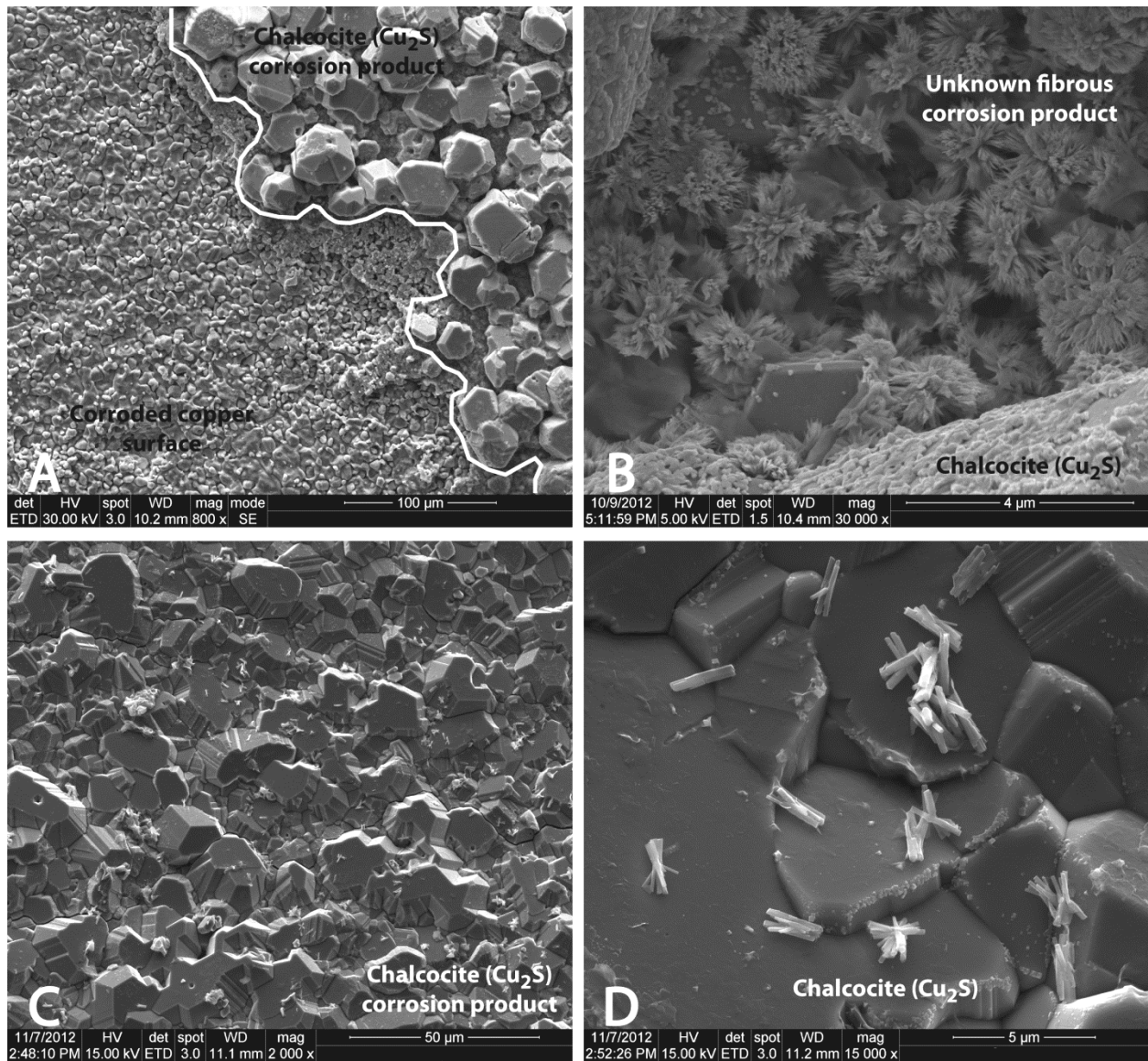


Figure 24. SEM image (plan view) of copper surface showing corroded copper surfaces and various interface reaction products from both ramped (EBS-4) and isothermal, 300 C (EBS-8) heating profiles. A) Boundary between the corroded copper surface and chalcocite (Cu₂S) from EBS-4. B) Unknown fibers occurring on the copper surface in between chalcocite growths from EBS-4. These fibers might be a late-stage oxide or chloride corrosion product upon depletion of sulfide. C) Intergrown chalcocite from EBS-8. D) Close-up of the chalcocite surface in panel C showing unknown short rods with a radiating texture.

4. Discussion

Geochemical modeling

The collection of aqueous samples composition during the experiments allows examination of the effects aqueous composition evolution has on the mineralogical alteration. Both, $a\text{Na}^+/\text{aH}^+$ and $a\text{K}^+/\text{aH}^+$ values at 120 °C tend to be scattered, but converge to a single solution composition as the reaction progresses to 300 °C (Figures 25 and 26). The $\text{SiO}_{2(\text{aq})}$ composition becomes saturated with respect to cristobalite beginning around 210 °C, but it appears montmorillonite and zeolite dissolution/alteration is controlling the silica activity.

The $a\text{Na}^+/\text{aH}^+$ and silica activities appear to be suitable for the clinoptilolite alteration and high-silicon analcime crystallization during the early reaction stages (Figure 25). However, this analcime formation was not observed until the long-term, 300 °C experiments, suggesting the delayed analcime formation appears to be a kinetic issue. Experimental work (Wilkin and Barnes 1998; Wilkin and Barnes 2000) indicates that analcime formation is significantly retarded at circum-neutral pH's and increased pressures.

The $a\text{K}^+/\text{aH}^+$ and silica activities early in the reaction plot within the K-clinoptilolite stability field, but the solution evolution shift the aqueous data into the illite ($\text{K}_{0.85}\text{Al}_2(\text{Si}_{3.15}\text{Al}_{0.85})\text{O}_{10}(\text{OH})_2$) stability field (Figure 25). Much like the analcime formation, the solution chemistry imparts controls on the illitization rates. High sodium and silica activities along with limited aluminum availability probably retarded illite formation via a illite-smectite transition state. However, direct precipitation of fibrous illite appears to have occurred which is further supported by Figure 26.

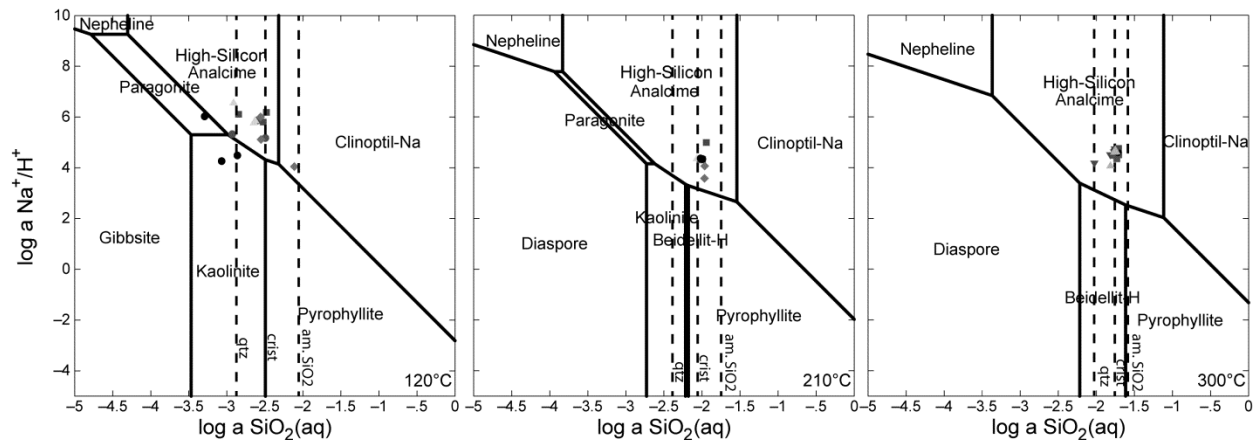


Figure 25. Log $a\text{Na}^+/\text{aH}^+$ and Log $a\text{SiO}_{2(\text{aq})}$ data from the a) 120 °C solution chemistries, b) 210 °C solution chemistries, and c) 300 °C solution chemistries plotted on a Na-H₂O-SiO₂ phase diagram. Analcime thermodynamic data has been adjusted to a high-silicon analcime ($\text{Na}_{0.75}\text{Al}_{0.75}\text{Si}_{2.25}\text{O}_6 \cdot 1.13\text{H}_2\text{O}$) after Neuoff et al. (2004).

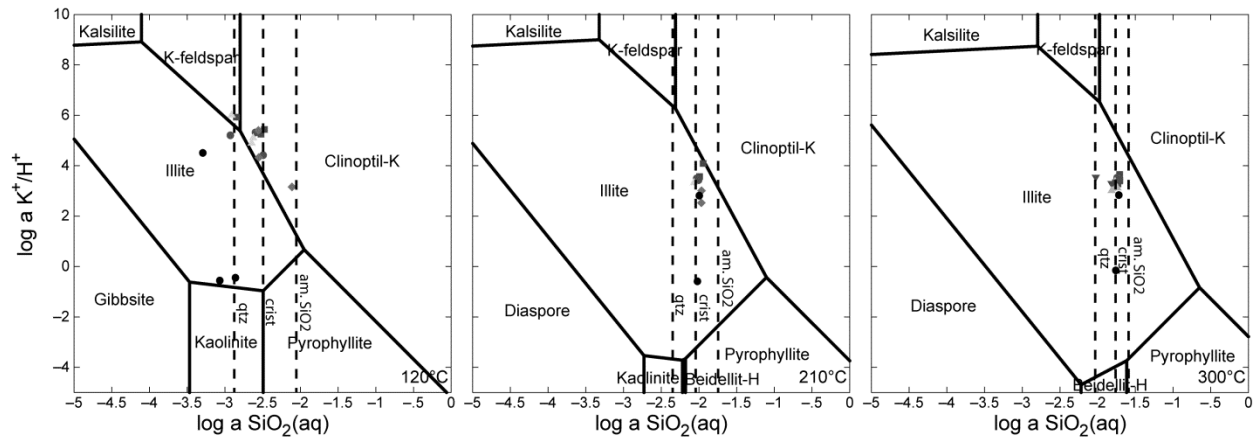
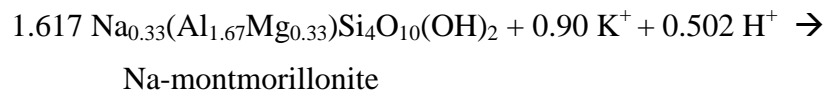


Figure 26. Log aK^+/aH^+ and Log $aSiO_2(aq)$ data from the a) 120 °C solution chemistries, b) 210 °C solution chemistries, and c) 300 °C solution chemistries plotted on a K-H₂O-SiO₂ phase diagram.

Absence of Smectite Illitization

There was no evidence of illite-smectite mixed-layering from any of the experiments conducted in this investigation. Many reports (Perry and Hower 1970; Reynolds and Hower 1970; Hower et al. 1976; Altaner 1989; Mosser-Ruck et al. 2001) indicate that smectite illitization occurs during diagenesis under elevated temperatures with a reactive K⁺ source via the following reaction scheme (assuming aluminum conservation)



This general reaction is believed to go through a sequence starting with a K-montmorillonite phase followed by various stages of illite-smectite mixed-layering leading into a discrete illite phase (Moore and Reynold 1997). It is evident that early in the experiments K⁺ is exchanged into the montmorillonite interlayer generating a Na-rich solution. Changes in solution chemistry and mineralogical data indicate that 11 to 20 % of the exchangeable cations in the initial montmorillonite were replaced with K⁺. Montmorillonite and clinoptilolite at this stage in the reaction appear to be buffering synthetic groundwater to high Na⁺ and low K⁺ activities. Maintaining relatively high Na⁺ activity with a limited supply of K⁺ has been shown in experimental data (Eberl and Hower 1977; Eberl et al. 1978; Roberson and Lahann 1981; Mosser-Ruck et al. 1999) to significantly retard smectite illitization rates. The cation exchange reactions associated with montmorillonite and clinoptilolite appear to be facilitating illitization retardation.

However, experimental results from Whitney and Velde (1993) and Mosser-Ruck et al. (1999) show K-saturated Wyoming montmorillonite in a Na-rich solution can still produce an I/S with about 29 to 40 % non-expandable (illitic) component under the same time and temperature

parameter of the current investigation. These results indicate that even in a Na-rich system, illitization still can occur provided there is a sufficient K^+ supply available in the system (i.e., K-bearing minerals). An example of this process has been argued that the observed smectite illitization in the Gulf Coast sediment is tied directly to the availability of K^+ from the dissolution of K-feldspars (Hower et al. 1976). Bulk K_2O content in Gulf Coast sediments tend to range from 2.27 to 3.68 wt. % with K_2O concentrations increasing (1.98 to 5.65 wt. %) in the $< 0.1 \mu m$ size fraction (Hower et al. 1976). However, there is much less K_2O associated with the bentonite (0.572 wt.%) used in this investigation with even less K_2O (0.174 wt.%) in the $< 2 \mu m$ fraction. It is uncertain if this is enough K_2O to overcome the Na-rich system. If there is an external source of K^+ (e.g., host rock or groundwater) then illitization possibly could proceed.

There have been no satisfactory explanations as to why K^+ is necessary for illitization reactions to proceed, considering illitic materials are defined by the layer charge, in which the interlayer cations have no direct control over the layer charge (Moore and Reynolds 1997). Illitic materials have an increased layer charge ($z \sim 0.6 - 0.9$) compared to montmorillonite ($z \sim 0.2 - 0.6$) due to higher amounts of Al-substitution into the tetrahedral sheet (Moore and Reynolds 1997). In fact, there have been numerous reported occurrences (Bannister 1943; Frey 1969; Środoń 1999) of Na-illite (i.e., brammalite) and ordered Na-I/S (~ 0.80 illite) in nature. This leads to the question as to why the presence of Na^+ , Ca^{2+} , Mg^{2+} significantly retards the illitization rates, whereas K^+ facilitates illitization. However, experimental data does indicate Na-illite and Na-I/S start reacting at much higher temperatures than those at which K^+ equivalents react (Eberl and Hower 1977; Eberl 1978). In light of this evidence, illitization is probably not directly related to K^+ , Na^+ , Ca^{2+} , or Mg^{2+} concentrations, but these elements likely have an indirect influence by changing the minerals' phase equilibria.

Solutions saturated with respect to cristobalite probably contributed to the illitization retardation. The silica activity in these experiments is controlled by silicate mineral dissolution and alteration. Systems with high silica activity should have a significant influence on illitization rates because illite formation is sensitive to Al^{3+} and Si^{4+} concentrations. But, it is important to consider the difference between closed systems such as these experiments versus repositories environments that are open to the surrounding environment. Many processes that are described above might be mitigated in an open system where solutes can move in and out of the environment.

Authigenic Illite

Even though there is an absence of illite-smectite mixed layering there is direct evidence that fibrous illite directly crystallized from solution. The formation controls of fibrous illite are not well understood, but has been suggested that high silica activities, slightly alkaline to mildly acidic solution, and rapid crystallization facilitates the formation of a fibrous morphology (Small et al. 1992). Additionally, it has been suggested that fibrous illite is partially due to organic sorption on the (010) faces poisoning growth along [010] direction and forcing crystallization in the [100], $[\bar{1}10]$, and $[\bar{1}\bar{1}0]$ directions (Small et al. 1992; Small 1993; Güven 2001). However, these fibrous illites are metastable in the illite growth phase and will eventually ripen into a more stable platy morphology (Small et al. 1992).

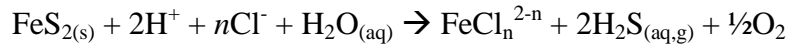
Clinoptilolite-to-analcime transformation

We have shown that at higher silica activities (i.e., cristobalite saturation) clinoptilolite is altered to a high-silica analcime (Si/Al ~2.89) under experimental repository conditions. This zeolite alteration reaction has not been observed within a bentonite under repository-type experiments. Previous studies (Smyth 1982; Kerrisk 1983; Duffy 1984; Bish and Aronson 1993; Chipera and Bish 1997; Wilkin and Barnes 1998; 2000; Bish et al. 2003; Cheshire et al. 2013) have linked changes in Na^+ , Al^{3+} , and Si^{4+} activities with the replacement of clinoptilolite with analcime. Increased Na^+ activity under elevated temperatures ($T > 84^\circ\text{C}$) has been suggested to promote alteration of clinoptilolite to analcime (Smyth 1982). Alternatively, it has been argued (Kerrisk 1983; Duffy 1984; Bish and Aronson 1993) that when silica activity is saturated with respect to quartz, clinoptilolite is destabilized compared to analcime. They (Kerrisk 1983; Duffy 1984; Bish and Aronson 1993) also suggested that when silica activity is cristobalite or opal saturated, clinoptilolite is the more stable phase and analcime will not crystallize. However, experimental work from Wilkin and Barnes (1998) indicate silica activity influences clinoptilolite alteration by affecting the reaction affinity rather than controlling the reaction equilibrium. Wilkin and Barnes (1998) show that analcime can form in an environment saturated with respect to cristobalite provided there is a sufficient change in the Na^+ and/or Al^{3+} activities. Natural paragenetic sequences suggest that clinoptilolite to analcime may progress at temperatures as low as $75 - 90^\circ\text{C}$ (Smyth 1982; Masuda et al. 1996), the current study produced analcime formation only during the long-term, 300°C experiments. Reaction kinetics in nuclear repository conditions is an important variable that needs to be further considered. Analcime might form in the low-temperature experiments with longer reaction times. Evolution of zeolites associated with bentonite has been suggested (Masuda et al. 1996) to be a major factor in the stability of smectite through the control of pore-water chemistry. Solubility and kinetic studies on clinoptilolite and analcime show that at higher pH's (9 - 10) solutions saturated with respect to analcime rapidly precipitate analcime with rates varying from $0.067\ \mu\text{m/h}$ (138 bar) to $0.016\ \mu\text{m/h}$ (345 bar) at 175°C . (Wilkin and Barnes 2000) However, analcime growth rates were significantly retarded at circum-neutral pH's, to the point no analcime was observed during experiments lasting up to 26 days with temperatures $> 100^\circ\text{C}$. (Wilkin and Barnes 1998) Analcime retardation at circum-neutral pH's could explain the lack of analcime formation in the ramped experiments, which were only at 300°C for 1 week and consistently obtained pH values of 6 - 7.

Silica is released during clinoptilolite alteration, thereby contributing to authigenic silica mineral formation (e.g., cristobalite, opal-C, quartz). There is a ~ 17 % volume (assuming quartz formation) decrease associated with analcime crystallization. Given that there is a ~ 13 wt. % clinoptilolite in the bentonite, a clinoptilolite-to-analcime volume loss will translate into ~ 2% volume loss in the bulk bentonite. It is uncertain how much volume loss will be recovered in response to the montmorillonite swelling due to the water loss in the zeolite alteration reaction. Additionally, analcime and feldspar formation sequesters aqueous Al^{3+} , thereby potentially limiting illitization. Aluminum availability, in addition to silica, alkali, and alkaline earth activities, probably is a crucial step for the long-term stability of bentonite-based engineered barriers.

Sulfide destabilization

Production of $\text{H}_2\text{S}_{(\text{aq,g})}$ is most likely related to pyrite solubility in a chloride-bearing solution (Crerar et al. 1978; Ohmoto et al. 1994).



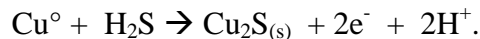
The highly reducing nature of the experimental system easily preserves the $\text{H}_2\text{S}_{(\text{aq,g})}$ species. Sulfide-induced corrosion of the waste canisters is the primary concern in repository systems (Börjesson et al. 2010). The Swedish Nuclear Fuel and Waste Management Company (SKB) have emplaced fairly strict sulfur specifications (sulfide content < 0.5 wt.%; total sulfur < 1 wt.%) for the bentonite buffer used in their repositories (Börjesson et al. 2010).

Metal-bentonite reaction interface

Results from these experiments have shown the more dynamic environment associated with this system is at the bentonite-metal interface. Fe-rich phyllosilicates (i.e., trioctahedral, Fe-rich saponite and chlorite) are crystallized on steel surfaces forming a reactive substrate with a high surface area compared to the original steel surfaces. Alternatively, chalcocite (Cu_2S) crystallized on the copper surfaces due to available H_2S from the decomposition of pyrite in the hydrothermal environment. It is evident that the formation of these surface bound minerals is from the direct crystallization from solution in the localized environments surrounding the metal plates. However, it is not yet well documented to what extent these authigenic minerals will have an effect on the repository system.

Synthetic Fe-saponites have been crystallized in dilute solutions and gels of silica, Fe-, Al-chlorides at temperatures up to 850 °C and pHs of 8.5 – 9.5 (Kloprogge et al. 1999). This is consistent with a partial dissolution of the steel plates contributing ferrous iron into a fluid phase with silica and aluminum, thereby facilitating Fe-saponite (smectite) crystallization with the steel surfaces acting as a growth substrate. Further, Fe-saponite alteration into chlorite has been suggested (Mosser-Ruck et al., 2010) in the presence of ferrous iron at temperatures approaching 300 °C and near-neutral pHs. The lack of chlorite consistency in our experiments is unexplained, but could be related to the ferrous iron availability.

Copper corrosion in a sulfide-bearing, compacted bentonite environment has been suggested to be a function of both sulfate reducing bacteria growth conditions (e.g., available carbon, sulfate concentrations, and electron donors) and geochemical parameters effecting sulfide diffusion (e.g., bentonite density, fluid content, and ferrous iron concentrations) to the copper surfaces (Pederson 2010). The overall reaction associated with sulfide-induced copper corrosion is



Under the anoxic and high temperature repository conditions, chloride and sulfide corrosion will be the primary (non-radiolytic) mechanism affecting waste canisters. Biotic sulfate reduction probably will be minimal at high-temperature conditions therefore, the dominant sulfide source is likely from sulfide minerals associated with the original bentonite. Mitigating sulfide-induced corrosion might be achieved by maintaining a high bentonite density thereby restricting sulfide diffusion (Pederson 2010).

One of the big unknowns regarding the steel and copper surface alteration is whether surface passivation is occurring. This could be an important factor to consider in the long-term modeling

of the repository system. There was no substantial change in the mineral thicknesses or surface coverage on both steel and copper between the ramped and isothermal, 300 °C experiments. This lack of mineral growth can be a clue in the possible steel or copper passivation, but can also be explained by depletion in the corrosive elements. In the case of copper, as sulfide is depleted from the system, chloride (in an anoxic environment) is the primary corrosive agent, subsequently altering the corrosion rate (King et al. 1992; Carlsson 2008). The fact that the reactant surface thicknesses do not change with temperature or run durations is critical. This has promising implications and needs to be investigated with further experiments. A long term experiment (ramp up – hold at 300 °C - ramp down) would be critical to understanding both passivation potential and general post heat pulse reactions.

Fe-phyllsilicates tend to have strong sorption properties towards actinides and other radioactive materials, therefore, they have the potential to provide added barrier properties for actinide containment. The dynamics and reactivity of actinide adsorption need to be incorporated into the long term repository performance evaluation models. However, this work has never been addressed in repository studies. Inclusion of a reactive, high surface-area canister into used-fuel repositories performance assessments should help provide a viable repository evaluation.

International EBS research

Experiments for international EBS research included two mixed buffer reactions and a heated bentonite sample at 20 wt. % free moisture intended for cooperative research with LBNL. The mixed buffer experiments (bentonite-graphite, bentonite-quartz sand) using the same water chemistry and ratios as the experiments detailed above were conducted to investigate potential mineralogic/petrologic changes to mixed buffer systems (Jobmann and Buntebarth, 2009) of interest to the German nuclear repository program. The cooperative study with LBNL involved heating Colony, Wyoming bentonite to 300 °C with 20 wt. % free moisture. The reaction products would be geologically characterized by LANL while thermal mechanical properties would be conducted by LBNL.

Mixed buffer experiments

Jobmann and Buntebarth (2009) conducted studies of bentonite – graphite and bentonite – quartz sand to determine if the clay buffer heat conduction could be enhanced to values similar to the host rock. The authors used bentonite, quartz sand, and a variety of graphites in their experimental runs. Temperatures spanned from 35 to 150 °C and a uniaxial 2MPa pressure was applied. Jobmann and Buntebarth (2009) determined that the necessary conductivity could not be obtained with quartz, but that the addition of 15 wt% graphite was able to achieve heat conductivity values ($2.5 \text{ W m}^{-1}\text{K}^{-1}$) in the mixed buffer similar to that of Opalinus Clay. Our ramped heating experiments (Table 2) for bentonite – graphite (EBS-7, 20 wt. % pre experiment, 12 wt. % post experiment graphite) and bentonite – quartz (EBS-9, 20 wt.% pre experiment 15 wt. % post experiment quartz) were developed to examine mineralogic/petrologic parameters coincident to the experiments of Jobmann and Buntebarth (2009). The only significant change in our post experiment reaction products, other than a reduction in carbon and quartz sand, was a decrease in the amount of clinoptilolite. However, as with the other ramped experiments, there was no attendant development of analcime. Further petrographic examinations will be performed on these product run materials.

High-temperature, 20 wt. % free moisture bentonite

A cooperative research activity initiated between LBNL and one of our authors (FAC) resulted in a plan to investigate Colony bentonite under “dry” peak heat repository conditions. As noted above, the bentonite with 20 wt. % free moisture (Stripa brine composition), was subjected to 300 °C for 7 weeks. The experiment (EBS-12) was concluded on May 30, 2013. Our laboratory will conduct mineralogic/petrologic characterization of the run products, while LBNL will perform thermo-mechanical studies on the same materials. The combined results will be utilized by the DECALOVEX modeling team. As seen in Table 2 the bentonite in EBS-12 reacts in a similar manner to all the other experiments conducted for 6 weeks at 300 °C. That is, clinoptilolite reacts to analcime, and no illitization was observed. The only mineralogic change from the other long term 300 °C experiments is an increase in cristobalite/ opal-C (10 wt. %). Further characterization and thermodynamic modeling should help explain this change in reactant products.

5. Potential EBS mineralogic/petrologic effects on geological repository - Conclusions

There have been a large number of investigations on bentonite stability under various repository conditions (Madsen 1998; Meunier et al. 1998; Pusch and Kasbohm 2002; Guillaume et al. 2003; Guillaume et al. 2004; Wilson et al. 2006; Marty et al. 2010; Mosser-Ruck et al. 2010; Ferrage et al. 2011). Yet, there remain questions regarding bentonite’s overall stability and more importantly whether montmorillonite will remain relatively unaltered through the repository life-time. After initial used-fuel emplacement there will be a pulse of heat flowing into the bentonite buffer producing an environment in which montmorillonite do not typically occur. However, many believe that the initial heat pulse will start to decay after about 100 to 1,000 years (Wersin et al. 2007). The repository is expected to remain dry during the initial 100 to 1,000 years and therefore illitization should be kept to a minimum as there is a limited supply of Al^{3+} and K^{+} available for interaction (Wersin et al. 2007). The buffering capacity of montmorillonite should maintain a Na-rich system even if a wet environment should occur, thereby inhibiting illitization. Additionally, the very low hydraulic conductivity ($\sim 3 \times 10^{-13}$ m/s) of the bentonite should help inhibit the redistribution or influx of Al^{3+} and K^{+} further retarding illitization (Pusch and Kasbohm 2002; Wersin et al. 2007).

Most often repository investigations focus on the MX-80 bentonite from Wyoming. The slightly different bentonite used in this investigation contains ~12 wt. % clinoptilolite, while MX-80 has ~2 wt. % calcite and no clinoptilolite. It is expected mineralogical variation will play a key role in the bentonite stability. For example, the presence of clinoptilolite develops reactions that have not been documented in bentonite buffer systems (Cheshire et al. 2013). Natural paragenetic sequences indicate that clinoptilolite to analcime may progress at temperatures as low as 90 – 100 °C (Smyth 1982). However, analcime formation does not occur until the long-term, 300 °C conditions indicating reaction kinetics are essential in the repository validation.

The Swedish Nuclear Fuel and Waste Management Company (SKB) have emplaced fairly strict sulfur specifications (sulfide content < 0.5 wt. %; total sulfur < 1 wt. %) for the bentonite buffer used in their repositories (Börjesson et al. 2010). Results from these experiments have shown that sulfide release from pyrite deposition will interact with waste canisters in various manners depending on the canister composition.

There have been a number of similar investigations on bentonite stability under various repository conditions and in contact with various metals replicating possible canister compositions (Guillaume et al. 2003; Guillaume et al. 2004; Wilson et al. 2006; Mosser-Ruck et al. 2010; Ferrage et al. 2011). These investigations tend to focus on the Fe-bearing phases (i.e., Fe-saponite, vermiculite, chlorite, and 7Å phases (odinite, berthierine, cronstedtite)) forming during their experiments. Newly formed Fe-rich phyllosilicates in the current investigation are primarily associated with the steel plate-bentonite interface and magnetite particles. Away from these Fe-rich zones there was little to no clay alteration. These observations agree well with the model results from Marty et al. (2010), in which the Fe-rich phases are associated with bentonite/steel interface. Bentonite not in contact with the steel waste container does not show the formation of these Fe-rich phyllosilicates. The occurrence of Fe-rich phyllosilicates most likely will not form in the bentonite away from the waste container because there is a low abundance of iron in the system.

Thermodynamic modeling (Marty et al., 2010) of MX-80 under repository conditions indicates the bentonite barrier system will develop three discrete alteration zones post-closure: 1) zone of mass transport of groundwater through bentonite, 2) middle zone where bentonite stays fairly unreacted, and 3) and inner zone where waste container has a strong influence on the bentonite alteration. Results from this experimental series would suggest that our experimental design corresponds to the outer zone in contact with groundwater and the inner zone influenced by the waste canister. The initial mineralogical composition and closed system of our reaction setup however changes the environment compared to modeled systems by Marty et al. (2010).

These experimental results demonstrate that understanding the mineralogical composition of bentonite barrier materials and the possible alteration pathways is essential in designing a high-level radioactive waste repository. The combination of a Na-rich environment, limited K⁺ supply, and precipitation of Al-bearing minerals (analcime and feldspars) appear to have inhibited the formation of illite-smectite mixed-layers. This is important considering many researchers have argued that illite formation is detrimental to the long-term stability of a used fuel repository. Even though mineral reactions do take place, there are added properties that potentially will compensate for the alteration of clinoptilolite to analcime (e.g., swelling of smectite due to water absorption and a potential of sealing cracks via silica precipitation). Further work needs to be done to better understand the kinetics of analcime formation in a bentonite barrier system and what impact these reactions have on the barrier's mechanical and physical properties.

6. FY14 Experimental program

Research objectives for the upcoming year will be a natural progression of experimental results obtained in FY12-FY13. For FY14, an emphasis will be put on characterizing the results of the 10 major experiments accomplished and producing peer-reviewed journal manuscripts (zeolites transformations and metal interface mineral growth).

Going forward, there will be three major experimental campaigns. The first would be to incorporate the repository wall rock (granite) into our present components. We would run a series of high pressure, temperature experiments containing brine – bentonite – metal – granite. These experiments would provide the first insights into how minerals (and cation exchange) from the enclosing repository rocks would affect EBS components.

The second major experiment theme would be to run long term (i.e., 6 month) experiments that replicate the complete thermal pulse event (ramp up to temperature – hold at 300 °C – ramp down to ambient temperature) of a repository. One run would consist of brine – bentonite – steel, while the second would include the additional component of granite. Critical information would be gleaned from petrographic information, which would allow us to trace mineral transitions through P, T, T (pressure, temperature, time) space. These experiments would be the first to duplicate the events occurring during a thermal pulse and will provide data on irreversible mineral transformations.

The third research theme would be further investigation of the formation of illite or lack thereof. Experiments this year indicated that illite does not form in the chemical compositional space of our studies. Later experiments allowed the growth of fibrous illite in a K⁺ dominated system. Although we now have narrowed down the potential growth mechanisms and chemical parameters needed, further investigation is still needed. These critical experiments are required since many repository systems consider illitization of bentonite as a constraint on EBS designs.

Other research that will be ongoing include: (1) further investigation of Fe-saponite and chalcocite reaction surfaces on steel and copper, respectively, as potential passivating agents, and (2) cation transfer and exchange between the aqueous geochemistry and aluminosilicate matrix. The transition from clinoptilolite to analcime in bentonite matrix is important due to the loss of water from the zeolite's structure, the volume contraction, the release of SiO₂, and the change in retardation factors of the zeolites. If time and resources permit, EBS component system (brine – bentonite) reactions with Opalineous clay will be conducted at elevated pressure and temperature.

Characterization techniques we would like to include in FY14 are: sulfur isotopic analyses of chalcocite growths, transmission electron microscopy, Raman spectroscopy, neutron tomography, focused ion beam microscopy, acoustic measurements to capture elastic moduli of the metals, electrochemical impedance spectroscopy to determine whether reacted metal have become passive, and various synchrotron techniques.

The proposed lines of study are presented in bullet form below for easy reference.

- Finish 300° C experiment characterizations.
- Repeat EBS reactions at 300° C for 6 weeks incorporating wall rock material (granite).
- Provide information on complete repository thermal pulse event, using long term (6 month) experiments.
- Investigate the chlorite formation kinetics.
- Further detailed studies on Fe-saponite, chalcocite growth at metal interface with bentonite.
- Further investigation of SiO₂ precipitation and aluminosilicate formation.
- Investigate further methods for the characterization of the solid phase reaction products, e.g., S isotopes, TEM, Raman spectroscopy, neutron tomography, FIBS, PDF, acoustic measurements of metals, and various synchrotron techniques.

7. References

- Altaner, S.P. (1989) Calculation of K diffusional rates in bentonite beds. *Geochimica et Cosmochimica Acta*, 53, 923-931.
- Bannister, R.A. (1943) Brammalite (sodium-illite) a new mineral from Llandebie, South Wales. *Mineralogical Magazine*, 26, 304-307.
- Bish, D.L. and Aronson, J.L. (1993) Paleogeothermal and paleohydrologic conditions in silicic tuff from Yucca Mountain, Nevada. *Clays and Clay Minerals*, 41, 148-161.
- Bish, D.L., Vaniman, D.T., Chipera, S.J., and Carey, J.W. (2003) The distribution of zeolites and their effects on the performance of a nuclear waste repository at Yucca Mountain, Nevada, U.S.A. *American Mineralogist*, 88, 1889-1902.
- Blanc, P. and Vieillard, P. (2010) Thermochemie: Estimation of the thermodynamic properties of dehydrated phyllosilicates. Bureau de Recherches Géologiques et Minières Technical Report, RP-57798-FR, pp. 64.
- Börjesson, L., Gunnarsson, D., Johannesson, L-E., and Jonsson, E. (2010) Design, production and initial state of the buffer. Svensk Kärnbränslehantering Technical Report, TR-10-15, pp. 89.
- Broxton, D.E., Bish, D.L., and Warren, R.G. (1987) Distribution and chemistry of diagenetic minerals at Yucca Mountain, Nye County, Nevada. *Clays and Clay Minerals*, 35, 89-110.
- Carlsson, T. (2008) Interactions between copper corrosion products and MX-80 bentonite. Svensk Kärnbränslehantering Working Report, TR-08-46, pp. 24.
- Cheshire, M.C., Caporuscio, F.A., Jové-Colón, C., and McCarney, M.K. (2013) Alteration of clinoptilolite into high-silica analcime within a bentonite barrier system under used nuclear fuel repository conditions. Proceeding from the 14th International High-Level Radioactive Waste Management Conference, 410-415.
- Chipera, S.J. and Bish, D.L. (1997) Equilibrium modeling of clinoptilolite-analcime equilibria at Yucca Mountain, Nevada, USA. *Clays and Clay Minerals*, 42, 226-239.
- Chipera, S.J. and Bish, D.L. (2002) FULLPAT: a full-pattern quantitative analysis program for X-ray powder diffraction using measured and calculated patterns. *Journal of Applied Crystallography*, 35, 744-749.
- Chung, F.H. (1974a) Quantitative interpretations of X-ray diffraction patterns of mixtures. I. Matrix flushing method for quantitative multicomponent analysis. *Journal of Applied Crystallography*, 7, 519-525.
- Coombs, D.S. and Whetten, T. (1967) Composition of analcime from sedimentary and burial metamorphic rocks. *Geological Society of America Bulletin*, 78, 269-282.

- Couture, R.A. (1985) Steam rapidly reduces the swelling capacity of bentonite. *Nature*, 318, 50-52.
- Crerar, D.A., Susak, N.J., Borcsik, M., and Schwartz, S. (1978) Solubility of the buffer assemblage pyrite + pyrrhotite + magnetite in NaCl solution from 200 to 350 °C. *Geochimica et Cosmochimica Acta*, 42, 1427-1437.
- Duffy, C.J. (1984) Hydrothermal geochemistry. Research and Development Related to the Nevada Nuclear Waste Storage Investigation July 1 – September 30, 1982. Eds., Wolfsberg, K. and Vaniman, D.T. Los Alamos National Lab Report, LA-10032-PR, pp. 76.
- Eberl, D. (1978) Reaction series for dioctahedral smectites. *Clays and Clay Minerals*, 26, 327-340.
- Eberl, D. and Hower, J. (1977) The hydrothermal transformation of sodium and potassium smectite into mixed-layer clay. *Clays and Clay Minerals*, 25, 215-227.
- Eberl, D., Whitney, G., and Khourym, H. (1978) Hydrothermal reactivity of smectite. *American Mineralogist*, 63, 401-409.
- Ferrage, E., Vidal, O., Mosser-Ruck, R., Cathelineau, M., and Cuadros, J. (2011) A reinvestigation of smectite illitization in experimental hydrothermal conditions: Results from X-ray diffraction and transmission electron microscopy. *American Mineralogist*, 96, 207-223.
- Frape, S.K., Blyth, A., Blomqvist, R., McNutt, R.H., and Gascoyne, M. (2003) Deep Fluids in the Continents: II. Crystalline Rocks, *Treatise on Geochemistry*, 5, J. I. Drever, ed., 541-580.
- Frey, M. (1969) A mixed-layer paragonite/phengite of low-grade metamorphic origin. *Contribution to Mineralogy and Petrology*, 24, 63-65.
- Guillaume, D., Neaman, A., Cathelineau, M., Mosser-Ruck, R., Peiffert, C., Abdelmoula, M., Dubessy, J., Villieras, F., Baronnet, A., and Michau, N., (2003) Experimental synthesis of chlorite from smectite at 300 °C in the presence of metallic Fe. *Clay Minerals*, 38, 281-302.
- Guillaume, D., Neaman, A., Cathelineau, M., Mosser-Ruck, R., Peiffert, C., Abdelmoula, M., Dubessy, J., Villieras, F., and Michau, N., (2004) Experimental study of the transformation of smectite at 80 to 300 °C in the presence of Fe oxides. *Clay Minerals*, 39, 17-34.
- Güven, N. (2001) Mica structure and fibrous growth of illite. *Clays and Clay Minerals*, 49, 189-196.
- Hower, J., Eslinger, E.V., Hower, M.E., and Perry, E.A. (1976) Mechanism of burial metamorphism of argillaceous sediments. *Geological Society of America Bulletin*, 87, 725-737.

- Jobmann, M. and Buntebarth, G. (2009) Influence of graphite and quartz addition on the thermo-physical properties of bentonite for sealing heat-generating radioactive waste. *Applied Clay Science*, 44, 206-210.
- Jové-Colón, C.F., et al. (2011) Disposal systems evaluations and tool development – engineered barrier system (EBS) evaluation (Fuel cycle research and development). Sandia National Laboratory, FCRD-USED-2011-000132, 16-48.
- Karnland, O. (2010) Chemical and mineralogical characterization of the bentonite buffer for the acceptance control procedure in a KBS-3 repository. Svensk Kärnbränslehantering Technical Report, TR-10-60, pp. 29.
- Kerrisk, J.F. (1983) Reaction-path calculations of groundwater chemistry and mineral formation at Rainier Mesa, Nevada. Los Alamos National Lab Report, LA-9912-MS, pp. 41
- King, F., Litke, C.D., and Ryan, S.R. (1992) A mechanistic study on the uniform corrosion of copper in compacted Na-montmorillonite/sand mixtures. *Corrosion Science*, 33, 1979-1995.
- Kloprogge, J.T., Komarneni, S., and Amonette, J.E. (1999) Synthesis of smectite clay minerals: A critical review. *Clays and Clay Minerals*, 47, 529-554.
- Kohyama, N., Shimoda, S., and Sudo, T. (1973) Iron-rich saponite (ferrous and ferric forms). *Clays and Clay Minerals*, 21, 229-237.
- Madsen, F.T. (1998) Clay mineralogical investigations related to nuclear waste disposal. *Clay Minerals*, 33, 109-129.
- Marty, N.C.M., Fritz, B., Clément, A., and Michau, N. (2010) Modelling the long term alteration of the engineered bentonite barrier in an underground radioactive waste repository. *Applied Clay Science*, 47, 82-90.
- Masuda, H., O'Neil, J.R., Jiang, W-T, and Peacor, D.R. (1996) Relation between interlayer composition of authigenic smectite, mineral assemblages, I/S reaction rate and fluid composition in silicic ash of the Nankai Trough. *Clays and Clay Minerals*, 44, 443-459.
- Meunier, A., Velde, B., and Griffault, L. (1998) The Reactivity of Bentonites: a Review. An Application to Clay Barrier Stability for Nuclear Waste Storage. *Clay Minerals*, 33, 187-196
- Moore, D. M. and Reynolds, R.C. (1997) *X-ray Diffraction and the Identification and Analysis of Clay Minerals*. Oxford University Press, pg. 377.
- Mosser-Ruck, R., Cathelineau, M., Baronnet, A., and Trouiller, A. (1999) Hydrothermal reactivity of K-smectite at 300 °C and 100 bar: dissolution-crystallization process and non-expandable dehydrated smectite formation. *Clay Minerals*, 34, 275-290.

- Mosser-Ruck, R., Cathelineau, M., Guillaume, D., Charpentier, D., Rousset, D., Barres, O., and Michau, N. (2010) Effects of Temperature, pH, and Iron/Clay and Liquid/Clay Ratios on Experimental Conversion of Dioctahedral Smectite to Berthierine, Chlorite, Vermiculite, or Saponite. *Clays and Clay Minerals*, 58, 280-291
- Mosser-Ruck, R., Pironon, J., Cathelineau, M., and Trouiller, A. (2001) Experimental illitization of smectite in a K-rich solution. *European Journal of Mineralogy*, 13, 829-840.
- Neuhoff, P.S., Hovis, G.L., Balassone, G., and Stebbins, J.F. (2004) Thermodynamic properties of analcime solid solutions. *American Journal of Science*, 304, 21-66.
- Nutt, M. Voegelé, M., Jove Colon, C.F., Wang, Y., Howard, R., Blink, J., Liu, H.H., Hardin, E., and Jenni, K. (2011) Used fuel disposition campaign disposal research and development road map (Fuel cycle research and development). Sandia National Laboratory.
- Ohmoto, H., Hayashi, K-I, and Kajisa, Y. (1994) Experimental study of the solubilities of pyrite in NaCl-bearing aqueous solutions at 250-350 °C. *Geochimica et Cosmochimica Acta*, 58, 2169-2185.
- Pederson, K. (2010) Analysis of copper corrosion in compacted bentonite clay as a function of clay density and growth conditions for sulfate-reducing bacteria. *Journal of Applied Microbiology*, 108, 1094-1104.
- Perry, E.A. and Hower, J. (1970) Burial diagenesis of Gulf Coast polytomic sediments. *Clays and Clay Minerals*, 18, 165-177.
- Pouchou J.L. and Pichoir F. (1985) "PAP" $\phi(\rho z)$ correction procedure for improved quantitative microanalysis. *Microbeam Analysis*. Ed. Armstrong, J.T. San Francisco Press, pp. 104-106.
- Pusch, R. (1979) Highly compacted sodium bentonite for isolating rock-deposited radioactive waste products. *Nuclear Technology*, 45, 153-157.
- Pusch, R. and Kasbohm, J. (2002) Alteration of MX-80 by hydrothermal treatment under high salt content conditions. *Svensk Kärnbränslehantering Technical Report*, TR-02-06, pp. 44.
- Reynolds, R.C. and Hower, J. (1970) The nature of interlayering in mixed-layer illite-montmorillonite. *Clays and Clay Minerals*, 18, 25-36.
- Roberson, H.E. and Lahann, R.W (1981) Smectite to illite conversion rates: Effects of solution chemistry. *Clays and Clay Minerals*, 29, 129-135.
- Seyfried, J.R., Janecky, D.R., and Berndt, M.E. (1987) Rocking autoclaves for hydrothermal experiments II. The flexible reaction-cell system. *Hydrothermal Experimental Techniques*. Eds. Ulmer, G.C. and Barnes, H.L. John Wiley and Sons, pp. 216 - 239
- Small, J.S. (1993) Experimental determination of the rates of precipitation of authigenic illite and kaolinite in the presence of aqueous oxalate and comparison to the K/Ar ages of authigenic illite in reservoir sandstones. *Clays and Clay Minerals*, 41, 191-208.

- Small, J.S., Hamilton, D.L., and Habesch, S. (1992) Experimental simulation of clay precipitation within reservoir sandstones 2: Mechanism of illite formation and controls on morphology. *Journal of Sedimentary Petrology*, 62, 520-529.
- Smyth, J.R. (1982) Zeolite stability constraints on radioactive waste isolation in zeolite-bearing volcanic rocks. *Journal of Geology*, 90, 195-201.
- Środoń, J. (1999) Nature of mixed-layer clays and mechanisms of their formation and alteration. *Annual Review of Earth and Planetary Sciences*, 27, 19-53.
- Wersin, P., Johnson, L.H., and McKinley, I.G. (2007) Performance of the bentonite barrier at temperatures beyond 100° C: A critical review. *Physics and Chemistry of the Earth*, 32, 780-788.
- Whitney, G. and Velde, B. (1993) Changes in particle morphology during illitization: An experimental study. *Clays and Clay Minerals*, 41, 209-218.
- Wilkin, R.T. and Barnes, H.L. (1998) Solubility and stability of zeolites in aqueous solution: I. Analcime, Na-, and K-clinoptilolite. *American Mineralogist*, 83, 746-761.
- Wilkin, R.T. and Barnes, H.L. (2000) Nucleation and growth kinetics of analcime from precursor Na-clinoptilolite. *American Mineralogist*, 85, 1329-1341.
- Wilson, J., Cressey, G., Cressey, B., Cuadros, J., Ragnarsdottir, K.V., Savage, D., and Shibata, M. (2006) The effect of iron on montmorillonite stability (II) Experimental investigation. *Geochimica et Cosmochimica Acta*, 70, 323-336.

**Thermodynamic Database (TDB): Recommendations and
Guidelines on Future TDB Development
(Part IV)**

1. Thermodynamic Data: Progress

Thermodynamic data are essential for understanding and evaluating geochemical processes, as by speciation-solubility calculations, reaction-path modeling, or reactive transport simulation. These data are required to evaluate both equilibrium states and the kinetic approach to such states (via the affinity term or its equivalent in commonly used rate laws). These types of calculations and the data needed to carry them out are a central feature of geochemistry in many applications, including water-rock interactions in natural systems at low and high temperatures. Such calculations are also made in engineering studies, for example studies of interactions involving man-made materials such as metal alloys and concrete. They are used in a fairly broad spectrum of repository studies where interactions take place among water, rock, and man-made materials. Waste form degradation, engineered barrier system performance, and near-field and far-field transport typically incorporate some level of thermodynamic modeling, requiring the relevant supporting data.

The development of thermodynamic databases has a long history in geochemistry (e.g., Garrels and Christ, 1965; Helgeson et al., 1969; Helgeson et al., 1978, Johnson et al., 1992; Robie and Hemingway, 1995), paralleled by related and applicable work in the larger scientific community (e.g., Wagman et al., 1982, 1989; Cox et al., 1989; Barin and Platzki, 1995; Binneweis and Milke, 1999). Unfortunately, the National Bureau of Standards (now the National Institutes of Science and Technology) no longer generally addresses thermodynamic data pertaining to aqueous, mineral, and gas species, its last work being the compilation of Wagman et al. (1982) and the errata published in 1989. IUPAC, whose efforts in this area were generally limited to data pertaining to key species only (a small subset), has not done much in this area since the publication of the Cox et al. (1989) report. The standards organizations have been basically inactive regarding thermodynamic data of interest to geochemical and repository studies for over twenty years. For radionuclide elements, much of this void has been filled by the European Nuclear Energy Agency (NEA), which has sponsored a series of review volumes (e.g., Grenthe et al., 1992 [1: uranium]; Silva et al., 1995 [2: americium]; Rard et al., 1999 [3: technetium]; Lemire et al., 2001 [4: neptunium and plutonium]; Guillaumont et al., 2003 [5: update on uranium, neptunium, plutonium americium, and technetium]; Gamsjäger et al., 2005 [6: nickel]; and Olin et al., 2005 [7: selenium]).

The thermodynamic database for dilute systems is widely used in the geochemistry community for a variety of applications involving rock/water interactions. It builds on the work of Prof. Helgeson and his students (see BSC, 2007a for many applicable references, including ones to the SUPCRT92 code and associated database), and covers a significant range of temperature (25-300°C). The last version of this thermodynamic database covers 86 chemical elements, 1219 aqueous species, 1156 minerals and other solids species, and 128 gas species. Many data for actinide species have been adopted from the Nuclear Energy Agency (NEA) series of volumes on actinide thermodynamics (see references given in BSC, 2007a), and the appropriate temperature extrapolations have been applied.

Progress in FY13 has continued to focus on the basic foundation of a thermodynamic database, namely values for *key data* associated with specific chemical species (solid, gas, aqueous) on which data for other species depend. This direction was taken after generating new estimates of thermodynamic properties of various complex clays and related sheet silicates. At that time, it was noted that some of the inputs derived from the mineral data of Helgeson et al. (1978) either

needed correction or seemed weakly supported. This further suggested the likelihood of necessary wholesale correction to the Helgeson et al. (1978) in regard to the aluminosilicate minerals. This sort of correction would affect the calculated relationships of clay minerals and related sheet silicates, including the illites and chlorite, among themselves and with other silicates and aluminosilicates. Also, understanding the needed corrections is required to evaluate the possible benefit of replacing the Helgeson et al. (1978) dataset with the similar but more modern one of Holland and Powell (2011). At this time we believe that it is necessary to settle various key data issues in order to properly move forward with either one. Once the key data issues are resolved, corrections would be needed to either for use in UFD applications. These corrections are needed to assure accurate calculation of solubilities and mineral phase relationships, particularly in the relative low temperature range (<300°C).

It is infeasible to re-do the many thousands, if not tens of thousands of experiments that contribute to the existing literature on thermodynamic data of potential significance to the UFD and similar geochemical applications. Therefore, it is necessary to re-evaluate a large body of historical data collected in a timespan of about a century and only do new experiments as absolutely required, not only to fill gaps but to resolve discrepancies in the data that cannot otherwise be resolved. Therefore, this is mostly a task of re-evaluating existing data.

A major problem with thermodynamic data is that data are typically dependent on other data. For example, Gibbs energies and enthalpies cannot be measured absolutely. The convention is to define them in terms of formation from the chemical elements in their standard reference forms. The standard reference forms are usually the thermodynamically stable forms at 298.15K and 1 bar pressure. An exception is white phosphorus, which in modern work is mostly used in place of the stable red form.

The Gibbs energy of formation is related to the enthalpy of formation is:

$$\Delta G_{f,i}^o = \Delta H_{f,i}^o - T\Delta S_{f,i}^o$$

where $\Delta G_{f,i}^o$ is the (standard molar) Gibbs energy of formation, $\Delta H_{f,i}^o$ is the (standard molar) enthalpy of formation, T is the absolute temperature, and $\Delta S_{f,i}^o$ is the (standard molar) entropy of formation. The Gibbs energy and enthalpy of formation are generally tabulated along with the absolute (standard molar) entropy (S^o), not the entropy of formation. The entropy of formation of a chemical substance is related to the absolute entropy of the substance by:

$$\Delta S_{f,i}^o = S_i^o - \sum_{\varepsilon} \nu_{\varepsilon,i} S_{\varepsilon}^o$$

where ε denotes a chemical element, $\nu_{\varepsilon,i}$ is the stoichiometric coefficient of the element in the i -th chemical substance, and S_{ε}^o is the absolute (standard molar) entropy of the element in its reference state.

The use of two reference forms for phosphorus has caused trouble. Consider two USGS compilations of thermodynamic data. Robie and Hemingway (1995) give the same thermodynamic data for PO_4^{3-} (within precision) as the earlier compilation of Robie et al. (1978) (See Table 8 in Appendix E). However, the earlier work uses *red* phosphorus as the reference form for P (entropy of 22.85 J/mol-K), while the later one uses the *white* form (41.09 J/mol/K). This is indicative that something is clearly wrong here.

Recommended values for elemental entropies have varied somewhat over time. Table 1 (Appendix E) lists the recommended values from nine relatively modern authoritative sources. Problem areas are noted in this table. One can see that discrepancies do exist, but most are relatively small. Older sets of recommended values are given in Tables 2 and 3 (Appendix E). In Table 1, the units are modern (Joule units, not calorie units) and the standard pressure is one bar. In Table 2, the values are given in calorie units and the standard pressure is 1 atm (1.013 bar). In Table 3, the values are given in Joule units but the standard pressure is again 1 atm. The difference in standard pressure causes no discrepancies for condensed phases, but does matter for gases.

The importance of elemental entropies in relating Gibbs energies to enthalpies clearly defines these entropies as the first group of key data. One would think that every compilation of thermodynamic data would begin with a selection and presentation of these data. However, that is generally not the case, and the elemental reference forms are more often treated as ordinary chemical species and scattered about the data tables following whatever general arrangement of chemical species is employed. As many of even the modern data compilations do not exist in computerized or other searchable form, this creates something of an impediment to making corrections to data that one may wish to adopt in one's own work. Many of the compilations do include words to the effect that corrections have been made where necessary. However, there is no objective evidence as to how rigorously this may have been practiced.

Tables 1-3 (Appendix E) were created in part to look at trends and gaps in the available data for elemental entropies. However, they were also created to serve as an easy reference in evaluating whether or not such corrections may have been made or to make such corrections if needed.

In general, we prefer the NEA-TDB values (included in Table 1) for future thermodynamic database work. These include the data from Cox et al. (1989) [the last CODATA report]. However, there are still a fair number of gaps; only 50 elements are covered. Barin and Platzki (1995) covers many more elements (89). It is probably a good place to start in filling gaps for a UFD thermodynamic database. However, direct evaluation of original sources should be made, along with a search for and evaluation of any data in the newer literature.

Entropy values are generally easy to obtain by calorimetry. Usually the sample remains intact. Other means of obtaining values are possible, but this is the most common. The situation is more challenging for obtain Gibbs energy data or enthalpy data. To obtain Gibbs energy data, a system of chemical components must be in equilibrium and one of these must be the chemical species of interest. To obtain enthalpy data, the idea is to completely react the sample, producing other chemical species. Gibbs energies and enthalpies both may be sensitive to the exact nature of the chemical species of interest, and in the case of minerals, there are often issues of proper characterization of chemical composition, crystallinity, particle size, etc.

In theory, one could just obtain enthalpy of formation data or everything of interest and then calculate the corresponding Gibbs energies. One could then just use equilibrium measurements as a means of test. However, it has been found that Gibbs energies can often give higher accuracy (cf. Helgeson et al., 1978). This is particularly important because what geochemists and others are more often trying to do is calculate equilibria or reaction rates that depend on distances from equilibria. The reality is that what we have today is a mixed set of results. It is somewhat unfortunate that both Gibbs energies and enthalpies are tied to elemental reference forms, as those reference forms are tied to a particular oxidation state (zero), while the oxidation states in

chemical species of interest may be different. Much of the uncertainty associated with a given Gibbs energy of formation or enthalpy of formation may be associated with relating the elemental reference forms to forms that represent the oxidation states in the species of interest. This appears to be a problem with aluminum, in regard to the relation of Al metal (the reference form) to the form common in minerals (Al[III]). Again, however, establishing the appropriate key data is the way to proceed. Such a key datum might be the Gibbs energy or enthalpy of corundum (Al₂O₃).

Table 4 (Appendix E) shows a selection of key data for aqueous species and minerals taken from the slop98.dat datafile associated with SUPCRT92. This includes the mineral data of Helgeson et al. (1978), with corrections in the case of Ca-bearing aluminosilicates performed in March, 1990. SUPCRT92 is very important to the UFD because it (along with the NEA-TDB database as developed at the time) were used to develop the dilute systems database in Wolery and Jové Colón (2007). Table 5 (Appendix E) shows the slop98.dat (SUPCRT92) key data converted to Joule units alongside the corresponding data from NEA-TDB (through volume 12). Various discrepancies are marked. The NEA-TDB data for the aqueous phosphate species were validated by Rard and Wolery (2007). The corresponding slop98.dat data are incorrect, and in fact were superseded in a SUPCRT92 data file used to update the dilute systems thermodynamic database in Wolery and Jové Colón (2007). We note that SiO₂(aq) (used in slop98.dat) and Si(OH)₄(aq) (used in NEA-TDB) are in fact the same species, just differing in formally assigned H₂O. Correcting for this, the two value sets are copacetic. However, in the development of the dilute systems database (Wolery and Jové Colón, 2007), different data were assigned that correspond to the “Rimstidt” paradigm, which is consistent with modern thinking among most geochemists (cf. BSC, 2007a). These data are shown in Table 6 (Appendix E).

Table 7 (Appendix E) similar shows the same key data from the last two NBS compilations, the NBS 270 series and Wagman et al. (1982). The first uses *calorie* units, the second, *Joule* units. Table 8 similar shows the same key data from the last two USGS compilations, Robie et al., (1978) and Robie and Hemingway (1995). Both use Joule units.

Tables 4-8 (Appendix E) are intended to support further UFD thermodynamic database development by providing ready access to key data from important compilations, and thus to assist in developing a single set of key data to use in further development of the UFD thermodynamic database. One would think, as for the entropies of the elements, that such key data would be identified and presented in one place in any compilation. However, that is, again, not generally the case. It may be necessary to refer to these older key data sets in evaluating other, non-key data, as they may depend on data in these sets.

A major problem of concern is aluminum, because Helgeson et al. (1978) after careful consideration of a body of conflicting data obtained one resolution, while USGS investigators (e.g., Robie and Hemingway, 1995) came to a different resolution. The main problem seems to be relating Al[III] in some form to Al metal (the elemental reference form).

A closer look at the Helgeson et al. (1978) paper (supported by discussions with Dr. K.J. Jackson, one of Prof. Helgeson's former students) indicates that in building most of the aluminosilicate data from mineral-mineral phase equilibrium data, kaolinite (Al₂Si₂O₅(OH)₄) was used as an anchor mineral for the Al₂O₃ component. However, Helgeson et al. did not use calorimetric data for the Gibbs energy of kaolinite. Instead, they estimated the Gibbs energy from a solubility (*log K*) approach. The solubility data were taken from a natural system, in

which groundwater as assumed to be in equilibrium with kaolinite and gibbsite. This is not an approach that most investigators today (if not then) would prefer. The resulting Gibbs energy for kaolinite was used to derive Gibbs energies for some other aluminosilicates, and so forth in a somewhat complex chain. We are engaged in attempting corrections to the Helgeson et al. (1978) approach to deriving kaolinite data, which of course depends on gibbsite data. We are also looking at the USGS approach to this issue. Holland and Powell (1985) developed their database using corundum as the key aluminum mineral, so that needs to be looked at as well.

2. Recommendations for Future Database Development

The following are recommendations for future thermodynamic database development and improvements:

- Continue evaluation of a large body of historical data reported over the last century
- Future database should use NEA-TDB data where feasible (post-Nickel volume)
- Consider Barin and Platzki a source of thermodynamic data to backfill NEA-TDB gaps
- Perform experiments to populate unknown data and resolve discrepancies only when absolutely required
- Establish key data for aluminum using Gibbs energy or enthalpy of corundum (Al_2O_3) to resolve discrepancies between Helgeson (1978) and Robie/Hemingway (1995), also incorporating Holland/Powell (1985) data
- Update SUPCRT92 mineral data for consistency with desired key data
- Maybe replace the SUPCRT92 mineral data with the Holland and Powell (2011) data, adjusting for consistency with the desired key data
- Put the SUPCRT92 functionality for calculating thermodynamic properties as a function of temperature and pressure into Cantera
- Collaborate with European investigators (Thereda, Pitzer, benchmarking)
- Fully update working databases at opportune times (e.g., do official releases)
- Take another look at temperature and pressure extrapolation of data for aqueous species for which HKF EoS data are not available
- Address high-ionic strength model data (Pitzer model, others)
- Include surface complexation modeling improvements as well as chemical thermodynamic data improvements

Additionally, other than work on dilute and concentrated solution databases (e.g., Wolery and Jové Colón 2007), the US has largely abandoned thermodynamic database development. Some of the last collections of U.S. thermodynamic data are from Bureau of Mines (no longer an entity) in 1995, USGS in 1995 and NBS (now NIST) in 1982. International efforts have continued, including those of France (2007), Belgium (2007), Sweden (2006), Finland (2007), Spain (2003), Japan (2005) with many of these relying heavily on the Swiss Nagra/PSI data, and the NEA-TDB program performs critical review on data.

A DOE thermodynamic database would be of interest to many DOE programs, including those in DOE-NE, DOE-EM, DOE-FE and Office of Science. Since several international repository programs have made progress on the development of thermodynamic data in parallel to US efforts, it would be beneficial for DOE to integrate international thermodynamic data into a

multi-program DOE database. Specific guidance on the creation, population and review of such a database would be required. Requirements for a DOE thermodynamic database should include:

- QA/QC – traceable, reproducible, consistent, uncertainty
- Integration with other national and international programs
- Benchmarking (possibly against NEA-TDB)
- Include geochemical reactions, redox, sorption, ion exchange
- Ability to handle both dilute and concentrated systems strengths (pitzer, debye-huckel, etc.)
- Data for elevated temperature and pressure
- Portability to multiple systems, programs, countries
- Open source format

3. Outline for Guidelines on Thermodynamic Database (TDB) Development and Programmatic goals

Why TDBs are important to nuclear waste disposal?

As delineated in previous sections, thermodynamic databases (TDB) are key inputs to models for the evaluation of chemical/geochemical interactions between fluids (gas or liquids) with engineered and natural barrier materials and waste components in repository environments. A fundamental modeling requirement in geochemical modeling is to calculate chemical equilibria in multiphase multicomponent systems between aqueous solutions, gases, and solids for a large comprehensive set of chemical reactions. Therefore, demonstrated adequacy of these sets of thermodynamic data needs to be established for confidence in the estimation of material solubility and evaluation of phase stability under various environmental conditions.

The strong reliance and confidence in the use of TDBs is demonstrated by documented decade's effort in producing these critically-assessed and comprehensive data sets not only for radioactive waste management and repository safety assessment but also in scientific fields such as material and chemical sciences. As noted in Section 1, given the limitations to be encountered with thermodynamic data gaps, we should consider other types of data such as adequate kinetic data. This type of data can be used to complement the analysis of metastable equilibria or cases where systems may be dominated by chemical disequilibria.

The importance of historical TDB development efforts

Section 1 discusses the importance of past efforts in TDB development (Cox et al., 1989; Robie and Hemingway, 1995; Rossini, 1952; Wagman et al., 1982). Relevant to nuclear waste repository science are the comprehensive assessments conducted by the Nuclear Energy Agency (NEA) and documented in a series of volumes targeting actinide elements but also other ancillary data for a wide range of chemical components (Guillaumont et al., 2003; Rand et al., 2008; Rard et al., 1999). A major effort in creating a large unified TDB (BSC 2007a) mainly derived from existing TDB compilations like the NEA but also reviewed, refined, and revised these data when necessary. Moreover, the legacy of repository science programs also advanced evaluation methodologies for analysis and estimation of thermodynamic data and conducted verification and validation (V&V) of data through internally-consistent modeling of multiphase equilibria.

All these efforts concluded that TDBs are evolving entities in need of constant expansion and refinement to encompass complex chemical systems that in many cases dominate in natural and engineered repository environments.

Another important aspect of the TDB development is thermodynamic consistency between data sets produced by various research programs. In this regard, the evaluation procedure for critically-reviewed and/or published data obtained from multiple sources needs to follow guidelines to ensure consistency in the retrieval and derivation of thermodynamic data. These guidelines and associated conventions have been to a large extent established by various entities (OECD-NEA, NIST-JANAF, IUPAC) and are based on well-established procedures for TDB development. The guidelines advanced by the OECD-NEA will be adopted here since these:

- were updated in the last 13 years and have undergone peer scrutiny from experts in TDB development
- are consistent with other guidelines used in national and international efforts in TDB development
- satisfy the needs and compliance assessments for confidence in data selection, quality, and reliability

Key guidelines for TDB development

Following the OECD-NEA (Grenthe et al., 2013; Wanner, 1999a, b; Wanner and Östhols, 2000) and IUPAC (Cohen et al., 2008) guidelines and conventions, the proposed procedure for TDB development is as follows:

- **Focus on the chemical phase composition and environmental conditions for the system of interest.** For example, what are the main compositions and phases in engineered and natural materials of interest to the repository environment, including fluid chemistry? It is important to narrow down the composition of the chemical system of interest keeping in mind pressure and temperature limits that could limit data availability along with representative phase composition (e.g., end-member vs. solid solutions).
- **Quality assessment (QA) of data sources.** This include, but not limited to, previous and current critical reviews and/or assessments for data selection such as quality, uncertainty quantification, evaluation of experimental results, temperature and pressure corrections, extrapolations, and estimations. This also encompasses consistency checks with standard state conventions and the use of widely adopted key thermodynamic data including historical data compilations. It should be noted that some of these QA assessments are cross-cut other TDB evaluation items described hereafter.
- **Standards and conventions.** Maintain the usage of sanctioned standards (e.g., IUPAC, OECD-NEA) for symbols, terminology, units, conversion factors, chemical formulae / nomenclature, and physical constants. Chemical reactions delineating equilibria for equilibrium constants (ligand formation, aqueous ion complexation), redox potentials, and pH should be formulated consistent with those conventionally defined within the aforementioned handbook databases and/or the scientific literature elsewhere.

- **Extrapolations to zero ionic strength.** This item is particularly important for the retrieval of thermodynamic data from solubility experiments based on the evaluation of equilibrium constants and computation aqueous species activities. These calculations are based on the estimation of activity coefficient corrections as a function of ionic strength and temperature. Consistency in the theoretical approaches for the computation of activity coefficients and thus activities of aqueous species is the key to the evaluation of multiphase multicomponent interactions. There are several adequate approaches and methods consistent with the existing standards to extrapolate activity coefficients to infinite dilution. However, these corrections need to be valid not only for a given range of concentrations or ionic strengths but also as a function of temperature. For nominally dilute systems, the specific interaction theory (SIT), Davies equation, and the extended Debye-Hückel approach such as b-dot (Helgeson et al., 1981) have been widely adopted in the retrieval of thermodynamic data such as the OECD-NEA and Shock et al (1997), respectively. The Pitzer approach has also been extensively adopted for modeling concentrated solutions and salt solubilities relevant to geologic environments and has been expanded to industrial applications. All these approaches for activity coefficient corrections are considered sufficiently adequate for the purposes of evaluating thermodynamic data. However, a decision must be made in selecting one or more with wide applicability and usage in geochemical codes. Pitzer and b-dot approaches are the likely candidates given their broad acceptance and extensive use in geochemical codes (e.g., EQ3/6, Geochemist Workbench).
- **Extrapolation of thermodynamic data to elevated temperatures.** Temperature is a very relevant parameter to TDB development given its importance to the long-term disposal of heat generating nuclear waste. It is also, in many cases, a glaring limitation of TDBs where data for aqueous and solid phase at above-ambient temperatures tends to be lacking. This is particularly true for alumino-silicate phases such as clays and zeolites where thermodynamic data representative of hydrothermal conditions is either scant or non-existent. In such cases, methods to estimate and extrapolate thermodynamic parameters as a function of temperature are necessary to fill these data gaps. This also calls for evaluation of alternate approaches to tie reference key thermodynamic data for mineral solids and revisit what was done for alumino-silicate minerals in the widely-adopted SUPCRT92 database. Temperature extrapolations are commonly represented by heat capacity expressions represented by polynomials for a given range of temperatures. Temperature extrapolations in many TDB compilations are based on heat capacities since these are readily obtained from direct thermodynamic measurements. Integration of heat capacity with respect to temperature provides the necessary data to develop the enthalpy and Gibbs functions commonly used in the thermodynamic database compilations (Robie and Hemingway, 1995). Other extrapolations such as those based on approximations like the assumption of zero heat capacity of reaction at all temperatures leads to the van't Hoff formulation. This type of approximation is usually considered when there is very

little or non-existent data at elevated temperatures. Temperature extrapolations based on such an approach require justification and a clear elucidation of the potential uncertainties arising from using such methods. It should be noted that the use of such approaches under limited temperature ranges not far exceeding ambient are acceptable. For example, the isocoulombic/isoelectric method has been used in a previous TDB development to retrieve thermodynamic data for several actinide species at elevated temperatures (Wolery and Jové Colón, 2007). Extensive work has been conducted by Helgeson et al. (1981) and his students (1997) to evaluate the thermodynamic properties of aqueous solutions resulting in the revised Helgeson–Kirkham–Flowers equation-of-state (HKF EoS) for aqueous solutions. This approach is widely accepted by many researchers who have adopted it in the evolution of experimental data therefore furthering the consistency in the adopted method used in many thermodynamic extrapolations. There are a myriad of methods that could be considered but it's recommended to use those that have been widely used thus establishing their reliance in the geochemical modeling. The review by Puigdomènech et al. (1999) provides a good summary on this topic.

- **Evaluation of uncertainties.** Evaluation of uncertainties is also an important topic and one that usually comes under lots of scrutiny. The main reason is that the statistical evaluation of thermodynamic data is often fraught with very limited experimental data sets with no information on the measurement errors and their propagation. Also, discrepancies between different data sets for the same type of measurement could impose uncertainty biasing and/or broadening of its uncertainty bounds. These are mainly a consequence of limited data availability which is exacerbated by the difficulties of obtaining data at high temperatures or at conditions far from ambient. Still, in some cases, the evaluation of uncertainty is possible even when difficulties due to the insufficient number of data points are usually encountered. The evaluation of uncertainties for thermodynamic database has been widely discussed in handbooks and it's well described by Wanner (1999a). The treatment of outliers or inconsistent data sets requires expert judgment of whether the data should be either considered or discarded for meeting certain criteria for uncertainty evaluation. Error propagation often requires assumptions about the systematic errors when obtaining the data. There are approaches that apply to situations where these systematic errors are assumed to be small and independent of the variables considered in the analysis.
- **Peer-review evaluation.** A critically-assessed peer-review of thermodynamic data requires the participation of two groups:
 - The investigators who generated the TDB and performed the evaluations
 - Independent reviewers that will analyzed the work conducted by the investigators

Independent reviewers provide an additional layer of scrutiny of a comprehensive assessment of thermodynamic data and are performed by a selected group of subject-

matter experts. The work conducted by the investigators is expected to be exhaustive and to the level of judicious review to meet a high level of quality and confidence in the developed TDB. Details of the procedures for peer-review and that of independent reviewer are discussed in detail by Wanner (1999b).

- **Benchmarking.** Benchmarking is another important activity for testing the developed TDB and also evaluates the adequacy and confidence of the thermodynamic models in the retrieval of data, particularly in extrapolations as a function of composition, pressure, and temperature. Benchmarks depend on the data parameters that need to be tested and are usually based on predefined calculations performed using curated data with an established pedigree serving as the basis for such tests. The design of these benchmarks should be focused on recognized gaps that can impact TDB development and its application to modeling of repository performance. For example, existing gaps include extrapolation to high temperatures, sorption data, key thermodynamic data for aluminosilicate, and formalization of retrieval methods that are tractable and transparent. The build-up of benchmark test cases are subject to concurrence of parties involved in the TDB development.
- **Dissemination of data and documentation.** The developed TDB and related documentation should be open-source and available to all the participants or interested parties through a web-based portal with password controlled access. Reporting guidelines should include quarterly reports, technical documentation, benchmarking test cases results, announcements, and other relevant information describing the TDB development. The TDB should be available in various formats to conform with the input structure of various computer codes. Only authorized and approved versions of the TDB and related documentation should be available through this channel.

It is crucial that the TDB development involve existing activities (e.g., THEREDA, CHNOSZ) for the build-up and analysis of data for multicomponent multiphase systems, for example:

- Establish alliances with international activities particularly in benchmark test case development and validation such as THEREDA. Such approach would cover both assessments of data and modeling uncertainties.
- Develop integrated and concerted approach of information passing and data assessment between the involved parties. Such an approach would permit the maintenance of consistency in the evaluation of thermodynamic parameters across various TDB activities.
- Thermodynamic analysis of sorption data such as ion exchange and surface adsorption should also be considered in this effort. However, consistency between thermodynamic data derived for minerals and aqueous solutions with those for sorption is a very challenging endeavor since no accepted convention for the thermodynamic analysis of sorption data has been established. Moreover, such

consistency is mainly specific to individual studies (e.g., clay sorption) with strong ties to certain model representations. A potential approach would be to exploit existing K_d databases and couple this with surface complexation models (“smart K_d ’s”) to capture key couplings on material transport.

- Evaluate alternate theoretical approaches to analyzed gaps in thermodynamic data at elevated temperatures. For example, exploit the use of first principles *ab initio* methods to retrieve mineral heat capacities and other thermal properties to evaluate temperature dependencies where data is limited, non-existent, or just simply difficult to obtain.

The involved parties should include technical staff at US national laboratories (see Table 1) and international institutions with expertise on TDB development. It should be noted this is a preliminary list of potential institutions based on their established contributions to TDB development and it could accept more parties with demonstrated interest in this concerted effort.

It should be noted that the proposed guidelines are consistent with the integrated Used Fuel Disposition (UFD) Data Management Plan described in the document “Integration Plan for Used Fuel Disposition (UFD) Data Management (FCRD-USED-2011-000386)” by Wang (2011). Specific points of consistency with the UFD Data Management Plan and activities are:

- Traceability, transparency and reproducibility (T²R)
- Flexibility and reusability
- Transferability and data inquiry capability
- Internal consistency and completeness
- Access controls

The benchmarking activity is consistent with the development and establishment of test cases within the realm of testing conditions in the UFD Data Management Plan. That is, the establishment of testing conditions shouldn’t be limited to experimental activities and can extend to coordinated activities for database testing. In addition, other activities described in the UFD Data Management Plan are aligned with these TDB development guidelines such as technical data collection and model development, configuration management, and related QA activities. A proposed example of a 3-year timeline for various TDB development activities is shown in Table 2. The preliminary activities described in this timeline should be conducted in parallel with other activities allowing for synergistic collaboration of multiple partners.

Technical analysis of TDB development will be discussed in detail in another section. The data acceptance criteria to be followed still needs to be assessed through a concerted effort of all involved parties.

This assessment should be consistent with that developed in other national and international repository science programs with programmatic requirements applicable to TDB development, for example:

- **Sufficient adequacy for system description and model integration.** This is important for the adequacy of technical bases and justifications for the data to be used in system performance assessment in the modeling coupled processes.
- **Adequate characterization of data uncertainties.** Suitable representation of data uncertainties of parameter values is defensible to reasonably describe variabilities and bounding assumptions.
- **Data compatibility with other existing data (i.e., thermodynamic consistency).** For example, data needs to be cross-checked to ensure internal consistency, mainly assessed through benchmarking.

Table 1. List of potential institutions and personnel with common interests in TDB development

Institutions (USA & International)	Personnel	Remarks
Sandia National Laboratories (SNL)	Carlos F. Jové Colón, David Sassani, Yifeng Wang, Don Reed, Philippe Weck, Yonliang Xiong	Expertise covers both experimental and theoretical assessments for evaluation and retrieval of thermodynamic data
Lawrence Livermore National Laboratories (LLNL)	Mark Sutton, Mavrik Zavarin, and Thomas Wolery (Retired)	Longstanding experience in TDB, geochemical modeling and associated code development.
Arizona State University (ASU)	Everett Shock, Jeffery Dick	Emphasis on biogeochemical and microbial systems
National Institute of Standard of Technology (NIST)		
International: Paul Scherrer Institute (Switzerland) EMPA (Switzerland) NAGRA (Switzerland) CNRS (France) BRGM (France) OECD-NEA (France) THEREDA Database Project (Germany) Karlsruhe Institute of Technology (KIT; Germany) Helmholtz Zentrum Dresden Rossendorf (HZDR; Germany) Japan Nuclear Cycle Dev. Inst. (JNC; Japan)	Extensive list of researchers with experience in TDB research	Wide-ranging expertise in TDB development: <ul style="list-style-type: none"> • Thermodynamic modeling of fluid-mineral interactions including surface and sorption phenomena • TDB development for minerals, radioactive materials, cementitious phases, sorption • Geosphere and engineered barrier transport

Table 2. Example of a preliminary 3-year timeline for various TDB development activities

Phase	Project Name	Lead Labs	2013 (Fall)	2014 (Winter)	2014 (Spring)	2014 (Summer)	2014 (Fall)	2015 (Winter)	2015 (Spring)	2015 (Summer)	2015 (Fall)	2016 (Winter)	2016 (Spring)	2016 (Summer)
	TDB Development Plan													
	Research Scope Definition Phase													
1.1.1	Define TDB objectives and partners	SNL, LLNL, Int. Partners												
1.1.2	Define TDB requirements & criteria	SNL & LLNL												
1.1.3	Define relevant component & phases	SNL & LLNL												
1.1.4	Define relevant benchmarks & tests	SNL, LLNL, Int. Partners												

Table 2 (Cont.). Example of a preliminary 3-year timeline for various TDB development activities

Phase	Project Name	Lead Labs	2013 (Fall)	2014 (Winter)	2014 (Spring)	2014 (Summer)	2014 (Fall)	2015 (Winter)	2015 (Spring)	2015 (Summer)	2015 (Fall)	2016 (Winter)	2016 (Spring)	2016 (Summer)
1.2	Technical R&D TDB Selection Phase													
1.2.1	Define database selection approach	SNL, LLNL, Int. Partners												
1.2.2	Catalog TDB sets for consideration	SNL, LLNL, Int. Partners												
1.2.3	Describe TDB Analysis Methodologies	SNL, LLNL, Int. Partners												
1.2.4	Evaluate data selection	SNL, LLNL, Int. Partners												
1.2.5	Submit TDB evaluation for review	SNL, LLNL, Int. Partners												

Table 2 (Cont.). Example of a preliminary 3-year timeline for various TDB development activities

Phase	Project Name	Lead Labs	2013 (Fall)	2014 (Winter)	2014 (Spring)	2014 (Summer)	2014 (Fall)	2015 (Winter)	2015 (Spring)	2015 (Summer)	2015 (Fall)	2016 (Winter)	2016 (Spring)	2016 (Summer)
1.3	Benchmarking and Reporting Phase													
1.3.1	Develop and select benchmarking tests	SNL, LLNL, Int. Partners												
1.3.2	Documentation and review of benchmarking	SNL, LLNL, Int. Partners												
1.3.3	Submit interim report for peer-review	SNL, LLNL, Int. Partners												
1.4	-Peer-reviews													
1.4.1	Identify and select reviewers	SNL, LLNL, Int. Partners												
1.4.2	Document and report peer-review results	SNL, LLNL, Int. Partners												
1.4.3	Assess peer-review comments	SNL, LLNL, Int. Partners												
1.4.4	Finalized report for open dissemination	SNL, LLNL, Int. Partners												

4. References

- Anderson, G.M., Castet, S., Schott, J. and Mesmer, R.E. 1991. "The density model for estimation of thermodynamic parameters of reactions at high temperatures and pressures." *Geochimica et Cosmochimica Acta*, 55, 1769–1779.
- Barin, I. and Platzki, G. 1995. *Thermochemical Data of Pure Substances*. 3rd Edition. Two volumes. New York, New York: VCH Publishers.
- Binnewies, M. and Milke, E. 1999. *Thermochemical Data of Elements and Compounds*. New York, New York: Wiley-VCH.
- Berman, R.G. 1988. "Internally-Consistent Thermodynamic Data for Minerals in the System $\text{Na}_2\text{O-K}_2\text{O-CaO-MgO-FeO-Fe}_2\text{O}_3\text{-Al}_2\text{O}_3\text{-SiO}_2\text{-TiO}_2\text{-CO}_2$." *Journal of Petrology*, 29, 445-522.
- BSC (Bechtel SAIC Company) 2007a. *Qualification of Thermodynamic Data for Geochemical Modeling of Mineral–Water Interactions in Dilute Systems*. ANL-WIS-GS-000003 REV 01. Las Vegas, Nevada: Bechtel SAIC Company. DOC.20070619.0007.
- BSC (Bechtel SAIC Company) 2007b. *In-Drift Precipitates/Salts Model*. ANL-EBS-MD-000045 REV 03. Las Vegas, Nevada: Bechtel SAIC Company. DOC.20070306.0037.
- CODATA. 1972. Report of the ICSU-CODATA Task Group on Key Values for Thermodynamics, November, 1971. *Journal of Chemical Thermodynamics* 4, 331-336.
- CODATA. 1975. CODATA Recommended Key Values for Thermodynamics, 1973. Report of the CODATA Task Group on Key Values for Thermodynamics, November, 1973. *Journal of Chemical Thermodynamics* 7, 1-3.
- CODATA. 1976. CODATA Recommended Key Values for Thermodynamics, 1975. Report of the CODATA Task Group on Key Values for Thermodynamics, 1975. *Journal of Chemical Thermodynamics* 8, 603-605.
- CODATA. 1977. CODATA Recommended Key Values for Thermodynamics, 1976. Report of the CODATA Task Group on Key Values for Thermodynamics, 1976. *Journal of Chemical Thermodynamics* 9, 705-706.
- CODATA. 1978. CODATA Recommended Key Values for Thermodynamics, 1977. Report of the CODATA Task Group on Key Values for Thermodynamics, 1977. *Journal of Chemical Thermodynamics* 10, 903-906.
- Chase, M.W., Jr., editor. 1998. *NIST-JANAF Thermochemical Tables, Fourth Edition*. *Journal of Physical and Chemical Reference Data*, Monograph No. 9. The American Institute of Physics, Woodbury, New York. 1963 p. ISBN 1-56396-831-2.
- Chase, M.W., Jr., Davies, C.A., Downey, J.R., Jr., Frurip, D.J., McDonald, R.A., and Syverud, A.N. 1985. *JANAF Thermochemical Tables Third Edition*, *Journal of Physical and Chemical Reference Data* 14, Supplement No. 1. American Chemical Society, Washington, DC and American Institute of Physics, New York, for the National Bureau of Standards. 1856 p.

- Cohen, E.R. et al., 2008. *Quantities, Units, and Symbols in Physical Chemistry*, IUPAC Green Book (3rd edition). IUPAC and RSC Publishing, Cambridge.
- Cox, J.D.; Wagman, D.D.; and Medvedev, V.A., eds. 1989. *CODATA Key Values for Thermodynamics*. CODATA Series on Thermodynamic Values. New York, New York: Hemisphere Publishing Company.
- Gamsjäger, H.; Bugajski, J.; Gajda, T.; Lemire, R.J.; and Preis, W. 2005. *Chemical Thermodynamics of Nickel*. Chemical Thermodynamics. Volume 6. New York, New York: Elsevier.
- Garrels, R.M., and Christ, C.L. 1965 *Solutions, Minerals, and Equilibria*. Boston, Massachusetts: Jones and Bartlett Publishers
- Garrels, R.M., and Mackenzie, F.T. 1967. Origin of the chemical compositions of some springs and lakes. In *Equilibrium Concepts in Natural Water Systems*. American Chemical Society, *Advances in Chemistry Series 67*, 222-242
- Greenberg, J.P. and Moller, N. 1989. "The Prediction of Mineral Solubilities in Natural Waters: A Chemical Equilibrium Model for the Na-K-Ca-Cl-SO₄-H₂O System to High Concentration from 0 to 250°C." *Geochimica et Cosmochimica Acta* 53, 2503–2518.
- Grenthe, I.; Fuger, J.; Konings, R.J.M.; Lemire, R.J.; Muller, A.B.; Nguyen-Trung, C.; and Wanner, H. 1992. *Chemical Thermodynamics of Uranium*. Chemical Thermodynamics. Volume 1. Amsterdam, The Netherlands: North-Holland Publishing Company.
- Grenthe, I., Mompean, F., Spahiu, K., 2013. *Guidelines For The Extrapolation To Zero Ionic Strength (TDB-2)*, OECD-NEA, Issy-les-Moulineaux, France.
- Guillaumont, R.; Fanghänel, T.; Fuger, J.; Grenthe, I.; Neck, V.; Palmer, D.A.; and Rand, M.H. 2003. Update on the Chemical Thermodynamics of Uranium, Neptunium, Plutonium, Americium and Technetium. Mompean, F.J.; Illemassene, M.; Domenech-Orti, C.; and Ben Said, K., eds. *Chemical Thermodynamics*. Volume 5. Amsterdam, The Netherlands: Elsevier.
- Gurvich, L.V., Veyts, I.V., and Alcock, C.B., Editors. 1989. *Thermodynamic Properties of Individual Substances, Fourth Edition*. Volume 1. Elements O, H(D, T), F, Cl, Br, I, He, Ne, Ar, Kr, Xe, Rn, S, N, P and Their Compounds. Hemisphere Publishing Corporation, Taylor & Francis Group, New York. 952 p.
- Gurvich, L.V., Veyts, I.V., and Alcock, C.B., Editors. 1991. *Thermodynamic Properties of Individual Substances, Fourth Edition*. Volume 2. Elements C, Si, Ge, Sn, Pb, and Their Compounds. Hemisphere Publishing Corporation, Taylor & Francis Group, New York. 952 p.
- Gurvich, L.V., Veyts, I.V., Iorish, V.S., and Alcock, C.B., Editors. 1993. *Thermodynamic Properties of Individual Substances, Fourth Edition*. Volume 3. Elements B, Al, Ga, In, Tl, Be, Mg, Ca, Sr, Ba and Their Compounds. CRC Press, Inc., Taylor & Francis Inc., New York. 448 p.
- Helgeson, H.C. 1969. "Thermodynamics of Hydrothermal Systems at Elevated Temperatures and Pressures." *American Journal of Science*, 267(6), 729-804.

- Helgeson, H.C.; Delany, J.M.; Nesbitt, H.W.; and Bird, D.K. 1978. "Summary and Critique of the Thermodynamic Properties of Rock Forming Minerals." *American Journal of Science*, 278-A. New Haven, Connecticut: Yale University, Kline Geology Laboratory.
- Hemingway, B.S., and Robie, R.A. 1977a. Enthalpies of formation of low albite (NaAlSi₃O₈), Gibbsite (Al(OH)₃) and NaAlO₂: revised values for $\Delta H^{\circ}_f, 298$ and $\Delta G^{\circ}_f, 298$ of some aluminosilicate minerals. *U.S. Geological Survey Journal of Research* 5, 413-429.
- Hemingway, B.S., and Robie, R.A. 1977b. The entropy and Gibbs free energy of formation of the aluminum ion. *Geochimica et Cosmochimica Acta* 41, 1402-1404.
- Holland, T.J.B. 1989. "Dependence of Entropy on Volume for Silicate and Oxide Minerals: A Review and a Predictive Model." *American Mineralogist*, 74, 5-13.
- Holland, T.J.B., and Powell, R. 1985. "An Internally Consistent Thermodynamic Dataset with Uncertainties and Correlations: 2. Data and Results." *Journal of Metamorphic Geology*, 3, 343-370. [The authors refer to this paper as "DS2".]
- Holland, T.J.B., and Powell, R. 1990. "An Enlarged and Updated Internally Consistent Thermodynamic Dataset with Uncertainties and Correlations: The System K₂O-Na₂O-CaO-MgO-MnO-FeO-Fe₂O₃-Al₂O₃-TiO₂-SiO₂-C-H₂-O₂." *Journal of Metamorphic Geology*, 8, 89-124. [The authors (cf. Powell and Holland, 1993) refer to this paper as "DS4".]
- Holland, T.J.B., and Powell, R. 1998. "An Internally Consistent Thermodynamic Dataset for Phases of Petrological Interest." *Journal of Metamorphic Geology*, 16, 309-343.
- Holland, T.J.B., and Powell, R. 2011. "An Improved and Extended Consistent Thermodynamic Dataset for Phases of Petrological Interest, Involving a New Equation of State for Solids." *Journal of Metamorphic Geology*, 29, 333-383.
- Hummel, W.; Berner, U.; Curti, E.; Pearson, F.J.; and Thoenen, T. 2002. *Nagra/PSI Chemical Thermodynamic Data Base 01/01*. Parkland, Florida: Universal Publishers.
- Johnson, J.W.; Oelkers, E.H.; and Helgeson, H.C. 1992. "SUPCRT92: A Software Package for Calculating the Standard Molal Thermodynamic Properties of Minerals, Gases, Aqueous Species, and Reactions from 1 to 5000 Bar and 0 to 1000°C." *Computers & Geosciences*, 18, (7), 899-947. New York, New York: Pergamon Press.
- Kelley, K.K. 1932. *Contributions to the Data on Theoretical Metallurgy. I. Entropies of the Elements and Inorganic Substances*. United States Department of Commerce. Bureau of Mines Bulletin 350. United States Government Printing Office, Washington, DC. 149 p.
- Kelley, K.K., and King, E.G. 1961. *Contributions to the Data on Theoretical Metallurgy. XIV. Entropies of the Elements and Inorganic Compounds*. United States Department of the Interior. Bureau of Mines Bulletin 592. United States Government Printing Office, Washington, DC. 149 p.
- Lemire, R.J., Fuger, J., Nitsche, H., Potter, P., Rand, M.H., Rydberg, J., Spahiu, K., Sullivan, J.C., Ullman, W.J., Vitorge, P., and Wanner, H. 2001. *Chemical Thermodynamics of Neptunium and Plutonium. Chemical Thermodynamics. Volume 4*. New York, New York: Elsevier.
- Lewis, G.N., and Gibson, G.E. 1917. The Entropy of the Elements and the Third Law of Thermodynamics. *Journal of the American Chemical Society* 39, 2554-2581.

- Lewis, G.N., Gibson, G.E., and Latimer, W.M. 1922. A Revision of the Entropies of the Elements. *Journal of the American Chemical Society* 44, 1008-1017.
- McBride, B.J., Gordon, S., and Reno, M.A. 2001. Thermodynamic Data for Fifty Reference Elements. NASA Technical Paper 3287/REV1. National Aeronautics and Space Administration.
- Olin, A.; Noläng, B.; Öhman, L-O.; Osadchii, E.G.; and Rosén, E. 2005. Chemical Thermodynamics of Selenium. Mompean, F.J.; Perrone, J.; and Illemassène, M., eds. *Chemical Thermodynamics*. Volume 7. Amsterdam, The Netherlands: Elsevier.
- Pabalan, R.T. and Pitzer, K.S. 1987. "Thermodynamics of Concentrated Electrolyte Mixtures and the Prediction of Mineral Solubilities to High Temperatures for Mixtures in the System Na-K-Mg-Cl-SO₄-OH-H₂O." *Geochimica et Cosmochimica Acta*, 51(9), 2429-2443
- Pankratz, L.B. 1982. Thermodynamic Properties of Elements and Oxides. United States Department of the Interior, Bureau of Mines Bulletin 672. United States Government Printing Office, Washington, DC. 509 p.
- Pankratz, L.B., Stuve, J.M., and Gokcen, N.A. 1984. Thermodynamic Data for Mineral Technology. United States Department of the Interior, Bureau of Mines Bulletin 677. United States Government Printing Office, Washington, DC. 355 p.
- Parker, V.B., Wagman, D.D., and Evans. 1971. Selected Values of Chemical Thermodynamic Properties. Tables for the Alkaline Earth Elements (Elements 92 Through 97 in the Standard Order of Arrangement. National Bureau of Standards Technical Note 270-6. United States Government Printing Office, Washington, DC. 106 p.
- Parker, V.B. and Khodakovskii, I.L. 1995. "Thermodynamic Properties of the Aqueous Ions (2+ and 3+) of Iron and the Key Compounds of Iron." *Journal of Physical and Chemical Reference Data*, 24, (5), 1699-1745. Washington, D.C.: American Chemical Society.
- Pitzer, K.S. 1991. "Ion Interaction Approach: Theory and Data Correlation." Chapter 3 of *Activity Coefficients in Electrolyte Solutions*. 2nd Edition. Pitzer, K.S., ed. Boca Raton, Florida: CRC Press.
- Powell, R., and Holland, T.J.B. 1985a. "An Internally Consistent Thermodynamic Dataset with Uncertainties and Correlations: 1. Methods and a Worked Example." *Journal of Metamorphic Geology*, 3, 327-342. [The authors refer to this paper as "DS1".]
- Powell, R., and Holland, T.J.B. 1985b. "An Internally Consistent Thermodynamic Dataset with Uncertainties and Correlations: 3. Applications to Geobarometry, Worked Examples and a Computer Program." *Journal of Metamorphic Geology*, 6, 173-204. [The authors refer to this paper as "DS3".]
- Powell, R., and Holland, T.J.B. 1993a. "The Applicability of Least Squares in the Extraction of Thermodynamic Data from Experimentally Bracketed Mineral Equilibria." *American Mineralogist*, 78, 107-112.
- Powell, R., and Holland, T.J.B. 1993b. "On the Formulation of Simple Mixing Models for Complex Phases." *American Mineralogist*, 78, 1174-1180.

- Powell, R., and Holland, T.J.B. 2006. "Mineral Activity-Composition Relations and Petrological Calculations Involving Cation Equipartition on Multisite Minerals: A Logical Inconsistency." *Journal of Metamorphic Geology*, 24, 851-861.
- Rand, H., Mompean, F.J., Perrone, J., Illemassène, M., 2008. *Chemical Thermodynamics of Thorium*. OECD Publishing, 900 pp.
- Ransom, B. and Helgeson, H.C. 1993. "Compositional End Members and Thermodynamic Components of Illite and Dioctahedral Aluminous Smectite Solid Solutions." *Clays and Clay Minerals* 41(5), 537-550.
- Ransom, B. and Helgeson, H.C. 1994a. "Estimation of the Standard Molal Heat Capacities, Entropies, and Volumes of 2:1 Clay Minerals." *Geochimica et Cosmochimica Acta*, 58 (21), 4537-4547.
- Ransom, B. and Helgeson, H.C. 1994b. "A Chemical and Thermodynamic Model of Aluminous Dioctahedral 2:1 Layer Clay Minerals in Diagenetic Processes: Regular Solution Representation of Interlayer Dehydration in Smectite." *American Journal of Science* 294, 449-484.
- Ransom, B. and Helgeson, H.C. 1995. "A Chemical and Thermodynamic Model of Aluminous Dioctahedral 2:1 Layer Clay Minerals in Diagenetic Processes: Dehydration of Dioctahedral Aluminous Smectite as a Function of Temperature and Depth in Sedimentary Basins." *American Journal of Science* 295, 245-281.
- Rard, J.A., and Wolery, T.J., 2007. The Standard Chemical-Thermodynamic Properties of Phosphorus and Some of its Key Compounds and Aqueous Species: An Evaluation of Differences between the Previous Recommendations of NBS/NIST and CODATA, *Journal of Solution Chemistry*, v. 36, p. 1585-1599.
- Rard, J.A.; Rand, M.H.; Anderegg, G.; and Wanner, H. 1999. *Chemical Thermodynamics of Technetium*. Sandino, M.C.A., and Östholms, E., eds. *Chemical Thermodynamics* 3. Amsterdam, The Netherlands: Elsevier.
- Robie, R.A., and Waldbaum, D.R. 1968. *Thermodynamic Properties of Minerals and Related Substances at 298.15K (25.0°C) and One Atmosphere (1.013 Bars) Pressure and at Higher Temperatures*. U.S. Geological Survey Bulletin 1259, United States Government Printing Office, Washington, DC. 256 p.
- Robie, R.A., Hemingway, B.S. , and Fischer, J.R. 1978. *Thermodynamic Properties of Minerals and Related Substances at 298.15K and 1 Bar (105 Pascals) Pressure and at Higher Temperatures*. U.S. Geological Survey Bulletin 1452, United States Government Printing Office, Washington, DC. 456 p. [Reprinted with corrections, 1979]
- Robie, R.A., and Hemingway, B.S. 1995. *Thermodynamic Properties of Minerals and Related Substances at 298.15 K and 1 Bar (10⁵ Pascals) Pressure and at Higher Temperatures*. Bulletin 2131. Reston, Virginia: U.S. Geological Survey.
- Rodebush, W.H., and Rodebush, E. 1929. "Thermodynamic Quantities: Values of the Heat Capacity, Entropy, Heat Content and 'Thermodynamic Potential' for Pure Substances between 0 and 298°K." p. 84-91 in Washburn, E.W. (Editor-in-Chief). 1929. *International Critical Tables of Numerical Data, Physics, Chemistry and Technology*, Volume V.

Published for the National Research Council by McGraw-Hill Book Company, New York.
Digital accessibility at <http://chla.library.cornell.edu/c/chla/browse/title/2944761.html>.

- Rossini, F.D., Wagman, D.D., Evans, W.H., Levine, S., and Jaffe, I. 1952. Selected Values of Chemical Thermodynamic Properties. U.S. Department of Commerce, National Bureau of Standards. Circular of the National Bureau of Standards 500. United States Government Printing Office, Washington, DC. 1268 p.
- Schumm, R.H., Wagman, D.D. Bailey, S., Evans, W.H., and Parker, V.B., 1973. Selected Values of Chemical Thermodynamic Properties. Tables for the Lanthanide (Rare Earth) Elements (Elements 62 Through 76 in the Standard Order of Arrangement. National Bureau of Standards Technical Note 270-7. United States Government Printing Office, Washington, DC. 75 p.
- Silva, R.J.; Bidoglio, G.; Rand, M.H.; Robouch, P.B.; Wanner, H.; and Puigdomenech, I. 1995. Chemical Thermodynamics of Americium. Chemical Thermodynamics. Volume 2. Amsterdam, The Netherlands: Elsevier.
- Stull, D.R., and Sinke, G.C. 1956. Thermodynamic Properties of the Elements. Advances in Chemistry Series 18. American Chemical Society, Washington, DC
- Stull, D.R., and Prophet, H. 1971. JANAF Thermochemical Tables, Second Edition. United States Department of Commerce, National Bureau of Standards. NSRDS-NBS 37. United States Government Printing Office, Washington, DC. 1141 p.
- Tardy, Y., and Garrels, R.M. 1974. "A Method of Estimating the Gibbs Energies of Formation of Layer Silicates." *Geochimica et Cosmochimica Acta* 38(7), 1101-1116.
- Tardy, Y., and Duplay, J. 1992. "A Method of Estimating the Gibbs Free Energies of Formation of Hydrated and Dehydrated Clay Minerals." *Geochimica et Cosmochimica Acta* 56(16), 3007-3029
- Vieillard, P. 1994a. "Prediction of Enthalpy of Formation Based on Refined Crystal Structures of Multisite Compounds: Part 1. Theories and Examples." *Geochimica et Cosmochimica Acta* 58(19), 4049-4063.
- Vieillard, P. 1994b. "Prediction of Enthalpy of Formation Based on Refined Crystal Structures of Multisite Compounds: Part 2. Application to Minerals Belonging to the System $\text{Li}_2\text{O}-\text{Na}_2\text{O}-\text{K}_2\text{O}-\text{BeO}-\text{MgO}-\text{CaO}-\text{MnO}-\text{FeO}-\text{Fe}_2\text{O}_3-\text{Al}_2\text{O}_3-\text{SiO}_2-\text{H}_2\text{O}$. Results and Discussion." *Geochimica et Cosmochimica Acta*, 58(19), 4065-4107.
- Vieillard, P. 2000. "A New Method for the Prediction of Gibbs Free Energies of Formation of Hydrated Clay Minerals Based on the Electronegativity Scale." *Clay and Clay Minerals*, 48(4), 459-473.
- Wagman, D.D., Evans, W.H., Parker, V.B., Halow, I, Bailey, S.M., and Schumm, R.H. 1968. Selected Values of Chemical Thermodynamic Properties. Tables for the First Thirty-Four Elements in the Standard Order of Arrangement. National Bureau of Standards Technical Note 270-3. United States Government Printing Office, Washington, DC. 264 p.
- Wagman, D.D., Evans, W.H., Parker, V.B., Halow, I, Bailey, S.M., and Schumm, R.H. 1969. Selected Values of Chemical Thermodynamic Properties. Tables for Elements 35 Through

- 53 in the Standard Order of Arrangement. National Bureau of Standards Technical Note 270-4. United States Government Printing Office, Washington, DC. 141 p.
- Wagman, D.D., Evans, W.H., Parker, V.B., Halow, I., Bailey, S.M., Schumm, R.H. , and Churney, K.L. 1971. Selected Values of Chemical Thermodynamic Properties. Tables for Elements 54 Through 61 in the Standard Order of Arrangement. National Bureau of Standards Technical Note 270-5. United States Government Printing Office, Washington, DC. 37 p.
- Wagman, D.D., Evans, W.H., Parker, V.B., Schumm, R.H. , and Nuttall, R.L. 1981. Selected Values of Chemical Thermodynamic Properties. Compounds of Uranium, Protactinium, Thorium, Actinium, and the Alkali Metals. National Bureau of Standards Technical Note 270-8. United States Government Printing Office, Washington, DC. 134 p.
- Wagman, D.D.; Evans, W.H.; Parker, V.B.; Schumm, R.H.; Halow, I.; Bailey, S.M.; Churney, K.L.; and Nuttall, R.L. 1982. "The NBS Tables of Chemical Thermodynamic Properties, Selected Values for Inorganic and C₁ and C₂ Organic Substances in SI Units." *Journal of Physical and Chemical Reference Data*, 11, (Supplement No. 2), 2-276 - 2-282. Washington, D.C.: American Chemical Society.
- Wagman, D.D.; Evans, W.H.; Parker, V.B.; Schumm, R.H.; Halow, I.; Bailey, S.M.; Churney, K.L.; and Nuttall, R.L. 1989. "Erratum: The NBS Tables of Chemical Thermodynamic Properties, Selected Values for Inorganic and C₁ and C₂ Organic Substances in SI Units." *Journal of Physical and Chemical Reference Data*, 18, (4), 2-276 - 2-282, 1807-1812. Washington, D.C.: American Chemical Society.
- Walter, J.V., and Helgeson, H.C. 1977. Calculation of the thermodynamic properties of aqueous silica and the solubility of quartz and its polymorphs at high pressures and temperatures. *American Journal of Science* 277, 1315-1351.
- Wang, Y., Simpson, M., Painter, S., Liu, H.-H., and Kersting, A.B. 2011. Natural System Evaluation and Tool Development – FY11 Progress Report: Fuel Cycle Research and Development. Document FCRD-USED-2011-000223 (originated from Sandia National Laboratories).
- Wanner, H., 1999a. Guidelines For The Assignment Of Uncertainties (TDB-3), OECD-NEA, Issy-les-Moulineaux, France.
- Wanner, H., 1999b. Guidelines For The Independent Peer Review Of TDB Reports (TDB-6), OECD-NEA, Issy-les-Moulineaux, France.
- Wanner, H., Östholms, E., 2000. Standards and Conventions for TDB Publications, OECD-NEA, Issy-les-Moulineaux, France.
- Wolery, T.J., and Sutton, M. 2011. Generic Natural Systems Evaluation - Thermodynamic Database Development and Data Management. LLNL-TR-500113, Lawrence Livermore National Laboratory, Livermore, CA. [LLNL input to SNL milestone M41UF034002: Initiating Natural System Database Design]
- Wolery, T.J. 2012. FY12 Thermodynamic Properties Report: Thermodynamic Database Development, With Emphasis On Complex Clay Minerals. LLNL-TR-554331, Lawrence Livermore National Laboratory, Livermore, CA. [milestone M4FT-12LL0806041]

**Thermodynamic Modeling: Clay Hydration, Ion Exchange,
and First Principle Calculations of Mineral Thermodynamic
Properties at Elevated Temperatures**

(Part V)

1. Thermodynamic Modeling of Smectitic Clay Hydration: Na-Ca-Mg-K-Al-Si-H₂O System

Initial work on the thermodynamic modeling of smectite clay hydration was described in Jové Colón et al. (2012) advancing results for a Na-smectite. The current analysis was expanded to other smectite end-member compositions defined by most common monovalent and divalent cations in clay such as K, Ca, and Mg. This section will also describe the application of this modeling approach in the prediction of smectite molar volumes as a function of relative humidity which determines the extent of swelling pressures in the barrier material. For completeness, a description of the importance of swelling clay to EBS and the thermodynamic modeling methodology will be yet again described in this part of the report with some modifications.

Clay swelling properties such as that observed for bentonite plays a key role in EBS performance since these materials can comprise the main barrier component in the near- and far-field domains. For this reason, clay barrier materials have a high degree of exposure to thermal, mechanical, and hydrological (i.e., THM) phenomena in nuclear waste repository environments. The swelling behavior of bentonite clay and water transport through this barrier material has been identified by various repository research programs as key aspects of the barrier performance (Karnland, 1997; Karnland et al., 2007; Kim et al., 2011). Among the most important geomechanical characteristic of bentonite clay in nuclear waste disposal concepts is the ability to swell in response to hydration which induces sealing and self-healing of potential fast flow paths structures such as joints and cracks therefore decreasing bulk permeability (Kim et al., 2011). Another important property is the ability of clays to sorb aqueous species providing also a chemical barrier to contaminant transport. On the other hand, clay expansive properties can be undesirable during backfill emplacement due to material cracking and phase disaggregation when exposed to moisture (Dueck et al., 2008). Moreover, hydro-mechanical properties of the swelling clay can be affected by varying levels of saturation and elevated temperatures (Akesson et al., 2009; Dueck et al., 2008; Karnland et al., 2008). It is expected that the clay backfill material will remain relatively unsaturated during most of the repository post-closure performance period, even at various levels of episodic resaturation. Many experimental studies of clay barrier materials have been conducted at various scales including full-scale *in situ* heating tests (Fernandez and Villar, 2010; Gens et al., 2009; Samper et al., 2008; Sanchez et al., 2010, 2012; Villar et al., 2007). Other studies have been focused on clay swelling behavior at a smaller (mineral) scale to better understand conditions in geologic environments (Dueck et al., 2008; Karnland, 1997; Karnland et al., 2007; Liu and Lin, 2005; Ransom and Helgeson, 1995). Knowledge of clay thermodynamic properties is critical to the evaluation and prediction of the smectite clay phase stability relations when assessing their interaction with fluids. As a result of these interactions, swelling generates changes in the smectite volume that could significantly affect the stability of the clay phase. Moreover, the few experimental data sets for swelling clay hydration are limited to a few compositions and ambient temperatures. This calls for the need of developing models to evaluate clay swelling in response to hydration exploiting the use of chemical equilibrium and thermodynamic relations along with the existing data to make predictions about clay stability and phase equilibria (Ransom and Helgeson, 1994a, b, 1995; Vidal and Dubacq, 2009; Vieillard et al., 2011). Such a model can be used to describe the non-linear volumetric behavior of smectite swelling based on existing clay hydration studies. Further, it could serve as the basis for the description of swelling pressures of a “free” or unconfined expansive clay as a function of relative humidity (RH) and solid composition.

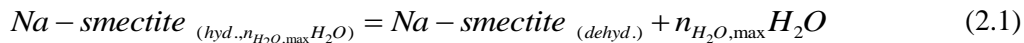
2. Thermodynamic Modeling Using the Cantera Code Suite

Cantera is a general purpose open-source object-oriented constitutive modeling toolkit to simulate problems related to chemical thermodynamics, kinetics, and transport processes (Moffat and Jové Colón, 2009). Cantera can perform similar types of equilibrium speciation calculations as those obtained from computer codes using mass action law formulations (e.g., EQ3/6) in aqueous systems and also simulate interactions between solution, solid, and gas phases. The GEM approach is used by Cantera to compute chemical equilibrium between the considered phases having a distinct set of properties and constituents (Karpov et al., 1997; Kulik et al., 1998; Smith and Missen, 1982). That is, Cantera is based on the specification of chemical potentials for all species in all phases instead of invoking prescribed input mass action law reactions. Chemical equilibria is computed by minimizing the total Gibbs energy of the system through optimization of component abundances using the Villars-Cruise-Smith (VCS) approach, described in detail by Smith and Missen (1982).

Cantera being object-oriented (C++) provides for a versatile and yet robust environment for the use and application of class objects to various types of thermodynamic problems adding the much needed flexibility in code development to evaluate specific processes. Cantera also accepts various types of thermodynamic data inputs including those consistent with the buildup of the EQ3/6 thermodynamic databases including parameters for the Helgeson-Kirkham-Flowers (HKF) equation of state (EoS) (Shock and Helgeson, 1988) used in calculations of thermodynamic properties of aqueous species at elevated pressures and temperatures. It also includes EoS expressions and parameters for the thermodynamic and volumetric properties of liquid and gas phases. For example, the International Association for the Properties of Water and Steam (IAPWS) Equation-of-State (EoS) formulation for H₂O by Wagner and Prúß (2002) is included in Cantera to compute the thermodynamic and volumetric properties of H₂O as a function of temperature and pressure.

2.1 Modeling Approach and Discussion

Estimation methods for the thermodynamic properties of clays have been developed capturing the compositional properties of layered silicates. Ransom and Helgeson (1994a, 1995) developed a solid solution mixing model to describe the hydration/dehydration of smectite clay solely based on the H₂O content within the interlayer region. No other sheet components in the smectite mineral structure are exchanged in the hydration/dehydration process making it suitable for studying partially saturated clay (Vieillard et al., 2011). The approach of Ransom and Helgeson (1994a, 1995) is based on a regular solid solution mixing between hydrated and dehydrated end-member components allowing for the application of mixing thermodynamic formalisms to describe chemical equilibria as a function of clay hydration. Their model can be expressed by the following reaction for Na-smectite dehydration:



where $Na - smectite_{(hyd., n_{H_2O, max} H_2O)}$ and $Na - smectite_{(dehyd.)}$ delineate the fully hydrated and dehydrated Na-smectite, respectively. $n_{H_2O, max}$ stands for the maximum number of moles of H₂O in the clay structure. The mass action law expression for reaction 2.1 is given by:

$$K = \frac{a_{Na-smectite (dehyd.)} a_{H_2O}^{n_{H_2O,max}}}{a_{Na-smectite (hyd., n_{H_2O,max} H_2O)}} \quad (2.2)$$

where the $a_{Na-smectite (dehyd.)}$ and $a_{Na-smectite (hyd., n_{H_2O,max} H_2O)}$ are the activities of the dehydrated and hydrated Na-smectite phase, respectively. Similarly, reaction (2.1) applies to smectitic clays having other cationic composition such as K, Ca, and Mg. a_{H_2O} denotes the activity of H₂O in the aqueous phase. The treatment of a_{H_2O} by Ransom and Helgeson (1994a) is to directly equate this parameter to the RH given by the clay swelling experimental data. Such equivalent designation of RH with a_{H_2O} is consistent with the liquid standard state reference for H₂O.

Other clay hydration models have been advanced (Vidal and Dubacq, 2009; Vieillard et al., 2011), however, their modeling basis is still consistent with the fundamental treatment of Ransom and Helgeson (1994a). Vidal and Dubacq (2009) developed a model based on the gradual stepwise evolution of clay dehydration using a non-ideal solid solution mixing model between a mica phase and smectite clay at various hydration levels (0.7, 2, 4, and 7 moles H₂O per O₁₀(OH)₂ in the interlayer region). In this model, the hydration levels correspond to the number of water layers in the clay interlayer domain. The model is parameterized in accord with estimations of thermodynamic properties of anhydrous and hydrous clays and hydration/dehydration experimental data from the literature. Vieillard et al. (2011) advanced a model also based on that by Ransom and Helgeson (1994a, 1995) consistent with hydration/dehydration data using the Margules formalism to represent a non-ideal solid solution between the anhydrous and hydrous smectite clay end-members. Their approach also accounts for the treatment of all thermodynamic entities (G° , H° , S°) in the evaluation of the excess Gibbs energy of mixing. Their model is also validated against experimental data for hetero- and homo-ionic smectites at different temperatures. All these models, even with their differences, provide a reasonable representation of the existing experimental data of smectite hydration behavior and related thermodynamic properties.

The model developed in the current study closely follows the approach of Vieillard et al. (2011) using the Margules formalism to represent a non-ideal solid solution or mixing between hydrated and dehydrated smectite clay end-members given by Equations (2.3) through (2.5) to compute chemical equilibrium between smectite and H₂O phase as a function of RH:

$$H^{EX} = X_{smect. hyd.} X_{smect. dehyd.} (W_{H1} + W_{H2} X_{smect. dehyd.}) \quad (2.3)$$

$$S^{EX} = X_{smect. hyd.} X_{smect. dehyd.} (W_{S1} + W_{S2} X_{smect. dehyd.}) \quad (2.4)$$

$$G^{EX} = H^{EX} - TS^{EX} \quad (2.5)$$

G^{EX} , H^{EX} , and S^{EX} are the excess Gibbs energy, enthalpy, and entropy for the smectite solid mixed phase. $X_{smect. hyd.}$ and $X_{smect. dehyd.}$ represent the mole fractions of hydrated and dehydrated smectite end-members, respectively. W_{H1} and W_{H2} correspond to the Margules parameters for the enthalpy term. Similarly, W_{S1} and W_{S2} denotes the Margules parameters for the entropy term. The model is implemented using the Cantera code suite for computation of chemical equilibria and a description is given in Section 1.1, and Moffat and Jové Colón (2009). It was

implemented in the form of C++ code that explicitly accounts for the thermodynamic properties of the clay solid solution (including end-members) and the gas state of H₂O when computing chemical equilibria as a function of RH. Therefore, the properties of all phases are properly captured in the computation of Gibbs energies by the GEM method in Cantera. The treatment of the H₂O phase in this work is different from that in Ransom and Helgeson (1994a, 1995), Vidal and Dubacq (2009), and Vieillard et al. (2011). Here the smectite solids interact with the stable phase of H₂O in the gas phase at the partial pressures and temperature that corresponds to the RH conditions in the experiments and delineated by the data. This treatment is important as to ensure thermodynamic consistency with the stable H₂O phase corresponding to the experimental methods when defining the theoretical equilibrium relations of this process.

The thermodynamic properties (H° and S°) of the Na-smectite at 25°C is that of dehydrated Na end-member beidellite obtained from thermodynamic estimations described in Jové Colón et al. (2012). Since the current model is developed to be closely consistent with that of Vieillard et al. (2011), the properties of the hydrated clay end-member were retrieved to be partially consistent with those of their work. H° and S° for hydrated end-member were retrieved by using the enthalpy (ΔH_{hyd}°) and entropy of hydration (ΔS_{hyd}°) given in Vieillard et al. (2011) and those for dehydrated Na beidellite described in this report. The computation of the number of moles of H₂O per O₁₀(OH)₂ (clay half-cell) or $n_{H_2O,il}$ in the clay interlayer is given by:

$$n_{H_2O,il} = X_{Na-beid,hyd} n_{H_2O,max} \quad (2.9)$$

where $X_{Na-beid,hyd}$ denotes the mole fraction of hydrated Na beidellite component. The value of $n_{H_2O,max}$, is still a matter of debate. Vidal and Dubacq (2009) adopts a value of 7 whereas Ransom and Helgeson (1994a) estimated a value of 4.5. The value of 5.5 adopted by Vieillard et al. (2011) was based on the attainment of adequate fits to the adsorption/desorption data for the considered clay compositions. For consistency with Vieillard et al. (2011), the adopted value of $n_{H_2O,max}$ in this study is taken as 5.5. It should be noted that the Grand Canonical Monte Carlo (GCMC) and molecular dynamic (MD) simulations described in part VI of this report predict $n_{H_2O,max}$ value of 4.5, in excellent agreement with the work Ransom and Helgeson (1994a). The thermodynamic and physical properties of H₂O are computed using the IAPWS EoS formulation by Wagner and Pruß (2002) implemented in Cantera. The computation of RH is performed by specifying the partial pressure ($P_{H_2O,gas}$) and mass of H₂O (treated as a pure phase) in linear increments until saturation (i.e., RH \approx 1) is reached. RH is calculated at 25°C from the ratio of H₂O gas density ($\rho_{H_2O,gas}$) to that of this phase at saturation ($\rho_{H_2O,gas,sat}$). This is equivalent to the ratio of H₂O partial pressure ($P_{H_2O,gas}$) multiplied by the fugacity coefficient (χ_{H_2O}) to that of H₂O partial pressure at saturation ($P_{H_2O,sat}^\circ$):

$$RH = a_{H_2O} = \frac{f_{H_2O}}{P_{H_2O,sat}^\circ} = \frac{\chi_{H_2O} P_{H_2O}}{P_{H_2O,sat}^\circ} = \frac{\rho_{H_2O,gas}}{\rho_{H_2O,gas,sat}} \quad (2.10)$$

where $\rho_{H_2O,gas}$ is computed from the IAPWS EoS in Cantera at each increment in pressure for each equilibrium step in the calculation. The regression analysis to retrieve the Margules parameters was conducted using the DAKOTA (Adams et al., 2012) optimization package along

with iterative analyses to evaluate and adjust the Margules terms and S° of the hydrated smectite end-member. The adjustment of the S° parameter the hydrated Na-smectite end-member was needed to refine the data fitting through the entire RH range. However, these adjustments were relatively minimal relative to the expected values for the Na smectite hydrated end-member used in this study. The optimization procedure consisted of minimization of least squared differences between model prediction and reported isotherm data in the form of an objective function using a nongradient-based optimization routine in the DAKOTA SCOLIB library (Adams et al., 2012). The experimental data of Cases et al. (1992) and Berend et al. (1995) as reported by Vieillard et al. (2011) and model fits described therein were used in the isotherm fitting procedure.

The experimental data given by Cases et al. (1992) and Berend et al. (1995) was corrected by Vieillard et al. (2011) for H₂O surface coverage as a function of RH. Ransom and Helgeson (1994a, 1995) describe the hysteretic behavior of H₂O adsorption and desorption isotherms as non-representative of an equilibrium state for these processes. This is based on the definition of chemical equilibrium as applied to clay swelling requiring the derivatives of their thermodynamic properties are exact differentials by definition. The two isotherms can then be used as reversal bounding limits to “bracket” the retrieval of equilibrium values for the Margules parameters. The theoretical equilibrium curve was obtained by computing the mean values of the Margules parameters between the adsorption/desorption curves closely corresponding to that given by Vieillard et al. (2011). The Margules parameter values given by Vieillard provided good initial points to the fitting strategy yielding the shape of the isotherm curves but shifted from the actual data likely due to differences in end-member thermodynamic data. Figures 2.1 through 2.4 show the Cantera results for the adsorption, desorption, and theoretical equilibrium curves for Na, K, Ca, and Mg smectites. Overall, the modeling results are in excellent agreement with the sigmoidal fits obtained by Vieillard et al. (2011). Overall, fitting of the desorption data at low RH values for most smectites was not possible due to limitations of the Margules two-term formulation to retrieve fitting parameters that could represent $n_{H_2O,il}$ through the whole RH range. The curves for divalent cations (Ca, Mg) smectites consistently show larger number of interlayer waters relative to monovalent cation (Na, K). This behavior is consistent with other clay swelling studies where Ca-Mg smectite exhibit more swelling relative to that of Na smectite (Likos and Wayllace, 2010). The analysis for Mg-smectite was done for two data sets reported by Vieillard et al. (2011). According to Vieillard et al. (2011), the reason for evaluating two data sets has to do with reproducibility issues in the original data.

Thermodynamic Analysis of Smectite Volumetric Properties

The thermodynamic model implementation described above allows for evaluation of clay hydration to advance predictions on the stability relations of these phases as a function of relative humidity at ambient temperatures. This approach also permits the retrieval of other smectite clay properties such as molar volumes as a function of RH. The computation of clay molar volumes can be related to the equilibrium mole fractions of hydrated and dehydrated smectite as obtained in fitting the isotherms and the end-member molar volumes:

$$V_{RH}^\circ = X_{smect. hyd.} V_{E-M, smect. hyd.}^\circ + X_{smect. dehyd.} V_{E-M, smect. dehyd.}^\circ \quad (2.11)$$

V_{RH}° is the molar volume of the bulk smectite phase, $V_{E-M, smect. hyd.}^\circ$ and $V_{E-M, smect. dehyd.}^\circ$ stand for the molar values of the hydrated and dehydrated beidellite end-members, respectively. The mole fractions

$X_{smect. hyd.}$ and $X_{smect. dehyd.}$ are computed by the Cantera equilibrium model as a function of RH. The values for $V_{E-M, smect. dehyd.}^{\circ}$ and $V_{E-M, smect. hyd.}^{\circ}$ are 133.13 cm³/mol and 210.21 cm³/mol, respectively, and were retrieved from the MD simulations described in part V of this report. These values were adopted for all the considered smectite compositions. As mentioned previously, the value of 210.21 cm³/mol for $V_{E-M, smect. hyd.}^{\circ}$ corresponds to $n_{H_2O, max}$ equal to 4.5. Alternatively, values for $V_{E-M, smect. dehyd.}^{\circ}$ can be obtained from the clay thermodynamic database development described in part IV of Jové Colón et al. (2012) whereas $V_{E-M, smect. hyd.}^{\circ}$ is reported by Vidal and Dubacq (2009) for various clay phases. The values listed by Vidal and Dubacq (2009) for $V_{E-M, smect. hyd.}^{\circ}$ is 256 cm³/mol for $n_{H_2O, max}$ equal to 7. The larger $V_{E-M, smect. hyd.}^{\circ}$ can be ascribed to also a larger $n_{H_2O, max}$ relative to that obtained from MD simulations. It should be noted that the Cantera simulations and fitting of isotherm data were conducted assuming an $n_{H_2O, max}$ value of 5.5. Although there might be a slight inconsistency between the adopted $n_{H_2O, max}$ value of 4.5 (MD simulations) for $V_{E-M, smect. hyd.}^{\circ}$ and that of 5.5 used in the Cantera simulations, the resulting effect on the computed molar volumes should be minor and would not affect the shape of the volumetric profile as a function of RH.

Figure 2.5 shows the computed molar volumes for each of the beidellite compositions considered in this study. These curves are solely based on the theoretical equilibrium isotherms. Bounding adsorption/desorption isotherm curves can be easily calculated but were omitted from the figure for clarity. As expected, the volumetric curve profiles for the smectite compositions map the hydration/dehydration curve as a function of RH. There is also a clear consistency between the molar volume predictions and smectite clay swelling behavior observed in other studies. This is exemplified by the overall larger molar volumes observed in divalent relative to monovalent cation smectites, particularly for K-beidellite. The latter is known to not swell much relative to Na-beidellite and the divalent cation beidellites due to the low hydration affinity in the clay interlayer.

The implication of this thermodynamic analysis for the volumetric properties of swelling clay is that it can be related to “free” or unconfined state of this phase. Some models have been proposed to account for volumetric changes or expansion of the clay phase as a function of RH and/or its relationship to suction (Likos and Lu, 2006; Likos and Wayllace, 2010; Tang and Cui, 2009, 2010). For example, the work of Likos and Lu (2006) and Likos and Wayllace (2010) focuses on developing methods to evaluate and predict changes in clay volume and swelling pressure phenomena through couple interactions in the clay phase at multiple scales. The expansive BBM described in part II of this report is another example. Other studies have been focused on this type of multi-scale coupled interactions to capture these type complexities in swelling clay media (Murad, 1999a, b, 2010; Murad et al., 1995; Murad and Cushman, 1997, 2000). Given that RH and temperature strongly influences coupled chemo-mechanical processes in the EBS, expansion and refinement of current THM models need to incorporate information from thermodynamic models to accurately represent complex swelling phenomena within relevant periods of repository performance.

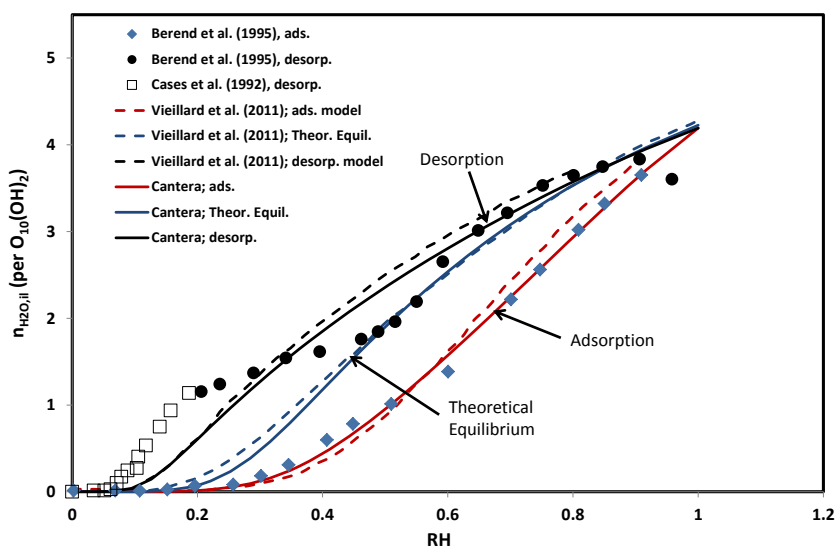


Figure 2.1. Plot of the of the number of moles of H_2O (per $\text{O}_{10}(\text{OH})_2$) ($n_{\text{H}_2\text{O},il}$) for the Na-smectite clay interlayer versus RH for adsorption/desorption experimental and computed isotherms using Cantera. Notice the excellent agreement between the computed and model isotherms of Vieillard et al. (2011) for adsorption, desorption, and theoretical equilibrium.

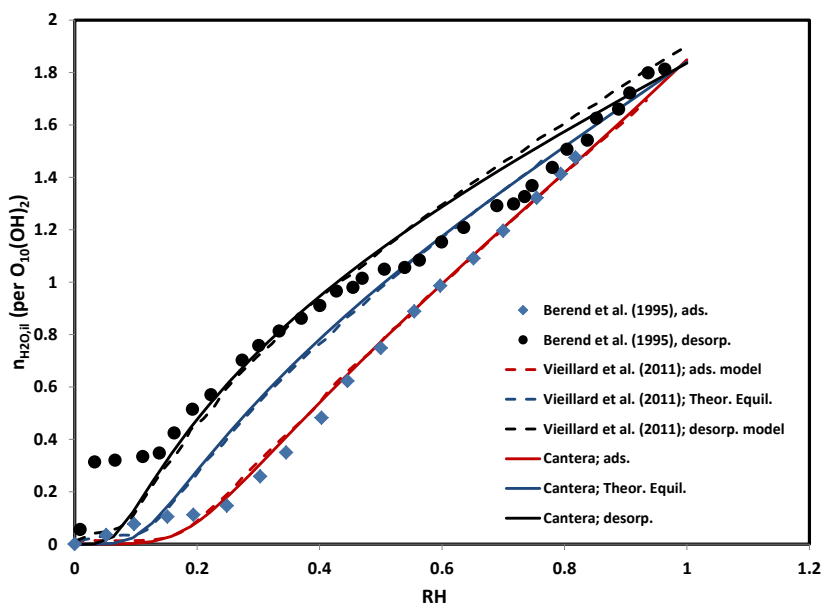


Figure 2.2. Plot of the of the number of moles of H_2O (per $\text{O}_{10}(\text{OH})_2$) ($n_{\text{H}_2\text{O},il}$) for the K-smectite the clay interlayer versus RH for adsorption/desorption experimental and computed isotherms using Cantera. Symbols for adsorption, desorption, theoretical equilibrium curves as in Figure 2.1.

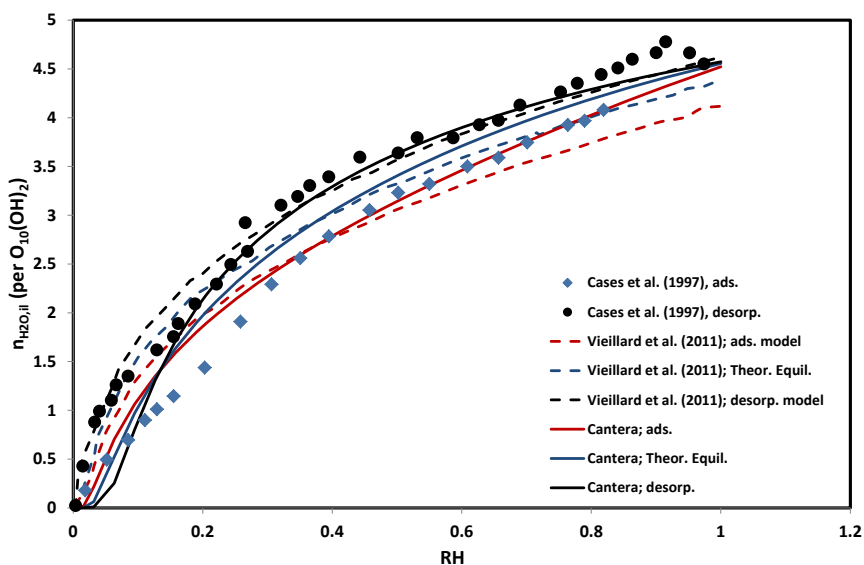


Figure 2.3. Plot of the of the number of moles of H₂O (per O₁₀(OH)₂) ($n_{H_2O,il}$) for the Ca-smectite the clay interlayer versus RH for adsorption/desorption experimental and computed isotherms using Cantera. Symbols for adsorption, desorption, theoretical equilibrium curves as in Figure 2.1. Notice the different extent of hydration between monovalent Na and K smectites.

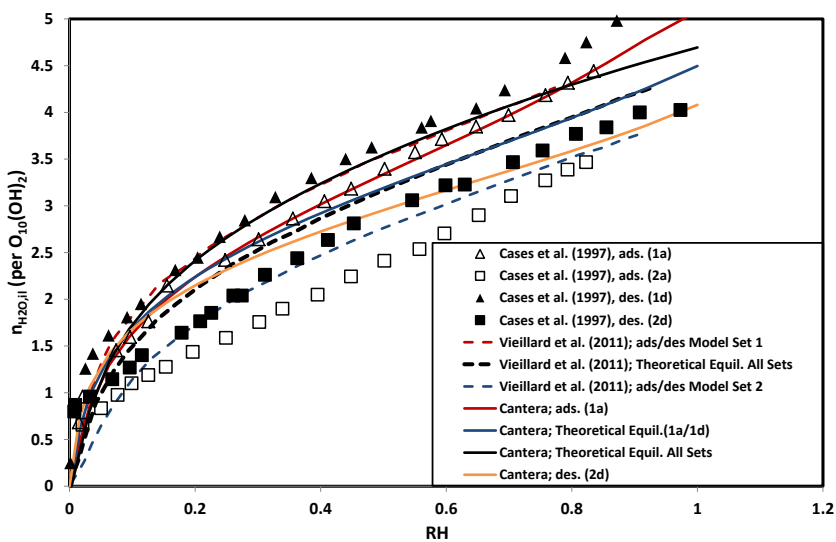


Figure 2.4. Plot of the of the number of moles of H₂O (per O₁₀(OH)₂) ($n_{H_2O,il}$) for the Mg-smectite the clay interlayer versus RH for adsorption/desorption experimental and computed isotherms using Cantera. Symbols for adsorption, desorption, theoretical equilibrium curves as in Figure 2.1. Notice that there are two sets of fits for each experimental data set (see text).

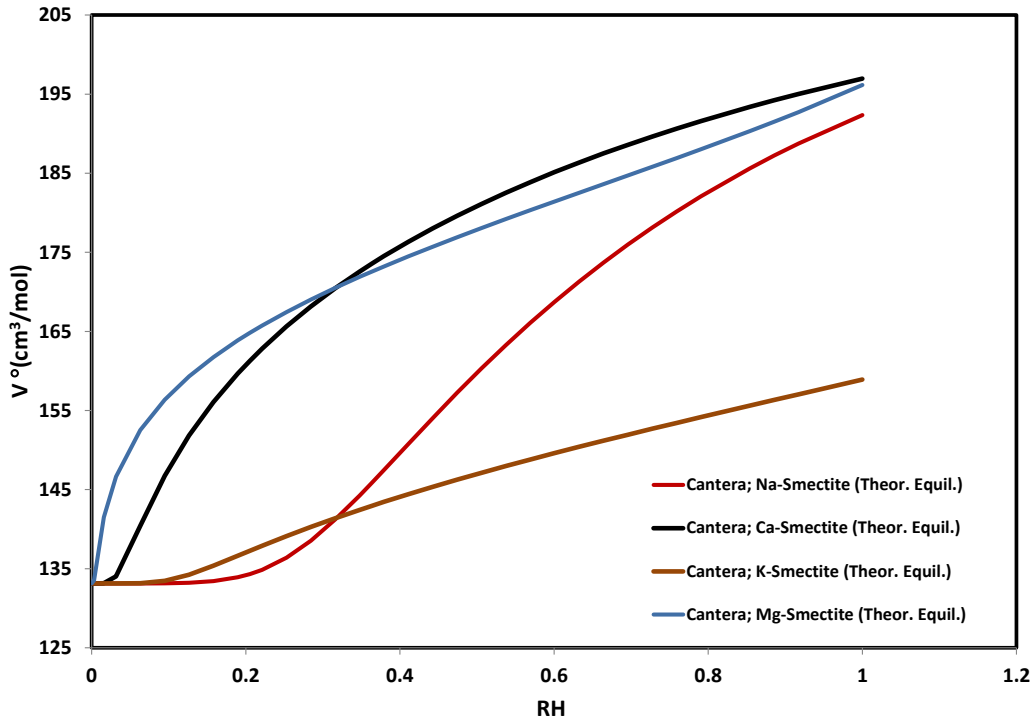


Figure 2.5. Computed molar volumes for each of the beidellite compositions considered in this study. The depicted curves are solely based on the theoretical equilibrium isotherms.

Thermodynamic Analysis of Smectite Ion Exchange

Minerals such as clay and zeolites exhibit cation exchange properties that are important to barrier performance given its controls on contaminant mass transport and sorption processes during interactions with aqueous solutions (Fletcher and Sposito, 1989b; Pabalan, 1994; Tournassat et al., 2011). The literature on clay ion exchange is rather extensive particularly in soil science research and the reader is referred to the works of Sposito (1984, 2008). Clay material in particular is a major component of the EBS and sorption plays a crucial role in hindering radionuclide transport in the near- and far-field regions.

The previous section describes the application of the Cantera Margules representation to the simulation of clay hydration/dehydration as a function of RH. Similarly, the same approach will be exploited here to describe Na-Ca cation exchange in clay as function of Na^+ concentration on the basis of a solid solution mixing and excess thermodynamic quantities. Thermodynamic modeling of ion exchanged using the Margules approach has been previously used by Pabalan (1994) for cation exchange in the zeolite mineral clinoptilolite. It should be noted that other methods in the modeling of cation exchange have been adopted in clays such as the Gaines-Thomas and the use of Vanselow selectivity coefficients (Tournassat et al., 2011). The cation exchange equilibrium reaction can be simply written as:



The cation exchange data to develop this approach is from Sposito et al. (1983a) and (Sposito et al., 1983b). The data is given in the form of equivalent charge fractions for the solid (E_{Na}) and solution (\tilde{E}_{Na}) defined by (Sposito et al., 1983a; Tournassat et al., 2011):

$$E_{Na} = \frac{n_{Na}}{n_{Na} + 2n_{Ca}} \quad (2.13)$$

$$\tilde{E}_{Na} = \frac{[Na^+]}{0.05} \quad (2.14)$$

where n_{Na} and n_{Ca} are the moles of Na and Ca in the exchanger phase, respectively. $[Na^+]$ denotes the aqueous concentration of Na^+ and the value of 0.05 stands for the total normality of the solution. Na- and Ca-beidellite end-members with thermodynamic data reported in Jové Colón et al. (2012) were used in the development of this model. The Margules parameters were iteratively adjusted to bound the fits in incremental steps of \tilde{E}_{Na} to the experimental data (Sposito et al., 1983a; Sposito et al., 1983b). Figure 2.6 shows the modeling results in very good agreement with the experimental data. The use of the Margules approach to model solid solution mixing can be applied to various types of geochemical processes with Cantera. Such a modeling methodology can be expanded to multicomponent multiphase phase equilibria in a complex system as observed in clay interactions with other barrier materials at EBS interfaces.

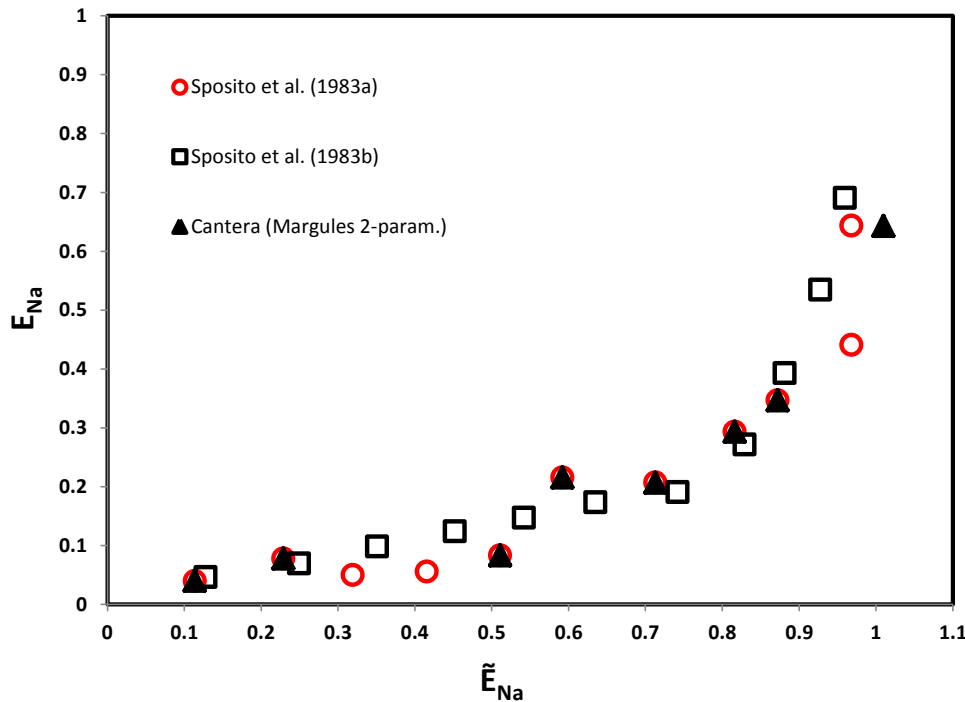


Figure 2.6. Plot of equivalent charge fractions for the clay solid and aqueous solution of Na-Ca cation exchange.

Thermodynamic Modeling of Surface Complexation

Another application of sorption modeling with Cantera is to represent surface complexation reactions on a mineral surface. There are several approaches to conduct this type of surface complexation modeling (SCM) but the most commonly adopted ones (whether electrostatic or non-electrostatic) is through the use of intrinsic surface complexation constants capturing the effects of mineral surface charge and background electrolyte concentration on solute adsorption (Davis et al., 1998; Davis and Kent, 1990; Dzombak and Morel, 1990; Goldberg and Criscenti, 2008; Goldberg et al., 2007). Although these types of approaches have been widely used in the evaluation of sorption data, there is the inherent limitation of unifying these with established thermodynamic concepts used to describe fluid-mineral equilibria in geochemical modeling. This limiting aspect in solution-mineral equilibrium and solute adsorption coupling is described in detail by Kulik (2002) and Kulik (2009). The main hurdle in linking these concepts lies in delineating reference and/or standard states of adsorbed species along with the “surface phase” to conform with thermodynamic definitions adopted in chemical equilibria. For example, interactions with surfaces are usually defined by a finite number of available sites for reaction for a given mass of sorbent. Then, the issue is reaching consensus on the amount of surface sites recognized as a reference state in which surface thermodynamic properties of adsorbed species for a particular type surface solid can then be defined. Moreover, these quantities need to be described within a thermodynamically consistent framework of properties between aqueous, solids, and adsorbed species along with standard thermodynamic data of the elements. Another difficulty is that surface complexation models can have variants for which intrinsic complexation reactions, surface parameters, and related constants are specific to the model. However, there have been some studies advancing methodologies to define standard states of mineral surfaces and adsorbed species consistent with surface complexation modeling (Kulik, 2002; Sverjensky, 2003).

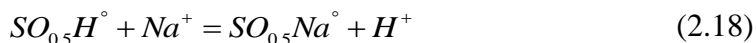
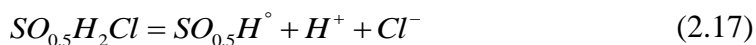
Cantera has been used to conduct surface thermodynamic modeling of surface growth through chemical vapor deposition process. Using Cantera object-oriented structure, a non-electrostatic surface complexation has been developed and tested in the modeling of surface charge data for rutile (TiO_2) as a function of pH. The reason for choosing this oxide is because the relatively large set of experimentally-derived surface speciation data mainly from the same research group (Machesky et al., 1998; Ridley et al., 1999). The Cantera surface complexation model implementation is composed of two parts (see Figure 2.7):

- Pitzer class to model aqueous phase speciation using the Pitzer thermodynamic approach
- A surface kinetics class uses a pseudo-state-state kinetic method to achieve equilibrium concentrations of surface species.

This is an example of a combined equilibrium aqueous speciation passing information to a surface kinetics model built using an object-oriented computational tool. The model is coded to run in a titration mode starting at pH~2.5 up to pH~9. First, the solution chemistry is speciated using the Pitzer object and then the aqueous concentrations is passed to the relevant species in the surface kinetic reactions defined in the next paragraph.

The model implementation requires a fixed site density taken as $2.0\text{e-}10$ mol/cm² consistent with the total surface site density advanced by Kulik (2002) in his standard state definition of surface

species. The pseudo state-state method is defined by the forward kinetics of four surface complexation reactions based on Kulik (2002):



Initial values for thermodynamic data for the surface species (those beginning with “S”) in reactions 2.15 to 2.18 were taken from Kulik (2000). The standard entropies were retained as those from Kulik (2000) but the enthalpies were adjusted to fit the surface charge data for rutile. The forward rates for each reaction were arbitrarily set to one. Figure 2.8 shows the results of the surface charge modeling of rutile in good agreement within the bounds of the experimental data sets. Multiple iterations in the data fitting exhibit a large degree of robustness demonstrated by the highly stable computation of steady-state surface concentrations. These results are promising given that this is an initial implementation of this thermodynamic modeling approach. There are some deviations from the data trend between pH~6 to pH~7. It was difficult to get a better fit to in this pH region without compromising other fitted parts of the surface charge profile. Maybe addition of other surface reaction and/or other surface species are needed to further evaluate this deviations. It should be also noted that fitting the data beyond pH 9 is also difficult since the trend flattens at pH~9. As mentioned previously, further evaluation using a larger set of surface complexation reactions including those involving solutes.

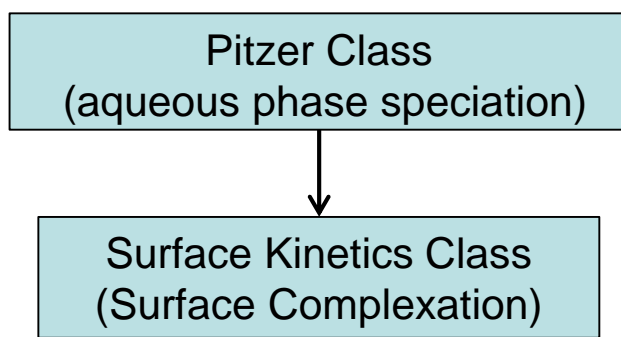


Figure 2.7. Cantera structure of the thermodynamic implementation of a surface complexation model based on steady-state surface kinetics.

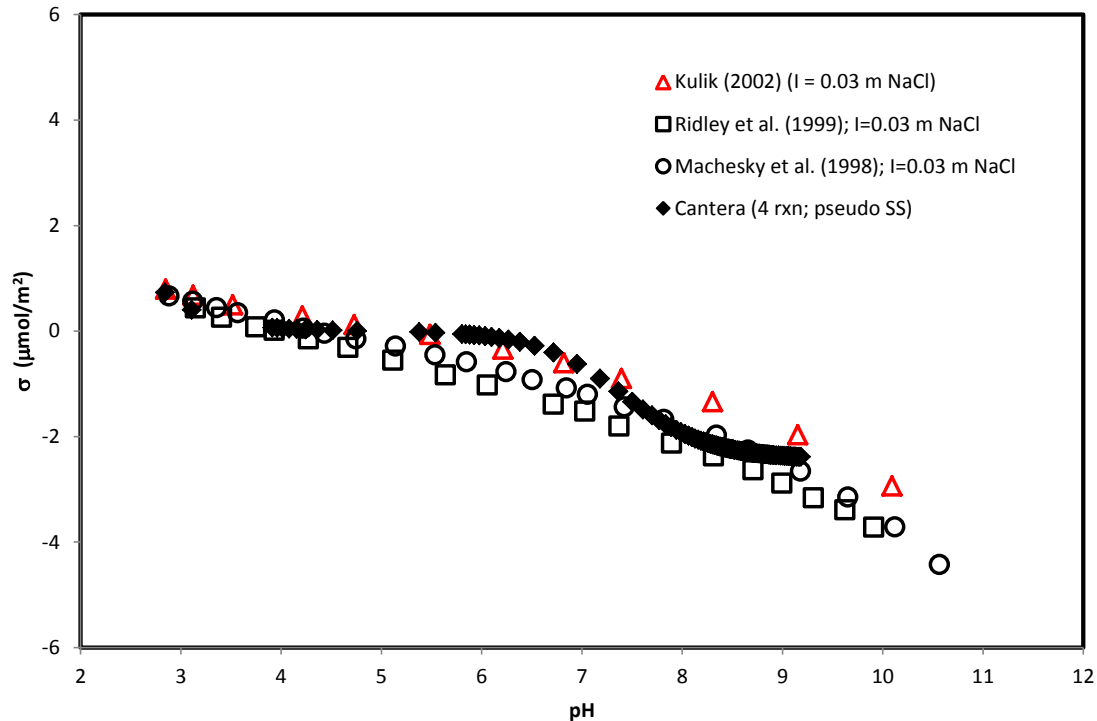


Figure 2.8. Cantera prediction of the surface charge profile for rutile (TiO_2) as a function of pH. The shown experimental data was used to bound the thermodynamic parameter fitting of the surface species.

3. Generating Thermodynamic Data for Geochemical and Used Fuel Degradation Models: A First-Principles Study of Salt Minerals

3.1 Background

Thermodynamic parameters for engineered barrier systems (EBS) materials and natural system (NS) minerals are critical to assess their stability and behavior in geologic used nuclear fuel disposal environments for safety assessments. In particular, thermodynamic data gaps and research needs exist regarding the NS minerals surrounding the waste package (e.g. complex salts, clays, granite...).

The main objectives of the present investigation are to use first-principles methods (without the need for any experimental input) to:

- Calculate missing thermodynamic data needed for EBS and NS models, as a fast, systematic, and early way to avoid using expensive and time-consuming real materials and to complement experiments.
- Provide an independent assessment of existing experimental thermodynamic data and resolve contradictions in existing calorimetric data.
- Validate our computational approach using high-quality calorimetric data.

In particular, understanding the structure–properties relationship of individual, defect-free salt minerals is a crucial first step toward deciphering and predicting the complex thermal behavior of mixed-salt systems for nuclear waste disposal in geological repositories in salt formations.

In this study, we report density functional calculations of the thermal properties of crystalline anhydrite (CaSO_4), bischofite ($\text{MgCl}_2 \cdot 6\text{H}_2\text{O}$) and polyhalite ($\text{K}_2\text{SO}_4 \cdot \text{MgSO}_4 \cdot 2\text{CaSO}_4 \cdot 2\text{H}_2\text{O}$) carried out within the generalized gradient approximation. Our approach consists of using salt mineral structures previously optimized using density functional theory (DFT) (Weck et al., 2013) and utilizing density functional perturbation theory (DF-PT) to calculate the phonon and thermal properties of these minerals for further comparison with calorimetric data.

Marine evaporites tend to form thick salt dome basins or bedded salts deposits and are usually the focus of extensive research and mining activities. All evaporites are ionic salts containing the major ions Na^+ , Ca^{2+} , Mg^{2+} , K^+ , Cl^- , SO_4^{2-} and CO_3^{2-} in varying proportions, along with structural water and other less common ionic constituents (e.g., Ba^{2+} , Sr^{2+} , Br^- , Li^+ , I^- and $\text{B}(\text{OH})_4^-$) with various degrees of coordination. Approximately eighty different 14 salt minerals have been identified in evaporite deposits, although only a few are considered important rock formers (Stewart, 1963, Warren, 2010).

The most representative salts that appear in these chemogenic deposits can generally be divided among three major mineral classes: the carbonates (e.g., dolomite, calcite, magnesite), the sulfates (e.g., anhydrite, gypsum, kieserite, polyhalite), and the chlorides (e.g., halite, sylvite, carnallite, kainite, bischofite). Minerals precipitate from sea water in reverse order of their solubilities, carbonate minerals first, followed by sulfate minerals, and finally chloride minerals. The nature of the salts formed also depends on the salinity of the seawater: below 15‰ salinity, dolomite, fluorite, celestite, gypsum, anhydrite, magnesite, and other minerals are precipitated, while halite forms at *ca.* 25‰ salinity, and above 30–35‰ salinity, sylvite, carnallite, bischofite, kainite, polyhalite, and langbeinite occur. Among those salts, anhydrite (CaSO_4) and the triple salt polyhalite ($\text{K}_2\text{SO}_4 \cdot \text{MgSO}_4 \cdot 2\text{CaSO}_4 \cdot 2\text{H}_2\text{O}$) are inversely related, and the polyhalite disappearance coincides with the formation of the double salt carnallite ($\text{KCl} \cdot \text{MgCl}_2 \cdot 6\text{H}_2\text{O}$) (Hardie and Eugster, 1980). Bischofite ($\text{MgCl}_2 \cdot 6\text{H}_2\text{O}$) eventually forms as part of a final invariant assemblage of several salts and solution (Hardie and Eugster, 1980). These four minerals are abundantly distributed in rock salt formations, such as the well-known Permian Salado Formation of Texas and New Mexico or the Permian Zechstein II potash deposit in Germany (Hardie and Eugster, 1980, Phillips, 1947). The Salado Formation is the host to the Waste Isolation Pilot Plant (WIPP), an operating US Department of Energy geological repository for the permanent disposal of defense-related transuranic waste (DOE, 1996), located 42 km East of Carlsbad in southeastern New Mexico. Rock salt mining of the the Permian Zechstein II potash deposit (Staßfurt series) in Germany started in 1927 in the region of the Asse, Lower Saxony, and stopped in 1963. From 1965 until 1978, low- and intermediate-level radioactive wastes were disposed in the Asse salt mine permanently at 750- and 511-meter depths (Gaertner et al., 2008).

To the best of our knowledge, this study is among the first-step assessments of the accuracy of first-principles calculations in modeling systematically salt minerals with complex crystal structures. This DFT approach is expected to provide a systematic, detailed and accurate description of the structures and electronic and thermodynamic properties of salt minerals. Only in recent years have first-principles approaches been used to assess the properties and stability of

salt minerals and other geomaterials. Such rigorous methodology would exploit robust computational methods in the assessment of thermodynamic properties for solids that can be used to not only complement existing knowledge of phase equilibria but also fill data gaps with accurate estimates, particularly at elevated temperatures.

Details of our computational approach are given in the next section, followed by a discussion of our computational thermodynamic properties and comparison with available calorimetric data in the next section.

3.2 Computational Methods

A schematic representation of the three-step computational approach used in this report is displayed in Figure 1. The first step consists of a crystal structure optimization using density functional theory (DFT), followed by a calculation of phonon frequencies using density functional perturbation theory (DFPT), and, finally, a phonon analysis is carried out to derive the thermodynamics properties of the crystalline system investigated.

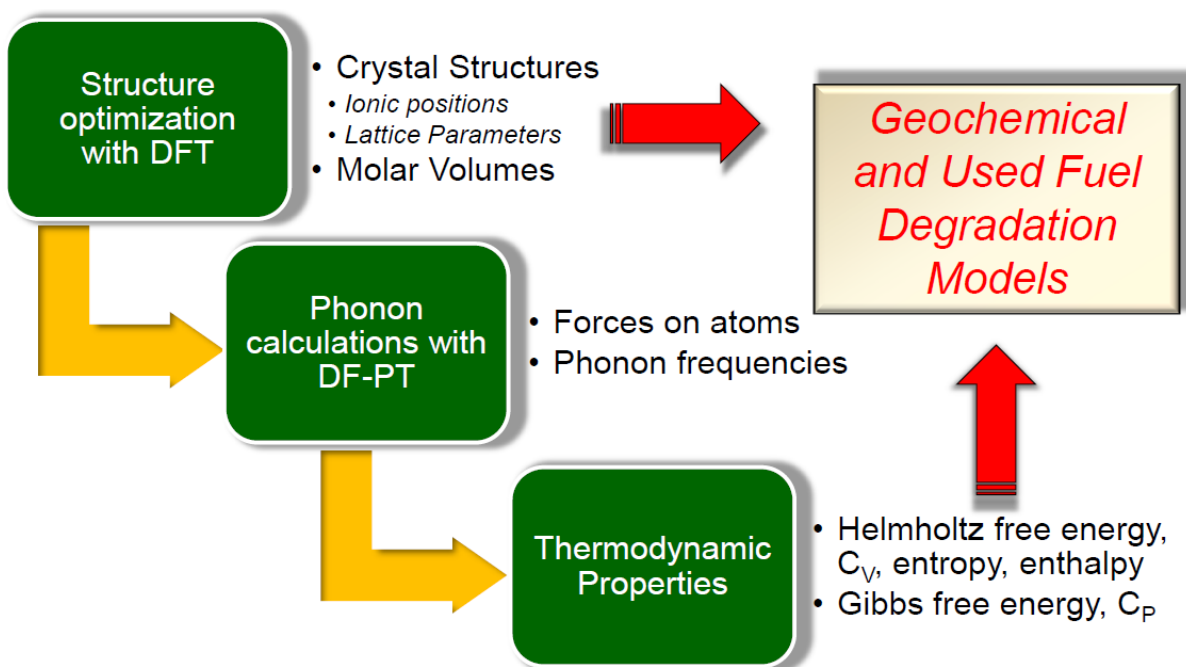


Figure 3.1. Schematic representation of the three-step computational approach used to calculate the thermal properties of crystalline systems using first-principles methods.

The equilibrium structures the salt minerals were optimized (Weck et al. 2013) using the Vienna ab initio simulation package (VASP) (Kresse, 1996). The exchange-correlation energy was calculated using the generalized gradient approximation (GGA), with the parameterization of Perdew, Burke, and Ernzerhof (PBE) (Perdew et al., 1996). The interaction between valence electrons and ionic cores was described by the projector augmented wave (PAW) method (Blochl, 1994a, Kresse, 1999). The outer electrons were treated explicitly as valence electrons in the Kohn-Sham (KS) equations and the remaining core electrons together with the nuclei were

represented by PAW pseudopotentials. The KS equation was solved using the blocked Davidson iterative matrix diagonalization scheme (Davidson, 1983). The plane-wave cutoff energy for the electronic wavefunctions was set to 500 eV, ensuring the total energy of the system to be converged to within 1 meV/atom.

All structures were optimized with periodic boundary conditions applied. Ionic relaxation was carried out using the quasi-Newton method and the Hellmann-Feynman forces acting on atoms were calculated with a convergence tolerance set to 0.01 eV/Å. Structural optimizations and properties calculations were carried out using the Monkhorst-Pack special k-point scheme (Monkhorst and Pack, 1976). The following k-point meshes were used for integrations in the Brillouin zone (BZ) of bulk systems: 3×5×3 for anhydrite and 3×3×3 for bischofite and polyhalite. The tetrahedron method with Bloechl corrections was used for BZ integrations (Bloechl, 1994b). Ionic and cell relaxations of the bulk structures were performed simultaneously, without symmetry constraints. Periodic unit cells were used in the calculations, with 24 atoms for CaSO₄ (Z = 4), 42 atoms for MgCl₂·6H₂O (Z = 2) and 30 atoms for K₂SO₄·MgSO₄·2CaSO₄·2H₂O (Z = 1).

The equilibrium structures the salt minerals were used to build a set of supercells. The forces exerted on atoms of the set of supercells were calculated using DFPT with VASP at the GGA/PBE level of theory and phonon frequencies were computed. Phonon analysis was performed at constant equilibrium volume in order to derive isochoric thermal properties (e.g., the phonon (Helmholtz) free energy, the entropy and the isochoric heat capacity).

The Helmholtz free energy was calculated using the following formula:

$$F = \frac{1}{2} \sum \hbar\omega + k_B T \sum \ln[1 - e^{-\hbar\omega/k_B T}].$$

The entropy was computed using the expression:

$$S = -k_B \sum \ln[1 - e^{-\hbar\omega/k_B T}] - \frac{1}{T} \sum \frac{\hbar\omega}{e^{\hbar\omega/k_B T} - 1}.$$

The heat capacity at constant volume was calculated using the formula:

$$C_V = \sum k_B \left[\frac{\hbar\omega}{k_B T} \right]^2 \frac{e^{\hbar\omega/k_B T}}{[e^{\hbar\omega/k_B T} - 1]^2}.$$

Further analysis from a set of phonon calculations in the vicinity of each computed equilibrium crystal structure was carried out to obtain thermal properties at constant pressure (e.g., the Gibbs free energy and the isobaric heat capacity) within a quasi-harmonic approximation (QHA). The QHA mentioned here introduces volume dependence of phonon frequencies as a part of anharmonic effect. A part of temperature effect can be included into the total energy of electronic structure through the phonon (Helmholtz) free energy at constant volume, but thermal properties at constant pressure are what we want to know. Therefore, some transformation from a function of volume V to a function of pressure p is needed.

The Gibbs free energy is defined at a constant pressure by the transformation:

$$G(T, p) = \min_V [U(V) + F_{phonon}(T; V) + pV],$$

where \min_V [function of V] means to find unique minimum value in the brackets by changing volume. Since volume dependencies of energies in electronic and phonon structures are different,

volume giving the minimum value of the energy function in the square brackets shifts from the value calculated only from electronic structure even at $T = 0$ K. By increasing temperature, the volume dependence of phonon free energy changes, then the equilibrium volume at temperatures changes.

The heat capacity at constant pressure versus temperature was also derived as the second derivative of the Gibbs free energy with respect to T , i.e.:

$$C_P = -T \frac{\partial^2 G}{\partial T^2}.$$

In order to derive the enthalpy function, $(H_T - H_{298.15})T^{-1}$, and the Gibbs energy function, $(G_T - H_{298.15})T^{-1}$, the thermal evolutions of the isobaric heat capacity calculated from first-principles were first fitted using a nonlinear least-squares regression to a Haas-Fisher-type polynomial, i.e.,

$$C_p(T) = a + bT + cT^{-2} + dT^{-0.5} + eT^2.$$

The enthalpy function was then computed by analytical integration of the fit to the isobaric heat capacity using the formula:

$$(H_T - H_{298.15})T^{-1} = \int_{298.15}^T (a + bT + cT^{-2} + dT^{-0.5} + eT^2)dT.$$

The Gibbs energy function was then computed using the following expression:

$$(G_T - H_{298.15})T^{-1} = (H_T - H_{298.15})T^{-1} - S_T,$$

where S_T is the entropy calculated from first-principles.

3.3 Results and Discussion

The optimized crystal unit cells of anhydrite, bischofite and polyhalite are displayed in Figure 3.2. The calculated structures were found to be in overall good agreement with available X-ray or neutron diffraction data (Hawthorne and Ferguson, 1975; Agron and Busing, 1985; Bindi, 2005).

The thermal properties, per formula unit, of anhydrite, bischofite and polyhalite derived from phonon calculations using density functional perturbation theory at the GGA/PBE level are displayed in Figures 3.3 to 3.5. Both the thermal properties at constant equilibrium volume (i.e. the total internal energy, the Helmholtz free energy, the entropy and the molar isochoric heat capacity) and the thermal properties at constant pressure (i.e. the Gibbs free energy and the molar isobaric heat capacity) are represented.

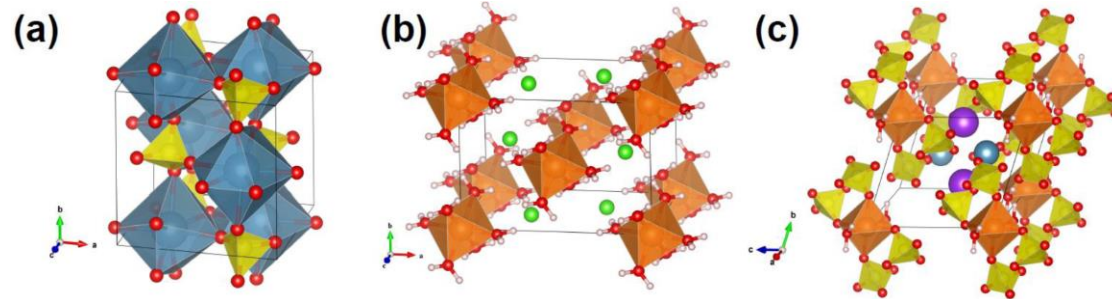


Figure 3.2. The crystal unit cells of (a) anhydrite (CaSO_4 ; space group $Amma$, $Z = 4$), (b) bischofite ($\text{MgCl}_2 \cdot 6\text{H}_2\text{O}$; space group $C2/m$, $Z = 2$) and (c) polyhalite ($\text{K}_2\text{SO}_4 \cdot \text{MgSO}_4 \cdot 2\text{CaSO}_4 \cdot 2\text{H}_2\text{O}$; $P-1$, $Z = 1$) relaxed at the GGA/PBE level of theory. Color legend: K, purple; Ca, blue; Mg, orange; O, red; Cl, green; H, white; S, yellow.

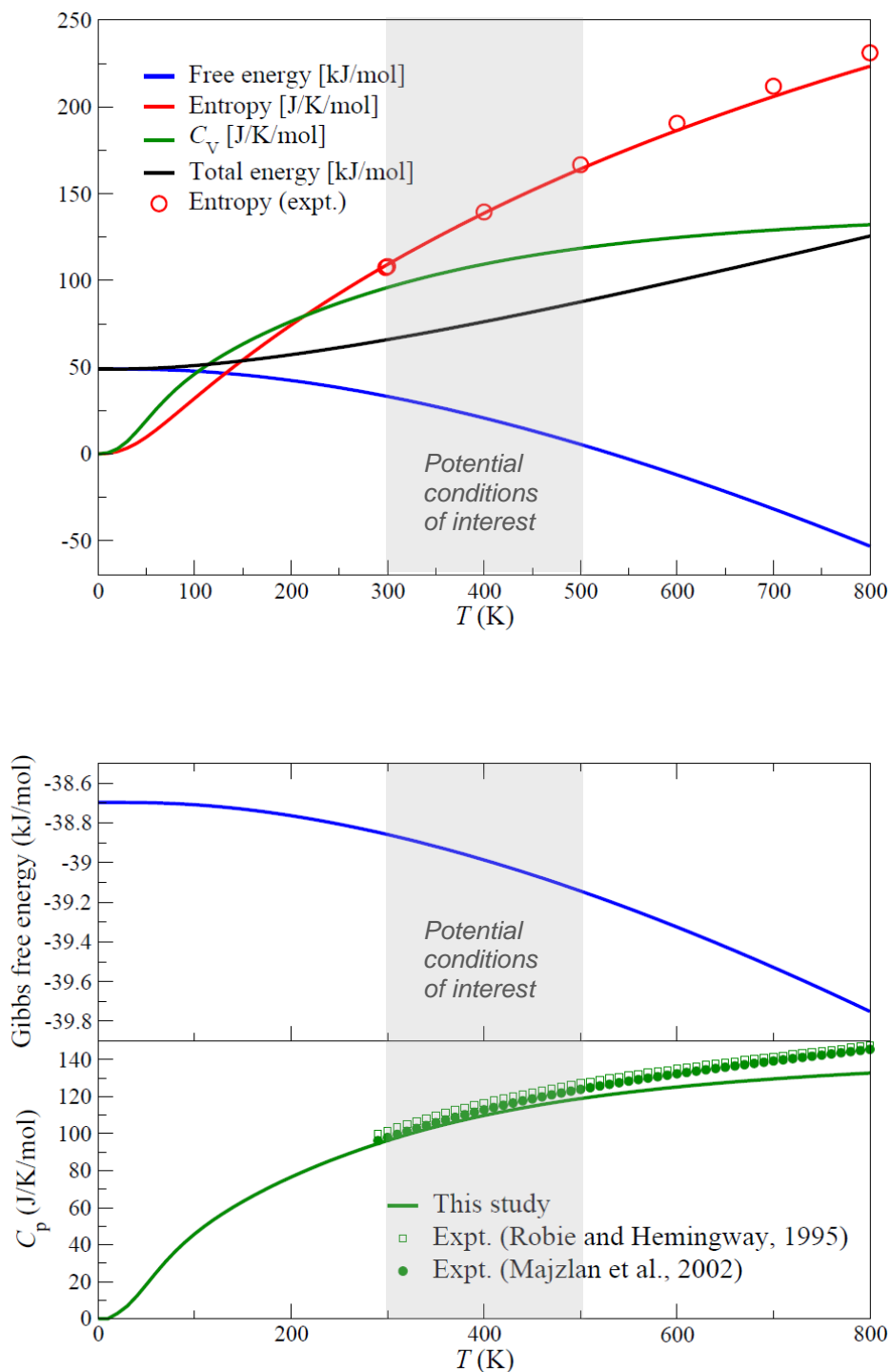


Figure 3.3. Thermal properties of anhydrite (per formula unit) calculated at the GGA/PBE level of theory. Top: thermal properties at constant equilibrium volume. Bottom: Thermal properties at constant pressure. Experimental data for the entropy are from Robie and Hemingway (1995); the isobaric heat capacity measured by Robie and Hemingway (1995) and by Majzlan et al. (2002) are also displayed. Potential thermal conditions of interest nuclear waste disposal in geological repositories are indicated as a shaded area.

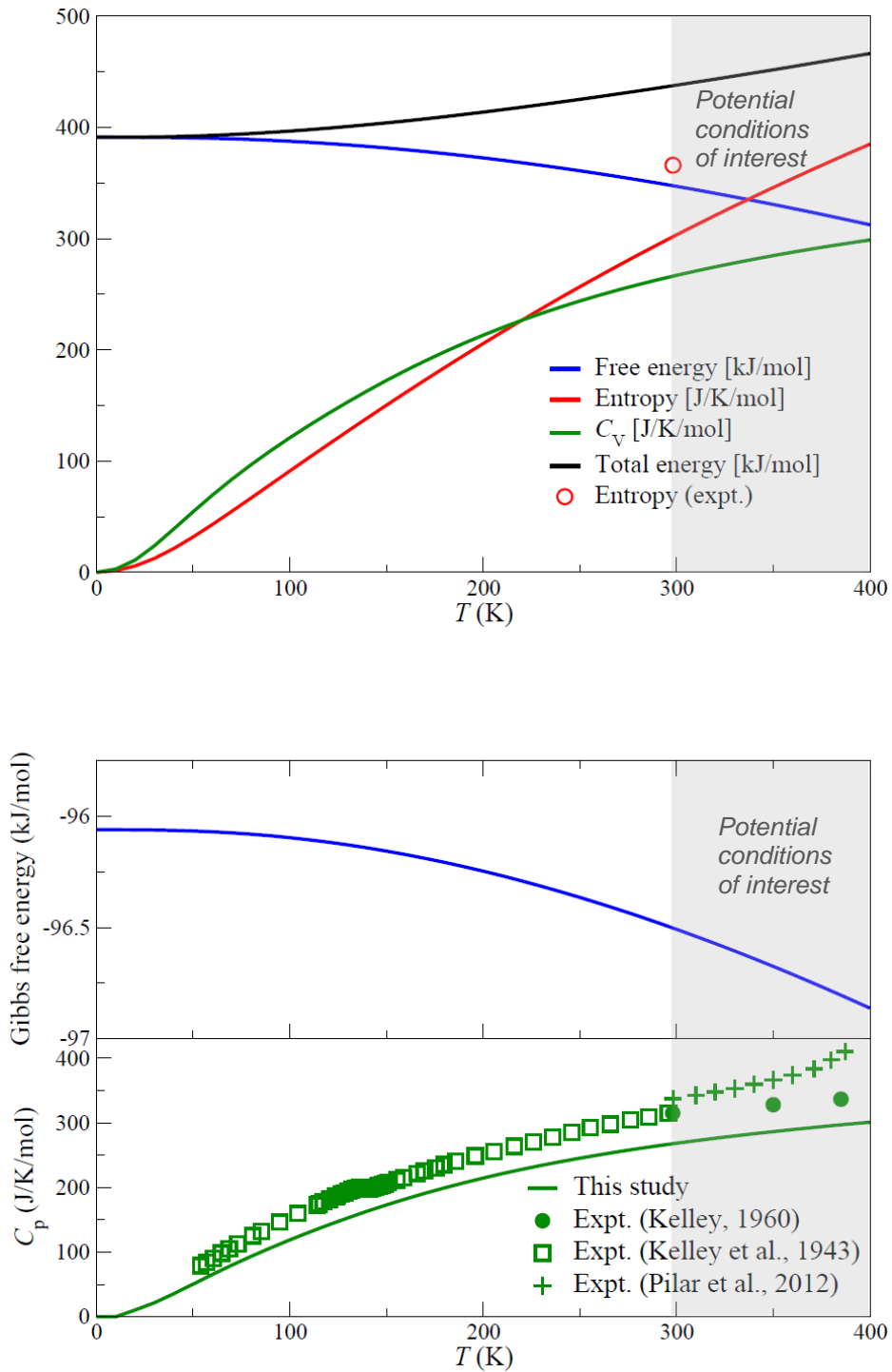


Figure 3.4. Thermal properties of bischofite (per formula unit) calculated at the GGA/PBE level of theory. Top: thermal properties at constant equilibrium volume. Bottom: Thermal properties at constant pressure. Experimental data for the entropy and isobaric heat capacity are from Pilar et al. (2012), Kelley and Moore (1943), Kelley (1960). Potential thermal conditions of interest nuclear waste disposal in geological repositories are indicated as a shaded area.

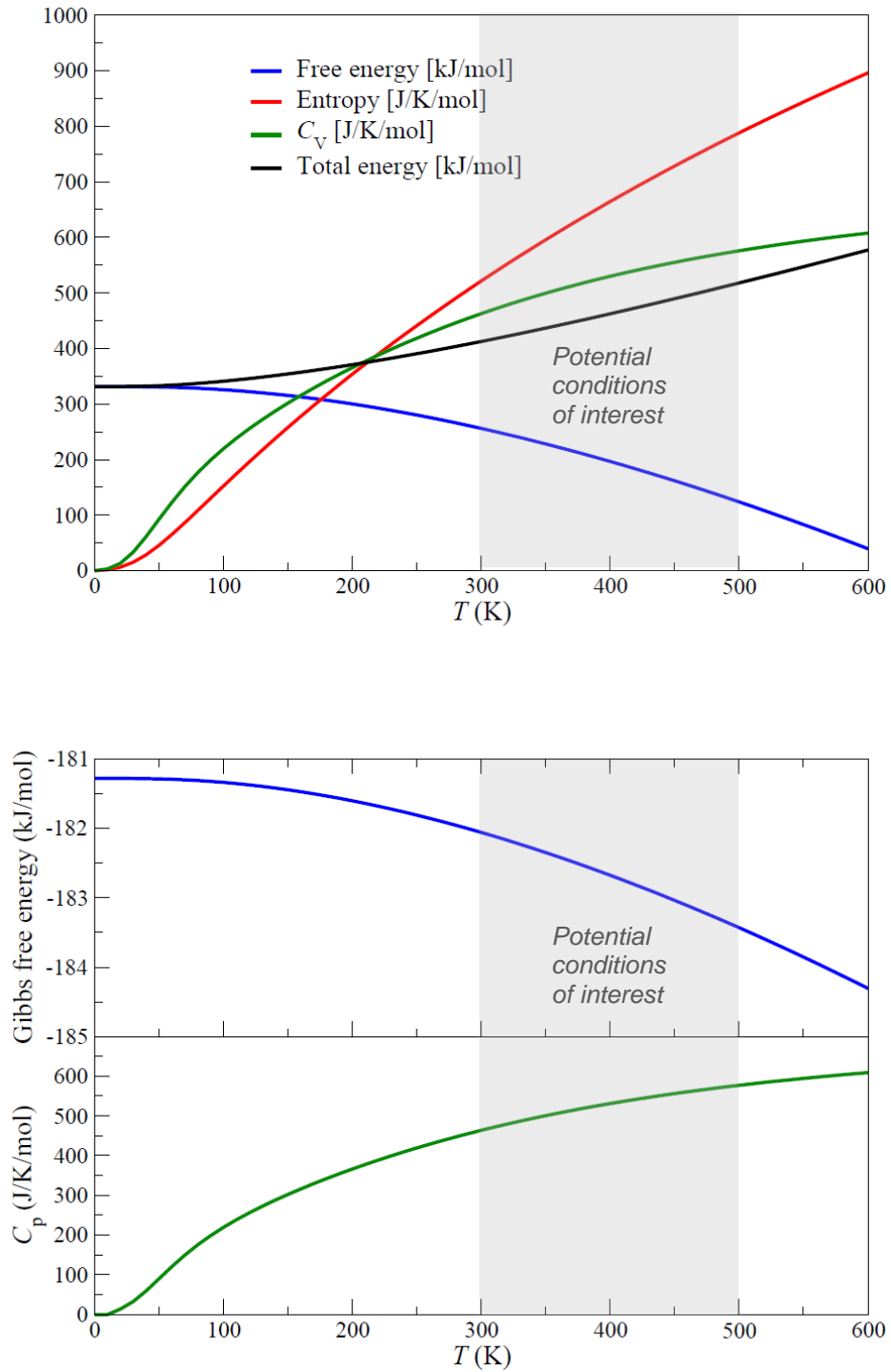


Figure 3.5. Thermal properties of polyhalite (per formula unit) calculated at the GGA/PBE level of theory. Top: thermal properties at constant equilibrium volume. Bottom: Thermal properties at constant pressure. Potential thermal conditions of interest nuclear waste disposal in geological repositories are indicated as a shaded area.

For anhydrite, excellent agreement is observed up to 800 K between the calculated entropy and the experimental values, for a reference pressure of 1 bar for the standard state, reported by Robie and Hemingway (Robie and Hemingway, 1995), with calculations underestimating experiment with a maximum deviation of *ca.* 3% at 800 K (cf. Fig. 3.3). The computed molar isobaric heat capacity also shows good agreement from room temperature up to about 500 K with the calorimetric data reported by Robie and Hemingway (Robie and Hemingway, 1995) and by Majzlan et al. (Majzlan et al., 2002). Both sets of differential scanning calorimeter (DSC) results were fitted to a Haas-Fisher polynomial within the range of *ca.* 245–1100 K and the 95% confidence interval of the measured C_P was found to typically vary from 1 to 2% of the measured value at low temperature up to 2 to 5% at high temperature (Majzlan et al., 2002). At room temperature, first-principles calculations underestimate by 1.7 and 5.2% the calorimetric data of Majzlan et al. and Robie and Hemingway, respectively, while these differences increase to *ca.* 4 and 6% at 500 K. At higher temperature, this theory/experiment agreement progressively degrades as the quasi-harmonic approximation breaks down; although calculations qualitatively reproduce the variation of C_P at high temperature, the measured heat capacity is larger than its computed value by as much as 8–10% at 800 K.

Limited experimental thermal data exist on bischofite (cf. Fig. 3.4). The reference value of the entropy of bischofite measured at 298.15 K and 1 bar by Kelley and Moore (Kelley and Moore, 1943) was used here for comparison. The experimental isobaric heat capacity of bischofite reported by Kelley and Moore between 54.1 and 295.8 K is displayed in Fig. 3.4; in the 298–385 K temperature range, the Maier-Kelley polynomial, $C_P = a + bT + cT^{-2}$, based on the calorimetric measurements of Kelley (Kelley, 1960, Pabalan and Pitzer, 1987) was used. As shown in Fig. 4, discrepancies of 17 % for the entropy and of 11–14 % for the isobaric heat capacity are found between the values computed in this study and the calorimetric measurements (Kelley and Moore, 1943, Kelley, 1960). Surprisingly, the agreement between computed and empirical C_P values improves as the temperature ramps up from 298 to 385 K, although one would expect a slight deterioration of this agreement due the breakdown of the QHA. Recently, Pilar and co-workers (Pilar et al., 2012) also reported measurements of C_P in the temperature range 298.15–387.15 K (cf. Fig. 3.4). However, large discrepancies are observed, especially towards the high end of the temperature range considered, between these recent data and both the experimental data of Kelley (Kelley, 1960) and calculations. Such discrepancies may stem in part from the phase transition occurring from bischofite to magnesium dichloride tetrahydrate ($\text{MgCl}_2 \cdot 4\text{H}_2\text{O}$) near 370 K (Sugimoto et al., 2007, Pilar et al., 2012). Therefore, a comprehensive experimental reinvestigation of the thermal properties of bischofite seems timely. Alternatively, the use of dispersion corrections in DFT calculations is likely to improve slightly the agreement between computed and measured thermodynamic data.

The predicted thermal properties of polyhalite are shown in Fig. 3.5 for temperatures up to 600 K. However, no calorimetric data are currently available for comparison, to the best of our knowledge. Experimental characterization of the thermal properties and the stability field of this compound are also needed.

In order to derive the enthalpy function, $(H_T - H_{298.15})T^{-1}$, and the Gibbs energy function, $(G_T - H_{298.15})T^{-1}$, the thermal evolutions of the isobaric heat capacity calculated from first-principles for anhydrite, bischofite and polyhalite were first fitted using a nonlinear least-squares regression to a Haas-Fisher-type polynomial with the resulting optimized coefficients given in Table 3.1.

Table 3.1. Coefficients of the Haas-Fisher heat capacity polynomial $C_p(T)$ for anhydrite, bischofite and polyhalite. The range of validity of the fit is 290–800 K.

Compound	$a \times 10^3$ (T^0)	$b \times 10^{-2}$ (T^1)	$c \times 10^6$ (T^2)	$d \times 10^4$ ($T^{0.5}$)	$e \times 10^{-5}$ (T^2)	SSD ^a
Anhydrite	0.30118	-7.885	1.3832256	-0.344036	2.20	0.004
Bischofite	0.54893	-6.226	0.1263209	-0.463856	4.94	0.349
Polyhalite	1.48458	-40.386	6.9100067	-1.711348	12.73	0.041

^a Sum of squared differences between calculated and fitted data.

The enthalpy function was then computed by analytical integration of the fit to the isobaric heat capacity and the Gibbs energy function was then computed using the S_T entropy calculated from first-principles. Results for the computed enthalpy function and Gibbs energy function for anhydrite, bischofite and polyhalite are shown in Figure 3.6, along with the experimental data from Robie and Hemingway (1995) for anhydrite. The computed enthalpy function for anhydrite underestimates experimental results by a maximum of *ca.* 5% at 800 K. The calculated Gibbs energy function overestimates and underestimates experimental data by *ca.* 1% at 298 K and 800 K, respectively. The thermal variations of the computed enthalpy and Gibbs energy functions for bischofite and polyhalite are predicted to be similar to anhydrite.

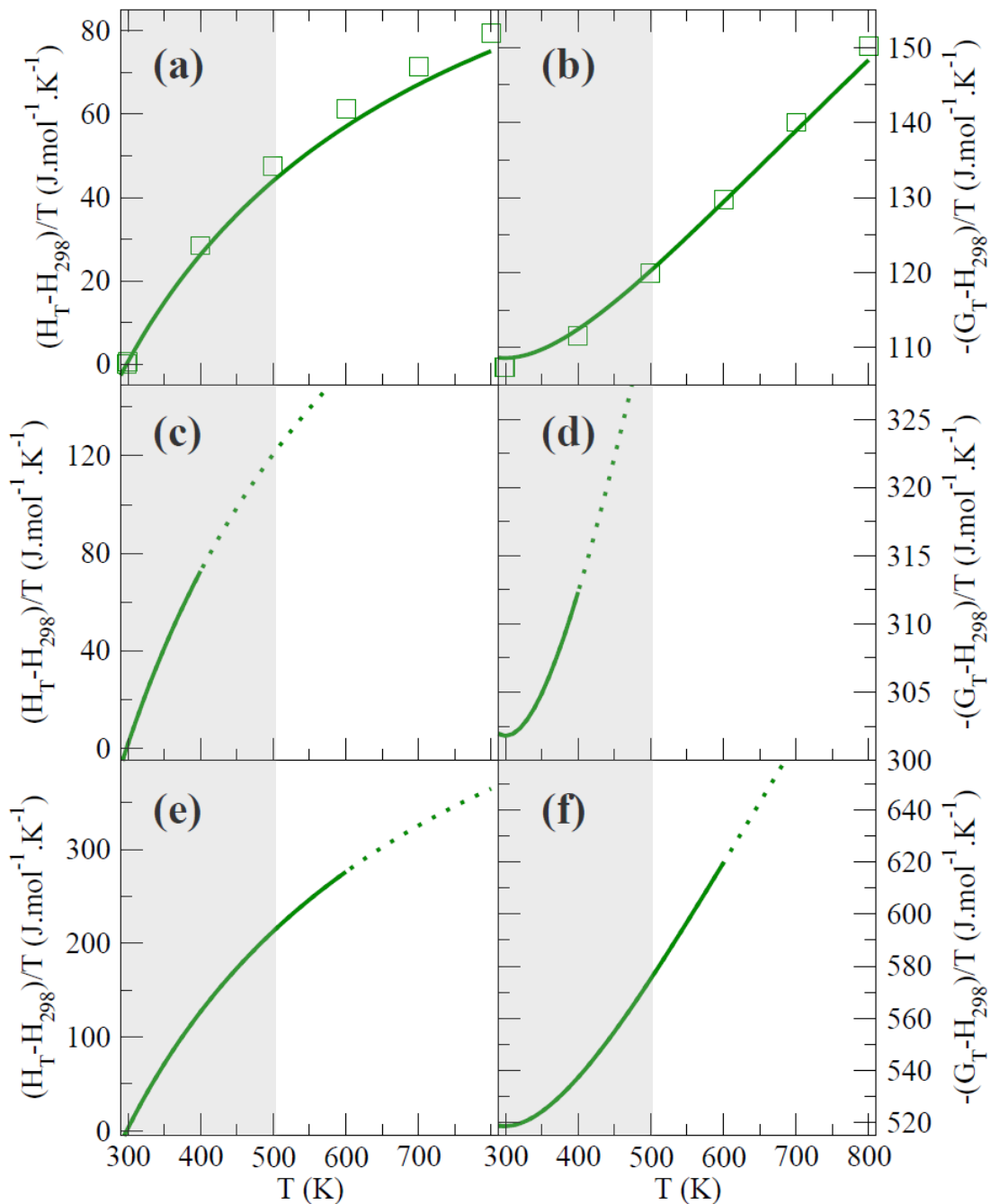


Figure 3.6. Enthalpy function (left column) and Gibbs energy function (right column) per formula unit for anhydrite [(a) and (b)], bischofite [(c) and (d)] and polyhalite [(e) and (f)] calculated at the GGA/PBE level of theory. Experimental data for anhydrite from Robie and Hemingway (1995) (squares) are also displayed. The calculated functions beyond the range of estimated stability of the salt minerals are represented as dotted lines. Potential thermal conditions of interest nuclear waste disposal in geological repositories are indicated as a shaded area.

3.4 Conclusions

In summary, DFT calculations of the structures and thermodynamic properties of crystalline anhydrite, bischofite and polyhalite were carried out within the generalized gradient approximation. The relaxed structures are found to be in overall good agreement with experimental XRD data, with some slight overestimation by 2-4% of the computed equilibrium volume compared to experimental estimates. Phonon analysis using density functional perturbation theory was also carried out for anhydrite, bischofite, and polyhalite, in order to derive both their isochoric and isobaric thermal properties. The computed entropy and isobaric heat capacity for anhydrite reproduce experimental data up to 800 K to within 3% and 10%, respectively, while further experimental work is needed to assess our theoretical predictions for other salts. This methodology will be applied in a systematic way to other salt minerals (e.g. dehydrated bischofite phases, gypsum,...) and other NS and EBS models to expand the applicability of this data set to more realistic systems. Such an expanded data set will facilitate investigation of phase behavior at a wide range of temperature and pressure conditions in natural evaporate deposits, as well as studies of nuclear waste disposal in geological repositories.

3.5 Planned FY14 Work on Thermodynamic Modeling

Planned FY14 work will be focused on:

- TDB development for barrier materials at elevated temperatures and pressures (in conjunction with LLNL). Evaluate benchmarking and other guidelines for TDB development, particularly the establishment of international partnership. Also, examine the inclusion of sorption database development within this effort.
- Thermodynamic description of clay interactions and phase relations at high temperatures and pressures based on LANL experimental work on barrier material interactions.
- Expand and further testing of GEM models for phase equilibria, ion exchange, and surface complexation with the Cantera code suite. Test Cantera with a multiphase multicomponent equilibria problem that includes aqueous, solid, and surface reactions.

4. References

- Adams, B. M., Dalbey, K. R., Eldred, M. S., Swiler, L. P., Bohnhoff, W. J., Eddy, J. P., Vigil, D. M., Hough, P. D., and Lefantzi, S., 2012, DAKOTA, A Multilevel Parallel Object-Oriented Framework for Design Optimization, Parameter Estimation, Uncertainty Quantification, and Sensitivity Analysis: Version 5.2+ User's Manual (SAND2010-2183): Sandia National Laboratories, SAND2010-2183.
- Agron, P. A., Busing, W. R. (1985). Magnesium dichloride hexahydrate, $MgCl_2 \cdot 6H_2O$, by neutron diffraction. *Acta Crystallographica Section C*, 41 (1), 8–10.
- Akesson, M., Jacinto, A. C., Gatabin, C., Sanchez, M., and Ledesma, A., 2009, Bentonite THM behaviour at high temperatures: experimental and numerical analysis: *Geotechnique*, v. 59, no. 4, p. 307-318.
- Berend, I., Cases, J. M., Francois, M., Uriot, J. P., Michot, L., Masion, A., and Thomas, F., 1995, Mechanism of Adsorption and Desorption of Water-Vapor by Homoionic Montmorillonites .2. The Li^+ , Na^+ , K^+ , Rb^+ and Cs^+ - Exchanged Forms: *Clays and Clay Minerals*, v. 43, no. 3, p. 324-336.
- Cases, J. M., Berend, I., Besson, G., Francois, M., Uriot, J. P., Thomas, F., and Poirier, J. E., 1992, Mechanism of Adsorption and Desorption of Water-Vapor by Homoionic Montmorillonite .1. The Sodium-Exchanged Form: *Langmuir*, v. 8, no. 11, p. 2730-2739.
- Cohen, E. R., Cvitas, T., Frey, J. G., Holstrom, B., Kuchitsu, K., Marquardt, R., Mills, I., Pavese, F., Quack, M., Stohner, J., Strauss, H. L., Takami, M., and Thor, A. J., 2008, *Quantities, Units, and Symbols in Physical Chemistry*, IUPAC Green Book (3rd edition), Cambridge, IUPAC and RSC Publishing.
- Copps, K. D., and Carnes, B. R., 2013, SIERRA Verification Module: Encore User Guide – Version 4.2 (2013-3344): Sandia National Laboratories, 279 pp.
- Cox, J. D., Wagman, D. D., and Medvedev, V. A., 1989, CODATA key values for thermodynamics, New York, Hemisphere Pub. Corp., xiii, 271 p. p.:
- Cygan, R. T., Liang, J.-J., and Kalinichev, A. G., 2004, Molecular models of hydroxide, oxyhydroxide, and clay phases and the development of a general force field: *Journal of Physical Chemistry B*, v. 108, no. 4, p. 1255-1266.
- Davidson, E. R. (1983). In G. Dierksen, & S. Wilson (Eds.), *Methods in Computational Molecular Physics* (Vol. 113, p. 95). New York, NY: NATO Advanced Study Institute, Series C, Plenum.
- Davis, J. A., Coston, J. A., Kent, D. B., and Fuller, C. C., 1998, Application of the surface complexation concept to complex mineral assemblages: *Environmental Science & Technology*, v. 32, no. 19, p. 2820-2828.
- Davis, J. A., and Kent, D. B., 1990, Surface complexation modeling in aqueous geochemistry *Reviews in Mineralogy and Geochemistry*, v. 23, no. 1, p. 177-260.
- DOE (1996). Appendix SOTERM. DOE/CAO 1996-2184. In: Title 40 CFR Part 191 Compliance Certification Application. U.S. DOE Carlsbad Area Office, Carlsbad, NM.

- Dueck, A., Borgesson, L., Goudarzi, R., Lonnqvist, M., and Akesson, M., 2008, Humidity-induced water absorption and swelling of highly compacted bentonite in the project KBS-3H: *Physics and Chemistry of the Earth*, v. 33, p. S499-S503.
- Dzombak, D. A., and Morel, F. M. M., 1990, *Surface Complexation Modeling: Hydrous Ferric Oxide* Wiley-Interscience, 416 p.:
- Fernandez, A. M., and Villar, M. V., 2010, Geochemical behaviour of a bentonite barrier in the laboratory after up to 8 years of heating and hydration: *Applied Geochemistry*, v. 25, no. 6, p. 809-824.
- Ferrage, E., Lanson, B., Michot, L. J., and Robert, J. L., 2010, Hydration Properties and Interlayer Organization of Water and Ions in Synthetic Na-Smectite with Tetrahedral Layer Charge. Part 1. Results from X-ray Diffraction Profile Modeling: *Journal of Physical Chemistry C*, v. 114, no. 10, p. 4515-4526.
- Fletcher, P., and Sposito, G., 1989, The Chemical Modelling of Clay/Electrolyte Interactions for Montmorillonite Clay Minerals, v. 24, p. 375-391.
- Gaertner, G., Stockmann, N., Fricke, H., Wallmueller, R. (2008). Geological characterization of the Asse salt mine for mining, disposal of radioactive waste, and proof of long-term safety. In: Rempe, N. T. (Ed.), *Deep Geologic Repositories*. Geological Society of America *Reviews in Engineering Geology*, pp. 41–52.
- Gens, A., Sanchez, M., Guimaraes, L. D., Alonso, E. E., Lloret, A., Olivella, S., Villar, M. V., and Huertas, F., 2009, A full-scale in situ heating test for high-level nuclear waste disposal: observations, analysis and interpretation: *Geotechnique*, v. 59, no. 4, p. 377-399.
- Goldberg, S., and Criscenti, L., 2008, Modeling adsorption of metals and metalloids by soil components, *Biophysico-chemical processes of heavy metals and metalloids in soil environments*. John Wiley & Sons, Hoboken, NJ. Modeling adsorption of metals and metalloids by soil components, p. 215-264.
- Goldberg, S., and Criscenti, L., 2008, Modeling adsorption of metals and metalloids by soil components, *Biophysico-chemical processes of heavy metals and metalloids in soil environments*. John Wiley & Sons, Hoboken, NJ. Modeling adsorption of metals and metalloids by soil components, p. 215-264.
- Goldberg, S., Criscenti, L. J., Turner, D. R., Davis, J. A., and Cantrell, K. J., 2007, Adsorption-desorption processes in subsurface reactive transport modeling: *Vadose Zone Journal*, v. 6, no. 3, p. 407-435.
- Grenthe, I., Mompean, F., and Spahiu, K., 2013, *Guidelines For The Extrapolation To Zero Ionic Strength (TDB-2)*: OECD-NEA.
- Guillaumont, R., Agency, O. N. E., and Mompean, F. J., 2003, *Update on the chemical thermodynamics of uranium, neptunium, plutonium, americium and technetium*, Elsevier Science & Technology Books.
- Hardie, L. A., Eugster, H. P. (1980). *Evaporation of seawater: calculated mineral sequences*. *Science (New York, N.Y.)* 208 (4443), 498–500.

- Helgeson, H. C., Kirkham, D. H., and Flowers, G. C., 1981, Theoretical Prediction of the Thermodynamic Behavior of Aqueous-Electrolytes at High-Pressures and Temperatures .4. Calculation of Activity-Coefficients, Osmotic Coefficients, and Apparent Molal and Standard and Relative Partial Molal Properties to 600-Degrees-C and 5 Kb: American Journal of Science, v. 281, no. 10, p. 1249-1516.
- Jové Colón, C. F., Caporuscio, F. A., Levy, S. S., Blink, J. A., Greenberg, H. R., Halsey, W. G., Fratoni, M., Sutton, M., Wolery, T. J., Rutqvist, J., Liu, H. H., Birkholzer, J., Steefel, C. I., and Galindez, J., 2011, Disposal Systems Evaluations and Tool Development - Engineered Barrier System (EBS) Evaluation, p. 1-192.
- Jové Colón, C. F., Greathouse, J. A., Teich-McGoldrick, S., Cygan, R. T., Hadgu, T., Bean, J. E., Martinez, M. J., Hopkins, P. L., Argüello, J. G., Hansen, F. D., Caporuscio, F. A., and Cheshire, M., et al., 2012, Evaluation of Generic EBS Design Concepts and Process Models: Implications to EBS Design Optimization (FCRD-USED-2012-000140): U.S. Department of Energy.
- Karnland, O., 1997, Bentonite swelling pressure in strong NaCl solutions - Correlation between model calculations and experimentally determined data: Swedish Nuclear Fuel and Waste Management Co.
- Karnland, O., Nilsson, U., Weber, H., and Wersin, P., 2008, Sealing ability of Wyoming bentonite pellets foreseen as buffer material - Laboratory results: Physics and Chemistry of the Earth, v. 33, p. S472-S475.
- Karnland, O., Olsson, S., Nilsson, U., and Sellin, P., 2007, Experimentally determined swelling pressures and geochemical interactions of compacted Wyoming bentonite with highly alkaline solutions: Physics and Chemistry of the Earth, v. 32, no. 1-7, p. 275-286.
- Karpov, I. K., Chudnenko, K. V., and Kulik, D. A., 1997, Modeling chemical mass transfer in geochemical processes: Thermodynamic relations, conditions of equilibria, and numerical algorithms: American Journal of Science, v. 297, no. 8, p. 767-806.
- Kelley, K. K. (1960). Contributions to the data on theoretical metallurgy. 13. High temperature heat-content, heat-capacity, and entropy data for the elements and inorganic compounds. U.S. Bur. of Mines Bull., 584, 232.
- Kim, J. S., Kwon, S. K., Sanchez, M., and Cho, G. C., 2011, Geological Storage of High Level Nuclear Waste: Ksce Journal of Civil Engineering, v. 15, no. 4, p. 721-737.
- Kelley, K. K., Moore, G. E. (1943). Specific Heats at Low Temperatures of Hydrates of Magnesium Chloride. Journal of the American Chemical Society, 65 (12), 2340-2342.
- Kresse, G. (1996). Efficient iterative schemes for ab initio total-energy calculations using a plane-wave basis set. Physical Review B 54 (16), 11169-11186.
- Kresse, G. (1999). From ultrasoft pseudopotentials to the projector augmented-wave method. Physical Review B, 59 (3), 1758-1775.
- Kulik, D. A., 2000, Thermodynamic properties of surface species at the mineral-water interface under hydrothermal conditions: a Gibbs energy minimization single-site 2pKa triple-layer model of rutile in NaCl electrolyte to 250°C: Geochimica Et Cosmochimica Acta, v. 64, no. 18, p. 3161-3179.

- , 2002, Gibbs energy minimization approach to modeling sorption equilibria at the mineral-water interface: Thermodynamic relations for multi-site-surface complexation: *American Journal of Science*, v. 302, no. 3, p. 227-279.
- , 2009, Thermodynamic concepts in modeling sorption at the mineral-water interface: *Reviews in Mineralogy and Geochemistry*, v. 70, no. 1, p. 125-180.
- Likos, W. J., and Lu, N., 2006, Pore-scale analysis of bulk volume change from crystalline interlayer swelling in Na⁺- and Ca²⁺-smectite: *Clays and Clay Minerals*, v. 54, no. 4, p. 515-528.
- Likos, W. J., and Wayllace, A., 2010, Porosity Evolution of Free and Confined Bentonites during Interlayer Hydration: *Clays and Clay Minerals*, v. 58, no. 3, p. 399-414.
- Liu, C. W., and Lin, W. S., 2005, A smectite dehydration model in a shallow sedimentary basin: Model development: *Clays and Clay Minerals*, v. 53, no. 1, p. 55-70.
- Machesky, M. L., Wesolowski, D. J., Palmer, D. A., and Ichiro-Hayashi, K., 1998, Potentiometric titrations of rutile suspensions to 250°C: *Journal of Colloid and Interface Science*, v. 200, no. 2, p. 298-309.
- Majzlan, J., Navrotsky, A., Neil, J. M., 2002. Energetics of anhydrite, barite, celestine, and anglesite: A high-temperature and differential scanning calorimetry study. *Geochimica et Cosmochimica Acta*, 66 (10), 1839–1850.
- Moffat, H. K., and Jové Colón, C. F., 2009, Implementation of Equilibrium Aqueous Speciation and Solubility (EQ3 type) Calculations into Cantera for Electrolyte Solutions: Sandia National Laboratories, SAND2009-3115.
- Monkhorst, H., & Pack, J. (1976). Special Points for Brillouin-Zone Integrations. *Physical Review B*, 13(12), 5188-5192.
- Murad, M. A., 1999a, Thermomechanical model of hydration swelling in smectitic clays: I Two-scale mixture-theory approach: *International Journal for Numerical and Analytical Methods in Geomechanics*, v. 23, no. 7, p. 673-696.
- , 1999b, Thermomechanical model of hydration swelling in smectitic clays: II - Three-scale inter-phase mass transfer: Homogenization and computational validation: *International Journal for Numerical and Analytical Methods in Geomechanics*, v. 23, no. 7, p. 697-719.
- , 2010, Swelling and Shrinking of Porous Materials: From Colloid Science to Poromechanics: *Anais Da Academia Brasileira De Ciencias*, v. 82, no. 1, p. 1-2.
- Murad, M. A., Bennethum, L. S., and Cushman, J. H., 1995, A Multiscale Theory of Swelling Porous-Media .1. Application to One-Dimensional Consolidation: *Transport in Porous Media*, v. 19, no. 2, p. 93-122.
- Murad, M. A., and Cushman, J. H., 1997, A Multiscale Theory of Swelling Porous Media .2. Dual Porosity Models for Consolidation of Clays Incorporating Physicochemical Effects: *Transport in Porous Media*, v. 28, no. 1, p. 69-108.
- , 2000, Thermomechanical theories for swelling porous media with microstructure: *International Journal of Engineering Science*, v. 38, no. 5, p. 517-564.

- NAGRA, 2002, Demonstration of disposal feasibility for spent fuel, vitrified high-level waste and long-lived intermediate-level waste: NAGRA (National Cooperative for the Disposal of Radioactive Waste).
- Nutt, M., Voegele, M., Jove-Colon, C., Wang, Y., Howard, R., Blink, J., Liu, H.-H., Hardin, E., and Jenni, K., 2011, Used Fuel Disposition Campaign Disposal Research and Development Roadmap (Fuel Cycle Research and Development), Prepared for U.S. Department of Energy Used Fuel Disposition Campaign FCR&D-USED-2011-000065
- Pabalan, R. T., Pitzer, K. S. (1987). Thermodynamics of concentrated electrolyte mixtures and the prediction of mineral solubilities to high temperature for mixtures in the system Na-K-Mg-Cl-SO₄-OH-H₂O. *Geochimica et Cosmochimica Acta*, 51, 2429–2443.
- Pabalan, R. T., 1994, Thermodynamics of ion exchange between clinoptilolite and aqueous solutions of Na⁺/K⁺ and Na⁺/Ca²⁺: *Geochimica et Cosmochimica Acta*, v. 58, no. 21, p. 4573-4590.
- Pilar, R., Pilar, R., Svoboda, L., Honcova, P., Oravova, L. (2012). Study of magnesium chloride hexahydrate as heat storage material. *Thermochimica Acta*, 546, 81 – 86.
- Perdew, J. P., Burke, K., Ernzerhof, M. (1996). Generalized Gradient Approximation Made Simple. *Physical Review Letters*, 77 (18), 3865–3868.
- Plimpton, S., 1995, Fast Parallel Algorithms for Short-Range Molecular Dynamics: *J Comp Phys*, v. 117, p. 1-19.
- Puigdomènech, I., Rard, J. A., Plyasunov, A. V., and Grenthe, I., 1999, Temperature Corrections to Thermodynamic Data and Enthalpy Calculations (TDB-4): OECD-NEA.
- Rand, H., Mompean, F. J., Perrone, J., and Illemassène, M., 2008, Chemical Thermodynamics of Thorium, OECD Publishing, 900 p.:
- Ransom, B., and Helgeson, H. C., 1994a, A Chemical and Thermodynamic Model of Aluminous Dioctahedral-2/1 Layer Clay-Minerals in Diagenetic Processes - Regular Solution Representation of Interlayer Dehydration in Smectite: *American Journal of Science*, v. 294, no. 4, p. 449-484.
- , 1994b, Estimation of the Standard Molal Heat-Capacities, Entropies, and Volumes of 2/1-Clay-Minerals: *Geochimica Et Cosmochimica Acta*, v. 58, no. 21, p. 4537-4547.
- , 1995, A Chemical and Thermodynamic Model of Dioctahedral 2-1 Layer Clay-Minerals in Diagenetic Processes - Dehydration of Dioctahedral Aluminous Smectite as a Function of Temperature and Depth in Sedimentary Basins: *American Journal of Science*, v. 295, no. 3, p. 245-281.
- Rard, J. A., Sandino, C. A., Östhols, E., and Agency, O. N. E., 1999, Chemical thermodynamics of technetium, North-Holland.
- Ridley, M. K., Machesky, M. L., Wesolowski, D. J., and Palmer, D. A., 1999, Calcium adsorption at the rutile-water interface: A potentiometric study in NaCl media to 250°C: *Geochimica et Cosmochimica Acta*, v. 63, no. 19, p. 3087-3096.

- Robie, R. A., and Hemingway, B. S., 1995, Thermodynamic properties of minerals and related substances at 298.15 K and 1 bar (105 pascals) pressure and at higher temperatures, Denver, CO, U.S. G.P.O., U S Geological Survey bulletin, v. 2131, 461 p.:
- Rossini, F. D., 1952, Selected values of chemical thermodynamic properties, Washington, U.S. G.P.O., Circular of the National Bureau of Standards, v. 500, 1268 p.:
- Samper, J., Zheng, L., Montenegro, L., Fernandez, A. M., and Rivas, P., 2008, Coupled thermo-hydro-chemical models of compacted bentonite after FEBEX in situ test: Applied Geochemistry, v. 23, no. 5, p. 1186-1201.
- Sanchez, M., Gens, A., and Olivella, S., 2010, Effect of thermo-coupled processes on the behaviour of a clay barrier submitted to heating and hydration: Anais Da Academia Brasileira De Ciencias, v. 82, no. 1, p. 153-168.
- , 2012, THM analysis of a large-scale heating test incorporating material fabric changes: International Journal for Numerical and Analytical Methods in Geomechanics, v. 36, no. 4, p. 391-421.
- Shock, E. L., and Helgeson, H. C., 1988, Calculation of the Thermodynamic and Transport-Properties of Aqueous Species at High-Pressures and Temperatures - Correlation Algorithms for Ionic Species and Equation of State Predictions to 5 kb and 1000oC: Geochimica Et Cosmochimica Acta, v. 52, no. 8, p. 2009-2036.
- Shock, E. L., Sassani, D. C., Willis, M., and Sverjensky, D. A., 1997, Inorganic species in geologic fluids: Correlations among standard molal thermodynamic properties of aqueous ions and hydroxide complexes: Geochimica et Cosmochimica Acta, v. 61, no. 5, p. 907-950.
- Smith, W. R., and Missen, R. W., 1982, Chemical reaction equilibrium analysis: theory and algorithms, New York, Wiley, 364 p.:
- Sposito, G., 1984, The surface chemistry of soils, Oxford University Press, 234 p.:
- , 2008, The chemistry of soils, Oxford university press.
- Sposito, G., Holtzclaw, K. M., Charlet, L., Jouany, C., and Page, C. L., 1983a, Sodium-Calcium and Sodium-Magnesium Exchange on Wyoming Bentonite in Perchlorate and Chloride Background Ionic Media: Soil Science Society of America Journal, v. 47, no. 1, p. 51-56.
- Sposito, G., Holtzclaw, K. M., Jouany, C., and Charlet, L., 1983b, Cation Selectivity in Sodium-Calcium, Sodium-Magnesium, and Calcium-Magnesium Exchange on Wyoming Bentonite at 298 K: Soil Science Society of America journal, v. 47, no. 5, p. 917-921.
- Sverjensky, D. A., 2003, Standard states for the activities of mineral surface sites and species: Geochimica Et Cosmochimica Acta, v. 67, no. 1, p. 17-28.
- Sugimoto, K., Dinnebier, R. E., Hanson, J. C. (2007). Structures of three dehydration products of bischofite from in situ synchrotron powder diffraction data ($MgCl_2 \cdot nH_2O$; $n=1,2,4$). Acta Crystallographica Section B-Structural Science, 63 (2), 235–242.
- Tang, A.-M., and Cui, Y.-J., 2009, Modelling the thermo-mechanical volume change behaviour of compacted expansive clays: arXiv preprint arXiv:0904.3614.

- , 2010, Effect of mineralogy on the thermo-hydro-mechanical parameters of MX80 bentonite: *Journal of Rock Mechanics and Geotechnical Engineering*, v. 2, no. 1, p. 91-96.
- Tournassat, C., Bizi, M., Braibant, G., and Crouzet, C., 2011, Influence of montmorillonite tactoid size on Na–Ca cation exchange reactions: *Journal of Colloid and Interface Science*, v. 364, p. 443-454.
- Vidal, O., and Dubacq, B., 2009, Thermodynamic modelling of clay dehydration, stability and compositional evolution with temperature, pressure and H₂O activity: *Geochimica Et Cosmochimica Acta*, v. 73, no. 21, p. 6544-6564.
- Vieillard, P., Blanc, P., Fialips, C. I., Gailhanou, H., and Gaboreau, S., 2011, Hydration thermodynamics of the SWy-1 montmorillonite saturated with alkali and alkaline-earth cations: A predictive model: *Geochimica Et Cosmochimica Acta*, v. 75, no. 19, p. 5664-5685.
- Vikhrenko, V. S., 2011, Heat Conduction – Basic Research, Rijeka, Croatia, InTech, 392 p.:
- Villar, M. V., Fernandez, A. M., Gomez, R., Barrenechea, J. F., Luque, F. J., Martin, P. L., and Barcala, J. M., 2007, State of a bentonite barrier after 8 years of heating and hydration in the laboratory: *Scientific Basis for Nuclear Waste Management XXX*, v. 985, p. 593-598.
- Wagman, D. D., Evans, W. H., Parker, V. B., Schumm, R. H., Halow, I., Bailey, S. M., Churney, K. L., and Nuttall, R. L., 1982, The NBS Tables of Chemical Thermodynamic Properties - Selected Values for Inorganic and C-1 and C-2 Organic-Substances in Si Units: *Journal of Physical and Chemical Reference Data*, v. 11, p. 1-407.
- Wagner, W., and Pruss, A., 2002, The IAPWS formulation 1995 for the thermodynamic properties of ordinary water substance for general and scientific use: *Journal of Physical and Chemical Reference Data*, v. 31, no. 2, p. 387-535.
- Wang, Y., 2011, Integration Plan for Used Fuel Disposition (UFD) Data Management (FCRD-USED-2011-000386), U.S. Department of Energy, Used Fuel Disposition Campaign, p. 1-20.
- Wanner, H., 1999a, Guidelines For The Assignment Of Uncertainties (TDB-3): OECD-NEA.
- , 1999b, Guidelines For The Independent Peer Review Of TDB Reports (TDB-6): OECD-NEA.
- Wanner, H., and Östhols, E., 2000, Standards and Conventions for TDB Publications: OECD-NEA.
- Weck, P., Kim, E., Jové-Colón, C., and Sassani, D. (2013). First-Principles Modeling of Salt Minerals: Structures and Properties of Anhydrite, Bischofite, Polyhalite and Carnallite. *Geochimica et Cosmochimica Acta*, submitted.
- Wersin, P., Johnson, L. H., and McKinley, I. G., 2007, Performance of the bentonite barrier at temperatures beyond 100°C: A critical review: *Physics and Chemistry of the Earth*, v. 32, no. 8-14, p. 780-788.
- Wolery, T. J., and Jové Colón, C. F., 2007, Qualification of Thermodynamic Data for Geochemical Modeling of Mineral–Water Interactions in Dilute Systems (ANL-WIS-GS-000003 REV 01): Las Vegas, Nevada, Sandia National Laboratories; OCRWM Lead Laboratory for Repository Systems, p. 412 pp.

**Molecular Dynamic (MD) Study on the Swelling
Properties of Montmorillonite and Beidellite Clays:
Comparison of Temperature, Cation, and Charge
Substitution Effects
(Part VI)**

1. Introduction

Smectites are abundant, naturally occurring clays that readily swell in the presence of water. Understanding the swelling process is important for many reasons including scientific curiosity, environmental considerations, and engineering safety. For example, smectite clays are used commercially in cosmetics, pharmaceuticals, construction materials, and as catalysts (Amato, 2013; Carretero, 2002; Hanczyc et al., 2003; Carretero and Pozo, 2009; Macewan, 1948). The swelling properties of clays also affect their use as engineered barriers, including those used in nuclear waste repositories, and in borehole stability during drilling for oil and gas (Anderson et al., 2010; Coulon et al., 1987; Galle, 1998; Montes-H et al., 2005).

Smectite clays are a natural product of the weathering and decomposition of igneous rocks and are commonly occurring in the environment (Zoltai, 1984). Formed in a ‘T-O-T’ layered pattern made from tetrahedral (T) silicate sheets surrounding octahedral (O) aluminum sheets, smectite clay layers are approximately 10 Å thick. Isomorphic substitutions can occur in either the tetrahedral or octahedral sheets resulting in a net negative charge that is counter balanced by cations located in the interlayer between individual clay sheets. The interaction between negatively charged clay sheets and positively charged interlayer cations serves to anchor multiple clay sheets together. Interestingly, in the presences of water these cations become hydrated and the clay swells.

The extent to which clay swells is influenced by several variables that can be subdivided into two categories: 1) thermodynamic variables and 2) chemical variables. Thermodynamic variables include temperature (Morodome and Kawamura, 2009), external pressure (Smith et al., 2006) humidity (water chemical potential) (Mooney et al., 1952), and salt concentration (osmotic pressure) (Anderson et al., 2010) while chemical variables include surface charge density (Slade et al., 1991), charge location (Greathouse and Sposito, 1998; Liu et al., 2008), and cation species (Boek et al., 1995b; Chang et al., 1997; Mooney et al., 1952).

In this study, we investigate the influence of temperature, cation species, and charge location on the crystalline swelling of smectite clays. Specifically, the swelling curves of Na⁺- Cs⁺- Ca²⁺- Mg²⁺- montmorillonite and beidellite clays were simulated at T = 298 K and 425 K. First, we discuss the d-spacing for dry clays and one-layer and two-layers hydrates as a function of cation species and charge location. We then report the one-dimensional density profiles for these states along with the cation-water and cation-clay surface oxygen coordination numbers. Finally, we discuss the effect of increasing temperature on the clay swelling states.

2. Model and Method

Molecular Dynamics Simulations

The model systems represent end members in smectite minerals and in cation species. Both clay mineral models have a layer charge of -0.75 e/unit cell contained exclusively in the octahedral (montmorillonite) or tetrahedral (beidellite) sheets. The general chemical formula for sodium montmorillonite studied in this work can be expressed as Na_{0.75}Si₈ [Mg_{0.75}Al_{3.25}]O₂₀(OH)₂•nH₂O while the chemical formula for beidellite can be expressed as Na_{0.75}[Si_{7.25}Al_{0.75}] Al₄O₂₀(OH)₄•nH₂O. Representative snapshots of the clay mineral models and their corresponding unit cell formulae are shown in Figure 1.

The simulation supercell consisted of 5 orthogonal clay layers, each containing 40 unit cells, with water contents ranging from dry clay to 14.25 H₂O per clay unit cell in increments of 0.75 H₂O per clay unit cell. Negative layer charge was created by randomly substituting Mg for Al in the octahedral sheet (montmorillonite) or Al for Si in the tetrahedral sheet (beidellite). Ten different charge configurations were created for each clay type with the charge sites randomly distributed through out each layer and obeying Loewenstein's substitution rule (Loewenstein, 1954), i.e., substitution sites cannot be adjacent to each other. The configuration with the lowest potential energy was chosen for the simulations.

Force field parameters include van der Waals and electrostatic atomic interactions and were taken from the Clayff force field (Cygan et al., 2004). Clayff is an established energy force field successfully used in a wide range of mineral and environmental applications involving the accurate modeling of structure, thermodynamics, spectroscopy, physical properties, adsorption, and transport behavior of minerals and other environmental phases. The clayff force field is particularly appropriate to this work in elucidating the effects of substitution sites as it treats coordinating oxygen differently based on the local substitution pattern. The flexible SPC water of Teleman et al. is used in conjunction with the clayff force field (Teleman et al., 1987).

Molecular dynamic simulations were performed using the LAMMPS (Plimpton, 1995) simulation package in the isobaric-isothermal ensemble at atmospheric pressure and T = 298 and 425 K. Pressure was controlled independently in the x, y, and z directions, and the temperature was controlled with a Nosé-Hoover thermostat (Martyna et al., 1994; Parrinello and Rahman, 1981; Shinoda et al., 2004; Tuckerman et al., 2006). The coupling constants for the barostat and thermostat are 100 and 1000 time steps respectively. A time step of 0.5 fs was used, and periodic boundaries were applied in all directions. Short-range interactions were truncated at 10 Å, and long-range electrostatics were computed with the particle-particle particle-mesh solver and an accuracy of $1e10^{-4}$.

Independent simulations were performed for each water content, cation, and clay species. Simulations were initialized with cations located in the midplane of the interlayer near charge substitution sites, and waters were inserted above and below the cation layer (Chang et al., 1995). Systems were randomized in the NVT ensemble by freezing the clay and cation atoms while allowing the waters to move as the temperature was ramped from T = 298 to 1000 K over 100 ps. The cations were then allowed to move along with the waters, and the system was run for another 100 ps at T = 1000 K. The temperature was ramped down to either T = 298 or 425 K over 100 ps. Finally, systems were equilibrated in the NPT ensemble for 1 ns before data was collected over 3 ns to obtain thermodynamic and structural properties. Structural data was collected every 50 ps, while thermodynamic data was collected every 0.5 ps.

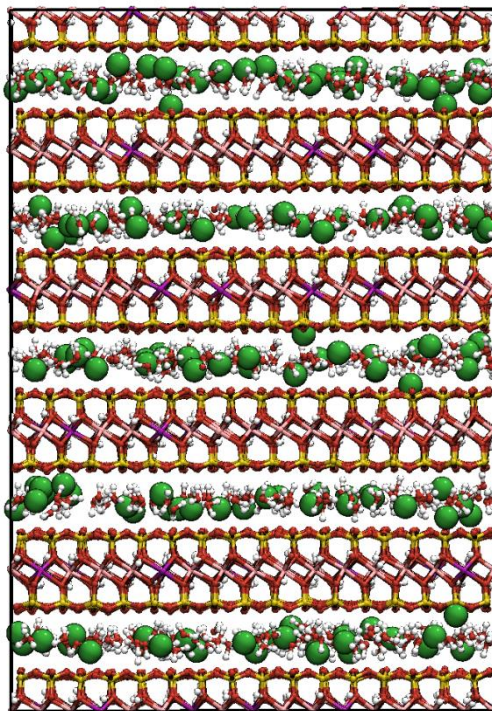


Figure 1. A snapshot (*ac* plane) of the orthogonal Na-montmorillonite simulation supercell containing 210 water molecules in each of the five clay interlayers. The atomistic color code is as follows: octahedral Mg - purple, interlayer sodium cations - green, silicon atoms - yellow, oxygen atoms – red, hydrogen atoms – white, aluminum atoms pink.

2.1 GCMC Simulations Methodology

Water adsorption isotherms at 300 K were obtained from GCMC simulations using the Towhee code (Martin, 2013) in the grand canonical ensemble (μ VT), where μ is the chemical potential of water. Model systems consisted of $4 \times 4 \times 2$ supercells of M-montmorillonite and M-beidellite ($M = \text{Na}, \text{Cs}, \text{Ca}, \text{Mg}$) as described above. Initial configurations of the clay layers were obtained from energy minimization of the dry clays, and layer atoms remained fixed at these coordinates during the subsequent GCMC simulations. Likewise, water molecules were treated as rigid bodies using the SPC/E model (Berendsen et al., 1987). Values of the water chemical potential were related to relative humidity (equivalent to H_2O vapor partial pressures P/P_0 ; P_0 being the partial pressure at saturation) based on the saturation chemical potential of SPC/E water ($-49.0 \text{ kJ}\cdot\text{mol}^{-1}$) (Botan et al., 2011) and the relationship between pressure and chemical potential for an ideal gas (Frenkel and Smit, 2002). Two d-spacings were chosen for all clay models, corresponding to the one-layer (12.0 \AA) and two-layer (15.0 \AA) hydrates as seen in the MD swelling curves. Models were also created corresponding to plateau regions in the MD swelling curves for Mg (13.5 \AA) and Ca (14.5 \AA) clays. Interlayer cations were initially placed in the midplane between clay layers directly above (below) layer charge sites. As in the MD simulations, short-range interactions were truncated at 10 \AA , and long-range electrostatics were computed using Ewald summation with an accuracy of 1.0×10^{-4} . GCMC moves were made according to the following probabilities: 40% configurational-bias insertion or deletion, 15%

intrabox configurational-bias molecule transfer, 15% molecule regrowth, 15% center-of-mass translation, and 15% rotation about the center of mass. Only moves involving water molecules were allowed for the first 2.5×10^7 steps to allow the water molecules to equilibrate in the accessible interlayer region. For the remaining 7.5×10^7 steps, translation moves of interlayer cations were also included with a 10% relative probability (90% of the translation moves involved water molecules). Configurations and energies were stored over the final 5.0×10^7 steps for analysis.

3. Results and Discussion

3.1 Swelling Curves

The swelling and potential energy curves for Na^+ - Cs^+ - Ca^{2+} - Mg^{2+} -montmorillonite at $T = 298$ K were calculated and are shown in Figure 2. Uncertainties in the d-spacing values from the simulations are less than the symbol size in the swelling plots. The overall stepwise swelling behavior of montmorillonite agrees well with previous simulations and experimental studies, and it is clear that the cation species has an important effect on clay swelling (Boek et al., 1995b; Cases et al., 1992; Karaborni et al., 1996; Meleshyn and Bunnenberg, 2005; Mooney et al., 1952). For each clay type, the water content corresponding to the swelling state is chosen based plateaus in the swelling curves. The calculated values for the d-spacing are presented in Table 1.

Comparing the monovalent cations cesium and sodium, it is clear that Cs-montmorillonite has a larger interlayer space than Na-montmorillonite. This is consistent with Cs having a larger ionic radius than Na (1.84 \AA compared to 1.16 \AA) (Burgess, 1988). Na-montmorillonite shows distinct transitions between the dry clay, one-layer, and two-layer hydration states while the Cs-montmorillonite shows only a distinct transition from the dry clay to the mono-hydrated clay. For dry clay, the interlayer spacing for Cs-montmorillonite is 10.53 \AA while it is slightly smaller value of 9.35 \AA for Na-montmorillonite. These values are consistent with previously calculated experimental values of $10.7\text{-}11.2 \text{ \AA}$ (Berend et al., 1995; Calvet, 1973; Chiou and Rutherford, 1997; Mooney et al., 1952; Rutherford et al., 1997) and $9.55 - 9.8 \text{ \AA}$ (Berend et al., 1995; Calvet, 1973; Cases et al., 1992; Chiou and Rutherford, 1997; Fripiat et al., 1965; Fu et al., 1990; Keren and Shainberg, 1975; Kraehenbuehl et al., 1987; Mooney et al., 1952; Posner and Quirk, 1964; Rutherford et al., 1997) and with previously calculated simulated values of $10.39 - 10.8 \text{ \AA}$ (Liu et al., 2008; Marry et al., 2002) and $9.68 - 10.3 \text{ \AA}$ (Boek et al., 1995a, b; Hensen and Smit, 2002; Marry et al., 2002; Tao et al., 2010) for Cs and Na montmorillonite, respectively. It should be noted that the previously reported results represent a range of charge site locations and charge densities. The values of 12.28 \AA for the mono-hydrated Cs clay and 12.17 for the mono-hydrated sodium clay are again consistent with previously calculated experimental values of $11.9\text{-}12.6 \text{ \AA}$ (Berend et al., 1995; Chiou and Rutherford, 1997; Rutherford et al., 1997) and $12.3\text{-}12.6 \text{ \AA}$ (Berend et al., 1995; Cases et al., 1992; Fu et al., 1990; Kraehenbuehl et al., 1987; Mooney et al., 1952) and simulated values of $12.1\text{-}12.7 \text{ \AA}$ (Liu et al., 2008; Marry et al., 2002; Whitley and Smith, 2004) and $12.0\text{-}12.4 \text{ \AA}$ (Boek et al., 1995b; Chang et al., 1995; Hensen and Smit, 2002; Karaborni et al., 1996; Marry et al., 2002; Whitley and Smith, 2004) for Cs and Na montmorillonite, respectively. For Na-montmorillonite, the value of the interlayer for the two-layer hydrated is 14.91 \AA , which is close to but slightly lower than the reported experimental and simulation data of $14.9\text{-}15.55 \text{ \AA}$ (Berend et al., 1995; Calvet, 1973; Cases et al., 1992; Chiou and Rutherford, 1997; Fripiat et al., 1965; Fu et al., 1990; Keren and Shainberg, 1975; Kraehenbuehl

et al., 1987; Mooney et al., 1952; Posner and Quirk, 1964) and 15.2-15.5 Å (Boek et al., 1995b; Chang et al., 1995; Hensen and Smit, 2002; Karaborni et al., 1996; Marry et al., 2002; Whitley and Smith, 2004), respectively. Cs-montmorillonite does not form a two-layer hydrate in nature (Berend et al., 1995; Calvet, 1973), but for comparison we report the value of the simulated two-layer hydrate with a d-spacing of 15.00 Å. Na-montmorillonite has been observed to form a three-layer hydrate at higher water content, but we do not investigate those systems in this work.

The divalent cations swell more rapidly than the monovalent cations, which is consistent with predicted behavior based on hydration energies (Mooney et al., 1952; Whitley and Smith, 2004). Experimentally, magnesium and calcium montmorillonite are known to only form two-layer hydrates (Morodome and Kawamura, 2009). As illustrated in Figure 2, there is a distinct plateau at the two-layer hydrate for Ca-montmorillonite and a smaller, less pronounced plateau at lower water concentrations. This artificial one-layer hydrate for Ca-montmorillonite has been seen before in simulation (Tao et al., 2010) and corresponds to an interlayer spacing of 11.95 Å. The two-layer hydrate for this clay corresponds to an interlayer spacing of 14.61 Å and is slightly smaller than experimental values 15.4-16.0 (Fripiat et al., 1965; Mooney et al., 1952; Posner and Quirk, 1964). The swelling curve for Mg-montmorillonite exhibits a single plateau between 3 and 6 water molecules per clay unit cell, and it forms a two-layer hydrate with an interlayer spacing of 13.61 Å. This is consistent with simulated of 13.83 Å (Meleshyn and Bunnenberg, 2005) and experimental values of 13.9 and 14.85 Å (Bishop et al., 1994; Laird, 1999).

The effect of charge location on smectite d-spacing is determined by comparing the swelling curves of montmorillonite with beidellite, Table 1 and Figure 3. Our clays represent extreme end-member case studies in which the montmorillonite charge is completely buried in the octahedral layer while the beidellite clay has only shallow charge located in the tetrahedral layer. There is a lack of experimental data that compares charge site locations in smectite clays. This is understandable given that in natural clays it is hard to control the charge location, clay composition, and charge density at the same time. Fortunately, computer simulation offers the advantage of complete control over the sample properties, and the consistency between the montmorillonite data and previously reported experimental and simulation data gives us confidence to extend or simulations to study beidellite.

In general, the interlayer spacing for beidellite is slightly smaller than for montmorillonite. Specifically, the interlayer spacing of a dry clay is slightly larger for Na⁺- and Cs⁺-montmorillonite than for Na⁺- and Cs⁺- beidellite, while it is the same for the divalent cations. In the one-layer hydration state, Cs and Ca - montmorillonite exhibit a slightly larger d-spacing compared to the same cations in beidellite, while this trend is reversed for the sodium clays. In the two-layer hydrated, montmorillonite exhibits a larger d-spacing than beidellite for each of the studied cations.

Previously reported simulation data is limited and the conclusions that can be drawn are varied. For example, Liu et al. reported that the layer spacing increased for three different water contents as the charge was shifted from the octahedral layers to the tetrahedral layers (Liu et al., 2008). However, their data shows no significant trend within the reported error. Chávez-Páez et al. reported smaller values for an Otay montmorillonite in which the charge density was entirely located in the octahedral layer as compared to a Wyoming montmorillonite where a quarter of the charge was shifted from the octahedral to the tetrahedral sheets. However, for this study with a calcium cation species, the charge density was not kept consistent between the two different samples. Skipper et al. reported that the basal spacing increases with increasing tetrahedral

charge layer for a sodium montmorillonite (Skipper et al., 1995). They attributed this to the counter ions binding to directly above the tetrahedral charge sites in an inner-sphere complex, and a comparison is made between the swelling states of a Wyoming montmorillonite being larger than for a pyrophyllite. However, this study uses a different clay and water model than is used in this study. Future work might focus on determining the stable swelling states from free energies using a narrower step size between water contents than was used there. This might help refine the data and conclusions.

Table 1. Values of interlayer spacing for montmorillonite and beidellite as a function of interlayer cation species. The interlayer spacing is given in angstroms, and the parenthetical values are the corresponding number of water molecules per clay unit cell for each state.

	Dry clay		One-layer hydrate		Two-layer hydrate	
	Mont.	Beid.	Mont.	Beid.	Mont.	Beid.
Na ⁺	9.35	9.42	12.17 (3.75)	12.26 (3.75)	14.91 (8.25)	14.87 (8.25)
Cs ⁺	10.53	10.93	12.28 (3)	12.27 (3)	15.00 (7.5)	14.93 (7.5)
Ca ²⁺	9.35	9.32	11.95 (2.25)	11.94 (2.25)	14.61 (7.5)	14.39 (7.5)
Mg ²⁺	9.30	9.30	--	12.17 (2.25)	13.61 (4.5)	3.51 4.5)

3.2 Potential Energies

The change in potential energy $\Delta U(N)$ of adding a water molecule into the clay interlayer as compared to dry clay was calculated as a function of increasing water content:

$$\Delta U(N) = (\langle U(N) \rangle - \langle U(0) \rangle) / N \quad (1)$$

where $\langle U(N) \rangle$ is the average potential energy of the clay-water system containing N water molecules and $\langle U(0) \rangle$ is the average potential energy of the dry clay system. The results for montmorillonite and beidellite are presented in Figures 2 and 3, respectively. These data can be compared to the value of the internal energy of bulk SPC/E water of -41.4KJ/mol; the value for SPC/E is used as a proxy for the SPC water of Teleman that is used in this study, which has not been calculated. During the first stage of hydration for the monovalent cations, the energy drops significantly below this bulk water value. Then as hydration continues, the hydration energy rises before leveling off. For the divalent cations, the hydration energy drops significantly below the value for the monovalent cations before continuously increasing as hydration continues. In the first phase of hydration at low water content, the hydration energies for beidellite are significantly lower than for montmorillonite, showing that it is energetically more favorable to add a water molecule to as system with the charge sites located in the tetrahedral layer as compared to the octahedral layer.

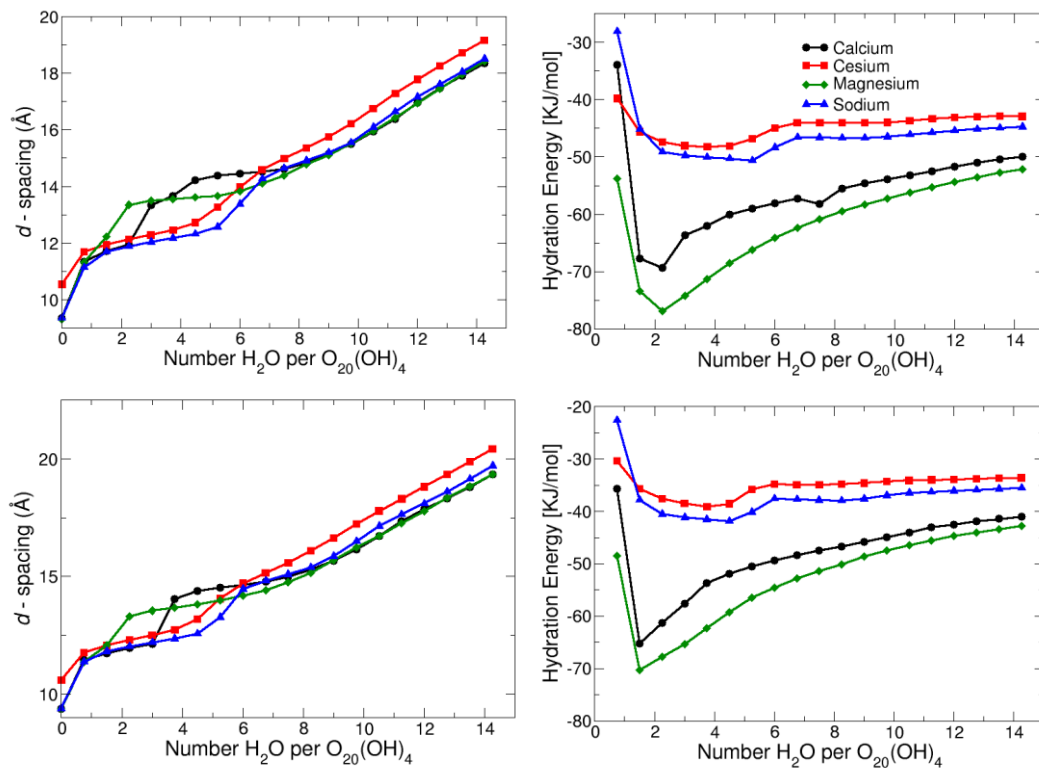


Figure 2: Montmorillonite swelling curves (left) and hydration energy (right) as a function of water content at $T= 298$ K (top) and 425 K (bottom). Symbols represent different interlayer cations and are defined as the following: calcium – black circles, cesium – red squares, magnesium – green diamonds, and sodium – blue triangles. Error bars are smaller than symbols.

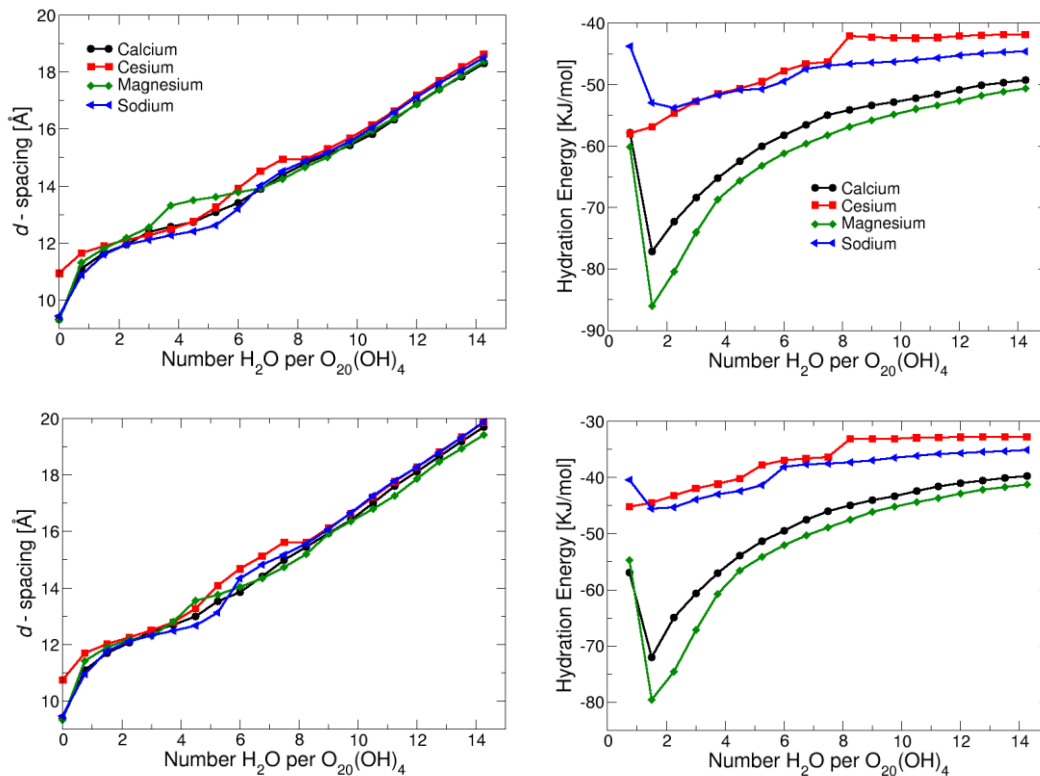


Figure 3: Beidellite swelling curves (left) and hydration energy (right) as a function of water content at $T = 298$ K (top) and 425 K (bottom). Symbols represent different interlayer cations and are defined as the following: calcium – black circles, cesium – red squares, magnesium – green diamonds, and sodium – blue triangles. Error bars are smaller than symbols.

3.3 Temperature Effects

The effects of temperature on the d-spacing can be seen in Figures 2 and 3. In general, increasing temperature shifts the swelling curves to higher d-spacing. This is consistent with the experimental work of Morodome and Kawamura (2009) that examined the effects of increasing temperature on the swelling behavior of Na-montmorillonite. This trend is examined in detail for sodium smectites in Figure 4. For Na^+ -montmorillonite, the swelling curves at both temperatures show distinct one and two-layer hydration states, and the increase in basal spacing occurred at similar water contents. The shift to larger interlayer spacing is most prominent in the transitions regions and the least prominent in the one-layer hydration state. The swelling curves of Na^+ -beidellite shows similar trends as those of Na^+ -montmorillonite; however, the plateau characterizing the two-layer hydration state is lost at the higher temperature for this clay.

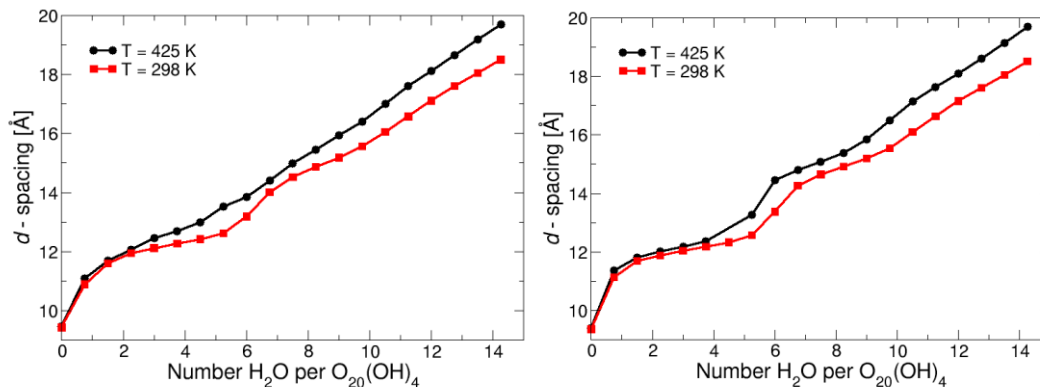


Figure 4. Swelling curves for Na^+ - beidellite (left) and Na^+ - montmorillonite at $T = 298 \text{ k}$ (red squares) and $T = 425 \text{ K}$ (black circles).

3.4 Interlayer Molecular Structure

For each cation-clay combination, the distributions of cations and water molecules in the interlayer were calculated for select hydration states and are shown as one-dimensional density profiles in Figures 5 and 6. These profiles represent the average cation and water molecule locations across all five interlayers.

For montmorillonite, we show the one-layer and two-layer hydrate structures for Na^+ , Cs^+ , and Ca^{2+} cations and the structure corresponding to the two-layer Mg^{2+} cation along with the structure for a water content double that of the two-layer hydrate, Figure 5. We see that the cesium cations remain close to the surface as the water content increases rather than forming a single layer at the interlayer midplane. The two cesium peaks spread apart as the water content increases allowing the cesium to maintain a relatively constant distance from the clay surface regardless of water content. In the mono-hydrated state, the sodium cations split into three peaks: two, very small peaks close to the clay surface and a more prominent peak in the middle of the interlayer. As the water content increases and a two-layer hydrate forms, the sodium forms a single peak at the midplane. Like sodium, calcium also splits into three peaks in the mono-hydrated state. However, we see the water peak also splits with a sharp middle peak and two smaller shoulders forming between the calcium ions. In the two-layer hydrate, the calcium peaks combine to form a single peak at the midplane of the interlayer. For the Mg^{2+} cation, the density profile corresponding to the two-layer hydrate chosen based on the swelling curves shows a single cation peak at the midplane, but also a splitting of the water oxygens into four peaks. At a higher water content that corresponds to a d-spacing of 15.1 \AA the water oxygen peaks collapse from four to two while the Mg^{2+} ion remains at the midplane.

Comparing the montmorillonite density profiles with those for beidellite, Figure 6, it is clear that the charge location has a strong effect on the atomistic structuring in the clay interlayer. We see that there is a tendency for the cations in the beidellite interlayer to remain closer to the clay surface than for those in the montmorillonite interlayer. For example, in mono-hydrated beidellite the interlayer sodium ions form two, equally distributed peaks that are offset from the midplane towards the clay surface as compared to Na^+ -montmorillonite structure that has a prominent peak at the midplane of the interlayer, Figure 7. In the two-layer hydrate, the Na^+ ions split to form three peaks as compared to the single peak in the montmorillonite structure.

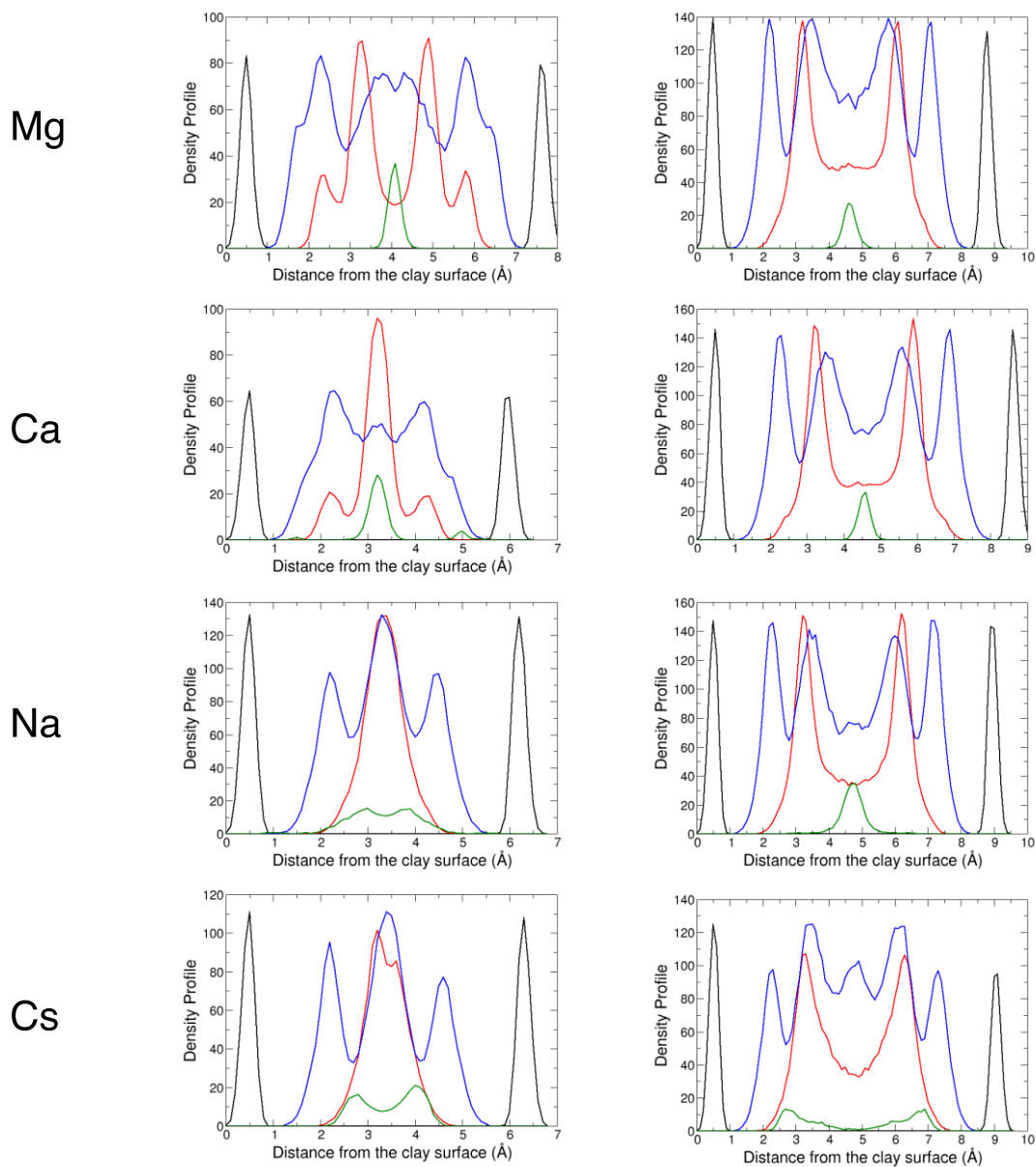


Figure 5. Density profiles for montmorillonite showing various interlayer cation species (green), water oxygens (red), water hydrogens (blue), and clay surface oxygens (black). The density profiles correspond to the following water contents per clay unit cells in the left/right-hand columns: Cs^+ 3/7.5; Na^+ 3.75/8.25; Ca^{2+} 2.25/7.5; Mg^{2+} 4.5/9.

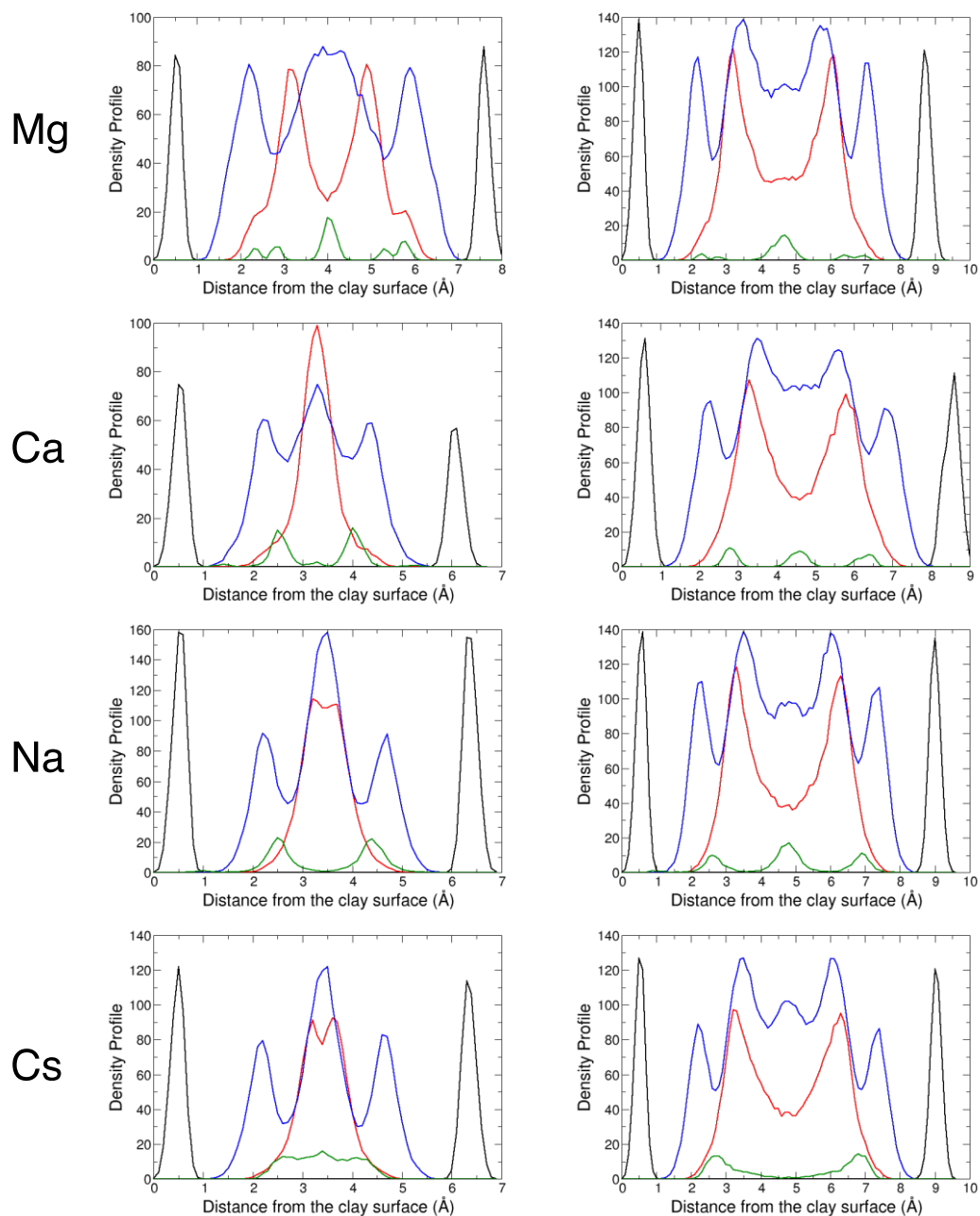


Figure 6. Density profiles for beidellite showing various interlayer cation species (green), water oxygens (red), water hydrogens (blue), and clay surface oxygens (black). The density profiles correspond to the following water contents per clay unit cells in the left/right-hand columns: Cs^+ 3/7.5; Na^+ 3.75/8.25; Ca^{2+} 2.25/7.5; Mg^{2+} 4.5/8.25.

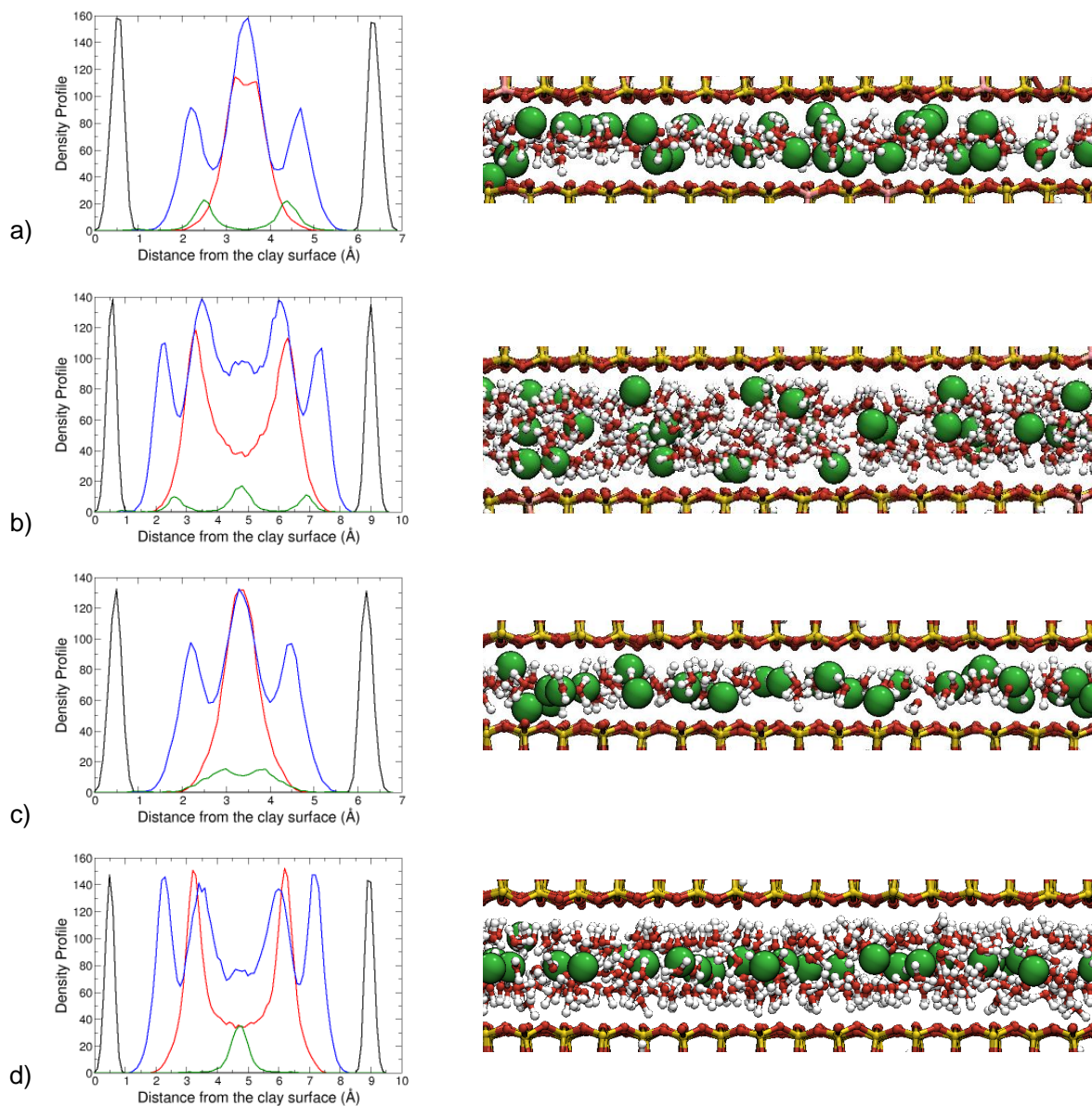


Figure 7. Atomistic snapshots corresponding to the density profiles for a) one-layer Na^+ -beidellite, b) two-layer Na^+ -beidellite, c) one-layer Na^+ -montmorillonite, and d) two-layer Na^+ -montmorillonite. The density profiles show the structure of the sodium cations (green), water oxygens (red), water hydrogen (blue), and clay surface oxygen (black). The atomistic snapshots illustrate the structure of the sodium cations (green), water oxygen (red), water hydrogen (white), clay surface oxygen (red), and the clay silicon atoms (yellow).

GCMC Simulations: Results

Water adsorption isotherms from the GCMC simulations are shown in Supporting Information. Adsorption loadings are given in units of water molecules per unit cell (H₂O/u.c.) for consistency with the MD swelling curves. Isotherms for the Na-clays are consistent with published results for Na-montmorillonite from GCMC simulations (Hensen et al., 2001; Smith et al., 2006) and experiment (Ferrage et al., 2010). Atomic density profiles of interlayer ions and water molecules (Supplemental Information in Appendix F: Figures S3 through S10) for the 12.0 Å and 15.0 Å phases are representative of one-layer and two-layer hydrates, respectively. The initial water uptake corresponds to ion hydration (Smith et al., 2006), followed by a gradual increase in adsorbed water until a maximum loading is reached. For each ion, the maximum loading (Table 2) is similar for montmorillonite and beidellite. For the one-layer hydrates (12.0 Å), the maximum loading correlates with ionic radius and ion hydration enthalpy. Clays containing the smaller divalent ions with their high hydration energies can accommodate more water. Although the sodium ion has a nearly identical radius as a calcium ion, the much smaller hydration enthalpy results in a substantially lower water content for the 12.0 Å phase. Clays containing the much larger and weakly hydrating cesium ion have even fewer water molecules. For the two-layer hydrates (15.0 Å), the presence of outer-sphere surface complexes for Na-, Ca-, and Mg- clays results in a consistent water content regardless of ion properties. The maximum loading for the sodium clays is slightly lower than that of the divalent cations because a small fraction of sodium ions form inner-sphere surface complexes with the basal surfaces. Cesium ions form exclusively inner-sphere surface complexes in the virtual 15.0 Å phase, resulting in a lower water content.

As a validation of our GCMC methods, we note that the maximum water contents for the Na-clays at 12.0 Å (4.3 H₂O/u.c.) and 15.0 Å (9.0 H₂O/u.c.) are in excellent agreement with experimentally determined water contents for a low-charge Na-saponite: 4.0 H₂O/u.c. – 4.5 H₂O/u.c. for the one-layer hydrate and 8.6 H₂O/u.c. – 9.6 H₂O/u.c. for the two-layer hydrate (Ferrage et al., 2010). The divalent ions also form stable swelling states at 14.5 Å (Ca-montmorillonite) and 13.5 Å (Mg-montmorillonite and Mg-beidellite). Similar findings have been reported from diffraction experiments for Ca- and Mg-montmorillonite, where they are described as intermediate states at 14.0 Å (Ferrage et al., 2005).

Table 2. Maximum Loadings (H₂O/u.c.) from GCMC Simulations at *d*-spacings of 12.0 Å and 15.0 Å.^a

interlayer ion	radius (Å)	$-\Delta H_{\text{hyd}}$ (kJ·mol ⁻¹)	montmorillonite		beidellite	
			12.0 Å	15.0 Å	12.0 Å	15.0 Å
Na ⁺	1.16	406	4.3	9.0	4.0	9.1
Cs ⁺	1.81	276	3.7	8.0	3.6	8.2
Ca ²⁺	1.14	1577	5.0	9.3 (8.5) ^b	5.0	9.5
Mg ²⁺	0.86	1921	5.4	9.4 (7.2) ^b	5.4	9.7 (7.1) ^b

^a Ionic radii and hydration enthalpies (ΔH_{hyd}) are shown for reference.

^b Values in parentheses correspond to plateau regions in the MD swelling curves (14.5 Å for Ca-montmorillonite, 13.5 Å for Mg-montmorillonite and Mg-beidellite).

The GCMC results can also be used to correlate relative humidity (RH) with thermodynamically stable states from the MD swelling curves. The minimum RH value at which the maximum water loading is achieved in the two-layer hydrate phases are shown in Table 3. Adsorption isotherms of the one-layer hydrate phases do not show the characteristic S-shaped curve as seen in the two-layer hydrate phases. We therefore assume that the one-layer hydrate phase is dominant at low RH, which is consistent with experimental findings for Na-saponite (Ferrage et al., 2010) and Na-montmorillonite (Ferrage et al., 2005). For cations that are known to form two-layer hydrates (Na⁺, Ca²⁺, Mg²⁺), Table 3 indicates that these phases begin to form at RH values of 0.45 – 0.50, in agreement with experimentally determined values of approximately 0.50 and 0.60 for low-charge Na-saponite (Ferrage et al., 2010) and Na-montmorillonite (Ferrage et al., 2005), respectively. Additionally, we note that the intermediate states for Ca- and Mg-clays form at RH values between 0.25 – 0.40, consistent with the experimental observation of these same states at RH values between 0.20 – 0.40 (Ferrage et al., 2005). Finally, by comparing MD swelling curves with GCMC adsorption isotherms, we can assign approximate RH ranges to gravimetric water contents corresponding to plateau regions in the MD swelling curves (Table 3).

Table 3. Comparison of RH at Maximum Loading from GCMC Simulations^a with Water Content from MD Simulations^b.

	<i>d</i> (Å)	Na		Ca		Mg	
		RH	H ₂ O/u.c.	RH	H ₂ O/u.c.	RH	H ₂ O/u.c.
Montmorillonite	13.5					0.35	2.25
	14.5			0.40	4.50		
	15.0	0.45	8.25	0.50	8.25	0.45	9.00
Beidellite	13.5					0.25	3.75
	15.0	0.45	8.25	0.50	7.50	0.45	8.25

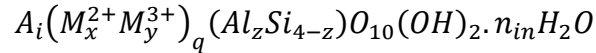
^a Lowest RH values at which the water content was within 0.5 H₂O/u.c. of the fully saturated system (RH = 1.0) at the indicated *d*-spacing.

^b Lowest water content (H₂O/u.c.) corresponding to the indicated *d*-spacing from the MD simulations.

4. Comparing energetic information from molecular simulations and experimental adsorption data for montmorillonite swelling

The purpose of this analysis is to interrogate the molecular dynamics simulation results described in Sections 1 through 3 for Na⁺, Cs⁺, Mg²⁺, Ca²⁺-montmorillonite to elucidate the thermodynamics of clay swelling and compare to the few thermodynamic values that have been extracted from existing experimental data. These preliminary results suggest that the thermodynamics of clay swelling may be determined from molecular dynamics simulation results once a common set of definitions are established between the continuum and molecular-scale models implemented. The data used in this report includes simulation results from the largest molecular simulations conducted on montmorillonite swelling, and therefore the best simulation statistics accumulated for these systems. These simulation results are compared to the only experimental data available for these systems which are discussed in Cases et al. (1992, 1997) and Bérend et al. (1995).

In this document, the generalized structural formula for 1 mol of smectite based on a half unit cell is expressed using the formula provided by Vieillard et al. (2011):



where A is an interlayer cation (Na⁺, K⁺, Ca²⁺, or Mg²⁺), M²⁺ and M³⁺ represent divalent and trivalent cations, respectively, the subscripts i, x, y, and z designate the number of moles of the respective cations per half unit cell in the various structural sites, q stands for the number of occupied octahedral sites per moles of the mineral (dioctahedral, x+y = q = 2; or trioctahedral, x + y = q = 3), and n_{in} denotes the number of moles of interlayer H₂O in the smectite formula.

4.1 Solid Solution Model

Vieillard et al. (2011) consider the silicate layers of the mineral as inert substrate for the interlayer hydration reactions. Partially hydrated smectites can therefore be considered as solid solutions between hydrous and anhydrous smectite end members. The heat of adsorption of water per mole of water on a smectite is given by:

$$\Delta H_{ads} = \frac{(U_1 - U_2)}{(n_1 - n_2)} \quad (2)$$

As the specific surface area of the solid is not constant, U represents a contribution to the heat of immersion and heat of hydration. The heat of immersion is defined as the heat from external H₂O, the heat of hydration is defined as the heat from internal H₂O. The integral hydration enthalpy is defined as

$$\Delta \tilde{H}_{hyd} = \frac{1}{n_m} \int_{x_{hs}=0}^{x_{hs}=1} \overline{\Delta H}_{hyd} * d(x_{hs}) \quad (3)$$

where $\overline{\Delta H}_{hyd}$ is the partial molar hydration enthalpy in kJ/mol H₂O, x_{hs} is the mole fraction of hydrated clay end member, and n_m represents the maximum number of moles of water that can be included in the smectite on the basis of the half cell.

In order to develop a solid solution model for montmorillonites, Vieillard et al. (2011) uses the experimentally acquired calorimetric data of the heat of adsorption and paired adsorption-desorption isotherms for smectites from Cases et al. (1992, 1997) and Bérend et al. (1995). Integral enthalpies of hydration are extracted from their experimental measurements of heat of adsorption. In the figures in this report, the experimental data plotted are these extracted integral enthalpies of hydration as provided in Figures 2, 4, 6, and 8 in Vieillard et al. (2011). Vieillard et al. (2011) chose the maximum number of water molecules $n_m = 5.5$ in order to fit the adsorption-desorption isotherms of Cases et al. (1992, 1997) and Bérend et al. (1995).

4.2 Energies Derived from Molecular Simulation

Smith (1998) calculates the hydration energy, the isosteric heat of adsorption, and the immersion enthalpy from classical molecular simulations. He chooses to define

$$\Delta U = \frac{\langle U(N) \rangle - \langle U(0) \rangle}{N} \quad (4)$$

as the hydration energy. $\langle U(N) \rangle$ is the average hydrated potential energy where N is the number of interlayer water molecules adsorbed on the clay. The partial molar enthalpy corresponds to the change in enthalpy of a clay mineral of specified water content per mole of water, upon adsorption of an additional infinitesimal amount of water. The negative of the differential (or partial molar) enthalpy is called the isosteric heat of adsorption (q_{st}). This can be calculated from molecular simulation using the following expression

$$q_{st}(\bar{N}) = -\frac{\langle U(N) \rangle - \langle U(N') \rangle}{N - N'} + RT \quad (5)$$

where \bar{N} is the average of N and N' . The clay immersion energy is defined by

$$Q_d = N[\Delta U(N) - U_{bulk}] \quad (6)$$

where the d subscript indicates the dry-clay reference state, $\Delta U(N)$ is the hydration energy defined in Eqn. (4) and U_{bulk} is the mean interaction energy of SPC/E water (-41.4 kJ/mol). The reference hydration state is sometimes taken to correspond to the first immersion energy minimum instead of the dry-clay reference state.

4.3 Approach and Results

Calculating Integral Hydration Energies and Enthalpies from Molecular Simulation

The integral hydration energies were calculated from molecular simulation starting with the expression provided by Vieillard et al. (2011) and in Eqn. (3) above. Assuming a fully-hydrated montmorillonite contains 5.5 H₂O molecules per half unit cell, x_{hs} was calculated for each level of hydration simulated. Two methods were used to derive the integral hydration energy from the molecular simulation results. In Method 1, the integral hydration energy for $x_{hs} = 0$ to $x_{hs} = 0.068$, for example, was calculated as

$$\Delta \tilde{H}_{hyd} = \int_{x_{hs}=0}^{x_{hs}=0.068} \overline{\Delta H}_{hyd} * d(x_{hs}) = [\overline{\Delta H}_{hyd}(x_{hs})]_0^{0.068} \quad (6)$$

and the value of $\overline{\Delta H}_{hyd}$ was taken to be equal to

$$\frac{\langle U(N) \rangle - \langle U(N') \rangle}{N - N'} \quad (7)$$

where N and N' are the number of water molecules in the molecular simulation corresponding to $x_{hs} = 0.068$ and $x_{hs} = 0$. In this way, $\Delta\tilde{H}_{hyd}$ was calculated for each increment and summed to obtain $\Delta\tilde{H}_{hyd}$ from $x_{hs} = 0$ to $x_{hs} = 1$. In Method 2, Eqn. (4) is used for each increment from $x_{hs} = 0$ to $x_{hs} = f_{hs}$, and then multiplied by the maximum fraction of hydration (f_{hs}) in that increment. Notice that both Methods 1 and 2 depend on Vieillard et al.'s (2011) assumption that 5.5 H₂O/half unit cell is equivalent to $x_{hs} = 1$. The results for these plots are provided in Figure 8. There is reasonably good agreement between the MD simulation and experimental data at low hydration levels for Cs⁺ and Na⁺, but this agreement disappears at higher hydration levels where changes in experimentally-derived hydration enthalpies decrease with increasing hydration. The MD simulation results do not exhibit this trend. One possible reason for this difference is that Vieillard et al.'s (2011) experiments are for the SWy-1 montmorillonite which has Al^{III} in both the tetrahedral and octahedral sheets and Mg, Fe^{II}, and Fe^{III} in the octahedral sheet while the simulations have been performed on compositionally simpler montmorillonite with no Al^{III} in the tetrahedral sheet and only Mg substitution in the octahedral sheet. In addition, real montmorillonite samples may have mixed layering, where the degree of substitution in each layer differs, while the simulations were performed with layers of identical composition. Further experiments and simulations would be required to fully understand how these variables impact integral hydration energies. The slopes for the Ca²⁺ and Mg²⁺ integral hydration energies derived both from experiments and calculations are similar, however the energies determined from experimental data are consistently lower than those determined experimentally.

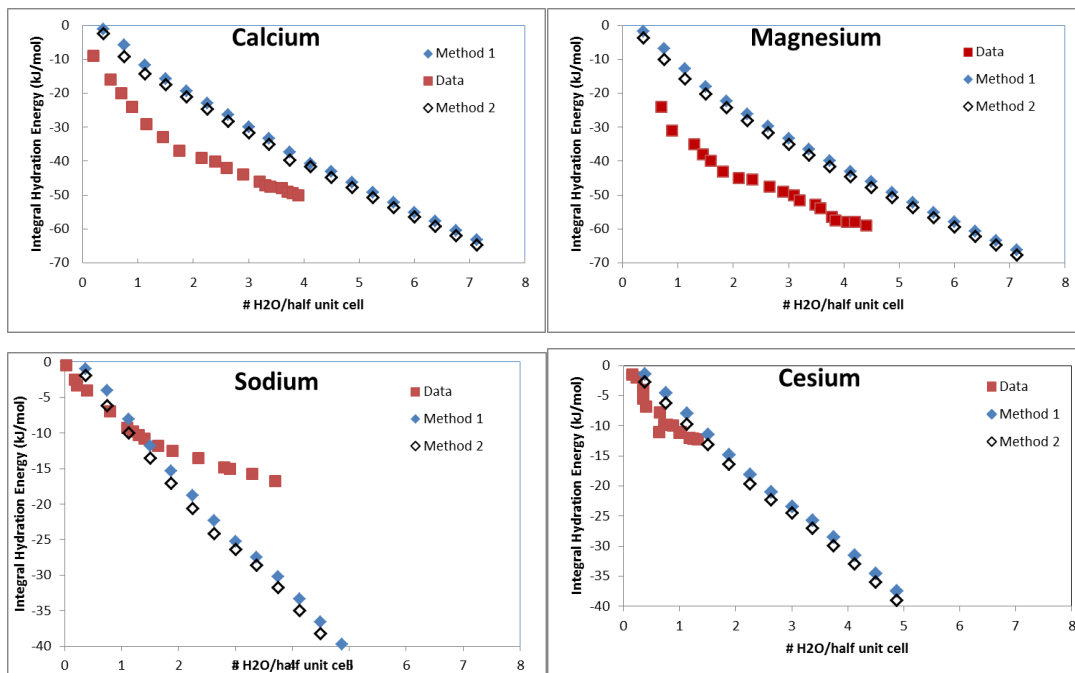


Figure 8. Integral hydration energies as a function of water concentration in montmorillonite interlayers. The data are extracted from figures in Vieillard et al. (2011). The two methods to calculate the integral hydration energies are described in the text.

While Vieillard et al.'s (2011) model fits the data of Cases et al. (1992, 1997) and Bérend et al. (1995) reasonably well using $n_m = 5.5$, this assumption is not imbedded in the experimental data plotted. Figure 9 illustrates that the calculated integral hydration enthalpies are sensitive to the n_m selected and that the best match between the experimental data and the molecular simulation results may require different n_m depending on the interlayer cation. For example, the predicted integral hydration energies for the Ca^{2+} -montmorillonite match the experimental data better using $n_m = 4.5$, and those for Na^+ -montmorillonite match the experimental data better using $n_m = 6.5$. This is not entirely unreasonable, as both the ion and its hydration shell may influence the number of water molecules present in the fully-hydrated clay interlayer.

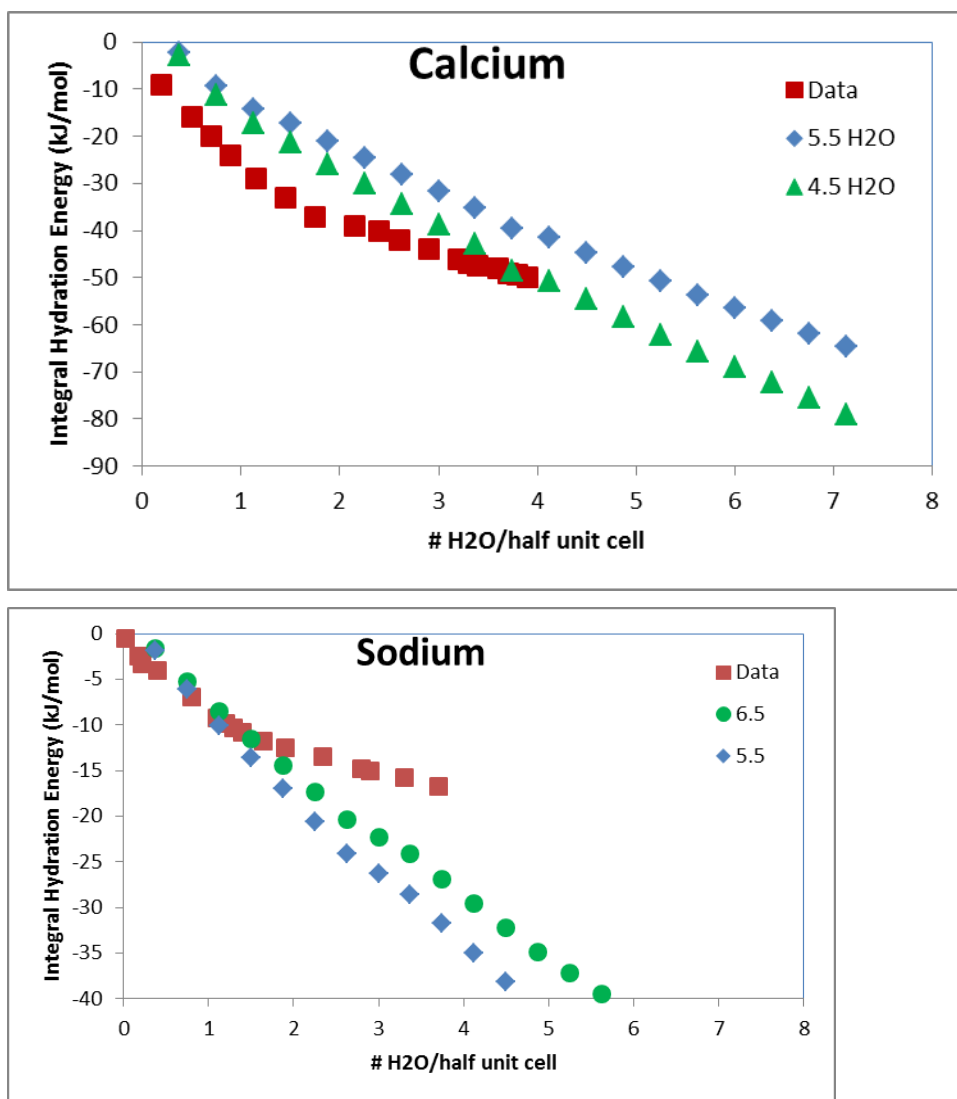


Figure 9. Comparison of integral hydration energies for calcium and sodium. The calculated points derived from molecular simulation data using Method 2 with two different maximum water contents.

Isosteric Heat of Adsorption and Immersion Energy

Using Eqn. (5), $\langle U(N) \rangle$ is taken to be the $\langle PE \rangle$ reported for the entire simulation cell, which contains 5 interlayer regions. Then N ranges from 0 to 2850, in increments of 150 water molecules. The number of half unit cells in the simulation cell is 400. The results are presented in Figure 10. For Cs-montmorillonite, Smith (1998) calculates $q_{st}(\bar{N})$ to range from 30 – 55 kJ/mol. Our calculated $q_{st}(\bar{N})$ ranges from 34 – 54 kJ/mol. Comparing our results to those of Smith (1998), it appears that the maximum and minimum isosteric heats of adsorption occur at similar, although not identical, montmorillonite water contents. This suggests that our post-processing approach matches that of Smith (1998) and that comparisons can be made between calculated isosteric heats of adsorption for Cs^+ , Na^+ , Ca^{2+} , and Mg^{2+} . Smith (1998) suggests that oscillations about the bulk SPC/E water vaporization enthalpy (~ 44 kJ/mol) indicate an enthalpic driving force for further hydration (> 44 kJ/mol) or dehydration (< 44 kJ/mol) upon equilibration of the clay with bulk water.

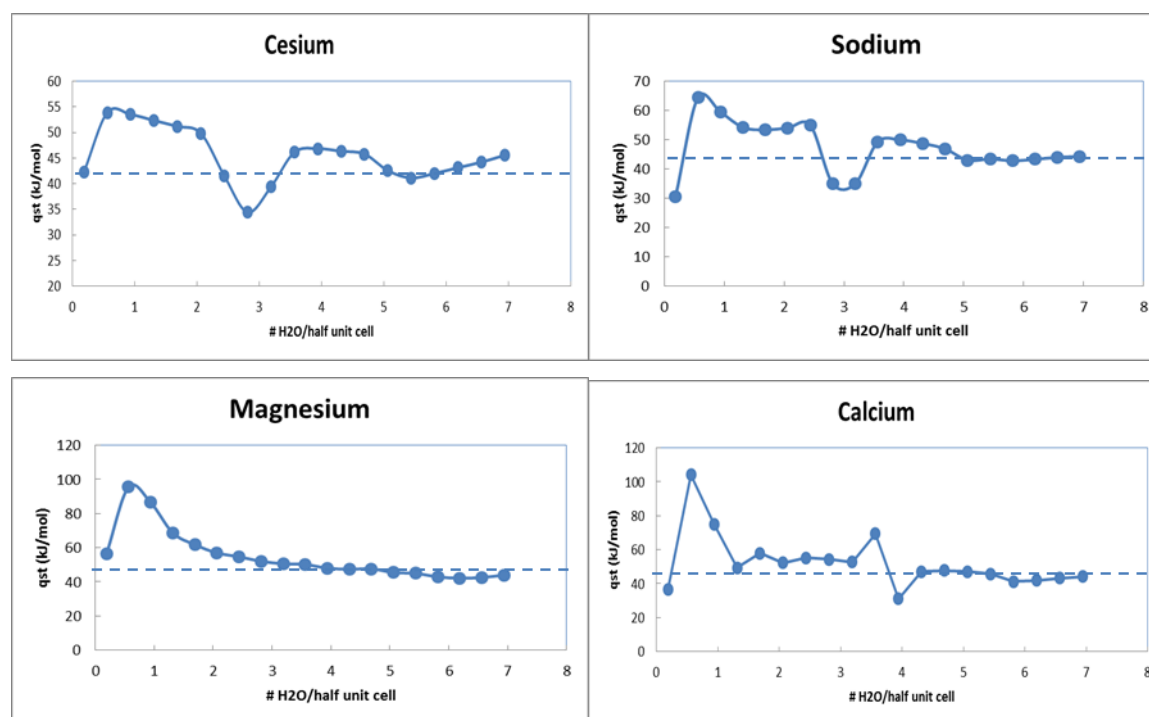


Figure 10. Isosteric heat of adsorption calculated using method of Smith (1998). The dotted lines approximate the mean vaporization energy of bulk SPC/E water. Isosteric heats of adsorption above the line suggest an enthalpic drive for further hydration and those below the line suggest an enthalpic drive for dehydration.

Montmorillonite immersion energies calculated using Eqn. (6) are illustrated in Figure 11. The reference state used is the dry clay. Compared to Smith (1998), the maxima and minima in the immersion energy curves for Cs-montmorillonite occur at similar water contents. The immersion energy minimum calculated by Smith is $60 \text{ J/g}_{\text{clay}}$ compared to our calculated immersion energy minimum of $38 \text{ J/g}_{\text{clay}}$, which is in fact more consistent with the experimental results of Bérend et al. (1995) who report immersion enthalpies of between $30\text{-}40 \text{ J/g}_{\text{clay}}$ for Li^+ , Rb^+ , and Cs^+ -exchanged montmorillonites. Bérend et al. (1995) also reports an experimentally determined immersion enthalpy of $70 \text{ J/g}_{\text{clay}}$ that compares well to our calculated immersion energy of $79 \text{ J/g}_{\text{clay}}$ for Na^+ -montmorillonite. Cases et al. (1997) determined immersion enthalpies of $148 \text{ J/g}_{\text{clay}}$ and $130 \text{ J/g}_{\text{clay}}$ for Mg^{2+} and Ca^{2+} -exchanged montmorillonites respectively. Our calculated immersion energies for the divalent cations may be comparable to those determined by Cases et al. (1997); however, the immersion energy curves for the divalent ions do not exhibit energy minima. Therefore it is difficult to determine which calculated energies correspond to those reported from experiment. Assuming that the experimental enthalpies are reported for $2.25 \text{ H}_2\text{O}$ per half unit cell, the calculated immersion enthalpies are very similar to those determined experimentally ($154 \text{ J/g}_{\text{clay}}$ and $122 \text{ J/g}_{\text{clay}}$ for Mg^{2+} and Ca^{2+} respectively).

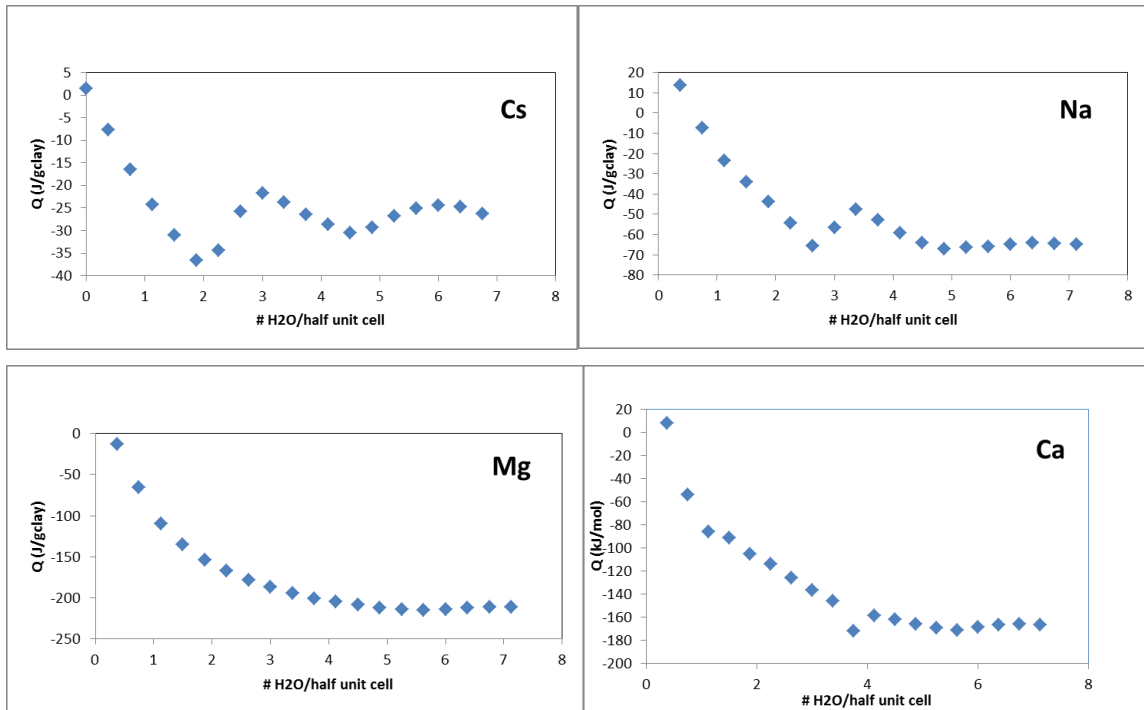


Figure 11. Immersion energies calculated using Eqn. (5). The dry-clay reference state is implemented.

4.4 Summary

This research suggests that molecular dynamics simulations on clay minerals such as montmorillonite can be useful to retrieve thermodynamic parameters to evaluate clay swelling properties where synthetic data is very limited or non-existent. Calculated integral hydration energies for Cs^+ and Na^+ -montmorillonites are shown to be in good agreement with experimentally-derived hydration enthalpies at low hydration levels. The calculated integral hydration energies for the divalent cations are consistently higher than those determined from experiment; however changes in energy from increasing water content are very similar in both datasets. Discrepancies between calculated and experimentally-derived integral hydration energies may be due to different montmorillonite compositions, the presence of mixed clay layers in the experiments, or the somewhat arbitrary definition of 5.5 water molecules per half-unit-cell as representative of a fully-hydrated clay, regardless of interlayer cation.

Our calculated isosteric heats of adsorption for Cs^+ -montmorillonite are similar to those reported by Smith (1998). The calculated isosteric heat of adsorption curve for Mg^{2+} -montmorillonite is significantly different in shape from those for Cs^+ -, Na^+ -, and Ca^{2+} -montmorillonites. Unfortunately, experimental values for the isosteric heats of adsorption are not available for comparison. Calculated immersion energies for both the monovalent and divalent cations are surprisingly consistent with those determined experimentally. In sum, this research demonstrates that molecular dynamics simulations can reproduce experimentally-derived thermodynamic properties for clay swelling and should be useful for investigating how clay swelling properties will vary as a function of temperature and interlayer cations over the lifetime of a repository.

5. References

- Amato, I., 2013, Concrete Solutions: Nature, v. 494, no. 7437, p. 300-301.
- Anderson, R. L., Ratcliffe, I., Greenwell, H. C., Williams, P. A., Cliffe, S., and Coveney, P. V., 2010, Clay swelling - A challenge in the oilfield: Earth-Science Reviews, v. 98, no. 3-4, p. 201-216.
- Berend, I., Cases, J. M., Francois, M., Uriot, J. P., Michot, L., Masion, A., and Thomas, F., 1995, Mechanism of Adsorption and Desorption of Water-Vapor by Homoionic Montmorillonites .2. The Li⁺, Na⁺, K⁺, Rb⁺ and Cs⁺-Exchanged Forms: Clays and Clay Minerals, v. 43, no. 3, p. 324-336.
- Berendsen, H. J. C., Grigera, J. R., and Straatsma, T. P., 1987, The Missing Term in Effective Pair Potentials: Journal of Physical Chemistry, v. 91, no. 24, p. 6269-6271.
- Bishop, J. L., Pieters, C. M., and Edwards, J. O., 1994, Infrared Spectroscopic Analyses on the Nature of Water in Montmorillonite: Clays and Clay Minerals, v. 42, no. 6, p. 702-716.
- Boek, E. S., Coveney, P. V., and Skipper, N. T., 1995a, Molecular modeling of clay hydration: A study of hysteresis loops in the swelling curves of sodium montmorillonites: Langmuir, v. 11, no. 12, p. 4629-4631.
- , 1995b, Monte Carlo molecular modeling studies of hydrated Li-, Na-, and K-smectites: Understanding the role of potassium as a clay swelling inhibitor: Journal of the American Chemical Society, v. 117, no. 50, p. 12608-12617.
- Botan, A., Rotenberg, B., Marry, V., Turq, P., and Noetinger, B., 2011, Hydrodynamics in Clay Nanopores: The Journal of Physical Chemistry C, v. 115, no. 32, p. 16109-16115.
- Burgess, J., 1988, Ions in solution: Basic principles of chemical interactions, New York, NY, Halsted Press: a division of John Wiley & Sons.
- Calvet, R., 1973, Hydration of Montmorillonite and Diffusion of Exchangeable Cations .1. Hydration of Montmorillonite Saturated by Monovalent Cations: Annales Agronomiques, v. 24, no. 1, p. 77-133.
- Carretero, M. I., 2002, Clay minerals and their beneficial effects upon human health. A review: Applied Clay Science, v. 21, no. 3-4, p. 155-163.
- Cases, J. M., Berend, I., Besson, G., Francois, M., Uriot, J. P., Thomas, F., and Poirier, J. E., 1992, Mechanism of Adsorption and Desorption of Water-Vapor by Homoionic Montmorillonite .1. The Sodium-Exchanged Form: Langmuir, v. 8, no. 11, p. 2730-2739.
- Cases, J.M., I. Bérend, M. Francois, J.P. Uriot, L.J. Michot, and F. Thomas (1997) Mechanism of adsorption and desorption of water vapor by homoionic montmorillonite: 3. The Mg²⁺, Ca²⁺, Sr²⁺, and Ba²⁺ exchanged forms. Clays and Clay Minerals, 45, 8-22.
- Chang, F. R. C., Skipper, N. T., and Sposito, G., 1995, Computer simulation of interlayer molecular structure in sodium montmorillonite hydrates: Langmuir, v. 11, no. 7, p. 2734-2741.
- , 1997, Computer simulation of alkali metal cation-montmorillonite hydrates: Abstracts of Papers of the American Chemical Society, v. 213, p. 39-GEOC.

- Chiou, C. T., and Rutherford, D. W., 1997, Effects of exchanged cation and layer charge on the sorption of water and EGME vapors on montmorillonite clays: *Clays and Clay Minerals*, v. 45, no. 6, p. 867-880.
- Coulon, H., Lajudie, A., Debrabant, P., Atabek, R., Jorda, M., and Andre-Jehan, R., 1987, Choice of French clays as engineered barrier components for waste disposal: *Scientific Basis for Nuclear Waste Management X*, p. 813-824.
- Cygan, R. T., Liang, J. J., and Kalinichev, A. G., 2004, Molecular models of hydroxide, oxyhydroxide, and clay phases and the development of a general force field: *Journal of Physical Chemistry B*, v. 108, no. 4, p. 1255-1266.
- Ferrage, E., Lanson, B., Michot, L. J., and Robert, J. L., 2010, Hydration Properties and Interlayer Organization of Water and Ions in Synthetic Na-Smectite with Tetrahedral Layer Charge. Part 1. Results from X-ray Diffraction Profile Modeling: *Journal of Physical Chemistry C*, v. 114, no. 10, p. 4515-4526.
- Ferrage, E., Lanson, B., Sakharov, B. A., and Drits, V. A., 2005, Investigation of smectite hydration properties by modeling experimental X-ray diffraction patterns: Part I. Montmorillonite hydration properties: *American Mineralogist*, v. 90, no. 8-9, p. 1358-1374.
- Frenkel, D., and Smit, B., 2002, *Understanding Molecular Simulation: From Algorithms to Applications*, San Diego, Academic Press, 638 p.:
- Fripiat, J. J., Jelli, A., Poncelet, G., and Andre, J., 1965, Thermodynamic Properties of Adsorbed Water Molecules and Electrical Conduction in Montmorillonites and Silicas: *Journal of Physical Chemistry*, v. 69, no. 7, p. 2185-&.
- Fu, M. H., Zhang, Z. Z., and Low, P. F., 1990, Changes in the Properties of a Montmorillonite-Water System during the Adsorption and Desorption of Water - Hysteresis: *Clays and Clay Minerals*, v. 38, no. 5, p. 485-492.
- Galle, C., 1998, Gas migration and breakthrough pressure in a compacted clay for the engineered barrier of a deep disposal: *Bulletin De La Societe Geologique De France*, v. 169, no. 5, p. 675-680.
- Greathouse, J., and Sposito, G., 1998, Monte Carlo and molecular dynamics studies of interlayer structure in Li(H₂O)(3)-smectites: *Journal of Physical Chemistry B*, v. 102, no. 13, p. 2406-2414.
- Hanczyc, M. M., Fujikawa, S. M., and Szostak, J. W., 2003, Experimental models of primitive cellular compartments: Encapsulation, growth, and division: *Science*, v. 302, no. 5645, p. 618-622.
- Hensen, E. J. M., and Smit, B., 2002, Why clays swell: *Journal of Physical Chemistry B*, v. 106, no. 49, p. 12664-12667.
- Hensen, E. J. M., Tambach, T. J., Blik, A., and Smit, B., 2001, Adsorption isotherms of water in Li-, Na-, and K-montmorillonite by molecular simulation: *Journal Of Chemical Physics*, v. 115, no. 7, p. 3322-3329.
- Isabel Carretero, M., and Pozo, M., 2009, Clay and non-clay minerals in the pharmaceutical industry Part I. Excipients and medical applications: *Applied Clay Science*, v. 46, no. 1, p. 73-80.

- Karaborni, S., Smit, B., Heidug, W., Urai, J., and vanOort, E., 1996, The swelling of clays: Molecular simulations of the hydration of montmorillonite: *Science*, v. 271, no. 5252, p. 1102-1104.
- Keren, R., and Shainberg, I., 1975, Water-Vapor Isotherms and Heat of Immersion of Na-Ca-Montmorillonite Systems .1. Homoionic Clay: *Clays and Clay Minerals*, v. 23, no. 3, p. 193-200.
- Kraehenbuehl, F., Stoeckli, H. F., Brunner, F., Kahr, G., and Muellervonmoos, M., 1987, Study of the Water-Bentonite System by Vapor Adsorption, Immersion Calorimetry and X-Ray Techniques .1. Micropore Volumes and Internal Surface-Areas, Following Dubinin Theory: *Clay Minerals*, v. 22, no. 1, p. 1-9.
- Laird, D. A., 1999, Layer charge influences on the hydration of expandable 2 : 1 phyllosilicates: *Clays and Clay Minerals*, v. 47, no. 5, p. 630-636.
- Liu, X., Lu, X., Wang, R., and Zhou, H., 2008, Effects of layer-charge distribution on the thermodynamic and microscopic properties of Cs-smectite: *Geochimica Et Cosmochimica Acta*, v. 72, no. 7, p. 1837-1847.
- Loewenstein, W., 1954, The Distribution of Aluminum in the Tetrahedra of Silicates and Aluminates: *American Mineralogist*, v. 39, no. 1-2, p. 92-96.
- Macewan, D. M. C., 1948, Clay Minerals as Catalysts and Adsorbents: *Nature*, v. 162, no. 4109, p. 195-196.
- Marry, V., Turq, P., Cartailier, T., and Levesque, D., 2002, Microscopic simulation of structure and dynamics of water and counterions in a monohydrated montmorillonite: *Journal of Chemical Physics*, v. 117, no. 7, p. 3454-3463.
- Martin, M. G., 2013, MCCCSTowhee: a tool for Monte Carlo molecular simulation: *Molecular Simulation*, p. in press, DOI 10.1080/08927022.08922013.08828208.
- Martyna, G. J., Tobias, D. J., and Klein, M. L., 1994, Constant-Pressure Molecular-Dynamics Algorithms: *Journal of Chemical Physics*, v. 101, no. 5, p. 4177-4189.
- Meleshyn, A., and Bunnenberg, C., 2005, Swelling of Na/Mg-montmorillonites and hydration of interlayer cations: A Monte Carlo study: *Journal of Chemical Physics*, v. 123, no. 7.
- Montes-H, G., Marty, N., Fritz, B., Clement, A., and Michau, N., 2005, Modelling of long-term diffusion-reaction in a bentonite barrier for radioactive waste confinement: *Applied Clay Science*, v. 30, no. 3-4, p. 181-198.
- Mooney, R. W., Keenan, A. G., and Wood, L. A., 1952, Adsorption of water vapor by montmorillonite. II. Effect of exchangeable ions and lattice swelling as measured by X-ray diffraction: *Journal of the American Chemical Society*, v. 74, no. 6, p. 1371-1374.
- Morodome, S., and Kawamura, K., 2009, Swelling behavior of Na- and Ca-montmorillonite up to 150 degrees C by in situ X-ray diffraction experiments: *Clays and Clay Minerals*, v. 57, no. 2, p. 150-160.
- Parrinello, M., and Rahman, A., 1981, Polymorphic Transitions in Single-Crystals - a New Molecular-Dynamics Method: *Journal of Applied Physics*, v. 52, no. 12, p. 7182-7190.

- Plimpton, S., 1995, Fast parallel algorithms for short-range molecular dynamics: *Journal of Computational Physics*, v. 117, no. 1, p. 1-19.
- Posner, A. M., and Quirk, J. P., 1964, Changes in Basal Spacing of Montmorillonite in Electrolyte Solutions: *Journal of Colloid Science*, v. 19, no. 9, p. 798.
- Rutherford, D. W., Chiou, C. T., and Eberl, D. D., 1997, Effects of exchanged cation on the microporosity of montmorillonite: *Clays and Clay Minerals*, v. 45, no. 4, p. 534-543.
- Shinoda, W., Shiga, M., and Mikami, M., 2004, Rapid estimation of elastic constants by molecular dynamics simulation under constant stress: *Physical Review B*, v. 69, no. 13.
- Skipper, N. T., Sposito, G., and Chang, F. R. C., 1995, Monte Carlo simulation of interlayer molecular structure in swelling clay minerals. 2. Monolayer hydrates: *Clays and Clay Minerals*, v. 43, no. 3, p. 294-303.
- Slade, P. G., Quirk, J. P., and Norrish, K., 1991, Crystalline Swelling of Smectite Samples in Concentrated NaCl Solutions in Relation to Layer Charge: *Clays and Clay Minerals*, v. 39, no. 3, p. 234-238.
- Smith, D.E. (1998) Molecular computational simulations of the swelling properties and interlayer structure of cesium montmorillonite. *Langmuir*, 14, 5959-5967.
- Smith, D. E., Wang, Y., Chaturvedi, A., and Whitley, H. D., 2006, Molecular simulations of the pressure, temperature, and chemical potential dependencies of clay swelling: *Journal of Physical Chemistry B*, v. 110, no. 40, p. 20046-20054.
- Tao, L., Tian, X. F., Yu, Z., and Tao, G., 2010, Swelling of K^+ , Na^+ , and Ca^{2+} -montmorillonites and hydration of interlayer cations: a molecular dynamics simulation: *Chinese Physics B*, v. 19, no. 10.
- Teleman, O., Jonsson, B., and Engstrom, S., 1987, A molecular dynamics simulation of a water model with intramolecular degrees of freedom: *Molecular Physics*, v. 60, no. 1, p. 193-203.
- Tuckerman, M. E., Alejandre, J., Lopez-Rendon, R., Jochim, A. L., and Martyna, G. J., 2006, A Liouville-operator derived measure-preserving integrator for molecular dynamics simulations in the isothermal-isobaric ensemble: *Journal of Physics a-Mathematical and General*, v. 39, no. 19, p. 5629-5651.
- Vieillard, P., P. Blanc, C. I. Fialips, H. Gailhanou, and G. Gaboreau (2011) Hydration thermodynamics of the SWy-1 montmorillonite saturated with alkali and alkaline-earth cations: A predictive model. *Geochimica et Cosmochimica Acta*, 75, 5664-5685.
- Whitley, H. D., and Smith, D. E., 2004, Free energy, energy, and entropy of swelling in Cs-, Na-, and Sr-montmorillonite clays: *Journal of Chemical Physics*, v. 120, no. 11, p. 5387-5395.
- Zoltai, T. a. S., J.H., 1984, *Mineralogy Concepts and Principles*, Burgess Publishing Company

**Disposal Systems Evaluation Framework (DSEF)
Version 3.0 User Manual
(Part VII)**

1. Overview

The Disposal Systems Evaluation Framework (DSEF) has been developed at Lawrence Livermore National Laboratory (LLNL) to formalize and facilitate the development and documentation of repository conceptual design options for a range of waste forms, geologic environments, repository design concepts, and repository operating modes. DSEF is one component of the Engineered Barrier System (EBS) family of work packages at several national laboratories led by Sandia National Laboratories (SNL), in support of the DOE Office of Nuclear Energy, specifically of the Used Fuel Disposition (UFD) Campaign within the Office of Used Nuclear Fuel Disposition Research and Development (NE-53).

DSEF is a knowledge management system that allows the user to intelligently access and draw data from a case library of hundreds of completed thermal analyses (currently 721 cases in the library), and draw input from databases of material properties and repository development cost data (currently the data in these databases are drawn from more than 100 references).

The core functionality of DSEF is provided by a Microsoft Office Excel 2010 workbook with macros and form controls that create a structured environment and walk the user through the steps of creating the input data required to perform disposal system evaluations internally and by interfacing with external programs. The user can choose to work with built-in data from the case library of previous analysis cases, from the material property databases, or can define their own input descriptions and data.

DSEF uses the Excel **worksheet protection** (implemented on a sheet by sheet basis) to prevent inadvertent over-writing of formulas with data. When worksheet protection is enabled, the user can see all underlying formulas, and enter data in unprotected cells (the unprotected cells generally correspond to the yellow highlighted cells). Worksheet protection also prevents restructuring the files (adding or deleting rows or columns) and changing the formatting, as well as preventing access to the Visual Basic Editor to prevent modification of the macros. If the user needs to modify the worksheet structure, formulas, or macros, they can contact LLNL to get the password to unprotect the worksheets. However, care should be taken in making any modifications, since the macros and formulas are dependent in some cases on the current structure, range names, and macro subroutines

DSEF is set up to retrieve the results of external thermal analysis program runs, summarize them graphically, and provide a template for adding the new results to the Case Library. The Case Library worksheet in DSEF is set up to create a Case Library data record for each new analysis case, at the top of the list of prior cases. Therefore, a separate DSEF file (with unique name) should be saved for each run that is to be archived. Users should submit a copy of their DSEF files to LLNL so that their results can be added to the overall Case Library and made available to other laboratories and stakeholders. LLNL will maintain the DSEF Case Library and make the most current files available on the SNL SharePoint site. The Revision History sheet documents the file evolution.

One of the key objectives of DSEF is to allow the user to compare the results of thermal analyses to the thermal constraints of the design components. These comparisons can then be used to consider design, layout, and operating mode modifications to find combinations that can meet the thermal constraints for a given combination of waste form, geologic medium, surface storage time, and system concept of operation.

DSEF has built-in capabilities to allow a user to graphically compare and contrast material property data, with statistical data summaries for the selected data sets. This is done at the push of a control button, where the user can then select a range or a collection of individual sets of data for comparison, with the freedom to select the placement location of the comparison plot.

As part of the assessment of design concept feasibility, DSEF includes the capability to evaluate the costs of repository design, licensing, construction, maintenance, closure and performance confirmation based on the methodology defined in Carter 2012 and Hardin 2012b. The costs also include waste packages and program integration costs. Similar to the thermal analysis Case Library, DSEF includes five sets of cost data input values from the five generic repository design cases defined in Carter 2012 and Hardin 2012b as example reference cases. The cost data for these five cases can be displayed on the INPUTS worksheet as examples of the cost calculations documented in the subject references, and they can be used directly or over-ridden by user supplied input to analyze different repository design concepts.

Interfaces with various repository analysis codes are possible for further DSEF development. Version 3.0 currently provides input to, and retrieves output data from; several Mathcad Version 15 thermal-analytical models developed at LLNL (see Appendix G).

This User Manual describes the structure and use of the various types of worksheets contained in the DSEF Version 3.0 workbook. Most of the worksheets are fully operational. Some worksheets are placeholders pending potential future development. A Beta test Version 2.0 of the software was delivered previously to the SNL Lead, Carlos Jove-Colon, and the DOE Manager, William Spezialetti; their comments greatly improved the software and this User Manual. The DSEF Version 2.0 Beta Test Excel file and the draft DSEF Version 2.0 User Manual delivered in September and August 2012 respectively met the requirements of Deliverable M4FT-12LL0806043. The DSEF Version 2.1 Excel spreadsheet, Mathcad thermal-analytical model, and the original issue of the DSEF User Manual for Version 2.1 (LLNL-TR-629812) were issued as in March 2013, and posted to the SNL SharePoint server for distribution.

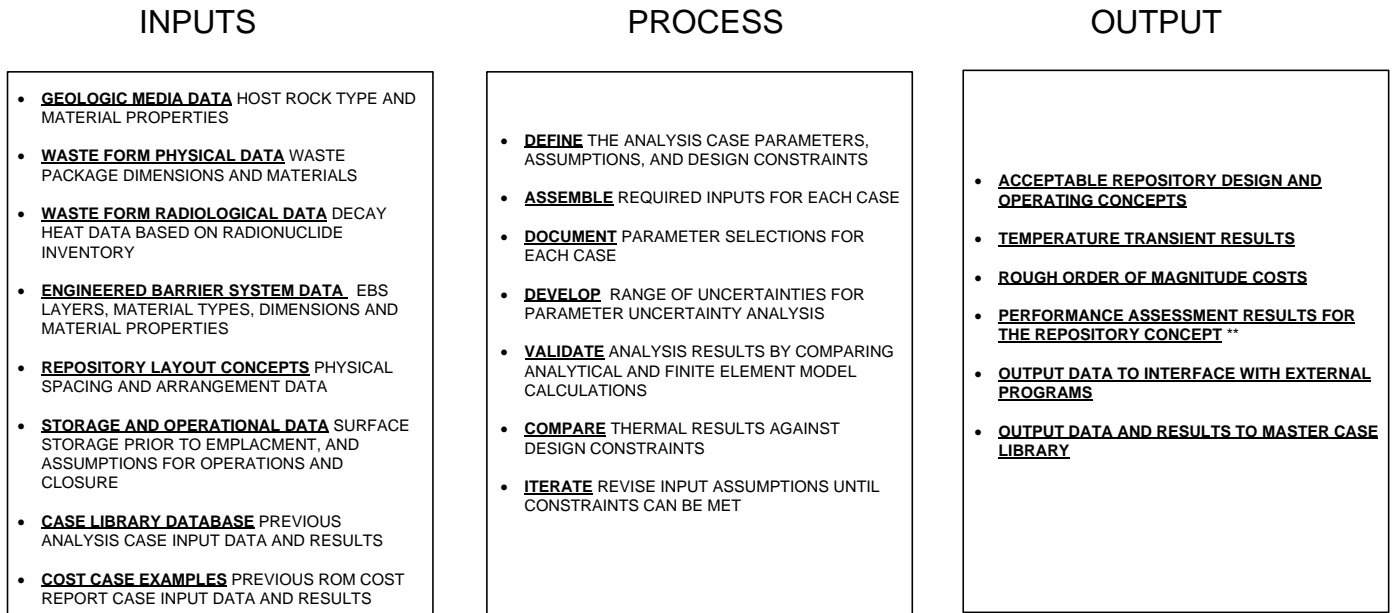
2. Information Flow

As in the DSEF Version 1.0 Progress Report (Sutton 2011), waste forms are examined with respect to three fuel cycles: open (once through), modified open (partial recycle), and closed (full recycle). The six heat-producing waste types from these cycles (one from open, two from modified open, and three from closed) are identified as examples with dimensions, mass, reactor burnup and decay heat properties. Seven disposal environments were initially identified, with the four key mined and saturated repositories (granite, salt, clay/shale and deep borehole) being part of the base case for DSEF evaluations. Together with six fuel types and four pre-emplacement aging times (10, 50, 100, and 200 years), 120 base case models were proposed (including 1 and 4-PWR-assembly options for SNF waste packages in granite, clay, and salt). Additional repository concepts, geological environments, operating modes, waste packages sizes, and spent fuel burnup cases were analyzed and documented in DSEF Version 2.1 (expanding the number of cases in the Case Library to 300) and in Version 3.0 (expanding the number of cases to 721).

Figure 1 is a high-level overview of the structure and approach that is implemented in DSEF to help the user gather the necessary input data, define an analysis case, and compare results to design constraints. It is used in an iterative manner to focus in on feasible repository design

concepts for a given combination of heat generating high-level radioactive waste in a given geologic medium using selected repository design and operating concepts.

Figure 1- DSEF Input-Process-Output diagram

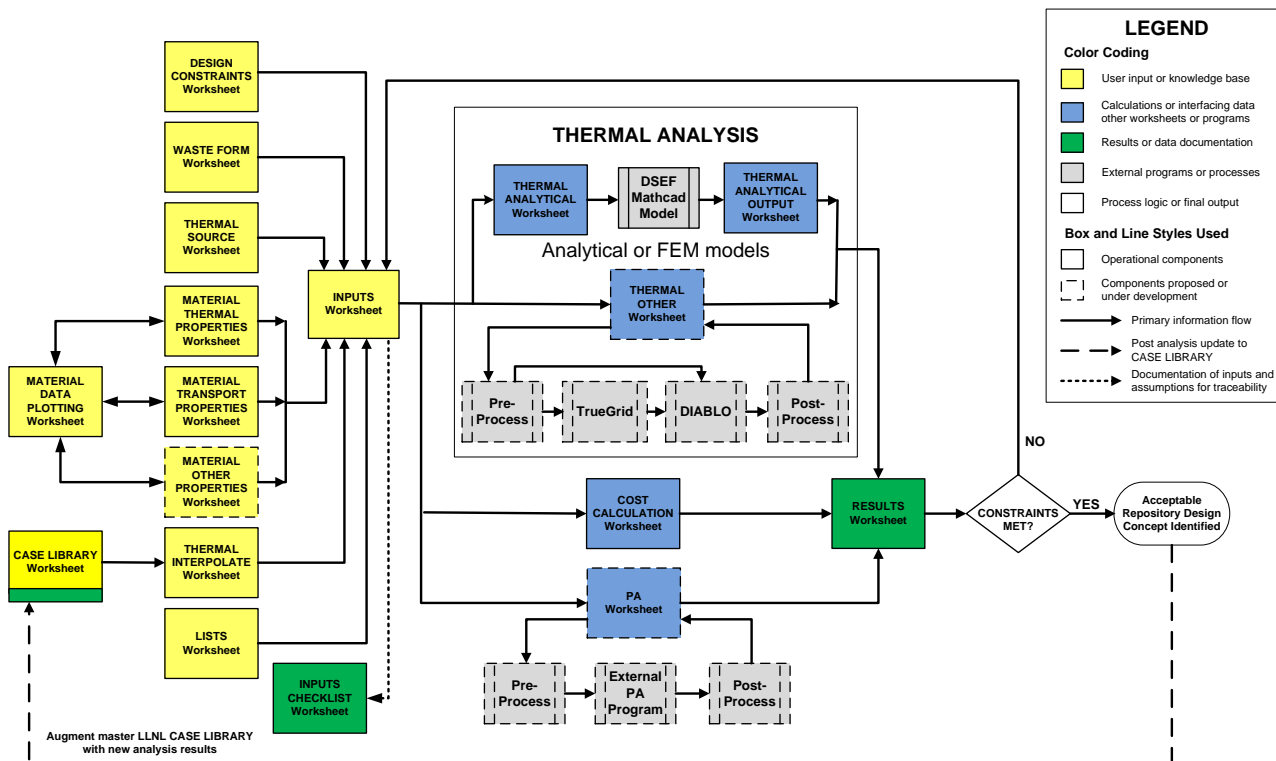


Notes:

**Not currently implemented in DSEF VERSION 3.0.

Figure 2 shows the detailed information flow in DSEF that implements the approach defined in the input-process-output diagram shown in Figure 1. It shows how DSEF can be used to identify feasible repository disposal concepts. TruGrid and DIABLO are used as examples of interfacing external analysis programs. The user could easily substitute CUBIT for the TruGrid as an alternate mesh generation program, and SINDA-G, ARIA, Albany, TOUGH2 or TOPAZ for DIABLO as other possible finite element model thermal analyzers. A good example of this is the application of Albany for 2-D and 3-D thermal analysis as described in part I.

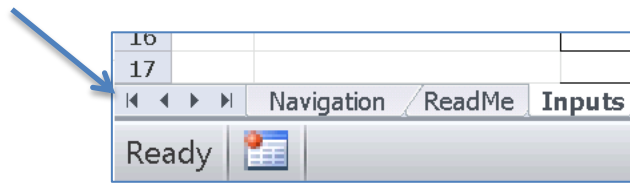
Figure 2 – Example of the information flow in DSEF



3. Finding Your Way Around – the NAVIGATION, README, LISTS and REV HISTORY Worksheets

Hyperlinks are available throughout the worksheets in the DSEF workbook to help you navigate quickly to related input and data source pages. The NAVIGATION worksheet in DSEF is the first worksheet tab, which allows users to quickly move to any worksheet and can be found by clicking on the Excel control for scrolling through the worksheet tabs. It is shown in Figure 3, with the arrow pointing to the “go to the first tab” button. Clicking on that will always take you to the NAVIGATION worksheet.

Figure 3 – Using the Excel tab navigation bar



On the NAVIGATION worksheet, there are two lists as shown in Figure 4. The list on the left shows the names of the worksheets in the sequence that they appear in the DSEF workbook. The list on the right consists of the same names but sorted alphabetically and hyperlinked to the worksheets themselves. Using the control shown in Figure 3 and the hyperlinks shown in Figure 4 enables quick navigation to any worksheet with two simple mouse clicks.

The README worksheet gives a brief overview of DSEF. At the bottom, there is an “Information Flow” description that explains the relationships between many of the worksheets. That part of the README worksheet serves the same purpose as this User Manual, but can be updated more easily when minor modifications and improvements are made to DSEF.

The LISTS worksheet is a tool primarily used by the DSEF Development Team. It is a central location for all drop-down lists and look-up tables used by other worksheets. Some advanced users may choose to view this worksheet to globally see the range of choices in these lists and to recommend additional choices to the DSEF Development Team.

The REV HISTORY worksheet documents the development history of DSEF. Advanced users may choose to view this worksheet to determine comparability of runs with earlier DSEF versions with current runs.

Figure 4 – The two lists of worksheets in the NAVIGATION worksheet

Worksheets in order of appearance	Hyperlinks to Worksheets in alphabetical order
Navigation (this sheet)	Case Library
Readme	Cost Calculations
Inputs	Cost References
Inputs Checklist	Design Constraints
Case Library	Environment
Thermal-Interpolate	Inputs
Results	Inputs Checklist
Interface Parameters	Interface Parameters
Design Constraints	Lists
Waste Form	Material Data Plotting
Environment	Materials
Thermal	Materials-Other Properties
Thermal-Source	Materials-References
Thermal-Analytical	Materials-Thermal Properties
Thermal-Analytical Output	Materials-Transport Properties
Thermal-FEM	Navigation (this sheet)
Performance Assessment	Performance Assessment
Cost Calculations	Readme
Cost References	Results
Materials	Rev History
Material Data Plotting	Thermal
Materials-Thermal Properties	Thermal-Analytical
Materials-Transport Properties	Thermal-Analytical Output
Materials-Other Properties	Thermal-FEM
Materials-References	Thermal-Interpolate
Rev History	Thermal-Source
Lists	Waste Form

4. Getting Started – Working with the DSEF Workbook

Opening DSEF for the First Time – Enabling the Macros

DSEF is a Microsoft Excel workbook with macros, and therefore has a file extension of “.xlsm” is used instead of the typical “.xlsx” for a workbook without macros. The macros developed in the built-in Visual Basic for Applications (VBA) programming language allow DSEF to automate a number of process steps coupled with the use of Form controls (such as command buttons and drop-down lists).

The first time that you open the DSEF workbook, you may get a prompt at the top of the workbook (below the Ribbon) notifying you that macros have been disabled for your protection and asking you if you want to enable macros. **In order for the Form controls to work, you must enable macros.** If you do not see this prompt, and the drop-down lists and other controls do not respond, you must change some settings in Excel. A detailed step-by-step procedure is outlined in Appendix F, complete with screen shots that point out exactly which options to select.

The Color Coding Conventions for Types of Cells and Information in DSEF

The DSEF file includes a significant amount of error checking and messages, and uses color codes for hyperlinks, errors, and inputs. Color coding conventions to help you recognize where input is needed, and where input is being used from other worksheets are the following:

- **Yellow highlighted cells:** Input cells or controls that help you select or input data
- **White highlighted cells:** Normal cells that contain data or formulas
- **Cells with a gray background and blue lettering** contain hyperlinks to other worksheets
- **Light gray highlighting of cells with black text** is used to distinguish different subsets of analysis cases for some of the CASE CATALOGs and some of the cases in the CASE LIBRARY. It is also used to distinguish the five cost case example data sets available on the INPUTS worksheet
- Light blue highlighted cells: Cells that retrieve data from other worksheets
- Cross-check / Caution cells:
 - **White background with black text** - Cross-check cells that provide confirmation of valid input
 - **Light red background with red text** – Cross-check cells that caution the user of a potential inconsistency when the cross-check confirmation fails
- **Green arrows and text:** Point to cells that have special range names used in formulas elsewhere

Working with the Form Controls

There are several kinds of Form controls used in DSEF, and for the most part, their use is straightforward (such as command buttons and check boxes). Figure 5 and Figure 6 show two examples.

The Form controls can serve three purposes

- They allow you to select from a pre-defined set of options, or allow you to enter a “user defined” option
- They can automatically run a macro program based on the selection you made. For example the control shown in Figure 5 runs a macro that copies the decay heat data for the selected waste form **from** a library of decay heat data on the THERMAL-SOURCE worksheet **to** the named range that defines the decay heat that will be used in the current analysis.
- They can limit the range of values you can use. For example the spinner control shown in Figure 6 only allows values between 5 years and 300 years of surface storage.

Figure 5 – A drop-down list to select the waste form

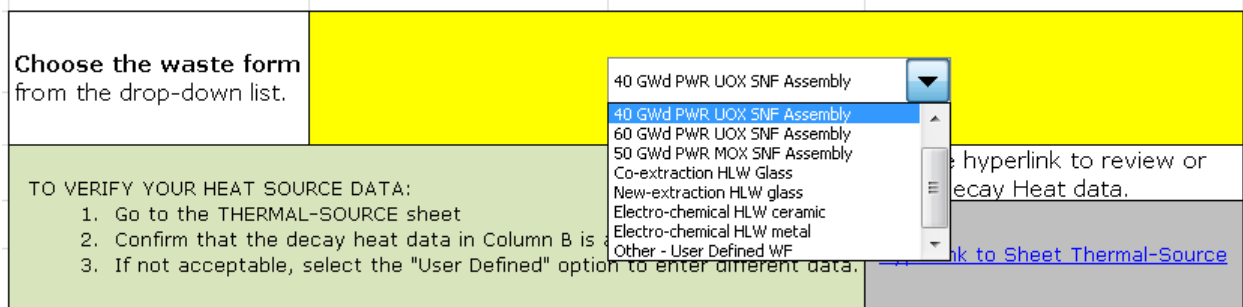


Figure 6 – A spinner control to select the number of assemblies in a waste package



In a number of cases, the data entry sections of the DSEF worksheet will look different depending on the selections you make using these controls. This is done by using conditional formatting to hide unused data entry cells and to display others, and by running macros that can hide some of the other controls.

Naming and Saving Files

DSEF is a template and is provided as a read-only, macro-enabled (xlsm), Excel spreadsheet. You must use the SAVE-AS menu command to save a DSEF workbook with your own data in it. The INPUTS worksheet helps you construct a file name with a standard set of information that will be common to all users and has a macro button to save the file (to the current directory) using the file name DSEF itself constructs. It is highly recommended you use this capability, rather than manually using the SAVE-AS Excel command. The name will include the DSEF version, date, your initials, and some information about waste form and medium from other selections you make on the INPUTS worksheet. The name will also include text that you specify after picking from the initial menus, and also a case number if you do multiple runs based on a similar configuration.

Suggested file name =

DSEF [Version]-[date]-[user's initials]-[waste form & geologic medium]-[a 4 to 30 character case description]-[case number of up to 6 alpha numeric characters].xlsm

After new design cases have been analyzed using DSEF and an external thermal analyzer like Mathcad, the DSEF file will include the results of your analysis on the RESULTS and THERMAL-ANALYTICAL OUTPUT worksheets, and will have a new data record for the analyzed design case on the CASE LIBRARY worksheet (just below the Case Catalog and the list of references).

As described in Section 11 of the User Manual, you can use a macro button on the THERMAL-ANALYTICAL OUTPUT worksheet to format the results written by Mathcad, and after doing that, you need to manually save this file using the FILE SAVE command in Excel. A copy of the completed DSEF file should be sent to LLNL to allow consolidation and augmenting of the master Case Library, thereby allowing updating and sharing of the new information between laboratories via the SNL SharePoint website.

5. The Starting Point to Define an Analysis Case - the INPUTS Worksheet

The central data entry worksheet in DSEF is the INPUTS worksheet. This worksheet builds the analysis case in steps (which are numbered and shown on the left edge). The user can proceed linearly through the worksheet, from top to bottom following the instructions on the worksheet, and completely define the analysis case. DSEF also provides two types of assistance in addition to the linear process:

- Hyperlinks to other worksheets are provided to allow the user to inspect libraries of properties (see Section 12). Some of these worksheets include tools to organize and/or visualize information being considered. The user can then return to the INPUTS worksheet (via another hyperlink, or by manual navigation) and input the parameter.
- Numbered cases in the CASE LIBRARY (see Section 7). The user can select a prior case number in several places on the INPUTS worksheet, resulting in pre-population of some input cells. The user can then overwrite parameters that are different than the “reference” case being used for that set of parameters in the INPUTS worksheet. The user can also use a hyperlink to jump to the THERMAL INTERPOLATE worksheet, which has tools to organize and visualize selected parameters for a selected set of cases (see Figure 22 Side-by-side case comparison table).

For experienced users, the cells in the linear process that require decisions or inputs are colored, allowing fast input without reading all the instructions for each use of DSEF.

Automatic Entry of Inputs

The power of DSEF can be used to automatically fill in many of the inputs by simply selecting a CASE LIBRARY case number. Different reference cases can be used for the natural and engineered barrier properties and configurations. Ideally, users can select a common reference

case number to set the starting inputs for both NBS and EBS (DSEF won't stop you from using different cases, but it will alert you if you have). An example is shown in Figure Figure 77.

Figure 7 - An example of some of the cross-checks and cautions displayed in the INPUTS worksheet

Designation of Case from Sheet "Case Library" for Initial EBS parameter data values					
Table1: Summary of EBS Component Selection Using CASE:			23	<-- EBS_case_select	CAUTION - The NBS and EBS case selections don't match!
CAUTION - The waste form for selected case does not match the waste form selected above!			CROSS-CHECK - The waste package spacing for selected case matches the spacing entered above.		
CROSS-CHECK - The waste package capacity for selected case matches the waste package capacity selected above.			CROSS-CHECK - The drift/borehole spacing for the selected case matches the spacing entered above.		
Case Number	DSEF Case Descriptionn	Waste Form	WP Capacity	EBS Components	Design Mode (Enclosed/Open)
23	Salt 4-UOX-40, Storage time=10 y, WP spacing=20 m, Drift/borehole spacing=20 m, EBS based on 200°C properties	UOX-40	4	WP, crushed Salt (to 3.048 m, calc rad = 4 m)	Enclosed

DSEF has several different constructs to use existing data. Some situations provide drop-down lists of data selections, and others have single data entry value displays and over-ride options. An example of the second approach is shown in Figure 8, in which the yellow override cells change the reference-case-populated values to the left. The resulting set of values (some from the pre-population and others from the overrides) are shown to the right of the yellow cells.

Figure 8 - An example of one of the ways DSEF lets you use data from the case library, or override the data with user input

Default EBS Component Names	User Input Names for EBS Components	EBS Component Names	Component Radial Thickness, m for Case 229	User Input Component Radial Thickness	Component Radial Thickness	Inner Radius m	Outer Radius m
Waste Form		Waste Form	0.89		0.89	N/A	0.89
Canister		Canister	0		0	0.89	0.89
Waste Package		Waste Package	0.11		0.11	0.89	1
Buffer		Buffer	0	0.1	0.1	1	1.1
Envelope	Buffer Layer 2	Buffer Layer 2	0	0.2	0.2	1.1	1.3
Backfill		Backfill	1.225	0.925	0.925	1.3	2.225
Liner		Liner	0.025		0.025	2.225	2.25
					Host Rock Inner Radius, m ---->	2.25	

Steps in the INPUTS Worksheet Process

The INPUTS worksheet is designed to guide the user in developing an analysis case in a structured manner. To assist new or infrequent users, instructions are provided near the entry fields. Color conventions are used to enable frequent users to move through the steps quickly, skipping those instructional fields. For all users, DSEF checks many of the inputs for consistency and provides feedback in cells labeled "Cross-Check".

The user should follow these steps sequentially in the DSEF INPUTS worksheet:

- Step 1 provides the user with the DSEF version number. No action is required, but the user should be aware that DSEF evolution from version to version could compromise comparability of results with earlier runs. The REV HISTORY worksheet documents the changes.

- Step 2 builds the case name and includes a macro for the initial saving of the file using the case name. The user inputs the date, their initials, some descriptive text, and a case number. Because the case name includes the geologic medium and the waste form, the user also selects (from pull-down lists) those parameters in Step 2. Step 2 also includes a macro button that allows the user to “Clear Previous Thermal Output Results” if the same Excel file is being used as a starting point to prepare multiple analysis cases.
- Step 3 selects the waste package capacity, in terms of the number of spent nuclear fuel assemblies or high-level waste canisters. A spinner control enables selection of integer numbers. A check box enables input of a non-integer number (for the situations of rod consolidation or non-standard canister sizes).
- Step 4 selects the storage time, which is the time between removal from the reactor flux to the emplacement in the repository.
- Step 5 selects the repository depth. Three inputs are required: depth, surface temperature, and geothermal gradient. DSEF uses these three inputs to calculate the initial temperature at the repository horizon (which is the initial temperature of the infinite medium in the THERMAL-ANALYTICAL worksheet approach). DSEF also uses the depth in the COST CALCULATIONS worksheet.
- Step 6 develops the repository layout. The THERMAL-ANALYTICAL worksheet uses a two-dimensional model that calculates thermal response from a central waste package, its axial neighbors, and its lateral neighbors. Thus, axial spacing and lateral spacing are the two inputs. Spacing values are center-to-center. The THERMAL-ANALYTICAL worksheet approach calculates the temperature near a central waste package with four axial (point source) neighbors on each end, and four line-source lateral neighbors on each side. For in-drift emplacement, axial spacing is between waste packages, and lateral spacing is between drifts. For horizontal borehole emplacement, axial spacing is between waste packages, and lateral spacing is between boreholes. For vertical boreholes with one waste package per borehole, the two-dimensional approximation turns each WP to be horizontal, with the axis aligned with the axis of the turned WPs in each neighboring borehole; thus, the axial spacing is the borehole spacing, and the lateral spacing is the drift spacing (the boreholes are drilled in the drift floor). For deep borehole emplacement, the axial spacing is between waste packages, and the lateral spacing is between boreholes (this only calculates one plane of the repository, but lateral spacing is wide enough that the adjacent planes can be ignored).
- Step 7 specifies the natural system material name and properties (thermal conductivity and thermal diffusivity). The user is invited to enter a case number for display of values from that reference case, directly to the left of the yellow input cells. The user may override any or all of these values in the input cells. Directly to the right of the input

cells are the values DSEF will use (which are the displayed reference case values if no values are directly input). Hyperlinks to the CASE LIBRARY and the MATERIALS worksheets are provided to enable the user to view available cases and material properties, prior to making their input choices.

- Step 8 specifies the EBS material names, radial thicknesses, thermal conductivities, and thermal diffusivities. EBS layers include the waste form, canister, waste package, buffer, envelope, backfill, and liner. The drift or borehole radius is the outer radius of the liner. The inner three layers are provided for dimensional purposes only; the THERMAL-ANALYTICAL worksheet treats everything inside of the waste package outer radius to be a thermal source with a thermal flux imposed at that location. The outer four layers can be renamed to accommodate a variety of designs. If a layer thickness is zero, it is as if that layer does not exist in the THERMAL-ANALYTICAL worksheet approach. As in Step 7, the user is invited to enter a case number for display of values from that reference case, which may be a different reference case than used in the Step 7. Table 8.B in DSEF, part of which is shown in Figure 8, allows the user to keep the reference case values or override them with user input (where the yellow cells are provided for user input). Table 8.C. displays a summary of the data that will be used, and that is passed to the THERMAL-ANALYTICAL worksheet, which is the interface with the Mathcad component of DSEF. Hyperlinks to the CASE LIBRARY worksheet and the MATERIALS worksheet are provided to enable the user to view prior runs and the assembled set of reference properties, prior to making their input choices. Finally, in Table 8.D, the user specifies a second in-rock compliance point. The Mathcad component of DSEF will calculate temperature history (and the value and time of peak temperature) at this location in addition to the outer radius of the waste package, all of the EBS component interfaces, and the drift/borehole radius. The Mathcad component returns the results of the transient temperature calculations to the THERMAL-ANALYTICAL OUTPUT worksheet.
- Step 9 specifies the parameters required to calculate the thermal behavior of an “open mode” repository design concept that includes pre-closure ventilation. These parameters include the ventilation duration and the subsequent unventilated duration during which backfill is emplaced, the ventilation efficiency, the rock wall emissivity, and the waste package emissivity. As in the preceding steps, the user is provided with the reference values from the EBS reference case (from Step 8), and can make their own direct inputs or overrides. The resulting values are shown to the right of the yellow input cells. The step ends with a hyperlink to the THERMAL worksheet which manages the calculation and documentation of the thermal performance. The user should return to this point in the INPUTS worksheet afterward, to address the COST calculation, should it be desired.

- Step 10 specifies the input parameters necessary to generate an approximate cost for the design choices made above. For costing, the entire repository must be specified, rather than the central waste package and neighbors specified above for the thermal performance calculations. Figure 9 shows an example of the repository-level cost input data, where the user enters the repository capacity (MTU) and annual receipt rate (MTU/yr) as well as other variables. The user can also choose one of five example cost calculation cases from the Carter/Hardin model for comparison purposes (see Section 9 on the COST worksheets). Figure 10 shows an example of user data entry for high and low range contingency percentages.
- Step 11 allows the user to input and output constraint data. The user supplies a constraint value for minimum lateral spacing of drifts for drift structural stability that is used to cross-check the repository design concept input data. The other constraint inputs are all related to temperature criteria for maximum waste package surface temperature, and maximum EBS and NBS material thermal constraints. The calculated results are checked against these constraint values, and the RESULTS worksheet displays a color-coded set of temperature compliance results as well as displaying quantitative margins (see Figure 11).
- Step 12 allows the user to document and check the single analysis reference case that was defined in steps 1 to 11. Step 12 sends the user to the INPUTS CHECKLIST worksheet, which allows the user to track the status of the input data entry, and provides a place to document decisions and data-selection choices, identify references used, and add notes with respect to the data entries. To perform a "one-off" parameter sensitivity study, proceed to Step 13.
- Step 13 allows the user to either select a "single" calculation mode that uses all of the input data for the reference case defined in Steps 1 through 12, or to select a "parametric" study calculation mode. Figure 12 shows the options available for parametric studies, where the basic inputs have been set, but the user can then define up to 10 data values for one of six possible parameters – waste package spacing, drift spacing, storage time, ventilation duration, rock thermal conductivity, and backfill thermal conductivity. Caution should be taken because the single value already input will be overwritten for the thermal, but not in the cost calculation. Therefore, the user is encouraged to choose to make one of the parametric values match the "single" value input defined in Steps 1 through 12 for easier comparison with the other parametric input results.
- Step 14 sends the user to the RESULTS worksheet, which displays the inputs and results in a reviewable and printable format.

Figure 9 – Example of repository level cost input data with Carter/Hardin example case data

Note: The light blue cells below are input elsewhere. The user should consider the options and consider overriding if appropriate. Consultation of the 5 cases documented in FCRD-UFD-2012-000211, Rev. 1 can be informative. The yellow cells need to be input directly. One can consult the data directly on the LISTS worksheet as shown in the data tables named "Table_Shafts_5_Case", "Table_Surface_Facility_Costs_5_Case", "Table_Assumptions_5_Case", "Table_Ramps_Drifts_5_Case", "Table_O_and_M_Unit_Cost_Assumptions_5_Case" or for any single case by selecting one of the standard cases and looking at Column D in the table immediately below.

FCRD-UFD-2012-000211, Rev 1 Case description

The cell one row down and one column to the left is where one selects "User Defined" or one of the Carter cases - simply click on it to show the menu

Repository operations related inputs	Thermal Calculation Related Inputs	ROM Cost Case 4 - Clay/Shale (open)	User Defined Over-ride Inputs		
MTU per Repository	140,000	140	140000	<-- Repository_MTU	
Repository Annual Waste Throughput (MTU/yr)	3,000	30	3000	<-- Repository_MTU_per_year	
Waste Package Capacity	21	21	21	<-- WP_capacity_for_cost	
Ventilation Duration (yr)	250	25	250	<-- Ventilation_Duration	
Ventilation Surface Facility Annual Costs (MM\$/yr)		1	1	<-- Vent_Surface_Facility_Annual_Cost	
Ventilation Operations Unit Cost per Emplacement Drift Length (\$/m-yr)		50	50	<-- Vent_Operations_per_Drift_Length_Unit_Cost	
Closure Duration (yr)	10	10	10	<-- Closure_Duration	
Closure Facility Annual Cost (MM\$/yr)		10	10	<-- Closure_Surface_Facility_Annual_Cost	

Select Cost Case or User Defined
 Select one of the 5 repository concept cost cases defined in FCRD-UFD-2012-000211, Rev 1 (Generic Repository ROM Cost Study; Joe T. Carter, Phillip O. Rodwell, and Mark Dupont (SRNL), Sept. 5, 2012), or select "User Defined" to input your own data.

Figure 10 – Example of cost contingency input data

For User-Defined Cases, the DSEF team recommends the User consult the contingencies for the 5 Carter cases. These can be seen in "Table_Contingencies_Carter_5_Case" or for any single case by selecting one of the standard cases and looking at Column D in the table immediately below. Those values can be "pasted-special" in Column C immediately below.

		Case Related Description				
Contingency Factors	User Defined Inputs	RDM Cost Case 4 - Clay/Shale (open)	User Defined Over-ride Inputs			
Facility Design & Startup - Low	5%	5%		5%	<-- Contingency_Facility_Design_and_Startup_Low	
Facility Design & Startup - High	53%	53%		53%	<-- Contingency_Facility_Design_and_Startup_High	
Surface Facility Construction - Low	5%	5%		5%	<-- Contingency_Surface_Facility_Construction_Low	
Surface Facility Construction - High	53%	53%		53%	<-- Contingency_Surface_Facility_Construction_High	
Subsurface Facility Construction - Low	5%	5%		5%	<-- Contingency_Subsurface_Facility_Construction_Low	
Subsurface Facility Construction - High	53%	53%		53%	<-- Contingency_Subsurface_Facility_Construction_High	
Ventilation Construction & Startup - Low	5%	5%		5%	<-- Contingency_Ventilation_Construction_and_Startup_Low	
Ventilation Construction & Startup - High	53%	53%		53%	<-- Contingency_Ventilation_Construction_and_Startup_High	
Operations & Maintenance - Low	5%	5%		5%	<-- Contingency_Operations_and_Maintenance_Low	
Operations & Maintenance - High	34%	34%		34%	<-- Contingency_Operations_and_Maintenance_High	
Closure Costs - Low	10%	10%		10%	<-- Contingency_Closure_Costs_Low	
Closure Costs - High	50%	10%		70%	<-- Contingency_Closure_Costs_High	
Waste Packages - Low	5%	5%		5%	<-- Contingency_Waste_Packages_Low	
Waste Packages - High	30%	30%		30%	<-- Contingency_Waste_Packages_High	
Regulatory & Licensing - Low	5%	5%		5%	<-- Contingency_Regulatory_and_Licensing_Low	
Regulatory & Licensing - High	3%	3%		3%	<-- Contingency_Regulatory_and_Licensing_High	
Monitoring - Low	10%	10%		10%	<-- Contingency_Monitoring_Low	
Monitoring - High	50%	50%		50%	<-- Contingency_Monitoring_High	
Performance Confirmation - Low	5%	5%		5%	<-- Contingency_Performance_Confirmation_Low	
Performance Confirmation - High	43%	43%		43%	<-- Contingency_Performance_Confirmation_High	
Program Integration - Low	10%	10%		10%	<-- Contingency_Program_Integration_Low	
Program Integration - High	50%	50%		50%	<-- Contingency_Program_Integration_High	

Figure 11 – Example of comparison of thermal results against thermal constraints from the RESULTS worksheet

Number of parametric sensitivity study cases = 3							
Summary of Peak Temperatures and Times		Ventilation Duration 200, yr		Ventilation Duration 250, yr		Ventilation Duration 300, yr	
Location	Radius, m	Peak Temp, C	TooR, yr	Peak Temp, C	TooR, yr	Peak Temp, C	TooR, yr
Second Compliance Point	5.25	183.58	600.00	175.39	680.00	167.86	705.00
Peak Rock	2.25	200.19	525.00	190.62	600.00	182.25	665.00
Liner inner surface	2.23	200.20	525.00	190.63	600.00	182.26	665.00
Backfill inner surface	1.00	237.70	455.00	225.19	515.00	214.34	580.00
Envelope inner surface	1.00	237.70	455.00	225.19	515.00	214.34	580.00
WP surface	1.00	237.70	455.00	225.19	515.00	214.34	580.00
Comparison against Thermal Constraints							
Location / medium	Thermal Constraint, °C	Margin (Constraint - Peak Temp)		Margin (Constraint - Peak Temp)		Margin (Constraint - Peak Temp)	
Host rock / Clay	100	-100.2		-90.6		-82.3	
Liner	None	N/A		N/A		N/A	
Backfill	120	-117.7		-105.2		-94.3	
Envelope	None	N/A		N/A		N/A	
Buffer	None	N/A		N/A		N/A	
WP surface	300	62.3		74.8		85.7	

Figure 12 – Example of parametric study input data from Step 13 on the INPUTS worksheet

Single or parametric calculation		Select Mode <input type="radio"/> Single <input checked="" type="radio"/> Parametric Options <input type="radio"/> WP Spacing <input type="radio"/> Drift Spacing <input type="radio"/> Storage Time <input checked="" type="radio"/> Ventilation Duration <input type="radio"/> Rock Conductivity <input type="radio"/> Backfill Conductivity	Base value of Ventilation Duration = 250	Ventilation Duration	<-- Calculation_mode
Fill in up to 10 values, starting at the top (with no blank rows in the middle)	Value 1	200		<--- Cells reserved for user defined data	
	Value 2	250		<--- Cells reserved for user defined data	
	Value 3	300		<--- Cells reserved for user defined data	
	Value 4			<--- Cells reserved for user defined data	
	Value 5			<--- Cells reserved for user defined data	
	Value 6			<--- Cells reserved for user defined data	
	Value 7			<--- Cells reserved for user defined data	
	Value 8			<--- Cells reserved for user defined data	
	Value 9			<--- Cells reserved for user defined data	
	Value 10			<--- Cells reserved for user defined data	
	Number of Values Entered	3	<-- Parametric_data_count	<--- Cells reserved for user defined data	
Minimum	Maximum	Average	Single Case Value	Variable Units	
200	300	250	250	yr	
CROSS-CHECK: Average of the range equals the single case value					
The single case value is used in the cost estimate, and the parametric values are used in the thermal calculations.					

6. The INPUTS CHECKLIST Worksheet

The INPUTS CHECKLIST worksheet provides a checklist to follow the user's progress in developing an analysis case, and provides documentation for the combination of built-in options chosen versus new user-defined inputs. It also provides a convenient location to document the references and to make explanatory notes to supplement the DSEF data options chosen. Figure 13 shows an example of the checklist style documentation structure of the INPUTS CHECKLIST worksheet. The INPUTS CHECKLIST worksheet also includes a section at the bottom that echoes all of the cross-check and caution warnings that are utilized on the INPUTS worksheet.

If sufficient display monitor space is available, the user can open both the INPUTS and INPUTS CHECKLIST worksheets side-by-side. As decisions are made on the INPUTS worksheet, the cells in the INPUTS CHECKLIST worksheet are automatically populated. The two columns to the right are places the user can document references used and to place notes on the thought process or rationale for the decisions made. The INPUTS CHECKLIST worksheet is narrow enough to be printed for hard-copy retention of case definition.

Figure 13 - Example from a section of the inputs checklist

Category of input	Subcategory	Subcategory	Data from the INPUTS sheet	References for User defined inputs	Notes
Natural Barriers System - Geologic media		Media type	Clay		
		Thermal conductivity	1.75		
		Thermal diffusivity	6.45E-07		
		Transport properties			
		Constraint temp. °C	100		
Waste form properties		Mechanical properties			
		SNF type	40 GW/d PWR UOX SNF Assembly		
		SNF burnup	See SNF type		
		Number of assemblies	32		
Waste form / waste package geometry		Waste package description	Assembly waste package		
		Decay heat source data			
		Waste form outer radius, m	0.89		
		Waste package outer radius, m	1.000		
		Waste package length, m	5		
		Waste package material	Carbon Steel		
Engineered Barriers System - Layer data	EBS layer 4 - closest to waste package	Waste package wall thickness	0.11		
		Layer descriptive name	Buffer		
		Layer material	None		
		Layer thermal kth	N/A		
		Layer thickness, m	0		
	EBS layer 3 - inner mid-layer	Layer outer radius, m	1		
		Constraint temp. °C	None		
		Layer descriptive name	Envelope		
		Layer material	None		
		Layer thermal kth	N/A		
	EBS layer 2 - inner mid-layer	Layer thickness, m	0		
		Layer outer radius, m	1		
		Constraint temp. °C	None		
		Layer descriptive name	Backfill		
		Layer material	70% Bentonite 30% Sand		
	EBS layer 1 - closest to host rock	Layer thermal kth	1.2		
		Layer thickness, m	1.225		
		Layer outer radius, m	2.225		
		Constraint temp. °C	120		
		Layer descriptive name	Liner		
		Layer material	Steel		
		Layer thermal kth	46		
		Layer thickness, m	0.025		

7. Reviewing Previous Analyses – the CASE LIBRARY and the THERMAL-INTERPOLATE Worksheets

DSEF provides user-friendly ways to rapidly access and compare a large number of completed thermal analysis cases through the combination of the CASE LIBRARY and the THERMAL-INTERPOLATE worksheets. The CASE LIBRARY is a flat-file database contained in a named range called the *Interp_Data_Table*. THERMAL INTERPOLATE directly predicts new results by using linear interpolation to get a first-order prediction of the effects of potential changes in a selected set of independent variables.

The database table currently has 721 records (rows) with 56 fields (columns) of data. Figure 14 shows the data fields. DSEF Version 2.1 included 300 analysis cases in the database. DSEF Version 3.0 added cases 301 to 401 from Greenberg 2013a, and cases 402 to 721 from Greenberg 2013b.

The CASE LIBRARY also includes an easy-to-use CASE CATALOG that categorizes the cases in the library and allows the user to quickly jump to a relevant record. Figure 15 through Figure 21 show the CASE CATALOG tables for enclosed mode cases, open mode cases, open mode sensitivity cases, required ventilation calculations, and dual-purpose canister calculations respectively. Each table includes a macro button to jump to the selected case in the CASE LIBRARY.

The “enclosed” mode referred to for Figure 15 means that the space between the waste package and drift or borehole wall is filled with engineered barrier components such as a buffer or backfill. In Figure 15, “Salt 200” is an abbreviation for cases with the thermal properties of salt within the EBS region being evaluated at 200°C, as opposed to the properties in the host rock which were evaluated at 100°C. For “Salt 100” cases, all properties were evaluated at 100°C.

Follow these steps to use the Case Catalog tables to examine specific case records in the library:

- Examine the Case Catalog tables to select a case of interest
- Click on the catalog case number of interest
- Click on the “*Jump to Selected Case*” macro button. This utilizes the Excel “freeze panes” feature to place the data field names at the top of the screen, with the first record being the selected case.
- Just above the field names (after the jump), there is another macro button that says “*Click Here to Go Back to the Case Library*”. Clicking on that macro button will put you back at the particular case catalog table you were looking at when you selected the case to review.
- Also above the field names, there is a counter for the “Number of Filtered Rows”. When looking at the Case Library the user can click on the Excel menu choice DATA – FILTER to set the auto-filter mode on. In this mode, the Case Library data can be filtered to identify specific sets of cases that meet the filter criteria. The number of filtered cases is displayed in the cell with the counter. Note that the DATA – FILTER operation will not work while the normal DSEF worksheet protection is enabled. A password must be used to first “unprotect” the worksheet before filtering. Contact LLNL if you need the password.

Figure 14 - The data fields used in the CASE LIBRARY

Columns in Interp_Data_Table		Columns in Interp_Data_Table (continued)	
1	Case Number	29	Envelope Wall kth, W/m-K
2	Case Description	30	Backfill kth, W/m-K
3	Design Mode	31	Liner kth, W/m-K
4	Date of Calc	32	Rock k _{th} , W/m-K
5	Reference Document	33	Rock alpha, m ² /s
6	Author / Org	34	Time Out of Reactor (Storage Time, yr)
7	Geologic Medium	35	Depth of Repository Horizon, m
8	Waste Form	36	Ambient T, °C
9	WP Capacity (# SNFAs or Canisters)	37	Center to Center Axial Spacing, m
10	WP Length, m	38	Center to Center Lateral Spacing, m
11	EBS Components	39	Time of Peak T at Rock Wall, yr
12	Waste Form Outer/ Canister Inner Radius, m	40	Peak Rock Wall T, °C
13	Canister Wall Thickness m	41	% Contribution to Peak Rock Wall T from Central WP
14	WP Wall Thickness m	42	% Contribution to Peak from Axial Neighbor WPs
15	Buffer Thickness m	43	% Contribution to Peak from Lateral Neighbor WP Lines
16	Envelope Thickness m	44	Time of Peak WP T, yr
17	Backfill Thickness m	45	Peak WP T, °C
18	Liner Thickness m	46	Third T Location
19	Calculated Rock Wall Radius, m	47	Time of T at Third Location (Note 1)
20	Canister Wall Material	48	Third Location T, °C (Note 1)
21	WP Wall Material	49	Ventilation thermal efficiency %
22	Buffer Material	50	Ventilation Period (yr)
23	Envelope Material	51	Backfill Duration
24	Backfill Material	52	Time of Operation
25	Liner Material	53	Rock Wall Emissivity
26	Canister Wall kth, W/m-K	54	Waste Package Emissivity
27	WP Wall kth, W/m-K	55	Single Case or Parameter Studied
28	Buffer kth, W/m-K	56	Number of Parameter Values in Study

Figure 15 - The enclosed mode analysis case catalog

Case Number Catalog for Enclosed Mode Analysis Cases							
Disposal Scenarios			Click Here to Jump to Selected Case				
Geology	Waste Form	Assemblies / WP	10 Year Storage	50 Year Storage	100 Year Storage	200 Year Storage	
Granite	4-UOX-60-SNFA	4	1	55	109	163	
	4-UOX-40-SNFA	4	2	56	110	164	
	1-UOX-60-SNFA	1	3	57	111	165	
	1-UOX-40-SNFA	1	4	58	112	166	
	4-MOX-50-SNFA	4	5	59	113	167	
	1-MOX-50-SNFA	1	6	60	114	168	
	Co-Extraction	1	7	61	115	169	
	New Extraction Glass	1	8	62	116	170	
	EC-Ceramic	1	9	63	117	171	
	EC-Metal	1	10	64	118	172	
Clay	4-UOX-60-SNFA	4	11	65	119	173	
	4-UOX-40-SNFA	4	12	66	120	174	
	1-UOX-60-SNFA	1	13	67	121	175	
	1-UOX-40-SNFA	1	14	68	122	176	
	4-MOX-50-SNFA	4	15	69	123	177	
	1-MOX-50-SNFA	1	16	70	124	178	
	Co-Extraction	1	17	71	125	179	
	New Extraction Glass	1	18	72	126	180	
	EC-Ceramic	1	19	73	127	181	
	EC-Metal	1	20	74	128	182	
Salt 100	4-UOX-60-SNFA	4	21	75	129	183	
	1-UOX-60-SNFA	1	24	78	132	186	
	4-MOX-50-SNFA	4	33	87	141	195	
	1-MOX-50-SNFA	1	35	89	143	197	
	Co-Extraction	1	40	94	148	202	
	New Extraction Glass	1	41	95	149	203	
	EC-Ceramic	1	42	96	150	204	
	EC-Metal	1	43	97	151	205	
	Salt 200	1-UOX-60-SNFA	1	25	79	133	187
		1-UOX-40-SNFA	1	26	80	134	188
2-UOX-60-SNFA		2	27	81	135	189	
2-UOX-40-SNFA		2	28	82	136	190	
3-UOX-60-SNFA		3	29	83	137	191	
3-UOX-40-SNFA		3	30	84	138	192	
4-UOX-60-SNFA		4	22	76	130	184	
4-UOX-40-SNFA		4	23	77	131	185	
12-UOX-60-SNFA		12	31	85	139	193	
12-UOX-40-SNFA		12	32	86	140	194	
1-MOX-50-SNFA		1	36	90	144	196	
2-MOX-50-SNFA		2	37	91	145	199	
3-MOX-50-SNFA		3	38	92	146	200	
4-MOX-50-SNFA		4	34	88	142	196	
12-MOX-50-SNFA		12	39	93	147	201	
Co-Extraction		1	44	98	152	206	
New Extraction Glass		1	45	99	153	207	
EC-Ceramic		1	46	100	154	208	
EC-Metal		1	47	101	155	209	
Deep Borehole		1-UOX-60-SNFA	1	48	102	156	210
	1-UOX-40-SNFA	1	49	103	157	211	
	1-MOX-50-SNFA	1	50	104	158	212	
	Co-Extraction	0.291	51	105	159	213	
	New Extraction Glass	0.291	52	106	160	214	
	EC-Ceramic	0.291	53	107	161	215	
	EC-Metal	0.291	54	108	162	216	

Figure 16 - The open mode analysis base case catalog

Case Number Catalog for Open Mode Analysis Cases					
Catalog of Base Cases			Click Here to Jump to Selected Case		
Disposal Scenarios		50 Year Storage		100 Year Storage	
Geology	Waste Form	LLNL-TR-572252 Case #	CASE LIBRARY Case Number	LLNL-TR-572252 Case #	CASE LIBRARY Case Number
Clay	4-UOX 40	#13	217	#14	218
	4-UOX 60	#15	219	#16	220
	12-UOX 40	#17	221	#18	222
	12-UOX 60	#19	223	#20	224
	21-UOX 40	#21	225	#22	226
	21-UOX 60	#23	227	#24	228
	32-UOX 40	#25	229	#26	230
	32-UOX 60	#27	231	#28	232
Alluvium	4-UOX 40	#41	233	#42	234
	4-UOX 60	#43	235	#44	236
	12-UOX 40	#45	237	#46	238
	12-UOX 60	#47	239	#48	240
	21-UOX 40	#49	241	#50	242
	21-UOX 60	#51	243	#52	244
	32-UOX 40	#53	245	#54	246
	32-UOX 60	#55	247	#56	248

Figure 17 - The open mode sensitivity studies case catalog

Case Number Catalog for Open Mode Analysis Cases												
Catalog of Open Mode Sensitivity Study Cases		Click Here to Jump to Selected Case										
Media	Parameter Studied											
Clay	Ventilation Thermal Efficiency All cases assume - 21-UOX, 40 GWd/MTHM, 50 yr Storage, 300 yr total Operation, 310 yr backfill	Variable Value	50%	60%	70%	75%	80%	90%				
		LLNL-TR-572252 Case #	#21a	#21b	#21c	#21	#21d	#21e				
		CASE LIBRARY Case #	249	250	251	225	252	253				
Clay	Ventilation Duration All cases assume - 21-UOX, 40 GWd/MTHM, 50 yr Storage, Ventilation Eff. 90%	Variable Value	250 yr, DS=30	200 yr, DS=30	150 yr, DS=30	100 yr, DS=30	50 yr, DS=30	50 yr, DS=40	50 yr, DS=50			
		LLNL-TR-572252 Case #	#21e	#21f	#21g	#21h	#21i	#21j	#21k			
		CASE LIBRARY Case #	253	254	255	256	257	258	259			
Clay	Drift / Borehole Spacing All cases assume - 21-UOX or 32-UOX, 40 GWd/MTHM, 50 yr Storage, 300 yr close	Variable Value	30 m, WP=21	40 m WP=21	50 m WP=21	60 m WP=21	70 m WP=21	30 m WP=32	40 m WP=32	50 m WP=32	60 m WP=32	70 m WP=32
		LLNL-TR-572252 Case #	#21	#21w	#21x	#21y	#21z	#25	#25a	#25b	#25c	#25d
		CASE LIBRARY Case #	225	260	261	262	263	229	264	265	266	267
Generic	Host Rock Thermal Conductivity (W/m-K) All cases assume - 21-UOX, 40 and 60 GWd/MTHM, 50 yr Storage	Variable Value	kth=1 BU=40	kth=2 BU=40	kth=3 BU=40	kth=4 BU=40	kth=5 BU=40	kth=1 BU=60	kth=2 BU=60	kth=3 BU=60	kth=4 BU=60	kth=5 BU=60
		LLNL-TR-572252 Case #	#57	#58	#59	#60	#61	#62	#63	#64	#65	#66
		CASE LIBRARY Case #	277	278	279	280	281	282	283	284	285	286
Clay	Backfill Thermal Conductivity All cases assume - 21-UOX, 40 GWd/MTHM, 50 yr Storage, 300 yr close, 10 yr backfill	Variable Value	kth=1 BU=40	kth=2 BU=40	kth=3 BU=40	kth=4 BU=40	kth=5 BU=40					
		LLNL-TR-572252 Case #	#67	#68	#69	#70	#71					
		CASE LIBRARY Case #	268	269	270	271	272					
Clay #21's Alluvium #49's	Uncertainty in Rock Properties All cases assume - 21-UOX, 40 GWd/MTHM, 50 yr Storage, 300 yr close, 10 yr backfill	Variable Value	-2 std. dev.	-1 std. dev.	Mean	+1 std. dev.	+2 std. dev.	-2 std. dev.	-1 std. dev.	Mean	+1 std. dev.	+2 std. dev.
		LLNL-TR-572252 Case #	21m	21r	21	21s	21n	49a	49c	49	49d	49b
		CASE LIBRARY Case #	273	287	225	288	274	275	289	241	290	276
Clay	Design Test Cases All cases assume - 21-UOX, 40 GWd/MTHM, cases 72-74, 50 yr storage, cases 75-77, 100 yr storage	Variable Value	No backfill	backfill kth=2	backfill kth=1.2	backfill kth=0.6	rDW = 5.25 m	No backfill	backfill kth=2	backfill kth=1.2	backfill kth=0.6	rDW = 5.25 m
		LLNL-TR-572252 Case #	72	73	73b	73a	74	75	76	76b	76a	77
		CASE LIBRARY Case #	291	292	293	294	295	296	297	298	299	300

Figure 18 - Case number catalog for repository layout and required ventilation trade studies in clay/shale (1 of 2)

Case Number Catalog for Repository Layout and Required Ventilation Trade Studies in Clay / Shale																			
Catalog of Open Mode Sensitivity Study Cases				Click Here to Jump to Selected Case															
LLNL-TR-638880 - Required Ventilation Time Trade Study in clay/shale, as a function of Temperature Criteria (TC), Drift spacing, Storage time, and Waste package spacing Cases analyzed for 2013 IHLRWM conference paper LLNL-CONF-614294				12-PWR waste package DSEF cases 221 (t-store 50) and 222 (t-store 100)				21-PWR waste package DSEF cases 225 (t-store 50) and 226 (t-store 100)				32-PWR waste package DSEF cases 229 (t-store 50) and 230 (t-store 100)							
				WP Spacing, m				Waste Package Spacing, m								Waste Package Spacing, m			
				TC	Dr Sp, m	t-store, yr	10		10		15		20		10		15		20
LLNL-TR-638880 Case #	CASE LIBRARY Case #	LLNL-TR-638880 Case #	CASE LIBRARY Case #				LLNL-TR-638880 Case #	CASE LIBRARY Case #	LLNL-TR-638880 Case #	CASE LIBRARY Case #	LLNL-TR-638880 Case #	CASE LIBRARY Case #	LLNL-TR-638880 Case #	CASE LIBRARY Case #	LLNL-TR-638880 Case #	CASE LIBRARY Case #			
100	30	50	221-1	301	225-1	315	225-10	333	225-19		342	229-1	351	229-10	369	229-19	378		
100	30	100	222-1	302	226-1	316						230-1	352						
100	45	50	221-2	303	225-2	317	225-11	334	225-20		343	229-2	353	229-11	370	229-20	379		
100	45	100	222-2	304	226-2	318						230-2	354						
100	60	50	221-3	305	225-3	319	225-12	335	225-21		344	229-3	355	229-12	371	229-21	380		
100	60	100	222-3	306	226-3	320						230-3	356						
120	30	50	221-4	307	225-4	321	225-13	336	225-22		345	229-4	357	229-13	372	229-22	381		
120	30	100	222-4	308	226-4	322						230-4	358						
120	45	50	221-5	309	225-5	323	225-14	337	225-23		346	229-5	359	229-14	373	229-23	382		
120	45	100	222-5	310	226-5	324						230-5	360						
120	60	50	221-6	311	225-6	325	225-15	338	225-24		347	229-6	361	229-15	374	229-24	383		
120	60	100	222-6	312	226-6	326						230-6	362						
140	30	50	221-7	313	225-7	327	225-16	339	225-25		348	229-7	363	229-16	375	229-25	384		
140	30	100	222-7	314	226-7	328						230-7	364						
140	45	50			225-8	329	225-17	340	225-26		349	229-8	365	229-17	376	229-26	385		
140	45	100			226-8	330						230-8	366						
140	60	50			225-9	331	225-18	341	225-27		350	229-9	367	229-18	377	229-27	386		
140	60	100			226-9	332						230-9	368						

Figure 19 - Case number catalog for repository layout and required ventilation trade studies in clay/shale (2 of 2)

Case Number Catalog for Repository Layout and Required Ventilation Trade Studies in Clay / Shale								
Catalog of Open Mode Sensitivity Study Cases			Click Here to Jump to Selected Case					
LLNL-TR-638880 - Required Ventilation Time Trade Study in clay/shale, as a function of Temperature Criteria (TC), Drift spacing, Storage time, and Waste package spacing Additional base cases to extend WP spacing to 30 m and Drift spacing to 90 m				32-PWR waste package, 40 GWd/MT burnup				
				DSEF base case 229				
				Waste Package Spacing				
				10		20		30
Clay/shale	TC	Dr Sp	LLNL-TR-638880 Case #	CASE LIBRARY Case #	LLNL-TR-638880 Case #	CASE LIBRARY Case #	LLNL-TR-638880 Case #	CASE LIBRARY Case #
	100	30	229-1	351	229-19	378	229-67	393
	100	60	229-3	355	229-21	380	229-64	394
	100	90	229-37	387	229-49	390	229-61	395
	120	30	229-4	357	229-22	381	229-68	396
	120	60	229-6	361	229-24	383	229-65	397
	120	90	229-38	388	229-50	391	229-62	398
	140	30	229-7	363	229-25	384	229-69	399
	140	60	229-9	367	229-27	386	229-66	400
	140	90	229-39	389	229-51	392	229-63	401

Figure 20 - Case number catalog for scoping thermal analysis of alternative DPC disposal concepts in clay/shale (subset 1)

Case Number Catalog for Scoping Thermal Analysis of Alternative DPC Disposal Concepts in Clay / Shale (subset 1)										
Catalog of Open Mode Sensitivity Study Cases		Click Here to Jump to Selected Case								
Case # Definition Table (Each parametric study case in LLNL-TR-639869 includes ten DSEF transient calculations)		LLNL-TR-639869 - Repository Layout and Thermal Gradient Trade Study for Large Waste Packages in Clay-Shale 32-PWR WP, 40 GWd/MT, Storage time = 50 years, Drift spacing = 70 m DSEF base case 229								
		Ventilation Duration (yr)								
		100		75		50		25		
Waste Package Spacing (m)	CP2* (m)	LLNL-TR-639869 Case #	CASE LIBRARY Case #	LLNL-TR-639869 Case #	CASE LIBRARY Case #	LLNL-TR-639869 Case #	CASE LIBRARY Case #	LLNL-TR-639869 Case #	CASE LIBRARY Case #	
15	1	500-1	402	500-6	452	500-11	502	500-16	552	
	2	500-2	403	500-7	453	500-12	503	500-17	553	
	3	500-3	404	500-8	454	500-13	504	500-18	554	
	4	500-4	405	500-9	455	500-14	505	500-19	555	
	5	500-5	406	500-10	456	500-15	506	500-20	556	
16	1	500-1	407	500-6	457	500-11	507	500-16	557	
	2	500-2	408	500-7	458	500-12	508	500-17	558	
	3	500-3	409	500-8	459	500-13	509	500-18	559	
	4	500-4	410	500-9	460	500-14	510	500-19	560	
	5	500-5	411	500-10	461	500-15	511	500-20	561	
17	1	500-1	412	500-6	462	500-11	512	500-16	562	
	2	500-2	413	500-7	463	500-12	513	500-17	563	
	3	500-3	414	500-8	464	500-13	514	500-18	564	
	4	500-4	415	500-9	465	500-14	515	500-19	565	
	5	500-5	416	500-10	466	500-15	516	500-20	566	
18	1	500-1	417	500-6	467	500-11	517	500-16	567	
	2	500-2	418	500-7	468	500-12	518	500-17	568	
	3	500-3	419	500-8	469	500-13	519	500-18	569	
	4	500-4	420	500-9	470	500-14	520	500-19	570	
	5	500-5	421	500-10	471	500-15	521	500-20	571	
19	1	500-1	422	500-6	472	500-11	522	500-16	572	
	2	500-2	423	500-7	473	500-12	523	500-17	573	
	3	500-3	424	500-8	474	500-13	524	500-18	574	
	4	500-4	425	500-9	475	500-14	525	500-19	575	
	5	500-5	426	500-10	476	500-15	526	500-20	576	
20	1	500-1	427	500-6	477	500-11	527	500-16	577	
	2	500-2	428	500-7	478	500-12	528	500-17	578	
	3	500-3	429	500-8	479	500-13	529	500-18	579	
	4	500-4	430	500-9	480	500-14	530	500-19	580	
	5	500-5	431	500-10	481	500-15	531	500-20	581	
21	1	500-1	432	500-6	482	500-11	532	500-16	582	
	2	500-2	433	500-7	483	500-12	533	500-17	583	
	3	500-3	434	500-8	484	500-13	534	500-18	584	
	4	500-4	435	500-9	485	500-14	535	500-19	585	
	5	500-5	436	500-10	486	500-15	536	500-20	586	
22	1	500-1	437	500-6	487	500-11	537	500-16	587	
	2	500-2	438	500-7	488	500-12	538	500-17	588	
	3	500-3	439	500-8	489	500-13	539	500-18	589	
	4	500-4	440	500-9	490	500-14	540	500-19	590	
	5	500-5	441	500-10	491	500-15	541	500-20	591	
23	1	500-1	442	500-6	492	500-11	542	500-16	592	
	2	500-2	443	500-7	493	500-12	543	500-17	593	
	3	500-3	444	500-8	494	500-13	544	500-18	594	
	4	500-4	445	500-9	495	500-14	545	500-19	595	
	5	500-5	446	500-10	496	500-15	546	500-20	596	
24	1	500-1	447	500-6	497	500-11	547	500-16	597	
	2	500-2	448	500-7	498	500-12	548	500-17	598	
	3	500-3	449	500-8	499	500-13	549	500-18	599	
	4	500-4	450	500-9	500	500-14	550	500-19	600	
	5	500-5	451	500-10	501	500-15	551	500-20	601	

Figure 21 - Case number catalog for scoping thermal analysis of alternative DPC disposal concepts in clay/shale (subset 2)

Case Number Catalog for Scoping Thermal Analysis of Alternative DPC Disposal Concepts in Clay / Shale (subset 2)									
Catalog of Open Mode Sensitivity Study Cases		Click Here to Jump to Selected Case							
Case # Definition Table (Each parametric study case in LLNL-TR-639869 includes ten DSEF transient calculations)		LLNL-TR-639869 - Repository Layout and Thermal Gradient Trade Study for Large Waste Packages in Clay-Shale 32-PWR WP, 60 GWd/MT, Storage time = 50 years, Drift spacing = 70 m or 90 m, Ventilation = 150 years DSEF base case 231							
		WP spacing ranges from 16 to 34 m				WP spacing ranges from 32 to 50 m			
		Drift spacing = 90 m		Drift spacing = 70 m		Drift spacing = 90 m		Drift spacing = 70 m	
WP Spacing (m)	CP2* (m)	LLNL-TR-639869 Case #	CASE LIBRARY Case #	LLNL-TR-639869 Case #	CASE LIBRARY Case #	LLNL-TR-639869 Case #	CASE LIBRARY Case #	LLNL-TR-639869 Case #	CASE LIBRARY Case #
16	1	500-21	602	500-26	652				
	2	500-22	603						
	3	500-23	604						
	4	500-24	605						
	5	500-25	606						
18	1	500-21	607	500-26	653				
	2	500-22	608						
	3	500-23	609						
	4	500-24	610						
	5	500-25	611						
20	1	500-21	612	500-26	654				
	2	500-22	613						
	3	500-23	614						
	4	500-24	615						
	5	500-25	616						
22	1	500-21	617	500-26	655				
	2	500-22	618						
	3	500-23	619						
	4	500-24	620						
	5	500-25	621						
24	1	500-21	622	500-26	656				
	2	500-22	623						
	3	500-23	624						
	4	500-24	625						
	5	500-25	626						
26	1	500-21	627	500-26	657				
	2	500-22	628						
	3	500-23	629						
	4	500-24	630						
	5	500-25	631						
28	1	500-21	632	500-26	658				
	2	500-22	633						
	3	500-23	634						
	4	500-24	635						
	5	500-25	636						
30	1	500-21	637	500-26	659				
	2	500-22	638						
	3	500-23	639						
	4	500-24	640						
	5	500-25	641						
32	1	500-21	642	500-26	660	500-32	662	500-27	672
	2	500-22	643					500-28	673
	3	500-23	644					500-29	674
	4	500-24	645					500-30	675
	5	500-25	646					500-31	676
34	1	500-21	647	500-26	661	500-32	663	500-27	677
	2	500-22	648					500-28	678
	3	500-23	649					500-29	679
	4	500-24	650					500-30	680
	5	500-25	651					500-31	681
36	1					500-32	664	500-27	682
	2							500-28	683
	3							500-29	684
	4							500-30	685
	5							500-31	686
38	1					500-32	665	500-27	687
	2							500-28	688
	3							500-29	689
	4							500-30	690
	5							500-31	691
40	1					500-32	666	500-27	692
	2							500-28	693
	3							500-29	694
	4							500-30	695
	5							500-31	696
42	1					500-32	667	500-27	697
	2							500-28	698
	3							500-29	699
	4							500-30	700
	5							500-31	701
44	1					500-32	668	500-27	702
	2							500-28	703
	3							500-29	704
	4							500-30	705
	5							500-31	706
46	1					500-32	669	500-27	707
	2							500-28	708
	3							500-29	709
	4							500-30	710
	5							500-31	711
48	1					500-32	670	500-27	712
	2							500-28	713
	3							500-29	714
	4							500-30	715
	5							500-31	716
50	1					500-32	671	500-27	717
	2							500-28	718
	3							500-29	719
	4							500-30	720
	5							500-31	721

Once the user finds a case of interest that may be used as a starting point for a new variation or analysis, the INPUTS worksheet can automatically populate some of the key data inputs from the selected case, so that the user can either accept it as is, or input their own values. This is discussed in Section 5.

The THERMAL-INTERPOLATE worksheet includes two tools that can be used to develop a new analysis case from the ensemble of existing runs. The first tool allows the user to compare and contrast combinations of cases and data fields from a set of comparison cases, using the worksheet template shown in Figure Figure 22. Following the color conventions introduced in Section 4, the yellow highlighted cells along the left column and in the top row of Figure Figure 22 allow the user to enter case numbers on the left, and selected data fields (from Figure Figure 14) on the top row.

Once the case numbers and selected data fields have been reviewed in the first tool, the user can select two appropriate case numbers for the interpolation. For example, in Figure Figure 23, the Case 225 and 260 rows show results for open mode drift spacing (i.e., lateral spacing) of 30 m and 40 m. The user is responsible to select cases in which other potential independent variables are identical or at least very similar. In these two cases, the geologic medium, the waste package capacity, the burnup, the waste package spacing (i.e., axial spacing), the surface storage time, and the ventilation duration are identical, as shown in the case description. The user can verify these parameters by inputting their parameter numbers (from the list in Figure Figure 14) on the top row of Figure Figure 22 (the first tool). Other parameters should also be checked using Figure 23 (including thermal conductivities, thermal diffusivities, and EBS dimensions).

Once the two cases are chosen, the user proceeds to the second tool on the THERMAL-INTERPOLATE worksheet, which requires two case numbers, an independent variable, and a dependent variable. Based on the discussion above, lateral spacing could be the independent variable for interpolating between cases 225 and 260. Consider the case where the waste package peak temperature is the dependent variable, with a desired value of 150°C, as an example of using the tool. Figure 23, panel (a), displays that example, with a linearly-predicted peak waste package temperature of 154.72°C at a lateral spacing of 35 m, obtained from the peak temperatures previously calculated for lateral spacing of 30 and 40 m. The user can simply iterate on the lateral spacing until the interpolated result is as close as desired to the target value. It should be noted that the tool also will extrapolate, but the user should be wary of extrapolating a significant distance.

Figure 23, panel (b), shows the error message if the user inadvertently specifies the same point for each end of the interpolation. Figure 23, panel (c), shows an example of one of the drop-down lists and some of the choices for independent variables.

Figure 22 - Side-by-side case comparison table

Side by side Case Comparison Section - see the CASE LIBRARY for additional description of the categories of cases in the library										
Column # -->	2	40	39	45	44	21	38	37	50	
Case Number	Case Description	Peak Rock Wall T, °C	Time of Peak T at Rock Wall, yr	Peak WP T, °C	Time of Peak WP T, yr	WP Wall Material	Center to Center Lateral Spacing, m	Center to Center Axial Spacing, m	Ventilation Period (yr)	
225	Open Mode Case 21, Clay 21-UOX-40, Storage time=50 y, WP spacing=10 m, Drift/borehole spacing=30 m, Base case for sensitivity studies in clay, WP=21, 40 Gwd/MT UOX TS=50	134.592	593	164.099	488	Carbon Steel	30	10	250	
260	Open Mode Case 21w, Clay 21-UOX-40, Storage time=50 y, WP spacing=10 m, Drift/borehole spacing=40 m, Sensitivity to Drift Spacing = 40 m	116.053	641	145.345	470	Carbon Steel	40	10	250	
55	Granite 4-UOX-60, Storage time=50 y, WP spacing=10 m, Drift/borehole spacing=20 m	100.7	87	141.2	65	Steel	20	10	NA	

Figure 23 - The template for variable interpolation between relevant cases

(a) – Good selection with no error messages.

Independent variable (Select column name)		Dependent variable (Select column name)	
Lateral Spacing, m		Peak Waste Package T, °C	
Interpolation Table Column #	38	Interpolation Table Column #	45
WARNING!!! CHOOSE CASES IN WHICH ALL OTHER INDEPENDENT VARIABLES ARE ROUGHLY EQUAL.	Case Number	Independent Variable	Dependent Variable
	225	X_1 30	Y_1 164.099
	OK	X 35	Y 154.722
	260	X_2 40	Y_2 145.345

(b) – An example of an error message that helps guide the user

Independent variable (Select column name)		Dependent variable (Select column name)	
Lateral Spacing, m		Peak Waste Package T, °C	
Interpolation Table Column #	38	Interpolation Table Column #	45
WARNING!!! CHOOSE CASES IN WHICH ALL OTHER INDEPENDENT VARIABLES ARE ROUGHLY EQUAL.	Case Number	Independent Variable	Dependent Variable
	225	X_1 30	Y_1 164.099
	Reselect	X 35	Y #DIV/0!
	225	X_2 30	Y_2 164.099
			Select Cases with Different Independent Variable Values

(c) – An example of what the drop down lists contain (they scroll to other selections besides the ones shown here)

Independent variable (Select column name)		Dependent variable (Select column name)	
Lateral Spacing, m		Peak Waste Package T, °C	
Interpolation Table Column #	38	Interpolation Table Column #	45
CHOOSE CASES IN WHICH ALL OTHER INDEPENDENT VARIABLES ARE ROUGHLY EQUAL.	Case Number	Independent Variable	Dependent Variable
	5	X_1 30	Y_1 164.099
	OK	X 35	Y 154.722
	260	X_2 40	Y_2 145.345

8. Getting a Quick Overview of the Latest Analysis – the RESULTS and the THERMAL-ANALYTICAL OUTPUT Worksheets

The RESULTS worksheet contains a concise summary of the input data from both the INPUTS worksheet; the THERMAL-SOURCE worksheets (providing both tabular and graphical summaries of the decay heat data; and results of the COST CALCULATIONS worksheet used in the current analysis case. The output data also includes results from the THERMAL-ANALYTICAL OUTPUT worksheet, including the plots shown later in Section 11 (Figure 36 and Figure

37).

Section 1 of the RESULTS worksheet summarizes the input data as follows:

- 1.A. Case Name and User Information.
- 1.B. Waste Characteristics and Waste Package Capacity.
- 1.C. Repository Design - including layout and ventilation system data.
- 1.D. Host Rock – including geometry, properties, and temperature.
- 1.E. EBS Components – including geometry, material names, and material properties.
- 1.F. Decay Heat – including both tabular and graphical representations.

Section 2 of the RESULTS worksheet summarizes the analysis results as follows:

- 2.A. Peak and Transient Temperature Results – these include peak temperatures and the times of the peaks for the host rock wall, the various EBS component interface locations, and the waste package surface. Figure Figure 11 shows an example of the peak temperature results summary and the results compared to the thermal constraints. When a parametric study is performed in DSEF (as described in Step 12 on the INPUTS sheet), and shown in Figure 12, the full set of peak temperature values and times of the peaks for the parametric study are shown on the RESULTS worksheet, but the graphical results are only shown for the first case of the parametric study, or the single analysis case if no parametric study is performed. The RESULTS worksheet provides a hyperlink to the THERMAL-ANALYTICAL OUTPUT worksheet to allow the user to examine the full set of transient tabular and graphical results when a parametric study is analyzed.
- 2.B. Potential New Case Library Data Entry – this section provides a hyperlink to the CASE LIBRARY, just below the Case Catalog where the current analysis results are displayed in the form of a Case Library record.

- 2.C. Cost Results – this section shows the overall summary of raw, low contingency, and high contingency cost data from the COST CALCULATIONS worksheet (see Figure 28 from Section 9 of this user manual), as well as a short summary of the emplacement drift length calculation based on the thermal analysis model, that is used in the cost calculations.

Note that when the Mathcad component of DSEF returns a table of peak temperatures and times, and one or more sets of transient temperatures (one set for each parametric sensitivity study case) to the THERMAL-ANALYTICAL OUTPUT worksheet, the Excel formatting is lost. There is a macro button on the top of the worksheet which needs to be pressed once to restore the formatting, which makes the results easier to read. There is another macro button which is used to clear all of the transient results in the event the user wishes to use the same Excel file with a few modifications to evaluate another case. There is a similar macro button to clear previous transient results provided on the INPUTS worksheet in Step 2.G.

The COST Worksheets

As part of the assessment of design concept feasibility, DSEF includes the capability to evaluate the costs of constructing and operating a repository concept that uses the design values from the DSEF INPUTS worksheet. In DSEF Version 2.1, the cost calculations were limited to mining and backfill costs of the repository subsurface only. Version 3.0 extends the cost model to include the total system cost.

Rough order-of-magnitude (ROM) cost data were developed in Carter 2012, and presented in Hardin 2012b, and referred to here as the Carter/Hardin cost model. DSEF Version 3.0 has been revised to address all of the cost categories covered in the Carter/Hardin model. The cost categories have been slightly regrouped to take advantage of repository design details available in DSEF, but are generally comparable to the Carter/Hardin results.

Specifically, the Carter/Hardin model includes two high-level cost categories of “Facility Design, Construction, and Startup”, and “Operations & Maintenance”. The DSEF calculations use five cost categories whose total is comparable to the total of the two Carter/Hardin categories; the DSEF categories are “Facility Design and Startup”, “Surface Facility Construction”, “Subsurface Facility Construction”, “Ventilation”, and “Operations and Maintenance”. It should be noted that DSEF construction categories include all such construction, while Carter/Hardin include the first phase of construction in their first category, and subsequent modular construction as part of O&M. Also, DSEF includes both construction and O&M for ventilation in the “Ventilation” category. The remaining Carter/Hardin categories are directly comparable to DSEF categories. These are “Closure”, “Waste Package costs”, “Regulatory & Licensing”, “Monitoring”, “Performance Confirmation”, and “Program Integration”.

The DSEF approach was to match the Carter/Hardin costs for their five base cases, for the sum of the first two Carter/Hardin cost categories, for each of the other six Carter/Hardin cost categories, and for the overall total. This was accomplished by calculating costs as the product of a unit cost times the number of units (meters of excavation, number of waste packages, years of operation, etc.), or as the sum of several of these products. The unit costs were specified to

produce agreement with the Carter/Hardin costs and to maintain as much consistency and logic as possible across the five disparate base cases.

The DSEF INPUTS worksheet now includes over 80 new input categories to address these calculations, and includes a set of five example cases that were analyzed in by Hardin and Carter using a drop-down menu to select the example case, and then providing the sample case data for each input so that it can either be used or over-ridden by providing user input for the current analysis case.

Note that the DSEF geologic material selection of “granite” corresponds to the crystalline rock type, and the geologic material selection of “alluvium” corresponds to the sedimentary rock type in the cost cases below.

The five example cost cases are defined in the Carter/Hardin model as follows:

1. Crystalline (enclosed) - Vertical borehole emplacement is used with a copper waste package (e.g., Swedish KBS-3 concept) with a clay buffer installed at emplacement. Access drifts are backfilled with low-permeability clay-based backfill at closure (Hardin 2012b, Section 1.4.5.1).
2. Generic Salt Repository (enclosed) – A repository in bedded salt in which carbon steel waste packages are placed on the floor in drifts or alcoves, and immediately covered (backfilled) with run-of-mine salt (Hardin 2012b, Section 1.4.5.2).
3. Clay/Shale (enclosed) – SNF or HLW is emplaced in blind, steel-lined horizontal borings constructed from access drifts. SNF is emplaced in carbon steel packages with a clay buffer. HLW glass is emplaced in stainless steel pour canisters, within a steel liner (Hardin 2012b, Section 1.4.5.3).
4. Shale Unbackfilled (open) – A repository in a thick shale formation constructed so that ventilation is maintained for at least 50 to 100 years after waste emplacement. Emplacement drifts are not backfilled at closure, but all other openings are backfilled to provide waste isolation (Hardin 2012b, Section 1.5.1).
5. Sedimentary Backfilled (open) – Constructed in sedimentary rock so that ventilation is maintained for at least 50 to 100 years after waste emplacement. All waste emplacement and other openings are backfilled with low-permeability clay-based backfill prior to repository closure (Hardin 2012b, Section 1.5.2).

The specific data for these cases is captured in a set of Excel lookup tables on the DSEF LISTS worksheet, and then used as described above on the INPUTS worksheet. DSEF provides a hyperlink to the relevant section of the LISTS worksheet that allows the user to examine the cost data summary tables if desired. The user can also see all the inputs for a single Carter/Hardin base case by simply selecting it. Then, the user can copy the values desired for a user design case, row by row, as appropriate, and then change to User-Defined in the case selection menu. The unit cost data were extracted from both Carter 2012 and Hardin 2012b, or were back calculated to match the Carter results in each category listed above. A number of the key reference tables from Hardin 2012b are included on the COST REFERENCES worksheet.

Figure 24, Figure 24, and Figure 26 summarize the five example cases from the Carter/Hardin model, and Figure 27

is an example of the detailed cost data for one of the examples (where the details for all of them are shown on the COST REFERENCES worksheet).

Figure 24- Summary of waste package numbers for the 5 example cost cases (From Hardin 2012b Tables 2.1-1 and 4-1)

Table 2.1-1 -Numbers of Different Size Waste Packages for a 140,000 MT SNF Repository

	4-PWR/9-BWR	12-PWR/24-BWR	21-PWR/44-BWR
PWR	52,250	17,417	9,952
BWR	30,333	11,375	6,205
Total	82,583	28,792	16,157

Table 4-1 - Summary of Waste Package Numbers for 5 Disposal Concepts

	Package Capacity (PWR/BWR)	140,000 MT Repository		Disposal Overpack
		Total Waste Packages	Annual Waste Packages	Material
Crystalline (enclosed)	4/9	82,583	1,757	Copper
Generic Salt Repository (enclosed)	12/24	28,792	616	Carbon Steel
Clay/Shale (enclosed)	4/9	82,583	1,757	Carbon Steel
Shale Unbackfilled (open)	21/44	16,157	344	Carbon Steel
Sedimentary Backfilled (open)	21/44	16,157	344	Carbon Steel

Figure 25- Summary of mined opening length and volume for the 5 example cost cases (From Hardin 2012b Table 4-2)

Table 4-2 - Summary of Mined Opening Length and Volume for 5 Disposal Concepts

	Access Drift		Disposal Drifts/ Borings		Service Drift		Repository Total	
	Length (m)	Volume (m³)	Length (m)	Volume (m³)	Length (m)	Volume (m³)	Length (m)	Volume (m³)
Crystalline (enclosed)	8.3E5	2.7E7	8.3E5	1.8E6	2.3E5	7.7E6	1.9E6	3.7E7
Generic Salt Repository (enclosed)	3.1E5	1.7E7	3.5E5	4.4E6	1.3E5	7.2E6	7.9E5	2.9E7
Clay/Shale (enclosed)	3.9E5	9.2E6	8.3E5	4.6E6	3.7E5	8.7E6	1.6E6	2.3E7
Shale Unbackfilled (open)	7.7E4	2.2E6	1.4E5	2.3E6	9.3E4	2.2E6	3.1E5	6.7E6
Sedimentary Backfilled (open)	8.5E4	2.0E6	2.2E5	3.5E6	5.8E4	1.4E6	3.6E5	6.9E6

Figure 26- Summary of shaft and ramp quantities for the 5 example cost cases

(From Hardin 2012b Table 4-3)

Table 4-3 - Summary of Shaft and Ramp Quantities for a 140,000 MT SNF Repository

	Air Intake	Rock Waste	Ventilation Exhaust	Waste Emplacement	
				Shafts	Ramps
Crystalline (enclosed)	1	1	2	1	0
Generic Salt Repository (enclosed)	1	1	2	1	0
Clay/Shale (enclosed)	1	1	2	0	1
Shale Unbackfilled (open)	8	1	4	0	1
Sedimentary Backfilled (open)	10	1	5	0	1

Figure 27– Cost example case 1 - crystalline (enclosed) repository drift panel detail summary

(From Hardin 2012b Table 4.1-1 and 4.1-2)

Table 4.1-1 - Crystalline (enclosed) Repository Drift Panel Detail Summary

Drift/Boring Function	Diameter (m)	Length (m)	Number (per panel)	Total Length (m)	Spacing (m)	Closure
Waste Emplacement	1.66	10	1,200	12,000	10	Bentonite clay backfilled at emplacement and shield plug installed
Access Drifts	6.5	1000	12	12,000	20	Backfilled with 30% bentonite clay and 70% crushed rock
Service Drifts	5.5	326 1100	4 2	3,352	N/A	Backfilled with 30% bentonite clay and 70% crushed rock
Panel Total				27,352		

Table 4.1-2 - Crystalline (enclosed) Concept Repository Waste Emplacement Details

Emplacement Mode	PWR/BWR Package Size	Waste Package Spacing (m)	Waste Packages per Emplacement Drift	Waste Packages Per Panel	Waste Package Description
Vertical Borehole	4/9	10	100 WP per 1,000 m segment	1200	Stainless steel SNF canister with 5 cm thick copper overpack

As shown on the NAVIGATION worksheet in Figure 4, there are two cost-related worksheets

- COST CALCULATIONS

- COST REFERENCES

The COST CALCULATIONS worksheet (below the summary information described in the next two paragraphs) follows the Carter/Hardin model cost categories with the changes described above. Depending on the availability of source data, the calculations can be done at three increasing levels of detail. In some cases, there are detailed data on unit costs, and a specific measure of the number of units is available, such as cost per unit volume to excavate emplacement drifts, and emplacement drift lengths. In this case, the calculation could start at level 3 (the most detailed) and build up the costs of subsurface construction to be added together at level 2 or level 1. In other cases, the detailed information may not be available, so the user can put data in at level 2 for several cost components to be summed up at level 1. If there isn't enough detail to break the calculation down further, such as for regulatory & licensing, then the user may enter the data at level 1. As on the INPUTS worksheet, data transferred from other worksheets or data areas in DSEF is shown in light blue, and cells that allow the user to override or directly input data are highlighted in yellow. It is recommended that the user do the overrides in the INPUTS worksheet. Overrides in the COST CALCULATIONS worksheet persist even if the user makes changes in INPUTS, so the user should scan the COST CALCULATIONS override columns to avoid inadvertent overrides for subsequent cases.

The top-left section of the COST CALCULATION worksheet summarizes the raw costs in each category as well as the low and high contingency values. Figure 28 shows an example of the top-left section. The low contingency values are copied from the three-level detailed table below it (as described in the preceding paragraph), and the raw and high contingency values are calculated in the summary table, using the contingencies selected in the INPUTS worksheet. As detailed in the Carter/Hardin model documentation, the values applied for low and high contingency adjustment vary by the cost calculation category. The lookup tables in the LISTS worksheet (which supply contingency values to the INPUTS sheet for the five Carter/Hardin examples) assume the low contingency value is 5% in most cases (except where it is given explicitly by Carter). These lookup tables also include high contingency values that were derived from the summary low and high contingency cost results in Carter/Hardin. This approach yielded good agreement with the five example cases, as shown below. Since the DSEF modeling was based on matching the low contingency values, the raw cost values were obtained by dividing the low contingency calculated values by 1 plus the low contingency, and the high contingency values were then calculated by multiplying the raw cost values by 1 plus the high contingency.. A table showing the general rules for applying contingency factors that were used in the Carter/Hardin model is included in the COST REFERENCES worksheet. The user can override the recommended contingency values in INPUTS.

Figure 28– Cost summary table example as shown on the RESULTS worksheet

Cost in MM\$	Current Case		
	Case evaluation below is ROM cost study case: ROM Cost Case 4 - Clay/Shale (open)		
Cost Category	Raw	Low Contingency	High Contingency
Facility Design & Startup	\$705	\$740	\$1,080
Surface Facility Construction	\$1,303	\$1,368	\$1,997
Subsurface Facility Construction	\$1,744	\$1,831	\$2,674
Ventilation	\$1,938	\$2,035	\$2,971
O&M (not including ventilation)	\$6,714	\$7,050	\$9,024
Upper Half Subtotal	\$12,404	\$13,024	\$17,746
Closure	\$1,296	\$1,425	\$2,203
Waste Package costs	\$2,616	\$2,747	\$3,406
Regulatory & Licensing	\$397	\$417	\$434
Monitoring	\$3,019	\$3,320	\$4,528
Performance Confirmation	\$400	\$420	\$571
Program Integration	\$3,393	\$3,732	\$5,089
Lower Half Subtotal	\$11,120	\$12,061	\$16,230
Total	\$23,524	\$25,085	\$33,977

The five Carter/Hardin cost cases (that had detailed costing in unreleased documentation) were used to construct the DSEF cost model, using cost results summarized by Carter and Hardin at the category level. That comparison is documented on the top-right section of the COST CALCULATIONS worksheet, where the DSEF calculated numbers are compared to the “Low and High Contingency” numbers from Carter/Hardin. The comparisons are shown in Figure 29 through Figure 33, and are generally within 5% of the total costs. In a number of cases, the DSEF modeling was based on estimating some scaling factors, such as scaling backfill costs for emplacement drifts per unit volume or length while accounting for a volume reduction fraction due to drift inverts. The Carter/Hardin unit costs were shifted slightly to allow for this kind of user input, while still calculating a reasonable total backfill cost.

Figure 29– Cost summary table comparing Carter/Hardin Case 1 (Crystalline Enclosed) results with DSEF results

Costs in MM\$	DSEF	Carter	DSEF/ Carter	DSEF	Carter	DSEF/ Carter
Cost Category	Low	Low	Low %	High	High	High %
Facility DC&S		\$3,754			\$5,495	
Facility D&S	\$1,026			\$1,498		
Surface	\$1,368			\$1,997		
Subsurface	\$12,484			\$18,227		
Ventilation	\$0			\$0		
O&M (incl some constr)		\$17,545			\$22,475	
O&M (n/i ventilation)	\$7,050			\$9,024		
Upper Half Subtotal	\$21,928	\$21,299	103%	\$30,746	\$27,970	110%
Closure	\$9,698	\$9,563	101%	\$13,224	\$13,704	96%
WPs	\$16,682	\$17,489	95%	\$20,685	\$21,647	96%
Regulatory & Licensing	\$424	\$424	100%	\$441	\$441	100%
Monitoring	\$10,436	\$10,685	98%	\$14,231	\$14,571	98%
PC	\$420	\$411	102%	\$571	\$561	102%
Integration	\$1,575	\$1,575	100%	\$2,148	\$2,142	100%
Lower Half Subtotal	\$39,235	\$40,147	98%	\$51,300	\$53,066	97%
Total	\$61,163	\$61,446	100%	\$82,046	\$81,036	101%

Figure 30– Cost summary table comparing Carter/Hardin Case 2 (Salt Enclosed) results with DSEF results

Costs in MM\$	DSEF	Carter	DSEF/ Carter	DSEF	Carter	DSEF/ Carter
Cost Category	Low	Low	Low %	High	High	High %
Facility DC&S		\$3,896			\$5,595	
Facility D&S	\$1,015			\$1,482		
Surface	\$1,368			\$1,997		
Subsurface	\$2,893			\$4,224		
Ventilation	\$0			\$0		
O&M (incl some constr)		\$7,947			\$10,259	
O&M (n/i ventilation)	\$7,050			\$9,024		
Upper Half Subtotal	\$12,326	\$11,843	104%	\$16,727	\$15,854	106%
Closure	\$855	\$832	103%	\$1,322	\$1,363	97%
WPs	\$3,801	\$3,998	95%	\$4,713	\$4,950	95%
Regulatory & Licensing	\$368	\$368	100%	\$383	\$379	101%
Monitoring	\$4,646	\$4,580	101%	\$6,336	\$6,246	101%
PC	\$560	\$567	99%	\$762	\$773	99%
Integration	\$2,136	\$2,136	100%	\$2,913	\$2,907	100%
Lower Half Subtotal	\$12,366	\$12,481	99%	\$16,428	\$16,618	99%
Total	\$24,692	\$24,324	102%	\$33,155	\$32,472	102%

Figure 31– Cost summary table comparing Carter/Hardin Case 3 (Clay/Shale Enclosed) results with DSEF results

Costs in MM\$	DSEF	Carter	DSEF/ Carter	DSEF	Carter	DSEF/ Carter
Cost Category	Low	Low	Low %	High	High	High %
Facility DC&S		6,872			10,064	
Facility D&S	1,547			2,259		
Surface	1,368			1,997		
Subsurface	22,949			33,506		
Ventilation	0			0		
O&M (incl some constr)		26,884			34,525	
O&M (n/i ventilation)	7,050			9,024		
Upper Half Subtotal	\$32,914	\$33,756	98%	\$46,786	\$44,589	105%
Closure	5,199	5,556	94%	8,035	8,334	96%
WPs	7,185	7,542	95%	8,909	9,337	95%
Regulatory & Licensing	414	414	100%	431	429	100%
Monitoring	9,028	9,021	100%	12,311	12,302	100%
PC	756	758	100%	1,028	1,034	99%
Integration	2914	2,914	100%	3,974	3,965	100%
Lower Half Subtotal	\$25,496	\$26,205	97%	\$34,688	\$35,401	98%
Total	\$58,410	\$59,961	97%	\$81,474	\$79,990	102%

Figure 32– Cost summary table comparing Carter/Hardin Case 4 (Clay/Shale Open) results with DSEF results

Costs in MM\$	DSEF	Carter	DSEF/ Carter	DSEF	Carter	DSEF/ Carter
Cost Category	Low	Low	Low %	High	High	High %
Facility DC&S		3,303			4,711	
Facility D&S	740			1,080		
Surface	1,368			1,997		
Subsurface	1,831			2,674		
Ventilation	2,035			2,971		
O&M (incl some constr)		9,702			12,408	
O&M (n/i ventilation)	7,050			9,024		
Upper Half Subtotal	\$13,024	\$13,005	100%	\$17,746	\$17,119	104%
Closure	1,425	1,622	88%	2,203	2,515	88%
WPs	2,747	2,882	95%	3,406	3,569	95%
Regulatory & Licensing	417	417	100%	434	421	103%
Monitoring	3,320	3,395	98%	4,528	4,629	98%
PC	420	423	99%	571	576	99%
Integration	3732	3,732	100%	5,089	5,084	100%
Lower Half Subtotal	\$12,061	\$12,471	97%	\$16,231	\$16,794	97%
Total	\$25,085	\$25,476	98%	\$33,977	\$33,913	100%

Figure 33– Cost summary table comparing Carter/Hardin Case 5 (Sedimentary Open) results with DSEF results

Costs in MM\$	DSEF	Carter	DSEF/ Carter	DSEF	Carter	DSEF/ Carter
Cost Category	Low	Low	Low %	High	High	High %
Facility DC&S		5,410			7,599	
Facility D&S	1,282			1,872		
Surface	1,368			1,997		
Subsurface	1,923			2,807		
Ventilation	3,010			4,395		
O&M (incl some constr)		9,614			12,264	
O&M (n/i ventilation)	7,050			9,024		
Upper Half Subtotal	\$14,633	\$15,024	97%	\$20,095	\$19,863	101%
Closure	2,075	2,263	92%	3,207	3,558	90%
WPs	2,747	2,882	95%	3,406	3,569	95%
Regulatory & Licensing	668	668	100%	695	679	102%
Monitoring	3,780	3,775	100%	5,155	5,148	100%
PC	798	798	100%	1,085	1,088	100%
Integration	6878	6,878	100%	9,379	9,370	100%
Lower Half Subtotal	\$16,946	\$17,264	98%	\$22,927	\$23,412	98%
Total	\$31,579	\$32,288	98%	\$43,022	\$43,275	99%

The bottom section of the COST CALCULATION worksheet retains some of the emplacement drift mining calculations that were performed in DSEF Version 2.1, summarizing required drift length based on waste package capacity, drift dimensions, and waste package spacing information. In the future, this section could be expanded to calculate lengths of access drifts and service drifts for various layouts, as well as shaft and ramp counts and lengths.

The top section of the COST-REFERENCES worksheet includes tables extracted from Hardin 2012b summarizing the data and assumptions for the five example cases that DSEF displays on the cost section of the INPUTS worksheet. The bottom section of the COST-REFERENCES worksheet provides a number of web pages for current data related to backfill material properties and costs. However, this is neither an endorsement nor a recommendation for using these particular web pages, which were chosen as examples for a ballpark estimate as a starting point for the user.

9. The WASTE FORM Worksheet

The WASTE FORM worksheet summarizes the waste form and waste package dimensions assumed for all of the enclosed mode and open mode cases. Currently there is a limited set of sizes that have been considered. Figure 34 shows the tables of data from the enclosed mode and open mode repository design cases analyzed in FY11 and FY12 included on the WASTE FORM worksheet. The enclosed mode waste package dimensions were based on the reference international repository design concepts (see Hardin 2011).

Figure 35 shows is a lookup table for PWR waste form outer radius (waste package inner radius), and the geometric figures that form the basis for the development of the lookup table. The WASTE FORM worksheet also includes data on PWR and BWR fuel basket designs from storage cask vendor designs. This data was used to define the unit cell dimensions used in the PWR waste form radius lookup table. As shown on the WASTE FORM worksheet, a cross-check of the calculation methodology used to construct the table for the 21-PWR waste package inner radius agrees closely with the value assumed in the open mode thermal analysis for that waste package size.

Although not currently planned, other potential developments of this worksheet might be used to define an equivalent internal thermal conductivity for waste packages for the purpose of determining peak cladding or HLW glass temperatures during thermal transients. This has not been investigated until now since the waste package surface temperature results have been low enough that this does not appear to be an issue.

Figure 34– Tables from the WASTE FORM worksheet

Enclosed Mode Cases		
Waste Form	Geologic Medium	Waste Package Wall thickness (m)
SNF (UOX and MOX)	Granite	0.1
	Clay	0.11
	Salt	0.03
	Deep borehole	0.011
HLW (Co-X, New-X, EC-C, and EC-M)	Granite	0.01
	Clay	0.01
	Salt	0.01
	Deep borehole	0.011

Open Mode Cases		
Waste Form	Geologic Medium	Waste Package Wall thickness (m)
SNF (UOX)	Clay	0.11
	Alluvium	0.11

Open Mode Cases	
Waste Form	Waste Package Length (m)
SNF (UOX)	5

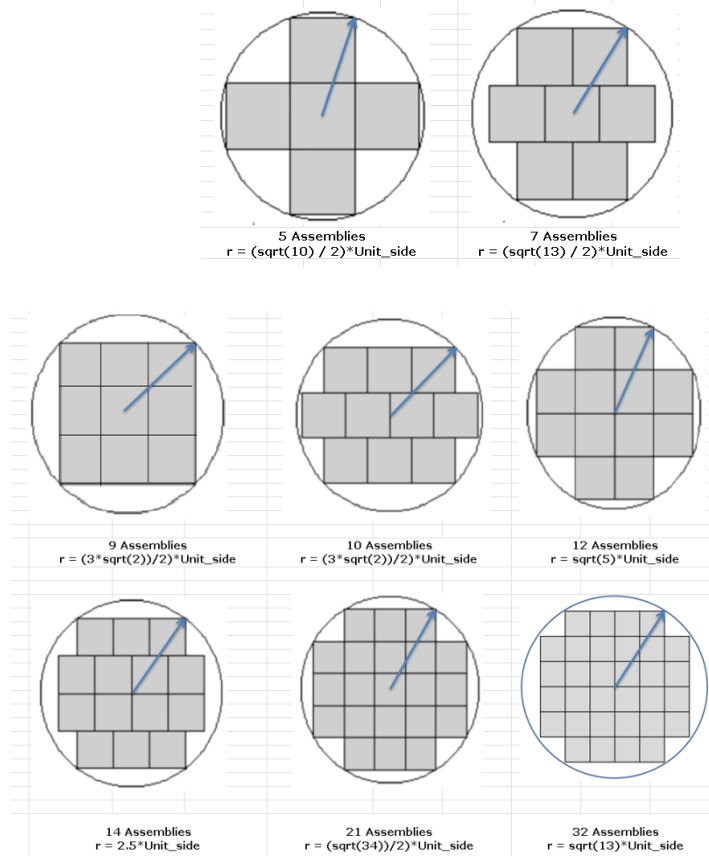
Open Mode Cases		
Number of SNF Assemblies	Waste Package Inner Radius (m)	Waste Package Outer Radius (m)
4	0.3	0.41
12	0.535	0.645
21	0.69	0.8
32	0.89	1

Enclosed Mode Cases	
Waste Form	Waste Package Length (m)
SNF (UOX and MOX)	5
HLW (Co-X, New-X, and EC-C)	4.572 (15 ft)
HWL (EC-M)	3.048 (10 ft)

Enclosed Mode Cases						
Number of Assemblies or Canisters	Geologic Medium	Waste Package Inner Radius (m)	Waste Package Outer Radius Granite (m)	Waste Package Outer Radius Clay (m)	Waste Package Outer Radius Salt (m)	Waste Package Outer Radius Deep Borehole (m)
1 SNF assembly	All Except Deep Borehole	0.19	0.29	0.3	0.22	
2 SNF assemblies		0.38	0.48	0.49	0.41	
3 SNF assemblies		0.38	0.48	0.49	0.41	
4 SNF assemblies		0.38	0.48	0.49	0.41	
12 SNF assemblies		0.555	0.655	0.665	0.585	
1 HLW canister		0.295	0.305	0.305	0.305	
1 assembly (with rod consolidation)	Deep Borehole	0.159				0.17
0.291 canisters (modified smaller radius HLW canister)		0.159				0.17

Figure 35- WASTE FORM worksheet – calculated waste form outer radius lookup table

Number of Assemblies	PWR Waste Form Outer Radius (m)
1	0.168
2	0.335
3	0.335
4	0.335
5	0.375
6	0.427
7	0.427
8	0.503
9	0.503
10	0.503
11	0.530
12	0.530
13	0.593
14	0.593
15	0.691
16	0.691
17	0.691
18	0.691
19	0.691
20	0.691
21	0.691
22	0.749
23	0.749
24	0.749
25	0.855
26	0.855
27	0.855
28	0.855
29	0.855
30	0.855
31	0.855
32	0.855



10. Defining Thermal Data Inputs and Outputs -the THERMAL Worksheets

As shown on the NAVIGATION worksheet in Figure 4, there are a series of thermal worksheets

- THERMAL
- THERMAL-ANALYTICAL
- THERMAL-ANALYTICAL OUTPUT
- THERMAL-FEM (see Section 13)
- THERMAL-INTERPOLATE (discussed in Section 7 with the CASE LIBRARY)
- THERMAL-SOURCE

These worksheets are all linked together by the main THERMAL worksheet. Besides including hyperlinks to the other worksheets, the THERMAL worksheet also displays plots of the decay heat chosen for the current analysis case on the THERMAL-SOURCE worksheet. The following describes the use of these other worksheets.

The THERMAL-ANALYTICAL Worksheet - Passing Input Data to Mathcad

The THERMAL-ANALYTICAL worksheet is the interface for passing data to the Mathcad thermal analytical component of DSEF. No numerical calculations are performed in this worksheet, but the formulas in the worksheet cells pull data from the INPUTS and THERMAL-SOURCE worksheets to a standard location cited in the Mathcad file.

The Mathcad file and the DSEF Excel file need to be in the same directory to facilitate the data transfer. As described in Appendix H, the Excel file name is entered in the Mathcad variable “file”. Before Mathcad can read the Excel file, the Excel file must be closed. By default the Mathcad DSEF file has the calculation mode set to manual, and the variable “Write_OK” is set to “No”. This allows the user to make adjustments and look at results prior to writing them back to the DSEF Excel file. To calculate a screen at a time as the user pages through the Mathcad file, press F9 or use the Mathcad TOOLS – CALCULATE menu to select CALCULATE NOW, alternatively the user can calculate the entire document by pressing CTRL-F9 or selecting the menu option TOOLS – CALCULATE - CALCULATE WORKSHEET. After reviewing the results in MathCad, set the variable “Write_OK” to “Yes” and recalculate the Mathcad document to write the results back to the Excel file in the THERMAL-ANALYTICAL OUTPUT worksheet. To preserve a record of the full Mathcad calculation, the user should print the file to a PDF file for future reference.

The THERMAL-ANALYTICAL OUTPUT Worksheet – Getting Results Back from Mathcad

After running an analysis case in Mathcad the summary of peak temperatures and times, and the full transient outputs are passed back to the THERMAL-ANALYTICAL OUTPUT worksheet, which in turn passes this data to the RESULTS worksheet of DSEF.

The THERMAL-ANALYTICAL OUTPUT worksheet also creates several kinds of plots. There are two plots that are specifically related to parametric studies, as shown in Figure 36. In addition to those plots, for each case in the parametric study two additional plots are provided. One showing the temperature transients at various locations within the EBS and at a second compliance point within the host rock, and another showing the contributions to the rock wall surface temperature are shown in Figure 37.

Figure 36- Example of parametric study plots on the THERMAL-ANALYTICAL OUTPUT worksheet

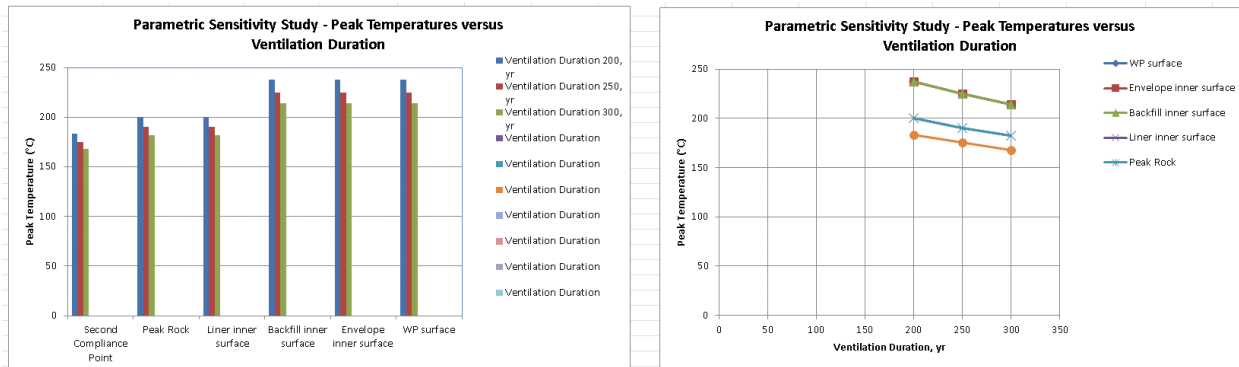
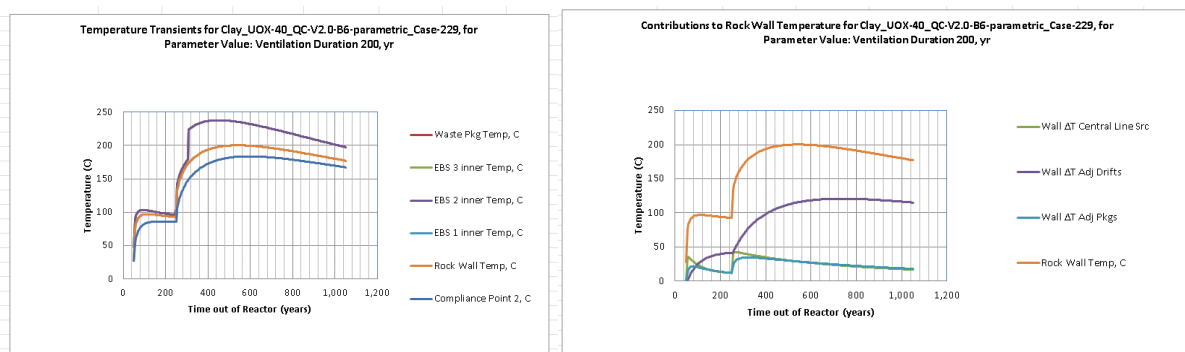


Figure 37- Example transient output data plotted in the THERMAL-ANALYTICAL OUTPUT worksheet



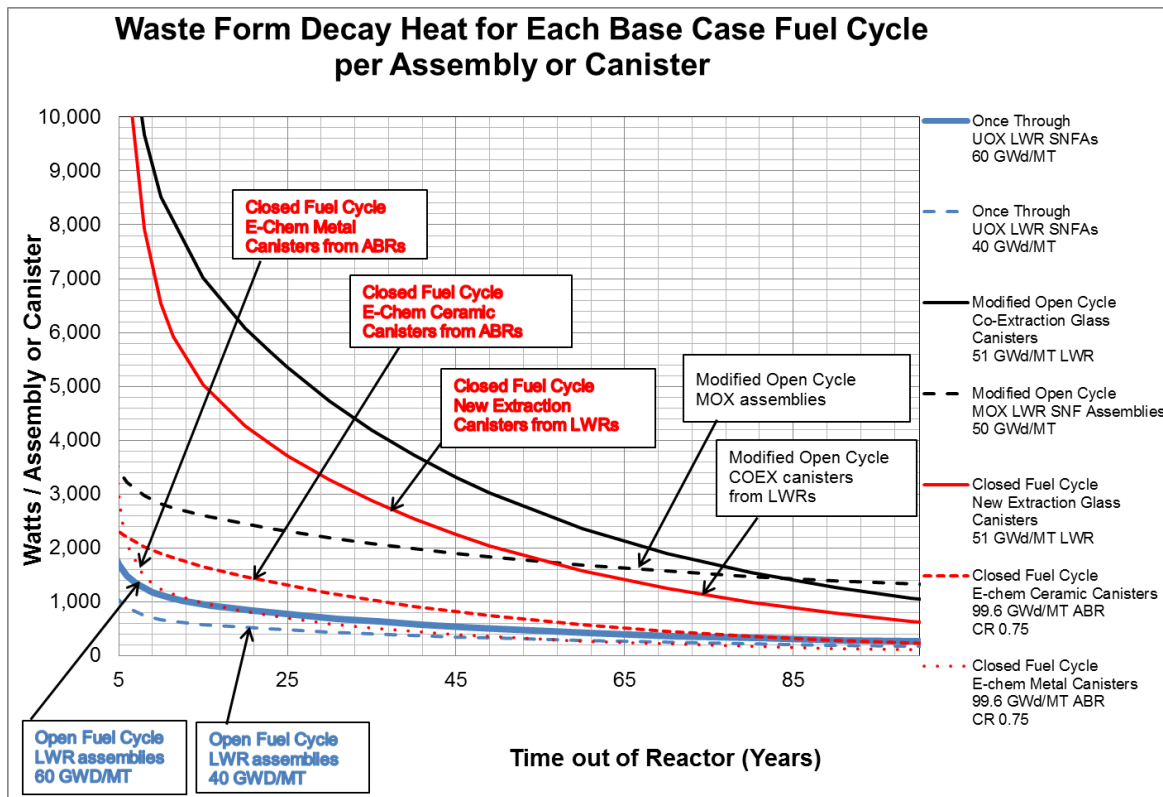
The THERMAL SOURCE Worksheet – Defining the Waste Form Decay Heat

The THERMAL SOURCE worksheet includes a fully documented set of decay heat curves for a set of seven waste forms previously analyzed from three potential fuel cycles

- A once-through LWR fuel cycle with UOX SNF of either 40 GWd/MTU or 60 GWd/MTU burnup
- A partial recycle fuel cycle with MOX SNF of 50 GWd/MTU burnup, and co-extraction glass HLW waste forms (COEX)
- A full recycle based on an Advanced Burner Reactor (ABR) with three HLW waste forms – new-extraction glass (NUEX), Electro-chemical ceramic (E-Chem Ceramic), and Electro-chemical metal (E-Chem Metal).

In addition to these options there is a user-defined option for input from another fuel cycle or modifications to any of the pre-defined cases. Figure 38 shows a plot of the pre-defined waste form decay heat data available for selection on the THERMAL-SOURCE worksheet (Greenberg 2012a).

Figure 38– Decay heat data built-in to the THERMAL-SOURCE worksheet



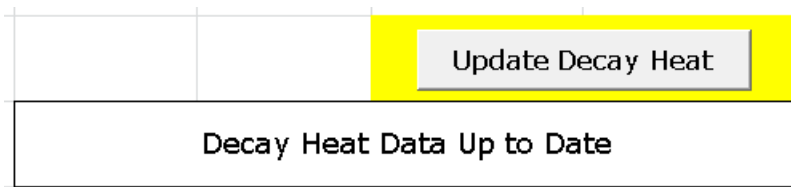
A drop-down list on the INPUTS worksheet allows the user to select one of these data sets, or choose to enter their own data. A prompt and a hyperlink are provided to go the THERMAL-SOURCE worksheet to examine the data, and to click on a macro button to update the decay heat input curve if necessary. Figure 39 shows an example of the “Update Decay Heat” macro button and the two types of prompts.

Figure 39- Examples of decay heat update caution and confirmation prompts

The caution prompt:



The confirmation prompt:



11. Finding and Comparing Material Properties - the MATERIALS Worksheets

As shown on the NAVIGATION worksheet in Figure 4, there are a series of material worksheets

- MATERIAL DATA PLOTTING
- MATERIALS
- MATERIALS-OTHER PROPERTIES (discussed in Section 13)
- MATERIALS-REFERENCES
- MATERIALS-THERMAL PROPERTIES
- MATERIALS-TRANSPORT PROPERTIES

These worksheets are all linked together by the main MATERIALS worksheet, which includes hyperlinks to the other materials worksheets, and then back to the INPUTS worksheet where the derived material properties will be used.

The MATERIAL DATA PLOTTING Worksheet

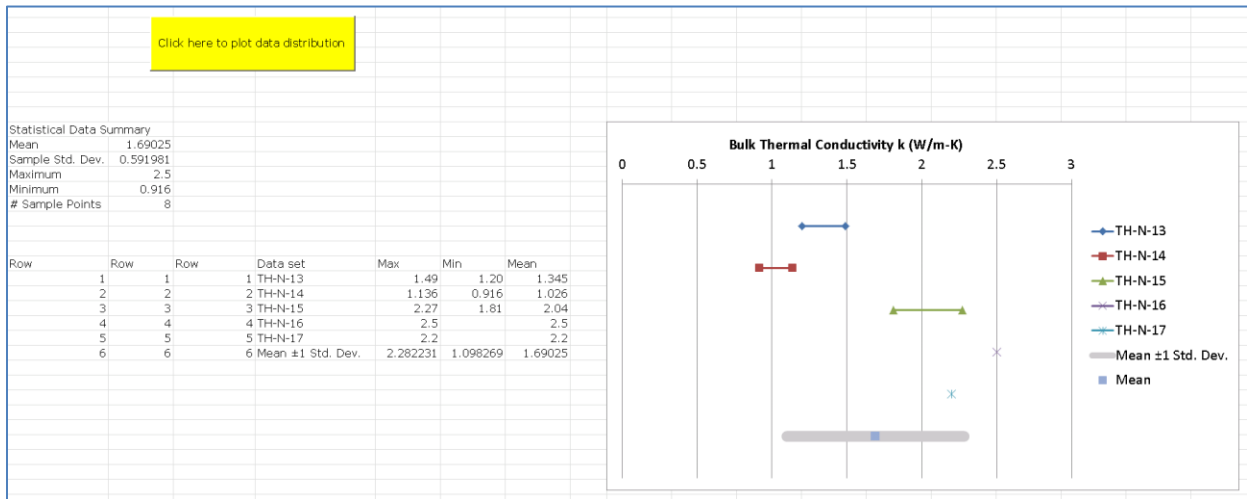
The MATERIAL DATA PLOTTING worksheet only contains a short list of instructions and a *Click here to plot data distribution* macro button. After clicking on that macro button a Select a Range user input box appears, as shown in Figure 40. At this point the user is free to navigate between material data worksheets by clicking on their tabs at the bottom of the screen, and then scrolling with the mouse to any set of data on those worksheets. The only restriction is that the range of data must be restricted to two yellow-highlighted columns, representing the high and low values of a single data parameter.

The range of data selected can be a continuous block of data values or a separate collection of different data sets (use the CTRL key with the mouse to select non-contiguous sets of data). Any blank rows in the middle of a range of data will be ignored. After clicking OK on the range selection box the user is returned to the MATERIAL DATA PLOTTING worksheet where they pick a location to place the statistical data and the plot, as shown in Figure 41 STOP. However, the user is not restricted to placing the output data and plot on this worksheet. It can be placed on any other worksheet by navigating to the new location before clicking OK to insert the plot.

Figure 40 - The first step – selecting the materials data to plot

TH-N-9	Clay	Opalinus clay				0	Ref. C-27, citing Ref. C-31, assumed to be isotropic
TH-N-10	Clay	Opalinus clay		1.38	1.24	1.31	Ref. C-27, (by inverse modeling, two boreholes) - perpendicular to bedding
TH-N-11	Clay	Opalinus clay				0.81	Ref. C-27, (by inverse modeling, two boreholes) - parallel to bedding
TH-N-12	Clay	Opalinus clay				1.87	Ref. C-27, (by inverse modeling, two boreholes) - parallel to bedding
TH-N-13	Clay	Opalinus clay		1.49	1.20	1.345	Ref. C-27, (by inverse modeling, two boreholes) - mean (assuming isotropic)
TH-N-14	Clay	Opalinus clay		1.136	0.916	1.026	Ref. C-27, citing C-32, for perpendicular to bedding
TH-N-15	Clay	Opalinus clay		2.27	1.81	2.04	Ref. C-27, citing C-32 for parallel to bedding
TH-N-16	Clay	Opalinus clay		2.5		2.5	Ref. C-18
TH-N-17	Clay	Opalinus clay		2.2		2.2	Ref. C-18, citing Ref. C-12
TH-N-18	Clay	Opalinus clay		2.5		2.5	Ref. C-18, citing Ref. C-33

Figure 41- Example output of the materials data plotting macro



The MATERIALS-THERMAL PROPERTIES Worksheet

The data records on the MATERIALS-THERMAL PROPERTIES worksheet are identified with a sequential data set number starting with TH-N (for natural material properties) or TH-E for engineered material properties. The natural property data is grouped into major categories of rock, and then subcategories, as shown in Figure 42.

Figure 42 - Example of data structure in the MATERIALS-THERMAL PROPERTIES worksheet

Data Set Number	Host Rock		Source Organization / Reference	Range		Mean	Bulk Thermal Conductivity Comments
	General Material Category	Specific Material Data Source		High Bulk Thermal Conductivity k (W/m-K)	Low Bulk Thermal Conductivity k (W/m-K)	Bulk Thermal Conductivity k (W/m-K)	
TH-N-1	Clay	Boom Clay	NIRAS/ONDRAF, Belgium Ref. C-01	1.69		1.69	Ref. C-01
TH-N-2	Clay	Clay - non-specific	Handbook of Heat Transfer, R-03	1.3		1.3	Ref. R-03, Table 2.35 - Thermophysical Properties of Miscellaneous Materials

The MATERIALS-TRANSPORT PROPERTIES Worksheet

The data records on the MATERIALS-TRANSPORT PROPERTIES worksheet are identified with a sequential data set number starting with TP-N (for natural material properties) or TP-E for engineered material properties. The natural property data is grouped into major categories of rock, and then subcategories, as shown in Figure 43.

Figure 43 - Example of data structure in the MATERIALS-TRANSPORT PROPERTIES worksheet

Data Set Number	Host Rock		Source Organization / Reference	Range		Mean	Permeability Comments
	General Material Category	Specific Material Subcategory		High Permeability (m ²)	Low Permeability (m ²)	Permeability (m ²)	
TP-N-1	Granite	Canadian Shield granite, measured values		1.00E-17	1.00E-19	5.05E-18	Ref. G-06
TP-N-2	Granite	Åspö diorite		1.00E-19	1.00E-20	5.5E-20	Ref. G-08 - for undisturbed rock

The MATERIALS-REFERENCES Worksheet

The MATERIALS-REFERENCES worksheet contains around 100 references that include both primary and secondary reference citations. These references are listed in groups with category letters as follows:

- A – alluvium
- C – clay
- EBS – engineered barrier materials
- G – granite
- R – general reference documents like handbooks or textbooks
- S – salt
- T – tuff

At LLNL a large number of these references are hyperlinked to the source documents on the network drive, but the distribution copy of DSEF Version 3.0 has all of these hyperlinks removed.

12.Placeholder worksheets for future development

No work is currently planned to develop these placeholder worksheets; however, their potential use is described below:

The INTERFACE PARAMETERS Worksheet

This worksheet has limited current operability, with the capability to read and write “comma delimited files”, which are universally accepted by most computer codes.

The DESIGN CONSTRAINTS Worksheet

This worksheet currently documents existing calculations and other references that formed the basis for assumed design constraints in previous calculations, and provides background

information for the users. Design constraint data are currently entered in Step 11 of the INPUTS worksheet. However, the DESIGN CONSTRAINTS worksheet could also allow documentation of experimental results and other information currently being developed that might form the basis for design constraints.

The ENVIRONMENT Worksheet

This worksheet is only a placeholder with no detailed description. This worksheet could be used to interface repository design an analysis to NEPA type of environmental impact statement related data such as passing the data on the volume of excavated muck, required concrete, and electricity / diesel fuel requirements – derived from the COST worksheets (for example).

The PERFORMANCE ASSESSMENT Worksheet

This worksheet is a placeholder intended to pass repository design data – repository layout and dimensions, material quantities and properties, and thermal transient data input to performance assessment external programs.

The MATERIALS-OTHER PROPERTIES Worksheet

This worksheet is a placeholder intended to gather property data and references for properties other than thermal or transport properties that already have data worksheets in DSEF. One example would be to have a worksheet for mechanical properties such as Young's Modulus, compressive strength, thermal expansion coefficients, etc. The data from such a worksheet could then be passed to ARIA or DIABLO to run thermal-mechanical analysis.

The THERMAL-FEM Worksheet

The THERMAL-FEM worksheet is a placeholder to interface with other Finite Element Model (FEM) thermal analysis codes, such as TOPAZ or DIABLO from LLNL, ARIA from SNL, SINDAG from ANL, etc. It is meant to be able to pass required inputs for those codes by pulling the problem/case definition information from other worksheets in DSEF.

This worksheet could function the way that the THERMAL-ANALYTICAL worksheet does to pass information to an external FEM code. It is expected that use of such codes would also include some post-processing of data to write the results back to the THERMAL-ANALYTICAL OUTPUT worksheet

13. References

- Carter 2012. Joe T. Carter, Phillip O. Rodwell, Mark DuPont, *Generic Repository ROM Cost Study*, FCRD-UFD-2012-000211 Rev 1, September 5, 2012
- Greenberg 2012a. Harris R. Greenberg, Montu Sharma, Mark Sutton, and Alethia V. Barnwell, *Repository Near-Field Thermal Modeling Update Including Analysis of Open Mode Design Concepts*, LLNL-TR-572252, Aug 2012
- Greenberg 2012b. Harris R. Greenberg, Montu Sharma and Mark Sutton, *Investigations on Repository Near-Field Thermal Modeling*, LLNL-TR-491099-Rev-2, November 2012
- Greenberg 2013a. H.R. Greenberg, J. A. Blink, and T. A. Buscheck, *Repository Layout and Required Ventilation Trade Studies in Clay/Shale using the DSEF Thermal Analytical Model*, LLNL-TR-638880, June 12, 2013.
- Greenberg 2013b. H. R. Greenberg, J. Wen, and T. A. Buscheck, *Scoping Thermal Analysis of Alternative Dual-Purpose Canister Disposal Concepts*, June 26, 2013
- Hardin 2011. Hardin, E., J. Blink, H. Greenberg, M. Sutton, M. Fratoni, J. Carter, M. DuPont and R. Howard 2011, *Generic Repository Design Concepts and Thermal Analysis (FY11)*. FCRD-USED-2011-000143 Rev. 2. December, 2011
- Hardin 2012a. E. Hardin, T. Hadgu, D. Clayton; R. Howard; H. R. Greenberg, J. Blink, M. Sharma, M. Sutton, J. Carter, M. DuPont and P. Rodwell, *Design Concepts/Thermal Load Management (FY11/12) Summary Report*, FCRD-UFD-2012-00219, August 2012
- Hardin 2012b. E. Hardin, T. Hadgu, D. Clayton; R. Howard; H. R. Greenberg, J. Blink, M. Sharma, M. Sutton, J. Carter, M. DuPont and P. Rodwell, *Repository Reference Disposal Concepts and Thermal Load Management Analysis*, FCRD-UFD-2012-00219, Rev. 2, November 2012
- Sutton 2011. Mark Sutton, James A. Blink, Massimiliano Fratoni, Harris R. Greenberg, William G. Halsey and Thomas J. Wolery, *Disposal Systems Evaluation Framework Version 1.0 Progress Report*, June 2011.

**Np(V) Sorption and Diffusion on Montmorillonite Clay
(Part VIII)**

1 Introduction

This progress report summarizes research conducted at LLNL within Work Package Number FT-13LL080603, Disposal Research – Generic Engineered Barrier System Evaluations. The research is focused on quantifying Np(V) sorption to and diffusion through montmorillonite clay which is the primary mineralogic component of proposed bentonite backfill material in certain nuclear waste repository scenarios.

1.1 Relevance of Np to Nuclear Waste Repositories

Neptunium (Np) is a transuranic element of particular concern to the development of nuclear waste repositories. The dominant isotope, ^{237}Np , has a long half-life (2.13×10^6 years) and high biological toxicity. In geological disposal scenarios, ^{237}Np will be one of the most radiologically significant contributors (Kaszuba and Runde, 1999; Wescott et al., 1995; Wilson et al., 1994). Dose calculations given in DOE (2002) suggested that Np will be a significant dose contributor at 50,000 years and the dominant dose contributor after 75,000 years (Figure 1).

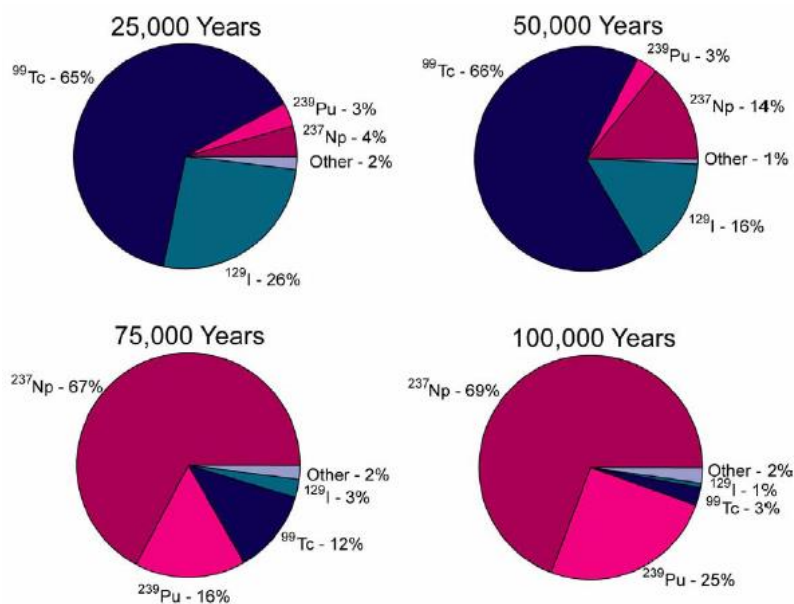


Figure 1. Fraction of mean total annual dose attributed to different radionuclides for the nominal scenario projected by the TSPA-SR model (DOE, 2002).

In 2003, scientists at the Electric Power Research Institute re-examined the potential dose rates (Apted et al., 2003) and produced less conservative risk estimates. While the estimated dose at 10,000 years was reported to be 0 mrem per year and the dose at 1 million years was about 3 mrem per year, Np was, nevertheless, identified as the dominant radionuclide contributing to longterm dose from a nuclear waste repository (Figure 2).

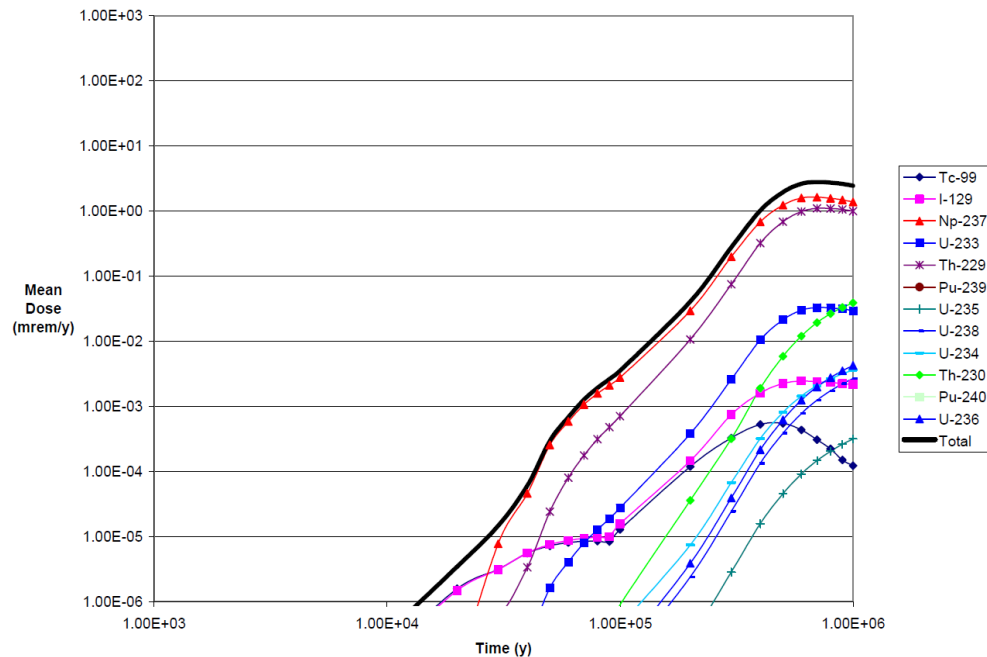


Figure 2. Annual dose attributed to different radionuclides for the IMARC 8.0, ICRP 72 dose conversion factor calculations reported in (Apted et al., 2003), page 4-18.

1.2 Np Reactive Transport

Based on our past experience and elsewhere, it is apparent that a detailed understanding of Np reactive transport within engineered barrier systems (e.g. clay backfill material) as well as the surrounding natural systems is essential.

The migration of Np through a repository near-field and the surrounding geosphere will be highly influenced by the nature and composition of the rock matrix. Montmorillonite is a major component of the bentonite barriers proposed in the geological nuclear waste repository designs of many countries (Dverstorp and Stromberg, 2013; Hoth et al., 2007; Nagra, 2002; Oecd, 2006). Montmorillonite may also be a dominant component of the repository host rock (e.g. Callovo-Oxfordian argillite at the French repository Cigeo) (Labalette et al., 2013). Thus, Np interaction with montmorillonite must be accurately parameterized in any performance assessment calculations.

Montmorillonite is a 2:1 smectite clay and consists of two SiO_4 tetrahedral (T) sheets bound to either side of an AlO_6 octahedral (O) sheet (expressed as T:O:T) (Dixon, 1989). Isomorphic substitutions of Al and Si give a permanent negative charge to the structure that is compensated by exchange cations. The electrostatic attraction between the charged layers and the exchangeable cations causes the cohesion of the T:O:T layers. As a result, the total cation exchange capacity is distributed between the inner surfaces in the interlayer spacing (interlamellar space) and the outer surfaces of the clay particles. In addition, the montmorillonite surface includes a pH-dependent charge associated with the broken silanol and aluminol edges of the T:O:T sheets. As a result, two mechanisms of sorption exist on montmorillonite: cation exchange at permanently charged sites and surface complexation on the variably charged silanol and aluminol edges.

The sorption of Np is controlled by both its redox and aqueous speciation (Bondietti and Francis, 1979; Kaszuba and Runde, 1999; Law et al., 2010). Under a wide range of oxic conditions, the pentavalent oxidation state, in the form of NpO_2^+ , will dominate (Choppin, 2006; Kaszuba and Runde, 1999). NpO_2^+ has a relatively low affinity to most minerals and rocks (Triay et al., 1993), resulting in its high environmental mobility.

Under aerobic conditions and at circumneutral pH values, Np(V) sorption to montmorillonite is likely to be dominated by surface complexation at the variably charged sorption sites (Bradbury and Baeyens, 2006; Turner et al., 1998b). However, at pH values below pH 6, cation exchange is expected to be the dominant sorption mechanism (Bradbury and Baeyens, 2006; Kozai et al., 1996; Nagasaki and Tanaka, 2000; Sabodina et al., 2006; Sakamoto et al., 1990; Turner et al., 1998b; Zavarin et al., 2012). Sorption by ion exchange is dependent on the composition of the clay exchange sites (Jensen, 1973), commonly occupied by Na^+ , K^+ , Mg^{2+} , and Ca^{2+} , which is, in turn, strongly dependent on the aqueous conditions and electrolyte composition. However, most of the studies in the literature have so far focused on Np(V)- Na^+ ion exchange.

While some data are available in the literature regarding diffusion of Np(V) in clay-containing rock or compacted clay materials (e.g. (Wu et al., 2009)), the nature of the diffusion process in these clay-rich materials is not fully understood. Furthermore, the effect of temperature has been studied only minimally and is essential to exploring repository performance under increasingly high heat loads. A basic observation from various authors is that the apparent retardation measured in batch sorption experiments differs significantly from the calculated retardation based on diffusion profiles through cores. This disparity between batch and core retardation measurements was summarized by Bourg et al. (2003). They proposed an alternative model that took into account diffusion within the interparticle pore space as well as the intralamellar space (Figure 3). Predicting diffusion is further complicated by the fact that the sorption mechanism (e.g. inner sphere, outer sphere, diffuse layer) will affect diffusion rates in the interlamellar space (Figure 4).

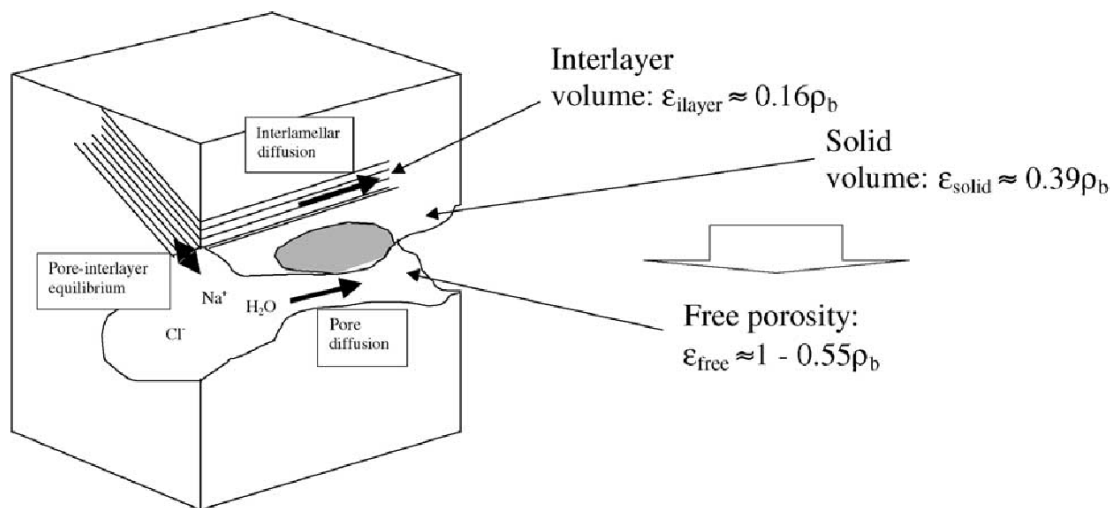


Figure 3. Example of an elementary volume of compacted bentonite, estimates of the volume fractions of interlayer porosity versus free porosity and effects on diffusion. After Bourg et al. (2003).

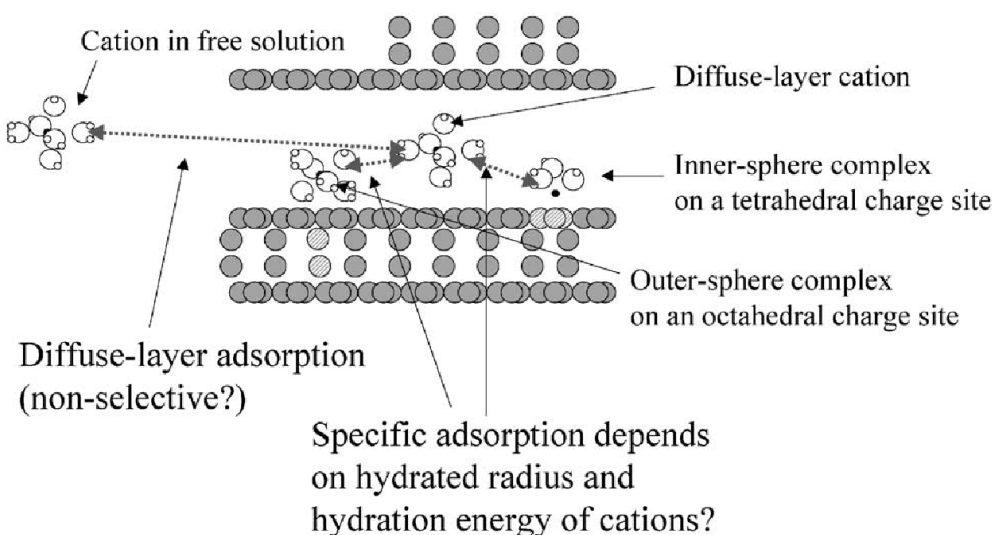


Figure 4. Example of diffuse-layer, outer-sphere, and inner-sphere interlayer adsorption processes. Each adsorption process may lead to unique diffusion rates. From (Bourg et al., 2003).

The aim of this study is to collect sorption data both experimentally and from the literature to develop a comprehensive model of Np ion exchange and surface complexation on montmorillonite. This model will be tested through a series of diffusion experiments using packed montmorillonite cores. The core diffusion experiments will examine the effect of temperature, solution conditions, and compaction on Np diffusion through an idealized montmorillonite repository backfill material and provide a dataset for detailed reactive transport model testing and calibration based on conceptual models proposed by Bourg et al. (2003) and others.

2 Development of a Np(V) Ion Exchange Model

The aim of the ion exchange study was to isolate the ion exchange mechanism of Np(V) sorption to montmorillonite. Np(V) exchange on homoionic Na, K, Ca and Mg-montmorillonite was determined experimentally at pH 4.5 using Na^+ , K^+ , Ca^{2+} , and Mg^{2+} as electrolyte cations at ionic strengths ranging from 0.001 to 0.1 M. This experimental data was then modeled to estimate selectivity coefficients for the exchange reactions. These coefficients are essential for accurate prediction of Np mobility in reactive transport models. The experimental work described herein was extracted from a manuscript to be submitted to the Journal of Contaminant Hydrology later in FY2013.

2.1 Materials and Methods

The montmorillonite used in the experiments was SWy-1 montmorillonite (Source Clays Repository of the Clay Minerals Society). It was preconditioned and purified using the procedure reported in Zavarin et al. (2012). Briefly, the montmorillonite was (1) pre-treated in a 0.001 M HCl solution to dissolve any soluble salts, (2) reacted with a H_2O_2 solution to minimize the reducing capacity of any impurities, (3) treated in a 0.1 M NaCl solution to produce a homoionic

clay suspension, (4) dialyzed in MQ H₂O (distilled–deionized water, 18.2 MΩ.cm resistivity) to remove excess salts, and (5) centrifuged at 180 g for 5 min and 2500 g for 6 hrs to remove the >2 μm and <50 nm particles from the suspension. The clay was then dried at 40 °C. The particles had a surface area of 31.5 m² g⁻¹ which is consistent with the reported value of 31.8 m² g⁻¹ (Clay Minerals Repository). XRD patterns were obtained on a Bruker D8 X-ray diffractometer and compared favorably with the montmorillonite. An obvious second mineral phase was not observed indicating that the prepared montmorillonite was relatively pure. Previously, a cation exchange capacity of 870 meq kg⁻¹ for the SWy-1 clay has been determined by Baeyens and Bradbury (2002) using a ²²Na isotopic dilution method.

Stock suspensions of the K, Ca or Mg exchanged montmorillonite were prepared by dialyzing 5 g of preconditioned Na-montmorillonite in 500 mL of 0.1 M KCl, CaCl₂ or MgCl₂, respectively. The electrolyte was changed every day for a period of one week. Following homoionization, the clays were washed repeatedly with MQ H₂O to remove excess salts. For sorption experiments, suspensions of 2 g L⁻¹ were prepared by diluting homoionized clays in the appropriate electrolyte at ionic strengths of 0.1, 0.01 and 0.001M.

The isotope ²³⁷Np was used in batch sorption experiments. Separation of ²³⁷Np from ²³³Pa was performed using the procedure of Pickett et al. (1994). The purified solution was analyzed using a Cary 500 UV-Vis spectrophotometer and the Np(V) oxidation state was verified by observation of a single absorption band at 979 nm (Waggener, 1958). For sorption experiments, ²³⁷Np stock solutions of 5×10⁻⁴, 5×10⁻⁵, and 5×10⁻⁶ M were prepared.

Np sorption isotherms were performed using the Na, K, Ca, and Mg-montmorillonite suspensions and spiking them with ²³⁷Np at initial concentrations between 2×10⁻⁸ and 5×10⁻⁶ M. Experiments were carried out in polyethylene tubes containing homoionic montmorillonite suspensions at three ionic strengths: 0.1, 0.01 and 0.001M. The pH was fixed to 4.5 in order to isolate cation exchange as the unique Np(V) sorption mechanism (Zavarin et al., 2012). Given the acidity associated with the Np stock following purification, the pH was readjusted to 4.5 with dilute HCl or 0.1 M NaOH as necessary following spiking. After spiking, the tubes were sealed and placed on an orbital shaker at room temperature for 6 days which is sufficient to achieve equilibrium (Zavarin et al., 2012). Due to the acidic nature of the Np(V) spike and the need to adjust solution pHs to 4.5, solution ionic strengths increased upon addition of Np(V). However, cation concentrations were monitored in all samples so as to account for any changes in solution composition.

The ²³⁷Np concentration was analyzed using a Perkin Elmer Liquid Scintillation Analyzer (LSA) model Tri-Carb 2900TR in alpha-beta discrimination mode. After the sorption period, total Np activity in the suspension ([Np]_{tot}) was counted to account for Np sorption to container walls. The difference between the theoretically added Np and the counted Np_{tot} was up to 13%, indicating some Np sorption to tube walls. Samples were then centrifuged at 7600 g for 2 h to achieve a < 30 nm particle size cut-off and Np activity in the supernatant ([Np]_{sol}) was determined. Na⁺, K⁺, Ca²⁺, and Mg²⁺ concentrations in the supernatant were determined by ion chromatography (IC) using a Dionex-ICS 600.

The thermodynamic database used for aqueous speciation was the NEA database including the hydrolysis and carbonate complexation constants selected by Lemire et al. (2001) and Neck et al. (1994). Activity correction was based on the Davies equation.

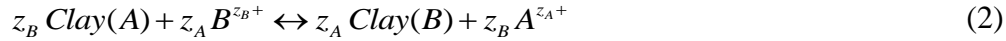
The distribution coefficient, K_d, was calculated by means of the following equation:

$$K_d = \frac{[\text{Np}]_{\text{tot}} - [\text{Np}]_{\text{sol}}}{[\text{Np}]_{\text{sol}}} \frac{1}{[\text{mont}]} \quad (1)$$

where [mont] is the montmorillonite concentration in the suspension (g mL⁻¹).

In this study, Np(V) speciation, Np sorption data fitting, and ion exchange simulations were carried out using the FIT4FD code (Zavarin et al., 2004b). The FIT4FD modeling of sorption data and determination of Np ion exchange selectivity coefficients was conducted by fitting all sorption isotherms simultaneously. The FIT4FD code allowed us to account for the unique cation composition of each sample and the associated measurement uncertainties. The simultaneous fitting of all ion exchange data ensured that the resulting ion exchange constants (and their associated uncertainties) were self-consistent across the entire range of solution compositions examined. Ion exchange selectivity coefficients were determined using both the Vanselow and Gaines-Thomas conventions, as we describe in detail in the following section.

The ion exchange reaction between a cation B, with charge z_B , in the aqueous phase and a cation A, with charge z_A , at the cation exchange sites of a clay can be represented by:



The cation exchange reaction can be described in terms of selectivity coefficients which indicate the sorption preference between two ions of different charge and size for the exchange site. An example of a calculation of the selectivity coefficient for an A/B exchange is shown in equation 3. In this case, selectivity coefficient values above 1 denote a higher affinity for cation B than for cation A. It should be noted that the selectivity coefficient is not a true thermodynamic exchange constant, since it has been shown to vary with factors such as the exchanger composition or the clay tactoid size (Jensen, 1973; Tournassat et al., 2011).

In the literature, various conventions are used to define selectivity coefficients. The Gaines-Thomas and the Vanselow conventions are commonly used in different speciation codes and by different authors (e.g. Gaines-Thomas convention (Bethke and Yeakel, 2009; Bolt, 1982; Bradbury and Baeyens, 2000; Bradbury and Baeyens, 2009; Maes and Cremers, 1977; Missana and García-Gutiérrez, 2007; Parkhurst and Appelo, 1999; Poinsot et al., 1999; Tournassat et al., 2007; Yariv and Cross, 1979); Vanselow convention (Bethke and Yeakel, 2009; Fletcher and Sposito, 1989; Parkhurst and Appelo, 1999; Schindler et al., 1987; Shaviv and Mattigod, 1985; Tournassat et al., 2007; Zavarin et al., 2004b)). In the case of homoivalent ion exchange where $z_A = z_B$, both conventions lead to equivalent selectivity coefficients. However, in the case of heterovalent ion exchange, the two conventions are not equivalent. Following the Gaines-Thomas convention (Gaines and Thomas, 1953), the selectivity coefficient (K_{GT}) is expressed by:

$${}^B_A K_{GT} = \frac{(E_B)^{z_A} (a_A)^{z_B}}{(E_A)^{z_B} (a_B)^{z_A}} \quad (3)$$

where a_A and a_B are the activities of the cations A and B respectively, and E_A and E_B are the equivalent fractional occupancies. The equivalent fractional occupancy is defined as the equivalents of sorbed cation per unit mass of clay (eq g⁻¹) divided by the cation exchange capacity CEC (eq g⁻¹). In the Vanselow convention (Mcbride; Sposito, 1981), the selectivity coefficient (KV) for the reaction is defined as follows:

$${}^B_A K_V = \frac{(M_B)^{z_A} (a_A)^{z_B}}{(M_A)^{z_B} (a_B)^{z_A}} \quad (4)$$

where M_A and M_B represent the mole fraction of the ion in the exchange phase. The mole fractional occupancy is defined as the moles of sorbed cation per mass (mol g^{-1}) divided by total moles in the clay exchange complex (mol g^{-1}).

2.2 Results and Discussion

2.2.1 Np(V) Speciation

The ion exchange of Np(V) will be dependent on its speciation in solution. NpO_2^+ is predicted to be the dominant aqueous species (> 94.5 %) at the pH value (4.5) and the highest ionic strength (0.1) used in these experiments. However we note that at pH 4.5 the uncharged species NpO_2Cl^0 will also be present, albeit as a minor component (< 5.5 %). For the same ionic strength, this percentage is slightly higher with divalent cation (Ca and Mg) electrolytes, due to the higher Cl^- concentration in the electrolyte. Nevertheless, the presence of NpO_2Cl^0 will not significantly affect the ion exchange behavior of Np over the range of solution compositions investigated.

2.2.2 Cation Composition of Batch Sorption Samples

Interpretation of Np ion exchange data requires consideration of the concentration of all cations in solution at equilibrium. This is important as the composition of the electrolyte varied due to adjustments in pH made to counter the acidity of the Np(V) spike addition and because the clay released trace amounts of other cations or impurities not removed during the homoionization process (Baeyens and Bradbury, 2004; Poinssot et al., 1999).

Figure 5 shows the concentrations of Na^+ , K^+ , Ca^{2+} , and Mg^{2+} measured in solution at the end of each experiment as a function of the final Np_{sol} concentration. Significant levels of Na^+ are present in each sample in addition to the principal cation. The Na^+ concentration in solution increases with Np concentration and follows the same trend for all four sets of “homoionic” ion exchange systems. The additional Na^+ cations are an artifact of the NaOH pH adjustment step as discussed previously. The significant concentration of Na and trace amounts of other cations found in all solutions will likely impact the ion exchange behavior of Np on montmorillonite. This effect was indeed observed in the Np sorption data and is described in the following section. Accordingly, it was necessary to account for the actual fluid ion composition of each experiment when determining Np selectivity coefficients.

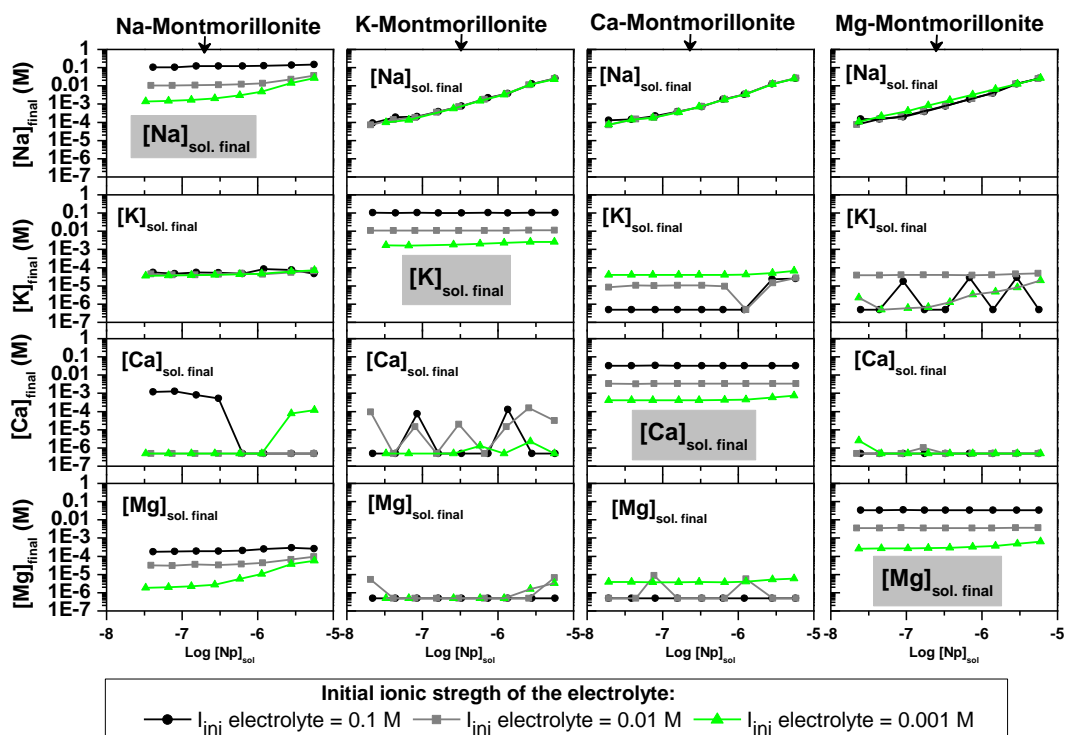


Figure 5. Cation composition of the electrolyte at the end of the experiment in the different system studied (Na, K, Ca and Mg-Montmorillonite) vs. Np loading in solution (measurements below detection limits are plotted as 5×10^{-7} M).

2.2.3 Np(V) Experimental Sorption Data

Np(V) sorption to homoionic montmorillonite (Na, K, Mg or Ca) suspended in corresponding electrolyte solutions (NaCl, KCl, MgCl₂ or CaCl₂, respectively) at three ionic strengths (0.1, 0.01 and 0.001 M) was measured over a range of initial Np concentrations (2.0×10^{-8} – 5.5×10^{-6} M). The percentage of sorbed Np as a function of the Np concentration in solution for the monovalent batch systems (Na/K-montmorillonite) and the divalent batch systems (Ca/Mg-montmorillonite) is plotted in Figure 6. There is an obvious difference in sorption behavior between Np(V) sorption in monovalent Na⁺/K⁺ solutions and divalent Ca²⁺/Mg²⁺ solutions. This difference in sorption is consistent with the greater selectivity for divalent cations in montmorillonite ion exchange reactions. At low ionic strength and at low Np concentrations, the percent Np(V) sorbed in Na⁺ and K⁺ experiments is between 20 and 30%. This represents a K_d on the order of 137-208 mL g⁻¹ which is significantly higher than the 24 ± 5 mL g⁻¹ reported by Zavarin et al. (2012) in 0.01 M NaCl which is, in turn, significantly higher than the 4-6 mL g⁻¹ reported by Turner et al. (1998b) in 0.1 M NaNO₃. Importantly, comparison of the Turner et al. (1998b), Zavarin et al. (2012), and present data demonstrates the ionic strength dependence of Np(V) sorption at low pH and thus provides strong evidence that sorption at low pH is dominated by ion exchange processes.

As the Np concentration increases, the percent Np sorbed decreases significantly for all cation systems (Figure 6). Importantly, the trend of lower sorption with increasing Np(V) concentration initially suggested that ion exchange is limited to low Np(V) concentrations. However, as shown

in Figure 5, careful examination of the background electrolyte composition indicates that the ionic strength of solutions tended to increase with the Np(V) concentration because of the acidic nature of the Np(V) spike and the need to neutralize the solution with NaOH. Thus, the apparent decrease in Np(V) ion exchange at higher Np(V) concentrations are more correctly attributed to changes in ionic strength, as we will demonstrate in the following modeling effort.

In the monovalent experiments, increasing the ionic strength decreases the percent Np(V) adsorbed, with minimal sorption seen at the highest ionic strength (Figure 6). The low sorption at high ionic strength is consistent with Zavarin et al. (2012) who reported a K_d of $<6 \text{ mL g}^{-1}$ in 1 M NaCl solutions. Such ionic strength dependence is consistent with the ion exchange mechanisms detailed in reactions (3) and (4) which imply that the extent of sorption of a cation will be dependent on the activity of the competing cation (Langmuir, 1997).

A decrease in Np(V) sorption with increasing ionic strength is less obvious in the divalent cation experiments (Figure 6). Sorption at the lowest divalent cation ionic strength and lowest Np(V) concentration falls just above the level of detection. Thus, we can conclude that $\frac{\text{NpO}_2^+}{\text{Na}^+} K$ and $\frac{\text{NpO}_2^+}{\text{K}^+} K$ selectivity coefficients are significantly greater than $\frac{\text{NpO}_2^+}{\text{Ca}^{2+}} K$ and $\frac{\text{NpO}_2^+}{\text{Mg}^{2+}} K$ s selectivity coefficients. Kozai et al. (1996) also reported lower Np(V) sorption on homoionic Ca- and Mg-montmorillonite relative to K- and Na-montmorillonite.

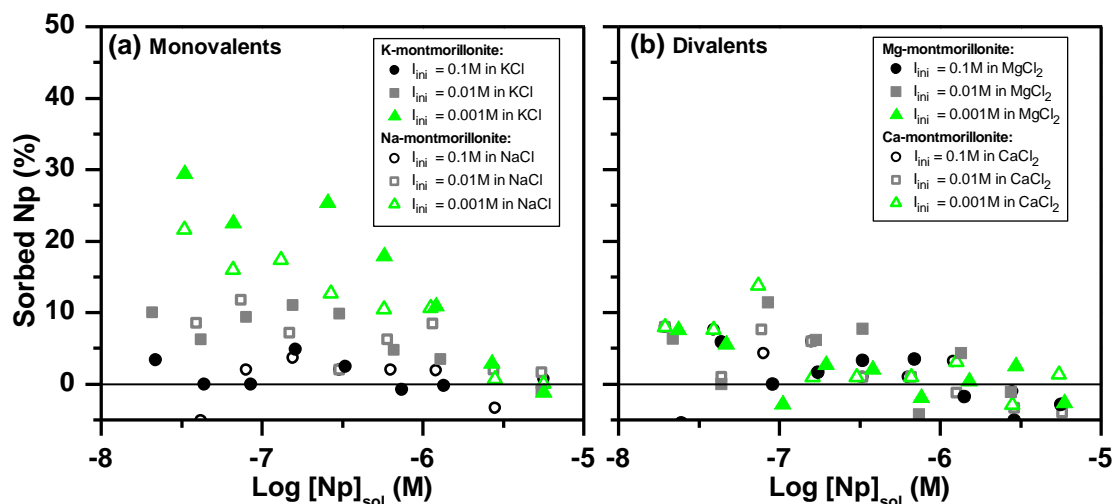


Figure 6. Percent Np sorbed to montmorillonite plotted vs. log Np concentration in solution at pH 4.5 and ionic strengths of 0.001 M, 0.01 M and 0.1 M in: (a) monovalent systems (Na/K-montmorillonite in NaCl/KCl) and (b) divalent systems (Ca/Mg-montmorillonite in CaCl₂/MgCl₂).

2.2.4 Modeling Np(V) Ion Exchange to Montmorillonite

For simple binary ion exchange experiments, the selectivity coefficient between two cations can be determined by fitting experimental data to equations 3 or 4. In the present case, this approach is not possible because exchange isotherm solution conditions vary both in ionic strength and the electrolyte cation composition. As a result, selectivity coefficients between cation pairs (e.g.

$\frac{\text{NpO}_2^+}{\text{Na}^+}K$, $\frac{\text{NpO}_2^+}{\text{K}^+}K$, $\frac{\text{NpO}_2^+}{\text{Ca}^{2+}}K$ and $\frac{\text{NpO}_2^+}{\text{Mg}^{2+}}K$ cannot be fitted individually. The FIT4FD code allows for the fitting of all batch isotherm data simultaneously and can account for the measured cation composition (i.e. Na, K, Ca, Mg, and Np) of each individual sample in the fitting process. In addition, uncertainties for each measured cation concentration can be accounted for in the minimization routine. In principle, data fitting could be performed such that selectivity coefficients, written as binary reactions, are allowed to vary simultaneously to reach a “best fit”. However, in reality, this approach leads to a poorly constrained problem. In addition, this approach leads to an unintended fitting of selectivity coefficients between the major cations (e.g. $\frac{\text{K}^+}{\text{Na}^+}K$, etc.) for which selectivity coefficients are well established in the literature. For example, if the data fitting yields $\log\left(\frac{\text{NpO}_2^+}{\text{Na}^+}K_V\right)$ and $\log\left(\frac{\text{NpO}_2^+}{\text{K}^+}K_V\right)$ selectivity coefficients of -0.34 and -0.31, respectively, it implies a $\log\left(\frac{\text{K}^+}{\text{Na}^+}K_V\right)$ selectivity coefficient of $(-0.34) - (-0.31) = -0.03$. However, this value contradicts the selectivity coefficient reported in the literature ($\log\left(\frac{\text{K}^+}{\text{Na}^+}K_V\right) = 0.26$ (Fletcher and Sposito, 1989)). To minimize the number of fitting parameters in our modeling effort and ensure consistency with published ion exchange selectivity coefficients between the major cations (i.e. $\frac{\text{K}^+}{\text{Na}^+}K$, $\frac{\text{Ca}^{2+}}{\text{Na}^+}K$, and $\frac{\text{Mg}^{2+}}{\text{Na}^+}K$), we limited our fitting parameter to $\frac{\text{NpO}_2^+}{\text{Na}^+}K$ while forcing the ion exchange selectivity coefficients between Np and the other major cations to be determined based on the major cation selectivity coefficients reported in the literature (e.g. $\log\left(\frac{\text{NpO}_2^+}{\text{K}^+}K_V\right) = \log\left(\frac{\text{NpO}_2^+}{\text{Na}^+}K_V\right) - \log\left(\frac{\text{K}^+}{\text{Na}^+}K_V\right)$).

A comprehensive table of Vanselow selectivity coefficients for many major and minor cations (but not Np) and montmorillonite was published by Fletcher and Sposito (1989). The relevant selectivity coefficients used in the present modeling effort are reproduced in Table 1. Note that reactions with clay edges as proposed by Fletcher and Sposito (1989) were not included in this analysis as they were found to be insignificant at the low pH examined here. A number of publications by Bradbury and Baeyens have applied the Gaines-Thomas convention to various cation ion exchange datasets (Baeyens and Bradbury, 1995; Baeyens and Bradbury, 1997). In these models, the selectivity coefficient $\log\left(\frac{\text{Ca}^{2+}}{\text{Na}^+}K_{GT}\right)$ was reported as 0.61. A $\log\left(\frac{\text{Mg}^{2+}}{\text{Na}^+}K_{GT}\right)$ selectivity coefficient was not reported. However, based on results from Fletcher and Sposito (1989), we assume that the Gaines-Thomas selectivity coefficient for Mg-Na ion exchange will be similar if not equivalent to Ca-Na. For homovalent ion exchange, the Vanselow and Gaines-Thomas conventions are equivalent. Thus, we use the $\frac{\text{K}^+}{\text{Na}^+}K$ value of Fletcher and Sposito (1989) in a Gaines-Thomas model without incurring any additional uncertainty (Table 1).

Importantly, all calculated ion exchange reaction constants contain some level of uncertainty. These uncertainties are a combination of measurement uncertainty and uncertainty associated with the choice of conceptual and numerical model. For example, Tournassat et al. (2011) determined that clay tactoid size and organization will affect the apparent ion exchange properties of clays. In addition, the composition of montmorillonites from different sources can lead to differences in measured ion exchange properties. These effects are not addressed in the

present modeling effort. However, it is acknowledged that the resulting Np selectivity coefficients are affected by our choice of a relatively simple conceptual model.

Table 1. Reaction constants for Na, K, Ca, and Mg ion exchange on montmorillonite based on the Vanselow and Gaines-Thomas conventions

Reaction	Log K_V^a	Log K_{GT}^b
Mont(Na) + $K^+ \leftrightarrow$ Mont(K) + Na^+	0.26	0.26 ^c
2 Mont(Na) + $Ca^{2+} \leftrightarrow$ Mont(Ca) + 2 Na^+	0.17	0.61
2 Mont(Na) + $Mg^{2+} \leftrightarrow$ Mont(Mg) + 2 Na^+	0.17	0.61 ^d

^a Fletcher and Sposito (1989a). K_a is equal to the Vanselow conditional equilibrium constant, K_V , assuming ideal mixing (i.e. activity coefficients for species on the solid phase are equal to one).

^b Baeyens and Bradbury (1995).

^c Based on $K_V = K_{GT}$ for homovalent ion exchange.

^d Assumed based on similar reaction constant reported for Ca^{2+} and Mg^{2+} in the Vanselow model.

Initially, all data were fit simultaneously while allowing only the $\frac{NpO_2^+}{Na^+}K$ selectivity coefficient to vary. All other coefficients were taken from Table 1 and the cation exchange capacity of SWy-1 was taken to be 870 meq kg⁻¹ (Baeyens and Bradbury, 1997). Both the Vanselow and Gaines-Thomas conventions were tested. The resulting constants are listed in Table 2. The $\log\left(\frac{NpO_2^+}{Na^+}K\right)$ selectivity coefficients based on the Vanselow and Gaines-Thomas conventions are -0.26 ± 0.03 and -0.14 ± 0.04 , respectively. The Np(V) selectivity coefficients with respect to K^+ , Ca^{2+} and Mg^{2+} were determined (Table 2) based on the fitted $\frac{NpO_2^+}{Na^+}K$ selectivity coefficient and the fixed major cation selectivity coefficients reported in Table 1. The $\frac{NpO_2^+}{Na^+}K$ selectivity coefficients determined using the Vanselow and Gaines-Thomas conventions are similar, as would be expected for homovalent exchange reactions. They are also within the range of selectivity coefficients reported in previous studies for Np-Na ion exchange on smectite ($\log\left(\frac{NpO_2^+}{Na^+}K\right) = 0.06$ to -0.75) (Bradbury and Baeyens, 2006; Gorgeon, 1994; Kozai et al., 1996; Kozai et al., 1993; Turner et al., 1998b; Zavarin et al., 2012). The slight difference in Vanselow and Gaines-Thomas selectivity coefficients is caused primarily by the differences in fixed $\frac{K^+}{Na^+}K$, $\frac{Ca^{2+}}{Na^+}K$ and $\frac{Mg^{2+}}{Na^+}K$ selectivity coefficients used in the two models as shown in Table 1. Residual errors reported in the FIT4FD code as WSOS/DF (weighted sum of squares divided by the degrees of freedom) (Zavarin et al., 2004b) were 2.48 using the Vanselow convention and 2.54 using the Gaines-Thomas convention, indicating a very small improvement in the fit to the experimental data with the Vanselow convention.

Table 2. Fitted ion exchange reaction constants for Np(V) .

N° free parameters		Vanselow		Gaines-Thomas	
		$\log K_V$	WSOS/DF	$\log K_{GT}$	WSOS/DF
1:	Np-Na	-0.26 (0.03) ^a	2.48	-0.14 (0.04)	2.54
	Np-K ^b	-0.52		-0.40	
	Np-Ca ^b	-0.69		-0.89	
	Np-Mg ^b	-0.69		-0.89	
2:	Np-Na	-0.34 (0.05)	2.43	-0.20 (0.05)	2.52
	K-Na	-0.03 (0.16)		0.01 (0.17)	
	Np-K ^b	-0.31		-0.21	
	Np-Ca ^b	-0.85		-1.01	
	Np-Mg ^b	-0.85		-1.01	

^a Values in parentheses are the uncertainties in the reported values (at one standard deviation).

^b Selectivity coefficients calculated from fitted Np-Na selectivity coefficient combined with fixed or fitted major cation selectivity coefficients.

A slightly better fit to the data can be achieved by varying the $\frac{\text{NpO}_2^+}{\text{Na}^+} K$ and $\frac{\text{K}^+}{\text{Na}^+} K$ selectivity coefficients simultaneously (WSOS/DF: 2.43 and 2.52 for the Vanselow and Gaines-Thomas conventions, respectively). However, the resulting $\frac{\text{NpO}_2^+}{\text{Na}^+} K$ selectivity coefficients do not change significantly from the earlier fit (Table 2). Furthermore, the fitted $\log\left(\frac{\text{K}^+}{\text{Na}^+} K\right)$ selectivity coefficients (Vanselow: -0.03; Gaines-Thomas: 0.01) deviate significantly from the reported values in the literature (Vanselow = Gaines-Thomas: 0.26) (Table 1). Thus, it appears that adjusting selectivity coefficients for the major cations is neither necessary nor justified in this case.

Figure 7 compares the Np isotherm data (presented as K_d rather than % sorbed) to the predicted values using a Vanselow fitted $\log\left(\frac{\text{NpO}_2^+}{\text{Na}^+} K_V\right)$ selectivity coefficient (-0.26) and associated values from Table 1. Given the low Np sorption in the divalent cation systems, values for corresponding Ca^{2+} and Mg^{2+} systems are averaged and presented together in the same plot. Figure 7 demonstrates that a single $\frac{\text{NpO}_2^+}{\text{Na}^+} K_V$ fitted selectivity coefficient is able to accurately predict Np(V) sorption to montmorillonite over the wide range solution conditions considered in this study.

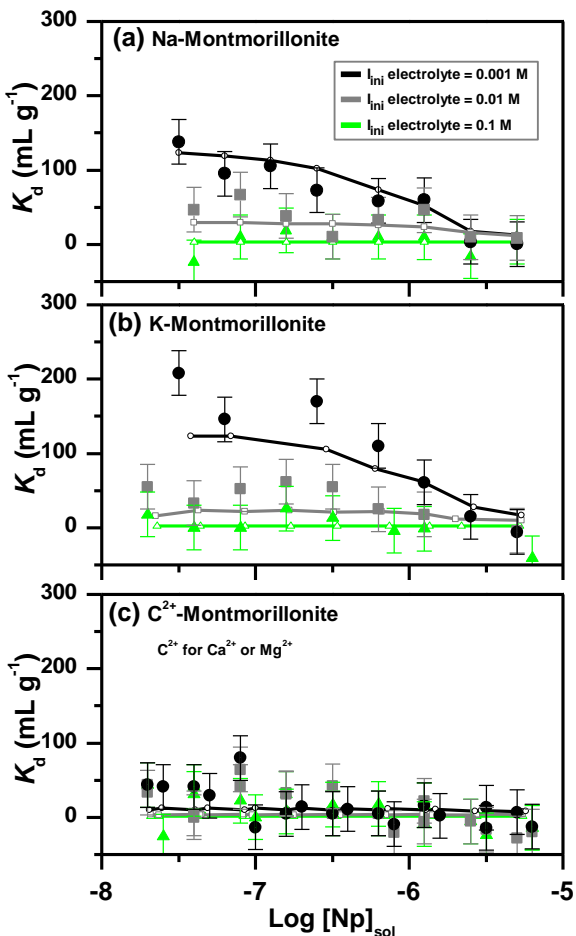


Figure 7. Experimental data (K_d) and model fit of Np(V) ion exchange (pH 4.5) on (a) Na-montmorillonite, (b) K-montmorillonite and (c) C^{2+} -montmorillonite. Predicted values based on the Vanselow convention, using parameters in Table 1 and fitted $\log\left(\frac{NpO_2^+}{Na^+} K_V\right) = -0.26$.

2.2.5 Simulation of Np(V) Sorption to Montmorillonite

In order to illustrate the independent effect of each major cation (Na, K, Ca or Mg) on Np ion exchange on montmorillonite without interference from other cations in the electrolyte, Np sorption in mono-electrolyte solutions was simulated using the Vanselow ion exchange model (1 free parameter) developed above. Figure 8 shows the predicted K_d values over a range of cation concentrations (0.0001 - 1 M). At equivalent electrolyte cation concentration, Np sorption is lower in divalent systems (Ca^{2+} and Mg^{2+}) than in monovalent systems (K^+ and Na^+). Further, the slope of the curves is lower in divalent systems, indicating that K_d is less affected by divalent cation concentration than monovalent Na^+ or K^+ concentration.

Such behaviour is consistent with the ionic exchange mechanism. In the ion exchange processes represented in equation 2, the theoretical dependence on ionic strength can be derived from equation 1 and equation 3. When the cation adsorbate B is present at trace level, the dependence can be expressed as follows (Baeyens and Bradbury, 1995):

$$z_A \cdot \text{Log}(K_d) = -z_B \text{Log}[A] + \text{Log} \left(\frac{{}^B K_{GT} (\text{CEC})^{z_A} \gamma_B^{z_A}}{z_B^{z_A} \gamma_A^{z_B}} \right) \quad (5)$$

where [A] is the concentration of the cation A in solution (M) and γ_A and γ_B are the solution activity coefficients of cations A and B. Thus, for a homovalent exchange ($\text{NpO}_2^+ \text{-Na}^+$ or $\text{NpO}_2^+ \text{-K}^+$) the dependence of the logarithm of the distribution coefficients ($\text{log}(K_d)$) with the logarithm of the concentration of the main ion of the electrolyte $\text{log}[A]$ is represented by a line with a slope of -1. For $\text{NpO}_2^+ \text{-Ca}^{2+}$ exchange, this dependence is a line with slope -0.5, as indicated by the simulation.

A result of the dependency of Np-montmorillonite exchange on ionic strength shown in Figure 8, is that high K_d values could be reached in waters with low Na^+ and K^+ concentrations and in the absence of divalent cations. For example, in waters with [Na] or [K] of 10^{-4} M, K_d values of 3800 mL g^{-1} and 2400 mL g^{-1} may be achieved. However, such conditions are not characteristic of typical natural waters.

It should be stressed that in these simulations (Figure 8) the intention was to focus solely on the ion exchange component. As a result, the contribution of surface complexation reactions to the overall K_d was not addressed. Turner et al. (1998) predicted much higher K_d values for Np sorption on montmorillonite in 0.1 M NaNO_3 electrolyte (100 to 1000 mL g^{-1}) than observed in the current simulations because of the contribution of Np(V) surface complexation. For a true estimation of total Np sorption (by ionic exchange and also by surface complexation), pH, anion composition, and redox conditions must also be taken into account.

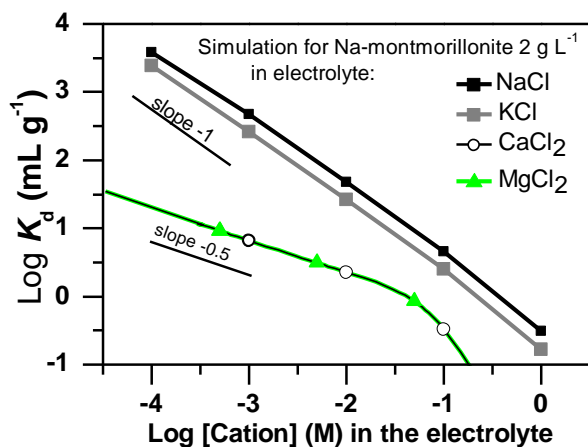


Figure 8. Simulation of Np(V) ionic exchange on montmorillonite (2 g L^{-1}) at pH 4.5 in pure electrolyte (NaCl , KCl , MgCl_2 and CaCl_2) for $[\text{Np}]_{\text{total}} = 5 \times 10^{-7}$ M. Predicted values with Vanselow convention, using parameters in Table 1 and fitted $\text{Np-Na } \text{Log}K_v = -0.26$.

2.3 Summary

The experimental data obtained in this study indicate that Np ionic exchange highly depends on the major cation composition of the aqueous system, being especially limited by the presence of divalent cations such as Ca^{2+} and Mg^{2+} in solution. In many geochemical scenarios under medium-acid pH conditions, Np(V) migration-retention can be highly influenced by NpO_2^+ ionic

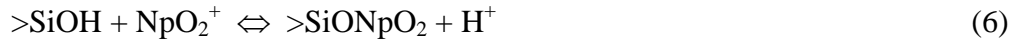
exchange on montmorillonite, which is a mineral ubiquitous in the environment. At basic conditions, ionic exchange becomes less significant and surface complexation of Np(V) will dominate.

A sorption model was developed on the basis of the experimental data, which is consistent with selectivity coefficients reported in the literature for the exchange between major cations on montmorillonite. The recommended selectivity coefficients for Np(V) ionic exchange on montmorillonite, according to the Vanselow convention, are as follows: $\log\left(\frac{\text{NpO}_2^+}{\text{Na}^+} K_V\right) = -0.26$, $\log\left(\frac{\text{NpO}_2^+}{\text{K}^+} K_V\right) = -0.52$, $\log\left(\frac{\text{NpO}_2^+}{\text{Ca}^{2+}} K_V\right) = -0.69$, $\log\left(\frac{\text{NpO}_2^+}{\text{Mg}^{2+}} K_V\right) = -0.69$. Their use in geochemical computer codes will allow better predictions of the Np(V) behaviour in the environment.

3 Development of a Np(V) Surface Complexation Model

In modeling radionuclide migration in the environment, distribution coefficients (K_d) are often used to model sorption. K_d s are typically reported as the ratio of total sorbed concentration (mol/g) to total aqueous concentration (mol/mL). Although the K_d approach can adequately describe the sorptive behavior of a particular sediment at a particular pH and solution composition, many factors that affect radionuclide sorption in geochemically dynamic environments cannot be accounted for. Surface complexation (SC) and ion exchange (IE) reactions provide a more mechanistic approach to modeling sorption and can account for the effect of changing environmental conditions on sorption. In this section, Np(V) sorption to aluminosilicate minerals is modeled using a non-electrostatic surface complexation model (NEM). Surface complexation is modeled using a generalized approach in which surface complexation to aluminosilicate $>\text{SiOH}$ or $>\text{AlOH}$ reactive sites is considered equivalent to the reactivity of aluminum oxide and silica reactive sites. The work presented in this section is a continuation of surface complexation modeling and database development efforts conducted at LLNL over the past decade (Zavarin and Bruton, 2004a; Zavarin and Bruton, 2004b; Zavarin et al., 2004a; Zavarin et al., 2012; Zavarin et al., 2005).

Minerals that exhibit variable surface charge (e.g. goethite, calcite, montmorillonite, etc.) can significantly reduce radionuclide mobility in the environment. The reduced mobility is partly a result of surface complexation (SC) reactions: reactions involving mineral surface functional groups and aqueous species. A typical SC reaction and associated equilibrium constant can be written in the following manner:



$$K = \frac{(>\text{SiONpO}_2)(\text{H}^+)}{(>\text{SiOH})(\text{NpO}_2^+)} \quad (7)$$

where $>\text{SiOH}$ is a surface functional group, NpO_2^+ is an aqueous species that reacts with the surface (to form $>\text{SiONpO}_2$), and H^+ is released as a result of the reaction. Just as for simple aqueous complexation reactions, the above SC reaction has an equilibrium reaction constant, K , that describes the relative activity of all species at equilibrium.

Factors that influence radionuclide surface complexation on a particular mineral and, thus, affect radionuclide migration include:

- Surface area
- pH
- Aqueous complexation
- Ionic strength
- Surface electrical charge

Since SC reactions occur at the mineral-water interface, surface complexation will be a function of the mineral surface area available for reaction. The pH can significantly affect surface complexation as well. For example, in equation 6, as the concentration of H^+ increases, a larger fraction of NpO_2^+ will remain in solution. Surface functional groups (e.g. $>SiOH$) may also become protonated/deprotonated as a function of pH which will affect surface complexation. Aqueous complexation will influence the concentration of aqueous species in solution; this will also affect surface complexation. For example, neptunium surface complexation decreases as a function of carbonate concentration in solution due to the formation of neptunyl carbonate complexes (neptunyl carbonate complexes remain primarily in the aqueous phase). Ionic strength may influence surface complexation by reducing the activity of aqueous species. Surface complexes as well as surface protonation and deprotonation may alter the electric double layer of the surface which can, in turn, influence surface complexation.

There are many models that describe surface complexation (non-electrostatic, constant capacitance, diffuse layer, triple layer, and others). Unlike the electrostatic models, the non-electrostatic model (Kurbatov et al., 1951) does not account for surface electrical charge and its effect on sorption. The electrostatic models typically contain one or more parameters that account for surface charge effects. Although the NEM approach over-simplifies the factors affecting surface complexation, several investigators have used this model approach to describe surface complexation (Bradbury and Baeyens, 1997; Davis et al., 1998; Zachara, 1995). Davis et al. (1998) argued that the NEM may be the most appropriate for complex environmental applications since the surface charging behavior of non-ideal natural mineral phases is not well known. In this report, this most simplified model is used to quantify radionuclide sorption and simulate radionuclide migration.

3.1 Non-Electrostatic Surface Complexation Model Development

Fitting NEM reactions to radionuclide sorption data was accomplished with the fitting program FITEQL (Herbelin and Westall, 1994). Data were typically retrieved from published sorption data using the Datathief 1.0.8 program (Huysen and Van Der Laan, 1992). While fitting the data, ionic strength, pH, and aqueous complexation were taken into account while electrostatic effects were ignored. The effect of ionic strength on ion activity was accounted for by the Davies equation. Aqueous complexation constants were based on the GEMBOCHS thermodynamic database version data.com.V8.R6 (Johnson and Lundeen, 1997). Note that Np(V) speciation constants from this database vary slightly from that used in the ion exchange model calibration (Lemire et al., 2001). All data will be fitted to a common speciation model at a later date.

Several authors have shown that sorption of radionuclides to aluminosilicate minerals can be related to surface complexation on alumina and silica surfaces since surface functional groups are comparable (Mckinley et al., 1995; Turner et al., 1996). In the following sections, this generalized aluminosilicate NEM model is used to fit published radionuclide-aluminosilicate

sorption data. Although the assumption that all $>AlOH$ or $>SiOH$ surface reactive sites are equivalent irrespective of the mineral substrate can only be defended in a very qualitative manner, the results presented below indicate that the relationship does hold true in many cases. Nevertheless, caution must be exercised when attempting to extrapolate generalized $>AlOH$ and $>SiOH$ NEM constants to aluminosilicate minerals for which data is not available. The equivalent reactivity of various aluminosilicate minerals should only be used as a validation effort for available data and extrapolation should only be attempted in a hypothetical manner.

In order to retain the most simplified approach to describing the reactive sites on aluminosilicate minerals, several simplifying assumption were made. These assumptions were held constant for all sorption data fits so as to produce a consistent set of NEM reactions. A single type of $>SiOH$ and/or $>AlOH$ reactive site was used to fit each data set. For all minerals, a site density of 2.31 sites/nm² was used. Dzombak and Morel (1990) used this site density for surface complexation modeling of hydrous ferric oxide surfaces. Turner (1995) also used this site density for a variety of minerals to minimize the number of fitting parameters and arrive at a uniform set of surface complexation reactions; this same approach is taken here.

The acidity constants used for $>AlOH$ and $>SiOH$ surface reactive sites were taken from SiO_2 and $\alpha-Al_2O_3$ diffuse layer model fits reported by Turner (1995). Depending on the SC model, surface acidity Log K constants can vary drastically. The diffuse layer model acidity constants were chosen for convenience. If acidity constants were varied during data fitting along with radionuclide surface complexation constants, less variability in LogK constants might be achieved. However, the limited data for most radionuclide–mineral sorption reactions do not merit additional fitting parameters in our NEM model.

McKinley et al. (1995) determined from transmission electron microscopy (TEM) measurements that SWy-1 montmorillonite broken edge sites (those that account for $>SiOH$ and $>AlOH$ sites) account for ~30% of the measured BET surface area (assuming 2.31 sites/nm²). Turner et al. (1996) reported similar values from particle size and crystallographic data but chemical methods resulted in much higher site concentrations. Several authors have used a surface complexation reactive site density equivalent to 10% of total BET surface area to model montmorillonite sorption results (Bertetti et al., 1998; Pabalan et al., 1998; Turner et al., 1998b). Their site density was based on potentiometric titration results of Wanner et al.(1994). Bertetti et al. (1998) used the same reduced effective surface area to account for reduced Np(V) sorption to clinoptilolite relative to quartz and α -alumina. In the following aluminosilicate fits to sorption data, 10% of BET surface area was used for all montmorillonite and clinoptilolite data fits. For all sorption fits, the pKa's for $>SiOH$ and $>AlOH$ sites were also held constant. This minimized the number of fitting parameters and resulted in a consistent set of surface complexation reactions.

For each Np(V)–mineral pair, NEM reaction constants are reported based on average fits to all available sorption data sets. However, fits to certain data sets were omitted from the database average when the quality of sorption data was questionable. The process of data rejection is rather subjective. Nevertheless, justification for data rejection is reported in the following section.

Table 3. Summary of reaction constants developed for Np(V) surface complexation to aluminosilicate minerals.

Sorption Type	Element Conc. ----- mol/l -----	Sorption Sites -----	Ionic Strength	pCO ₂	Species	log K	Comments	Refs.	
Np(V) on colloidal alumina	1E-14	9.97E-5	0.1	3.5	>AlONpO ₂	-2.31	pH curve	1	
					>AlONpO ₃ H ⁻	-13.59			
	1E-14	9.97E-5	0.1	0.05M	>AlONpO ₂	-2.18	pH curve	1	
					>AlONpO ₃ H ⁻	-10.19			
Np(V) on α-Al ₂ O ₃	1E-14	9.97E-5	0.1	3.5	>AlONpO ₂	-2.18	pH curve	2	
					>AlONpO ₃ H ⁻	-13.65			
	6E-6	6.71E-4	0.1	3.5	>AlONpO ₂	-2.49	pH curve	4	
					>AlONpO ₃ H ⁻	-13.62			
	6E-6	9.59E-6	0.1	3.5	>AlONpO ₂	-4.36	pH curve	4	
					>AlONpO ₃ H ⁻	-14.21			
1E-6	3.53E-6	0.01	none	>AlONpO ₂	-4.78	pH curve	5		
				>AlONpO ₃ H ⁻	-14.27				
1E-6	3.53E-6	0.01	none	>AlONpO ₂	-4.86	pH curve	5		
				>AlONpO ₃ H ⁻	-14.29				
Np(V) on SiO ₂	1.9E-7	4.6-6.4E-7	0.01	5E-5	>AlONpO ₂	-2.52	pH curve	3	
					>AlONpO ₃ H ⁻	-12.84			
	1.9E-9	4.6-6.4E-7	0.01	5E-5	>AlONpO ₂	-2.74	pH curve	3	
					>AlONpO ₃ H ⁻	-12.44			
	Np(V) on SiO ₂	1E-14	8.05E-4	0.1	3.5	>SiONpO ₂	-5.31	pH curve	2
						>SiONpO ₃ H ⁻	-12.90		
1E-7		4.6E-6	0.1	3.5	>SiONpO ₂	-3.59	pH curve	5	
					>SiONpO ₃ H ⁻	-11.77			
1E-7		9.2E-6	0.1	3.5	>SiONpO ₂	-3.74	pH curve	5	
					>SiONpO ₃ H ⁻	-11.59			
1E-6		4.6E-6	0.1	3.5	>SiONpO ₂	-3.90	pH curve	5	
					>SiONpO ₃ H ⁻	-12.06			
1E-6	4.6E-6	0.1	none	>SiONpO ₂	-3.82	pH curve	5		
				>SiONpO ₃ H ⁻	-12.03				
Np(V) on clinoptilolite	1E-6	2.33E-6 (Al), 1.32E-5 (Si)	0.1	3.5			average fit	5	
	1E-6	4.65E-6 (Al), 2.64E-5 (Si)	0.01	3.5					
			0.01	none					
Np(V) on montmorillonite	9.25E-7	7.66E-5 (Al,Si)	0.1	3.5			average fit	6	
	9.13E-7	7.59E-5 (Al,Si)	0.1	none					

REFERENCES: 1. (Righetto et al., 1988); 2. (Righetto et al., 1991); 3. (Allard et al., 1982); 4. (Nakayama and Sakamoto, 1991); 5. (Bertetti et al., 1998); 6. (Turner et al., 1998)

3.2 Np(V) on Aluminum Oxide

Several authors have examined the interaction of Np(V) with aluminum oxide minerals (Allard et al., 1982; Bertetti et al., 1998; Nakayama and Sakamoto, 1991; Righetto et al., 1991; Righetto et al., 1988). Sorption experiments were performed on both colloidal and larger particle size Al_2O_3 . Sorption experiments performed on colloidal material resulted in very low surface loading. During fitting, it was found that fitted NEM constants determined for colloidal and larger particle sorption experiments differed significantly. Np(V) sorbed more strongly to colloidal aluminum oxide even when surface area differences were accounted for. This difference may be indicative of surface structural differences between the two forms of aluminum oxide which may lead to differences in Np(V) affinities for these surfaces. Regardless of the underlying mechanisms, average NEM Log K constants were calculated for high and low surface area sorbing materials separately. Fitted NEM constants for each data set are listed in Table 3. Average NEM database constants (Table 4) were based on the low surface area aluminum oxide minerals.

Model results using average fitted NEM constants for colloidal aluminum oxide experiments are shown in Figures 9 to 12. For nearly all colloidal aluminum oxide sorption data, best fit Log K constants are quite similar resulting in a good match between the average Log K constants model results and data. The average values are -2.37 ± 0.55 and -13.62 for $>\text{AlONpO}_2$ and $>\text{AlONpO}_3\text{H}^-$, respectively. A standard deviation for the $>\text{AlONpO}_3\text{H}^-$ NEM constant could not be determined because it is an average of two values; its effect on sorption is significant only at very high pH where data are limited. Figure 10 shows the data and fit to sorption experiments conducted in 0.05 mol/L NaHCO_3 . In this case, the data fit is poor. Inadequate control of carbonate alkalinity in these experiments may, in part, have led to the poor fit. However, the underestimated sorption at high pH may also be indicative of formation of ternary Np(V)-carbonate surface complexes. The limited data available are not sufficient to justify additional NEM reactions.

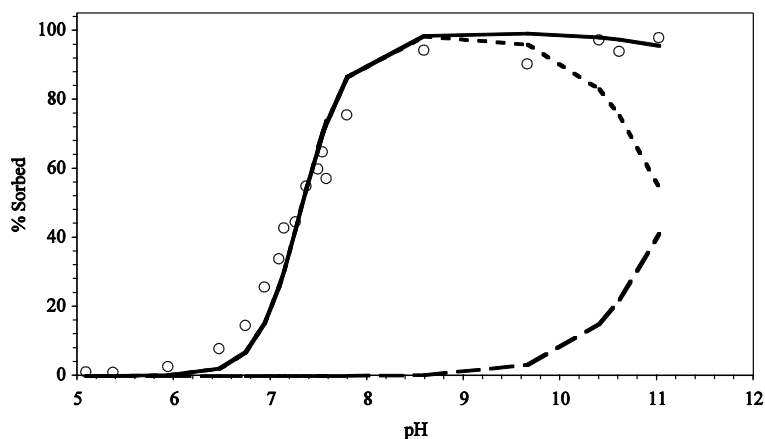


Figure 9. Sorption of 10^{-14} mol/L Np(V) on colloidal alumina. Solid lines represent data fits using average colloidal alumina NEM constants. Dashed lines represent contribution of $>\text{AlONpO}_2$ (short dash) and $>\text{AlONpO}_3\text{H}^-$ (long dash) to sorption. $I = 0.1$; 0.2 g/L Al_2O_3 ; 130 m^2/g Al_2O_3 ; open to air; data from Righetto et al. (1988).

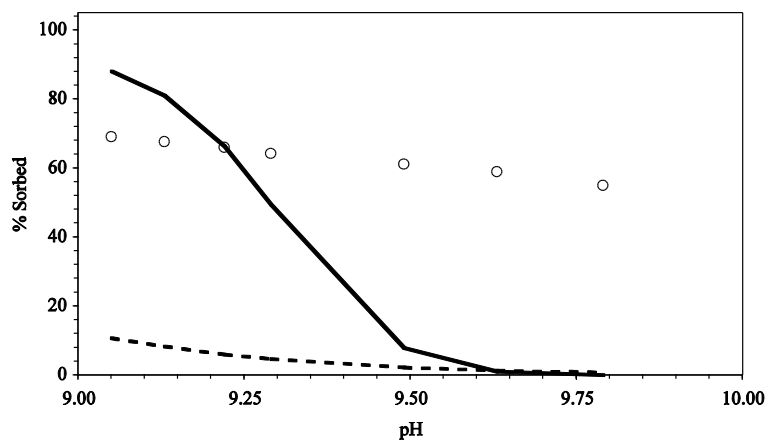


Figure 10. Sorption of 10^{-14} mol/L Np(V) on colloidal alumina. Solid lines represent data fits using average colloidal alumina NEM constants. Model fits produced assuming 0.05 mol/L HCO_3^- (solid line) or atmospheric CO_2 (dashed line); $I = 0.1$; 0.2 g/L Al_2O_3 ; 130 m^2/g Al_2O_3 ; open to air; data from Righetto et al. (1988).

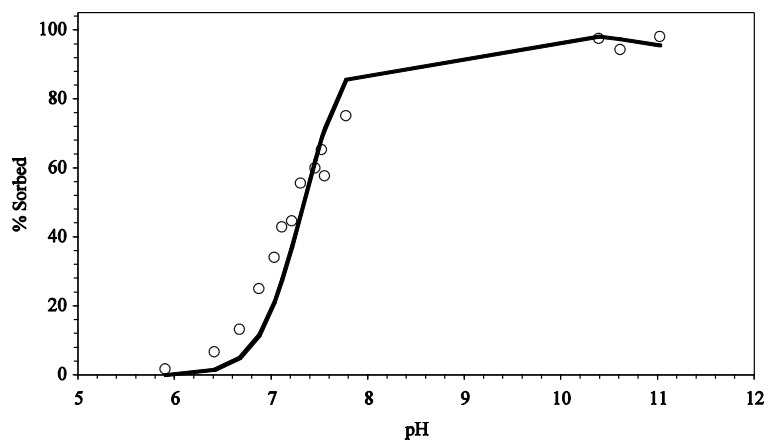


Figure 11. Sorption of 10^{-14} mol/L Np(V) on colloidal alumina. Solid line represents data fit using average colloidal alumina NEM constants. $I = 0.1$; 0.2 g/L Al_2O_3 ; 130 m^2/g Al_2O_3 ; open to air; data from Righetto et al. (1991).

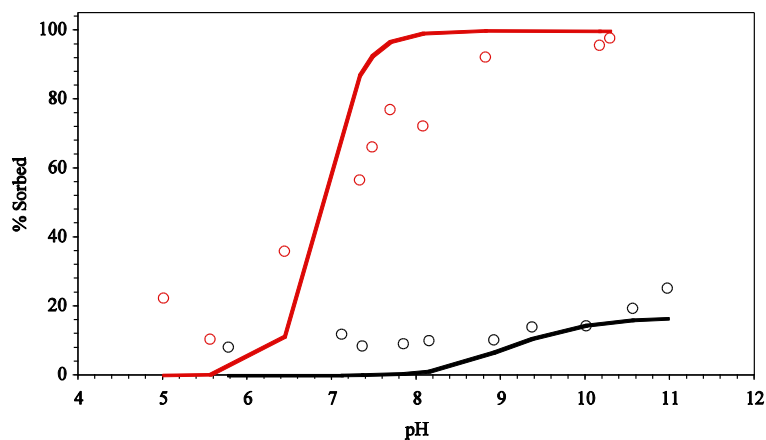


Figure 12. Sorption of 6×10^{-6} mol/L Np(V) on colloidal alumina ($175 \text{ m}^2/\text{g}$) (red) and low surface area α -alumina ($2.5 \text{ m}^2/\text{g}$) (black). Solid lines represent data fits using average colloidal alumina and α -alumina NEM constants. $I = 0.1$; $1 \text{ g/L Al}_2\text{O}_3$; open to air; data from Nakayama and Sakamoto (1991).

Several authors examined the sorption of Np(V) on aluminum oxide material of low surface area and relatively high surface loads (Allard et al., 1982; Bertetti et al., 1998; Nakayama and Sakamoto, 1991). The best fit NEM constants to data of Nakayama and Sakamoto (1991) and Bertetti et al. (1998) (Table 3 and Figures 12 and 13) are in good agreement. The best fit NEM constant to data of Allard et al. (1982) (Table 3 and Figure 14) is significantly higher. Since surface areas for these experiments were estimated from sieving results, it is likely that surface area estimates were too low, resulting in unusually high NEM constants. Ignoring the data of Allard et al. (1982), the average Log K constants for low surface area aluminum oxide data were estimated to be -4.67 ± 0.27 and -14.26 ± 0.04 for $>\text{AlONpO}_2$ and $>\text{AlONpO}_3\text{H}$, respectively.

The difference in NEM constants for the low surface area and high surface area aluminum oxide minerals is indicative of possible multiple-site binding on the aluminum oxide surface or differences in surface characteristics of colloidal and crystalline $\alpha\text{-Al}_2\text{O}_3$. However, the available data is rather limited. The lower NEM constants fit aluminosilicate sorption data suggesting that they may be more appropriate for modeling montmorillonite behavior. They are, therefore, reported in Table 4.

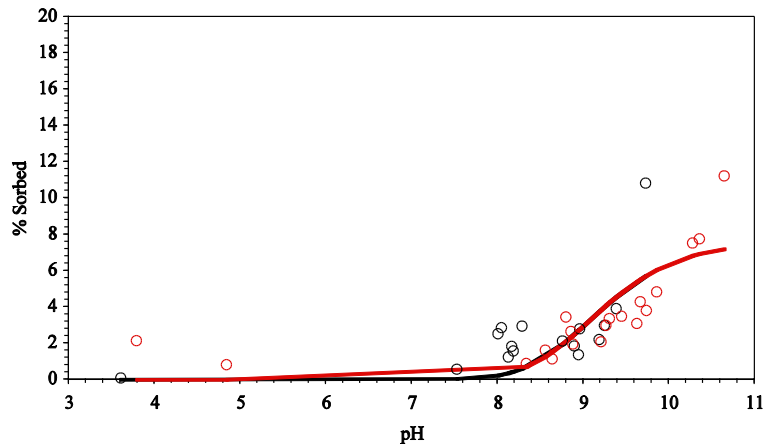


Figure 13. Sorption of 10^{-6} mol/L Np(V) on low surface area α -Al₂O₃ (two data sets). Solid lines represent data fits using average low surface area α -Al₂O₃ NEM constants. $I = 0.01$; 4 g/L Al₂O₃; 0.23 m²/g Al₂O₃; in the absence of CO₂; data from Bertetti et al. (1998).

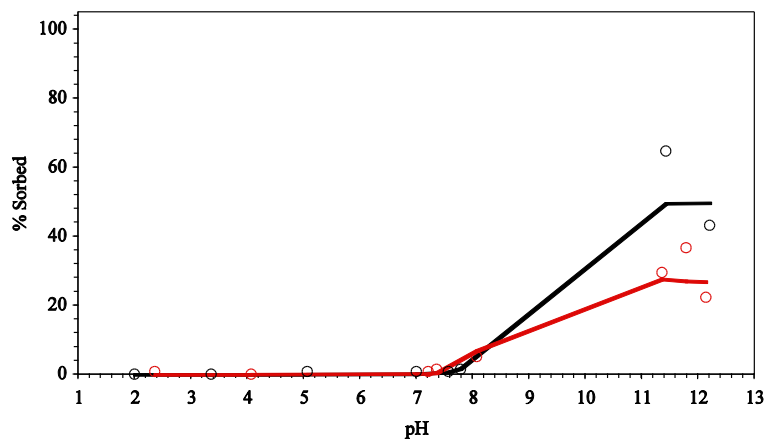


Figure 14. Sorption of 1.9×10^{-7} (red) and 1.9×10^{-9} (black) mol/L Np(V) on alumina. Solid lines represent data fits using best fit NEM constants. $I = 0.01$; 20 g/L alumina; 0.09-0.125 mm particle diameter; open to air; data from Allard et al. (1982).

3.3 Np(V) on Silica

Np(V) sorption to silica was examined by Righetto et al. (1991) and Bertetti et al. (1998) (Figures 15 to 17). The fitted NEM constants for the data of Righetto et al. (1991) are significantly lower than fitted NEM constants for the data of Bertetti et al. (1998) (Table 3). For the data of Righetto et al. (1991), an overestimated colloidal silica surface area could account for the low fitted NEM constant. This same pattern was observed with respect to fitted Am(III) NEM constants for the data reported by these same authors. The multiple data sets of Bertetti et al. (1998) all resulted in similar fitted NEM constants (Table 3). The average Log K constants using these data fits are -3.72 ± 0.15 and -12.16 for $>\text{SiONpO}_2$ and $>\text{SiONpO}_3\text{H}^-$, respectively. An error estimate could not be performed for $>\text{SiONpO}_3\text{H}^-$ because this surface species contributed to sorption only when CO₂ was absent from solutions. Only two data sets were reported by Bertetti et al. (1998) at low CO₂(g).

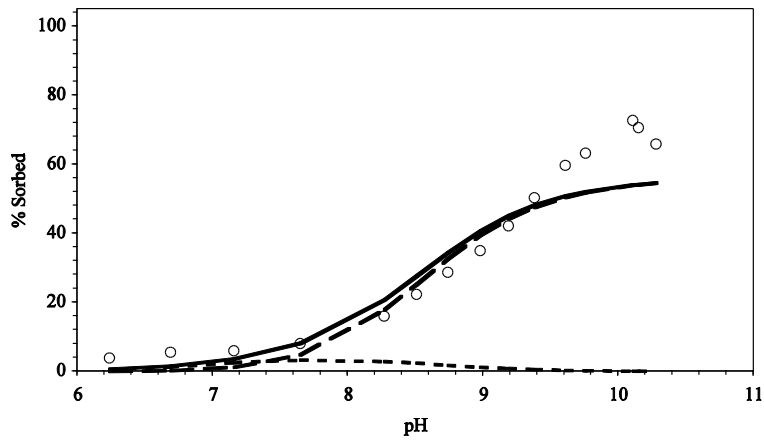


Figure 15. Sorption of 10^{-14} mol/L Np(V) on colloidal silica. Solid lines represent data fits using best fit NEM constants. Dashed lines represent contribution of individual surface species. $I = 0.1$; 1.2 g/L SiO_2 ; 175 m²/g SiO_2 from Turner (1995); open to air; data from Righetto et al. (1991).

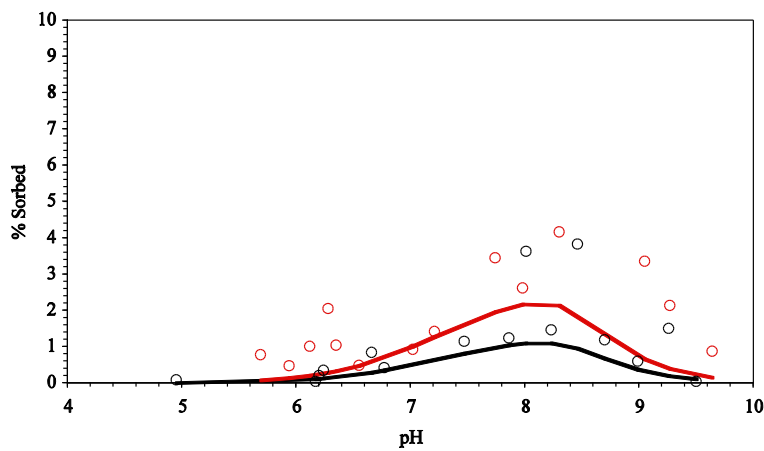


Figure 16. Sorption of 10^{-7} mol/L Np(V) to 40 g/L (black) and 80 g/L (red) SiO_2 . Solid lines represent model prediction using NEM constants from Table 4. $I = 0.1$; 0.03 m²/g SiO_2 ; open to air; data from Bertetti et al. (1998).

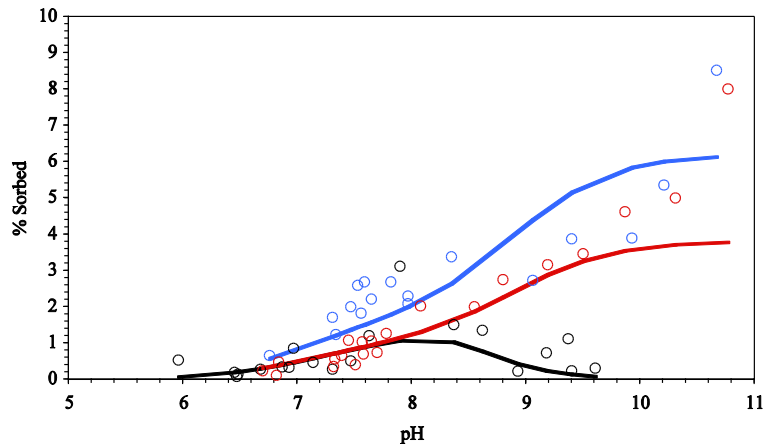


Figure 17. Sorption of 10^{-6} mol/L Np(V) on 40 g/L SiO₂ in air (black), 40 g/L SiO₂ w/o CO₂ (red), and 4 g/L fine grained SiO₂ w/o CO₂ (blue). Solid lines represent model prediction using NEM constants from Table 4. $I = 0.1$; $0.03 \text{ m}^2/\text{g}$ SiO₂; $0.5 \text{ m}^2/\text{g}$ fine grained SiO₂; data from Bertetti et al. (1998).

3.4 Np(V) on Aluminosilicates

Several authors have examined the interaction of Np(V) with aluminosilicates (Bertetti et al., 1998; Bertetti et al., 1995; Turner et al., 1998a). Turner et al. (1998a) hypothesized that Np(V) sorption to montmorillonite could be described by surface complexation to >AlOH and >SiOH sites at the edges of this layered clay mineral. Here, model results using average NEM constants determined for aluminum oxide and silica sorption experiments are compared to montmorillonite sorption data. Following the suggestion of Turner et al. (1998a), it was estimated that 10% of the BET surface area comprised reactive edge sites. Turner et al. (1998a) used an Al/Si reactive site ratio of 0.83:1; in our case, we used a ratio of 1:1. Data fits are shown in Figure 18. No adjustment of NEM constants was performed. Because two sets of NEM constants were calculated for aluminum oxides (colloidal and low surface area), fits to montmorillonite data were examined with both sets of values. Only the low surface area aluminum oxide constants fit montmorillonite data well even though surface loads on montmorillonite were relatively low. At $I = 0.1$, sorption at low pH was minor; indicating that ion exchange of Np(V) on montmorillonite was not significant under these experimental conditions. At lower ionic strength, ion exchange will become significant, as described in the previous section.

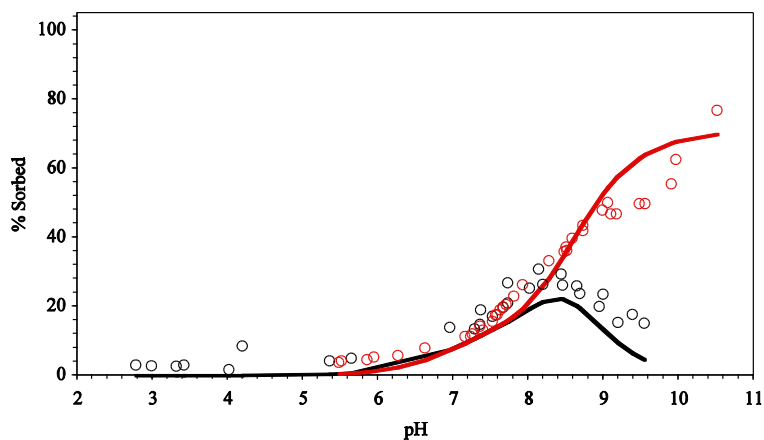


Figure 18. Sorption of $\sim 9 \times 10^{-7}$ mol/L Np(V) on montmorillonite in air (black) and w/o CO₂ (red). Solid lines represent model prediction using NEM constants from Table 4. $I = 0.1$; ~ 4 g/L montmorillonite; $97 \text{ m}^2/\text{g}$; 10% edge sites; 1:1 Si:Al site ratio; data from Turner et al. (1988a).

Sorption of Np(V) to clinoptilolite was evaluated in the same manner as for montmorillonite. Again, reactive surface sites were estimated to comprise 10% of the BET surface area. This new site density was determined from comparisons made by Bertetti et al. (1998) that showed clinoptilolite sorption to be equivalent to that of montmorillonite (on a surface area basis). The Al:Si reactive site ratio was estimated by the molar ratio of these elements in clinoptilolite. Pabalan (1994) measured the concentration of Al and Si in the clinoptilolite used in the experiments of Bertetti et al. (1998). The Al:Si ratio was found to be approximately 15:85, typical of clinoptilolites in general. This ratio was used to estimate the concentration of $>\text{AlOH}$ and $>\text{SiOH}$ reactive sites on the clinoptilolite surface. Results are presented in Figure 19. As in the case of Np(V) on montmorillonite, ion exchange under these experimental conditions was not significant, though a small amount of sorption at low pH was evident. Surprisingly, this relatively simple approach to surface complexation modeling adequately fit the observed sorption of Np(V) to clinoptilolite without any adjustment to the reaction constants independently developed for Np(V) sorption to alumina and silica.

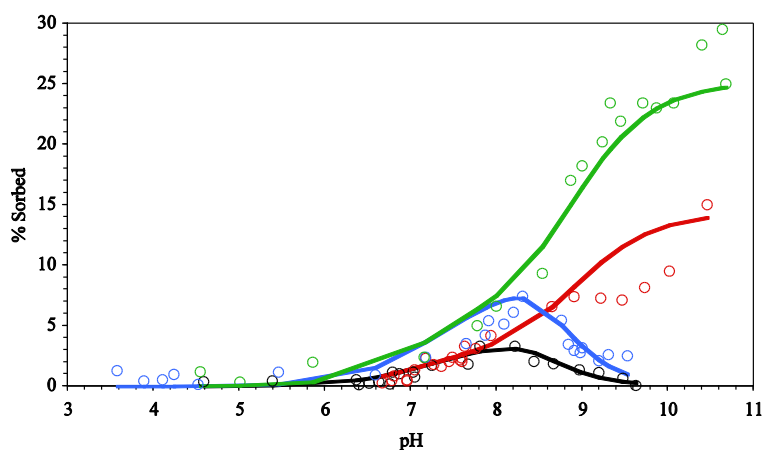


Figure 19. Sorption of 10^{-6} mol/L Np(V) on clinoptilolite with 4 g/L, $I = 0.1$, in air (black), 4 g/L, $I = 0.1$, w/o CO₂ (red), 8 g/L, $I = 0.01$, in air (blue), and 8 g/L, $I = 0.01$, w/o CO₂ (green). Solid lines represent model prediction using NEM constants from Table 4. $10.1 \text{ m}^2/\text{g}$ clinoptilolite; 10% reactive edge sites; 15:85 Al:Si site ratio; data from Bertetti et al. (1998).

3.5 Summary

Table 4 lists the average NEM constants that comprise a database of surface complexation reactions on aluminosilicate minerals. The acidity constants used for >AlOH and >SiOH surface reactive sites were taken from SiO₂ and α-Al₂O₃ diffuse layer model fits reported by Turner (1995). Depending on the SC model, surface acidity Log K constants can vary drastically. If acidity constants were varied during data fitting along with radionuclide surface complexation constants, less variability in Log K constants might be achieved. However, the limited data for most radionuclide–mineral sorption reactions do not merit additional fitting parameters in our NEM model.

Table 4. Average non-electrostatic surface complexation model constants for Np(V) sorption to aluminosilicates.

Reaction	# of Curves Evaluated	log K	Ref.
>AlOH ⇌ >AlO ⁻ + H ⁺		-9.73*	
>AlOH + H ⁺ ⇌ >AlOH ₂ ⁺		8.33*	
>SiOH ⇌ >SiO ⁻ + H ⁺		-7.20*	
>AlOH + NpO ₂ ⁺ ⇌ >AlONpO ₂ + H ⁺	9	-4.67±0.27	1-5†
>AlOH + NpO ₂ ⁺ + H ₂ O ⇌ >AlONpO ₃ H ⁻ + 2H ⁺		-14.26±0.04	
>SiOH + NpO ₂ ⁺ ⇌ >SiONpO ₂ + H ⁺	6	-3.72±0.15	2, 4
>SiOH + NpO ₂ ⁺ + H ₂ O ⇌ >SiONpO ₃ H ⁻ + 2H ⁺		-12.16	

* Surface acidity constants taken from Turner (1995) SiO₂ and α-Al₂O₃ diffuse layer surface complexation model data.

† 2 montmorillonite curves and 4 clinoptilolite curves fit using average aluminol/silanol sites (refs. 13 and 14).

REFERENCES: 1. (Righetto et al., 1988); 2. (Righetto et al., 1991); 3. (Allard et al., 1982); 4. (Nakayama and Sakamoto, 1991); 5. (Bertetti et al., 1998).

The NEM constants in Table 4 are valid only when they are used in conjunction with the listed acidity constants. In addition, all NEM constants are dependent on the aqueous speciation constants used to model the data. This is particularly important for actinides and lanthanides for which aqueous speciation can be very complex. Aqueous complexation constants were based on the GEMBOCHS thermodynamic data base version data.com.V8.R6 (Johnson and Lundeen, 1997).

Sorption of Np(V) to aluminum oxide, silica, and aluminosilicate minerals using a generalized NEM approach, in combination with Vanselow IE has been accomplished using a combination of new experimental data and a survey of data from the literature. Results indicate that generalized >SiOH and >AlOH reactive sites can be used to describe sorption on a variety of minerals. Although this generalized approach may result in greater uncertainty in mineral sorption constants (when compared to a mineral-dependent model), the number of equations necessary to describe sorption is minimized. This approach also minimizes the number of fitting parameters while retaining the principal pH, ionic strength, and surface loading effects.

The NEM and Vanselow IE constants described here are an attempt to arrive at a consistent simplified database of sorption constants that can be used in reactive transport simulations in chemically heterogeneous environments. The accuracy of the resulting equations is limited by the quality and quantity of available sorption data and the limitations of the generalized NEM approach used. The reactivity of natural minerals is complicated and cannot be assumed to

behave ideally. Thus, the validity of the NEM and Vanselow IE constants must always be evaluated with respect to the mineralogy and solution conditions of interest.

4 Comprehensive Approaches to Developing Ion Exchange and Surface Complexation Models for Nuclear Waste Repository Conditions

To date, we have taken the approach of developing a non-electrostatic surface complexation model in combination with ion exchange to simulate Np(V) sorption to montmorillonite. A combination of new experimental data and sorption data from the literature were used to quantify reaction constants that describe all available sorption data. This model provides the foundation for examining Np(V) diffusive reactive transport through montmorillonite clay. The compilation of raw sorption data will also allow us to test alternative approaches (new aqueous speciation models, alternative surface complexation models, uncertainty analyses) to modeling sorption.

The need to develop self-consistent surface complexation/ion exchange models, in concert with thermodynamic models, for nuclear waste repository performance assessment was identified many years ago (Bradbury and Baeyens, 1993). However, significant progress on this issue has been made only recently in various international nuclear waste repository programs (e.g. (Bradbury and Baeyens, 2009), (Dresden-Rosendorf, 2013), (Geckeis et al., 2013)). Hybrid approaches have also been attempted (Bradbury et al., 2010). The best path forward for developing such databases remains an open question (Geckeis et al., 2013), particularly in cases where generic repositories are being investigated resulting in a need to model radionuclide behavior over a very broad range of solution and mineralogic conditions.

One promising effort underway in Germany is the development of an open source database of surface complexation constants reported in the open literature (Dresden-Rosendorf, 2013). RES³T is a digital open source thermodynamic sorption database. It is mineral-specific and can therefore also be used for additive models of more complex solid phases such as rocks or soils. The database includes an integrated user interface to access selected mineral and sorption data and export data into formats suitable for other modeling software. Data records comprise mineral properties, specific surface areas, characteristics of surface binding sites and their protolysis, sorption ligand information, and surface complexation reactions. The database includes the following surface complexation models: Non-Electrostatic, Diffuse Double Layer, Constant Capacitance, Triple Layer, Basic Stern, and the 1-pK Model as extended to CD-MUSIC. The concept of strong and weak binding sites is also included. An extensive bibliography is included in the database, providing links to the original publications, but also to background information concerning surface complexation model theories, related software for data processing and modeling, and sorption experiment techniques. The intent of the database is help to substitute the present K_d approach in risk assessment studies to the more realistic description of sorption phenomena with SCM. The RES³T approach represents the first international attempt to produce a digital thermodynamic database for surface complexation equilibria from the vast amount of data available in the literature.

As an example, a query of Np(V) sorption to aluminosilicate minerals yields the output shown in Table 5. The majority of the Np(V) surface complexation constants available in the database are associated with the Diffuse Double Layer (DDL) model. However, some NEM surface complexation constants are reported and can be compared to values reported in Section 3. For example, the NEM logK reaction constant for formation of >SiONpO₂ on the silanol reactive site

reported to be -4.3 in the RES³T and compares well with our fitted value (Table 4, -3.72 ± 0.15). The comparison is not as promising for the aluminol reactive site $>AlONpO_2$ (-3.6 to -3.4 in RES³T compared to -4.67 ± 0.27 in Table 4). However, it should be noted that our analysis indicated that Np(V) sorption to aluminum oxides may depend on the mineral phase present (e.g. $Al(OH)_3$ vs. $\alpha-Al_2O_3$, Table 3).

One significant difficulty in directly utilizing reaction constants supplied in the RES³T database is that reported constants are dependent on the specific surface complexation model used in the referenced manuscript and the associated protonation/deprotonation constants, surface areas, site densities, and associated aqueous speciation constants and activity correction methods. This inconsistent application of surface complexation models in the literature limits our ability to develop self-consistent databases that would be directly applicable to reactive transport modeling efforts. Ideally, raw sorption data would be stored in a database from which one could develop surface complexation reaction constants based on preferred SCM modeling approaches and most up to date aqueous speciation databases. UFD program at LLNL is actively engaged with the RES³T group to evaluate options for a next generation RES³T database.

Table 5. Surface complexation reaction constants extracted from the RES³T database for Np(V) sorption to aluminosilicate minerals.

SCM	Mineral	Area m ² /g	SiteDensity sites/nm ²	pK ₁	pK ₂	logK	Chemical Equation	Literature Reference
DDL	Biotite	8	2.31	7.2	2.86		»Si-OH + NpO ₂ <1+> = »Si-OH-NpO ₂ <1+>	TS96
DDL	Kaolinite	24.5	2.31	7.2	4.09		»Si-OH + NpO ₂ <1+> = »Si-OH-NpO ₂ <1+>	WAT01b
DDL	Montmorillonite	9.7	1.257	7.2	4.05		»Si-OH + NpO ₂ <1+> = »Si-OH-NpO ₂ <1+>	TPB98a
DDL	Montmorillonite	97	2.31	7.2	3.04		»Si-OH + NpO ₂ <1+> = »Si-OH-NpO ₂ <1+>	WAT01b
DDL	Biotite	7.5	2.31	7.2	-4.17		»Si-OH + NpO ₂ <1+> = »Si-O-NpO ₂ + H<1+>	WAT01b
DDL	amorphous Silica	175	2.31	7.2	-12.54		»Si-OH + NpO ₂ <1+> + H ₂ O = »Si-O-NpO ₂ (OH)<1-> + 2 H<1+>	WAT01b
DDL	Biotite	8	2.31	7.2	-11.58		»Si-OH + NpO ₂ <1+> + H ₂ O = »Si-O-NpO ₂ (OH)<1-> + 2 H<1+>	TS96
DDL	Clinoptilolite	10.1	2.31	7.2	-13.2		»Si-OH + NpO ₂ <1+> + H ₂ O = »Si-O-NpO ₂ (OH)<1-> + 2 H<1+>	WAT01b
DDL	Biotite	8	2.31	8.33	9.73	4.15	»Al-OH + NpO ₂ <1+> = »Al-OH-NpO ₂ <1+>	TS96
DDL	Boehmite	175	2.31	6.85	9.05	3.89	»Al-OH + NpO ₂ <1+> = »Al-OH-NpO ₂ <1+>	WAT01b
DDL	Diaspore	0.11	2.31	8.33	9.72	5.5	»Al-OH + NpO ₂ <1+> = »Al-OH-NpO ₂ <1+>	WAT01b
DDL	Gibbsite	0.22	2.31	6.85	9.05	4.95	»Al-OH + NpO ₂ <1+> = »Al-OH-NpO ₂ <1+>	WAT01b
DDL	Clinoptilolite	10.1	2.31	8.33	9.73	3.27	»Al-OH + NpO ₂ <1+> = »Al-OH-NpO ₂ <1+>	WAT01b
DDL	Boehmite	175	2.31	6.85	9.05	-4.5	»Al-OH + NpO ₂ <1+> = »Al-O-NpO ₂ + H<1+>	WAT01b
DDL	Diaspore	0.11	2.31	8.33	9.72	-3.62	»Al-OH + NpO ₂ <1+> = »Al-O-NpO ₂ + H<1+>	WAT01b
DDL	Gibbsite	0.22	2.31	6.85	9.05	-3.53	»Al-OH + NpO ₂ <1+> = »Al-O-NpO ₂ + H<1+>	WAT01b
DDL	Gibbsite	0.8	2.31	8.33	9.73	-2.81	»Al-OH + NpO ₂ <1+> = »Al-O-NpO ₂ + H<1+>	WAT01b
DDL	Kaolinite	24.5	2.31	8.33	9.73	-4.04	»Al-OH + NpO ₂ <1+> = »Al-O-NpO ₂ + H<1+>	WAT01b
DDL	Alumina	130	2.31	6.85	9.05	-10.93	»Al-OH + NpO ₂ <1+> + H ₂ O = »Al-O-NpO ₂ (OH)<1-> + 2 H<1+>	WAT01b
DDL	Biotite	8	2.31	8.33	9.73	-12.39	»Al-OH + NpO ₂ <1+> + H ₂ O = »Al-O-NpO ₂ (OH)<1-> + 2 H<1+>	TS96
DDL	Biotite	7.5	2.31	8.33	9.72	-11.5	»Al-OH + NpO ₂ <1+> + H ₂ O = »Al-O-NpO ₂ (OH)<1-> + 2 H<1+>	WAT01b
DDL	Diaspore	0.11	2.31	8.33	9.72	-13.1	»Al-OH + NpO ₂ <1+> + H ₂ O = »Al-O-NpO ₂ (OH)<1-> + 2 H<1+>	WAT01b
DDL	Montmorillonite	9.7	1.043	8.33	9.73	-13.79	»Al-OH + NpO ₂ <1+> + H ₂ O = »Al-O-NpO ₂ (OH)<1-> + 2 H<1+>	TPB98a
DDL	Montmorillonite	97	2.31	8.33	9.72	-13.72	»Al-OH + NpO ₂ <1+> + H ₂ O = »Al-O-NpO ₂ (OH)<1-> + 2 H<1+>	WAT01b
DDL	Corundum	2.5	2.31	8.33	9.73	-8.23	2 »Al-OH + NpO ₂ <1+> = (»Al-O) ₂ -NpO ₂ <1-> + 2 H<1+>	WAT01b
DDL	Corundum	0.24	2.31	8.33	9.73	-8.23	2 »Al-OH + NpO ₂ <1+> = (»Al-O) ₂ -NpO ₂ <1-> + 2 H<1+>	WAT01b

SCM	Mineral	Area m ² /g	SiteDensity sites/nm ²	pK_1	pK_2	logK	Chemical Equation	Literature Reference
DDL	Montmorillonite	50	0.74673	6.05	7.79	1.33	»X-OH + NpO ₂ <1+> + CO ₃ <2-> = »X-O-NpO ₂ CO ₃ <2-> + H<1+>	TNOYS10
DDL	Montmorillonite	50	0.74673	6.05	7.79	2.85	»X-OH + NpO ₂ <1+> = »X-OH-NpO ₂ <1+>	TNOYS10
DDL	Montmorillonite	50	0.74673	6.05	7.79	-14	»X-OH + NpO ₂ <1+> + H ₂ O = »X-O-NpO ₂ (OH)<1-> + 2 H<1+>	TNOYS10
NE	amorphous Silica	0.1	12.04409	2.72	6.18	-4.3	»Si-OH + NpO ₂ <1+> = »Si-O-NpO ₂ + H<1+>	L93
NE	Gibbsite	0.8	10	5.7	9.4	-3.6	»Al-OH + NpO ₂ <1+> = »Al-O-NpO ₂ + H<1+>	DBMCB98
NE	Gibbsite	0.8	10	5.92	9.4	-3.44	»Al-OH + NpO ₂ <1+> = »Al-O-NpO ₂ + H<1+>	DMBC97
NE	Gibbsite	0.8	10	5.65	9.55	-3.41	»Al-OH + NpO ₂ <1+> = »Al-O-NpO ₂ + H<1+>	DMBC97
NE	Montmorillonite	35	1.37647	5	9.5	-12	»X-OH + NpO ₂ <1+> + H ₂ O = »X-O-NpO ₂ (OH)<1-> + 2 H<1+>	BB06
NE	Montmorillonite	35	1.37647	5	9.5	-2	»X-OH + NpO ₂ <1+> = »X-O-NpO ₂ + H<1+>	BB06
TL	Quartz	6	2.31	-2.3	6.8	-6.929	»Si-OH + NpO ₂ <1+> = »Si-O-NpO ₂ + H<1+>	KHL99

REFERENCES:

- Bradbury MH, Bayens B (2006) Modelling sorption data for the actinides Am(III), Np(V) and Pa(V) on montmorillonite. *Radiochim. Acta* 94, 619-625.
- Del Nero M, Ben Said K, Made B, Clement A, Bontems G (1998) Effect of pH and carbonate concentration in solution on the sorption of neptunium(V) by hydrargilite: Application of the Non-Electrostatic Model. *Radiochim. Acta* 81, 133-141.
- Del Nero M, Made B, Bontems G, Clement A (1997) Adsorption of neptunium(V) on hydrargilite. *Radiochim. Acta* 76, 219-228.
- Kohler M, Honeyman BD, Leckie JO (1999) Neptunium(V) sorption on hematite (α-Fe₂O₃) in aqueous suspension: The effect of CO₂. *Radiochim. Acta* 85, 33-48.
- Labonne N (1993): Role des matieres organiques dans les phenomenes de retention des actinides sur la silice. Ph.D. Thesis Université Paris XI-Orsay
- Tachi Y, Nakazawa T, Ochs M, Yotsuji, Suyama T, Seida T, Yamada N, Yui M (2010) Diffusion and sorption of neptunium(V) in compacted montmorillonite: effects of carbonate and salinity. *Radiochim. Acta* 98, 711-718.
- Turner DR, Pabalan RT, Bertetti FP (1998) Neptunium(V) sorption on montmorillonite: An experimental and surface complexation modeling study. *Clays Clay Min.* 46, 256-269.
- Turner DR, Sassman SA (1996) Approaches to sorption modeling for high-level waste performance assessment. *J. Contam. Hydrol.* 21, 311-332.
- Wang P, Anderko A, Turner DR (2001) Thermodynamic modeling of the adsorption of radionuclides on selected minerals. I. Cations. *Ind. Eng. Chem. Res.* 40, 4428-4443.

5 Diffusion Cell Experiments

While some data are available in the literature regarding diffusion of Np(V) in clay-containing rock or compacted clay materials (e.g. (Wu et al., 2009)), the nature of the diffusion process in these clay-rich materials is not fully understood. Furthermore, the effect of temperature has been studied only minimally and is essential to exploring repository performance under increasingly high heat loads. A focus of our experimental and modeling effort is to examine diffusion within the free pore space as well as the interlamellar space (Figure 3). The significance of Np(V) diffusion through the interlamellar space of montmorillonite will depend on the speciation of Np(V) in solution, its ability to access the interlamellar space via ion exchange processes, and the degree of clay compaction which will affect the relative abundance of interlamellar porosity versus free porosity (e.g. Figure 3). Np(V) diffusion through compacted clay will be examined at solution conditions that favor Np(V) sorption via ion exchange, that favor Np(V) sorption via surface complexation, that favor the presence of negatively charged Np(V) complexes in solution, and that favor the presence of a positively charged NpO_2^+ free ion. Each of these conditions will test the effects of interlamellar diffusion, charge exclusion, and pore connectivity which affect the apparent diffusion of Np(V) through an engineered clay barrier.

5.1 Materials and Methods

At present, instrumentation has been acquired and the appropriate experimental conditions are being explored based on our ion exchange/surface complexation model. The configuration of the diffusion cells is based on the original design by Van Loon et al. (2004) (Figure 20). The complete diffusion cell configuration during experiments is shown in Figure 21. Diffusion experiments will begin in late FY13.

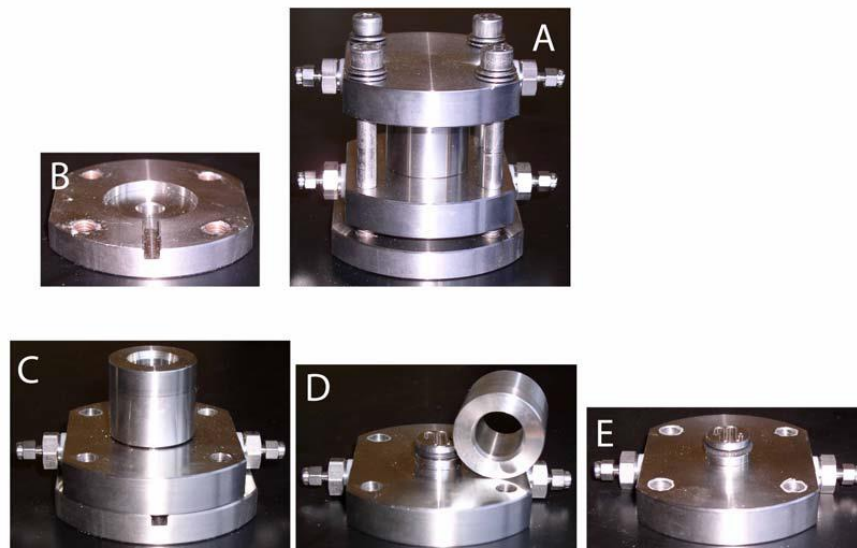


Figure 20. The diffusion cell (A) includes two ports on each side of the core to allow for continuous circulation of fluid on the upstream and downstream ends of the core. The bottom plate (B) is configured for a Burster miniature ring load sensor to monitor pressure. The central cylinder (C and D) holds the clay core between two O-rings. Fluid circulates at the top and bottom of the core through a sinusoidal flowpath (E) that ensures a uniform concentration across the ends of the core. The top and bottom of each core is isolated between two titanium porous (2 micrometer pore size) frits. Core dimension is 18.5 mm in diameter and 10 mm in length.

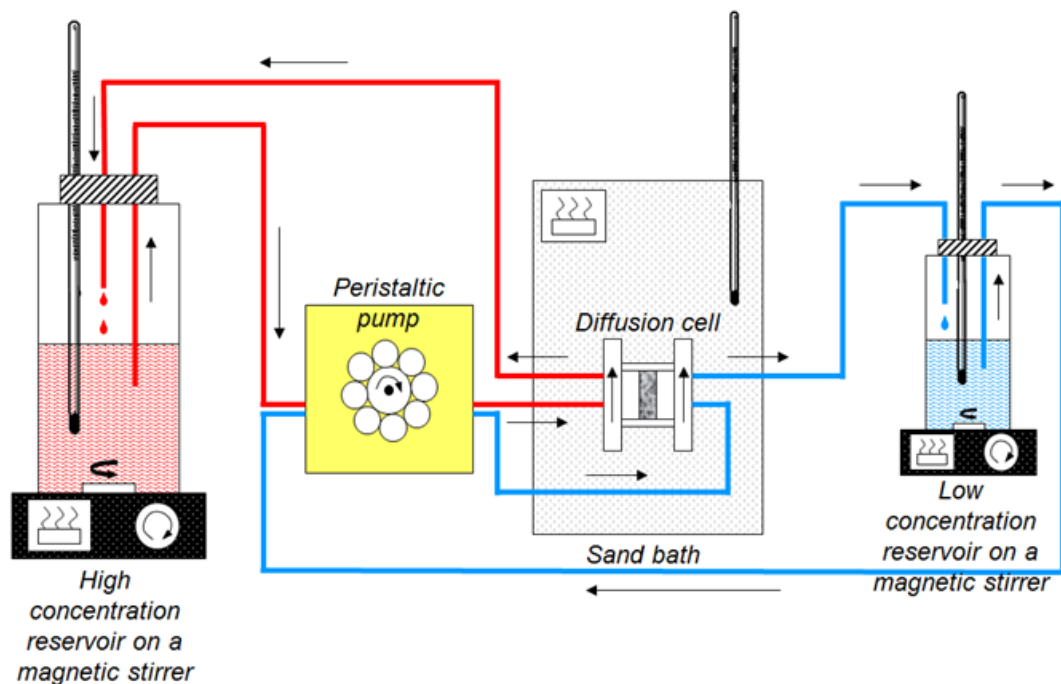


Figure 21. Configuration of diffusion cell under heated aerobic conditions. Temperature is maintain by hot plate (for reservoirs) and sand bath (for diffusion cell). Np(V) and solution composition in high concentration and low concentration reservoirs is monitored over time. If diffusion is observed across core, diffusion rate can be calculated directly. If Np(V) through diffusion is not observed, the core is disassembled and diffusion profile quantified using abrasive peeling, laser ablation ICP-MS, or secondary ion mass spectrometry (SIMS).

5.2 Characterization of Long-term Uranium Diffusion Experiments

In the Fall of 2013, a collaboration between LLNL and the Helmholtz Zentrum Dresden Rossendorf was initiated. As part of this collaboration, there was an opportunity to characterize U(VI) diffusion through compacted MX-80 bentonite cores using the same diffusion cell configuration described above (Figure 21). The unique nature of these experiments was that the diffusion cells had been allowed to run since 2006, providing an unprecedented 7 years of diffusive transport. Characterization of these samples also provided an opportunity to test various methods for characterizing core material.

Three cores were examined: compacted MX-80 bentonite with bulk densities of 1.3, 1.6, and 1.9 g/cm³. High and low concentration reservoirs contained saline solutions that were determined to represent equilibrium composition of bentonite porewaters at their specific dry bulk densities (Table 6). The U(VI) concentration in the high concentration reservoirs was set to 1E-6 mol/L while the downstream reservoir was uranium free. Tritium diffusion through the cores was measured, leading to effective diffusivities in the 1.3, 1.6, and 1.9 g/cm³ of 1.99×10^{-10} , 1.14×10^{-10} , and 4.05×10^{-11} m²/s, respectively.

While modeling and data analysis are still ongoing, the diffusion data are indicative of a significant decrease in U(VI) migration with increasing compaction (Figure 22). Some of this is the result of a reduction in total porosity in the compacted bentonite. However, additional effects

such as tortuosity and charge exclusion phenomena are likely playing a role as well. Numerical modeling of these data will provide a unique opportunity to quantify U(VI) diffusion in compacted clay over extended time periods.

Table 6. Composition of porewaters in equilibrium with MX-80 bentonite at the three bulk densities examined in these experiments.

Dry density (kg m ⁻³)	1300	1600	1900
Porosity	0.122	0.044	0.019
log P _{CO₂} (bar)	-3.42	-3.47	-3.65
pH	8.00	8.00	8.00
Ionic strength (M)	0.26	0.29	0.33
Na (M)	1.83 x 10 ⁻¹	2.07 x 10 ⁻¹	2.54 x 10 ⁻¹
K (M)	2.7 x 10 ⁻³	3.1 x 10 ⁻³	3.7 x 10 ⁻³
Mg (M)	1.0 x 10 ⁻²	1.2 x 10 ⁻²	1.5 x 10 ⁻²
Ca (M)	9.2 x 10 ⁻³	9.8 x 10 ⁻³	1.2 x 10 ⁻²
Sr (M)	8.1 x 10 ⁻⁵	8.6 x 10 ⁻⁵	1.1 x 10 ⁻⁴
Cl (M)	1.81 x 10 ⁻²	6.18 x 10 ⁻²	1.70 x 10 ⁻¹
SO ₄ (M)	1.02 x 10 ⁻¹	9.5 x 10 ⁻²	7.1 x 10 ⁻²
C _{inorg.} (M)	8.9 x 10 ⁻⁴	8.0 x 10 ⁻⁴	5.5 x 10 ⁻⁴
F (M)	2.2 x 10 ⁻⁴	2.2 x 10 ⁻⁴	1.9 x 10 ⁻⁴
Si (M)	1.8 x 10 ⁻⁴	1.8 x 10 ⁻⁴	1.8 x 10 ⁻⁴
N _{Na}	0.69	0.71	0.71
N _K	0.024	0.024	0.024
N _{Mg}	0.127	0.128	0.129
N _{Ca}	0.155	0.140	0.135
N _{Sr}	0.001	0.001	0.001

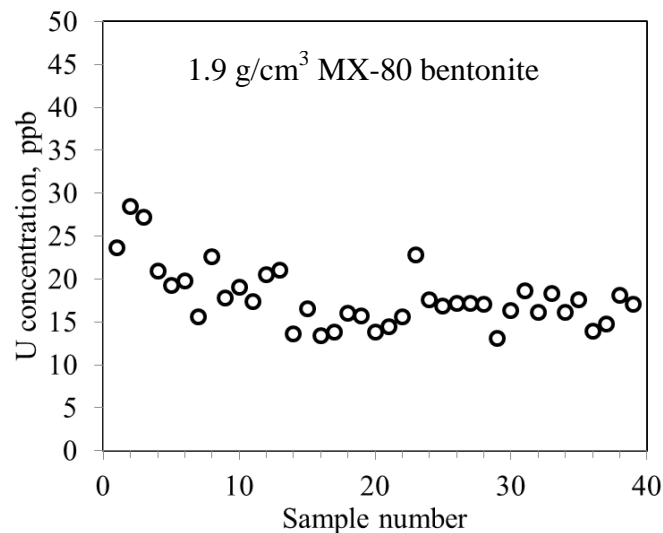
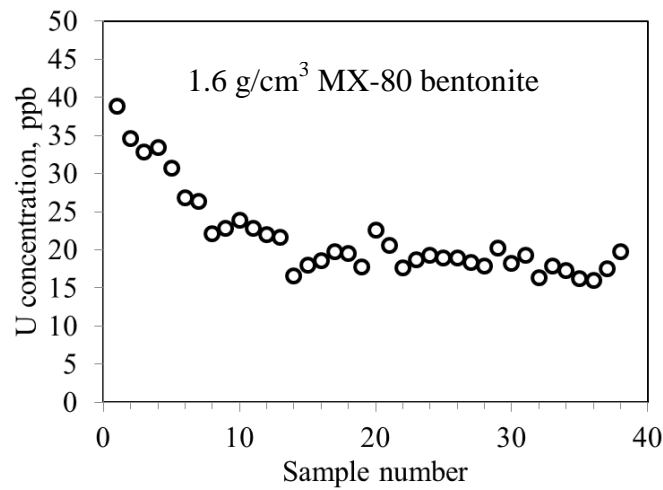
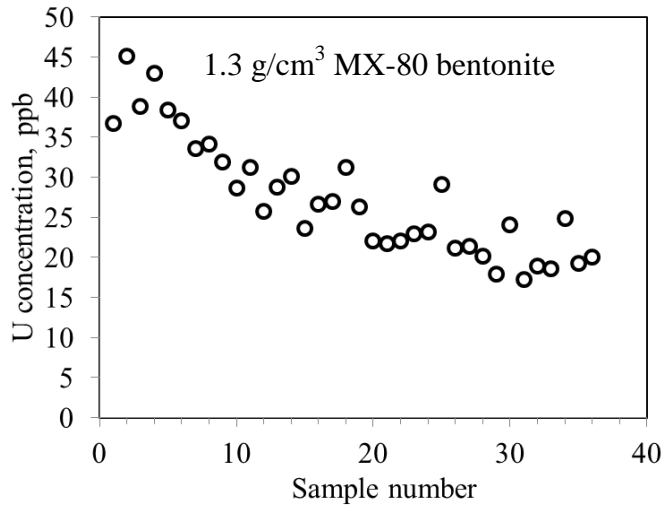


Figure 22. U(IV) diffusion profiles in compacted MX-80 bentonite cores after 7 years of diffusion. Each sample represents approximately a 100 micrometer section of core along the diffusion profile. Sample 1 is located at the high concentration side of the diffusion cell. U concentration is the desorbed U fraction in the core material after equilibration with 1 M HNO₃.

6. Planned FY14 Efforts

In FY14, we plan to continue our current experimental program looking at the diffusion of Np(V) in montmorillonite clay. At this time, the diffusion cells have been designed and made, a post doc was identified and hired, and the initial batch experiments and modeling were completed. The modeling will now focus on determining the experimental parameters needed for the diffusion cell experiments which will begin in late FY13 and continue into FY14. As data becomes available, we will be working with LBNL geochemists and modelers to provide insight into Np(V) diffusion through backfill material. We will also be working with LBNL experimentalist to compare our Np data with their parallel work on U diffusion.

We will begin FY14 effort by completing lab-scale Np diffusion experiments with compacted montmorillonite. The work will then extend to bentonite. Montmorillonite represents a pure end-member clay while bentonite contains montmorillonite along with a variety of additional minor phases (illite, quartz, feldspar, etc.) and is more representative of what might be used in a repository environment. In addition, we are actively discussing the possibility of examining Np(V) diffusion in altered bentonite material produced hydrothermally by F. Caporuscio (Cheshire et al., 2013). This would allow us to test the diffusive properties of bentonite backfill material that may have experienced high heat loading and mineral alteration. We will employ unique x-ray spectroscopic and electron-based imaging techniques available at LBNL and LLNL to evaluate actinide diffusion on the scale of mm. The collaboration with LBNL will allow us to develop a self-consistent diffusion model for both U(VI) and Np(V).

The proposed research will address the following FEPs/needs identified in the R&D Roadmap: 2.2.09.05 - radionuclide speciation and solubility in host rock; 2.2.09.55 - sorption of dissolved radionuclides in host rock; 2.2.09.59 - colloidal transport in host rock.

7. References

- Allard, B., Olofsson, U., Torstenfelt, B., Kipatsi, H., and Andersson, K., 1982. Sorption of actinides in well-defined oxidation states on geologic media. In: Lutze, W. (Ed.), Scientific basis for radioactive waste management - V. Elsevier Science Pub. Co.
- Apted, M., Ross, A., and Kessler, J., 2003. Scientific and Technical Priorities at Yucca Mountain. EPRI, Palo Alto, CA.
- Baeyens, B. and Bradbury, M. H., 1995. A quantitative mechanistic description of Ni, Zn and Ca sorption on Na-montmorillonite. Part II: Sorption measurements. PSI Bericht Nr. 95-11 and Nagra Technical Report NTB 95-05, Wetingen and Villigen (Switzerland).
- Baeyens, B. and Bradbury, M. H., 1997. A mechanistic description of Ni and Zn sorption on Na-montmorillonite .1. Titration and sorption measurements. *J. Contam. Hydrol.* 27, 199-222.
- Baeyens, B. and Bradbury, M. H., 2004. Cation exchange capacity measurements on illite using the sodium and cesium isotope dilution technique: effects of the index cation, electrolyte concentration and competition: modeling. *Clays Clay Miner.* 52, 421-431.
- Bertetti, F. P., Pabalan, R. T., and Almendarez, M. G., 1998. Studies on neptunium(V) sorption on quartz, clinoptilolite, montmorillonite, and α -alumina. In: Jenne, E. A. (Ed.), Adsorption of metals by geomedia. Academic Press, San Diego.
- Bertetti, F. P., Pabalan, R. T., Turner, D. R., and Almendarez, M. G., 1995. Neptunium(V) sorption behavior on clinoptilolite, quartz, and montmorillonite. In: Murphy, W. M. and Knecht, D. A. Eds.) Materials Research Society Symposium Proceedings. Materials Research Society, Boston, MA.
- Bethke, C. M. and Yeakel, S., 2009. The Geochemist's Workbench. Release 8.0. Essentials Guide.
- Bolt, G. H., 1982. Soil Chemistry. B. Physico-Chemical Models. Chapter 2. Elsevier.
- Bondietti, E. A. and Francis, C. W., 1979. Geologic Migration Potentials of Tc-99 and Np-237. *Nature* 203, 1337-1340.
- Bourg, I. C., Bourg, A. C. M., and Sposito, G., 2003. Modeling diffusion and adsorption in compacted bentonite: a critical review. *Journal of Contaminant Hydrology* 61, 293-302.
- Bradbury, M. H. and Baeyens, B., 1993. A general application of surface complexation modeling radionuclide sorption in natural systems. *J. Colloid Interface Sci.* 158, 364-371.
- Bradbury, M. H. and Baeyens, B., 1997. A mechanistic description of Ni and Zn sorption on Na-montmorillonite Part II: modelling. *J. Contam. Hydrol.* 27, 223-248.
- Bradbury, M. H. and Baeyens, B., 2000. A generalised sorption model for the concentration dependent uptake of caesium by argillaceous rocks. *J. Contam. Hydrol.* 42, 141-163.
- Bradbury, M. H. and Baeyens, B., 2002. Sorption of Eu on Na- and Ca-montmorillonites: Experimental investigations and modelling with cation exchange and surface complexation. *Geochim. Cosmochim. Acta* 66, 2325-2334.
- Bradbury, M. H. and Baeyens, B., 2006. Modelling sorption data for the actinides Am(III), Np(V) and Pa(V) on montmorillonite. *Radiochim. Acta* 94, 619-625.

- Bradbury, M. H. and Baeyens, B., 2009. Sorption modelling on illite. Part II: Actinide sorption and linear free energy relationships. *Geochim. Cosmochim. Acta* 73, 1004-1013.
- Bradbury, M. H., Baeyens, B., and Thoenen, T., 2010. Sorption Data Bases for Generic Swiss Argillaceous Rock Systems. Nagra, Wettingen, Switzerland.
- Cheshire, M. C., Caporuscio, F. A., Jové-Colon, C., and McCarney, M. K., 2013. Alteration of clinoptilolite into high-silica analcime within a bentonite barrier system under used nuclear fuel repository conditions 14th International High-Level Radioactive Waste Management Conference. American Nuclear Society, Albuquerque, NM.
- Choppin, G. R., 2006. Actinide speciation in aquatic systems. *Mar. Chem.* 99, 83-92.
- Davis, J. A., Coston, J. A., Kent, D. B., and Fuller, C. C., 1998. Application of the surface complexation concept to complex mineral assemblages. *Environmental Science and Technology* 32, 2820-2828.
- Dixon, J. B., 1989. *Minerals in Soil Environments*, 2nd Edition. Soil Science Society of America.
- DOE, 2002. Yucca Mountain Science and Engineering Report: Technical Information Supporting Site Recommendation Consideration. U.S. Department of Energy, Office of Civilian Radioactive Waste Management, North Las Vegas.
- Dresden-Rossendorf, H.-Z., 2013. RES³T - Rossendorf Expert System for Surface and Sorption Thermodynamics. RES³T - Rossendorf Expert System for Surface and Sorption Thermodynamics, Dresden, Germany.
- Dverstorp, B. and Stromberg, B., 2013. Initial review of a license application for a spent nuclear fuel repository in Sweden 14th International High-Level Radioactive Waste Management Conference. American Nuclear Society, Albuquerque, NM.
- Dzombak, D. A. and Morel, F. M. M., 1990. *Surface complexation modeling : hydrous ferric oxide*. Wiley, New York.
- Fletcher, P. and Sposito, G., 1989. The chemical modeling of clay electrolyte interactions for montmorillonite. *Clay Min.* 24, 375-391.
- Gaines, G. L. and Thomas, H. C., 1953. Adsorption studies on clay minerals II. A formulation of the thermodynamic of exchange adsorption. *J. Chem. Phys.* 21, 714-718.
- Geckeis, H., Lützenkirchen, J., Polly, R., Rabung, T., and Schmidt, M., 2013. Mineral–Water Interface Reactions of Actinides. *Chemical Reviews* 113, 1016-1062.
- Gorgeon, L., 1994. Contribution à la Modélisation Physico-Chimique de la Retention de Radioéléments à Vie Longue par des Matériaux Argileux, Université Paris.
- Herbelin, A. L. and Westall, J. C., 1994. FITEQL, A computer program for determination of chemical equilibrium constants from experimental data. Department of Chemistry, Oregon State University.
- Hoth, P., Wirth, H., Reinhold, K., Bräuer, V., Krull, P., and Feldrappe, H., 2007. *Endlagerung radioaktiver Abfälle in tiefen geologischen Formationen Deutschlands – Untersuchung und Bewertung von Tongesteinsformationen*. BGR Bundesanstalt für Geowissenschaften und Rohstoffe, Hannover.

- Huysen, K. and van der Laan, J., 1992. DataTheif. National Institute for Nuclear Physics and High Energy Physics, Amsterdam.
- Jensen, H. E., 1973. Potassium–calcium exchange equilibria on a montmorillonite and a kaolinite clay. *Agrochimica* 17, 181-190.
- Johnson, J. W. and Lundeen, S. R., 1997. GEMBOCHS thermodynamic datafiles for use with the EQ3/6 modeling package. Lawrence Livermore National Laboratory, Livermore.
- Kaszuba, J. P. and Runde, W. H., 1999. The aqueous geochemistry of neptunium: Dynamic control of soluble concentrations with applications to nuclear waste disposal. *Environ. Sci. Technol.* 33, 4427-4433.
- Kozai, N., Ohnuki, T., Matsumoto, J., Banba, T., and Ito, Y., 1996. A study of specific sorption of neptunium(V) on smectite in low pH solution. *Radiochim. Acta* 75, 149-158.
- Kozai, N., Ohnuki, T., and Muraoka, S., 1993. Sorption characteristics of neptunium by sodium-smectite. *J. Nucl. Sci. Technol. (Tokyo, Jpn.)* 30, 1153-1159.
- Kurbatov, M. H., Wood, G. B., and Kurbatov, J. D., 1951. Isothermal adsorption of cobalt from dilute solutions. *Journal of Physical Chemistry* 55, 1170-1182.
- Labalette, T., Harman, A., Dupuis, M. C., and Ouzounian, G., 2013. CIGÉO, the French geological repository project 14th International High-Level Radioactive Waste Management Conference. American Nuclear Society, Albuquerque, NM.
- Langmuir, D., 1997. *Aqueous Environmental Geochemistry*. Prentice-Hall, U.S.
- Law, G. T. W., Geissler, A., Lloyd, J. R., Livens, F. R., Boothman, C., Begg, J. D. C., Denecke, M. A., Rothe, J., Dardenne, K., Burke, I. T., Charnock, J. M., and Morris, K., 2010. Geomicrobiological Redox Cycling of the Transuranic Element Neptunium. *Environ. Sci. Technol.* 44, 8924-8929.
- Lemire, R. J., Fuger, J., Nitsche, H., Potter, P., Rand, M. H., Rydberg, J., Spahiu, K., Sullivan, J. C., Ullman, W. J., Vitorge, P., and Wanner, H., 2001. *Chemical Thermodynamics of Neptunium and Plutonium*. North-Holland by Elsevier, Amsterdam.
- Maes, A. and Cremers, A., 1977. Charge density effects in ion exchange. Part 1. Heterovalent exchange equilibria. *J. Chem. Soc. Faraday Trans.* 173, 1807-1814.
- McBride, M. B., 1994. *Environmental Chemistry of Soils* Oxford University Press, Oxford.
- McKinley, J. P., Zachara, J. M., Smith, S. C., and Turner, G. D., 1995. The influence of uranyl-hydrolysis and multiple site-binding reaction on adsorption of U(VI) to montmorillonite. *Clays and Clay Minerals* 45, 586-598.
- Missana, T. and García-Gutiérrez, M., 2007. Adsorption of bivalent ions (Ca(II), Sr(II) and Co(II)) onto FEBEX bentonite. *Phys. Chem. Earth* 32, 559-567.
- Nagasaki, S. and Tanaka, S., 2000. Sorption equilibrium and kinetics of NpO_2^+ on dispersed particles of Na-montmorillonite. *Radiochim. Acta* 88, 705-709.
- NAGRA, 2002. Project Opalinus Clay. Safety Report. Demonstration of disposal feasibility for spent fuel, vitrified high-level waste and long-lived intermediate-level waste (Entsorgungsnachweis). NTB 02-05. Nagra, Wettingen, Switzerland.

- Nakayama, S. and Sakamoto, Y., 1991. Sorption of neptunium on naturally-occurring iron-containing minerals. *Radiochimica Acta* 52-3, 153-157.
- Neck, V., Kim, J. I., and Kanellakopoulos, B., 1994. Thermodynamisches Verhalten von Neptunium(V) in konzentrierten NaCl- und NaClO₄-Lösungen, Tech. Rep. Kfk 5301. Kernforschungszentrum Karlsruhe, Karlsruhe, Germany.
- OECD, 2006. Safety of geological disposal of high-level and longlived radioactive waste in France—an international peer review of the “Dossier 2005 Argile” concerning disposal in the Callovo-Oxfordian formation. NEA No. 6178. OECD.
- Pabalan, R. T., 1994. Thermodynamics of ion-exchange between clinoptilolite and aqueous solutions of Na⁺/K⁺ and Na⁺/Ca²⁺. *Geochimica et Cosmochimica Acta* 58, 4573-4590.
- Pabalan, R. T., Turner, D. R., Bertetti, F. P., and Prikryl, J. D., 1998. Uranium VI sorption onto selected mineral surfaces: Key geochemical parameters. In: Jenne, E. A. (Ed.), *Adsorption of metals by geomedia*. Academic Press, San Diego.
- Parkhurst, D. L. and Appelo, C. A. J., 1999. User’s guide to PHREEQC—a computer program for speciation, batch-reaction, one-dimensional transport, and inverse geochemical calculations, USGS Report No. 99-4259.
- Pickett, D. A., Murrell, M. T., and Williams, R. W., 1994. Determination of femtogram quantities of protactinium in geologic samples by thermal ionization mass spectrometry. *Analytical Chemistry* 66, 1044-1049.
- Poinsot, C., Baeyens, B., and Bradbury, M. H., 1999. Experimental studies of Cs, Sr, Ni and Eu sorption on Na-illite and the modelling of Cs sorption, PSI Bericht Nr. 99-06.
- Righetto, L., Bidoglio, G., Azimonti, G., and Bellebono, I. R., 1991. Competitive actinide interaction in colloidal humic acid-mineral oxide systems. *Environmental Science and Technology* 25, 1913-1919.
- Righetto, L., Bidoglio, G., Marcandalli, B., and Bellebono, I. R., 1988. Surface interactions of actinides with alumina colloids. *Radiochimica Acta* 44/45, 73-75.
- Sabodina, M. N., Kalmykov, S. N., Sapozhnikov, Y. A., and Zakharova, E. V., 2006. Neptunium, plutonium and Cs-137 sorption by bentonite clays and their speciation in pore waters. *J. Radioanal. Nucl. Chem.* 270, 349-355.
- Sakamoto, Y., Konishi, M., Shirahashi, K., Senoo, M., and Moriyama, N., 1990. Adsorption behavior of neptunium for soil. *Radioact. Waste Manage. Environ. Restor.* 15, 13-25.
- Schindler, P. W., Liechti, P., and Westall, J. C., 1987. Adsorption of copper, cadmium and lead from aqueous solution to the kaolinite/water interface. *Neth. J. Agric. Sci.* 35, 219-230.
- Shaviv, S. and Mattigod, S. V., 1985. Cation exchange equilibria in soils expressed as cation-ligand complex formation. *Soil Sci. Soc. Am. J.* 49, 569-573.
- Sposito, G., 1981. *The Thermodynamics of Soil Solution*. Oxford University Press, Oxford.
- Tournassat, C., Bizi, M., Braibant, G., and Crouzet, C., 2011. Influence of montmorillonite tactoid size on Na–Ca cation exchange reactions. *J. Colloid Interface Sci.* 364, 443-454.
- Tournassat, C., Gailhanou, H., Crouzet, C., Braibant, G., Gautier, A., Lassin, A., Blanc, P., and Gaucher, E. C., 2007. Two cation exchange models for direct and inverse modelling of

- solution major cation composition in equilibrium with illite surfaces. *Geochim. Cosmochim. Acta* 71, 1098-1114.
- Triay, I. R., Robinson, B. A., Lopez, R. M., Mitchell, A. J., and Overly, C. M., 1993. Neptunium retardation with tufts and groundwaters from Yucca Mountain Proc 4th Annu Int Conf on High-Level Radioactive Waste Management. Am. Nuclear Soc., La Grange Park, IL.
- Turner, D. R., 1995. A uniform approach to surface complexation modeling of radionuclide sorption. Center for Nuclear Waste Regulatory Analyses, San Antonio.
- Turner, D. R., Pabalan, R. T., and Bertetti, F. P., 1998a. Neptunium(V) sorption on montmorillonite: An experimental and surface complexation modeling study. *Clays and Clay Minerals* 46, 256-269.
- Turner, D. R., Pabalan, R. T., and Bertetti, F. P., 1998b. Neptunium(V) sorption on montmorillonite: An experimental and surface complexation modeling study. *Clays Clay Miner.* 46, 256-269.
- Turner, G. D., Zachara, J. M., McKinley, J. P., and Smith, S. C., 1996. Surface charge properties and UO₂²⁺ adsorption of a subsurface smectite. *Geochimica et Cosmochimica Acta* 60, 3399-3414.
- Van Loon, L. R. and Soler, J. M., 2004. Diffusion of HTO, ³⁶Cl⁻, ¹²⁵I⁻ and ²²Na⁺ in Opalinus Clay: Effect of Confining Pressure, Sample Orientation, Sample Depth and Temperature. Paul Scherrer Institut, Villigen PSI, Switzerland.
- Waggener, W. C., 1958. Measurement of the absorption spectra of neptunium ions in heavy water solution from 0.35 to 1.85 μ . *Journal of Physical Chemistry* 62, 382-383.
- Wanner, H., Albinsson, Y., Karnl, O., Wieland, I., Wersin, P., and Charlet, L., 1994. The acid/base chemistry of montmorillonite. *Radiochimica Acta* 66/67, 733-738.
- Wescott, R. G., Lee, M. P., McCartin, T. J., Eisenberg, N. A., and Baca, R. G., 1995. NRC iterative performance assessment Phase 2: Development of capabilities for review of a performance assessment for a high-level waste repository. NUREG-1464. Nuclear Regulatory Commission, Washington, DC.
- Wilson, M. L., Gauthier, J. H., Barnard, R. W., Barr, G. E., Dockery, H. A., Dunn, E., Eaton, R. R., Guerin, D. C., Lu, N., Martinez, M. J., Nilson, R., Rautman, C. A., Robey, T. H., Ross, B., Ryder, E. E., Schenker, A. R., Shannon, S. A., Skinner, L. H., Halsey, W. G., Gansemer, J. D., Lewis, L. C., Lamont, A. D., Triay, I. R., Meijer, A., and Morris, D. E., 1994. Total-system performance assessment for Yucca mountain-SLN second iteration (TSPA-1993) volume 1 and 2. SAND93-2675. Sandia National Laboratories Albuquerque
- Wu, T., Amayri, S., Drebert, J., Loon, L. R. V., and Reich, T., 2009. Neptunium(V) Sorption and Diffusion in Opalinus Clay. *Environmental Science & Technology* 43, 6567-6571.
- Yariv, S. and Cross, H., 1979. *Geochemistry of Colloid Systems for Earth Sciences*. Chapter 2. Springer-Verlag.
- Zachara, J. M., P.L. Gassman, S.C. Smith, and D. Taylor 1995 Oxidation and adsorption of Co(II) EDTA²⁻ complexes in subsurface materials with iron and manganese oxides. *Geochim Cosmochim Acta* 59, 4449-4463.

- Zavarin, M. and Bruton, C. J., 2004a. A Non-Electrostatic Surface Complexation Approach to Modeling Radionuclide Migration at the Nevada Test Site: Aluminosilicates. Lawrence Livermore National Laboratory, Livermore.
- Zavarin, M. and Bruton, C. J., 2004b. A Non-Electrostatic Surface Complexation Approach to Modeling Radionuclide Migration at the Nevada Test Site: Iron Oxides and Calcite. Lawrence Livermore National Laboratory, Livermore.
- Zavarin, M., Carle, S. F., and Maxwell, R. M., 2004a. Upscaling Radionuclide Retardation - Linking the Surface Complexation and Ion Exchange Mechanistic Approach to a Linear Kd Approach. Lawrence Livermore National Laboratory, Livermore, California.
- Zavarin, M., Powell, B. A., Bourbin, M., Zhao, P., and Kersting, A. B., 2012. Np(V) and Pu(V) Ion Exchange and Surface-Mediated Reduction Mechanisms on Montmorillonite. *Environ. Sci. Technol.* 46, 2692-2698.
- Zavarin, M., Roberts, S. K., Hakem, N., Sawvel, A. M., and Kersting, A. B., 2005. Eu(III), Sm(III), Np(V), Pu(V), and Pu(IV) sorption to calcite. *Radiochimica Acta* 93, 93-102.
- Zavarin, M., Turner, G. D., and Westall, J. C., 2004b. FIT4FD. Modification of the Program FITEQL to Facilitate Rapid Evaluation of Complex Datasets, Livermore (CA).

Appendices

Appendix A

EMP standards and oxide detection limits for silicate analyses

Phlogopite (Synthetic): MgO = 0.02 wt.% , F = 0.11 wt.%

Albite (Amelia, NC, U.S.A, Rutherford mine): Na₂O = 0.02 wt.%

Labradorite (Chihuahua, Mexico): Al₂O₃ = 0.02 wt.%, SiO₂ = 0.02 wt.%, CaO = 0.01 wt.%

Tugtupite (Greenland): Cl = 0.01 wt.%

Adularia (St. Gotthard, Switzerland): K₂O = 0.01 wt.%

Titanite glass (Penn State): TiO₂ = 0.02 wt.%

Magnesiochromite (Synthetic): Cr₂O₃ = 0.04 wt.%

Rhodonite (unknown locality): MnO = 0.02 wt.%

Augite (unknown locality): FeO = 0.02 wt.%

Liebenbergite (synthetic): NiO = 0.06 wt.%

Gahnite: ZnO = 0.05 wt.%

Appendix B

Electron Microprobe Mineral Data

Fe-SAPONITE/CHLORITE

Oxide Abundance wt. %	SiO ₂	TiO ₂	Al ₂ O ₃	Cr ₂ O ₃	FeO*	MnO	MgO	NiO	ZnO	CaO	Na ₂ O	K ₂ O	F	Cl	Total
(6) Ave. EBS-2	33.96	0.02	12.83	1.35	30.94	0.38	1.95	1.34	0.03	1.32	1.62	0.61	0.13	0.41	86.66
<i>1σ</i>	3.48	0.03	0.97	1.39	3.53	0.15	0.34	0.93	0.02	0.67	0.27	0.29	0.09	0.29	0.60
Atoms per formula unit	Si	Ti	Al	Cr	Fe	Mn	Mg	Ni	Zn	Ca	Na	K	F	Cl	Sum
18 oxygen	4.87	0.00	2.17	0.16	3.74	0.05	0.42	0.16	0.00	0.20	0.45	0.11	0.06	0.10	12.32
<i>1σ</i>	0.49	0.01	0.20	0.26	0.88	0.03	0.11	0.17	0.00	0.16	0.09	0.08	0.07	0.11	0.40
12 oxygen	3.25	0.00	1.45	0.11	2.49	0.02	0.28	0.07	0.00	0.13	0.30	0.07	0.04	0.07	8.22

Table B1. EMPA of Fe-phyllsilicates grown on 304 SS plate during EBS-2. The Fe-phyllsilicates are a mixture of Fe-saponite and chlorite, therefore 18 oxygen (chlorite) and 12 oxygen (saponite) formula units were calculated.

SAPONITE

Oxide Abundance wt. %	SiO ₂	TiO ₂	Al ₂ O ₃	Cr ₂ O ₃	FeO*	MnO	MgO	NiO	ZnO	CaO	Na ₂ O	K ₂ O	F	Cl	Total
(8) Ave. EBS-6	36.20	0.01	12.95	0.02	33.99	0.22	0.83	0.01	0.01	0.67	0.98	0.32	0.03	0.04	86.24
<i>1σ</i>	0.81	0.01	0.95	0.01	0.89	0.10	0.04	0.01	0.01	0.18	0.39	0.17	0.03	0.03	1.71
Atoms per formula unit	Si	Ti	Al	Cr	Fe	Mn	Mg	Ni	Zn	Ca	Na	K	F	Cl	Sum
12 oxygen	3.42	0.00	1.44	0.00	2.69	0.02	0.12	0.00	0.00	0.07	0.18	0.04	0.01	0.01	7.974
<i>1σ</i>	0.15	0.00	0.20	0.00	0.10	0.00	0.20	0.00	0.00	0.04	0.17	0.05	0.02	0.01	0.110

Table B2. EMPA of Fe-saponite grown on low-carbon steel plates during EBS-6. There are other sulfides and oxides mixed within the saponite, therefore the atoms per formula unit should be considered as a guide and not the absolute saponite composition.

Pre-experiment clinoptilolite data

Oxide Abundance wt. %	SiO ₂	TiO ₂	Al ₂ O ₃	Cr ₂ O ₃	FeO*	MnO	MgO	NiO	ZnO	CaO	Na ₂ O	K ₂ O	F	Cl	Total
(9) Ave. mine run	71.28	0.01	12.6	0.01	0.09	0	0.3	0.01	0.01	0.95	4.57	0.2	0.02	0.00	90.03
<i>1σ</i>	2.19	0.01	0.33	0.01	0.02	0.01	0.34	0.01	0.01	0.63	1.31	0.13	0.04	0.00	2.21
Atoms per formula unit	Si	Ti	Al	Cr	Fe	Mn	Mg	Ni	Zn	Ca	Na	K	F	Cl	Sum
72 oxygen	30.02	0.00	6.26	0.00	0.03	0.03	0.19	0.00	0.00	0.43	3.73	0.11	0.03	0.00	40.78
<i>1σ</i>	0.06	0.00	0.04	0.00	0.00	0.00	0.07	0.00	0.00	0.10	0.35	0.02	0.02	0.00	0.2

Table B3. EMPA of clinoptilolite in the initial, unprocessed bentonite.

Post-experiment clinoptilolite data

Oxide Abundance wt. %	SiO ₂	TiO ₂	Al ₂ O ₃	Cr ₂ O ₃	FeO*	MnO	MgO	NiO	ZnO	CaO	Na ₂ O	K ₂ O	F	Cl	Total
(10) Ave. EBS-1	71.13	0.01	12.87	0.00	0.09	0.00	0.14	0.01	0.00	1.63	3.90	1.26	0.02	0.00	91.05
<i>1σ</i>	0.98	0.01	0.32	0.00	0.05	0.00	0.03	0.01	0.00	0.30	0.38	0.31	0.03	0.00	1.01
Atoms per formula unit	Si	Ti	Al	Cr	Fe	Mn	Mg	Ni	Zn	Ca	Na	K	F	Cl	Sum
72 oxygen	29.84	0.00	6.36	0.00	0.03	0.00	0.09	0.00	0.00	0.73	3.17	0.65	0.02	0.00	40.89
<i>1σ</i>	0.05	0.00	0.06	0.00	0.01	0.00	0.01	0.00	0.00	0.04	0.10	0.05	0.01	0.00	0.05

Table B4. EMPA of residual clinoptilolite in EBS-1 bentonite.

Analcime data

Oxide Abundance wt. %	SiO ₂	TiO ₂	Al ₂ O ₃	Cr ₂ O ₃	FeO*	MnO	MgO	NiO	ZnO	CaO	Na ₂ O	K ₂ O	F	Cl	Total
(10) Ave. EBS-5	69.96	0.00	19.29	0.01	0.17	0.01	0.01	0.00	0.00	1.89	4.47	0.07	0.07	0.02	95.95
<i>1σ</i>	0.76	0.01	0.25	0.01	0.04	0.01	0.02	0.01	0.01	0.18	0.23	0.02	0.04	0.02	0.57
Atoms per formula unit	Si	Ti	Al	Cr	Fe	Mn	Mg	Ni	Zn	Ca	Na	K	F	Cl	Sum
6 oxygen	2.33	0.00	0.76	0.00	0.01	0.00	0.00	0.00	0.00	0.07	0.29	0.00	0.01	0.00	3.45
<i>1σ</i>	0.04	0.00	0.05	0.00	0.00	0.00	0.00	0.00	0.00	0.03	0.06	0.00	0.01	0.00	0.04

Table B5. EMPA of authigenic analcime from EBS-5.

Appendix C

Solution Chemistry

Unfilter (UF) samples

Sample ID	1/0 UF	1/1 UF	1/2 UF	1/3 UF	1/4 UF	1/5 UF	1/6 UF	1/7 UF
Date analyzed	na	na	na	na	na	na	na	na
Date sampled		7/27/2011	8/1/2011	8/8/2011	8/11/2011	8/15/2011	8/22/2011	8/23/2011
Hours	0.00	23.55	144.00	308.90	381.80	479.30	645.00	670.00
Temp, C	25	118	121	120	212	212	300	22
pH	8.59	8.96	8.31	8.78	6.59	7.69	6.03	5.83
Al	<0.05	0.09(0)	<0.05	<0.05	0.38(1)	0.16(1)	1.10(0)	<0.05
B								
Ba	<0.05	0.09(0)	0.10(0)	0.12(0)	0.09(0)	0.14(0)	0.08(0)	0.02(0)
Br								
Ca	89(0)	35(0)	20(0)	19(0)	13(1)	11(0)	4(0)	10(0)
Cl	1045	1077	1131	1125	1225	1185	1128	1458
F	<0.2	<0.2	0.37	0.65	0.97	1.09	1.46	1.39
Fe	<0.5	<0.5	<0.5	<0.5	<0.5	1.1(0)	0.7(0)	<0.5
K	583(3)	457(0)	282(2)	203(1)	167(1)	152(1)	95(0)	37(0)
Li								
Mg								
Mn								
Na	167(2)	405(6)	590(15)	649(9)	640(10)	673(13)	590(10)	584(2)
NO2								
NO2-N								
NO3	<0.2	2.81	2.50	8.17	2.72	1.91	0.20	<0.2
NO3-N	<0.05	0.63	0.57	1.84	0.61	0.43	0.05	<0.05
PO4								
Si	1(0)	45(0)	88(1)	104(2)	286(1)	322(3)	550(1)	137(1)
SiO2	2(0)	97(0)	189(1)	223(4)	611(2)	689(7)	1176(3)	293(2)
SO4	47	64	109	352	154	155	59	201
Sr	0.05(0)	0.26(0)	0.25(0)	0.23(0)	0.13(0)	0.09(0)	<0.05	0.06(0)
Ti	<0.05	<0.05	<0.05	<0.05	0.09(1)	0.08(0)	0.11(0)	0.02(0)
Zn	<0.05	<0.05	<0.05	0.70	0.46(0)	0.41(0)	0.54(1)	0.04(0)
TDS	1934	2139	2326	2580	2816	2870	3056	2585
Cation	27	31	34	34	33	34	28	27
Anion	30	32	34	39	38	37	33	45
Balance	-0.07	-0.01	0.00	-0.07	-0.07	-0.04	-0.08	-0.26
Na/K	0.286	0.886	2.09	3.20	3.84	4.44	6.24	15.7

Sample ID	2/0 UF	2/1 UF	2/2 UF	2/3 UF	2/4 UF	2/5 UF	2/6 UF	2/7 UF
Date analyzed	na	na	na	na	na	na	na	na
Date sampled		7/27/2011	8/1/2011	8/8/2011	8/11/2011	8/15/2011	8/22/2011	8/22/2011
Hours	0.00	25	146	311	383	477	646	672
Temp, C	25	121	121	121	212	213	301	22
pH	8.59	7.91	8.54	7.70	6.77	6.44	6.16	6.21
Al	<0.05	0.05(1)	<0.05	<0.05	0.20(0)	0.14(2)	0.45(0)	3.50(5)
B								
Ba	<0.05	0.09(0)	0.08(0)	0.09(0)	0.09(0)	0.09(0)	0.09(0)	0.02(0)
Br								
Ca	89(0)	41(0)	20(0)	19(0)	19(0)	17(0)	4(0)	11(0)
Cl	1045	1067	1014	974	968	915	801	772
F	<0.2	<0.2	0.25	0.48	0.86	1.06	1.93	1.62
Fe	<0.5	<0.5	<0.5	<0.5	<0.5	<0.5	<0.5	<0.5
K	583(3)	468(0)	257(1)	167(0)	146(1)	117(1)	78(0)	44(1)
Li								
Mg								
Mn								
Na	167(2)	362(4)	536(3)	559(9)	563(14)	511(1)	428(7)	407(7)
NO2								
NO2-N								
NO3	<0.2	1.36	1.72	4.49	1.26	1.20	0.10	<0.2
NO3-N	<0.05	0.31	0.39	1.01	0.29	0.27	0.02	<0.05
PO4								
Si	1(0)	34(0)	76(0)	92(0)	262(1)	278(4)	510(2)	129(1)
SiO2	2(0)	73(0)	162(1)	196(0)	561(3)	596(9)	1092(4)	276(3)
SO4	47	64	105	115	115	197	40	114
Sr	0.05(0)	0.21(0)	0.16(0)	0.12(0)	0.09(0)	0.08(0)	<0.05	0.08(0)
Ti	<0.05	<0.05	<0.05	<0.05	0.09(0)	0.07(1)	0.10(0)	0.03(0)
Zn	<0.05	<0.05	0.63(1)	0.52(0)	0.67(0)	0.45(0)	0.64(1)	0.01(0)
TDS	1934	2077	2096	2036	2376	2356	2446	1629
Cation	27	30	31	29	29	26	21	20
Anion	30	31	31	30	30	30	23	24
Balance	-0.07	-0.03	0.00	-0.01	-0.01	-0.07	-0.06	-0.10
Na/K	0.286	0.774	2.09	3.36	3.84	4.37	5.48	9.16

Sample ID	3/0 UF	3/1 UF	3/2 UF	3/3 UF	3/4 UF	3/5 UF	3/6 UF
Date analyzed	na	05/10/12	05/10/12	05/10/12	05/10/12	05/15/12	05/10/12
Date sampled	na	3/22/2012	3/28/2012	4/4/2012	4/18/2012	4/25/2012	4/27/2012
Hours	0.00	72.3	215.2	388.6	719.6	912.1	935.2
Temp, C	25	120	121	120	212	303	22
pH	8.59	9.55	8.49	8.43	6.83	6.36	7.51
Al	<0.05	0.07(1)	<0.05	<0.05	0.45(1)	1.1(0)	12(0)
B		0.62(1)	1.55(1)	1.89(2)	8.68(1)	8(0)	7(0)
Ba	<0.05	<0.05	<0.05	0.06(1)	<0.05	<0.05	0.07(0)
Br		<0.2	<0.2	<0.2	<0.2	<0.2	<0.2
Ca	89(0)	15(1)	13(0)	12(0)	8(1)	3(0)	8(0)
Cl	1045	935	1200	873	868	744	782
F	<0.2	0.3	0.6	1.0	1.4	2.7	2.0
Fe	<0.5	<0.5	<0.5	<0.5	<0.5	<0.5	9(0)
K	583(3)	208(2)	181(1)	129(1)	86(1)	53(0)	21(0)
Li		0.22(0)	0.24(0)	0.31(0)	0.27(0)	0.25(1)	0.49(1)
Mg		<0.5	<0.5	<0.5	<0.5	<0.5	2.2
Mn		<0.05	<0.05	<0.05	<0.05	<0.05	<0.05
Na	167(2)	428(3)	585(7)	560(2)	516(2)	411(3)	534(7)
NO2		<0.2	<0.2	<0.2	<0.2	<0.2	<0.2
NO2-N		<0.06	<0.06	<0.06	<0.06	<0.06	<0.06
NO3	<0.2	1.6	0.9	<0.2	<0.2	<0.2	4.0
NO3-N	<0.05	0.35	0.20	<0.05	<0.05	<0.05	0.90
PO4		3	4	5	4	3	2
Si	1(0)	47(0)	70(1)	67(1)	242(6)	478(4)	156(2)
SiO2	2(0)	101(0)	150(1)	143(1)	518(13)	1022(8)	335(4)
SO4	47	90	145	131	130	44	154
Sr	0.05(0)	0.10(0)	0.12(0)	0.09(0)	<0.05	<0.05	0.06(0)
Ti	<0.05	<0.05	<0.05	<0.05	<0.05	<0.05	0.11(1)
Zn	<0.05	<0.05	<0.05	0.07(2)	<0.05	0.05(1)	0.06(1)
TDS	1934	2048	1949	1766	2530	2821	2261
Cation	27	25	31	28	25	20	26
Anion	30	28	37	27	28	22	26
Balance	-0.07	-0.07	-0.09	0.01	-0.05	-0.07	0.01
Na/K	0.286	2.06	3.24	4.33	5.99	7.71	24.9

Sample ID	4/0 UF	4/1 UF	4/2 UF	4/3 UF	4/4 UF	4/5 UF	4/6 UF	4/7 UF
Date analyzed	na	05/10/12	05/14/12	05/14/12	05/15/12	05/14/12	05/15/12	05/14/12
Date sampled	na	4/6/2012	4/12/2012	4/19/2012	4/26/2012	5/3/2012	5/10/2012	5/11/2012
Hours	0.00	42.7	186.7	355.5	523.3	690.9	858.7	884.8
Temp, C	25	120	120	119	212	212	305	1
pH	8.59	8.62	7.68	6.93	6.08	6.09	6.25	7.43
Al	<0.05	6.76(3)	1(0)	33(1)	1.0(0)	4(0)	1.1(0)	22(1)
B		0.67(2)	0.33(1)	1(0)	9(0)	8(0)	9(0)	8(0)
Ba	<0.05	0.13(0)	0.10(0)	0.21(1)	<0.05	0.07(0)	<0.05	0.12(1)
Br		<0.2	<0.2	<0.2	<0.2	<0.2	<0.2	<0.2
Ca	89(0)	16(1)	14(0)	21(0)	8(0)	9(0)	4(0)	15(0)
Cl	1045	1224	1257	1283	1271	1278	1169	1297
F	<0.2	0.6	0.6	0.9	0.8	0.5	1.4	1.7
Fe	<0.5	<0.5	1(0)	17(1)	<0.5	2(0)	<0.5	13(0)
K	583(3)	252(5)	182(1)	153(2)	112(1)	107(1)	91(1)	54(0)
Li		0.07(1)	0.11(1)	0.17(0)	0.21(1)	0.23(0)	0.29(1)	0.60(0)
Mg		1.3(0)	0.7(0)	7.5(6)	<0.5	0.8(0)	<0.5	5.5(3)
Mn		<0.05	<0.05	0.07(0)	<0.05	<0.05	<0.05	0.09(0)
Na	167(2)	598(8)	650(7)	683(6)	706(3)	673(6)	618(5)	789(2)
NO2		<0.2	<0.2	<0.2	<0.2	<0.2	<0.2	<0.2
NO2-N		<0.06	<0.06	<0.06	<0.06	<0.06	<0.06	<0.06
NO3	<0.2	1.6	0.4	0.3	<0.2	<0.2	<0.2	<0.2
NO3-N	<0.05	0.35	0.10	0.06	<0.05	<0.05	<0.05	<0.05
PO4		4	3	3	3	3	2	<0.2
Si	1(0)	85(1)	80(1)	218(11)	305(1)	303(2)	539(2)	291(4)
SiO2	2(0)	181(2)	171(1)	466(23)	652(2)	648(5)	1154(3)	624(9)
SO4	47	97	128	157	190	193	51	232
Sr	0.05(0)	0.22(0)	0.19(0)	0.30(0)	0.10(0)	0.10(0)	<0.05	0.25(0)
Ti	<0.05	0.07(0)	<0.05	0.30(1)	<0.05	<0.05	<0.05	0.19(2)
Zn	<0.05	0.08(2)	0.01(1)	0.06(1)	<0.05	0.05(2)	0.12(2)	0.08(2)
TDS	1934	1159	2197	1544	1682	1649	1933	1766
Cation	27	34	34	40	34	33	30	40
Anion	30	37	38	40	40	40	34	42
Balance	-0.07	-0.04	-0.06	0.00	-0.08	-0.10	-0.08	-0.02
Na/K	0.286	2.37	3.58	4.46	6.29	6.27	6.80	14.6

Sample ID	5/0 UF**	5/1 UF**	5/2 UF	5/3 UF	5/4 UF	5/5 UF	5/6 UF	5/7 UF
Date analyzed	7/27/2012	8/01/2012	7/27/2012	7/27/2012	7/27/2012	8/07/2012	8/21/2012	8/21/2012
Date sampled	7/2/2012	7/5/2012	7/12/2012	7/19/2012	7/26/2012	8/2/2012	8/14/2012	8/15/2012
Hours	0	72.95	242.05	411.53	578.87	747.68	1033.18	1041.47
Temp, C	10	302	303	302	302	302	302	18
pH	NA	5.81	5.75	5.84	5.84	6	5.92	NA
Al	<0.1	1.42(1)	<0.1	<0.1	<0.1	1.0(0)	0.9(0)	0.1(0)
B	0.18(0)	7.93(7)	9.98(2)	9.67(1)	10.42(1)	11(0)	8(0)	7(0)
Ba	<0.01	<0.1	<0.1	<0.1	<0.1	<0.1	<0.1	<0.1
Br	<0.2	<0.2	<0.2	<0.2	<0.2	<0.2	<0.2	<0.2
Ca	108(1)	3(0)	11.8(1)	<1	11.1(1)	8(0)	8(2)	19(1)
Cl	931	932	865	866	1186	1071	1052	1278
F	<0.2	1.47	<0.2	<0.2	<0.2	1.9	3.5	1.3
Fe	<1	<1	<1	<1	<1	<1	<1	<1
K	663(5)	92(1)	94(0)	88(0)	87(0)	78(1)	62(1)	49(0)
Li	<0.1	0.32(1)	<0.1	<0.1	<0.1	0.35(0)	<0.1	<0.1
Mg	<1	<1	<1	<1	<1	<1	<1	<1
Mn	<0.1	<0.1	<0.1	<0.1	<0.1	<0.1	<0.1	<0.1
Na	197(1)	613(3)	684(2)	676(1)	742(1)	636(8)	584(16)	776(6)
NO2	<0.2	<0.2	<0.2	<0.2	<0.2	<0.2	<0.2	<0.2
NO2-N	<0.06	<0.06	<0.06	<0.06	<0.06	<0.06	<0.06	<0.06
NO3	<0.2	<0.2	<0.2	<0.2	<0.2	<0.2	2.3	53.1
NO3-N	<0.05	<0.05	<0.05	<0.05	<0.05	<0.05	0.51	12
PO4	<0.2	<0.2	<0.2	<0.2	<0.2	<0.2	<0.2	<0.2
Si	<1.0	525(2)	558(1)	551(0)	554(0)	489(4)	507(9)	81(1)
SiO2	<2.14	1125(3)	1194(2)	1178(1)	1185(1)	1046(8)	1084(19)	173(1)
SO4	45.75	59	42	39	46	50	47	362
Sr	<0.1	<0.1	<0.1	<0.1	<0.1	<0.1	<0.1	<0.1
Ti	<0.2	<0.2	<0.2	<0.2	<0.2	<0.2	<0.2	<0.2
Zn	<0.1	<0.1	<0.1	<0.1	<0.1	0.17(2)	0.99(13)	0.72(2)
TDS	1946	2836	2901	2856	3266	2902	2853	2719
Cation	30	29	33	32	35	30	27	36
Anion	27	27	26	26	35	32	31	45
Balance	0.06	0.02	0.12	0.10	0.00	-0.03	-0.06	-0.11
Na/K	0.298	6.65	7.31	7.71	8.57	8.20	9.49	15.9

Sample ID	6/0 UF**	6/1 UF**	6/2 UF	6/3 UF	6/4 UF	6/5 UF	6/6 UF	6/7 UF	6/8 UF
Date analyzed	7/27/2012	7/27/2012	7/27/2012	7/27/2012	7/27/2012	8/07/2012	8/07/2012	8/21/2012	8/21/2012
Date sampled	7/2/2012	7/5/2012	7/12/2012	7/19/2012	7/26/2012	8/2/2012	8/6/2012	8/9/2012	8/10/2012
Hours	0	46.63	216.45	382.85	550.83	718.63	822.27	888.15	911.13
Temp, C	25	119	120	119	218	218	298	300	25
pH	9.52	9.43	6.98	7.13	6.12	6.34	6.13	6.47	6.45
Al	<0.1	<0.1	<0.1	<0.1	<0.1	0.4(0)	1.5(0)	1.6	1.5(0)
B	<0.1	1.4(0)	<0.1	2.76(1)	9.58(2)	12(0)	10(0)	7	7(0)
Ba	0.01(0)	<0.1	<0.1	<0.1	<0.1	<0.1	<0.1	<0.1	<0.1
Br	<0.2	<0.2	<0.2	<0.2	<0.2	<0.2	<0.2	<0.2	<0.2
Ca	102(3)	60(0)	51.4(1)	36.8(1)	15.3(1)	11(0)	8(0)	7	9(1)
Cl	362	301	396	410	541	583	509	507	489
F	<0.2	<0.2	<0.2	<0.2	<0.2	1.7	5.1	4.9	3.9
Fe	<1	<1	<1	<1	<1	<1	<1	<1	4(0)
K	8(0)	13(0)	<1	<1	<1	26(1)	13(0)	<1	<1
Li	<0.1	<0.1	<0.1	<0.1	<0.1	0.19(2)	0.12(1)	<0.1	<0.1
Mg	<1	<1	<1	<1	<1	<1	<1	<1	<1
Mn	<0.1	<0.1	<0.1	<0.1	<0.1	<0.1	<0.1	<0.1	<0.1
Na	187(4)	254(0)	383(1)	495(0)	478(1)	461(9)	350(5)	288	328(4)
NO2	<0.2	<0.2	<0.2	<0.2	<0.2	<0.2	<0.2	<0.2	<0.2
NO2-N	<0.06	<0.06	<0.06	<0.06	<0.06	<0.06	<0.06	<0.06	<0.06
NO3	<0.2	<0.2	70.2	<0.2	<0.2	<0.2	<0.2	<0.2	<0.2
NO3-N	<0.05	<0.05	15.84	<0.05	<0.05	<0.05	<0.05	<0.05	<0.05
PO4	<0.2	<0.2	<0.2	<0.2	<0.2	<0.2	<0.2	<0.2	<0.2
Si	<1	17(0)	24.5(0)	39.3(0)	272(0)	288(0)	543(7)	494	198(4)
SiO2	<2.14	36(0)	52(0)	84(0)	583(1)	617(0)	1161(15)	1058	424(8)
SO4	43	61	119	179	212	269	134	130	221
Sr	<0.1	<0.1	<0.1	<0.1	<0.1	<0.1	<0.1	<0.1	<0.1
Ti	<0.2	<0.2	<0.2	<0.2	<0.2	<0.2	<0.2	<0.2	<0.2
Zn	<0.1	<0.1	<0.1	<0.1	<0.1	<0.1	0.13(2)	0.61(5)	1.05(2)
TDS	702	701	1072	1208	1839	1982	2190	2004	1489
Cation	13	14	19	23	22	21	16	13	15
Anion	11	10	15	15	20	23	18	18	19
Balance	0.10	0.18	0.12	0.21	0.03	-0.03	-0.05	-0.15	-0.11
Na/K	22.9	19.3	na	na	na	17.6	27.9	na	na

Sample ID	7/0 UF	7/1 UF	7/2 UF	7/3 UF	7/4 UF	7/5 UF	7/6 UF	7/7 UF
Date analyzed	8/21/12	8/23/2012	2/25/2013	2/25/2013	2/25/2013	2/25/2013	2/25/2013	2/25/2013
Date sampled		8/22/2012	8/30/2012	9/6/2012	9/13/2012	9/20/2012	9/27/2012	9/28/2012
Hours	0	50.63	235.82	403.43	571.77	739.68	907.45	936.27
Temp, C	25	119	120	120	211	211	303	22
pH	6.69	9.64	8.33	7.44	6.33	6.2	6.17	6.16
Al	<0.1	0.35(0)	0.18(0)	0.14(1)	0.84(0)	0.58(0)	2.86(2)	0.75(2)
B	<0.1	1.3(0)	0.9(9)	2(0)	6(0)	7(0)	7(0)	7(0)
Ba	<0.1	0.3	<0.05	<0.05	<0.05	<0.05	<0.05	<0.05
Br	<0.2	<0.2	<0.5	<0.5	<0.5	<0.5	<0.5	<0.5
Ca	96(1)	34(1)	30(1)	25(0)	9(0)	7(0)	5(0)	8(1)
Cl	477	538	541	578	559	538	512	537
F	<0.2	<0.2	<0.5	<0.5	<0.5	<0.5	<0.5	<0.5
Fe	<1	<1	<0.5	<0.5	<0.5	<0.5	<0.5	0.8
K	<1	7(0)	13(0)	9(0)	11(0)	10(0)	10(0)	6(0)
Li	<0.1	<0.1	<0.05	<0.05	0.09(1)	0.11(1)	0.12(0)	0.23(1)
Mg	<1	<1	<0.5	<0.5	<0.5	<0.5	<0.5	<0.5
Mn	<0.1	<0.1	<0.05	<0.05	<0.05	<0.05	<0.05	<0.05
Na	153(1)	250(1)	335(4)	382(2)	378(0)	366(3)	298(2)	380(2)
NO2	<0.2	<0.2	<0.5	<0.5	<0.5	<0.5	<0.5	<0.5
NO2-N	<0.06	<0.06	<0.15	<0.15	<0.15	<0.15	<0.15	<0.15
NO3	<0.2	1.4	<0.5	<0.5	<0.5	<0.5	<0.5	<0.5
NO3-N	<0.05	0.31	<0.11	<0.11	<0.11	<0.11	<0.11	<0.11
PO4	<0.2	<0.2	<0.5	<0.5	<0.5	<0.5	<0.5	<0.5
Si	2(0)	16(0)	32(1)	48(0)	165(1)	235(2)	451(5)	264(3)
SiO2	5(0)	34(0)	69(3)	102(1)	353(2)	502(3)	965(11)	566(6)
SO4	46	68	128	187	221	215	134	221
Sr	<0.1	0.13	0.11	0.10	<0.05	<0.05	<0.05	<0.05
Ti	<0.2	<0.2	<0.1	<0.1	<0.1	<0.1	<0.1	<0.1
Zn	0.28	0.82	<0.05	<0.05	<0.05	<0.05	<0.05	<0.05
TDS	777	936	1118	1285	1538	1646	1934	1726
Cation	11	13	16	18	17	17	14	17
Anion	14	17	18	20	21	20	18	20
Balance	-0.11	-0.13	-0.04	-0.06	-0.09	-0.09	-0.12	-0.08
Na/K	na	38.3	26.0	44.2	35.8	37.0	30.2	66.5

Sample ID	8/0 UF	8/1 UF	8/2 UF	8/3 UF	8/4 UF	8/5 UF	8/6 UF	8/7 UF	8/8 UF
Date analyzed	8/21/2012	8/23/2012	2/25/2013	2/25/2013	2/25/2013	2/25/2013	2/25/2013	2/25/2013	02/25/13
Date sampled		8/23/2012	8/30/2012	9/6/2012	9/13/2012	9/20/2012	9/27/2012	10/4/2012	10/5/12 9:30
Hours	0	25.03	194.08	361.27	531.22	698.65	864.73	1033.13	1058.03
Temp, C	25	309	310	310	309	309	310	309	21
pH	6.69	6.16	6.07	6.02	6.06	6.16	6.17	6.13	5.91
Al	<0.1	2.94(5)	0.77(1)	1.49(1)	1.13(2)	1.04(1)	1.11(2)	1.22(1)	2.86(26)
B	<0.1	9.5(1)	8.3(0)	7.2(1)	7.1(1)	6.9(1)	6.6(0)	7.2(1)	4.9(0)
Ba	<0.1	<0.1	<0.05	<0.05	<0.05	<0.05	<0.05	<0.05	<0.05
Br	<0.2	<0.2	<0.5	<0.5	<0.5	<0.5	<0.5	<0.5	---
Ca	96(1)	7(1)	4(0)	4(0)	3(0)	4(0)	3(0)	4(0)	17(0)
Cl	477	509	489	452	434	414	406	392	306
F	<0.2	<0.2	<0.5	<0.5	<0.5	<0.5	<0.5	<0.5	---
Fe	<1	<1	<0.5	<0.5	<0.5	<0.5	<0.5	<0.5	5
K	<1	7(0)	11(0)	10(0)	11(0)	12(0)	13(0)	15(0)	12(0)
Li	<0.1	<0.1	0.13(1)	0.14(1)	0.16(1)	0.17(1)	0.18(1)	0.18(2)	0.22(2)
Mg	<1	<1	<0.5	<0.5	<0.5	<0.5	<0.5	0.8(2)	2.2(1)
Mn	<0.1	<0.1	<0.05	<0.05	<0.05	<0.05	<0.05	<0.05	<0.05
Na	153(1)	264(2)	263(1)	248(4)	237(1)	229(0)	222(1)	209(2)	204(1)
NO2	<0.2	<0.2	<0.5	<0.5	<0.5	<0.5	<0.5	<0.5	---
NO2-N	<0.06	<0.06	<0.15	<0.15	<0.15	<0.15	<0.15	<0.15	---
NO3	<0.2	0.94	<0.5	<0.5	<0.5	<0.5	<0.5	<0.5	---
NO3-N	<0.05	0.21	<0.11	<0.11	<0.11	<0.11	<0.11	<0.11	---
PO4	<0.2	<0.2	<0.5	<0.5	<0.5	<0.5	<0.5	<0.5	---
Si	2(0)	463(6)	408(1)	499(4)	462(5)	289(2)	500(3)	491(8)	353(0)
SiO2	5(0)	990(12)	874(3)	1068(8)	988(10)	619(4)	1069(6)	1050(17)	754(1)
SO4	46	19	58	69	85	90	93	98	190
Sr	<0.1	<0.1	<0.05	<0.05	<0.05	<0.05	<0.05	<0.05	0.10
Ti	<0.2	<0.2	<0.1	<0.1	<0.1	<0.1	<0.1	<0.1	<0.1
Zn	0.28	1.00	<0.05	<0.05	<0.05	<0.05	<0.05	<0.05	<0.05
TDS	777	1811	1710	1859	1767	1376	1814	1778	1497
Cation	11	12	12	11	11	11	10	10	11
Anion	14	15	15	14	14	14	14	13	13
Balance	-0.11	-0.10	-0.12	-0.12	-0.14	-0.13	-0.14	-0.15	-0.08
Na/K	na	36.7	23.0	25.6	21.1	19.2	17.6	14.1	17.5

Sample ID	9/0 UF	9/1 UF	9/2 UF	9/3 UF	9/4 UF	9/5 UF	9/6 UF	9/7 UF	9/8 UF
Date analyzed	2/25/2013	2/25/2013	2/25/2013	2/25/2013	2/25/2013	2/25/2013	2/25/2013	2/25/2013	2/25/2013
Date sampled		11/1/2012	11/8/2012	11/15/2012	11/21/2012	11/29/2012	12/4/2012	12/10/2012	12/11/2012
Hours	0	23.75	192.65	360.62	504.23	696.25	817.17	960.02	984.33
Temp, C	25	121	121	121	210	210	300	300	20
pH	7.16	8.98		7.2	6.55	6.39	6.28	6.13	6.54
Al	0.11(0)	0.26(0)	0.47(0)	0.43(0)	0.73(0)	0.69(1)	2.33(1)	2.22(1)	1.09(1)
B	0.9(0)	0.4(0)	0.8(0)	1.6(0)	5.6(0)	7.4(0)	7.0(1)	7.1(1)	6.8(0)
Ba	<0.05	<0.05	<0.05	<0.05	<0.05	<0.05	<0.05	<0.05	<0.05
Br	<0.5	<0.5	<0.5	<0.5	<0.5	<0.5	<0.5	<0.5	<0.5
Ca	96(1)	15(0)	18(0)	16(0)	8(0)	8(1)	5(0)	4(0)	7(0)
Cl	526	574	577	576	600	592	536	540	546
F	<0.5	<0.5	<0.5	<0.5	<0.5	<0.5	<0.5	<0.5	<0.5
Fe	<0.5	<0.5	<0.5	<0.5	<0.5	<0.5	<0.5	<0.5	<0.5
K	10(0)	6(0)	7(0)	8(0)	9(0)	13(0)	11(0)	12(0)	11(0)
Li	<0.05	<0.05	<0.05	0.06(0)	0.09(1)	0.10(0)	0.09(1)	0.11(1)	0.23(2)
Mg	<0.5	<0.5	<0.5	<0.5	<0.5	<0.5	<0.5	<0.5	0.7
Mn	<0.05	<0.05	<0.05	<0.05	<0.05	<0.05	<0.05	<0.05	<0.05
Na	175(2)	362(1)	398(5)	424(4)	409(2)	404(2)	331(0)	332(2)	374(2)
NO2	<0.5	<0.5	<0.5	<0.5	<0.5	<0.5	<0.5	<0.5	<0.5
NO2-N	<0.15	<0.15	<0.15	<0.15	<0.15	<0.15	<0.15	<0.15	<0.15
NO3	<0.5	<0.5	<0.5	<0.5	<0.5	<0.5	<0.5	<0.5	<0.5
NO3-N	<0.11	<0.11	<0.11	<0.11	<0.11	<0.11	<0.11	<0.11	<0.11
PO4	<0.5	<0.5	<0.5	<0.5	<0.5	<0.5	<0.5	<0.5	<0.5
Si	1.1(1)	18(0)	38(0)	55(0)	188(1)	255(1)	473(2)	508(2)	445(2)
SiO2	2(0)	38(0)	81(1)	118(1)	403(1)	545(2)	1013(4)	1088(5)	953(4)
SO4	55	131	172	222	246	248	163	150	232
Sr	<0.05	0.09	0.09	0.08	<0.05	<0.05	<0.05	<0.05	<0.05
Ti	<0.1	<0.1	<0.1	<0.1	<0.1	<0.1	<0.1	<0.1	<0.1
Zn	<0.05	<0.05	<0.05	<0.05	<0.05	<0.05	<0.05	<0.05	<0.05
TDS	865	1126	1255	1366	1682	1818	2069	2135	2132
Cation	13	17	18	19	18	18	15	15	17
Anion	16	19	20	21	22	22	19	19	20
Balance	-0.12	-0.06	-0.04	-0.04	-0.09	-0.09	-0.11	-0.10	-0.09
Na/K	18.0	62.7	54.6	53.8	45.1	31.6	29.5	28.5	33.9

Sample ID	10/0 UF	10/1 UF	10/2 UF	10/3 UF	10/4 UF	10/5 UF	10/6 UF	10/7 UF	10/8 UF
Date analyzed	3/05/2013	3/05/2013	3/05/2013	3/05/2013	3/05/2013	3/05/2013	3/05/2013	4/21/2013	4/21/2013
Date sampled		1/18/2013	1/24/2013	1/31/2013	2/7/2013	2/15/2013	2/21/2013	2/28/2013	2/28/2013
Hours	0	46.97	191.48	359.32	527.43	719.35	863.02	1031.35	1032.72
Temp, C	21	299	299	299	299	299	299	300	21
pH	6.36	6.45	6.00	6.21	6.57	6.27	6.53	6.39	6.30
Al	0.12(0)	1.54(2)	0.96(0)	0.93(0)	0.92(1)	0.86(0)	0.79(0)	1.28(1)	0.60(1)
B	1(0)	6(0)	10(0)	10(0)	10(0)	10(0)	10(1)	8(0)	6(0)
Ba	<0.05	<0.05	<0.05	<0.05	<0.05	<0.05	<0.05	<0.05	<0.05
Br	<0.5	<0.5	<0.5	<0.5	<0.5	<0.5	<0.5	<0.5	<0.5
Ca	43(2)	9(1)	7(0)	7(0)	7(0)	8(1)	9(0)	6(0)	25(0)
Cl	686	696	691	684	676	674	675	628	510
F	<0.5	<0.5	<0.5	<0.5	<0.5	<0.5	<0.5	<0.5	<0.5
Fe	<0.5	<0.5	<0.5	<0.5	<0.5	<0.5	<0.5	<0.5	<0.5
K	299(12)	148(1)	50(1)	32(1)	27(0)	33(0)	29(2)	31(0)	26(0)
Li	<0.05	<0.05	0.07(0)	0.08(0)	0.08(0)	0.08(0)	0.09(0)	0.20(0)	0.22(1)
Mg	<0.5	<0.5	<0.5	<0.5	<0.5	<0.5	<0.5	<0.5	<0.5
Mn	<0.05	<0.05	<0.05	<0.05	<0.05	<0.05	<0.05	<0.05	<0.05
Na	162(5)	369(4)	429(4)	443(8)	430(3)	458(4)	413(28)	396(1)	320(2)
NO2	<0.5	<0.5	<0.5	<0.5	<0.5	<0.5	<0.5	<0.5	<0.5
NO2-N	<0.15	<0.15	<0.15	<0.15	<0.15	<0.15	<0.15	<0.15	<0.15
NO3	<0.5	<0.5	<0.5	<0.5	<0.5	<0.5	<0.5	23.6	<0.5
NO3-N	<0.11	<0.11	<0.11	<0.11	<0.11	<0.11	<0.11	5.33	<0.11
PO4	<0.5	<0.5	<0.5	<0.5	<0.5	<0.5	<0.5	<0.5	<0.5
Si	2(0)	268(4)	432(3)	487(8)	499(0)	526(5)	513(28)	499(1)	321(2)
SiO2	3(0)	574(9)	925(6)	1043(16)	1068(0)	1125(12)	1097(60)	1068(3)	687(4)
SO4	31	42	87	95	115	124	124	188	198
Sr	<0.05	<0.05	<0.05	<0.05	<0.05	<0.05	<0.05	<0.05	0.17
Ti	<0.1	<0.1	<0.1	<0.1	<0.1	<0.1	<0.1	<0.1	<0.1
Zn	0.29	<0.05	0.22	<0.05	0.08	0.15	<0.05	<0.05	<0.05
TDS	1226	1846	2199	2315	2334	2433	2358	2351	1772
Cation	17	20	20	21	20	21	19	18	16
Anion	20	21	22	22	22	22	22	22	19
Balance	-0.09	-0.01	-0.03	-0.03	-0.05	-0.02	-0.07	-0.10	-0.08
Na/K	0.542	2.50	8.67	13.9	15.7	13.9	14.1	12.6	12.5

Sample ID	11/0 UF	11/1 UF	11/2 UF	11/3 UF	11/4 UF	11/5 UF	11/6 UF	11/7 UF	11/8 UF
Date analyzed	3/05/2013	2/26/2013	2/26/2013	2/26/2013	2/26/2013	4/21/2013	4/21/2013	4/21/2013	4/21/2013
Date sampled		2/1/2013	2/7/2013	2/14/2013	2/21/2013	2/28/2013	3/7/2013	3/14/2013	3/29/2013
Hours	0	48.58	194.05	360.87	530.40	697.15	863.02	1031.35	1032.72
Temp, C	21	300	299	300	300	300	300	300	300
pH	6.36	5.85	6.07	6.03	5.97	6.03	5.86	6.06	5.94
Al	0.12(0)	3.47(4)	2.60(1)	2.68(13)	1.85(1)	1.69(2)	1.57(2)	1.34(1)	0.17(1)
B	1(0)	9.2(0)	8.6(4)	8.7(5)	8.2(1)	8.4(0)	6.9(1)	6.7(0)	7.1(1)
Ba	<0.05	<0.05	<0.05	<0.05	<0.05	<0.05	<0.05	<0.05	<0.05
Br	<0.5	<0.5	<0.5	<0.5	<0.5	<0.5	<0.5	<0.5	<0.5
Ca	43(2)	4(1)	4(0)	5(0)	4(0)	6(1)	6(1)	6(1)	31(0)
Cl	686	714	723	719	722	710	730	727	724
F	<0.5	<0.5	<0.5	<0.5	<0.5	<0.5	<0.5	<0.5	<0.5
Fe	<0.5	<0.5	<0.5	<0.5	<0.5	<0.5	<0.5	<0.5	<0.5
K	299(12)	63(2)	31(1)	31(2)	29(1)	36(0)	32(0)	31(0)	30(0)
Li	<0.05	0.19(1)	0.20(1)	0.20(0)	0.21(1)	0.32(2)	0.23(0)	0.23(2)	0.28(1)
Mg	<0.5	<0.5	<0.5	<0.5	<0.5	<0.5	<0.5	<0.5	<0.5
Mn	<0.05	<0.05	<0.05	<0.05	<0.05	<0.05	<0.05	<0.05	<0.05
Na	162(5)	379(12)	412(11)	430(27)	417(5)	453(0)	430(5)	413(0)	472(2)
NO2	<0.5	<0.5	<0.5	<0.5	<0.5	<0.5	<0.5	<0.5	<0.5
NO2-N	<0.15	<0.15	<0.15	<0.15	<0.15	<0.15	<0.15	<0.15	<0.15
NO3	<0.5	<0.5	<0.5	<0.5	<0.5	<0.5	<0.5	<0.5	<0.5
NO3-N	<0.11	<0.11	<0.11	<0.11	<0.11	<0.11	<0.11	<0.11	<0.11
PO4	<0.5	<0.5	<0.5	<0.5	<0.5	<0.5	<0.5	<0.5	<0.5
Si	2(0)	436(7)	488(21)	520(38)	504(9)	493(4)	540(4)	504(4)	337(5)
SiO2	3(0)	933(15)	1045(45)	1113(81)	1079(19)	1054(9)	1156(8)	1078(9)	720(11)
SO4	31	95	162	174	179	186	203	193	271
Sr	<0.05	<0.05	<0.05	<0.05	<0.05	<0.05	<0.05	<0.05	0.38(0)
Ti	<0.1	<0.1	<0.1	<0.1	<0.1	<0.1	<0.1	<0.1	<0.1
Zn	0.29	0.18(5)	<0.05	0.09(3)	<0.05	<0.05	<0.05	<0.05	<0.05
TDS	1226	2202	2387	2482	2439	2455	2565	2456	2257
Cation	17	19	19	20	19	21	20	19	23
Anion	20	23	24	24	24	24	25	25	26
Balance	-0.09	-0.09	-0.11	-0.10	-0.12	-0.07	-0.11	-0.13	-0.07
Na/K	0.542	6.00	13.5	14.1	14.5	12.7	13.4	13.1	16.0

Filtered (F) Samples

Sample ID	1/0 F	1/1 F	1/2 F	1/3 F	1/4 F	1/5 F	1/6 F	1/7 F
Date analyzed	na	na	na	na	na	na	na	na
Date sampled		7/27/2011	8/1/2011	8/8/2011	8/11/2011	8/15/2011	8/22/2011	8/23/2011
Time, hrs	0.00	23.55	144.00	308.90	381.80	479.30	645.00	670.00
Temp, C	25	118	121	120	212	212	300	22
pH	8.59	8.96	8.31	8.78	6.59	7.69	6.03	5.83
Al	<0.05	0.06(2)	<0.05	<0.05	0.39(0)	0.15(1)	1.46(1)	<0.05
B								
Ba	<0.05	0.09(0)	0.10(0)	0.12(0)	0.10(0)	0.09(0)	0.08(0)	0.02(0)
Ca	89(0)	33(0)	18(0)	17(0)	14(0)	12(0)	3(0)	10(0)
Fe	<0.5	<0.5	<0.5	<0.5	<0.5	1.0(0)	<0.5	<0.5
K	583(3)	458(0)	276(1)	207(2)	174(1)	155(1)	98(1)	37(0)
Li								
Mg								
Mn								
Na	167(2)	403(3)	581(0)	687(8)	683(1)	690(5)	647(4)	584(2)
Si	1(0)	46(0)	87(1)	102(0)	296(2)	322(3)	584(1)	137(1)
SiO2	2(0)	98(1)	186(0)	217(1)	634(5)	690(6)	1250(2)	293(2)
Sr	0.05(0)	0.25(0)	0.24(0)	0.23(0)	0.13(0)	0.09(0)	<0.05	0.06(0)
Ti	<0.05	<0.05	<0.05	<0.05	0.07(0)	0.07(1)	0.11(1)	0.02(0)
Zn	<0.05	<0.05	<0.05	0.57(0)	0.60(0)	0.50(0)	0.52(0)	0.04(0)
Na/K	0.286	0.878	2.10	3.32	3.92	4.44	6.62	15.7

Sample ID	2/0 F	2/1 F	2/2 F	2/3 F	2/4 F	2/5 F	2/6 F	2/7 F
Date analyzed	na	na	na	na	na	na	na	na
Date sampled		7/27/2011	8/1/2011	8/8/2011	8/11/2011	8/15/2011	8/22/2011	8/22/2011
Time, hrs	0.00	25	146	311	383	477	646	672
Temp, C	25	121	121	121	212	213	301	22
pH	8.59	7.91	8.54	7.70	6.77	6.44	6.16	6.21
Al	<0.05	0.07(1)	<0.05	<0.05	0.16(1)	0.12(1)	0.47(0)	3.50(5)
B								
Ba	<0.05	0.08(0)	0.09(0)	0.09(0)	0.10(0)	0.10(0)	0.09(0)	0.02(0)
Ca	89(0)	39(1)	18(1)	18(0)	18(0)	17(0)	5(0)	11(0)
Fe	<0.5	<0.5	<0.5	<0.5	<0.5	<0.5	<0.5	<0.5
K	583(3)	469(7)	254(4)	170(1)	149(0)	119(2)	84(0)	44(1)
Li								
Mg								
Mn								
Na	167(2)	362(4)	540(7)	575(3)	568(12)	521(2)	452(1)	407(7)
Si	1(0)	34(0)	76(1)	94(1)	274(1)	284(3)	546(1)	129(1)
SiO2	2(0)	73(1)	164(2)	202(3)	586(3)	608(7)	1168(2)	276(3)
Sr	0.05(0)	0.20(0)	0.18(0)	0.12(0)	0.09(0)	0.08(0)	<0.05	0.08(0)
Ti	<0.05	<0.05	<0.05	<0.05	0.07(0)	0.07(0)	0.12(2)	0.03(0)
Zn	<0.05	<0.05	0.35(0)	0.44(0)	0.68(2)	0.40(1)	0.48(0)	0.01(0)
Na/K	0.286	0.773	2.13	3.39	3.82	4.38	5.40	9.16

Sample ID	3/1 F	3/2 F	3/3 F	3/4 F	3/5 F	3/6 F
Date analyzed	05/10/12	05/10/12	05/10/12	05/10/12	05/15/12	05/10/12
Date sampled	3/22/2012	3/28/2012	4/4/2012	4/18/2012	4/25/2012	4/27/2012
Hours	72.3	215.2	388.6	719.6	912.1	935.2
Temp, C	120	121	120	212	303	22
pH	9.55	8.49	8.43	6.83	6.36	7.51
Al	0.08(0)	<0.05	<0.05	0.44(0)	0.9	<0.05
B	0.61(1)	1.47(3)	3.40(4)	9.02(7)	8(0)	7(0)
Ba	0.10(0)	<0.05	0.08(0)	<0.05	<0.05	<0.05
Ca	12(0)	12(0)	12(0)	8(0)	4(0)	7(0)
Fe	<0.5	<0.5	<0.5	<0.5	<0.5	<0.5
K	202(3)	176(0)	134(1)	93(1)	58(1)	21(0)
Li	0.21(0)	0.23(0)	0.34(0)	0.31(0)	0.28(1)	0.51(0)
Mg	<0.5	<0.5	<0.5	<0.5	<0.5	<0.5
Mn	<0.05	<0.05	<0.05	<0.05	<0.05	<0.05
Na	422(4)	579(4)	556(5)	545(6)	430(3)	538(2)
Si	47(0)	81(0)	86(1)	265(4)	481(3)	118(1)
SiO2	100(1)	173(1)	185(2)	566(8)	1028(6)	252(3)
Sr	0.09(0)	0.11(0)	0.09(0)	<0.05	<0.05	0.05(0)
Ti	<0.05	<0.05	<0.05	<0.05	<0.05	<0.05
Zn	0.07(2)	<0.05	0.08(3)	<0.05	<0.05	0.01(1)
Na/K	2.09	3.29	4.16	5.85	7.44	26.0

Sample ID	4/1 F	4/2 F	4/3 F	4/4 F	4/5 F	4/6 F	4/7 F
Date analyzed	05/10/12	05/14/12	05/14/12	05/15/12	05/14/12	05/15/12	05/14/12
Date sampled	4/6/2012	4/12/2012	4/19/2012	4/26/2012	5/3/2012	5/10/2012	5/11/2012
Hours	42.7	186.7	355.5	523.3	690.9	858.7	884.8
Temp, C	120	120	119	212	212	305	1
pH	8.62	7.68	6.93	6.08	6.09	6.25	7.43
Al	0.10(1)	<0.05	10(0)	0.3(0)	0.14(1)	0.8(0)	13(1)
B	0.63(1)	0.25(2)	1(0)	9(0)	8(0)	9(0)	8(0)
Ba	0.10(1)	0.10(1)	0.19(0)	<0.05	0.09(0)	<0.05	0.15(0)
Ca	14(0)	14(0)	16(1)	9(1)	9(0)	4(0)	15(0)
Fe	<0.5	<0.5	5(0)	<0.5	<0.5	<0.5	10(1)
K	245(2)	180(1)	145(2)	116(1)	113(2)	88(1)	49(1)
Li	0.06(0)	0.11(0)	0.15(0)	0.22(1)	0.25(1)	0.28(1)	0.57(1)
Mg	<0.5	<0.5	3.0(0)	<0.5	<0.5	<0.5	2.6(1)
Mn	<0.05	<0.05	<0.05	<0.05	<0.05	<0.05	0.07(0)
Na	581(7)	651(4)	689(6)	717(7)	681(5)	606(10)	751(10)
Si	61(1)	86(0)	128(1)	312(3)	132(1)	450(7)	227(5)
SiO2	130(1)	185(0)	275(2)	668(7)	281(2)	963(16)	487(11)
Sr	0.19(0)	0.19(0)	0.23(0)	0.10(0)	0.10(0)	<0.05	0.23(0)
Ti	<0.05	<0.05	0.09(0)	<0.05	<0.05	<0.05	0.11(2)
Zn	<0.05	<0.05	<0.05	<0.05	<0.05	0.15(1)	0.08(2)
Na/K	2.38	3.62	4.76	6.16	6.00	6.90	15.3

Sample ID	5/1 F	5/1 F	5/2 F	5/3 F	5/4 F	5/5 F	5/6 F	5/7 F
Date analyzed	07/27/12	08/01/12	07/27/12	07/27/12	07/27/12	08/07/12	08/21/12	08/21/12
Date Sampled	7/2/2012	7/5/2012	7/12/2012	7/19/2012	7/29/2012	8/2/2012	8/14/2012	8/15/2012
Hours	0	72.95	242.05	411.53	578.87	747.68	1033.18	1041.47
Temp	10	302	303	302	302	302	302	18
pH	NA	5.81	5.75	5.84	5.84	6	5.92	NA
Al	<0.1	<0.1	<0.1	<0.1	<0.1	0.4(0)	0.9(0)	0.1(0)
B	1.15(1)	0.70(0)	9.81(2)	10.42(0)	11.48(1)	11(0)	7(0)	7(0)
Ba	<0.1	<0.1	<0.1	<0.1	<0.1	<0.1	<0.1	<0.1
Ca	107(1)	107(2)	<1	<1	12.6(1)	11(1)	9(1)	19(1)
Fe	<1	<1	<1	<1	<1	<1	<1	<1
K	706(7)	704(4)	96(0)	91(0)	94(0)	15(0)	56(1)	49(0)
Li	<0.1	<0.1	<0.1	<0.1	<0.1	0.14(1)	<0.1	<0.1
Mg	<1	<1	<1	<1	<1	<1	<1	<1
Mn	<0.1	<0.1	<0.1	<0.1	<0.1	<0.1	<0.1	<0.1
Na	258(2)	263(2)	693(2)	740(1)	789(1)	483(5)	582(9)	776(6)
Si	48(0)	47(0)	553(0)	584(0)	583(1)	318(3)	506(5)	81(1)
SiO2	103(0)	101(0)	1183(0)	1250(1)	1248(1)	681(6)	1082(11)	173(1)
Sr	<0.1	<0.1	<0.1	<0.1	<0.1	<0.1	<0.1	<0.1
Ti	<0.2	<0.2	<0.2	<0.2	<0.2	<0.2	<0.2	<0.2
Zn	<0.1	<0.1	<0.1	<0.1	<0.1	0.11(1)	0.84(9)	0.72(2)
Na/K	0.365	0.374	7.23	8.16	8.37	31.4	10.3	15.9

Sample ID	6/1 F	6/1 F	6/2 F	6/3 F	6/4 F	6/6 F	6/7 F	6/8 F
Date analyzed	07/27/12	07/27/12	07/27/12	07/27/12	08/07/12	08/07/12	08/21/12	08/21/12
Date Sampled	7/5/2012	7/12/2012	7/19/2012	7/26/2012	8/2/2012	8/6/2012	8/9/2012	8/10/2012
Hours	46.63	216.45	382.85	550.83	718.63	822.27	888.15	911.13
Temp	119	120	119	218	218	298	300	25
pH	9.43	6.98	7.13	6.12	6.34	6.13	6.47	6.45
Al	<0.1	<0.1	<0.1	<0.1	<0.1	1.5(0)	1.6(5)	0.1(0)
B	2.0(0)	<0.1	<0.1	5.08(1)	10.91(2)	9(0)	7(0)	6(0)
Ba	<0.1	<0.1	<0.1	<0.1	<0.1	<0.1	<0.1	<0.1
Ca	59(0)	71(0)	53.0(2)	41.7(1)	16.7(1)	10(0)	8(1)	10(1)
Fe	<1	<1	<1	<1	<1	<1	<1	<1
K	29(0)	17(0)	<1	22(0)	12(0)	12(0)	1(0)	<1
Li	<0.1	<0.1	<0.1	<0.1	<0.1	0.12(1)	<0.1	<0.1
Mg	<1	<1	<1	<1	<1	<1	<1	<1
Mn	<0.1	<0.1	<0.1	<0.1	<0.1	<0.1	<0.1	<0.1
Na	258(0)	302(0)	387(0)	518(0)	553(1)	351(4)	239(1)	313(5)
Si	13(0)	20(0)	24.9(0)	43.8(0)	309(0)	543(2)	414(5)	183(3)
SiO2	27(0)	43(0)	53(0)	94(0)	662(0)	1161(4)	885(11)	392(7)
Sr	<0.1	<0.1	<0.1	<0.1	<0.1	<0.1	<0.1	<0.1
Ti	<0.2	<0.2	<0.2	<0.2	<0.2	<0.2	<0.2	<0.2
Zn	<0.1	<0.1	<0.1	<0.1	<0.1	0.13(1)	0.83(2)	0.75(3)
Na/K	8.94	18.3	na	23.2	46.1	28.7	238	na

Sample ID	7/1 F	7/2 F	7/3 F	7/4 F	7/5 F	7/6 F	7/7 F
Date analyzed	08/23/12	02/25/13	02/25/13	02/25/13	02/25/13	02/25/13	02/25/13
Date Sampled	8/22/2012	8/30/2012	9/6/2012	9/13/2012	9/20/2012	9/27/2012	9/28/2012
Hours	50.63	235.82	403.43	571.77	739.68	907.45	936.27
Temp	119	120	120	211	211	303	22
pH	9.64	8.33	7.44	6.33	6.2	6.17	6.16
Al	0.26(1)	0.23(0)	0.13(2)	0.73(0)	0.60(0)	2.90(9)	0.16(0)
B	0.8(0)	1(0)	2(0)	6(0)	7(0)	7(0)	7(0)
Ba	<0.1	<0.05	<0.05	<0.05	<0.05	<0.05	<0.05
Ca	35(1)	28(0)	26(1)	9(0)	7(1)	5(1)	8(0)
Fe	<1	<0.5	<0.5	<0.5	<0.5	<0.5	<0.5
K	6(0)	12(0)	11(0)	11(0)	11(0)	11(0)	5(0)
Li	<0.1	<0.05	<0.05	0.12(0)	0.13(0)	0.15(0)	0.24(0)
Mg	<1	<0.5	<0.5	<0.5	<0.5	<0.5	<0.5
Mn	<0.1	<0.05	<0.05	<0.05	<0.05	<0.05	<0.05
Na	251(3)	357(3)	405(6)	365(2)	375(1)	307(1)	381(3)
Si	16(0)	33(1)	45(2)	185(3)	244(1)	477(3)	244(1)
SiO2	34(0)	70(3)	96(4)	396(5)	523(3)	1021(7)	522(3)
Sr	0.13(0)	0.12(0)	0.11(0)	<0.05	<0.05	<0.05	<0.05
Ti	<0.2	<0.1	<0.1	<0.1	<0.1	<0.1	<0.1
Zn	0.03(1)	<0.05	<0.05	<0.05	<0.05	<0.05	<0.05
Na/K	42.6	31.0	36.0	32.8	35.4	28.6	69.6

Sample ID	8/1 F	8/2 F	8/3 F	8/4 F	8/5 F	8/6 F	8/7 F	8/8 F
Date analyzed	08/23/12	02/25/13	02/25/13	02/25/13	02/25/13	02/25/13	02/25/13	02/25/13
Date sampled	8/23/2012	8/30/2012	9/6/2012	9/13/2012	9/20/2012	9/27/2012	10/4/2012	10/5/2012
Hours	25.03	194.08	361.27	531.22	698.65	864.73	1033.13	1058.03
Temp, C	25	118	121	120	212	212	300	22
pH	6.16	6.07	6.02	6.06	6.16	6.17	6.13	5.91
Al	2.91(1)	0.64(3)	1.42(0)	<0.05	<0.05	0.86(3)	0.62(1)	0.47(0)
B	9.4(1)	7.6(0)	7.5(0)	6.8(1)	6.8(0)	6.6(1)	6.4(1)	4.7(0)
Ba	<0.1	<0.05	<0.05	<0.05	<0.05	<0.05	<0.05	<0.05
Ca	6(1)	6(0)	5(0)	3(0)	3(0)	4(0)	4(0)	16(1)
Fe	<1	<0.5	<0.5	<0.5	<0.5	<0.5	<0.5	<0.5
K	7(0)	9(0)	10(0)	11(0)	12(0)	12(0)	12(0)	11(0)
Li	<0.1	0.14(1)	0.14(1)	0.16(1)	0.17(1)	0.18(1)	0.18(1)	0.23(2)
Mg	<1	<0.5	<0.5	<0.5	<0.5	<0.5	<0.5	<0.5
Mn	<0.1	<0.05	<0.05	<0.05	<0.05	<0.05	<0.05	<0.05
Na	258(1)	259(1)	247(1)	231(1)	228(1)	218(1)	213(2)	200(2)
Si	461(2)	350(2)	493(5)	43(0)	37(0)	385(2)	186(3)	336(2)
SiO2	986(5)	750(5)	1056(11)	91(0)	79(1)	824(4)	398(6)	719(5)
Sr	<0.1	<0.05	<0.05	<0.05	<0.05	<0.05	<0.05	0.10(0)
Ti	<0.2	<0.1	<0.1	<0.1	<0.1	<0.1	<0.1	<0.1
Zn	0.84(3)	<0.05	<0.05	<0.05	<0.05	<0.05	<0.05	<0.05
Na/K	36.0	27.3	25.2	21.2	19.1	18.2	17.1	18.0

Sample ID	9/0 F	9/1 F	9/2 F	9/3 F	9/4 F	9/5 F	9/6 F	9/7 F	9/8 F
Date analyzed	02/25/13	02/25/13	02/25/13	02/25/13	02/25/13	02/25/13	02/25/13	02/25/13	02/25/13
Date sampled		11/1/2012	11/8/2012	11/15/2012	11/21/2012	11/29/2012	12/4/2012	12/10/2012	12/11/2012
Hours	0	23.75	192.65	360.62	504.23	696.25	817.17	960.02	984.33
Temp, C	rt	121	121	121	210	210	300	300	20
pH	7.16	8.98		7.2	6.55	6.39	6.28	6.13	6.54
Al	0.25(0)	0.21(0)	0.47(0)	0.14(0)	0.62(0)	0.48(0)	2.41(1)	2.18(1)	0.81(1)
B	0.4(0)	0.4(0)	0.8(0)	1.7(0)	5.4(1)	7.0(0)	6.8(1)	6.8(1)	7.1(0)
Ba	<0.05	<0.05	<0.05	<0.05	<0.05	<0.05	<0.05	<0.05	<0.05
Ca	96(2)	15(0)	18(0)	16(0)	8(0)	8(0)	5(1)	4(0)	7(1)
Fe	<0.5	<0.5	<0.5	<0.5	<0.5	<0.5	<0.5	<0.5	<0.5
K	8(0)	6(0)	8(0)	8(0)	9(0)	11(0)	11(0)	10(0)	12(0)
Li	<0.05	<0.05	<0.05	0.06(0)	0.08(0)	0.08(1)	0.10(0)	0.11(1)	0.15(1)
Mg	<0.5	<0.5	<0.5	<0.5	<0.5	<0.5	<0.5	<0.5	0.7(0)
Mn	<0.05	<0.05	<0.05	<0.05	<0.05	<0.05	<0.05	<0.05	<0.05
Na	182(1)	356(3)	415(4)	423(3)	419(4)	414(2)	328(2)	313(2)	386(7)
Si	<0.5	18(0)	42(1)	57(0)	196(1)	261(3)	468(4)	476(5)	451(5)
SiO2	<1	38(0)	89(1)	122(1)	418(1)	559(6)	1002(8)	1019(10)	965(11)
Sr	<0.05	0.10(0)	0.10(0)	0.07(0)	<0.05	<0.05	<0.05	<0.05	<0.05
Ti	<0.1	<0.1	<0.1	<0.1	<0.1	<0.1	<0.1	<0.1	<0.1
Zn	<0.05	<0.05	<0.05	<0.05	<0.05	<0.05	<0.05	<0.05	<0.05
Na/K	22.4	62.2	49.2	55.8	46.0	37.5	30.9	30.6	32.3

Sample ID	10/1 F	10/2 F	10/3 F	10/4 F	10/5 F	10/6 F	10/7 F	10/8 F
Date analyzed	03/05/13	03/05/13	03/05/13	03/05/13	03/05/13	03/05/13	04/21/2013	04/21/2013
Date sampled	1/18/2013	1/24/2013	1/31/2013	2/7/2013	2/15/2013	2/21/2013	2/28/2013	2/28/2013
Hours	46.97	191.48	359.32	527.43	719.35	863.02	1031.35	1032.72
Temp, C	299	299	299	299	299	299	300	21
pH	6.45	6.00	6.21	6.57	6.27	6.53	6.39	6.30
Al	1.56(3)	0.91(1)	0.95(0)	0.87(2)	0.88(1)	0.83(0)	1.33(2)	0.40(0)
B	6(0)	10(0)	10(0)	10(0)	12(0)	10(0)	8(0)	5(0)
Ba	<0.05	<0.05	<0.05	<0.05	<0.05	<0.05	<0.05	<0.05
Ca	9(0)	7(0)	9(0)	9(1)	9(1)	9(0)	7(1)	23(0)
Fe	<0.5	<0.5	<0.5	<0.5	<0.5	<0.5	<0.5	<0.5
K	150(4)	53(0)	33(0)	29(0)	33(0)	29(0)	41(1)	27(0)
Li	<0.05	0.07(0)	0.08(0)	0.08(1)	0.08(0)	0.09(0)	0.30(1)	0.07(1)
Mg	<0.5	<0.5	<0.5	<0.5	<0.5	<0.5	<0.5	<0.5
Mn	<0.05	<0.05	<0.05	<0.05	<0.05	<0.05	<0.05	<0.05
Na	376(13)	451(4)	463(4)	453(2)	442(1)	431(2)	442(6)	355(1)
Si	310(13)	481(4)	534(2)	533(1)	539(1)	533(2)	598(4)	324(4)
SiO2	663(28)	1028(9)	1143(5)	1140(1)	1154(2)	1140(3)	1279(10)	692(9)
Sr	<0.05	<0.05	<0.05	<0.05	<0.05	<0.05	<0.05	0.18(0)
Ti	<0.1	<0.1	<0.1	<0.1	<0.1	<0.1	<0.1	<0.1
Zn	<0.05	<0.05	0.08(0)	<0.05	0.25(0)	<0.05	<0.05	<0.05
Na/K	2.51	8.48	14.1	15.4	13.3	14.7	10.9	12.9

Sample ID	11/1 F	11/2 F	11/3 F	11/4 F	11/5F	11/6F	11/7 F	11/8 F
Date analyzed	02/26/2013	02/26/2013	02/26/2013	02/26/2013	04/21/2013	04/21/2013	04/21/2013	04/21/2013
Date sampled	2/1/2013	2/7/2013	2/14/2013	2/21/2013	2/28/2013	3/7/2013	3/14/2013	3/29/2013
Hours	48.58	194.05	360.87	530.40	697.15	863.02	1031.35	1032.72
Temp, C	300	299	300	300	300	300	300	300
pH	5.85	6.07	6.03	5.97	6.03	5.86	6.06	5.94
Al	3.45(5)	1.98(1)	1.90(1)	1.88(2)	1.57(1)	1.63(1)	1.64(1)	0.27(1)
B	7.8(2)	8.1(0)	8.5(3)	7.8(1)	6.9(1)	7.2(0)	7.0(1)	7.1(0)
Ba	<0.05	<0.05	<0.05	<0.05	<0.05	<0.05	<0.05	<0.05
Ca	5(1)	4(0)	4(0)	4(1)	6(1)	6(1)	6(0)	35(1)
Fe	<0.5	<0.5	<0.5	<0.5	<0.5	<0.5	<0.5	<0.5
K	71(2)	33(0)	30(0)	29(0)	31(0)	31(0)	30(0)	34(0)
Li	0.20(1)	0.21(1)	0.21(1)	0.21(2)	0.24(1)	0.22(1)	0.21(2)	0.35(1)
Mg	<0.5	<0.5	<0.5	<0.5	<0.5	<0.5	<0.5	<0.5
Mn	<0.05	<0.05	<0.05	<0.05	<0.05	<0.05	<0.05	<0.05
Na	425(7)	438(11)	425(4)	412(3)	428(4)	425(2)	408(5)	499(7)
Si	491(6)	536(2)	506(9)	506(3)	521(5)	532(1)	473(4)	388(2)
SiO2	1051(14)	1146(4)	1082(18)	1083(6)	1116(11)	1138(1)	1011(9)	830(4)
Sr	<0.05	<0.05	<0.05	<0.05	<0.05	<0.05	<0.05	0.42(0)
Ti	<0.1	<0.1	<0.1	<0.1	<0.1	<0.1	<0.1	<0.1
Zn	<0.05	0.27(0)	<0.05	0.05(2)	<0.05	<0.05	<0.05	<0.05
Na/K	6.02	13.4	14.1	14.0	13.7	13.9	13.4	14.7

Appendix D

FIB-SEM Figures

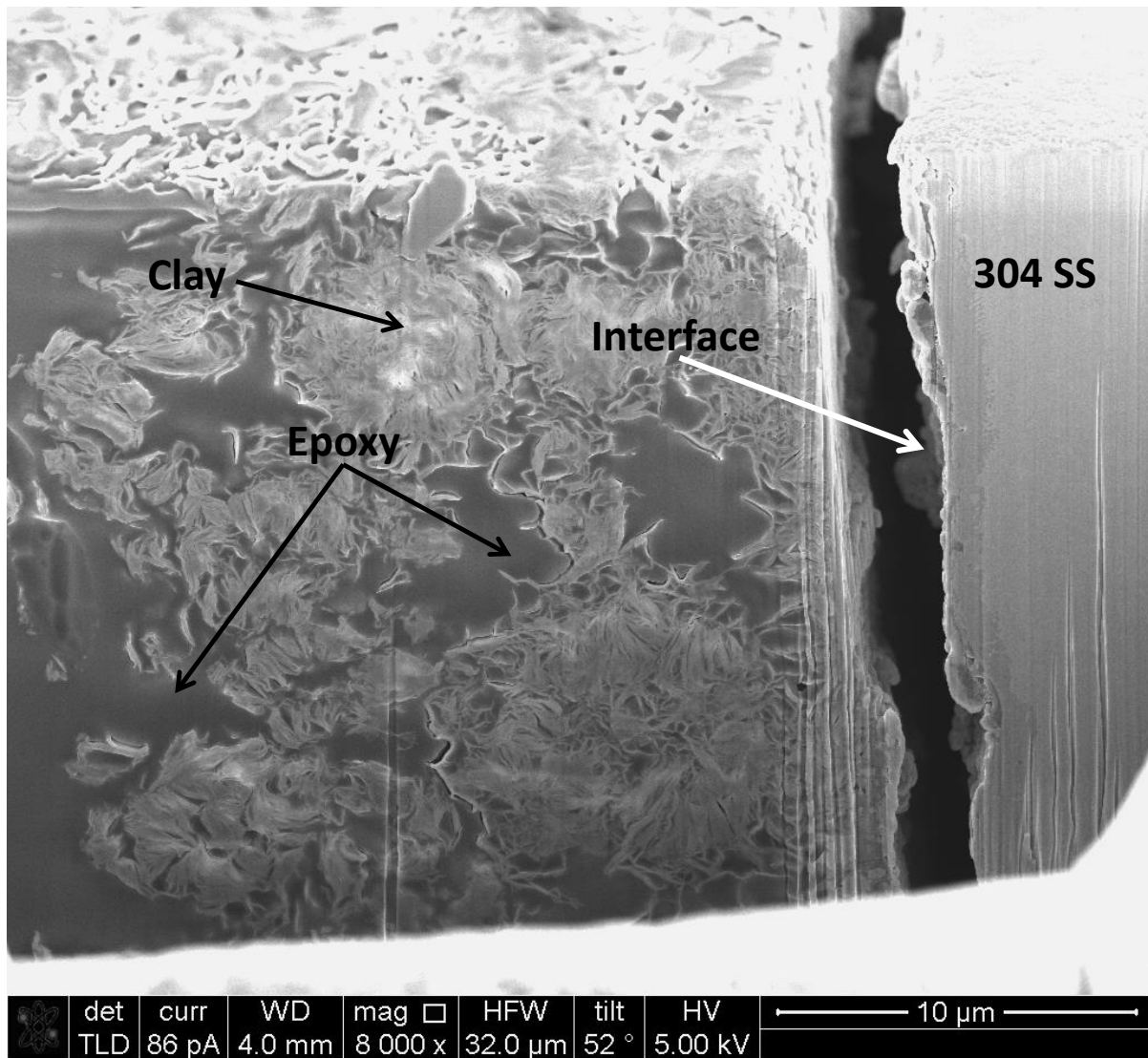


Figure S1. FIB-SEM analysis showing clay coating texture and interfacial domain with respect to 304 SS sample. The figure also shows the clay engulfment within the epoxy mount possibly causing the clay to “peel off” from the metal surface. The vertical striations are traces of the FIB milling cutting through the surface. FIB-SEM analysis conducted by Michael Rye at SNL.

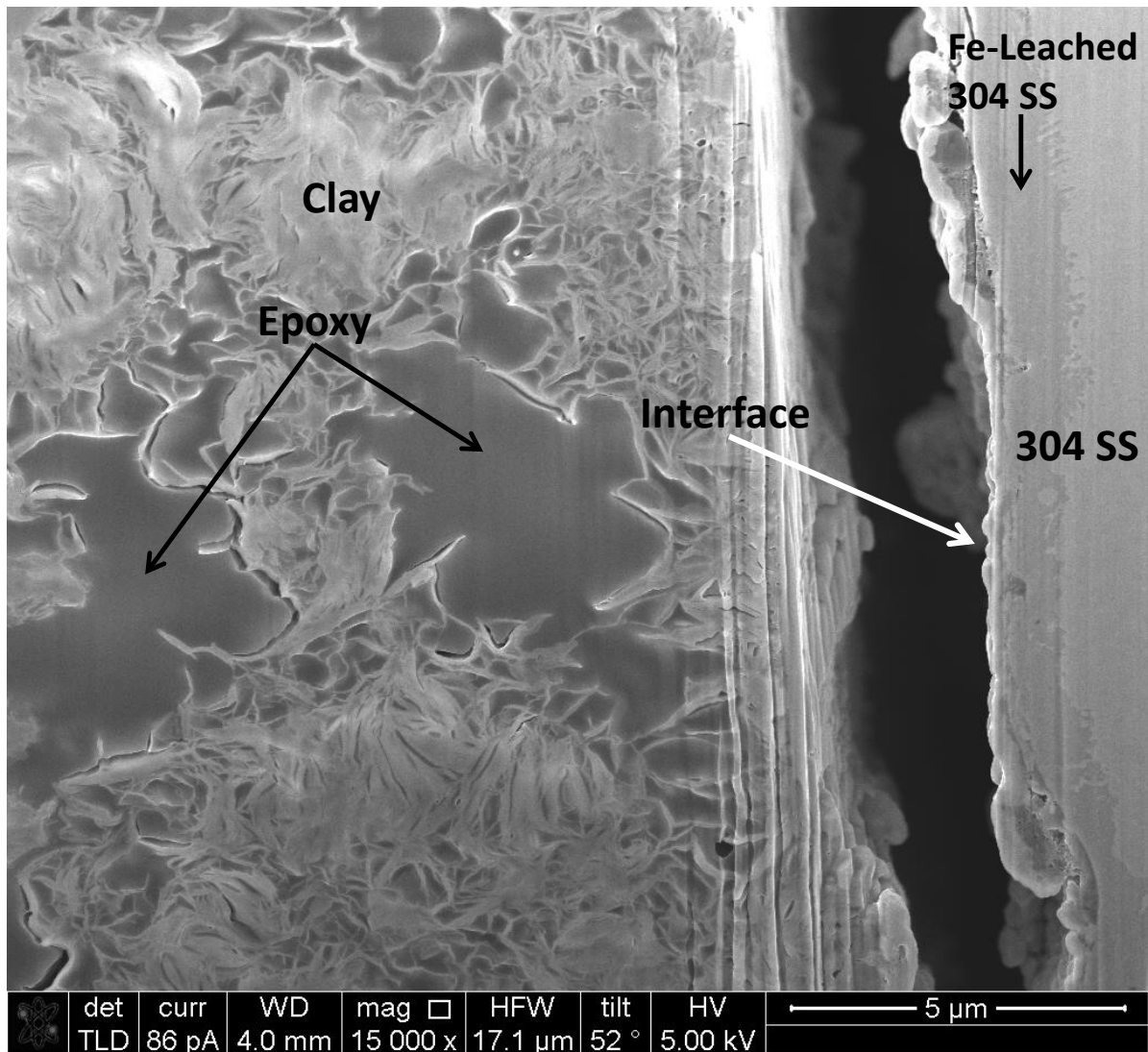


Figure S2. Close up snapshot of FIB-SEM picture shown in Figure S1 displaying clay coating texture and interfacial domain with respect to 304 SS sample. This picture depicts finer details of the clay metal interface showing a Fe-leached O-rich layer with a nearly constant thickness of approximately 1.5 – 2 microns. The vertical striations are traces of the FIB milling cutting through the surface. FIB-SEM analysis conducted by Michael Rye at SNL.

Appendix E

Thermodynamic Data Tables

Table 1. Entropies of the Chemical Elements in Their Standard Reference Forms. The data shown here represent “modern” era values characterized by the use of Joule units and a standard pressure of 1.0 bar. NEA-TDB data (light green) are generally preferred over values from other sources, but only cover a limited number of elements. Light orange background marks problematic or potentially problematic values. This table is taken from workbook TDProperties_Rev0_u3.xlsx.

Handle	USGS 1452	NBS 82	JANAF 3rd	CODATA 89	NEA TDB	Barin	NIST-JANAF	USGS 2131	Lange's
Element	Robie et al. 1978 J/mol-K	Wagman et al. 1982 J/mol-K	Chase et al. 1985 J/mol-K	Cox et al. 1989 J/mol-K	NEA TDB Series 1992- J/mol-K	Barin and Platzki 1995 J/mol-K	Chase (ed.) 1998 J/mol-K	Robie and Hemingway 1995 J/mol-K	Lange's Handbook 2005 J/mol-K
Ac		56.5							56.5
Ag	42.55	42.55		42.55	42.550	42.677		42.55	42.55
Al	28.35	28.33	28.275	28.30	28.300	28.275	28.275	28.30	28.30
Am					55.400	54.488			62.7
Ar	154.84	154.843	154.845	154.846	154.846	154.845	154.845		154.846
As	35.69	35.1			35.100	35.706		35.69	35.1
At2									121.3
Au	47.49	47.40				47.497		47.49	47.4
B	5.90	5.86	5.834	5.90	5.900	5.830	5.834	5.83	5.90
Ba	64.42	62.8	62.475		62.420	62.417	62.475	62.42	62.48
Be	9.54	9.50	9.440	9.50	9.500	9.440	9.440	9.50	9.50
Bi	56.74	56.74			56.740	56.735		56.74	56.7
Bk									
Br2	152.32	152.231	152.206	152.210	152.210	152.210	152.206	152.20	152.21
C	5.74	5.740	5.740	5.74	5.740	5.740	5.740	5.74	5.74
Ca	41.63	41.42	41.588	41.59	41.590	41.422	41.588	42.90	41.59
Cd	51.80	51.76		51.80	51.800	51.798		51.80	51.8
Ce	69.46	72.0				69.454		72.0	72.0

Table 2 (continued)

Handle	USGS 1452	NBS 82	JANAF 3rd	CODATA 89	NEA TDB	Barin	NIST-JANAF	USGS 2131	Lange's
Element	Robie et al. 1978 J/mol-K	Wagman et al. 1982 J/mol-K	Chase et al. 1985 J/mol-K	Cox et al. 1989 J/mol-K	NEA TDB Series 1992- J/mol-K	Barin and Platzki 1995 J/mol-K	Chase (ed.) 1998 J/mol-K	Robie and Hemingway 1995 J/mol-K	Lange's Handbook 2005 J/mol-K
Cf									
Cl2	223.08	223.066	223.079	223.081	223.081	223.117	223.079	223.08	233.08
Cm									
Co	30.04	30.04	30.067			30.041	30.067	30.04	30.0
Cr	23.64	23.77	23.618			23.640	23.618	23.62	23.8
Cs	85.23	85.23	85.147	85.23	85.230	85.147	85.147	85.23	85.23
Cu	33.15	33.150	33.164	33.15	33.150	33.164	33.164	33.14	33.15
Dy	74.89	74.77				74.894			75.6
Er	73.18	73.18				73.178			73.18
Es									
Eu	80.79	77.78				77.822			77.78
F2	202.79	202.78	202.789	202.791	202.791	202.795	202.789	202.79	202.791
Fe	27.28	27.28	27.321			27.280	27.321	27.09	27.32
Fm									
Fr		95.4							95.40
Ga	40.83	40.88	40.838			40.828	40.838		40.8
Gd	68.45	68.07				67.948			68.07
Ge	31.09	31.09		31.09	31.090	31.087		31.09	31.09
H	130.68	130.684	130.680	130.680	130.680	130.680	130.680	130.68	130.680
He	126.15	126.150	126.152	126.153	126.153	126.148	126.152		126.153
Hf	43.56	43.56	43.560			43.555	43.560		43.56
Hg	75.90	76.02	76.028	75.90	75.900	75.898	76.028	75.90	75.90

Table 2 (continued)

Handle	USGS 1452	NBS 82	JANAF 3rd	CODATA 89	NEA TDB	Barin	NIST-JANAF	USGS 2131	Lange's
Element	Robie et al. 1978 J/mol-K	Wagman et al. 1982 J/mol-K	Chase et al. 1985 J/mol-K	Cox et al. 1989 J/mol-K	NEA TDB Series 1992- J/mol-K	Barin and Platzki 1995 J/mol-K	Chase (ed.) 1998 J/mol-K	Robie and Hemingway 1995 J/mol-K	Lange's Handbook 2005 J/mol-K
Ho	75.02	75.3				75.019			75.3
I2	116.15	116.135	116.142	116.140	116.140	116.142	116.142	116.14	116.14
In	57.84	57.82				57.823			57.8
Ir	35.48	35.48				35.505			35.48
K	64.68	64.18	64.670	64.68	64.680	64.670	64.670	64.67	64.68
Kr	164.08	164.082	164.084	164.085	164.085	164.085	164.084		164.085
La	56.90	56.9				56.902			56.9
Li	29.12	29.12	29.085	29.12	29.120	29.080	29.085	29.09	29.12
Lr									
Lu	50.96	50.96				50.961			50.96
Md									
Mg	32.68	32.68	32.671	32.67	32.670	32.677	32.671	32.67	32.67
Mn	32.01	32.01	32.010			32.008	32.010	32.01	32.01
Mo	28.66	28.66	28.605			28.593	28.605	28.66	28.71
N2	191.61	191.61	191.609	191.609	191.609	191.609	191.609	191.61	191.609
Na	51.30	51.21	51.455	51.30	51.300	51.455	51.455	51.46	51.30
Nb	36.40	36.40	36.464			36.401	36.464		36.4
Nd	71.09	71.5				71.086			7.16
Ne	146.32	146.328	146.327	146.328	146.328	146.324	146.327		146.328
Ni	29.87	29.87	29.870		29.870	29.874	29.87	29.87	29.87
No									
Np					50.460	50.459			

Table 2 (continued)

Handle	USGS 1452	NBS 82	JANAF 3rd	CODATA 89	NEA TDB	Barin	NIST-JANAF	USGS 2131	Lange's
Element	Robie et al. 1978 J/mol-K	Wagman et al. 1982 J/mol-K	Chase et al. 1985 J/mol-K	Cox et al. 1989 J/mol-K	NEA TDB Series 1992- J/mol-K	Barin and Platzki 1995 J/mol-K	Chase (ed.) 1998 J/mol-K	Robie and Hemingway 1995 J/mol-K	Lange's Handbook 2005 J/mol-K
O2	205.15	205.138	205.147	205.152	205.152	205.147	205.147	205.15	205.152
Os	32.64	32.6				32.635			32.6
P	22.85	41.09	41.077	41.09	41.090	41.070	41.077	41.09	41.09
Pa		51.9				51.882			51.8
Pb	65.06	64.81	64.785	64.80	64.800	64.785	64.785	64.8	64.80
Pd	37.82	37.57				37.823			37.61
Pm									
Po									62.8
Pr	73.93	73.2				73.931			73.2
Pt	41.63	41.63				41.631		41.63	41.63
Pu	51.46				54.460	51.463			51.5
Ra		71							71
Rb	76.78	76.78	76.778	76.78	76.780	76.780	76.778		76.78
Re	36.53	36.86				36.526			36.9
Rh	31.54	31.51				31.505			31.51
Rn	176.23	176.21	176.235			176.231	176.235		176.235
Ru	28.53	28.53				28.535			28.53
S	31.80	31.80	32.056	32.054	32.054	32.056	32.056	32.05	32.054
Sb	45.52	45.69			45.520	45.522		45.52	45.7
Sc	34.64	34.64				34.644			34.64
Se	42.27	42.442			42.090	42.258		42.27	41.97
Si	18.81	18.83	18.820	18.81	18.810	18.820	18.820	18.81	18.81

Table 2 (continued)

Handle	USGS 1452	NBS 82	JANAF 3rd	CODATA 89	NEA TDB	Barin	NIST-JANAF	USGS 2131	Lange's
Element	Robie et al. 1978 J/mol-K	Wagman et al. 1982 J/mol-K	Chase et al. 1985 J/mol-K	Cox et al. 1989 J/mol-K	NEA TDB Series 1992- J/mol-K	Barin and Platzki 1995 J/mol-K	Chase (ed.) 1998 J/mol-K	Robie and Hemingway 1995 J/mol-K	Lange's Handbook 2005 J/mol-K
Sm	69.50	69.58				69.496			69.58
Sn	51.20	51.55		51.18	51.180	51.195		51.18	51.08
Sr	55.40	52.3	55.694		55.700	55.690	55.694	55.69	55.0
Ta	41.51	41.51	41.471			41.505	41.471		41.47
Tb	73.70	73.22				73.304			73.22
Tc					32.506	33.472			33.47
Te	49.50	49.71			49.221	49.497		49.71	49.70
Th	53.39	53.39		51.8	51.800	53.388		51.83	51.8
Ti	30.63	30.63	30.759	30.72	30.720	30.759	30.759	30.76	30.72
Tl	64.18	64.18				64.183			64.18
Tm	74.01	74.01				74.015			74.01
U	50.29	50.21		50.20	50.200	50.292		50.2	50.20
V	28.91	28.91	28.936			28.911	28.936	28.94	28.94
W	32.64	32.64	32.660			32.660	32.660	32.65	32.6
Xe	169.68	169.683	169.684	169.685	169.685	169.683	169.684		169.685
Y	44.43	44.43				44.434			44.4
Yb	59.83	59.87				59.831			59.87
Zn	41.63	41.63	41.717	41.63	41.630	41.631	41.717	41.63	41.63
Zr	38.99	38.99	38.869		39.080	38.869	38.869	38.87	39.0
Count	85	88	47	37	50	89	47	50	93

Notes: The Lange's Handbook value for Cl₂ of 233.08 J/mol-K is possibly a typo where the actual value should be 223.08 J/mol-K. The value for P given by Robie et al. (1978) differs because they use red phosphorus as the reference form instead of the now generally accepted white form. The NEA-TDB value for Pu is notably higher than the values given by other sources.

Table 2. Entropies of the Chemical Elements in Their Standard Reference Forms. The data shown here represent older historical era values characterized by the use of calorie units (1 cal = 4.184 joule) and a standard pressure of 1.0 atm (1.013 bar). This table is taken from workbook TDProperties_Rev0_u3.xlsx.. Still earlier data compilations by Lewis and Gibson (1917) and Lewis et al. (1922), which appear to be the earliest such compilations, are not included here, though they are given in the spreadsheet. Also in the spreadsheet is a small compilation that was included in the International Critical Tables of 1929 (which gave the data in Joule units, for 1 bar pressure). The data included here, though historical, is often found cited in later literature or in tracing the origin of data presented in later literature. Note that some sources use red phosphorus as the reference form for P instead of the now commonly accepted white form.

Handle	USBM 350	NBS 500	ACS 18	USBM 592	USGS 1259	NBS 270	JANAF 2nd	USBM 672
Element	Kelly 1932 cal/mol-K	Rossini et al. 1952 cal/mol-K	Stull and Sinke 1956 cal/mol-K	Kelley and King 1961 cal/mol-K	Robie and Waldbaum 1968 cal/mol-K	NBS 270-3 to 270-8 1968-1981 cal/mol-K	Stull and Prophet 1971 cal/mol-K	Pankratz 1982 cal/mol-K
Ac			15.00	15.0		13.5		
Ag	10.15	10.206	10.20	10.20	10.20	10.17		10.170
Al	6.75	6.769	6.77	6.77	6.77	6.77	6.769	6.776
Am								13.023
Ar	36.8	36.983	36.98	36.98		36.9822		36.983
As	8.4	8.4	8.40	8.4	8.40	8.4		8.534
At2			29.00	29.0				
Au	11.4	11.4	11.32	11.31	11.31	11.33		11.330
B		1.56	1.4	1.403	1.403	1.40	1.403	1.410
Ba		16	15.50	16.0	16.0	15.0		14.918
Be	2.14	2.28	2.28	2.28	2.28	2.27	2.280	2.270
Bi	13.8	13.6	13.58	13.5	13.56	13.56		13.560
Bk								
Br2	36.6	36.4	36.25	36.4	36.384	36.384	36.384	36.379
C	1.3	1.3609	1.37	1.36	1.372	1.372	1.359	1.372
Ca	9.95	9.95	9.95	9.95	9.95	9.90	9.932	9.940
Cd	12.30	12.3	12.37	12.37	12.38	12.37		12.380

Table 2 (continued)

Handle	USBM 350	NBS 500	ACS 18	USBM 592	USGS 1259	NBS 270	JANAF 2nd	USBM 672
Element	Kelly 1932 cal/mol-K	Rossini et al. 1952 cal/mol-K	Stull and Sinke 1956 cal/mol-K	Kelley and King 1961 cal/mol-K	Robie and Waldbaum 1968 cal/mol-K	NBS 270-3 to 270-8 1968-1981 cal/mol-K	Stull and Prophet 1971 cal/mol-K	Pankratz 1982 cal/mol-K
Ce	13.80	13.8	16.64	16.6	15.3	17.2		17.200
Cf								
Cl2	53.8	53.286	53.29	53.29	53.288	53.288	53.2890	53.290
Cm								17.200
Co	6.8	6.8	7.18	7.18	7.18	7.18	7.180	7.180
Cr	5.6	5.68	5.70	5.68	5.65	5.68		5.650
Cs		19.8	20.16	20.1		20.37	20.351	20.370
Cu	7.92	7.96	7.97	7.7	7.97	7.923	7.913	7.924
Dy			17.87	17.9		18.0		17.900
Er			17.48	17.5		17.49		17.490
Es								
Eu			17.00	17.0		18.59		18.600
F2		48.6	48.45	48.49	48.44	48.44	48.447	48.443
Fe	6.47	6.49	6.49	6.49	6.52	6.52	6.529	6.520
Fm								
Fr			22.50	22.5		22.8		
Ga	10.2	10.2	9.82	9.77		9.77		9.758
Gd		14	15.77	16.2		16.27		16.240
Ge		10.14	7.43	7.43		7.43		7.430
H2	31.23	31.211	27.39	31.21	31.208	31.208	31.208	31.207
He	30.13	30.126	30.13	30.13		30.1244		30.125
Hf		13.1	10.91	10.91	10.41	10.41		10.410

Table 2 (continued)

Handle	USBM 350	NBS 500	ACS 18	USBM 592	USGS 1259	NBS 270	JANAF 2nd	USBM 672
Element	Kelly 1932 cal/mol-K	Rossini et al. 1952 cal/mol-K	Stull and Sinke 1956 cal/mol-K	Kelley and King 1961 cal/mol-K	Robie and Waldbaum 1968 cal/mol-K	NBS 270-3 to 270-8 1968-1981 cal/mol-K	Stull and Prophet 1971 cal/mol-K	Pankratz 1982 cal/mol-K
Hg	18.5	18.5	18.19	18.17	18.17	18.17	18.171	18.140
Ho			17.77	18.0		18.0		17.930
I2	27.90	27.90	27.90	27.76	27.757	27.757	27.758	27.758
In		12.5	13.82	13.9		13.82		13.820
Ir	8.7	8.7	8.70	8.48		8.48		8.481
K	15.2	15.2	15.39	15.34	15.48	15.34	15.457	15.457
Kr	39.17	39.19	39.19	39.19		39.1905		39.191
La	13.7	13.7	13.60	13.6		13.6		13.600
Li	7.6	6.70	6.75	6.70	6.95	6.96	6.954	6.954
Lr								
Lu			11.75	11.8		12.18		12.180
Md								
Mg	7.77	7.77	7.81	7.81	7.81	7.81	7.814	7.810
Mn	7.3	7.59	7.65	7.64	7.65	7.65		7.650
Mo	6.83	6.83	6.83	6.82	6.85	6.85	6.837	6.850
N2	45.8	45.767	45.77	45.77	45.77	45.77	45.77	45.770
Na	12.2	12.2	12.21	12.24	12.24	12.24	12.298	12.298
Nb		8.3	8.73	9.0	8.70	8.70		8.700
Nd			17.50	17.5		17.1		17.100
Ne	35.0	34.948	34.95	34.95		34.9471		34.947
Ni	7.12	7.20	7.14	7.14	7.14	7.14		7.140
No								

Table 2 (continued)

Handle	USBM 350	NBS 500	ACS 18	USBM 592	USGS 1259	NBS 270	JANAF 2nd	USBM 672
Element	Kelly 1932 cal/mol-K	Rossini et al. 1952 cal/mol-K	Stull and Sinke 1956 cal/mol-K	Kelley and King 1961 cal/mol-K	Robie and Waldbaum 1968 cal/mol-K	NBS 270-3 to 270-8 1968-1981 cal/mol-K	Stull and Prophet 1971 cal/mol-K	Pankratz 1982 cal/mol-K
Np								12.060
O2	49.03	49.003	49.01	49.01	48.996	49.003	49.004	49.005
Os	7.8	7.8	7.80	7.8		7.8		7.800
P		10.6	(red) 5.46	9.80	(red)5.45	9.82	(red)5.450	9.820
Pa			12.40	12.4		12.4		12.400
Pb	15.63	15.51	15.49	15.49	15.55	15.49	15.484	15.490
Pd	8.9	8.9	9.05	9.06		8.98		9.013
Pm			17.21	17.2				
Po			15.00	15.0				
Pr			17.45	17.6		17.5		17.670
Pt	10.0	10.0	10.00	9.95	9.95	9.95		9.950
Pu								13.420
Ra		17	17.00	17.0		17		
Rb		16.6	18.22	18.1		18.35		18.350
Re		10	8.89	8.89		8.81		8.730
Rh	7.6	7.6	7.60	7.53		7.53		7.542
Rn	42.10	42.10	42.10	42.10		42.09		
Ru	6.9	6.9	6.90	6.82		6.82		6.839
S	7.6	7.62	7.62	7.62	7.60	7.60	7.631	7.661
Sb	10.5	10.5	10.92	10.92	10.92	10.92		10.880
Sc			9.00	9.0		8.28		8.280
Se		10.0	10.15	10.14	10.144	10.144		10.144

Table 2 (continued)

Handle	USBM 350	NBS 500	ACS 18	USBM 592	USGS 1259	NBS 270	JANAF 2nd	USBM 672
Element	Kelly 1932 cal/mol-K	Rossini et al. 1952 cal/mol-K	Stull and Sinke 1956 cal/mol-K	Kelley and King 1961 cal/mol-K	Robie and Waldbaum 1968 cal/mol-K	NBS 270-3 to 270-8 1968-1981 cal/mol-K	Stull and Prophet 1971 cal/mol-K	Pankratz 1982 cal/mol-K
Si	4.50	4.47	4.53	4.51	4.50	4.50	4.498	4.500
Sm			16.28	16.3		16.63		16.630
Sn	12.3	12.3	12.29	12.29	12.32	12.32		12.236
Sr		13.0	12.50	12.5	12.5	12.5		12.500
Ta	9.4	9.9	9.90	9.92		9.92		9.920
Tb			17.46	17.5		17.50		17.520
Tc		9	8.00	8.0				
Te		11.88	11.88	11.88	11.88	11.88		11.880
Th	13.6	13.6	12.76	12.8	12.76	12.76		12.760
Ti	6.6	7.24	7.33	7.30	7.32	7.32	7.325	7.320
Tl	15.5	15.4	15.35	15.35		15.34		15.340
Tm			17.06	17.1		17.69		17.690
U	11.1	12.03	12.03	12.03	12.00	12.00		12.000
V		7.05	7.01	7.02	6.91	6.91		6.915
W	8.0	8.0	8.04	7.80	7.80	7.80	7.806	7.800
Xe	40.51	40.53	40.53	40.53		40.529		40.530
Y			11.00	11.0		10.62		10.62
Yb			15.00	15.0		14.31		14.300
Zn	9.95	9.95	9.95	9.95	9.95	9.95		9.950
Zr	9.5	9.18	9.29	9.32	9.31	9.32	9.314	9.320
Count	55	73	92	92	50	88	29	88

Table 3. Entropies of the Chemical Elements in Their Standard Reference Forms. The data shown here represent late historical reports from CODATA in the 1970s. They are characterized by the use of Joule units in combination with a standard pressure of 1.0 atm (1.013 bar). This table is taken from workbook TDProperties_Rev0_u3.xlsx. Though superseded by the CODATA 1989 report, these data are occasionally cited in the later literature or in tracing the origin of data presented in later literature.

Handle	CODATA 71	CODATA 73	CODATA 75	CODATA 76	CODATA 77
Element	CODATA 1972 J/mol-K	CODATA 1975 J/mol-K	CODATA 1976 J/mol-K	CODATA 1977 J/mol-K	CODATA 1978 J/mol-K
Ac					
Ag		42.55	42.55	42.55	42.55
Al			28.35	28.35	28.35
Am					
Ar	154.732	154.732	154.732	154.732	154.732
As					
At2					
Au					
B			5.90	5.90	5.90
Ba					
Be				9.50	9.50
Bi					
Bk					
Br2	152.210	152.210	152.210	152.210	152.210
C	5.74	5.74	5.74	5.74	5.74
Ca				41.6	41.6
Cd					51.80
Ce					
Cf					
Cl2	222.965	222.965	222.965	222.965	222.965
Cm					
Co					
Cr					
Cs		85.23	85.23	85.23	85.23
Cu			33.15	33.15	33.15
Dy					
Er					
Es					

Table 3 (continued)

Eu					
F2			202.685	202.685	202.685
Fe					
Fm					
Fr					
Ga					
Gd					
Ge					31.09
H2	130.570	130.570	130.570	130.570	130.570
He	126.039	126.039	126.039	126.039	126.039
Hf					
Hg					75.90
Ho					
I2	116.139	116.139	116.139	116.139	116.139
In					
Ir					
K		64.68	64.68	64.68	64.68
Kr	163.971	163.971	163.971	163.971	163.971
La					
Li		29.12	29.12	29.12	29.12
Lr					
Lu					
Md					
Mg				32.68	32.68
Mn					
Mo					
N2	191.502	191.502	191.502	191.502	191.502
Na		51.30	51.30	51.30	51.30
Nb					
Nd					
Ne	146.214	146.214	146.214	146.214	146.214
Ni					
No					
Np					
O2	205.037	205.037	205.037	205.037	205.037
Os					
P				41.09	41.09
Pa					

Table 3 (continued)

Pb					64.80
Pd					
Pm					
Po					
Pr					
Pt					
Pu					
Ra					
Rb		76.78	76.78	76.78	76.78
Re					
Rh					
Rn					
Ru					
S					32.054
Sb					
Sc					
Se					
Si			18.81	18.81	18.81
Sm					
Sn					51.18
Sr					
Ta					
Tb					
Tc					
Te					
Th				53.39	53.39
Ti					
Tl					
Tm					
U				50.20	50.20
V					
W					
Xe	169.573	169.573	169.573	169.573	169.573
Y					
Yb					
Zn		41.63	41.63	41.63	41.63
Zr					
Count	12	19	24	30	36

Table 4. Key Thermodynamic Data from SUPCRT92 as Represented by the slop98.dat Data File. These data are in calorie units and correspond to a standard pressure of 1 bar. This table is taken from workbook TDProperties_Rev0_u3.xlsx. The data shown for H₂O(l) (light blue background) are not in the data file, but generated by a model built into the SUPCRT92 software. Light orange background marks items of concern. The data here for SiO₂(aq) were superseded in Wolery and Jové Colón (2007).

SUPCRT92 (slop98.dat, 1998)			
Species	ΔG°_f kcal/mol	ΔH°_f kcal/mol	S° cal/mol-K
O2(g)	0.0	0.0	49.029
H+	0.	0.	0.
OH-	-37.595	-54.977	-2.56
H2O(l)	-56.688	-68.317	16.7
F-	-67.340	-80.150	-3.15
Cl-	-31.379	-39.933	13.56
Br-	-24.870	-29.040	19.80
I-	-12.410	-13.600	25.50
SO4--	-177.930	-217.400	4.50
HS-	2.860	-3.850	16.3
NO3-	-26.507	-49.429	35.12
NH3(aq)	-6.383	-19.440	25.770
NH4+	-18.990	-31.850	26.57
PO4---	-243.500	-305.300	-53.0
HPO4--	-260.310	-308.815	-8.0
H2PO4-	-270.140	-309.820	21.6
H3PO4(aq)	-273.100	-307.920	38.000
CO2(aq)	-92.250	-98.900	28.100
CO3--	-126.191	-161.385	-11.95
HCO3-	-140.282	-164.898	23.53
SiO2(aq)	-199.190	-209.775	18.000
B(OH)3(aq)	-231.540	-256.820	37.000
BO2-	-162.240	-184.600	-8.9
Al+++	-115.609	-126.834	-77.7
AlO2-	-198.693	-222.125	-7.22
Pb++	-5.710	0.220	4.2
Zn++	-35.200	-36.660	-26.2
Cu+	11.950	17.132	9.7
Cu++	15.675	15.700	-23.2
Ni++	-10.900	-12.900	-30.8
Co++	-13.000	-13.900	-27.0

Table 4 (continued)

SUPCRT92 (slop98.dat, 1998)			
Species	ΔG°_f kcal/mol	ΔH°_f kcal/mol	S° cal/mol-K
Fe ⁺⁺	-21.870	-22.050	-25.3
Fe ⁺⁺⁺	-4.120	-11.850	-66.3
Mn ⁺⁺	-55.100	-52.900	-16.2
Mg ⁺⁺	-108.505	-111.367	-33.00
Ca ⁺⁺	-132.120	-129.800	-13.50
Sr ⁺⁺	-134.760	-131.670	-7.53
Ba ⁺⁺	-134.030	-128.500	2.3
Ra ⁺⁺	-134.200	-126.100	12.9
Li ⁺	-69.933	-66.552	2.70
Na ⁺	-62.591	-57.433	13.96
K ⁺	-67.510	-60.270	24.15
Rb ⁺	-67.800	-60.020	28.8
Cs ⁺	-69.710	-61.670	31.75

P(white)			
P(red)			
Quartz	-204.646	-217.650	9.880
Corundum	-374.824	-397.145	12.180
Gibbsite	-276.168	-309.065	16.750
AlCl ₃ .6H ₂ O			
Andalusite	-580.587	-615.866	22.200
Kyanite	-580.956	-616.897	20.000
Sillimanite	-580.091	-615.099	23.130
Calcite	-269.880	-288.552	22.150

Table 5. Key Thermodynamic Data from SUPCRT92 (as represented by the *slop98.dat* data file but converted to Joule units) and from NEA-TDB. This table is taken from workbook *TDProperties_Rev0_u3.xlsx*. Light orange background marks items of concern (including discrepant values). The SUPCRT92 data for aqueous phosphate species (red background) have been discredited.

SUPCRT92 (<i>slop98.dat</i> , 1998)				NEA-TDB (through vol. 12)			
Species	ΔG°_f kJ/mol	ΔH°_f kJ/mol	S° J/mol-K	Species	ΔG°_f kJ/mol	ΔH°_f kJ/mol	S° J/mol-K
O2(g)	0.000	0.000	205.137	O2(g)	0.000	0.000	205.152
H+	0.000	0.000	0.000	H+	0.000	0.000	0.000
OH-	-157.297	-230.024	-10.711	OH-	-157.220	-230.015	-10.900
H2O(l)	-237.183	-285.838	69.873	H2O(l)	-237.140	-285.830	69.950
F-	-281.751	-335.348	-13.180	F-	-281.523	-335.350	-13.800
Cl-	-131.290	-167.080	56.735	Cl-	-131.217	-167.080	56.600
Br-	-104.056	-121.503	82.843	Br-	-103.850	-121.410	82.550
I-	-51.923	-56.902	106.692	I-	-51.724	-56.780	106.450
SO4--	-744.459	-909.602	18.828	SO4--	-744.004	-909.340	18.500
HS-	11.966	-16.108	68.199	HS-	12.243	-16.300	67.000
NO3-	-110.905	-206.811	146.942	NO3-	-110.794	-206.850	146.700
NH3(aq)	-26.706	-81.337	107.822	NH3(aq)	-26.673	-81.170	109.040
NH4+	-79.454	-133.260	111.169	NH4+	-79.398	-133.260	111.170
PO4---	-1018.804	-1277.375	-221.752	PO4---	-1025.491	-1284.400	-220.970
HPO4--	-1089.137	-1292.082	-33.472	HPO4--	-1095.985	-1299.000	-33.500
H2PO4-	-1130.266	-1296.287	90.374	H2PO4-	-1137.152	-1302.600	92.500
H3PO4(aq)	-1142.650	-1288.337	158.992	H3PO4(aq)	-1149.367	-1294.120	161.912
CO2(aq)	-385.974	-413.798	117.570	CO2(aq)	-385.970	-413.260	119.360
CO3--	-527.983	-675.235	-49.999	CO3--	-527.900	-675.230	-50.000
HCO3-	-586.940	-689.933	98.450	HCO3-	-586.845	-689.930	98.400
SiO2(aq)	-833.411	-877.699	75.312	Si(OH)4(aq)	-1307.735	-1456.960	189.973
B(OH)3(aq)	-968.763	-1074.535	154.808	B(OH)3(aq)	-969.268	-1072.800	162.400
BO2-	-678.812	-772.366	-37.238	B(OH)4-			
Al+++	-483.708	-530.673	-325.097	Al+++	-491.507	-538.400	-325.000
AlO2-	-831.332	-929.371	-30.208	Al(OH)4-			
Pb++	-23.891	0.920	17.573	Pb++	-24.238	0.920	18.500
Zn++	-147.277	-153.385	-109.621	Zn++	-147.203	-153.390	-109.800
Cu+	49.999	71.680	40.585	Cu+			
Cu++	65.584	65.689	-97.069	Cu++	65.040	64.900	-98.000
Ni++	-45.606	-53.974	-128.867	Ni++	-45.773	-55.012	-131.800
Co++	-54.392	-58.158	-112.968	Co++			
Fe++	-91.504	-92.257	-105.855	Fe++			

Table 5 (continued)

SUPCRT92 (slop98.dat, 1998)			
Species	ΔG°_f kJ/mol	ΔH°_f kJ/mol	S° J/mol-K
Fe+++	-17.238	-49.580	-277.399
Mn++	-230.538	-221.334	-67.781
Mg++	-453.985	-465.960	-138.072
Ca++	-552.790	-543.083	-56.484
Sr++	-563.836	-550.907	-31.506
Ba++	-560.782	-537.644	9.623
Ra++	-561.493	-527.602	53.974
Li+	-292.600	-278.454	11.297
Na+	-261.881	-240.300	58.409
K+	-282.462	-252.170	101.044
Rb+	-283.675	-251.124	120.499
Cs+	-291.667	-258.027	132.842

NEA-TDB (through vol. 12)			
Species	ΔG°_f kJ/mol	ΔH°_f kJ/mol	S° J/mol-K
Fe+++			
Mn++			
Mg++	-455.375	-467.000	-137.000
Ca++	-552.806	-543.000	-56.200
Sr++	-563.864	-550.900	-31.500
Ba++	-557.656	-534.800	8.400
Ra++			
Li+	-292.918	-278.470	12.240
Na+	-261.953	-240.340	58.450
K+	-282.510	-252.140	101.200
Rb+			
Cs+	-291.456	-258.000	132.100

P(white)			
P(red)			
Quartz	-856.239	-910.648	41.338
Corundum	-1568.264	-1661.655	50.961
Gibbsite	-1155.487	-1293.128	70.082
AlCl ₃ .6H ₂ O			
Andalusite	-2429.176	-2576.783	92.885
Kyanite	-2430.720	-2581.097	83.680
Sillimanite	-2427.101	-2573.574	96.776
Calcite	-1129.178	-1207.302	92.676

P(white)	0.000	0.000	41.090
P(red)		-7.500	
Quartz	-856.287	-910.700	41.460
Corundum	-1582.257	-1675.700	50.920
Gibbsite			
AlCl ₃ .6H ₂ O			
Andalusite			
Kyanite			
Sillimanite			
Calcite			

Table 6. Correction of Data for SiO₂(aq) and Quartz from the “Fournier” Paradigm to the “Rimstidt” Paradigm. The correction for quartz is quite small. This correction was made in the construction of the Wolery and Jové Colón (2007). R =Rimstidt, F = Fournier.

		ΔG°_f kcal/mol	ΔH°_f kcal/mol	S° cal/mol-K
"Fournier"	SiO ₂ (aq)	-199.190	-209.775	18.000
"Rimstidt"	SiO ₂ (aq)	-199.540	-212.179	11.128
	$\Delta(R-F)$	-0.350	-2.404	-6.872

		ΔG°_f kJ/mol	ΔH°_f kJ/mol	S° J/mol-K
	SiO ₂ (aq)	-833.411	-877.699	75.312
	SiO ₂ (aq)	-834.875	-887.757	46.560
	$\Delta(R-F)$	-1.464	-10.058	-28.752

"Fournier"	Quartz	-204.646	-217.650	9.880
"Rimstidt"	Quartz	-204.656	-217.663	9.904
	$\Delta(R-F)$	-0.010	-0.013	0.024

	Quartz	-856.239	-910.648	41.338
"Rimstidt"	Quartz	-856.281	-910.702	41.438
	Quartz	-0.042	-0.054	0.100

Table 7. Key Thermodynamic Data from the Last Two NBS Efforts (as Represented by the slop98.dat Data File). This table is taken from workbook TDProperties_Rev0_u3.xlsx. Data for the preceding and first NBS effort (NBS 500, Rossini et al., 1952) are included in the spreadsheet. The aqueous phosphate species data have been discredited. The Gibbs energy value for $H_2PO_4^-$ from the NBS 270 series (red background) is likely a typo. Some calorie-Joule units conversions are shown between the left and right tables.

NBS 270-(3-8), Wagman et al. (1968) and others				NBS, Wagman et al. (1982)			
Species	ΔG°_f kcal/mol	ΔH°_f kcal/mol	S° cal/mol-K		ΔG°_f kJ/mol	ΔH°_f kJ/mol	S° J/mol-K
O2(g)	0	0	49.003		0	0	205.138
H+	0	0	0		0	0	0
OH-	-37.594	-54.970	-2.57		-157.244	-229.994	-10.75
H2O(l)	-56.687	-68.315	16.71		-237.129	-285.830	69.91
F-	-66.64	-79.50	-3.3		-278.79	-332.63	-13.8
Cl-	-31.372	-39.952	13.5		-131.228	-167.159	56.5
Br-	-24.85	-29.05	19.7		-103.96	-121.55	82.4
I-	-12.33	-13.19	26.6		-51.57	-55.19	111.3
SO4--	-177.97	-217.32	4.8		-744.53	-909.27	20.1
HS-	2.88	-4.2	15.0		12.08	-17.6	62.8
NO3-	-26.61	-49.56	35.0		-108.74	-205.0	146.4
NH3(aq)	-6.35	-19.19	26.6		-26.50	-80.29	111.3
NH4+	-18.97	-31.67	27.1	<-----	-79.31	-132.51	113.4
PO4---	-243.5	-305.3	-53.	-243.475	-1018.7	-1277.4	-222.
HPO4--	-260.34	-308.83	-8.0	-260.313	-1089.15	-1292.14	-33.5
H2PO4-	-260.17	-309.82	21.6	-270.143	-1130.28	-1296.29	90.4
H3PO4(aq)	-273.10	-307.92	37.8	-273.074	-1142.54	-1288.34	158.2
CO2(aq)	-92.26	-98.90	28.1		-385.98	-413.80	117.6
CO3--	-126.17	-161.84	-13.6		-527.81	-677.14	-56.9
HCO3-	-140.26	-165.39	21.8		-586.77	-691.99	91.2
H4SiO4(aq)	-314.7	-351.0	43.		-1316.6	-1468.6	180.

NBS 270-(3-8), Wagman et al. (1968) and others			
Species	ΔG°_f kcal/mol	ΔH°_f kcal/mol	S° cal/mol-K
H3BO3(aq)	-231.56	-256.29	38.8
B(OH)4-	-275.65	-321.23	24.5
Al+++	-116.	-127.	-76.9
Al(OH)4-	-310.2	-356.2	28.
Pb++	-5.83	-0.4	2.5
Zn++	-35.14	-36.78	-26.8
Cu+	11.95	17.13	9.7
Cu++	15.66	15.48	-23.8
Ni++	-10.9	-12.9	-30.8
Co++	-13.0	-13.9	-27.
Fe++	-18.85	-21.3	-32.9
Fe+++	-1.1	-11.6	-75.5
Mn++	-54.5	-52.76	-17.6
Mg++	-108.7	-111.58	-33.0
Ca++	-132.30	-129.74	-12.7
Sr++	-133.71	-130.45	-7.8
Ba++	-134.02	-128.50	2.3
Ra++	-134.2	-126.1	13.
Li+	-70.10	-66.56	3.2
Na+	-62.593	-57.39	14.1
K+	-67.70	-60.32	24.5
Rb+	-67.87	-60.03	29.04
Cs+	-69.79	-61.73	31.80

NBS, Wagman et al. (1982)			
Species	ΔG°_f kJ/mol	ΔH°_f kJ/mol	S° J/mol-K
H3BO3(aq)	-968.75	-1072.32	162.3
B(OH)4-	-1153.17	-1344.03	102.5
Al+++	-485.	-531.	-321.7
Al(OH)4-	-1305.3	-1502.5	102.9
Pb++	-24.43	-1.7	10.5
Zn++	-147.06	-153.89	-112.1
Cu+	49.98	71.67	40.6
Cu++	65.49	64.77	-99.6
Ni++	-45.6	-54.0	-128.9
Co++	-54.4	-58.2	-113.
Fe++	-78.90	-89.1	-137.7
Fe+++	-4.7	-48.5	-315.9
Mn++	-228.1	-220.75	-73.6
Mg++	-454.8	-466.85	-138.1
Ca++	-553.58	-542.83	-53.1
Sr++	-559.48	-545.80	-32.6
Ba++	-560.77	-537.64	9.6
Ra++	-561.5	-527.6	54.
Li+	-283.98	-278.49	13.4
Na+	-261.905	-240.12	59.0
K+	-283.27	-252.38	102.5
Rb+	-283.98	-251.17	121.50
Cs+	-292.02	-258.28	133.05

NBS 270-(3-8), Wagman et al. (1968) and others			
Species	ΔG°_f kcal/mol	ΔH°_f kcal/mol	S° cal/mol-K
P(white)	0	0	9.82
P(red)	-2.9	-4.2	5.45
Quartz	-204.75	-217.72	10.00
Corundum	-378.2	-400.5	12.17
Gibbsite	-546.7	-612.5	33.51
AlCl ₃ .6H ₂ O		-643.3	
Andalusite	-620.8	-655.9	22.28
Kyanite	-620.5	-656.4	20.03
Sillimanite	-627.6	-662.6	22.99
Calcite	-269.80	-288.46	22.2

----->
-
1582.389
-
2287.393
-
2597.427
-
2596.172
-
2625.878

NBS, Wagman et al. (1982)			
Species	ΔG°_f kJ/mol	ΔH°_f kJ/mol	S° J/mol-K
P(white)	0	0	41.09
P(red)	-12.1	-17.6	22.80
Quartz	-856.64	-910.94	41.84
Corundum	-1582.3	-1675.7	50.92
Gibbsite	-2310.21	-2586.67	136.90
AlCl ₃ .6H ₂ O	-2261.1	-2691.6	318.0
Andalusite	-2442.66	-2590.27	93.22
Kyanite	-2443.88	-2594.29	83.81
Sillimanite	-2440.99	-2587.76	96.11
Calcite	-1128.79	-1206.92	92.9

Table 8. Key Thermodynamic Data from the Last Two USGS Efforts as Represented by the *slop98.dat* Data File. This table is taken from workbook *TDPProperties_Rev0_u3.xlsx*. Data for the preceding and first USGS effort (Robie and Waldbaum, 1968) are included in the spreadsheet. The aqueous phosphate species data shown here have been discredited. Red background marks known erroneous values. Light orange background marks items of concern.

USGS: Robie et al. (1978)			
Species	ΔG°_f kJ/mol	ΔH°_f kJ/mol	S° J/mol-K
O2(g)	0.	0.	205.15
H+	0.	0.	0.
OH-	-157.328	-230.025	-10.71
H2O(l)	-237.141	-285.830	69.95
F-	-281.705	-335.350	-13.18
Cl-	-131.270	-167.080	56.73
Br-	-104.010	-121.500	82.84
I-	-51.915	-56.900	106.70
SO4--	-744.630	-909.270	20.00
HS-	12.100	-16.999	62.80
NO3-	-111.500	-207.400	146.94
NH3(aq)	-26.600	-80.2990	111.00
NH4+	-79.457	-133.260	111.17
PO4---	-1001.550	-1259.550	-222.00
HPO4--			
H2PO4-			
H3PO4(aq)			
H2CO3(aq)	-623.170	-699.650	187.00
CO3--	-527.900	-677.140	-56.90
HCO3-	-586.850	-691.990	91.20
H4SiO4(aq)	-1308.000	-1460.000	180.00

USGS: Robie and Hemingway (1995)			
Species	ΔG°_f kJ/mol	ΔH°_f kJ/mol	S° J/mol-K
O2(g)	0.0	0.0	205.15
H+	0.0	0.0	0.00
OH-	-157.3	-230.0	-10.7
H2O(l)	-237.1	-285.8	70.0
F-	-281.5	-335.4	-13.8
Cl-	-131.2	-167.1	56.60
Br-	-103.8	-121.4	82.55
I-	-51.7	-56.8	106.45
SO4--	-744.0	-909.3	18.5
HS-	44.8	16.3	67.0
NO3-	-110.8	-206.9	146.7
NH3(aq)			
NH4+	-79.4	-133.3	111.17
PO4---	-1001.6	-1259.6	-222.0
HPO4--			
H2PO4-			
H3PO4(aq)			
H2CO3(aq)	-623.2	-699.7	184.7
CO3--	-527.0	-675.2	-50.0
HCO3-	-586.8	-689.9	98.4
H4SiO4(aq)	-1307.8	-1460.0	180.0

USGS: Robie et al. (1978)			
Species	ΔG°_f kJ/mol	ΔH°_f kJ/mol	S° J/mol-K
H3BO3(aq)			
H2BO3-			
Al+++	-489.400	-531.000	-308.00
Al(OH)4-			
Pb++	-24.400	-1.700	10.00
Zn++	-147.260	-153.390	-109.60
Cu+	50.000	71.670	41.00
Cu++	65.520	64.770	-99.60
Ni++	-45.600	-54.000	-129.00
Co++	-54.400	-58.200	-113.00
Fe++	-78.870	-89.100	-138.00
Fe+++	-4.600	-48.500	-316.00
Mn++	-228.00	-220.700	-73.60
Mg++	-454.800	-466.850	-138.00
Ca++	-553.540	-542.830	-53.10
Sr++	-559.440	-545.800	-33.00
Ba++	-560.740	-537.640	9.60
Ra++			
Li+	-292.620	-278.455	11.30
Na+	-261.900	-240.300	58.41
K+	-282.490	-252.170	101.04
Rb+	-291.715	-251.120	120.46
Cs+	-283.625	-258.040	132.84

USGS: Robie and Hemingway (1995)			
Species	ΔG°_f kJ/mol	ΔH°_f kJ/mol	S° J/mol-K
H3BO3(aq)			
B(OH)4-			
Al+++	-489.4	-538.4	-332.
Al(OH)4-			
Pb++	-24.2	0.9	18.5
Zn++	-147.3	-153.4	-109.8
Cu+	50.0	71.7	40.60
Cu++	65.1	64.9	-98.0
Ni++	-45.6	-54.0	-128.9
Co++			
Fe++	-90.0	-91.1	-107.1
Fe+++	-16.7	-49.9	-280.0
Mn++	-228.1	-220.8	-73.60
Mg++	-455.4	-467.0	-137.0
Ca++	-553.6	-543.0	-56.2
Sr++	-563.8	-550.9	-31.5
Ba++	-555.4	-532.5	8.40
Ra++			
Li+	-292.9	-278.5	12.24
Na+	-261.5	-240.3	58.45
K+	-282.5	-252.1	101.20
Rb+			
Cs+	-291.5	-258.0	132.1

USGS: Robie et al. (1978)			
Species	ΔG°_f kJ/mol	ΔH°_f kJ/mol	S° J/mol-K
P(white)			
P(red)	0.	0.	22.85
Quartz	-856.288	-910.700	41.46
Corundum	-1582.228	-1675.700	50.92
Gibbsite	-1154.889	-1293.128	68.44
AlCl ₃ .6H ₂ O			
Andalusite	-2439.892	-2587.525	93.22
Kyanite	-2441.276	-2591.730	83.76
Sillimanite	-2438.988	-2585.760	96.11
Calcite	-1128.842	-1207.370	91.71

USGS: Robie and Hemingway (1995)			
Species	ΔG°_f kJ/mol	ΔH°_f kJ/mol	S° J/mol-K
P(white)	0.0	0.0	41.09
P(red)			
Quartz	-856.3	-910.7	41.5
Corundum	-1582.3	-1675.7	50.9
Gibbsite	-1154.9	-1293.1	68.4
AlCl ₃ .6H ₂ O			
Andalusite	-2441.8	-2589.9	91.4
Kyanite	-2443.1	-2593.8	82.8
Sillimanite	-2439.1	-2586.1	95.4
Calcite	-1128.5	-1207.4	91.7

Appendix F

Swelling properties of montmorillonite and beidellite clays: comparison of temperature, cation, and charge substitution effects

*Stephanie L. Teich-McGoldrick, Jeffery A. Greathouse, and Randall T. Cygan**
Sandia National Laboratories, Albuquerque, New Mexico 87185-0754 USA

Supporting Information

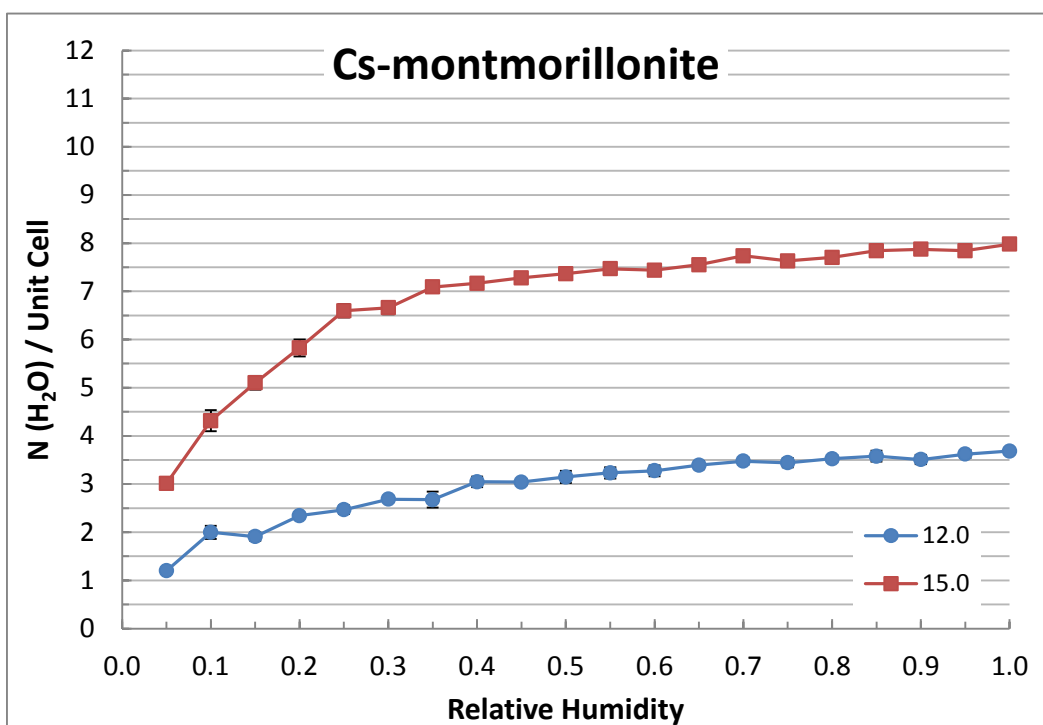
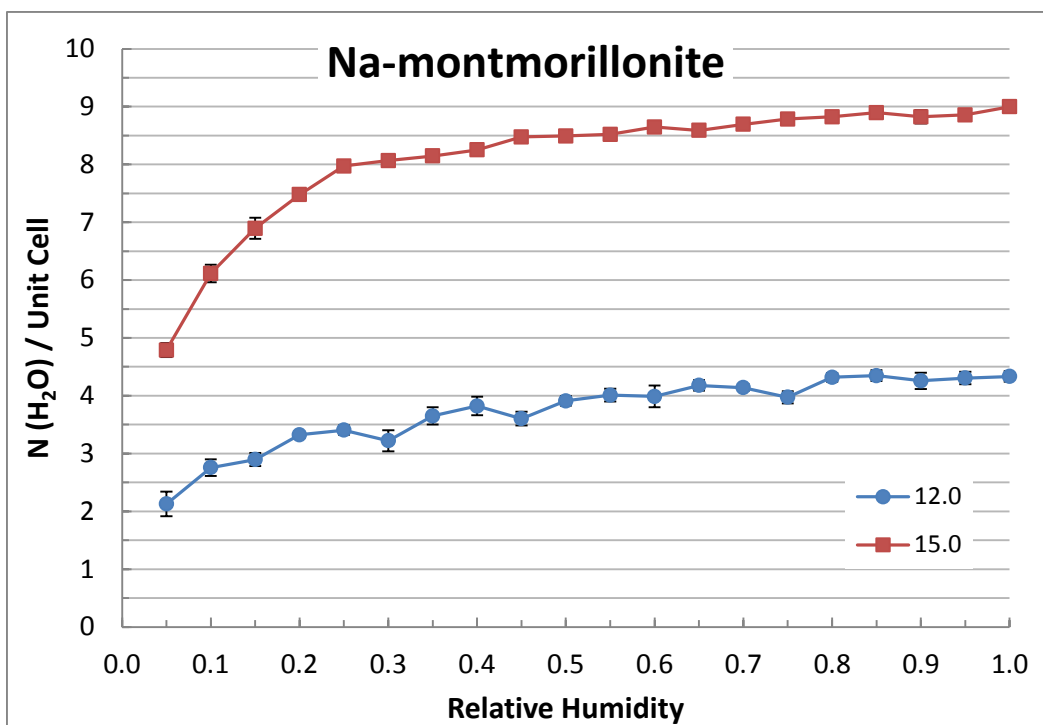


Figure S3. Water adsorption isotherms from GCMC simulations of Na-montmorillonite and Cs-montmorillonite. Fixed d -spacing values (Å) are given in the legend.

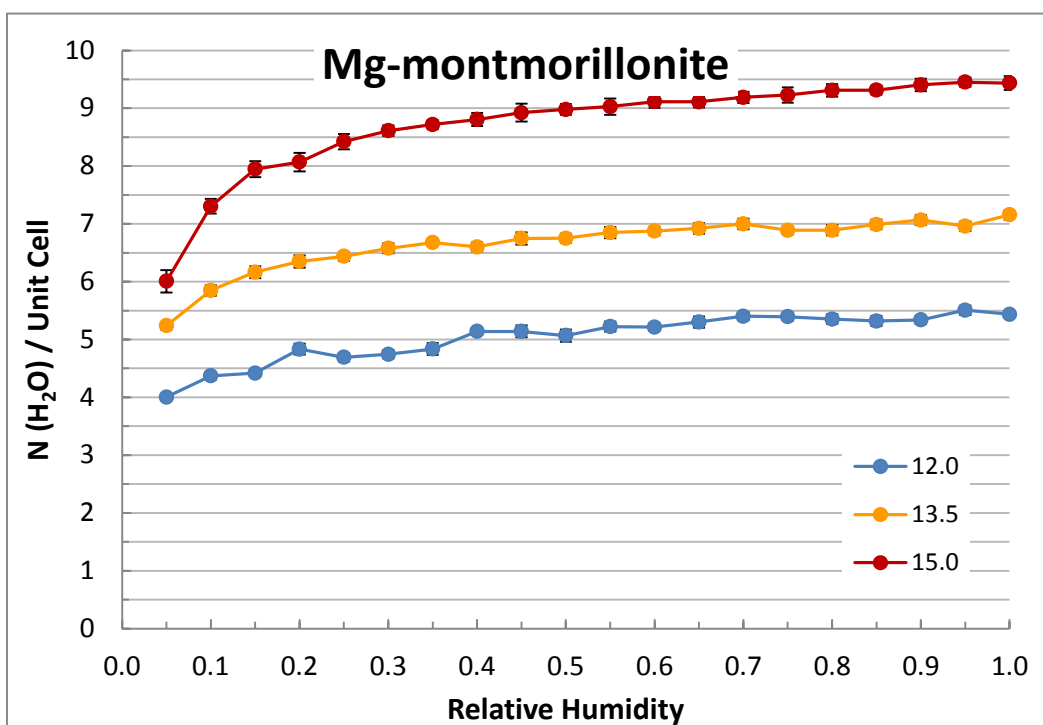
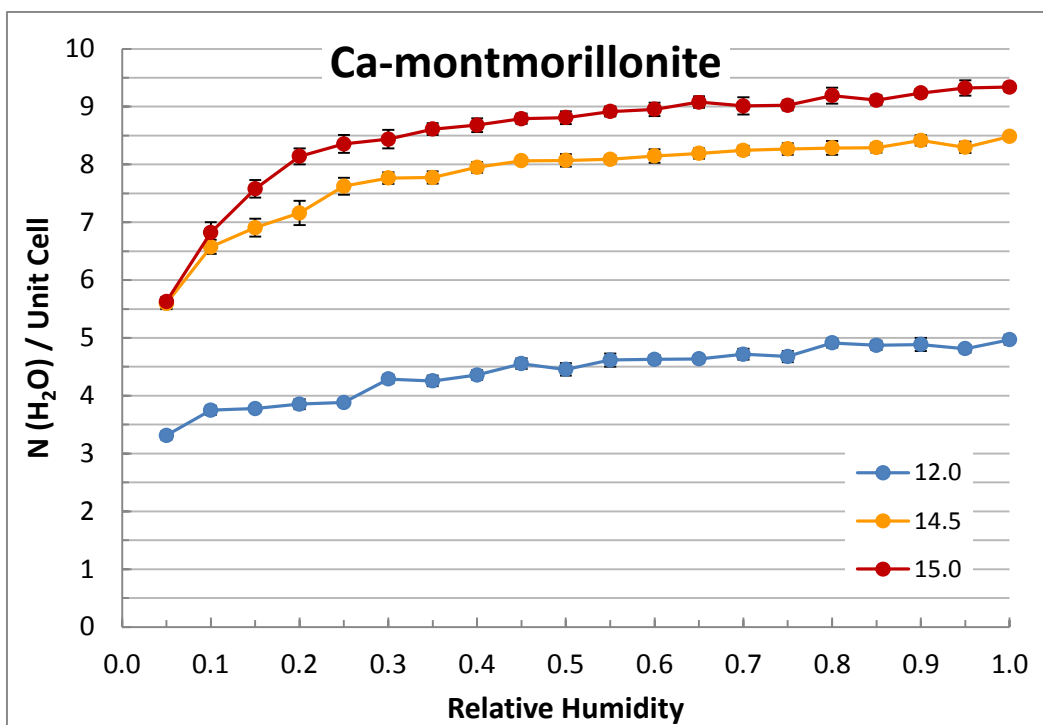


Figure S4. Water adsorption isotherms from GCMC simulations of Ca-montmorillonite and Mg-montmorillonite. Fixed d -spacing values (Å) are given in the legend.

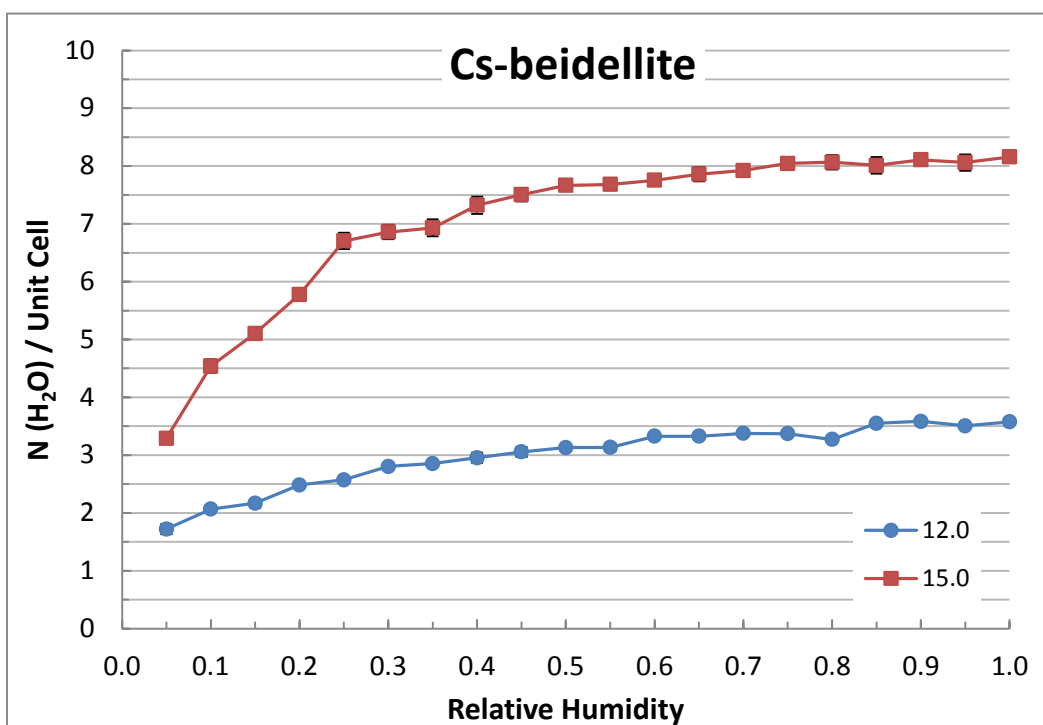
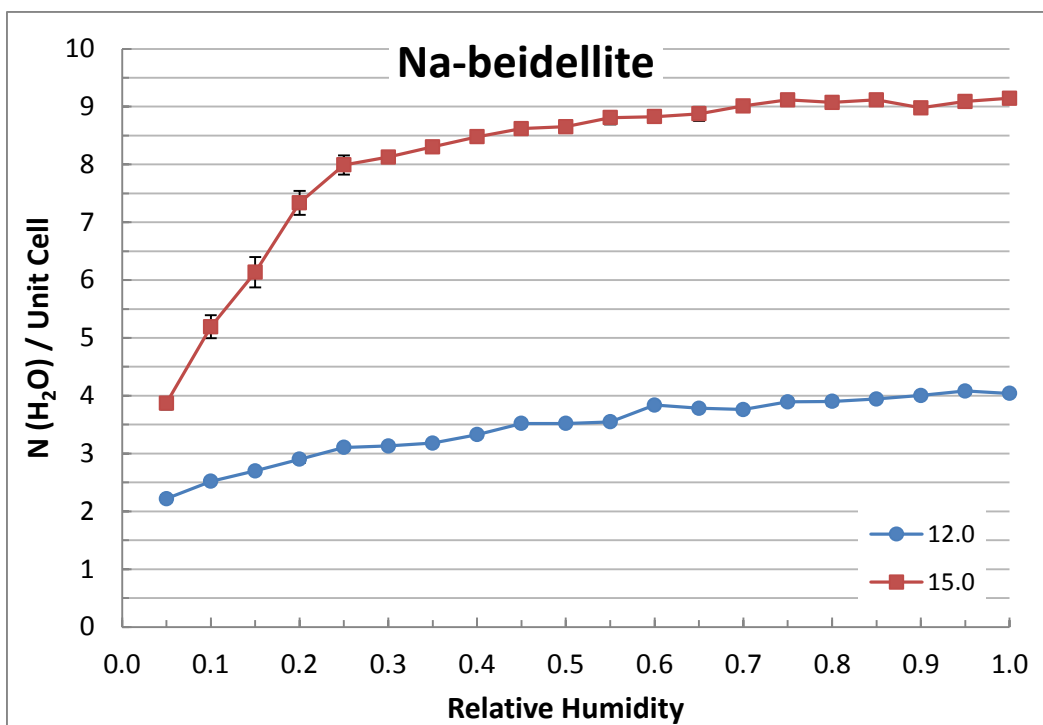


Figure S5. Water adsorption isotherms from GCMC simulations of Na-beidellite and Cs-beidellite. Fixed d -spacing values (Å) are given in the legend.

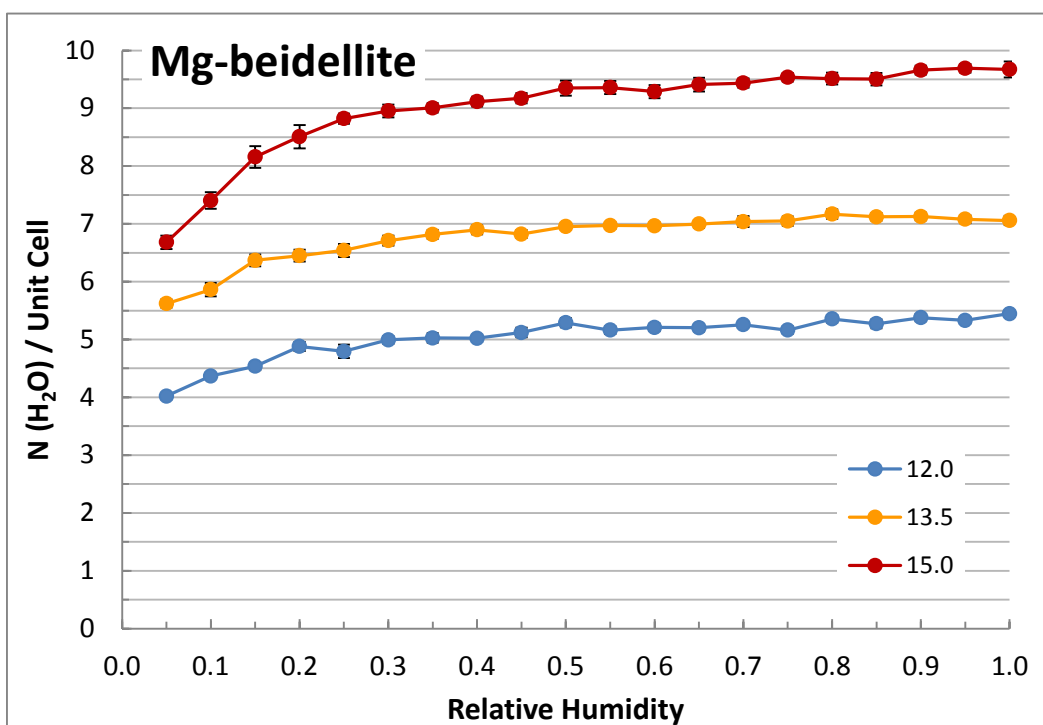
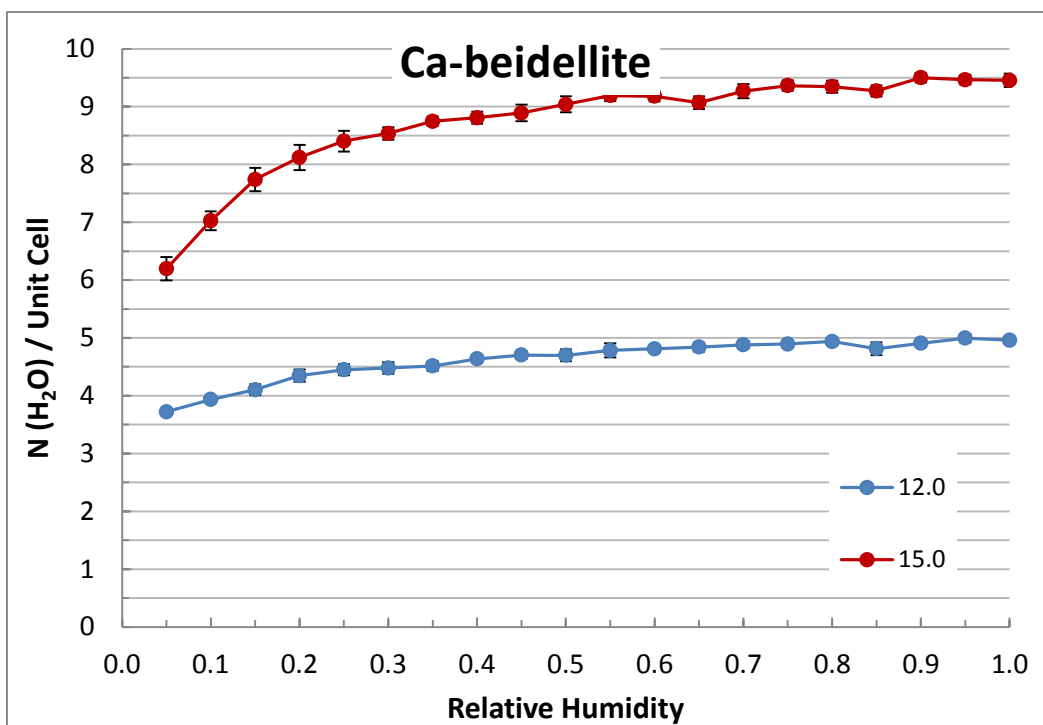


Figure S6. Water adsorption isotherms from GCMC simulations of Ca-beidellite and Mg-beidellite. Fixed d -spacing values (Å) are given in the legend.

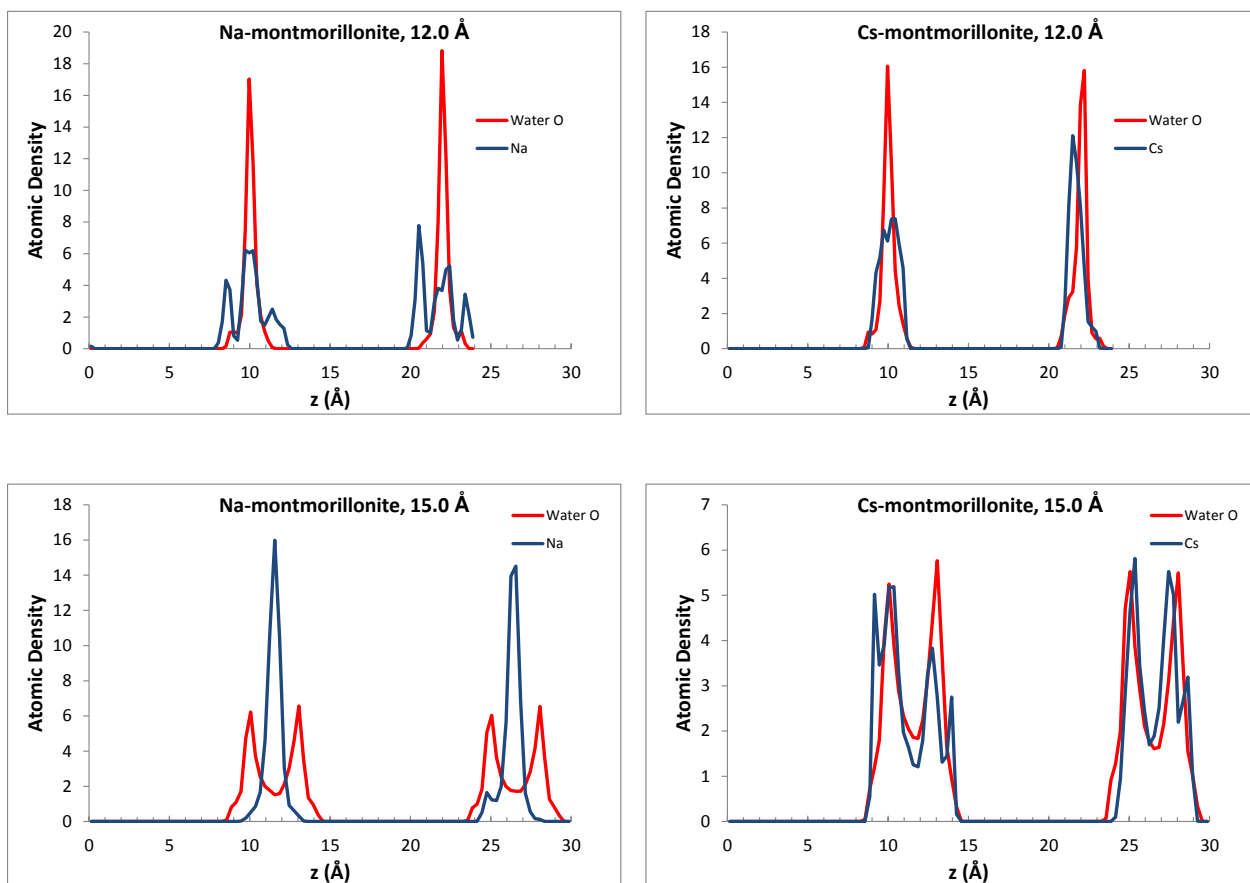


Figure S7. Interlayer cation and water atomic density profiles from GCMC simulations of Na-montmorillonite and Cs-montmorillonite.

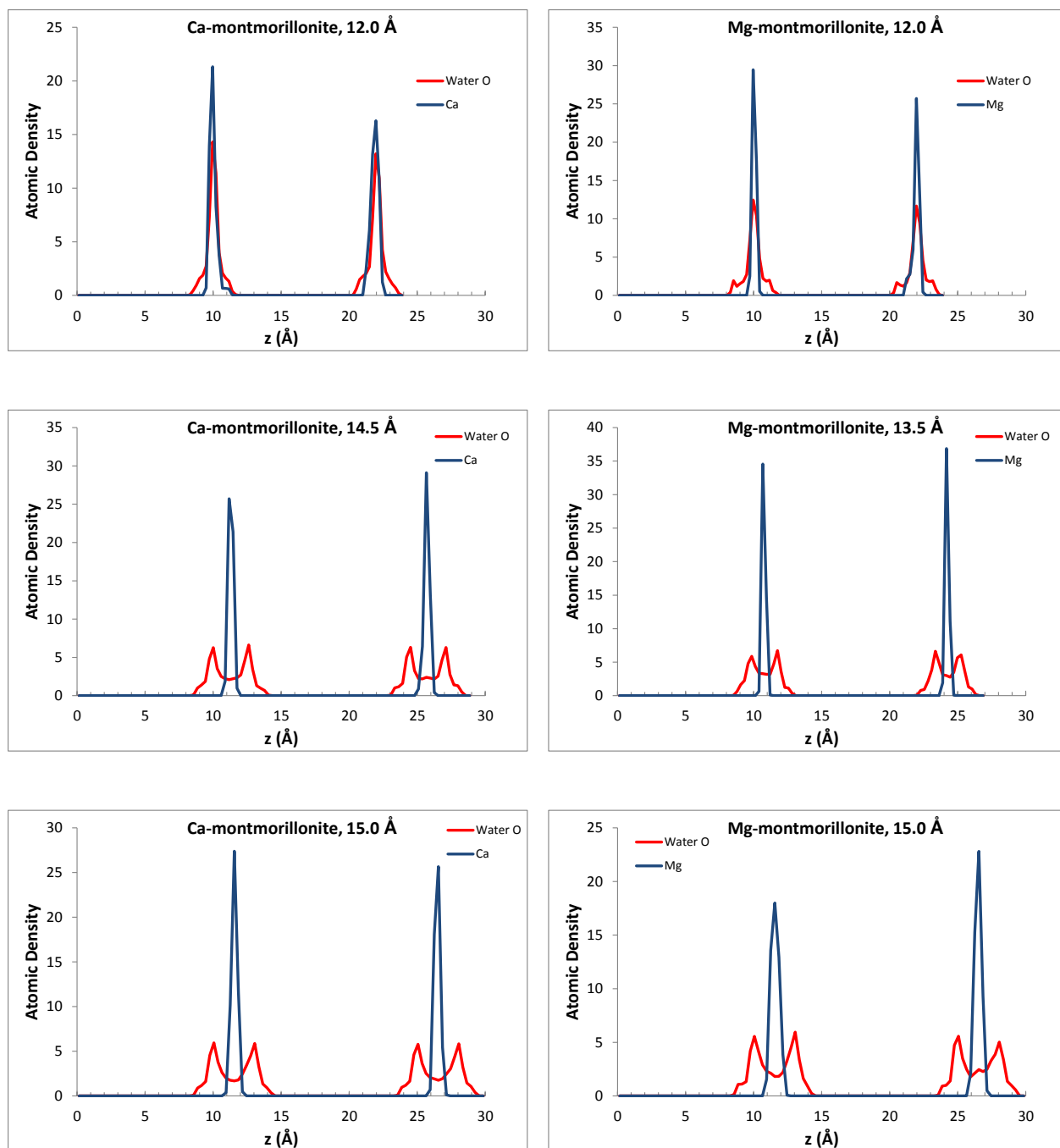


Figure S8. Interlayer cation and water atomic density profiles from GCMC simulations of Ca-montmorillonite and Mg- montmorillonite.

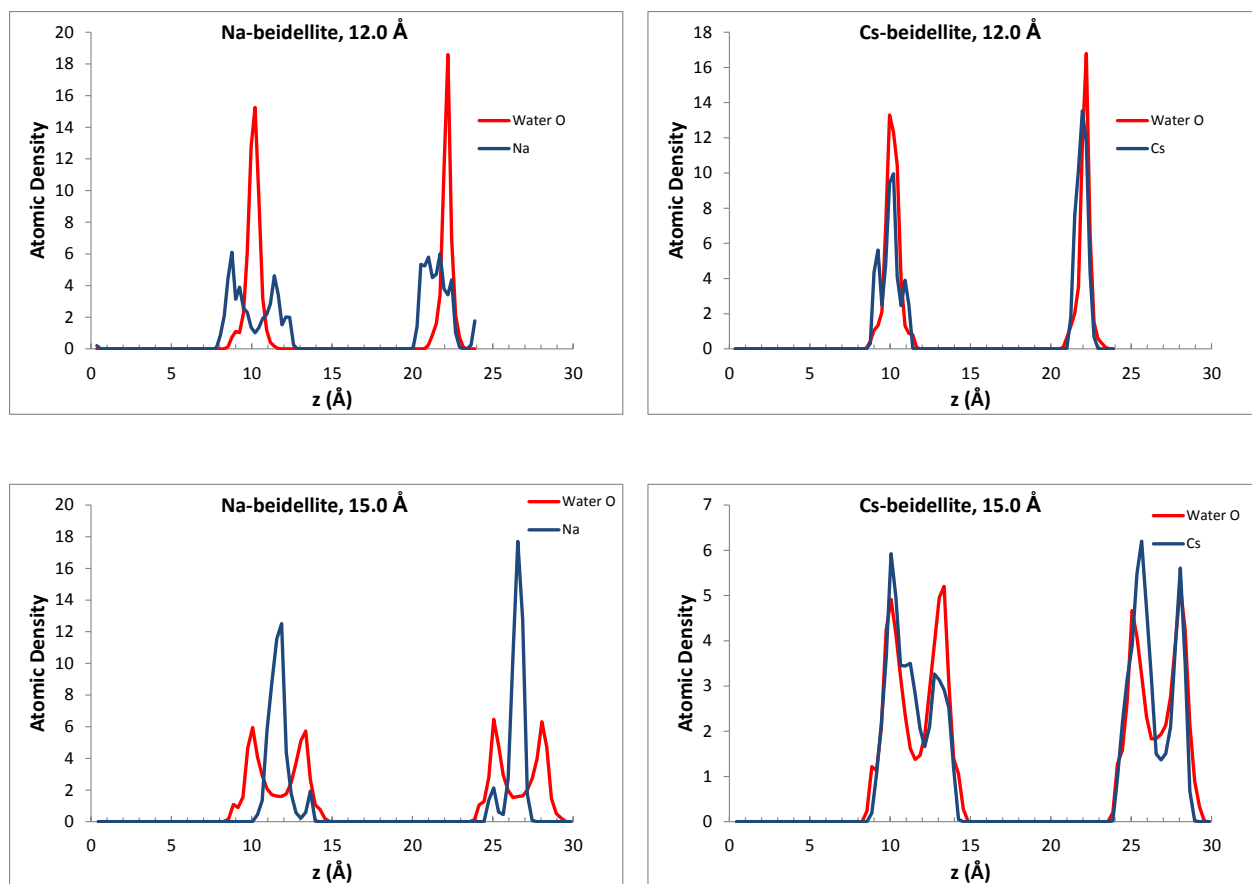


Figure S9. Interlayer cation and water atomic density profiles from GCMC simulations of Na-beidellite and Cs-beidellite.

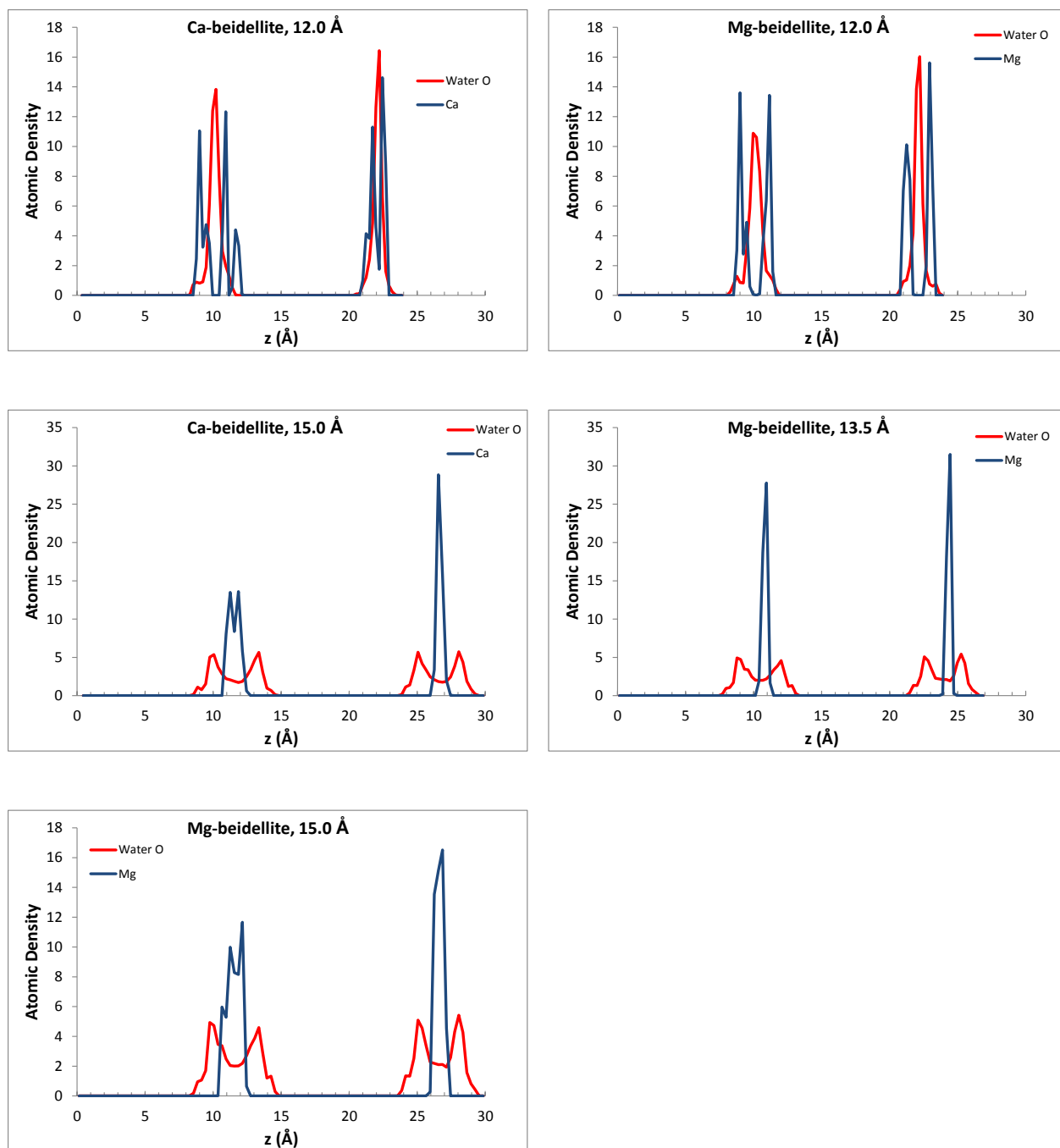


Figure S10. Interlayer cation and water atomic density profiles from GCMC simulations of Ca-beidellite and Mg-beidellite.

Appendix G

Setting up Excel to Allow the DSEF Macros to Work

In order for the Form controls in DSEF to work you must enable macros. If you weren't prompted to **ENABLE MACROS** when you first started DSEF, and the Form controls do not appear to be working, the steps outlined in this Appendix should resolve the problem.

Please follow Figures A.1 through A.7 and the steps outlined below:

Figure A-1– The FILE menu choices



- Figure A.1 - Click on the FILE menu
- Under HELP, select OPTIONS
- Figure A.2 shows the OPTIONS menu,
- Select the TRUST CENTER option
- Figure A.3 shows the TRUST CENTER button
- Click on the TRUST CENTER SETTINGS button
- Figure A.4 shows the TRUST CENTER options
- You need to select settings for
 - Macros
 - Message bar
- Suggested settings are shown in Figures A.5 – A.7

Figure A-2 – The *OPTIONS* menu choices

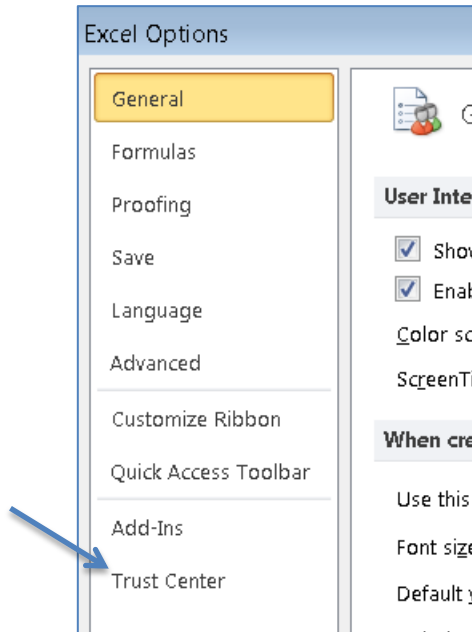


Figure A-3 – Select Trust Center Settings

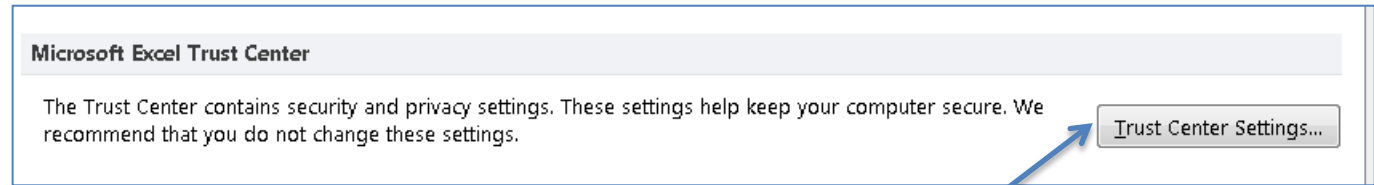


Figure A-4 – Trust Center Settings

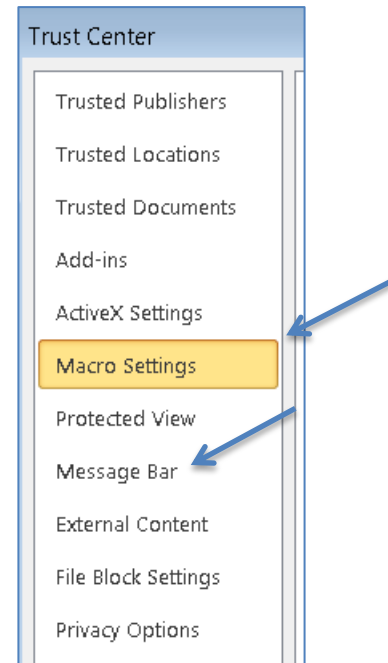


Figure A-5 – Prompt before enabling all controls with minimal restrictions

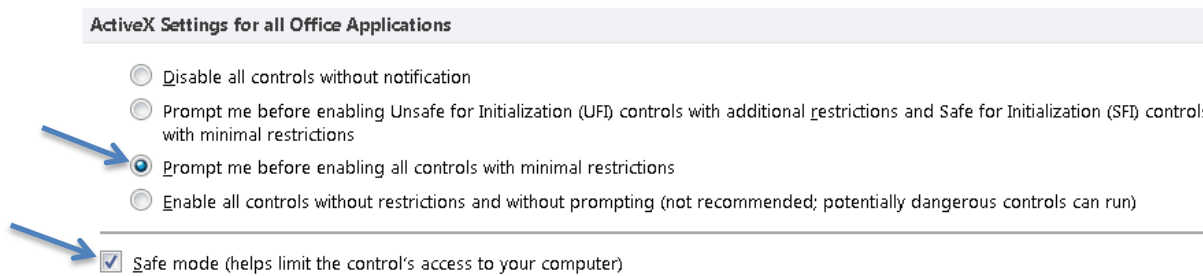


Figure A-6 – Macro settings

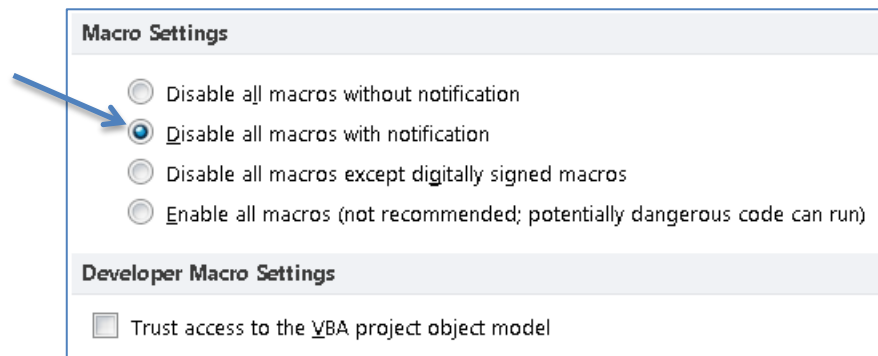
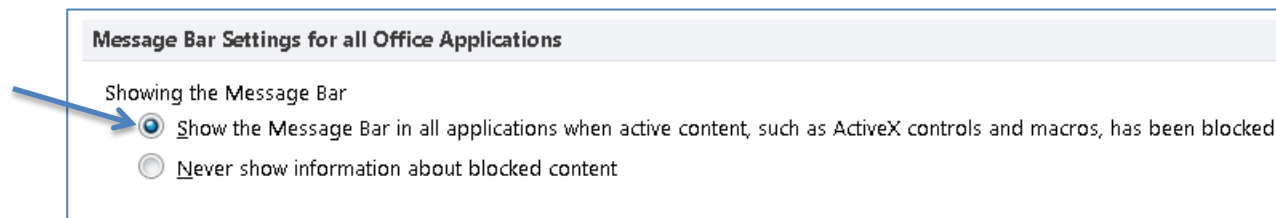


Figure A-7 – Message bar settings



Appendix H

The Mathcad Thermal-Analytical Component of DSEF

This appendix contains PDF pages of the two DSEF Version 3.0 Mathcad thermal-analytical models that receive input from the THERMAL-ANALYTICAL worksheet, and return transient and peak summary data to the THERMAL-ANALYTICAL OUTPUT worksheet in DSEF. The basic Mathcad thermal-analytical model was benchmarked against two different finite-element model (FEM) computer codes by ANL and by SNL. The benchmarking analyses are documented in Sections G.6.1 and G.6.2 of Greenberg 2012b respectively.

Section B.1 describes the use of the Mathcad thermal-analytical models, and their interface with the DSEF Excel spreadsheet.

Section B.2 documents the update to the parametric study analysis model documented in the DSEF Version 2.1 User Manual to add the capability to perform iterative analyses to determine required ventilation time. This one model can perform either parametric study case analyses when the input data sets the mode to “Parametric”, or individual case and iterative convergence modeling when the mode is set to “Single”. Section B.2 shows an example of a parametric study set of analysis cases.

Section B.3 documents the additional programming added to the parametric study analysis model to perform iterative analysis to determine required ventilation time necessary to meet input temperature constraint values for the drift wall (which is easily modified to apply the temperature constraint at other locations as well). This model was used to perform the analyses documented in Greenberg 2012a.

Section B.4 documents a new DSEF Version 3.0 Mathcad model that allows temperature and time-dependent thermal properties within the EBS layers of the model. The particular PDF file and Mathcad document example applies these to salt for temperature-dependent thermal conductivity and time-dependent crushed salt porosity to model consolidation of the crushed salt layer with time and heat. The data for the time-dependent crushed salt consolidation comes from a finite element model in Hardin 2012b (Figure C-5). This model provides proof-of-principle that the thermal-analytical model can accommodate more complex thermal property modeling than the constant properties assumed in models and analysis using earlier versions of DSEF. The thermal results of this new model have a better fit to the FEM model results for the 12-PWR 40-GWd/MT burnup waste stream with 50 years of surface storage documented in Hardin 2012b than was possible with previous analyses using constant salt properties in the EBS (see Greenberg 2012b, Section G.6.2).

With different temperature or time-depending functions, this methodology could be used to model moisture dependent properties covering dryout or re-wetting effects in other media. This would require other data or analysis to set the basic input functions, but then the benefits of the analytical-model approach could be applied to a broader class of problems.

B.1 Using the Mathcad models in conjunction with the DSEF Excel file

The Mathcad file and the DSEF Excel file need to be in the same directory to facilitate the data transfer. Before Mathcad can read the Excel file, the Excel file must be closed. By default the Mathcad DSEF file has the calculation mode set to manual, and the variable “Write_OK” is set to “No”. This allows the user to make adjustments and look at results prior to writing them back to the DSEF Excel file. To calculate a screen at a time as the user pages through the Mathcad file, press F9 or use the Mathcad TOOLS – CALCULATE menu to select CALCULATE NOW, alternatively the user can calculate the entire document by pressing CTRL-F9 or selecting the menu option TOOLS – CALCULATE - CALCULATE WORKSHEET. After reviewing the results in MathCad, set the variable “Write_OK” to “Yes” and recalculate the Mathcad document to write the results back to the Excel file in the THERMAL-ANALYTICAL OUTPUT worksheet. To preserve a record of the full Mathcad calculation, the user should print the file to a PDF file for future reference.

Working with the Mathcad component of DSEF – here are some key pointers for using the Mathcad file:

- Connecting to the DSEF Excel component – on the first page (page 1 of 21 of the PDF listing) assign the file name of the Excel file you want to work with to the variable “file”.
- The calculation mode setting in Mathcad – the calculation mode setting in the Mathcad component is set to “Manual” (under the Mathcad TOOLS menu selection). This gives the user more control when working with a large model, and also allows you to set variables that will turn on or delay writing back to the DSEF Excel file until you are ready. Pressing the F9 key, or using the Mathcad menu to select “Calculate Now” will process only the currently visible screen and variables, so you can work your way slowly through the file and see the data, section-by-section as it is being read in from the THERMAL-ANALYTICAL worksheet. Either pressing CTRL-F9, or using the menu to select “Calculate Worksheet” will initiate a complete calculation of the entire file.
- Writing the results back to the THERMAL-ANALYTICAL OUTPUT worksheet – on the first page of the PDF listing, use the variable “Write_OK” to “Yes” if you are ready to immediately write your calculated results back to the Excel file, or to “No” if you want to examine the results first. Setting the variable to “No” allows you to make changes in Mathcad to some of the input variables if you want to make adjustments to refine your design case to reach some desired goal. For example, if you wanted to find the required ventilation time to meet a given design constraint, you might want to adjust the ventilation time until the goal was met, and then go back and set “Write_OK” to “Yes”.
- Speeding up the calculations – on the bottom of page 11 of 21 in the PDF file, there are two variables “Counter” and “Step”. These variables set the number of time-steps and the size of the time-step in the main calculation loop for the transient calculations. If you

are doing a large number of parametric study cases, or covering a long time period, you may first want to set a large time-step to quickly get a ball-park answer, and then later rerun the case with a smaller time-step after you have adjusted some variables in your design case to try to optimize your results.

- Additional graphics in the Mathcad file – the Mathcad file includes a number of plots for working with the analysis that are not currently returned to the DSEF Excel component. These include a plot of the thermal resistance versus radius of the EBS layers before and after backfill is installed (see pages 5 and 6 of the PDF file), and a plot of the thermal gradients within the EBS at the time of the waste package peak temperature and the drift wall peak temperature (see page 19 of 21 in the PDF file).
- Selectively overriding input variables – After a variable has been assigned a value, either by reading it in from the DSEF Excel component or within the Mathcad component itself, the user can override the value and provide a new assignment. Mathcad notes the re-assignment by underlining the variable and displaying a message on mouse-over of the variable as you work. Care should be taken when re-assigning variables. The user is advised to make any re-assignments at the point where the variable is first assigned, so that the changes are easily identified. The notes section of the INPUTS CHECKLIST in the DSEF Excel component is the place to note any such changes that remain in effect when the final analysis results are returned to the Excel file.
- Printing the Mathcad Output – it should be noted that saving the Mathcad file after an analysis does not save the results, it just saves the problem setup and variables. To see the results again the Mathcad worksheet must be completely recalculated. This is not a problem for short calculations. However, for longer more complex calculations, or if you want to keep a record of intermediate design “test cases”, it is recommended that the user print the fully evaluated results to a PDF file or to a printer for traceability, and to create records for QA/QC purposes. The current Mathcad component has a header that lists the Mathcad file name.

B.2 The Mathcad parametric analysis and iterative convergence model – parametric study example

Step 13 on the DSEF INPUTS worksheet allows the user to either select a “single” calculation mode that uses all of the input data for the reference case defined in Steps 1 through 12, or to select a “parametric” study calculation mode. Figure shows the options available for parametric studies, where the basic inputs have been set, but the user can then define up to 10 data values for one of six possible parameters – waste package spacing, drift spacing, storage time, ventilation duration, rock thermal conductivity, and backfill thermal conductivity. The Mathcad model documented in this section is essentially the same as that documented in the Version 2.1 User Manual for running parametric study cases when “parametric” is selected as the study mode. The model looks slightly different because of the additional capabilities discussed in Section B.3, and because “collapsible” regions have been added to the Mathcad document to speed up review of results when using the iterative model discussed in Section B.3. The collapsible region boundaries appear as lines going across the entire page, with a drop-down arrow at the left-hand edge of the line.

The specific parametric study example case was taken from Greenberg 2012b, and is Case 500-1 in that report, which corresponds to DSEF Case Library case number 427. It is a parametric study of waste package spacing (with 10 values ranging from 15 to 24 m) for a large 32-PWR waste package having 40-GWd/MT burnup, with a drift spacing of 70 m, surface storage of 50 years, and 100 years of ventilation in a clay/shale repository design. As the last figure in the analysis shows, a waste package spacing of 23 m is required to achieve a maximum drift wall temperature of 100°C. Greenberg 2012b included analysis of thermal gradients into the host rock outside the drift wall by varying the depth of Compliance Point 2 (CP2), and in this example run CP2 = 1 m.

The program loop for the iterative convergence model appears on page 19 of 23 of the example output, but there are no results shown on pages 20 and 21 of 23, since the variable Iterate_OK = “No”, and thus the iterative model was not used.

DSEF R3.0 parametric and iterative model with collapsable areas - for rapid iteration.

Values over-written from DSEF Excel file to create case include: Drift_spacing, TC and t_{vent}.

Allow output transients to be written back to DSEF FILE

Case_name := "500-1"

Variables for repository symmetry and extent: Write_OK := "YES"

N_{drifts} := 4 N_{adj} := 4

REQUIRED REPOSITORY INPUT DATA (from DSEF):

file := "DSEF R3.0_2013Aug12_HRG-Clay_UOX-40_CP2=1m_DS70_Vent100_WP param_Case-500-1.xlsm"

sheet := "Thermal-Analytical"

DATA FOR ITERATION ON TEMPERATURE ACCEPTANCE CRITERIA:

TC := 100 T_{criteria} := (TC + 273.15)·K = 373.15K T_{criteria} = 100·°C

READ DSEF INPUT FILE

Input 1 = Operating Mode (enclosed or open)

Input_1 := READEXCEL(file,concat(sheet,"A5:B5"))

Input_1 := ("MODE = Open or Enclosed:" "Open") Mode := Input_1,2 = "Open"

t_{convergence} := 1·yr CONVERGE CRITERIA FOR REQUIRED VENTILATION TIME IN YEARS

SET THE VARIABLE ITERATE_OK TO "NO" TO TURN OFF THE AUTOMATIC CONVERGENCE CALCULATION, AND MANUALLY RESET IT TO "YES" IF YOU WANT TO FINE TUNE YOUR ANSWER:

Input_2 := READEXCEL(file,concat(sheet,"A7:B16")) **Input 2 = Case Definitions**

ITERATE_OK := "NO"

Input 3 = Ventilation Parameters (for Open Modes)

	"Host Media"	"Clay"
	"Rock thermal conductivity, W/m·K"	1.75
	"Rock thermal diffusivity, m ² /sec"	6.45 × 10 ⁻⁷
	"Repository Depth, m"	500
Input_2 =	"Surface temperature, °C"	15
	"Geothermal gradient, °C/km"	25
	"Ambient temperature at depth, °C"	27.5
	"Waste Package (axial) spacing, m"	20
	"Drift / Borehole (lateral) spacing, m"	70
	"Surface storage time, y"	50

Input_3 := READEXCEL(file,concat(sheet,"e7:f11"))

	"Ventilation Duration, yr"	100
Input_3 =	"Unventilated Closure Duration (Backfill Installation), yr"	10
	"Ventilation Thermal Efficiency, %"	0.75
	"Rock Wall Emissivity"	0.9
	"Waste Package Emissivity"	0.6

RT_name := Input_2,2 = "Clay"

$$k_{ht} := \text{Input}_2,2 \cdot \frac{\text{W}}{\text{m}\cdot\text{K}} = 1.75 \frac{\text{m}\cdot\text{kg}}{\text{K}\cdot\text{s}^3}$$

$$\alpha := \text{Input}_2,2 \cdot \frac{\text{m}^2}{\text{s}} = 6.45 \times 10^{-7} \frac{\text{m}^2}{\text{s}}$$

t_{vent} := if[(Mode = "Enclosed"), 0, Input_3, 2]·yr = 100·yr

t_{backfill} := if[(Mode = "Enclosed"), 0, Input_3, 2]·yr = 10·yr

V_{eff} := if[(Mode = "Enclosed"), 0, Input_3, 2] = 0.75

ε_{wall} := if[(Mode = "Enclosed"), 0.9, Input_3, 2] = 0.9

Mathcad DSEF 3.0 parametric and iterative convergence model - parametric study example for User's Manual.xmod

WP_depth := Input_24, 2 m = 500 m $\epsilon_{WP} := \text{if}[(\text{Mode} = \text{"Enclosed"}), 6, \text{Input}_35, 2] = 0.6$

$T_{\text{surface}} := (\text{Input}_25, 2 + 273.15) \text{K} = 288.15 \text{K}$

geothermal_gradient := Input_26, 2 $\frac{\text{K}}{\text{km}} = 0.025 \frac{\text{K}}{\text{m}}$

OVER-RIDE VENTILATION DURATION

$T_{\text{ambient}} := (\text{Input}_27, 2 + 273.15) \text{K} = 300.65 \text{K}$

WP_spacing := Input_28, 2 m = 20 m

OVER-RIDE DRIFT AND/OR WASTE PACKAGE SPACING

Drift_spacing := Input_29, 2 m = 70 m

$t_{\text{store}} := \text{Input}_210, 2 \text{ yr} = 50 \text{ yr}$

$t_{\text{operate}} := (t_{\text{store}} + t_{\text{vent}}) = 150 \text{ yr}$

T OPERATE = T STORE + T VENTILATE

$t_{\text{closure}} := t_{\text{operate}} + t_{\text{backfill}} = 160 \text{ yr}$

T CLOSURE = T OPERATE + TIME TO BACKFILL



Input 4 = ENGINEERED BARRIER SYSTEM DATA:

Input 5 = COMPLIANCE POINT 2 INPUT DATA

Input_4 := READEXCEL(file, concat(sheet, "A20:F27"))

Input_5 := READEXCEL(file, concat(sheet, "C32"))

Input_4 =	"Waste Form Outer Radius, m"	0.535	"N/A"	0.535	"UOX-40"	"N/A"
	"Canister"	0	0.535	0.535	"None"	"N/A"
	"Waste Package"	0.11	0.535	0.645	"Carbon Steel"	"N/A"
	"Buffer"	0	0.645	0.645	"None"	"N/A"
	"Envelope"	0	0.645	0.645	"None"	"N/A"
	"Backfill"	1.58	0.645	2.225	"70% Bentonite 30% Sand"	1.2
	"Liner"	0.025	2.225	2.25	"Steel"	46
"Host Rock Inner Radius, m -->"	NaN	2.25	NaN	NaN	NaN	

Input_5 = (3.25)

$r_{CP2} := \text{Input}_51, \text{m} = 3.25 \text{m}$

$r_{DW} := \text{Input}_48, 3, \text{m} = 2.25 \text{m}$

$r_{WP} := \text{Input}_49, 4, \text{m} = 0.645 \text{m}$

EBS_name1 := Input_47, 1 = "Liner"

EBS_material1 := Input_47, 5 = "Steel"

thickness1 := Input_47, 2, m = 0.025m

$r_1 := \text{Input}_47, 4, \text{m} = 2.25 \text{m}$

$k_1 := \text{Input}_47, 6 = 46$

$k_1 := \text{if}[(k_1 = \text{"N/A"}), 0, k_1] \frac{\text{W}}{\text{mK}} = 46 \frac{\text{W}}{\text{mK}}$

$$\begin{aligned} \text{EBS_name}_2 &:= \text{Input_46,1} = \text{"Backfill"} & \text{EBS_material}_2 &:= \text{Input_46,5} = \text{"70\% Bentonite 30\% Sand"} \\ \text{thickness}_2 &:= \text{Input_46,2} \cdot \text{m} = 1.38 \text{ m} & r_2 &:= \text{Input_46,4} \cdot \text{m} = 2.225 \text{ m} \\ k_2 &:= \text{Input_46,6} = 1.2 & k_2 &:= \text{if}[(k_2 = \text{"N/A"}), 0, k_2] \cdot \frac{\text{W}}{\text{m}\cdot\text{K}} = 1.2 \cdot \frac{\text{W}}{\text{m}\cdot\text{K}} \\ k_{\text{radiation}} &:= \text{if}[(\text{Mode} = \text{"Enclosed"}), k_2, 0] = 0 \cdot \frac{\text{W}}{\text{m}\cdot\text{K}} \end{aligned}$$

$$\begin{aligned} \text{EBS_name}_3 &:= \text{Input_45,1} = \text{"Envelope"} & \text{EBS_material}_3 &:= \text{Input_45,5} = \text{"Ncre"} \\ \text{thickness}_3 &:= \text{Input_45,2} \cdot \text{m} = 0 \text{ m} & r_3 &:= \text{Input_45,4} \cdot \text{m} = 0.645 \text{ m} \\ k_3 &:= \text{Input_45,6} = \text{"N/A"} & k_3 &:= \text{if}[(k_3 = \text{"N/A"}), 0, k_3] \cdot \frac{\text{W}}{\text{m}\cdot\text{K}} = 0 \cdot \frac{\text{W}}{\text{m}\cdot\text{K}} \end{aligned}$$

$$\begin{aligned} \text{EBS_name}_4 &:= \text{Input_44,1} = \text{"Buffer"} & \text{EBS_material}_4 &:= \text{Input_44,5} = \text{"Ncre"} \\ \text{thickness}_4 &:= \text{Input_44,2} \cdot \text{m} = 0 \text{ m} & r_4 &:= \text{Input_44,4} \cdot \text{m} = 0.645 \text{ m} \\ k_4 &:= \text{Input_44,6} = \text{"N/A"} & k_4 &:= \text{if}[(k_4 = \text{"N/A"}), 0, k_4] \cdot \frac{\text{W}}{\text{m}\cdot\text{K}} = 0 \cdot \frac{\text{W}}{\text{m}\cdot\text{K}} \end{aligned}$$

Define the total thermal resistance between the rock well and the waste package surface based on a heat flux per unit area, it is then applied to a heat flux is per unit length adjusting to area per unit length and q_l (W/m).

$$r_{\text{WP}} = 0.645 \text{ m} \quad r_4 = 0.645 \text{ m} \quad r_3 = 0.645 \text{ m} \quad r_2 = 2.225 \text{ m} \quad r_1 = 2.25 \text{ m} \quad r_{\text{DW}} = 2.25 \text{ m}$$

$$R_1(k_1) := \text{if}\left[\left[\text{thickness}_1 = 0 \vee (k_1 = \text{"N/A"})\right], 0, \frac{r_{\text{DW}}}{k_1} \cdot \ln\left(\frac{r_1}{r_2}\right)\right] \quad R_1(k_1) = 5.465 \times 10^{-4} \cdot \frac{\text{m}^2 \cdot \text{K}}{\text{W}} \quad \text{Thermal resistance}$$

$$\text{EBS_name}_1 = \text{"Liver"} \quad \text{EBS_material}_1 = \text{"Steel"}$$

ADDED CORRECTION FOR PARAMETRIC t_{closure} replaced t_{closure} with (t_{operate} + t_{backfill})

Revised R₂ to make it an explicit function of t_{operate} and t_{backfill}

$$R_2(k_2, t_{\text{operate}}, t_{\text{backfill}}) := \begin{cases} k_2 \leftarrow k_{\text{radiation}} \left[t < (t_{\text{operate}} + t_{\text{backfill}}) \right] + k_2 \left[t \geq (t_{\text{operate}} + t_{\text{backfill}}) \right] \\ \text{return if} \left[\left[(\text{thickness}_2 = 0) \vee (k_2 = 0) \right], 0, \frac{r_{\text{DW}}}{k_2} \cdot \ln\left(\frac{r_2}{r_3}\right) \right] \end{cases} \quad \frac{r_{\text{DW}}}{k_2} \cdot \ln\left(\frac{r_2}{r_3}\right) = 2.322 \cdot \frac{\text{m}^2 \cdot \text{K}}{\text{W}}$$

Mathcad DSEF 3.0 parametric and iterative convergence model - parametric study example for User's Manual.xmod

$$\text{EBS_name}_2 = \text{"Backfill"} \quad \text{EBS_material}_2 = \text{"70\% Bentonite 30\% Sand"} \quad R_2(k_2, 5\text{-yr}, 300\text{-yr}, 10\text{-yr}) = 0 \frac{\text{m}^2 \cdot \text{K}}{\text{W}} \quad R_2(k_2, 1000\text{-yr}, 300\text{-yr}, 10\text{-yr}) = 2.321741 \frac{\text{m}^2 \cdot \text{K}}{\text{W}}$$

$$R_3(k_3) = \text{if} \left[\left[\text{thickness}_3 = 0 \vee (k_3 = \text{"N/A"}) \right], 0, \frac{\rho_{\text{DW}}}{k_3} \ln \left(\frac{r_3}{r_4} \right) \right] \quad R_3(k_3) = 0 \frac{\text{m}^2 \cdot \text{K}}{\text{W}}$$

$$\text{EBS_name}_3 = \text{"Envelope"} \quad \text{EBS_material}_3 = \text{"None"}$$

$$R_4(k_4) = \text{if} \left[\left[\text{thickness}_4 = 0 \vee (k_4 = \text{"N/A"}) \right], 0, \frac{\rho_{\text{DW}}}{k_4} \ln \left(\frac{r_4}{r_{\text{WP}}} \right) \right] \quad R_4(k_4) = 0 \frac{\text{m}^2 \cdot \text{K}}{\text{W}}$$

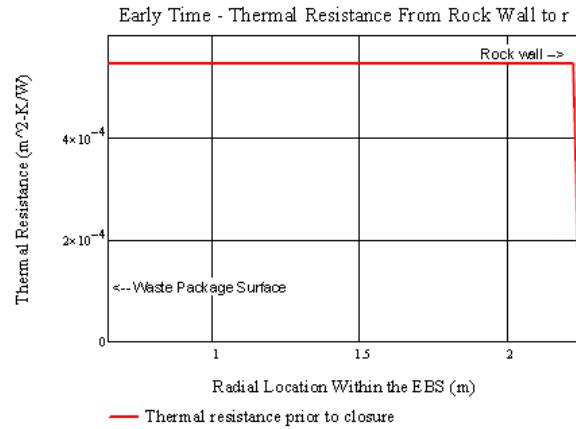
$$\text{EBS_name}_4 = \text{"Buffer"} \quad \text{EBS_material}_4 = \text{"None"}$$

$$R_{\text{Total}}(t, k_1, k_2, k_3, k_4) := R_1(k_1) + R_2(k_2, t, t_{\text{operate}}, t_{\text{backfill}}) + R_3(k_3) + R_4(k_4) \quad \text{Total thermal resistance between wall and waste package}$$

$$t_{\text{backfill}} = 10\text{-yr} \quad t_{\text{operate}} = 100\text{-yr}$$

$$R_{\text{continuous}}(t, r, k_1, k_2, k_3, k_4) := \begin{cases} k k_2 \leftarrow k_{\text{radiation}} \left[t < (t_{\text{operate}} + t_{\text{backfill}}) \right] + k_2 \left[t \geq (t_{\text{operate}} + t_{\text{backfill}}) \right] \\ R \leftarrow R_1(k_1) + R_2(k_2, t, t_{\text{operate}}, t_{\text{backfill}}) + R_3(k_3) + \text{if} \left[\left[\left(\text{thickness}_4 = 0 \right) \vee (k_4 = \text{"N/A"}) \right], 0, \frac{\rho_{\text{DW}}}{k_4} \ln \left(\frac{r_4}{r} \right) \right] \quad \text{if } r \leq r_4 \wedge r \geq r_{\text{WP}} \\ R \leftarrow R_1(k_1) + R_2(k_2, t, t_{\text{operate}}, t_{\text{backfill}}) + \text{if} \left[\left[\left(\text{thickness}_3 = 0 \right) \vee (k_3 = \text{"N/A"}) \right], 0, \frac{\rho_{\text{DW}}}{k_3} \ln \left(\frac{r_3}{r} \right) \right] \quad \text{if } r \leq r_3 \wedge r > r_4 \\ R \leftarrow R_1(k_1) + \text{if} \left[\left[\left(\text{thickness}_2 = 0 \right) \vee (k_2 = 0) \right], 0, \frac{\rho_{\text{DW}}}{k k_2} \ln \left(\frac{r_2}{r} \right) \right] \quad \text{if } r \leq r_2 \wedge r \geq r_3 \\ R \leftarrow \text{if} \left[\left[\left(\text{thickness}_1 = 0 \right) \vee (k_1 = \text{"N/A"}) \right], 0, \frac{\rho_{\text{DW}}}{k_1} \ln \left(\frac{r_1}{r} \right) \right] \quad \text{if } r \leq r_{\text{DW}} \wedge r \geq r_2 \\ R \leftarrow \text{"Invalid Radius"} \quad \text{otherwise} \\ \text{return } R \end{cases}$$

$$R_{\text{continuous}}(5\text{-yr}, r_{\text{WP}}, k_1, k_2, k_3, k_4) = 5.465 \times 10^{-4} \frac{\text{K} \cdot \text{s}^3}{\text{kg}} \quad R_{\text{continuous}}(1000\text{-yr}, r_{\text{WP}}, k_1, k_2, k_3, k_4) = 2.322288 \frac{\text{K} \cdot \text{s}^3}{\text{kg}}$$



$$r_{DW} = 2.25\text{m}$$

$$r_1 = 2.25\text{m} \quad \text{EBS_name}_1 = \text{"Liner"} \quad \text{EBS_material}_1 = \text{"Steel"}$$

$$r_2 = 2.225\text{m} \quad \text{Note that for "open modes", the backfill hasn't been emplaced at early time}$$

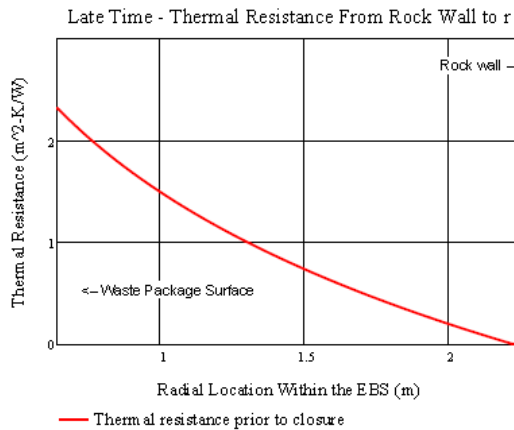
$$r_3 = 0.645\text{m} \quad \text{EBS_name}_3 = \text{"Envelope"} \quad \text{EBS_material}_3 = \text{"None"}$$

$$r_4 = 0.645\text{m} \quad \text{EBS_name}_4 = \text{"Buffer"} \quad \text{EBS_material}_4 = \text{"None"}$$

$$r_{WP} = 0.645\text{m}$$

$$R_1(k_1) = 5.465 \times 10^{-4} \frac{\text{m}^2 \cdot \text{K}}{\text{W}} \quad R_2(k_2, t_{\text{operate}}, t_{\text{backfill}}) = 0 \frac{\text{m}^2 \cdot \text{K}}{\text{W}} \quad R_3(k_3) = 0 \frac{\text{m}^2 \cdot \text{K}}{\text{W}} \quad R_4(k_4) = 0 \frac{\text{m}^2 \cdot \text{K}}{\text{W}}$$

$$R_{\text{Total}}(50\text{yr}, k_1, k_2, k_3, k_4) = 5.465 \times 10^{-4} \frac{\text{m}^2 \cdot \text{K}}{\text{W}}$$



$$r_{DW} = 2.25\text{m}$$

$$r_1 = 2.25\text{m} \quad \text{EBS_name}_1 = \text{"Liner"} \quad \text{EBS_material}_1 = \text{"Steel"}$$

$$r_2 = 2.225\text{m} \quad \text{EBS_name}_2 = \text{"Backfill"} \quad \text{EBS_material}_2 = \text{"70% Bentonite 30% Sand"}$$

$$r_3 = 0.645\text{m} \quad \text{EBS_name}_3 = \text{"Envelope"} \quad \text{EBS_material}_3 = \text{"None"}$$

$$r_4 = 0.645\text{m} \quad \text{EBS_name}_4 = \text{"Buffer"} \quad \text{EBS_material}_4 = \text{"None"}$$

$$r_{WP} = 0.645\text{m}$$

$$R_1(k_1) = 5.465 \times 10^{-4} \frac{\text{m}^2 \cdot \text{K}}{\text{W}} \quad R_2(k_2, t_{\text{closure}}, t_{\text{operate}}, t_{\text{backfill}}) = 2.322 \frac{\text{m}^2 \cdot \text{K}}{\text{W}} \quad R_3(k_3) = 0 \frac{\text{m}^2 \cdot \text{K}}{\text{W}}$$

$$R_{\text{Total}}(1000\text{yr}, k_1, k_2, k_3, k_4) = 2.322 \frac{\text{m}^2 \cdot \text{K}}{\text{W}}$$

INPUT 6 = WASTE FORM DATA

Input_6 := READEXCEL(file,concat(sheet,"A35:B38"))

$$\text{Input}_6 = \begin{pmatrix} \text{"Waste form short name"} & \text{"UOX-40"} \\ \text{"Waste form type"} & \text{"Assembly"} \\ \text{"Waste package capacity"} & 32 \\ \text{"Waste package length, m"} & 5 \end{pmatrix}$$

WF_name := Input_6[1,2 = "UOX-40"

WF_type := Input_6[2,2 = "Assembly"

WP_cap := Input_6[3,2 = 32

	Outside of the liner	Outside of the backfill	Outside of the envelope	Outside of the buffer
WP_length := Input_6[4,2 = 5 m	$A_1 = 2 \cdot \pi \cdot r_1 \cdot \text{WP_length} = 70.69 \text{ m}^2$	$A_2 = 2 \cdot \pi \cdot r_2 \cdot \text{WP_length} = 69.9 \text{ m}^2$	$A_3 = 2 \cdot \pi \cdot r_3 \cdot \text{WP_length} = 20.26 \text{ m}^2$	$A_4 = 2 \cdot \pi \cdot r_4 \cdot \text{WP_length} = 20.26 \text{ m}^2$
	$A_{DW} = 2 \cdot \pi \cdot r_{DW} \cdot \text{WP_length} = 70.686 \text{ m}^2$			$A_{WP} = 2 \cdot \pi \cdot r_{WP} \cdot \text{WP_length} = 20.263 \text{ m}^2$

CONSIDER THE ALTERNATE DESIGN CASE OF AN "OPEN MODE" DESIGN, WITH A CEMENTITIOUS LINER, BUT ONLY AIR BETWEEN THE LINER AND THE WASTE PACKAGE FOR THE FIRST 300 YEARS. ASSUME NO VENTILATION FOR 300 YEARS, AND THEN BACKFILL AT CLOSURE.

CALCULATE THE EQUIVALENT THERMAL RESISTANCE OF THE AIR GAP USING A LINEARIZED RADIATION HEAT TRANSFER COEFFICIENT. BASE THE COEFFICIENT ON THE ROCK WALL TEMPERATURE AT THE DRIFT, AND THE EQUIVALENT WASTE PACKAGE TEMPERATURE NECESSARY TO MOVE THE HEAT GENERATED AT THE WASTE PACKAGE AT ANY GIVEN TIME. THE EQUATION FOR THE RADIATION HEAT TRANSFER COEFFICIENT IS FROM INCROPERA AND DEWITT.

$A_{wall} := \text{WP_length} \cdot 2 \cdot \pi \cdot r_{DW} = 70.686 \text{ m}^2$

Stefan Boltzmann constant $\sigma := 5.670 \cdot 10^{-8} \frac{\text{W}}{\text{m}^2 \cdot \text{K}^4}$

Waste Package emissivity $\epsilon_{WP} = 0.6$

Rock wall or cementitious liner emissivity $\epsilon_{wall} = 0.9$

The basis for the rock and waste package emissivity assumed is F.P. Incropera and D.P. DeWitt, *Fundamentals of Heat and Mass Transfer*, 4th Edition, 1996, Table A-11, which shows a range of 0.88 to 0.93 is adapted from hemispherical emissivity of rock at around 300 K. This range is corroborated by the "Heat Transmission" section of Perry's Chemical Engineers Handbook, 6th Edition, 1984 (Table 10-17, pages 10-51 to 10-52) for normal emissivity of rough silica and rough fused quartz, ranging from 0.8 to 0.93. The waste package surface is assumed to be covered with dust and dirt. The emissivity values to the left were specified in DSEF, and should be changed there if necessary.

Reference for radiation heat transfer coefficient, h_{rad} , is from Incropera and DeWitt, Table 13.3 for concentric infinite cylinders (based on the inner surface as the heat source), and is also referenced in the YMP *Ventilation Model and Analysis Report*, ANL-EBS-MD-000030 REV 04, Oct. 2004, page 6-8.

$$h_{rad_infinite}(r_1, r_0, \epsilon_1, \epsilon_0) := \frac{\sigma}{\frac{1}{\epsilon_1} + \left(\frac{1 - \epsilon_0}{\epsilon_0} \right) \frac{r_1}{r_0}}$$

$$h_{rad_infinite}(r_{WP}, r_{DW}, \epsilon_{WP}, \epsilon_{wall}) = 3.338 \times 10^{-8} \frac{\text{W}}{\text{m}^2 \cdot \text{K}^4}$$

Usage is Q in watts = $h^* A^* (T_1^4 - T_0^4)$

For radiation between the liner and the envelope (both metal surfaces) use r_2 and r_3 , and assume the same emissivity for both surfaces.

$$Q_{\text{rad_infinite}}(r_1, r_o, \epsilon_i, \epsilon_o, L, T_{\text{cold}}, T_{\text{hot}}) := h_{\text{rad_infinite}}(r_1, r_o, \epsilon_i, \epsilon_o) (2\pi r_1 L) (T_{\text{hot}}^4 - T_{\text{cold}}^4) \quad Q_{\text{rad_infinite}}(r_3, r_2, \epsilon_{\text{WP}}, \epsilon_{\text{wall}}, \text{WP_length}, 300 \text{ K}, 600 \text{ K}) = 8.217 \times 10^4 \text{ W}$$

$$Q_{\text{L_rad_infinite}}(r_1, r_o, \epsilon_i, \epsilon_o, T_{\text{cold}}, T_{\text{hot}}) := h_{\text{rad_infinite}}(r_1, r_o, \epsilon_i, \epsilon_o) (2\pi r_1) (T_{\text{hot}}^4 - T_{\text{cold}}^4) \quad Q_{\text{L_rad_infinite}}(r_3, r_2, \epsilon_{\text{WP}}, \epsilon_{\text{wall}}, 300 \text{ K}, 600 \text{ K}) = 1.643 \times 10^4 \frac{\text{W}}{\text{m}}$$

Heat transfer by radiation from NIRAS/ONDRAF December 2005 Report Eef Weetjens and Xavier Sillen: *Thermal analysis of the Supercontainer concept 2D axisymmetric heat transport calculations*, Section 5.4.3. P.g 34, equation 29.

$$Q_{\text{L_infinite}}(r_1, r_o, \epsilon_i, \epsilon_o, T_{\text{cold}}, T_{\text{hot}}) := \frac{2\pi\sigma (T_{\text{hot}}^4 - T_{\text{cold}}^4)}{\frac{1-\epsilon_i}{\epsilon_i r_1} + \frac{1-\epsilon_o}{\epsilon_o r_o}} \quad Q_{\text{L_infinite}}(r_3, r_2, \epsilon_{\text{WP}}, \epsilon_{\text{wall}}, 300 \text{ K}, 600 \text{ K}) = 1.643 \times 10^4 \frac{\text{W}}{\text{m}}$$

This is the same as the Incropera and DeWitt result, $Q_{\text{L_rad_infinite}}$

Comparison of thermal radiation across a gap to conduction after the gap has been filled with backfill material.

$$Q_{\text{L_conduction_comparison}}(r_1, r_o, T_{\text{cold}}, T_{\text{hot}}) := \frac{2\pi r_o}{\frac{D W}{k_2} \ln\left(\frac{r_o}{r_1}\right)} (T_{\text{hot}} - T_{\text{cold}}) \quad Q_{\text{L_conduction_comparison}}(r_3, r_2, 300 \text{ K}, 600 \text{ K}) = 1.806 \times 10^3 \frac{\text{W}}{\text{m}}$$

$$Q_{\text{ratio}}(r_1, r_o, \epsilon_i, \epsilon_o, T_{\text{cold}}, T_{\text{hot}}) := \frac{Q_{\text{L_infinite}}(r_1, r_o, \epsilon_i, \epsilon_o, T_{\text{cold}}, T_{\text{hot}})}{Q_{\text{L_conduction_comparison}}(r_1, r_o, T_{\text{cold}}, T_{\text{hot}})} \quad Q_{\text{ratio}}(r_3, r_2, \epsilon_{\text{WP}}, \epsilon_{\text{wall}}, 300 \text{ K}, 600 \text{ K}) = 9.097$$

INPUT 7 = PARAMETRIC STUDY VARIABLE INPUT DATA

Input_7 := READEXCEL(file, concat(sheet, "F29:F41"))

```

Cases := Input_7[1] = 10
Parameter := Input_7[2] = "WP Spacing"
Parameter_units := Input_7[3] = "m"
ij := 1..Cases
Parameter_data[ij] := Input_7[ij+3]

Parameter_description[ij] := "Single Base Case" if Cases = 1
concat[num2str[Input_7[ij+3]], ", " , Input_7[3] otherwise
    
```

Input_7 =

1	10
2	"WP Spacing"
3	"m"
4	15
5	16
6	17
7	18
8	19
9	20
10	21
11	22
12	23
13	24

Parameter_data =

	1
1	15
2	16
3	17
4	18
5	19
6	20
7	21
8	22
9	23
10	24

Parameter_description =

	1
1	"15, m"
2	"16, m"
3	"17, m"
4	"18, m"
5	"19, m"
6	"20, m"
7	"21, m"
8	"22, m"
9	"23, m"
10	"24, m"

INPUT 8 = DECAY HEAT INPUT DATA PER UNIT SOURCE (ASSEMBLY OR CANISTER):

Input_8_size := READEXCEL(file,concat(sheet,"C43")) Input_8_size1 := 58 Decay_heat_range := concat["A43:B",num2str((Input_8_size1 + 42))] = "A43:B100"

Input_8 := READEXCEL(file,concat(sheet,Decay_heat_range))

Time_out_of_Reactor := Input_8⁽¹⁾.yr Decay_Heat_per_Cnt := Input_8⁽²⁾.W

Input_8 =

	1	2
1	5	1.029·10 ³
2	5.1	1.011·10 ³
3	5.5	949.125
4	5.75	916.671
5	6	887.984
6	8	742.948
7	10	670.028
8	11.5	634.239
9	15	576.929
10	20	...

Time_out_of_Reactor =

	1
1	5
2	5.1
3	5.5
4	5.75
5	6
6	8
7	10
8	11.5
9	15
10	...

.yr

Decay_Heat_per_Cnt =

	1
1	1.029·10 ³
2	1.011·10 ³
3	949.125
4	916.671
5	887.984
6	742.948
7	670.028
8	634.239
9	576.929
10	...

W

$Q(t) := \text{interp}(\text{cspline}(\text{Time_out_of_Reactor}, \text{Decay_Heat_per_Cnt}), \text{Time_out_of_Reactor}, \text{Decay_Heat_per_Cnt}, t)$

Ventilation efficiency for open systems is $V_{\text{eff}} = 0.75$ between t_{store} and t_{operate}

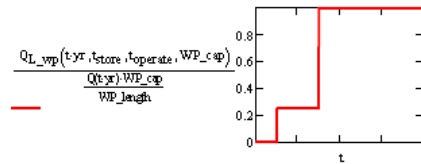
FUNCTION DEFINITION FOR ONE OUTPUT FILE

FORMULAS FOR CALCULATING THE TRANSIENT DRIFT WALL TEMPERATURE:

Central waste package:

$$Q_{L_wp}(t, t_{\text{store}}, t_{\text{operate}}, WP_{\text{cap}}) = \frac{Q(t) \cdot WP_{\text{cap}}}{WP_{\text{length}}} [1 - 1(t \leq t_{\text{store}})] [1 - V_{\text{eff}}(t \leq t_{\text{operate}})]$$

$$Q_{L_wp}(55\text{-yr}, t_{\text{store}}, t_{\text{operate}}, 12) = 177.365 \frac{\text{W}}{\text{m}}$$



Note - added r_{DW} as a function parameter to allow calculations at additional compliance points inside the rock, where r_{DW} would be replaced with newradius value.

$$DW_T_finite_line(t, r_{DW}, y, t_{store}, t_{operate}, WP_cap, Kth, \omega) := \int_0^t \frac{Q_{L_wp}(\tau, t_{store}, t_{operate}, WP_cap)}{8(\pi \cdot Kth) \cdot (t - \tau)} e^{-\frac{(r_{DW})^2}{4 \cdot \omega \cdot (t - \tau)}} \left[\operatorname{erf} \left[\frac{1}{2} \frac{\left(y + \frac{WP_length}{2} \right)}{\sqrt{\omega \cdot (t - \tau)}} \right] - \operatorname{erf} \left[\frac{1}{2} \frac{\left(y - \frac{WP_length}{2} \right)}{\sqrt{\omega \cdot (t - \tau)}} \right] \right] d\tau$$

Adjacent drifts:

$$Q_{L_avg}(t, t_{store}, t_{operate}, WP_cap, WP_spacing) := \frac{Q(t) \cdot WP_cap}{WP_spacing} [1 - 1(t \leq t_{store})] [1 - V_{eff}(t \leq t_{operate})]$$

Note - added r_{DW} as a function parameter to allow calculations at additional compliance points inside the rock, where r_{DW} would be replaced with newradius value.

$$DW_T_drifts(t, r_{DW}, t_{store}, t_{operate}, WP_cap, WP_spacing, Drift_spacing, Kth, \omega) := 2 \sum_{id=1}^{N_{drifts}} \int_0^t \frac{Q_{L_avg}(\tau, t_{store}, t_{operate}, WP_cap, WP_spacing)}{4(\pi \cdot Kth) \cdot (t - \tau)} e^{-\frac{[(r_{DW})^2 + (id \cdot Drift_spacing)^2]}{4 \cdot \omega \cdot (t - \tau)}} d\tau$$

Adjacent waste packages:

$$Q_{wp}(t, t_{store}, t_{operate}, WP_cap) := Q(t) WP_cap [1 - 1(t \leq t_{store})] [1 - V_{eff}(t \leq t_{operate})]$$

Note - added r_{DW} as a function parameter to allow calculations at additional compliance points inside the rock, where r_{DW} would be replaced with newradius value.

$$DW_T_adjacent_plgs(t, r_{DW}, t_{store}, t_{operate}, WP_cap, WP_spacing, Kth, \omega) := 2 \sum_{p=1}^{N_{adj}} \int_0^t \frac{Q_{wp}(\tau, t_{store}, t_{operate}, WP_cap)}{8 \cdot Kth \cdot \sqrt{\omega \cdot \pi}^{1.5} \cdot (t - \tau)^{1.5}} e^{-\frac{[(r_{DW})^2 + (p \cdot WP_spacing)^2]}{4 \cdot \omega \cdot (t - \tau)}} d\tau$$

This command specifies two rows of column headings for output parameter sensitivity runs

OutfileName := file = "DSEF R3.0_2013Aug12_HRG-Clay_UOX-40_CP2=1m,DS70,Vent100,WP param_Case-500-1.xlsm"

Out_sheet := "Thermal-Analytical Output"

This section specifies the column headings for output sensitivity studies

Cases = 10 Read in from Thermal-Analytical sheet in DSEF (Inputs_7)

i := 1..Cases

Parameter_vector_i := $\begin{cases} \text{"Base Case"} & \text{if Cases} = 1 \\ \text{concat(Parameter, " ", Parameter_description}_i) & \text{otherwise} \end{cases}$

	1
1	"WP Spacing 15, m"
2	"WP Spacing 16, m"
3	"WP Spacing 17, m"
4	"WP Spacing 18, m"
5	"WP Spacing 19, m"
6	"WP Spacing 20, m"
7	"WP Spacing 21, m"
8	"WP Spacing 22, m"
9	"WP Spacing 23, m"
10	"WP Spacing 24, m"

Parameter_vector =

heading₁ :=

concat("Parameter value: ", Parameter_vector _i)
""
""
""
""
""
""
""
""
""

heading₂ :=

"TooR (yr)"
"Wall ΔT Central Line Src"
"Wall ΔT Adj Drifts"
"Wall ΔT Adj Pkgs"
"Compliance Point 2, C"
"Rock Wall Temp, C"
"EBS 1 inner Temp, C"
"EBS 2 inner Temp, C"
"EBS 3 inner Temp, C"
"Waste Pkg Temp, C"

heading₁ := heading₁^T heading₂ := heading₂^T

Title_array₁ := stack(heading₁, heading₂)

	1	2	3	4	5
1	Parameter value: WP Spacing 16, m"	""	""	""	""
2	"TooR (yr)"	"Wall ΔT Central Line Src"	"Wall ΔT Adj Drifts"	"Wall ΔT Adj Pkgs"	...

For-Loop analysis returning the output time, three temperature contribution terms, and six temperatures

length(Parameter_data) = 10

r_{DW} = 2.25m

t_{store} = 50-yr

t_{vent} = 100-yr

Changed j vector to Parameter_data, Inserted row2 in row5 changed to k_{radiation} and k₂ from k₂ and k_{backfill} row 8 changed WP_spacej to WP_spacing.

r_{CP2} = 3.25m

t_{operate} = 150-yr

t_{closure} = 160-yr

Removed loop on "j", added r_{DW} into DW_T functions.

Note for enclosed modes k_{radiation} = k₂

DEFINE STEP SIZE FOR OUTDATA

Counter := 200

Step := 5

time_after_employment_analyzed := (Counter*Step.yr) + t_{store} = 1050.yr

ADDED CORRECTION FOR PARAMETRIC t_{closure}
replaced t_{closure} with (t_{operate} + t_{backfill})

```

outdata(ηDW, κCP2, tstore, toperate, WPcap, WPspacing, Driftspacing, Kth, α, k1, k2, k3, k4) :=
for i ∈ 1..Counter+1
|
| ti ← Step.i.yr + tstore - Step.1.yr
| kk2 ← kradiation[ti < (toperate + tbackfill)] + k2[ti ≥ (toperate + tbackfill)]
| Wall_deltaT_finite_linei ← DW_T_finite_line(ti, ηDW, 0, tstore, toperate, WPcap, Kth, α)
| Wall_deltaT_drifti ← DW_T_drift(ti, ηDW, tstore, toperate, WPcap, WPspacing, Driftspacing, Kth, α)
| Wall_deltaT_adj_pksi ← DW_T_adjacent_pks(ti, ηDW, tstore, toperate, WPcap, WPspacing, Kth, α)
| Wall_Ti ← Tambient + Wall_deltaT_finite_linei + Wall_deltaT_drifti + Wall_deltaT_adj_pksi
| CP2_deltaT_finite_linei ← DW_T_finite_line(ti, κCP2, 0, tstore, toperate, WPcap, Kth, α)
| CP2_deltaT_drifti ← DW_T_drift(ti, κCP2, tstore, toperate, WPcap, WPspacing, Driftspacing, Kth, α)
| CP2_deltaT_adj_pksi ← DW_T_adjacent_pks(ti, κCP2, tstore, toperate, WPcap, WPspacing, Kth, α)
| CP2_Ti ← Tambient + CP2_deltaT_finite_linei + CP2_deltaT_drifti + CP2_deltaT_adj_pksi
| Qi ← QL_WP(ti, tstore, toperate, WPcap)
| EBS_1i ← Wall_Ti +  $\frac{Q_i}{2\pi \cdot \eta_{DW}}$  · R1(k1)
| EBS_2i ←  $\begin{cases} EBS_{_1i} + \frac{Q_i}{2\pi \cdot \eta_{DW}} \cdot R_2(kk_2, t_i, t_{operate}, t_{backfill}) & \text{if } kk_2 \neq 0 \frac{W}{m \cdot K} \\ \left[ \frac{Q_i}{h_{rad\_infinite}(r_3, r_2, \epsilon_{WP}, \epsilon_{wall}) \cdot 2\pi \cdot r_3} + (EBS_{_1i})^4 \right]^{\frac{1}{4}} & \text{otherwise} \end{cases}$ 
| EBS_3i ← EBS_2i +  $\frac{Q_i}{2\pi \cdot \eta_{DW}}$  · R3(k3)
| WP_Ti ← EBS_3i +  $\frac{Q_i}{2\pi \cdot \eta_{DW}}$  · R4(k4)
| T1i ← CP2_Ti - 273.15K
| T2i ← Wall_Ti - 273.15K
| T3i ← EBS_1i - 273.15K
| T4i ← EBS_2i - 273.15K
| T5i ← EBS_3i - 273.15K
| T6i ← WP_Ti - 273.15K
| Data_array ← augment( $\frac{t}{yr}$ , Wall_deltaT_finite_line  $\frac{1}{K}$ , Wall_deltaT_drift  $\frac{1}{K}$ , Wall_deltaT_adj_pks  $\frac{1}{K}$ , T1  $\frac{1}{K}$ , T2  $\frac{1}{K}$ , T3  $\frac{1}{K}$ , T4  $\frac{1}{K}$ , T5  $\frac{1}{K}$ , T6  $\frac{1}{K}$ )

```

Mathcad DSEF 3.0 parametric and iterative convergence model - parametric study example for User's Manual.xmcd

ijj := 1..Cases Cases = 10

X_{ijj} := Parameter_data_{ijj} Parameter = "WP Spacing"

Temp_array_{ijj} :=
$$\begin{cases} \text{outdata}(\tau_{DW}, \kappa_{CP2}, t_{store}, t_{operate}, WP_{cap}, WP_{spacing}, Drift_{spacing}, K_{th}, \alpha, k_1, k_2, k_3, k_4) & \text{if Parameter = "Single"} \\ \text{outdata}(\tau_{DW}, \kappa_{CP2}, t_{store}, t_{operate}, WP_{cap}, WP_{spacing}, X_{ijj}, m, K_{th}, \alpha, k_1, k_2, k_3, k_4) & \text{if Parameter = "Drift Spacing"} \\ \text{outdata}(\tau_{DW}, \kappa_{CP2}, t_{store}, t_{operate}, WP_{cap}, X_{ijj}, m, Drift_{spacing}, K_{th}, \alpha, k_1, k_2, k_3, k_4) & \text{if Parameter = "WP Spacing"} \\ \text{outdata}(\tau_{DW}, \kappa_{CP2}, X_{ijj}, \gamma, t_{operate}, WP_{cap}, WP_{spacing}, Drift_{spacing}, K_{th}, \alpha, k_1, k_2, k_3, k_4) & \text{if Parameter = "Storage Time"} \\ \text{outdata}(\tau_{DW}, \kappa_{CP2}, t_{store}, t_{store} + X_{ijj}, \gamma, WP_{cap}, WP_{spacing}, Drift_{spacing}, K_{th}, \alpha, k_1, k_2, k_3, k_4) & \text{if Parameter = "Ventilation Duration"} \\ \text{outdata}(\tau_{DW}, \kappa_{CP2}, t_{store}, t_{operate}, WP_{cap}, WP_{spacing}, Drift_{spacing}, X_{ijj}, \frac{W}{mK}, \alpha, k_1, k_2, k_3, k_4) & \text{if Parameter = "Rock Conductivity"} \\ \text{outdata}(\tau_{DW}, \kappa_{CP2}, t_{store}, t_{operate}, WP_{cap}, WP_{spacing}, Drift_{spacing}, K_{th}, \alpha, k_1, X_{ijj}, \frac{W}{mK}, k_3, k_4) & \text{if Parameter = "Backfill Conductivity"} \\ \text{"Undefined"} & \text{otherwise} \end{cases}$$

File_array_{ijj} := stack(Title_array_{ijj}, Temp_array_{ijj})

□

File_array1 =

	1	2	3	4	5	6
1	"Parameter value: WP Spacing IS, m"
2	"ToR (γ)"	"Wall ΔT Central Line Src"	"Wall ΔT Adj Drift"	"Wall ΔT Adj Rcg"	"Compliance Point 2, C"	"Rock Wall Temp, C"
3	50	0	0	0	27.5	27.5
4	55	35.579	6.058·10 ⁻⁶	4.514	56.729	67.593
5	60	34.948	5.304·10 ⁻³	7.482	59.778	69.94
6	65	33.507	0.055	9.174	60.687	70.236
7	70	31.898	0.188	10.303	60.822	69.789
8	75	30.316	0.402	10.841	60.618	69.059
9	80	28.814	0.677	11.225	60.25	68.216
10	85	27.416	0.932	11.486	59.808	67.344
11	90	26.118	1.328	11.527	59.325	66.473
12	95	24.936	1.671	11.531	58.841	65.638
13	100	23.83	2.016	11.483	58.349	64.826
14	105	22.827	2.354	11.387	57.878	64.068
15	110	21.9	2.682	11.252	57.41	63.334
16	115	21.059	2.999	11.117	56.99	...

□

$$\text{Peak_values} = \begin{pmatrix} 102.266 & 31.5 & 99.137 & 285 & 96.413 & 285 & 93.988 & 285 & 91.828 & 260 & 89.914 & 230 & 88.231 & 235 & 86.66 & 235 & 85.276 & 230 & 84.019 & 230 \\ 115.262 & 210 & 112.287 & 205 & 109.734 & 190 & 107.536 & 190 & 105.602 & 185 & 103.927 & 185 & 102.391 & 185 & 101.064 & 180 & 99.912 & 175 & 98.88 & 175 \\ 115.285 & 210 & 112.311 & 205 & 109.759 & 190 & 107.561 & 190 & 105.628 & 185 & 103.952 & 185 & 102.417 & 185 & 101.09 & 180 & 99.939 & 175 & 98.907 & 175 \\ 231.735 & 160 & 229.391 & 160 & 227.373 & 160 & 225.623 & 160 & 224.095 & 160 & 222.753 & 160 & 221.567 & 160 & 220.514 & 160 & 219.576 & 160 & 218.736 & 160 \\ 231.735 & 160 & 229.391 & 160 & 227.373 & 160 & 225.623 & 160 & 224.095 & 160 & 222.753 & 160 & 221.567 & 160 & 220.514 & 160 & 219.576 & 160 & 218.736 & 160 \\ 231.735 & 160 & 229.391 & 160 & 227.373 & 160 & 225.623 & 160 & 224.095 & 160 & 222.753 & 160 & 221.567 & 160 & 220.514 & 160 & 219.576 & 160 & 218.736 & 160 \end{pmatrix}$$

Peak_Wall_T := (Peak_values^Q)₂ = 115.262



outsheet := "Thermal-Analytical Output!"

rows(Temp_array) = 201

rows(File_array) = 203

Transient output starting row in DSEF on the Thermal = 60

start_row := 100 end_row := start_row + rows(Temp_array) - 1 = 300

NOTE - USE File_array to write to stand-alone Excel files, and Temp_array to write back to the DSEF Excel file.

transient_case_cols := $\begin{pmatrix} \text{"A"} & \text{"J"} \\ \text{"L"} & \text{"U"} \\ \text{"W"} & \text{"AF"} \\ \text{"AH"} & \text{"AQ"} \\ \text{"AS"} & \text{"BB"} \\ \text{"BD"} & \text{"BM"} \\ \text{"BO"} & \text{"BX"} \\ \text{"BZ"} & \text{"CI"} \\ \text{"CK"} & \text{"CT"} \\ \text{"CV"} & \text{"DE"} \end{pmatrix}$

To write the transients for each case horizontally instead of vertically, the following location array includes 10 columns for each case with one column separating the cases.

iw := 1..Cases

start_row = 100

end_row = 300

transient_write_ranges_{iw} := concat[outsheet, (transient_case_cols^Q)_{iw}, num2str(start_row), ":", (transient_case_cols^Q)_{iw}, num2str(end_row)]

```

transient_write_range := "Thermal-Analytical Output!L100:U300"   peaks_write_range := concat(outsheet,"C6:V11") = "Thermal-Analytical Output!C6:V11"

transient_write_range = {
    "Thermal-Analytical Output!A100:J300"
    "Thermal-Analytical Output!L100:U300"
    "Thermal-Analytical Output!W100:AF300"
    "Thermal-Analytical Output!AH100:AQ300"
    "Thermal-Analytical Output!AS100:BE300"
    "Thermal-Analytical Output!BD100:BM300"
    "Thermal-Analytical Output!BO100:BX300"
    "Thermal-Analytical Output!BZ100:CI300"
    "Thermal-Analytical Output!CK100:CT300"
    "Thermal-Analytical Output!CV100:DE300"
}

Transient_size := (Counter Step)      Transient_size = (200 5)      Transient_size_range := concat(outsheet,"B92:C92") = "Thermal-Analytical Output!B92:C92"

```

```

Make writing an output file optional      t_vent = 100-yr
Write_file := Write_OK = "YES"          OutfileName = "DSEF R3.0_2013Aug12_HRG-Clay_UOX-40_CP2=1m,DS70,Vent100,WP param_Case-500-1.xls.m"
write_the_peaks(Write_file) := write_it ← WRITEEXCEL(Peak_values,OutfileName,peaks_write_range) if (Write_file = "Yes") ∨ (Write_file = "YES")
                                     "File written"
                                     write_it ← "No file written" otherwise

write_the_peaks(Write_file) = "File written"

write_the_transient_size(Write_file) := write_it ← WRITEEXCEL(Transient_size,OutfileName,Transient_size_range) if (Write_file = "Yes") ∨ (Write_file = "YES")
                                     "File written"
                                     write_it ← "No file written" otherwise

write_the_transient_size(Write_file) = "File written"

Write_file := Write_OK = "YES"          Cases = 10
inw := 1..Cases
write_the_transients(jj) := write_array ← Temp_arrayjj
                             write_it ← WRITEEXCEL(write_array,OutfileName,transient_write_rangejj) if (Write_file = "Yes") ∨ (Write_file = "YES")
                             "File written"
                             write_it ← "No file written" otherwise

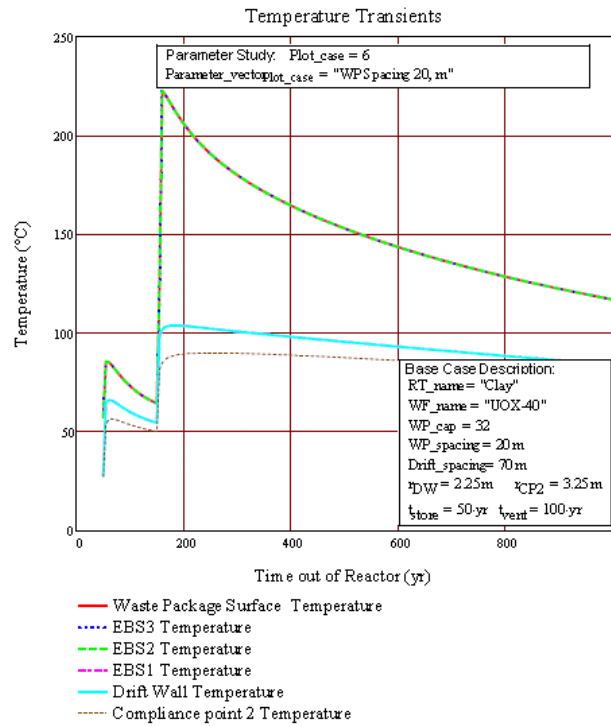
```

NOTE - USE File_array to write to stand-alone Excel files, and Temp_array to write back to the DSEF Excel file.

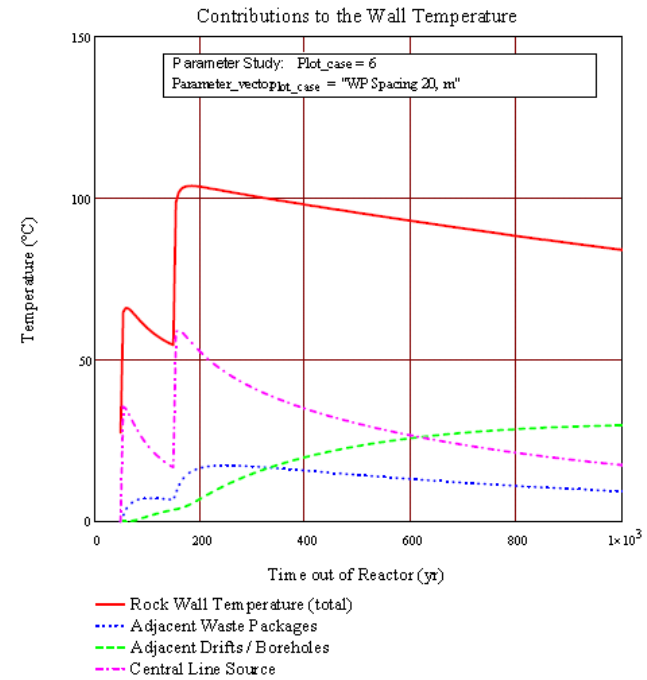
```
write_the_transients(i,v,w) =  
  ("File written"  
  "File written")
```

Plot_case := 6 Select parametric study case to plot (default plot is for case 1)

WP_plot := [(Temp_arrayPlot_case)^{10}] EBS3_T_plot := [(Temp_arrayPlot_case)^{9}] EBS2_T_plot := [(Temp_arrayPlot_case)^{8}] EBS1_T_plot := [(Temp_arrayPlot_case)^{7}] Wall_T_plot := [(Temp_arrayPlot_case)^{6}]
CP2_plot := [(Temp_arrayPlot_case)^{5}] Delta_WPvs_T_plot := [(Temp_arrayPlot_case)^{4}] Delta_drifts_T_plot := [(Temp_arrayPlot_case)^{3}] Delta_central_T_plot := [(Temp_arrayPlot_case)^{2}]



$$T_{EBS}(x,t,Wall_T,k_1,k_2,k_3,k_4) := Wall_T.K + \frac{Q_{L_wp}(t,t_{store},t_{operate},WP_cap)}{2 \cdot \pi \cdot r_{DW}} \cdot R_{continuous}(t,x,k_1,k_2,k_3,k_4)$$



$$Q_{L_wp}(110 \text{ yr}, t_{store}, t_{operate}, WP_cap) = 255.7 \frac{\text{W}}{\text{m}}$$

$$t_{rw} := [(Peak_values)^{Plot_case-2}]_2 = 185$$

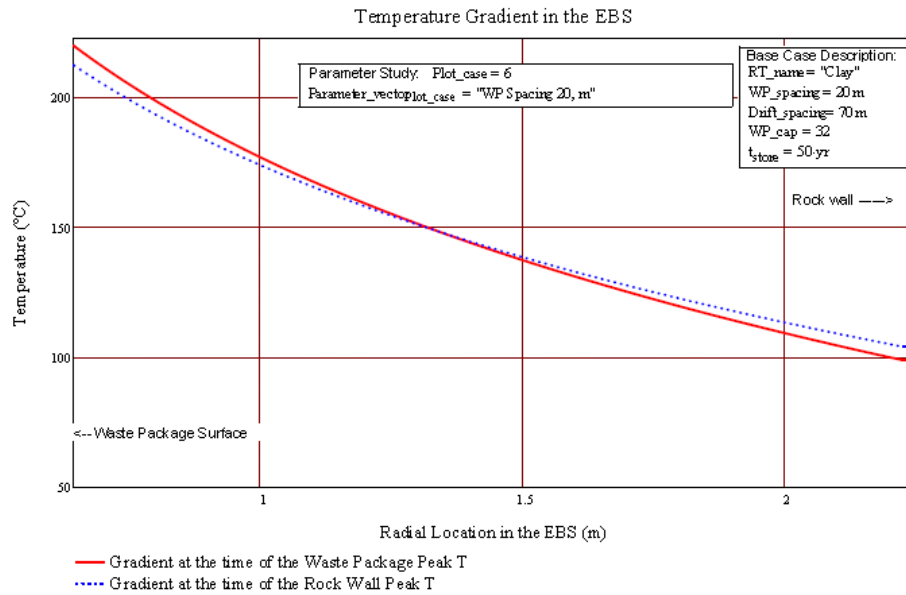
$$Wall_T_at_t_{rw} := [(Peak_values)^{Plot_case-2-1}]_2 = 103.927$$

$$WP_T_at_t_{rw} := [(Peak_values)^{Plot_case-2-1}]_6 = 222.753$$

$$t_{wp} := [(Peak_values)^{Plot_case-2}]_6 = 180$$

$$Wall_T_at_t_{wp} := \left[\left(\frac{Temp_array^{Plot_case}}{Step} \right)^{6} \right]_{\left(\frac{t_{wp} - t_{store}}{yr} \right)} = 98.739$$

$$WP_T_at_t_{wp} := \left[\left(\frac{Temp_array^{Plot_case}}{Step} \right)^{10} \right]_{\left(\frac{t_{wp} - t_{store}}{yr} \right)} = 214.369$$



OVERWRITE COUNTER AND STEP SIZE TO GET FINER CONVERGENCE ON THE ANSWER

$t_{vent} = 100 \text{ yr}$ OPTIONALLY OVERRIDE VENTILATION TIME TO SHORTEN ITERATION CONVERGENCE
 $ITERATE_OK := "No"$ $t_{convergence} = 1 \text{ yr}$

$t_{required_storage}(t_{operate}, T_{criteria}, t_{convergence}) :=$

```

timeOK ← t_operate - t_convergence
Peak_Wall_T_check ← (Peak_Wall_T + 273.15) · K
timeOK ← t_operate if Peak_Wall_T_check ≤ T_criteria
while Peak_Wall_T_check > T_criteria
    timeOK ← timeOK + t_convergence
    calc_array ← outdata(η_DW, ε_CP2, t_store, timeOK, WP_cap, WP_spacing, Drift_spacing, K_th, α, k_1, k_2, k_3, k_4)
    Peak_Wall_T_check ← (max(calc_array6) + 273.15) · K
return (
    (
        (
            Peak_Wall_T_check - 273.15K
        ) / K
    ) / (yr)
    outdata(η_DW, ε_CP2, t_store, timeOK, WP_cap, WP_spacing, Drift_spacing, K_th, α, k_1, k_2, k_3, k_4)
)
    
```

$Final_array :=$ $t_{required_storage}(t_{operate}, T_{criteria}, t_{convergence})$ if $ITERATE_OK = "YES"$
 "No Iteration Performed" otherwise

$t_{operate_required} := Final_array1 \text{ yr} = \bullet \text{ yr}$

$t_{vent_required} := t_{operate_required} - t_{store} = \bullet \text{ yr}$ **REQUIRED VENTILATION TIME NEEDED TO MEET $T_{criteria} = 100 \text{ °C}$**

$Peak_Wall_T_check := (Final_array2 + 273.15) \cdot K = \bullet \text{ °C}$

Result := stack(Title_array1, Final_array3)

NOTE THAT THIS SECTION WILL BE BLANK IF NO ITERATIVE ANALYSIS IS PERFORMED (Iterate_OK = "No")

Result = ■

Time_array := (Final_array3)⁽¹⁾

Peak_Temp(n) := max{(Final_array3)⁽⁶⁾} Peak_Temp(6) = ■

Peak_t(n) := lookup[Peak_Temp(n), (Final_array3)⁽⁶⁾, Time_array] Peak_t(6)1.yr = ■.yr

mn := 5..10 Peak_results_{mn-4,1} := Peak_Temp(mn) Peak_results_{mn-4,2} := Peak_t(mn)1

Peak_results = ■

CP2, time of peak
 Peak Wall T, time of peak
 Peak EBS 1, time of peak
 Peak EBS 2, time of peak
 Peak EBS 3, time of peak
 Waste Pkg T, time of peak

Array_row_at_Wall_T_peak := match[Peak_Temp(6), (Final_array3)⁽⁶⁾]₁ = ■

CP2_at_Wall_T_pk_t := [(Final_array3)⁽⁶⁾]_{Array_row_at_Wall_T_peak} = ■

Central_WP_delta := [(Final_array3)⁽²⁾]_{Array_row_at_Wall_T_peak} = ■

Adj_Drift_delta := [(Final_array3)⁽³⁾]_{Array_row_at_Wall_T_peak} = ■

Mathcad DSEF 3.0 parametric and iterative convergence model - parametric study example for User's Manual.xmcd

$$\text{Adj_WP_delta} := \left[(\text{Final_array3})^{(4)} \right]_{\text{Array_row_at_Wall_T_peak}} = \bullet$$

$$\text{Result_Vector} := \left(\frac{\text{WP_spacing}}{\text{m}}, \text{TC}, \frac{\text{Drift_spacing}}{\text{m}}, \text{Peak_results}_{6,1}, \text{Peak_results}_{6,2}, \text{Peak_results}_{2,1}, \text{Peak_results}_{2,2}, \text{CP2_at_Wall_T_pk_t}, \frac{\text{Vent_required}}{\text{yr}}, \text{Central_WP_delta}, \text{Adj_Drift_delta}, \text{Adj_WP_delta} \right)$$

Result_headings := ("WP Spacing" "Temp Criteria" "Drift Spacing" "Peak WP T" "Time of WP Peak" "Peak Wall T" "Time of Wall Peak" "Peak CP2 T" "Ventilation time" "Central WP delta" "Adj Drift delta" "Adj WP delta")

Result_Vector = ■

This is the result vector for transcription to the Excel case results tracking file

RV := augment(Result_headings^T, Result_Vector^T) T_ambient = 27.5 °C Contribution percentages at time of peak wall temperature

$$\text{Percent_central_WP_delta} := \frac{\text{Central_WP_delta}}{\text{Peak_Temp}(6) - \frac{\text{T_ambient} - 273.15 \text{ K}}{\text{K}}} \cdot 100 = \bullet$$

$$\text{Percent_adj_Drift_delta} := \frac{\text{Adj_Drift_delta}}{\text{Peak_Temp}(6) - \frac{\text{T_ambient} - 273.15 \text{ K}}{\text{K}}} \cdot 100 = \bullet$$

RV = ■

$$\text{Percent_adj_WP_delta} := \frac{\text{Adj_WP_delta}}{\text{Peak_Temp}(6) - \frac{\text{T_ambient} - 273.15 \text{ K}}{\text{K}}} \cdot 100 = \bullet$$

$$\text{Percent_central_WP_delta} + \text{Percent_adj_WP_delta} + \text{Percent_adj_Drift_delta} = \bullet$$

Plot temperature results as a function of parameter data

ip := 1 .. Cases

$$\text{Peak_WP_T}_{ip} := (\text{Peak_values}^{ip-2-1})_6$$

Peak_WP_T =

231.735
229.391
227.373
225.623
224.095
222.753
221.567
220.514
219.576
218.736

$$\text{Peak_EBS3_T}_{ip} := (\text{Peak_values}^{ip-2-1})_5$$

Peak_EBS3_T =

231.735
229.391
227.373
225.623
224.095
222.753
221.567
220.514
219.576
218.736

$$\text{Peak_EBS2_T}_{ip} := (\text{Peak_values}^{ip-2-1})_4$$

Peak_EBS2_T =

231.735
229.391
227.373
225.623
224.095
222.753
221.567
220.514
219.576
218.736

$$\text{Peak_EBS1_T}_{ip} := (\text{Peak_values}^{ip-2-1})_3$$

Peak_EBS1_T =

115.285
112.311
109.759
107.561
105.628
103.952
102.417
101.09
99.939
98.907

$$\text{Peak_Wall_T}_{ip} := (\text{Peak_values}^{ip-2-1})_2$$

Peak_Wall_T =

115.262
112.287
109.734
107.536
105.602
103.927
102.391
101.064
99.912
98.88

$$\text{Peak_CP2_T}_{ip} := (\text{Peak_values}^{ip-2-1})_1$$

Peak_CP2_T =

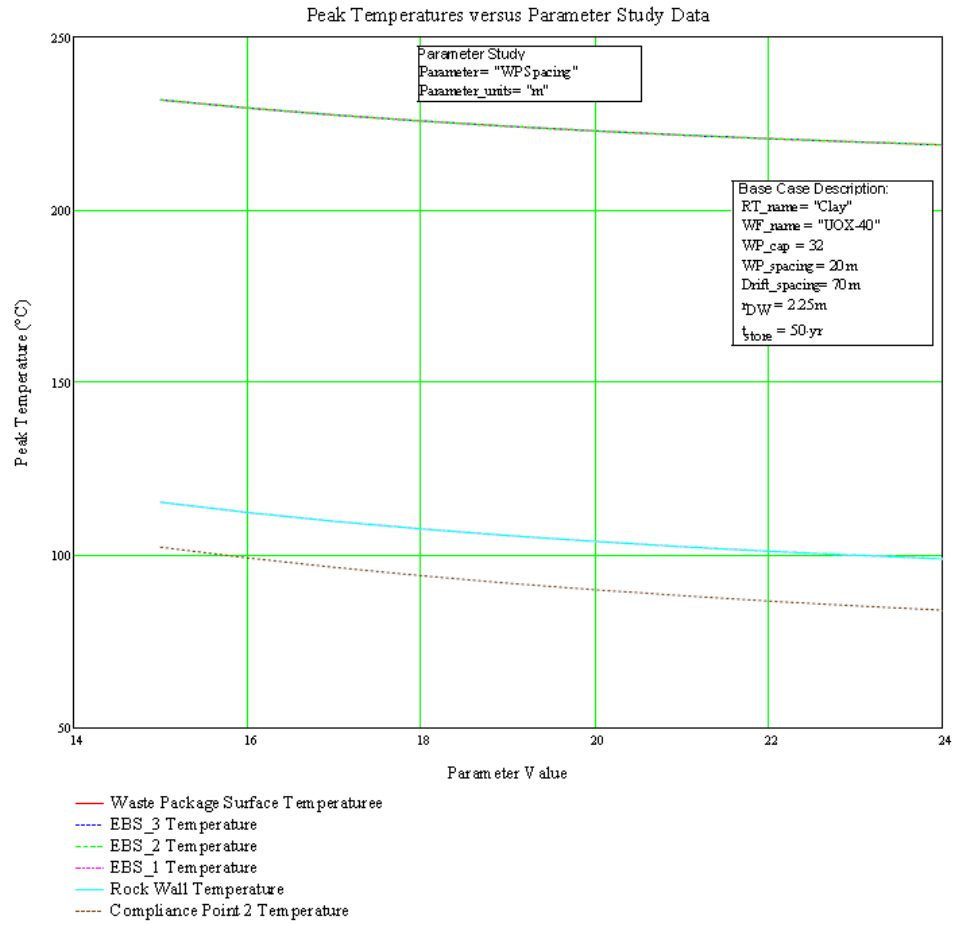
102.266
99.137
96.413
93.988
91.828
89.914
88.231
86.66
85.276
84.019

Parameter_data =

15
16
17
18
19
20
21
22
23
24

Parameter_vector =

"WP Spacing 15, m"
"WP Spacing 16, m"
"WP Spacing 17, m"
"WP Spacing 18, m"
"WP Spacing 19, m"
"WP Spacing 20, m"
"WP Spacing 21, m"
"WP Spacing 22, m"
"WP Spacing 23, m"
"WP Spacing 24, m"



B.3 The Mathcad parametric analysis and iterative convergence model – iterative convergence example

As noted in Section B.2, the iterative convergence programming loop started on page 19 of 23 of the Mathcad document. However, to perform an iterative convergence analysis to determine required ventilation time, a number of input variables must be set. First, the “Parameter” variable passed from the DSEF Excel file must be set to “Single”. Then the two critical variables of the iterative convergence study – the initial guess for required ventilation time (t_{vent}), and the target temperature criterion (TC) are set locally in the Mathcad document itself.

The next variable to be set turns the iterative loop on or keeps it off, and it is recommended to keep it initially off (Iterate_OK = “No”) unless, based on previous analysis in the Case Library, you already have a reasonable guess for the required ventilation time. This is recommended since a single non-iterative analysis with the Mathcad thermal-analytical model should take around 15 to 30 seconds. If the initial guess is a poor one and if the step size is small and close convergence is being required, then the iterative mode could take a long time to run. Before setting Iterate_OK to “Yes”, make sure the starting ventilation time results in a temperature that is above the temperature acceptance value. If you start with a ventilation time that already meets the acceptance criterion, then the convergence loop will just return the same starting ventilation time since it is already acceptable.

The example PDF file in this appendix set the temperature acceptance criterion at the drift wall of a clay/shale repository analysis at TC = 100°C. To speed up the iterative calculation process there are also three new input variables “Counter”, “Step”, and “Convergence” that allow initially larger and few calculation steps to quickly converge an analysis, and then optionally to make more smaller steps to cover the same time span but a more detailed transient if desired.

This specific example is from Greenberg 2013a, and is report case 225-19 (DSEF Case Library case number 342) and represents a required ventilation time calculation for a 21-PWR waste package with 40 GWd/MT burnup in a clay/shale repository, with a layout design of 30 m drift spacing and 20 m waste package spacing, to meet a temperature acceptance criterion of 100°C at the drift wall. The result presented originally was taken within 0.5 degrees and gave 100.1°C with 125 years of ventilation. To check more accurately and assure the temperature is below 100°C, the iterative convergence was turned on using Iterate_OK:=”YES”. In this case, we knew the answer, but just to demonstrate the convergence loop, we started the case off with a guess of $t_{vent} = 120$ years. The result showed that with 127 years of ventilation, we get a drift wall temperature of 99.93°C (shown on page 19 of 23 in the PDF printout).

Note that the last figure on page 23 of 23 is blank, since it is reserved to show parametric study results and this was a “Single” analysis.

DSEF R3.0 parametric and iterative model with collapsable areas - for rapid iteration.

Values over-written from DSEF Excel file to create cases potentially include TC and t_{vent} .

Allow output transients to be written back to DSEF FILE

Case_name := "225-19"

Variables for repository symmetry and extent:

Write_OK := "YES"

$N_{diffs} := 4$ $N_{adj} := 4$

REQUIRED REPOSITORY INPUT DATA (from DSEF):

file := "DSEF R3.0_2013Aug12_HRG-Clay_UOX-40_Iterative convergence example_Case-225-19.xlsm"

sheet := "Thermal-Analytical"

DATA FOR ITERATION ON TEMPERATURE ACCEPTANCE CRITERIA:

$TC := 100$ $T_{criteria} = (TC + 273.15) \cdot K = 373.15K$ $T_{criteria} = 100 \cdot ^\circ C$

READ DSEF INPUT FILE

$t_{convergence} := 1 \cdot yr$ CONVERGE CRITERIA FOR REQUIRED VENTILATION TIME IN YEARS

Input 1 = Operating Mode (enclosed or open)

Input_1 := READEXCEL(file,concat(sheet,"A5:B5"))

Input_1 = ("MODE = Open or Enclosed:" "Open") Mode := Input_1,2 = "Open"

SET THE VARIABLE ITERATE_OK TO "NO" TO TURN OFF THE AUTOMATIC CONVERGENCE CALCULATION, AND MANUALLY RESET IT TO "YES" IF YOU WANT TO FINE TUNE YOUR ANSWER:

Input_2 := READEXCEL(file,concat(sheet,"A7:B16")) **Input 2 = Case Definitions**

ITERATE_OK := "YES"

Input_2 =	"Host Media"	"Clay"
	"Rock thermal conductivity, W/m-K"	1.75
	"Rock thermal diffusivity, m ² /sec"	6.45×10^{-7}
	"Repository Depth, m"	500
	"Surface temperature, °C"	15
	"Geothermal gradient, °C/km"	25
	"Ambient temperature at depth, °C"	27.5
	"Waste Package (axial) spacing, m"	20
	"Drift / Borehole (lateral) spacing, m"	30
"Surface storage time, y"	50	

Input 3 = Ventilation Parameters (for Open Modes)

Input_3 := READEXCEL(file,concat(sheet,"e7:f11"))

Input_3 =	"Ventilation Duration, yr"	125
	"Unventilated Closure Duration (Backfill Installation), yr"	10
	"Ventilation Thermal Efficiency, %"	0.75
	"Rock Wall Emissivity"	0.9
	"Waste Package Emissivity"	0.6

RT_name := Input_2,2 = "Clay"

$t_{vent} := \text{if}[(\text{Mode} = \text{"Enclosed"}), 0, \text{Input}_3, 1, 2] \cdot yr = 125 \cdot yr$

$K_{th} := \text{Input}_2, 2 \cdot \frac{W}{m \cdot K} = 1.75 \frac{m \cdot kg}{K \cdot s^3}$

$t_{backfill} := \text{if}[(\text{Mode} = \text{"Enclosed"}), 0, \text{Input}_3, 2] \cdot yr = 10 \cdot yr$

$\alpha := \text{Input}_2, 2 \cdot \frac{m^2}{s} = 6.45 \times 10^{-7} \frac{m^2}{s}$

$V_{eff} := \text{if}[(\text{Mode} = \text{"Enclosed"}), 0, \text{Input}_3, 3] = 0.75$

$\epsilon_{wall} := \text{if}[(\text{Mode} = \text{"Enclosed"}), .9, \text{Input}_3, 4] = 0.9$

$WP_depth := Input_24, 2 \text{ m} = 500 \text{ m}$
 $T_{surface} := (Input_25, 2 + 273.15) \cdot K = 288.15 \text{ K}$
 $geothermal_gradient := Input_26, 2 \frac{K}{km} = 0.025 \frac{K}{m}$
 $T_{ambient} := (Input_27, 2 + 273.15) \cdot K = 300.65 \text{ K}$
 $WP_spacing := Input_28, 2 \text{ m} = 20 \text{ m}$
 $Drift_spacing := Input_29, 2 \text{ m} = 30 \text{ m}$
 $t_{store} := Input_210, 2 \text{ yr} = 50 \text{ yr}$

$\epsilon_{wpp} := \text{if}[(Mode = "Enclosed"), 6, Input_35, 2] = 0.6$

OVER-RIDE VENTILATION DURATION

$t_{vent} := 120 \text{ yr}$

OVER-RIDE DRIFT AND/OR WASTE PACKAGE SPACING

$t_{operate} := (t_{store} + t_{vent}) = 170 \text{ yr}$

T OPERATE = T STORE + T VENTILATE

$t_{closure} := t_{operate} + t_{backfill} = 180 \text{ yr}$

T CLOSURE = T OPERATE + TIME TO BACKFILL



Input 4 = ENGINEERED BARRIER SYSTEM DATA:

Input 5 = COMPLIANCE POINT 2 INPUT DATA

$Input_4 := \text{READEXCEL}(\text{file}, \text{concat}(\text{sheet}, "A20:F27"))$

$Input_5 := \text{READEXCEL}(\text{file}, \text{concat}(\text{sheet}, "C32"))$

Input_4 =	"Waste Form Outer Radius, m"	0.535	"N/A"	0.535	"UOX-40"	"N/A"
	"Canister"	0	0.535	0.535	"None"	"N/A"
	"Waste Package"	0.11	0.535	0.645	"Carbon Steel"	"N/A"
	"Buffer"	0	0.645	0.645	"None"	"N/A"
	"Envelope"	0	0.645	0.645	"None"	"N/A"
	"Backfill"	1.58	0.645	2.225	"70% Bentonite 30% Sand"	1.2
	"Liner"	0.025	2.225	2.25	"Steel"	46
	"Host Rock Inner Radius, m-->"	NaN	2.25	NaN	NaN	NaN

$Input_5 = (5.25)$

$r_{CP2} := Input_51 \text{ m} = 5.25 \text{ m}$

$r_{DW} := Input_48, 3 \text{ m} = 2.25 \text{ m}$

$r_{wpp} := Input_43, 4 \text{ m} = 0.645 \text{ m}$

$EBS_name_1 := Input_47, 1 = "Liner"$

$EBS_material_1 := Input_47, 5 = "Steel"$

$thickness_1 := Input_47, 2 \text{ m} = 0.025 \text{ m}$

$r_1 := Input_47, 4 \text{ m} = 2.25 \text{ m}$

$k_1 := Input_47, 6 = 46$

$k_1 := \text{if}[(k_1 = "N/A"), 0, k_1] \cdot \frac{W}{mK} = 46 \cdot \frac{W}{mK}$

$EBS_name_2 := Input_46_1 = "Backfill"$ $EBS_material_2 := Input_46_5 = "70\% \text{ Bentonite } 30\% \text{ Sand}"$
 $thickness_2 := Input_46_2 \cdot m = 1.58 \text{ m}$ $r_2 := Input_46_4 \cdot m = 2.225 \text{ m}$
 $k_2 := Input_46_6 = 1.2$ $k_2 := \text{if}[(k_2 = "N/A"), 0, k_2] \cdot \frac{W}{m \cdot K} = 1.2 \cdot \frac{W}{m \cdot K}$
 $k_{radiation} := \text{if}[(Mode = "Enclosed"), k_2, 0] = 0 \cdot \frac{W}{m \cdot K}$

$EBS_name_3 := Input_45_1 = "Envelope"$ $EBS_material_3 := Input_45_5 = "None"$
 $thickness_3 := Input_45_2 \cdot m = 0 \text{ m}$ $r_3 := Input_45_4 \cdot m = 0.645 \text{ m}$
 $k_3 := Input_45_6 = "N/A"$ $k_3 := \text{if}[(k_3 = "N/A"), 0, k_3] \cdot \frac{W}{m \cdot K} = 0 \cdot \frac{W}{m \cdot K}$

$EBS_name_4 := Input_44_1 = "Buffer"$ $EBS_material_4 := Input_44_5 = "None"$
 $thickness_4 := Input_44_2 \cdot m = 0 \text{ m}$ $r_4 := Input_44_4 \cdot m = 0.645 \text{ m}$
 $k_4 := Input_44_6 = "N/A"$ $k_4 := \text{if}[(k_4 = "N/A"), 0, k_4] \cdot \frac{W}{m \cdot K} = 0 \cdot \frac{W}{m \cdot K}$

Define the total thermal resistance between the rock wall and the waste package surface based on a heat flux per unit area, it is then applied to a heat flux is per unit length adjusting to area per unit length and q_1 (W/m)

$r_{WP} = 0.645 \text{ m}$ $r_4 = 0.645 \text{ m}$ $r_3 = 0.645 \text{ m}$ $r_2 = 2.225 \text{ m}$ $r_1 = 2.25 \text{ m}$ $r_{DW} = 2.25 \text{ m}$

$R_1(k_1) := \text{if} \left[\left[\text{thickness}_1 = 0 \vee (k_1 = "N/A") \right], 0, \frac{r_{DW}}{k_1} \cdot \ln \left(\frac{r_1}{r_2} \right) \right]$ $R_1(k_1) = 5.465 \times 10^{-4} \cdot \frac{m^2 \cdot K}{W}$ Thermal resistance

$EBS_name_1 = "Liner"$ $EBS_material_1 = "Steel"$

ADDED CORRECTION FOR PARAMETRIC $t_{closure}$ replaced $t_{closure}$ with $(t_{operate} + t_{backfill})$

Revised R_2 to make it an explicit function of $t_{operate}$ and $t_{backfill}$.

$R_2(k_2, t, t_{operate}, t_{backfill}) := \left| \begin{array}{l} k_2 \leftarrow k_{radiation} \left[t < (t_{operate} + t_{backfill}) \right] + k_2 \left[t \geq (t_{operate} + t_{backfill}) \right] \\ \text{return if} \left[\left[\text{thickness}_2 = 0 \right] \vee (k_2 = 0), \frac{r_{DW}}{k_2} \cdot \ln \left(\frac{r_2}{r_3} \right) \right] \end{array} \right.$ $\frac{r_{DW}}{k_2} \cdot \ln \left(\frac{r_2}{r_3} \right) = 2.322 \cdot \frac{m^2 \cdot K}{W}$

Mathcad DSEF 3.0 parametric and iterative model - example for User's Manual.xmcd

$$\text{EBS_name}_2 = \text{"Backfill"} \quad \text{EBS_material}_2 = \text{"70\% Bentonite 30\% Sand"} \quad R_2(k_2, 5\text{-yr}, 300\text{-yr}, 10\text{-yr}) = 0 \frac{\text{m}^2 \cdot \text{K}}{\text{W}} \quad R_2(k_2, 1000\text{-yr}, 300\text{-yr}, 10\text{-yr}) = 2.321741 \frac{\text{m}^2 \cdot \text{K}}{\text{W}}$$

$$R_3(k_3) = \text{if} \left[\left[\text{thickness}_3 = 0 \vee (k3 = \text{"N/A"}) \right], 0, \frac{\rho_{\text{DW}}}{k_3} \cdot \ln \left(\frac{r_3}{r_4} \right) \right] \quad R_3(k_3) = 0 \frac{\text{m}^2 \cdot \text{K}}{\text{W}}$$

$$\text{EBS_name}_3 = \text{"Envelope"} \quad \text{EBS_material}_3 = \text{"None"}$$

$$R_4(k_4) = \text{if} \left[\left[\text{thickness}_4 = 0 \vee (k4 = \text{"N/A"}) \right], 0, \frac{\rho_{\text{DW}}}{k_4} \cdot \ln \left(\frac{r_4}{r_{\text{WP}}} \right) \right] \quad R_4(k_4) = 0 \frac{\text{m}^2 \cdot \text{K}}{\text{W}}$$

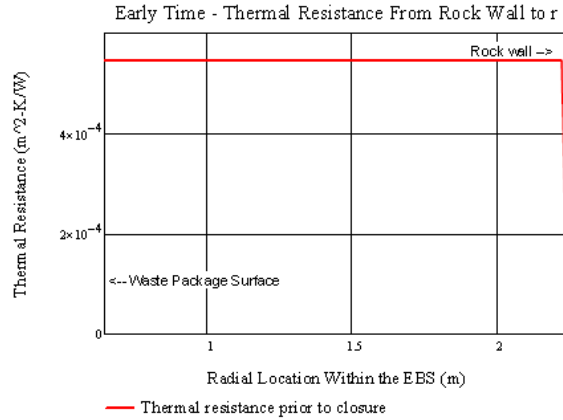
$$\text{EBS_name}_4 = \text{"Buffer"} \quad \text{EBS_material}_4 = \text{"None"}$$

$$R_{\text{Total}}(t, k_1, k_2, k_3, k_4) := R_1(k_1) + R_2(k_2, t, t_{\text{operate}}, t_{\text{backfill}}) + R_3(k_3) + R_4(k_4) \quad \text{Total thermal resistance between wall and waste package}$$

$$t_{\text{backfill}} = 10\text{-yr} \quad t_{\text{operate}} = 170\text{-yr}$$

$$R_{\text{continuous}}(t, r, k_1, k_2, k_3, k_4) := \begin{cases} k k_2 \leftarrow k_{\text{radiation}} \left[t < (t_{\text{operate}} + t_{\text{backfill}}) \right] + k_2 \left[t \geq (t_{\text{operate}} + t_{\text{backfill}}) \right] \\ R \leftarrow R_1(k_1) + R_2(k_2, t, t_{\text{operate}}, t_{\text{backfill}}) + R_3(k_3) + \text{if} \left[\left[\left(\text{thickness}_4 = 0 \right) \vee (k4 = \text{"N/A"}) \right], 0, \frac{\rho_{\text{DW}}}{k_4} \cdot \ln \left(\frac{r_4}{r} \right) \right] \text{ if } r \leq r_4 \wedge r \geq r_{\text{WP}} \\ R \leftarrow R_1(k_1) + R_2(k_2, t, t_{\text{operate}}, t_{\text{backfill}}) + \text{if} \left[\left[\left(\text{thickness}_3 = 0 \right) \vee (k3 = \text{"N/A"}) \right], 0, \frac{\rho_{\text{DW}}}{k_3} \cdot \ln \left(\frac{r_3}{r} \right) \right] \text{ if } r \leq r_3 \wedge r > r_4 \\ R \leftarrow R_1(k_1) + \text{if} \left[\left[\left(\text{thickness}_2 = 0 \right) \vee k k_2 = 0 \right], 0, \frac{\rho_{\text{DW}}}{k k_2} \cdot \ln \left(\frac{r_2}{r} \right) \right] \text{ if } r \leq r_2 \wedge r \geq r_3 \\ R \leftarrow \text{if} \left[\left[\left(\text{thickness}_1 = 0 \right) \vee (k1 = \text{"N/A"}) \right], 0, \frac{\rho_{\text{DW}}}{k_1} \cdot \ln \left(\frac{r_1}{r} \right) \right] \text{ if } r \leq r_{\text{DW}} \wedge r \geq r_2 \\ R \leftarrow \text{"Invalid Radius"} \text{ otherwise} \\ \text{return } R \end{cases}$$

$$R_{\text{continuous}}(5\text{-yr}, r_{\text{WP}}, k_1, k_2, k_3, k_4) = 5.465 \times 10^{-4} \frac{\text{K} \cdot \text{s}^3}{\text{kg}} \quad R_{\text{continuous}}(1000\text{-yr}, r_{\text{WP}}, k_1, k_2, k_3, k_4) = 2.322288 \frac{\text{K} \cdot \text{s}^3}{\text{kg}}$$



$$D_W = 2.25m$$

$$r_1 = 2.25m \quad EBS_name_1 = "Liner" \quad EBS_material_1 = "Steel"$$

$$r_2 = 2.225m \quad \text{Note that for "open modes", the backfill hasn't been emplaced at this time}$$

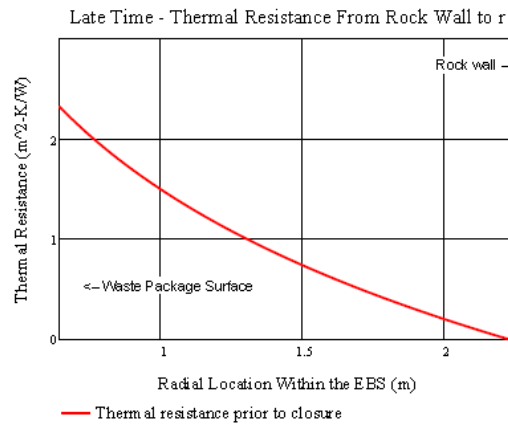
$$r_3 = 0.645m \quad EBS_name_3 = "Envelope" \quad EBS_material_3 = "None"$$

$$r_4 = 0.645m \quad EBS_name_4 = "Buffer" \quad EBS_material_4 = "None"$$

$$r_{WP} = 0.645m$$

$$R_1(k_1) = 5.465 \times 10^{-4} \frac{m^2 \cdot K}{W} \quad R_2(k_2, t_{operate}, t_{backfill}) = 0 \frac{m^2 \cdot K}{W} \quad R_3(k_3) = 0 \frac{m^2 \cdot K}{W} \quad R_4(k_4) = 0 \frac{m^2 \cdot K}{W}$$

$$R_{Total}(50yr, k_1, k_2, k_3, k_4) = 5.465 \times 10^{-4} \frac{m^2 \cdot K}{W}$$



$$D_W = 2.25m$$

$$r_1 = 2.25m \quad EBS_name_1 = "Liner" \quad EBS_material_1 = "Steel"$$

$$r_2 = 2.225m \quad EBS_name_2 = "Backfill" \quad EBS_material_2 = "70\% Bentonite 30\% Sand"$$

$$r_3 = 0.645m \quad EBS_name_3 = "Envelope" \quad EBS_material_3 = "None"$$

$$r_4 = 0.645m \quad EBS_name_4 = "Buffer" \quad EBS_material_4 = "None"$$

$$r_{WP} = 0.645m$$

$$R_1(k_1) = 5.465 \times 10^{-4} \frac{m^2 \cdot K}{W} \quad R_2(k_2, t_{closure}, t_{operate}, t_{backfill}) = 2.322 \frac{m^2 \cdot K}{W} \quad R_3(k_3) = 0 \frac{m^2 \cdot K}{W}$$

$$R_{Total}(1000yr, k_1, k_2, k_3, k_4) = 2.322 \frac{m^2 \cdot K}{W}$$

INPUT 6 = WASTE FORM DATA

Input_6 := READEXCEL(file,concat(sheet,"A35:B38"))

$$\text{Input}_6 = \begin{pmatrix} \text{"Waste form short name"} & \text{"UOX-40"} \\ \text{"Waste form type"} & \text{"Assembly"} \\ \text{"Waste package capacity"} & 21 \\ \text{"Waste package length, m"} & 5 \end{pmatrix}$$

WF_name := Input_6[1,2 = "UOX-40"

WF_type := Input_6[2,2 = "Assembly"

WP_cap := Input_6[3,2 = 21

	Outside of the liner	Outside of the backfill	Outside of the envelope	Outside of the buffer
WP_length := Input_6[4,2 = 5m	$A_1 := 2 \cdot \pi \cdot r_1 \cdot \text{WP_length} = 70.69 \text{ m}^2$	$A_2 := 2 \cdot \pi \cdot r_2 \cdot \text{WP_length} = 69.9 \text{ m}^2$	$A_3 := 2 \cdot \pi \cdot r_3 \cdot \text{WP_length} = 20.26 \text{ m}^2$	$A_4 := 2 \cdot \pi \cdot r_4 \cdot \text{WP_length} = 20.26 \text{ m}^2$
	$A_{DW} := 2 \cdot \pi \cdot r_{DW} \cdot \text{WP_length} = 70.686 \text{ m}^2$			$A_{WP} := 2 \cdot \pi \cdot r_{WP} \cdot \text{WP_length} = 20.263 \text{ m}^2$

CONSIDER THE ALTERNATE DESIGN CASE OF AN "OPEN MODE" DESIGN, WITH A CEMENTITIOUS LINER, BUT ONLY AIR BETWEEN THE LINER AND THE WASTE PACKAGE FOR THE FIRST 300 YEARS. ASSUME NO VENTILATION FOR 300 YEARS, AND THEN BACKFILL AT CLOSURE.

CALCULATE THE EQUIVALENT THERMAL RESISTANCE OF THE AIR GAP USING A LINEARIZED RADIATION HEAT TRANSFER COEFFICIENT. BASE THE COEFFICIENT ON THE ROCK WALL TEMPERATURE AT THE DRIFT, AND THE EQUIVALENT WASTE PACKAGE TEMPERATURE NECESSARY TO MOVE THE HEAT GENERATED AT THE WASTE PACKAGE AT ANY GIVEN TIME. THE EQUATION FOR THE RADIATION HEAT TRANSFER COEFFICIENT IS FROM INCROPERA AND DEWITT.

$A_{\text{wall}} := \text{WP_length} \cdot 2 \cdot \pi \cdot r_{DW} = 70.686 \text{ m}^2$

Stefan Boltzmann constant $\sigma := 5.670 \cdot 10^{-8} \frac{\text{W}}{\text{m}^2 \cdot \text{K}^4}$

Waste package emissivity $\epsilon_{WP} = 0.6$

Rock wall or cementitious liner emissivity $\epsilon_{\text{wall}} = 0.9$

The basis for the rock and waste package emissivity assumed is F.P. Incropera and D.P. DeWitt, *Fundamentals of Heat and Mass Transfer*, 4th Edition, 1996, Table A-11, which shows a range of 0.88 to 0.93 is adapted from hemispherical emissivity of rock at around 300 K. This range is corroborated by the "Heat Transmission" section of Perry's Chemical Engineers Handbook, 6th Edition, 1984 (Table 10-17, pages 10-51 to 10-52) for normal emissivity of rough silica and rough fused quartz, ranging from 0.8 to 0.93. The waste package surface is assumed to be covered with dust and dirt. The emissivity values to the left were specified in DSEF, and should be changed there if necessary.

Reference for radiation heat transfer coefficient, h_{rad} , is from Incropera and DeWitt, Table 13.3 for concentric infinite cylinders (based on the inner surface as the heat source), and is also referenced in the YMP *Ventilation Model and Analysis Report*, ANLEBS-MD-000030 REV 04, Oct. 2004, page 6-8.

$$h_{\text{rad_infinite}}(r_1, \epsilon_0, \epsilon_1, \epsilon_0) = \frac{\sigma}{\frac{1}{\epsilon_1} + \left(\frac{1 - \epsilon_0}{\epsilon_0}\right) \frac{r_1}{r_0}}$$

$$h_{\text{rad_infinite}}(r_{WP}, r_{DW}, \epsilon_{WP}, \epsilon_{\text{wall}}) = 3.338 \times 10^{-8} \frac{\text{W}}{\text{m}^2 \cdot \text{K}^4}$$

Usage is Q in watts = $h \cdot A \cdot (T_1^4 - T_0^4)$

For radiation between the liner and the envelope (both metal surfaces) use r_2 and r_3 , and assume the same emissivity for both surfaces.

$$Q_{rad_infinite}(r_1, r_o, \epsilon_1, \epsilon_o, L, T_{cold}, T_{hot}) := h_{rad_infinite}(r_1, r_o, \epsilon_1, \epsilon_o) \left(2 \cdot \pi \cdot r_1 \cdot L \cdot (T_{hot}^4 - T_{cold}^4) \right) \quad Q_{rad_infinite}(r_3, r_2, \epsilon_{WP}, \epsilon_{wall}, WP_length, 300\text{ K}, 600\text{ K}) = 8.217 \times 10^4 \text{ W}$$

$$Q_{L_rad_infinite}(r_1, r_o, \epsilon_1, \epsilon_o, T_{cold}, T_{hot}) := h_{rad_infinite}(r_1, r_o, \epsilon_1, \epsilon_o) \left(2 \cdot \pi \cdot r_1 \cdot (T_{hot}^4 - T_{cold}^4) \right) \quad Q_{L_rad_infinite}(r_3, r_2, \epsilon_{WP}, \epsilon_{wall}, 300\text{ K}, 600\text{ K}) = 1.643 \times 10^4 \frac{\text{W}}{\text{m}}$$

Heat transfer by radiation from NIRAS/ONDRAF December 2005 Report. Eef Weetjens and Xavier Sillen. *Thermal analysis of the Supercontainer concept 2D axisymmetric heat transport calculations*, Section 6.4.3. P g 34, equation 29.

$$Q_{L_infinite}(r_1, r_o, \epsilon_1, \epsilon_o, T_{cold}, T_{hot}) := \frac{2 \cdot \pi \cdot \sigma \cdot (T_{hot}^4 - T_{cold}^4)}{\frac{1 - \epsilon_1}{\epsilon_1 \cdot r_1} + \frac{1}{r_1} + \frac{1 - \epsilon_o}{\epsilon_o \cdot r_o}} \quad Q_{L_infinite}(r_3, r_2, \epsilon_{WP}, \epsilon_{wall}, 300\text{ K}, 600\text{ K}) = 1.643 \times 10^4 \frac{\text{W}}{\text{m}}$$

This is the same as the Incropera and DeWitt result, $Q_{L_rad_infinite}$

Comparison of thermal radiation across a gap to conduction after the gap has been filled with backfill material.

$$Q_{L_conduction_comparison}(r_1, r_o, T_{cold}, T_{hot}) := \frac{2 \cdot \pi \cdot r_o}{\frac{D_{DW}}{k_2} \cdot \ln\left(\frac{r_o}{r_1}\right)} (T_{hot} - T_{cold}) \quad Q_{L_conduction_comparison}(r_3, r_2, 300\text{ K}, 600\text{ K}) = 1.806 \times 10^3 \frac{\text{W}}{\text{m}}$$

$$Q_{ratio}(r_1, r_o, \epsilon_1, \epsilon_o, T_{cold}, T_{hot}) := \frac{Q_{L_infinite}(r_1, r_o, \epsilon_1, \epsilon_o, T_{cold}, T_{hot})}{Q_{L_conduction_comparison}(r_1, r_o, T_{cold}, T_{hot})} \quad Q_{ratio}(r_3, r_2, \epsilon_{WP}, \epsilon_{wall}, 300\text{ K}, 600\text{ K}) = 9.097$$

INPUT 7 = PARAMETRIC STUDY VARIABLE INPUT DATA

Input_7 := READEXCEL(file, concat(sheet, "F29:F41"))

0	
1	1
2	"Single"
3	"None"
4	""
5	""
6	""
7	""
8	""
9	""
10	""
11	""
12	""

Cases := Input_7[1] = 1

Parameter := Input_7[2] = "Single"

Parameter_units := Input_7[3] = "None"

ij := 1..Cases

Parameter_data[ij] := Input_7[ij+3]

Parameter_data = ("")

Parameter_description[ij] := | "Single Base Case" if Cases = 1
| concat[num2str[Input_7[(ij+3)], " ", Input_7[3]] otherwise

Parameter_description = ("Single Base Case")

INPUT 8 = DECAY HEAT INPUT DATA PER UNIT SOURCE (ASSEMBLY OR CANISTER):

Input_8_size := READExcel(file,concat(sheet,"C43")) Input_8_size1 = 58 Decay_heat_range := concat["A43:B",num2str((Input_8_size1 + 42))] = "A43:B100"
 Input_8 := READExcel(file,concat(sheet,Decay_heat_range))
 Time_out_of_Reactor := Input_8⁽¹⁾.yr Decay_Heat_per_Cnt := Input_8⁽²⁾.W

Input_8 =

	0	1
0	5	1.028·10 ³
1	5.1	1.011·10 ³
2	5.5	949.125
3	5.75	916.671
4	6	887.384
5	8	742.348
6	10	670.028
7	11.5	634.239
8	15	576.329
9	20	...

Time_out_of_Reactor =

	0
0	5
1	5.1
2	5.5
3	5.75
4	6
5	8
6	10
7	11.5
8	15
9	...

.yr

Decay_Heat_per_Cnt =

	0
0	1.028·10 ³
1	1.011·10 ³
2	949.125
3	916.671
4	887.384
5	742.348
6	670.028
7	634.239
8	576.329
9	...

W

$$Q(t) := \text{interp}(\text{spline}(\text{Time_out_of_Reactor}, \text{Decay_Heat_per_Cnt}), \text{Time_out_of_Reactor}, \text{Decay_Heat_per_Cnt}, t)$$

Ventilation efficiency for open systems is $V_{\text{eff}} = 0.75$ between t_{store} and t_{operate}

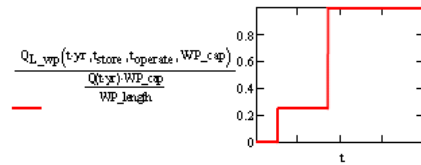
FUNCTION DEFINITION FOR ONE OUTPUT FILE

FORMULAS FOR CALCULATING THE TRANSIENT DRIFT WALL TEMPERATURE:

Central waste package:

$$Q_{L_wp}(t; t_{\text{store}}, t_{\text{operate}}, WP_{\text{cap}}) := \frac{Q(t) \cdot WP_{\text{cap}}}{WP_{\text{length}}} [1 - 1(t \leq t_{\text{store}})] [1 - V_{\text{eff}}(t \leq t_{\text{operate}})]$$

$$Q_{L_wp}(55\text{-yr}, t_{\text{store}}, t_{\text{operate}}, 12) = 177.365 \frac{\text{W}}{\text{m}}$$



Note - added r_{DW} as a function parameter to allow calculations at additional compliance points inside the rock, where r_{DW} would be replaced with newradius value.

$$DW_T_finite_line(t, r_{DW}, y, t_{store}, t_{operate}, WP_cap, Kth, \omega) = \int_0^t \frac{Q_{L_wp}(\tau, t_{store}, t_{operate}, WP_cap)}{8(\pi \cdot Kth)(t-\tau)} e^{-\frac{(r_{DW})^2}{4\omega(t-\tau)}} \left[\operatorname{erf} \left[\frac{1}{2} \frac{(y + \frac{WP_length}{2})}{\sqrt{\omega(t-\tau)}} \right] - \operatorname{erf} \left[\frac{1}{2} \frac{(y - \frac{WP_length}{2})}{\sqrt{\omega(t-\tau)}} \right] \right] d\tau$$

Adjacent drifts:

$$Q_{L_avg}(t, t_{store}, t_{operate}, WP_cap, WP_spacing) = \frac{Q(t) \cdot WP_cap}{WP_spacing} [1 - 1(t \leq t_{store})] [1 - V_{eff}(t \leq t_{operate})]$$

Note - added r_{DW} as a function parameter to allow calculations at additional compliance points inside the rock, where r_{DW} would be replaced with newradius value.

$$DW_T_drifts(t, r_{DW}, t_{store}, t_{operate}, WP_cap, WP_spacing, Drift_spacing, Kth, \omega) = 2 \sum_{id=1}^{N_{drifts}} \int_0^t \frac{Q_{L_avg}(\tau, t_{store}, t_{operate}, WP_cap, WP_spacing)}{4(\pi \cdot Kth)(t-\tau)} e^{-\frac{[(r_{DW})^2 + (id \cdot Drift_spacing)^2]}{4\omega(t-\tau)}} d\tau$$

Adjacent waste packages:

$$Q_{wp}(t, t_{store}, t_{operate}, WP_cap) = Q(t) \cdot WP_cap [1 - 1(t \leq t_{store})] [1 - V_{eff}(t \leq t_{operate})]$$

Note - added r_{DW} as a function parameter to allow calculations at additional compliance points inside the rock, where r_{DW} would be replaced with newradius value.

$$DW_T_adjacent_pkgs(t, r_{DW}, t_{store}, t_{operate}, WP_cap, WP_spacing, Kth, \omega) = 2 \sum_{ip=1}^{N_{adj}} \int_0^t \frac{Q_{wp}(\tau, t_{store}, t_{operate}, WP_cap)}{8 \cdot Kth \cdot \sqrt{\omega} \cdot \pi^{1.5} \cdot (t-\tau)^{1.5}} e^{-\frac{[(r_{DW})^2 + (ip \cdot WP_spacing)^2]}{4\omega(t-\tau)}} d\tau$$

This command specifies two rows of column headings for output parameter sensitivity runs

```
OutfileName := file = "DSEF R3.0_2013Aug12_HRG-Clay_UOX-40_Iterative convergence example_Case-225-19.xdsm"
Outsheet := "Thermal-Analytical Output"
```

This section specifies the column headings for output sensitivity studies

```
Cases = 1 Read in from Thermal-Analytical sheet in DSEF (Inputs_7)
i := 1..Cases
```

```
Parameter_vectori :=  $\begin{cases} \text{"Base Case"} & \text{if Cases} = 1 \\ \text{concat(Parameter, " ", Parameter\_descriptions)} & \text{otherwise} \end{cases}$ 
```

```
Parameter_vector = ("Base Case")
```

$$\text{heading1}_i := \begin{pmatrix} \text{concat("Parameter value: ", Parameter_vector}_i) \\ \text{""} \end{pmatrix}$$

$$\text{heading2} := \begin{pmatrix} \text{"TooR (yr)} \\ \text{"Wall } \Delta T \text{ Central Line Src"} \\ \text{"Wall } \Delta T \text{ Adj Drifts"} \\ \text{"Wall } \Delta T \text{ Adj Plugs"} \\ \text{"Compliance Point 2, C"} \\ \text{"Rock Wall Temp, C"} \\ \text{"EBS 1 inner Temp, C"} \\ \text{"EBS 2 inner Temp, C"} \\ \text{"EBS 3 inner Temp, C"} \\ \text{"Waste Plg Temp, C"} \end{pmatrix}$$

```
heading1i := heading1iT heading2 := heading2T
```

```
Title_arrayi := stack(heading1i, heading2)
```

```
Title_array2 = ■
```

For-Loop analysis returning the output time, three temperature contribution terms, and six temperatures

```
length(Parameter_data) = 1 rDW = 2.25m tstore = 50.yr tvent = 120.yr
rCP2 = 5.25m toperate = 170.yr
tclosure = 180.yr
```

Changed j vector to Parameter_data, inserted row2 in row5 changed to k_{radiation} and k₂ from k₂ and k_{backfill} row 8 changed WP_{spacej} to WP_{spacing}.

Removed loop on "j", added r_{DW} into DW_T functions.

Note for enclosed modes k_{radiation} = k₂

DEFINE STEP SIZE FOR OUTDATA

Counter := 200

Step := 5

time_after_employment_analyzed := (Counter*Step*yr) + t_{store} = 1050*yr

ADDED CORRECTION FOR PARAMETRIC t_{closure}
replaced t_{closure} with (t_{operate} + t_{backfill})

```

outdata(DW,CP2,tstore,toperate,WPcap,WPspacing,Driftspacing,Kth,α,k1,k2,k3,k4) :=
for i ∈ 1..Counter+1
  ti ← Step*i*yr + tstore - Step*1*yr
  kk2 ← kradiation[ti < (toperate + tbackfill)] + k2[ti ≥ (toperate + tbackfill)]
  Wall_deltaT_finite_linei ← DW_T_finite_line(ti,DWW,0,tstore,toperate,WPcap,Kth,α)
  Wall_deltaT_driftsi ← DW_T_drifts(ti,DWW,tstore,toperate,WPcap,WPspacing,Driftspacing,Kth,α)
  Wall_deltaT_adj_pkgsi ← DW_T_adjacent_pkgs(ti,DWW,tstore,toperate,WPcap,WPspacing,Kth,α)
  Wall_Ti ← Tambient + Wall_deltaT_finite_linei + Wall_deltaT_driftsi + Wall_deltaT_adj_pkgsi
  CP2_deltaT_finite_linei ← DW_T_finite_line(ti,CP2,0,tstore,toperate,WPcap,Kth,α)
  CP2_deltaT_driftsi ← DW_T_drifts(ti,CP2,tstore,toperate,WPcap,WPspacing,Driftspacing,Kth,α)
  CP2_deltaT_adj_pkgsi ← DW_T_adjacent_pkgs(ti,CP2,tstore,toperate,WPcap,WPspacing,Kth,α)
  CP2_Ti ← Tambient + CP2_deltaT_finite_linei + CP2_deltaT_driftsi + CP2_deltaT_adj_pkgsi
  Qi ← QL_wp(ti,tstore,toperate,WPcap)
  EBS_1i ← Wall_Ti +  $\frac{Q_i}{2\pi \cdot DWW} \cdot R_1(k_1)$ 
  EBS_2i ←  $\begin{cases} EBS_1 + \frac{Q_i}{2\pi \cdot DWW} \cdot R_2(kk_2, t_i, t_{operate}, t_{backfill}) & \text{if } kk_2 \neq 0 \frac{W}{mK} \\ \left[ \frac{Q_i}{h_{rad\_infinite}(r_3, r_2, \epsilon_{WP}, \epsilon_{wall}) \cdot 2\pi \cdot r_3} + (EBS_1)^4 \right]^{\frac{1}{4}} & \text{otherwise} \end{cases}$ 
  EBS_3i ← EBS_2i +  $\frac{Q_i}{2\pi \cdot DWW} \cdot R_3(k_3)$ 
  WP_Ti ← EBS_3i +  $\frac{Q_i}{2\pi \cdot DWW} \cdot R_4(k_4)$ 
  T1i ← CP2_Ti - 273.15K
  T2i ← Wall_Ti - 273.15K
  T3i ← EBS_1i - 273.15K
  T4i ← EBS_2i - 273.15K
  T5i ← EBS_3i - 273.15K
  T6i ← WP_Ti - 273.15K
  Data_array ← augment( $\frac{1}{yr}$ , Wall_deltaT_finite_line $\frac{1}{K}$ , Wall_deltaT_drifts $\frac{1}{K}$ , Wall_deltaT_adj_pkgs $\frac{1}{K}$ , T1 $\frac{1}{K}$ , T2 $\frac{1}{K}$ , T3 $\frac{1}{K}$ , T4 $\frac{1}{K}$ , T5 $\frac{1}{K}$ , T6 $\frac{1}{K}$ )

```

$jjj := 1..Cases$ $Cases = 1$

$X_{jjj} := Parameter_data_{jjj}$ $Parameter = "Single"$

$Temp_array_{jjj} :=$ $\left\{ \begin{array}{l} outdata\left(\rho_{DW}, \kappa_{CP2}, t_{store}, t_{operate}, WP_cap, WP_spacing, Drift_spacing, K_{th}, \omega, k_1, k_2, k_3, k_4 \right)$ if Parameter = "Single"
 $outdata\left(\rho_{DW}, \kappa_{CP2}, t_{store}, t_{operate}, WP_cap, WP_spacing, X_{jjj}, m, K_{th}, \omega, k_1, k_2, k_3, k_4 \right)$ if Parameter = "Drift Spacing"
 $outdata\left(\rho_{DW}, \kappa_{CP2}, t_{store}, t_{operate}, WP_cap, X_{jjj}, m, Drift_spacing, K_{th}, \omega, k_1, k_2, k_3, k_4 \right)$ if Parameter = "WFS spacing"
 $outdata\left(\rho_{DW}, \kappa_{CP2}, X_{jjj}, \gamma_r, t_{operate}, WP_cap, WP_spacing, Drift_spacing, K_{th}, \omega, k_1, k_2, k_3, k_4 \right)$ if Parameter = "Storage Time"
 $outdata\left(\rho_{DW}, \kappa_{CP2}, t_{store}, t_{store} + X_{jjj}, \gamma_r, WP_cap, WP_spacing, Drift_spacing, K_{th}, \omega, k_1, k_2, k_3, k_4 \right)$ if Parameter = "Ventilation Duration"
 $outdata\left(\rho_{DW}, \kappa_{CP2}, t_{store}, t_{operate}, WP_cap, WP_spacing, Drift_spacing, X_{jjj} \frac{W}{mK}, \omega, k_1, k_2, k_3, k_4 \right)$ if Parameter = "Rock Conductivity"
 $outdata\left(\rho_{DW}, \kappa_{CP2}, t_{store}, t_{operate}, WP_cap, WP_spacing, Drift_spacing, K_{th}, \omega, k_1, X_{jjj} \frac{W}{mK}, k_3, k_4 \right)$ if Parameter = "Backfill Conductivity"
"Undefined" otherwise

$File_array_{jjj} := stack(Title_array_{jjj}, Temp_array_{jjj})$



$File_array_1 =$ ■



Mathcad DSEF 3.0 parametric and iterative model - example for User's Manual.xmcd

```
transient_write_range := # peaks_write_range := concat(outsheet,"C6:V11") = "Thermal-Analytical Output!C6:V11"
```

```
transient_write_range = ("Thermal-Analytical Output!A100:J300")
```

```
Transient_size := (Counter Step) Transient_size = (200 5) Transient_size_range := concat(outsheet,"B92:C92") = "Thermal-Analytical Output!B92:C92"
```

Make writing an output file optional

```
t_vert = 120.yr
```

```
OutfileName = "DSEFR3.0_2013Aug12_HRG-Clay_UOX-40_iterative convergence example_Case-225-19.xdsm"
```

```
Write_file := Write_OK = "YES"
```

```
write_the_peaks(Write_file) := write_it ← WRITEEXCEL(Peak_values,OutfileName,peaks_write_range) if (Write_file = "Yes") ∨ (Write_file = "YES")  
"File written"  
write_it ← "No file written" otherwise
```

```
write_the_peaks(Write_file) = #
```

```
write_the_transient_size(Write_file) := write_it ← WRITEEXCEL(Transient_size,OutfileName,Transient_size_range) if (Write_file = "Yes") ∨ (Write_file = "YES")  
"File written"  
write_it ← "No file written" otherwise
```

```
write_the_transient_size(Write_file) = "File written"
```

```
Write_file := Write_OK = "YES"
```

```
Cases = 1
```

```
iwv := 1..Cases
```

NOTE - USE File_array to write to stand-alone Excel files, and Temp_array to write back to the DSEF Excel file.

```
write_the_transients(iwv) := write_array ← Temp_array  
write_it ← WRITEEXCEL(write_array,OutfileName,transient_write_range) if (Write_file = "Yes") ∨ (Write_file = "YES")  
"File written"  
write_it ← "No file written" otherwise
```

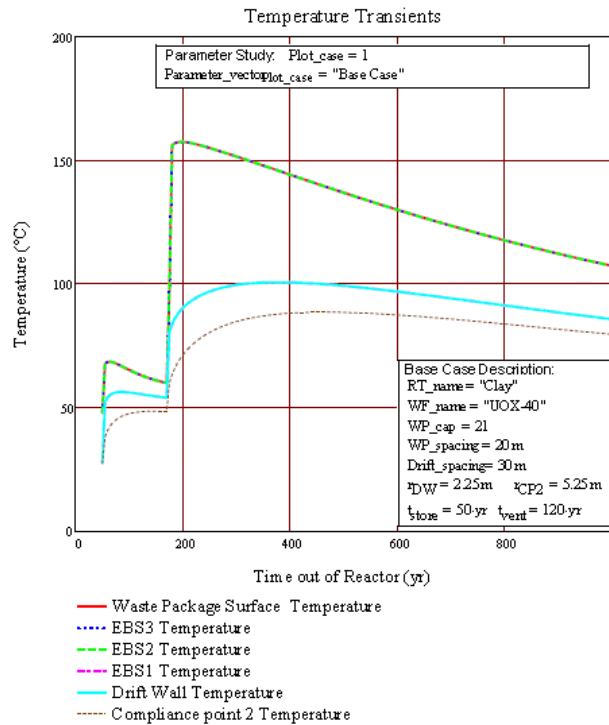
```
write_the_transients(iwv) = #
```

Plot_case := 1

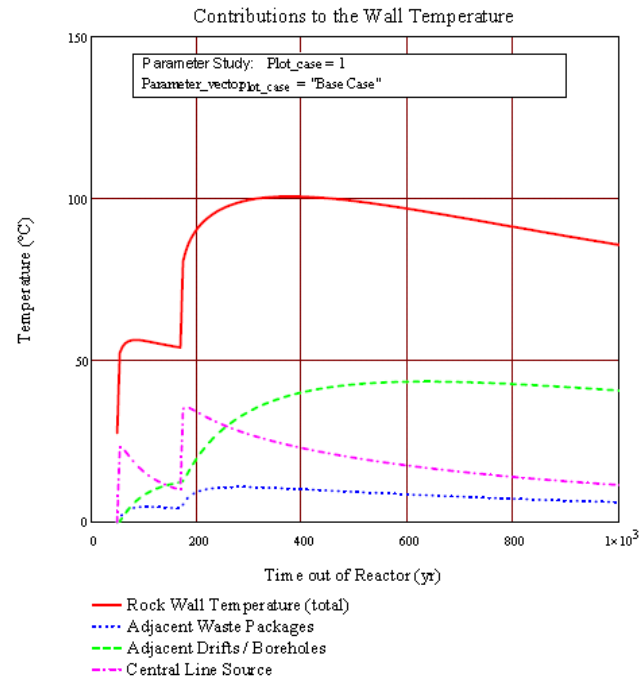
Select parametric study case to plot (default plot is for case 1)

WP_plot := [(Temp_arrayplot_case)¹⁰] EBS3_T_plot := [(Temp_arrayplot_case)⁶] EBS2_T_plot := [(Temp_arrayplot_case)⁸] EBS1_T_plot := [(Temp_arrayplot_case)⁷] Wall_T_plot := [(Temp_arrayplot_case)⁶]

CP2_plot := [(Temp_arrayplot_case)⁵] Delta_WP3_T_plot := [(Temp_arrayplot_case)⁴] Delta_difbs_T_plot := [(Temp_arrayplot_case)³] Delta_central_T_plot := [(Temp_arrayplot_case)²]



$$T_{EBS}(r, t, Wall_T, k_1, k_2, k_3, k_4) := Wall_T \cdot K + \frac{Q_{L_wp}(t_{store}, t_{operate}, WP_cap)}{2 \cdot \pi \cdot r \cdot DW} \cdot R_{continuous}(t, r, k_1, k_2, k_3, k_4)$$



$$Q_{L_wp}(110 \text{ yr}, t_{store}, t_{operate}, WP_cap) = 167.803 \frac{W}{m}$$

$$tt_{rw} := [(Peak_values)^{(Plot_case-2)}]_2 = 385$$

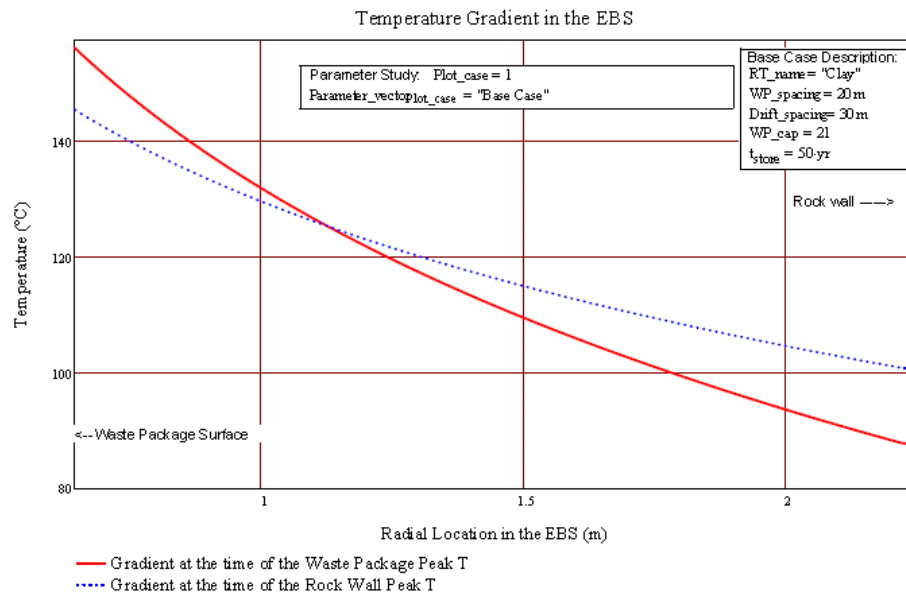
$$Wall_T_at_tt_{rw} := [(Peak_values)^{(Plot_case-2-1)}]_2 = 100.744$$

$$WP_T_at_tt_{rw} := [(Peak_values)^{(Plot_case-2-1)}]_6 = 157.563$$

$$tt_{wp} := [(Peak_values)^{(Plot_case-2)}]_6 = 195$$

$$Wall_T_at_tt_{wp} := \left[(Temp_arrayplot_case)^{(6)} \right] \left(\frac{tt_{wp} - t_{store}}{Step} \right) = 87.705$$

$$WP_T_at_tt_{wp} := \left[(Temp_arrayplot_case)^{(10)} \right] \left(\frac{tt_{wp} - t_{store}}{Step} \right) = 145.774$$



OVERRIDE COUNTER AND STEP SIZE TO GET FINER CONVERGENCE ON THE ANSWER

$t_{vent} = 120\text{-yr}$

OPTIONALLY OVERRIDE VENTILATION TIME TO SHORTEN ITERATION CONVERGENCE:

ITERATE_OK := "YES"

$t_{convergence} = 1\text{-yr}$

$$t_{required_storage}(t_{operate}, T_{criteria}, t_{convergence}) := \left(\begin{array}{l} \text{time}_{OK} \leftarrow t_{operate} - t_{convergence} \\ \text{Peak_Wall_T_check} \leftarrow (\text{Peak_Wall_T} + 273.15) \cdot K \\ \text{time}_{OK} \leftarrow t_{operate} \quad \text{if } \text{Peak_Wall_T_check} \leq T_{criteria} \\ \text{while } \text{Peak_Wall_T_check} > T_{criteria} \\ \quad \left(\begin{array}{l} \text{time}_{OK} \leftarrow \text{time}_{OK} + t_{convergence} \\ \text{calc_array} \leftarrow \text{outdata}(T_{DW}, \alpha_{CP2}, t_{store}, \text{time}_{OK}, \text{WP_cap}, \text{WP_spacing}, \text{Drift_spacing}, K_{th}, \alpha, k_1, k_2, k_3, k_4) \\ \text{Peak_Wall_T_check} \leftarrow (\max(\text{calc_array}) + 273.15) \cdot K \end{array} \right) \\ \text{return} \left(\begin{array}{l} \frac{\text{time}_{OK}}{\text{yr}} \\ \frac{\text{Peak_Wall_T_check} - 273.15 \cdot K}{K} \\ \text{outdata}(T_{DW}, \alpha_{CP2}, t_{store}, \text{time}_{OK}, \text{WP_cap}, \text{WP_spacing}, \text{Drift_spacing}, K_{th}, \alpha, k_1, k_2, k_3, k_4) \end{array} \right) \end{array} \right)$$

$\text{Final_array} := \left(\begin{array}{l} t_{required_storage}(t_{operate}, T_{criteria}, t_{convergence}) \quad \text{if } \text{ITERATE_OK} = \text{"YES"} \\ \text{"No Iteration Performed"} \quad \text{otherwise} \end{array} \right)$

$t_{operate_required} := \text{Final_array}_1 \text{ yr} = 177\text{-yr}$

$t_{vent_required} := t_{operate_required} - t_{store} = 127\text{-yr}$ **REQUIRED VENTILATION TIME NEEDED TO MEET $T_{criteria} = 100^\circ\text{C}$**

$\text{Peak_Wall_T_check} := (\text{Final_array}_2 + 273.15) \cdot K = 99.931^\circ\text{C}$

Result := stack(Title_array, Final_array3)

NOTE THAT THIS SECTION WILL BE BLANK IF NO ITERATIVE ANALYSIS IS PERFORMED (Iterate_OK = "No")

Result =

	1	2	3	4	5	6	7
1	"Parameter value: Base Case"						
2	"TooR (yr)"	"Wall ΔT Central Line Src"	"Wall ΔT Adj Drifts"	"Wall ΔT Adj Pkgs"	"Compliance Point 2, C"	"Rock Wall Temp, C"	"EBS 1 inner Temp, C"
3	50	0	0	0	27.5	27.5	27.513
4	55	23.349	0.269	1.181	38.116	52.299	52.311
5	60	22.931	1.341	2.422	40.833	54.195	54.206
6	65	21.989	2.532	3.206	42.678	55.227	55.238
7	70	20.933	3.643	3.728	43.983	55.804	55.814
8	75	19.895	4.644	4.085	44.978	56.124	56.133
9	80	18.909	5.536	4.332	45.748	56.278	56.287
10	85	17.992	6.332	4.501	46.352	56.325	56.333
11	90	17.14	7.042	4.612	46.831	56.294	56.302
12	95	16.364	7.675	4.681	47.21	56.22	56.227
13	100	15.639	8.245	4.719	47.518	56.103	56.111
14	105	14.98	8.756	4.735	47.767	55.972	55.979
15	110	14.372	9.214	4.728	47.957	55.814	55.82
16	115	13.82	9.628	4.71	48.116	55.658	...

Time_array := (Final_array3)^{1}

Peak_Temp(n) := max[(Final_array3)^{6}] Peak_Temp(6) = 99.931

Peak_t(n) := lookup[Peak_Temp(n), (Final_array3)^{6}, Time_array] Peak_t(6) 1_yr = 380_yr

mi := 5..10 Peak_results_m-4_1 := Peak_Temp(mi) Peak_results_m-4_2 := Peak_t(mi) 1

Peak_results = $\begin{pmatrix} 88.045 & 470 \\ 99.931 & 380 \\ 99.941 & 380 \\ 154.961 & 210 \\ 154.961 & 210 \\ 154.961 & 210 \end{pmatrix}$

CP2 . time of peak Array_row_at_Wall_T_peak := match[Peak_Temp(6), (Final_array3)^{6}]₁ = 67
 Peak Wall T, time of peak CP2_at_Wall_T_pk_t := [(Final_array3)^{6}]_{Array_row_at_Wall_T_peak} = 87.069
 Peak EBS 1, time of peak
 Peak EBS 2, time of peak
 Peak EBS 3, time of peak
 Waste Pkg T, time of peak
 Central_WP_delta := [(Final_array3)^{2}]_{Array_row_at_Wall_T_peak} = 23.638
 Adj_Drift_delta := [(Final_array3)^{3}]_{Array_row_at_Wall_T_peak} = 38.538
 Adj_WP_delta := [(Final_array3)^{4}]_{Array_row_at_Wall_T_peak} = 10.254

$$\text{Result_Vector} := \left(\frac{\text{WP_spacing}}{m} \quad \text{TC} \quad \frac{\text{Drift_spacing}}{m} \quad \text{Peak_results}_{6,1} \quad \text{Peak_results}_{6,2} \quad \text{Peak_results}_{2,1} \quad \text{Peak_results}_{2,2} \quad \text{CP2_at_Wall_T_pk} \quad t_{\text{vent_required}} \quad \text{Central_WP_delta} \quad \text{Adj_Drift_delta} \quad \text{Adj_WP_delta} \right)$$

Result_headings := ("WPSpacing" "Temp Criteria" "Drift Spacing" "Peak WP T" "Time of WP Peak" "Peak Wall T" "Time of Wall Peak" "Peak CP2 T" "Ventilation time" "Central WP delta" "Adj Drift delta" "Adj WP delta")

Result_Vector = (20 100 30 154.961 210 99.931 380 87.069 127 23.638 38.538 10.254) This is the result vector for transcription to the Excel case results tracking file

RV := augment(Result_headings^T, Result_Vector^T) T_ambient = 27.5 °C Contribution percentages at time of peak wall temperature

"WPSpacing"	20	Percent_central_WP_delta :=	$\frac{\text{Central_WP_delta}}{\text{Peak_Temp}(6) - \frac{T_{\text{ambient}} - 273.15 \text{ K}}{K}} \cdot 100 = 32.636$
"Temp Criteria"	100		
"Drift Spacing"	30		
"Peak WP T"	154.961	Percent_adj_Drift_delta :=	$\frac{\text{Adj_Drift_delta}}{\text{Peak_Temp}(6) - \frac{T_{\text{ambient}} - 273.15 \text{ K}}{K}} \cdot 100 = 53.207$
"Time of WP Peak"	210		
"Peak Wall T"	99.931	Percent_adj_WP_delta :=	$\frac{\text{Adj_WP_delta}}{\text{Peak_Temp}(6) - \frac{T_{\text{ambient}} - 273.15 \text{ K}}{K}} \cdot 100 = 14.157$
"Time of Wall Peak"	380		
"Peak CP2 T"	87.069		
"Ventilation time"	127		
"Central WP delta"	23.638		
"Adj Drift delta"	38.538		
"Adj WP delta"	10.254	Percent_central_WP_delta + Percent_adj_WP_delta + Percent_adj_Drift_delta =	100

Plot temperature results as a function of parameter data

ip := 1..Cases

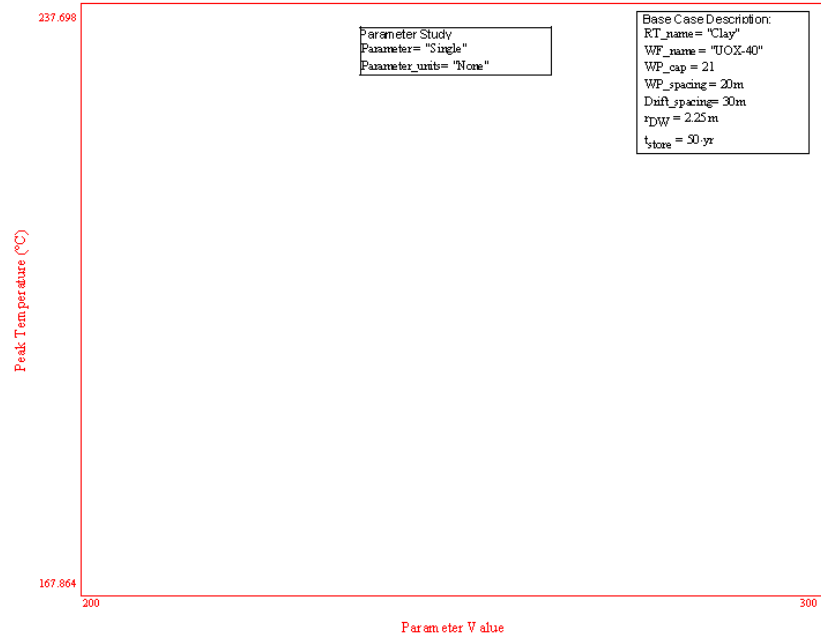
$$\text{Peak_WP_T}_{ip} := (\text{Peak_values}^{\langle \Phi-2-1 \rangle})_6 \quad \text{Peak_EBS3_T}_{ip} := (\text{Peak_values}^{\langle \Phi-2-1 \rangle})_5 \quad \text{Peak_EBS2_T}_{ip} := (\text{Peak_values}^{\langle \Phi-2-1 \rangle})_4 \quad \text{Peak_EBS1_T}_{ip} := (\text{Peak_values}^{\langle \Phi-2-1 \rangle})_3$$

$$\text{Peak_WP_T} = (157.563) \quad \text{Peak_EBS3_T} = (157.563) \quad \text{Peak_EBS2_T} = (157.563) \quad \text{Peak_EBS1_T} = (100.755)$$

$$\text{Peak_Wall_T}_{ip} := (\text{Peak_values}^{\langle \Phi-2-1 \rangle})_2 \quad \text{Peak_CP2_T}_{ip} := (\text{Peak_values}^{\langle \Phi-2-1 \rangle})_1$$

$$\text{Peak_Wall_T} = (100.744) \quad \text{Peak_CP2_T} = (88.663) \quad \text{Parameter_data} = ("") \quad \text{Parameter_vector} = ("Base Case")$$

Peak Temperatures versus Parameter Study Data



B.4 The Mathcad model with temperature and time dependent EBS thermal properties

This section documents a new DSEF Version 3.0 Mathcad model that allows temperature and time-dependent thermal properties within the EBS layers of the model. The PDF file and Mathcad document example shown applies these to salt for temperature-dependent thermal conductivity and time-dependent crushed salt porosity to model consolidation of the crushed salt layer with time and heat. The equations that implement these functions are shown on pages 2 and 3 of 24 in the PDF printout. The data for the time-dependent crushed salt consolidation comes from a finite element model in Hardin 2012b (Figure C-5). This model provides proof-of-principle that the thermal-analytical model can accommodate more complex thermal property modeling than the constant properties assumed in models and analysis using earlier versions of DSEF. The thermal results of this new model have a better fit to the FEM model results for the 12-PWR 40-GWd/MT burnup waste stream with 50 years of surface storage documented in Hardin 2012b than was possible with previous analyses using constant salt properties in the EBS (see Greenberg 2012b, Section G.6.2).

The EBS layer thermal conductivity values input by the DSEF Excel file have been replaced by the temperature and time-dependent functions at the beginning of the Mathcad document, and the programming loop shown on page 13 of 23 of the PDF file has been modified to use these new functions.

It should be noted that this model will work with all of the parametric study options except for parameter variations involving backfill thermal conductivity. The Mathcad model will convert any backfill thermal conductivity parameter study case into a “Single” analysis. The temperature and time-dependent EBS property functions will also work with the iterative convergence model.

With different temperature or time-dependence functions, this methodology could be used to model moisture-dependent properties covering dryout or re-wetting effects in other media. This would require other data or analysis to set the basic input functions, but then the benefits of the analytical-model approach could be applied to a broader class of problems.

DSEF R3.0 Single Model with collapsed areas - for rapid iteration cases

Allow output transients to be written back to DSEF FILE

Case_name := "229-61"

Variables for repository symmetry and extent:

Write_OK := "No"

$N_{drift} := 4$ $N_{adj} := 4$

NOTE - the Write_OK variable controls writing transient results back to Excel-DSEF, and Iterate_OK controls iterative convergence calculations for required ventilation times. This Mathcad model also allows temperature and time dependent thermal properties, and works with all DSEF parametric option cases except parametric cases involving backfill thermal conductivity.

REQUIRED REPOSITORY INPUT DATA (from DSEF):

file := "DSEF R3.0C_2013Jul29_HRG-Salt_UOX-40_Enclosed mode variable kth_Case-Kth-1.xlsm"

sheet := "Thermal-Analytical"

DATA FOR ITERATION ON TEMPERATURE ACCEPTANCE CRITERIA:

TC := 100 $T_{criteria} := (TC + 273.15) \cdot K = 373.15 \text{ K}$ $T_{criteria} = 100 \cdot ^\circ C$

READ DSEF INPUT FILE

Input 1 = Operating Mode (enclosed or open)

Input_1 := READEXCEL(file, concat(sheet, "A5:B5"))

Input_1 = ("MODE = Open or Enclosed:" "Enclosed") Mode := Input_1,2 = "Enclosed"

t_convergence := 1-yr **CONVERGE CRITERIA FOR REQUIRED VENTILATION TIME IN YEARS**

SET THE VARIABLE ITERATE_OK TO "NO" TO TURN OFF THE AUTOMATIC CONVERGENCE CALCULATION, AND MANUALLY RESET IT TO "YES" IF YOU WANT TO FINE TUNE YOUR ANSWER.

Input_2 := READEXCEL(file, concat(sheet, "A7:B16"))

ITERATE_OK := "NO"

Input 3 = Ventilation Parameters (for Open Modes)

Input_2 =	"Host Media"	"Salt"
	"Rock thermal conductivity, W/m-K"	5.4
	"Rock thermal diffusivity, m ² /sec"	2.661×10^{-6}
	"Repository Depth, m"	500
	"Surface temperature, °C"	15
	"Geothermal gradient, °C/km"	25
	"Ambient temperature at depth, °C"	27.5
	"Waste Package (axial) spacing, m"	20
	"Drift / Borehole (lateral) spacing, m"	20
	"Surface storage time, y"	50

Input_3 := READEXCEL(file, concat(sheet, "e7:f11"))

Input_3 =	"Ventilation Duration, yr"	"N/A"
	"Unventilated Closure Duration (Backfill Installation), yr"	"N/A"
	"Ventilation Thermal Efficiency, %"	"N/A"
	"Rock Wall Emissivity"	"N/A"
	"Waste Package Emissivity"	"N/A"

RT_name := Input_2,1,2 = "Salt"

$K_{th} := \text{Input}_{2,2} \frac{W}{m \cdot K} = 5.4 \frac{m \cdot kg}{K \cdot s^3}$

$\alpha := \text{Input}_{2,3} \frac{m^2}{s} = 2.661 \times 10^{-6} \frac{m^2}{s}$

WP_depth := Input_2,4,2 = 500 m

$T_{surface} := (\text{Input}_{2,5,2} + 273.15) \text{ K} = 288.15 \text{ K}$

$\text{geothermal_gradient} := \text{Input}_{2,6,2} \frac{K}{km} = 0.025 \frac{K}{m}$

$t_{vent} := \text{if}[(\text{Mode} = \text{"Enclosed"}), 0, \text{Input}_{3,1,2}] \text{ yr} = 0 \text{ yr}$

$t_{backfill} := \text{if}[(\text{Mode} = \text{"Enclosed"}), 0, \text{Input}_{3,2,2}] \text{ yr} = 0 \text{ yr}$

$V_{eff} := \text{if}[(\text{Mode} = \text{"Enclosed"}), 0, \text{Input}_{3,3,2}] = 0$

$\epsilon_{wall} := \text{if}[(\text{Mode} = \text{"Enclosed"}), 0.9, \text{Input}_{3,4,2}] = 0.9$

$\epsilon_{WP} := \text{if}[(\text{Mode} = \text{"Enclosed"}), 0.6, \text{Input}_{3,5,2}] = 0.6$

OVER-RIDE VENTILATION DURATION

DSEF R3.0_Mathcad with temperature and time dependent EBS thermal conductivity.xmod

$$T_{\text{ambient}} := (\text{Input}_{2,2} + 273.15) \text{ K} = 300.65 \text{ K}$$

$$\text{WP_spacing} := \text{Input}_{2,8,2} \text{ m} = 20 \text{ m}$$

$$\text{Drift_spacing} := \text{Input}_{2,9,2} \text{ m} = 20 \text{ m}$$

$$t_{\text{store}} := \text{Input}_{2,10,2} \text{ yr} = 50 \text{ yr}$$

OVER-RIDE DRIFT SPACING

$$t_{\text{operate}} := (t_{\text{store}} + t_{\text{vent}}) = 50 \text{ yr}$$

$$T_{\text{OPERATE}} = T_{\text{STORE}} + T_{\text{VENTILATE}}$$

$$t_{\text{closure}} := t_{\text{operate}} + t_{\text{backfill}} = 50 \text{ yr}$$

$$T_{\text{CLOSURE}} = T_{\text{OPERATE}} + \text{TIME TO BACKFILL}$$

Input 4 = ENGINEERED BARRIER SYSTEM DATA:

Input_4 := READEXCEL(file,concat(sheet,"A20:F27"))

Input_4 =	"Waste Form Outer Radius, m"	0.555	"N/A"	0.555	"UOX-40"	"N/A"
	"Canister"	0	0.555	0.555	"Carbon Steel"	"N/A"
	"Waste Package"	0.03	0.555	0.585	"Carbon Steel"	"N/A"
	"Salt Layer 1"	0.821	0.585	1.406	"75% Intact Salt at T4°C"	3.16
	"Salt Layer 2"	0.821	1.406	2.227	"75% Intact Salt at T3°C"	3.16
	"Salt Layer 3"	0.821	2.227	3.048	"75% Intact Salt at T2°C"	3.16
	"Salt Layer 4"	0.952	3.048	4	"Intact Salt 100°C"	4.2
"Host Rock Inner Radius, m ---->"	NaN	4	NaN	NaN	NaN	

Input 5 = COMPLIANCE POINT 2 INPUT DATA

Input_5 := READEXCEL(file,concat(sheet,"C32"))

$$\text{Input}_5 = (5.25)$$

$$r_{\text{CP2}} := \text{Input}_{5,1} \text{ m} = 5.25 \text{ m}$$

DATA AND FORMULAS TO ALLOW TRANSIENT THERMAL CONDUCTIVITY WITHIN THE EBS

SALT THERMAL CONDUCTIVITY AS A FUNCTION OF TEMPERATURE AND POROSITY

Thermal conductivity of intact and crushed salt, based on Reference:
 3-D Thermal Analyses of High-Level Waste Emplaced in a Generic Salt Repository
 AFCL-WAST-PMO-MI-DV-2009-000002; February, 2009. (D. J. Clayton, SNL, and C. W. Gable, Los Alamos).

$$k_{\text{intact}_0} := 5.4 \frac{\text{W}}{\text{m}\cdot\text{K}} \quad k_{\text{intact}}(T) := k_{\text{intact}_0} \left(\frac{300\text{ K}}{T} \right)^{1.14} \quad \text{Where } T \text{ is in Kelvin}$$

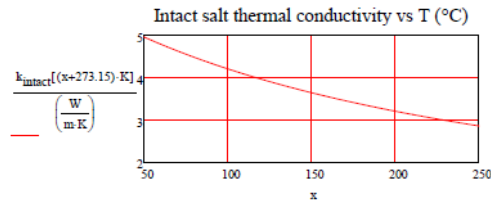
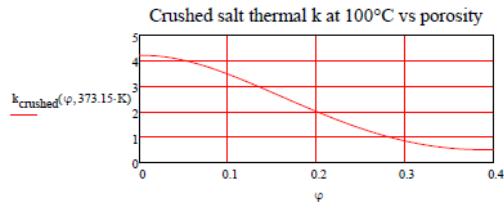
$$k_{\text{intact}}(372.15\text{ K}) = 4.224 \frac{\text{W}}{\text{m}\cdot\text{K}}$$

$$k_{\text{cs}}(\varphi) := (-270\varphi^4 + 370\varphi^3 - 136\varphi^2 + 1.5\varphi + 5) \cdot 1.08 \frac{\text{W}}{\text{m}\cdot\text{K}} \quad \text{Where } \varphi \text{ is porosity}$$

$$k_{\text{crushed}}(\varphi, T) := k_{\text{cs}}(\varphi) \left(\frac{300\text{ K}}{T} \right)^{1.14}$$

$$k_{\text{crushed}}[0, (273.15 + 27.5)\text{ K}] = 5.4 \frac{\text{W}}{\text{m}\cdot\text{K}}$$

$$k_{\text{crushed}}[0, (273.15 + 100)\text{ K}] = 4.2 \frac{\text{W}}{\text{m}\cdot\text{K}}$$



$k_{consolidate}$ is based on an initial porosity of φ_0 and a final porosity of φ_1 , and assumes a linear increase over time $t_{consolidate}$ $\varphi_0 := 0.20$ $\varphi_1 := 0.02$ $t_{consolidate} := 10\text{-yr}$

For comparison with SNL calculation (E. Hardin, T. Hadgu, D. Clayton, R. Howard, H. Greenberg, J. Blink, M. Sharma, M. Sutton, J. Carter, M. Dupont, P. Rodwell. *Repository Disposal Concepts and Thermal Load Management Analysis*. FCRD-UFD-2012-00219 Rev. 2. November, 2012) assume an initial crushed salt porosity $\varphi_0 = 0.20$, and use a piece-wise linear function to fit a set of data representing the time-dependent consolidation of crushed salt (from FCRD-UFD-2012-00219 figure C-5), where the first column is time in years, and the second column is porosity fraction.

$$\text{Consolidation_data_array} := \begin{pmatrix} 0 + \frac{t_{store}}{yr} & 0.20 \\ 20 + \frac{t_{store}}{yr} & 0.09 \\ 40 + \frac{t_{store}}{yr} & 0.06 \\ 60 + \frac{t_{store}}{yr} & 0.05 \\ 95 + \frac{t_{store}}{yr} & 0.04 \\ 200 + \frac{t_{store}}{yr} & 0.02 \\ 1000 + \frac{t_{store}}{yr} & 0.02 \end{pmatrix}$$

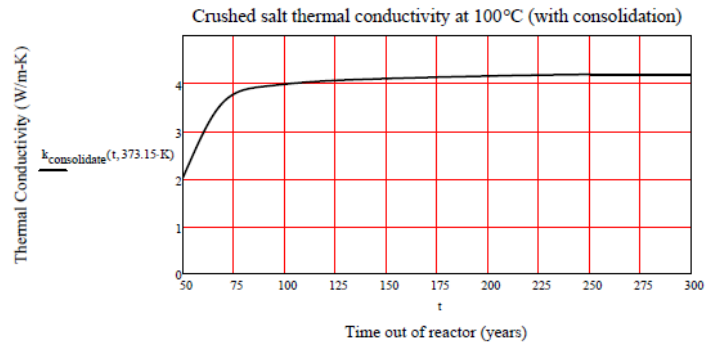
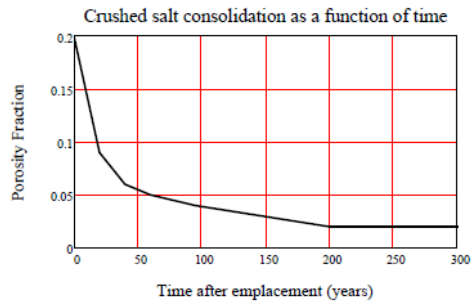
$$SS := \text{lspline}(\text{Consolidation_data_array}^{(1)}, \text{Consolidation_data_array}^{(2)})$$

$$\text{Porosity}(t) := \text{interp}(SS, \text{Consolidation_data_array}^{(1)}, \text{Consolidation_data_array}^{(2)}, t)$$

$$\text{Porosity}(50) = 0.2 \quad \text{Porosity}(80) = 0.068$$

$$k_{consolidate}(t, T) := \begin{cases} k_{crushed}(\text{Porosity}(t), T) & \text{if } [t \leq (\text{Consolidation_data_array}^{(1)})_6] \\ k_{crushed}[(\text{Consolidation_data_array}^{(2)})_6, T] & \text{otherwise} \end{cases}$$

$$k_{consolidate}\left(\frac{t_{store}}{yr}, 373.15\text{-K}\right) = 2.011 \frac{\text{W}}{\text{m}\cdot\text{K}}$$



DSEF R3.0_Mathcad with temperature and time dependent EBS thermal conductivity.xmod

$$r_{DW} := \text{Input}_{4,8,3} \text{ m} = 4 \text{ m}$$

$$r_{WP} := \text{Input}_{4,3,4} \text{ m} = 0.585 \text{ m}$$

$$\text{EBS_name}_1 := \text{Input}_{4,7,1} = \text{"Salt Layer 4"}$$

$$\text{thickness}_1 := \text{Input}_{4,7,2} \text{ m} = 0.952 \text{ m}$$

$$k1 := \text{Input}_{4,7,6} = 4.2$$

$$\text{EBS_name}_2 := \text{Input}_{4,6,1} = \text{"Salt Layer 3"}$$

$$\text{thickness}_2 := \text{Input}_{4,6,2} \text{ m} = 0.821 \text{ m}$$

$$k2 := \text{Input}_{4,6,6} = 3.16$$

$$k_{\text{radiation}}(t, T2) := \text{if}(\text{Mode} = \text{"Enclosed"}, k_2(t, T2), 0)$$

$$\text{EBS_name}_3 := \text{Input}_{4,5,1} = \text{"Salt Layer 2"}$$

$$\text{thickness}_3 := \text{Input}_{4,5,2} \text{ m} = 0.821 \text{ m}$$

$$k3 := \text{Input}_{4,5,6} = 3.16$$

$$\text{EBS_name}_4 := \text{Input}_{4,4,1} = \text{"Salt Layer 1"}$$

$$\text{thickness}_4 := \text{Input}_{4,4,2} \text{ m} = 0.821 \text{ m}$$

$$k4 := \text{Input}_{4,4,6} = 3.16$$

$$\text{EBS_material}_1 := \text{Input}_{4,7,5} = \text{"Intact Salt 100°C"}$$

$$r_1 := \text{Input}_{4,7,4} \text{ m} = 4 \text{ m}$$

$$k_1 := \text{if}[(k1 = \text{"N/A"}), 0, k1] \cdot \frac{\text{W}}{\text{m} \cdot \text{K}} = 4.2 \cdot \frac{\text{W}}{\text{m} \cdot \text{K}}$$

$$\text{EBS_material}_2 := \text{Input}_{4,6,5} = \text{"75% Intact Salt at T2°C"}$$

$$r_2 := \text{Input}_{4,6,4} \text{ m} = 3.048 \text{ m}$$

$$k_2 := \text{if}[(k2 = \text{"N/A"}), 0, k2] \cdot \frac{\text{W}}{\text{m} \cdot \text{K}} = 3.16 \cdot \frac{\text{W}}{\text{m} \cdot \text{K}}$$

$$\text{EBS_material}_3 := \text{Input}_{4,5,5} = \text{"75% Intact Salt at T3°C"}$$

$$r_3 := \text{Input}_{4,5,4} \text{ m} = 2.227 \text{ m}$$

$$k_3 := \text{if}[(k3 = \text{"N/A"}), 0, k3] \cdot \frac{\text{W}}{\text{m} \cdot \text{K}} = 3.16 \cdot \frac{\text{W}}{\text{m} \cdot \text{K}}$$

$$\text{EBS_material}_4 := \text{Input}_{4,4,5} = \text{"75% Intact Salt at T4°C"}$$

$$r_4 := \text{Input}_{4,4,4} \text{ m} = 1.406 \text{ m}$$

$$k_4 := \text{if}[(k4 = \text{"N/A"}), 0, k4] \cdot \frac{\text{W}}{\text{m} \cdot \text{K}} = 3.16 \cdot \frac{\text{W}}{\text{m} \cdot \text{K}}$$

$$k_{\text{intact}}(T) := \text{if}[(k1 = \text{"N/A"}), 0, k_{\text{intact}}(T)]$$

THE FOLLOWING FORMULAS ASSUME 75% CONTACT WITH INTACT SALT AND 25% CONTACT WITH CRUSHED SALT.

$$k_{\text{intact}}(t, T2) := \text{if}[(k2 = \text{"N/A"}), 0, 0.75 \cdot k_{\text{intact}}(T2) + 0.25 \cdot k_{\text{consolidate}}\left(\frac{t}{\text{yr}}, T2\right)]$$

$$k_{\text{intact}}(t, T3) := \text{if}[(k2 = \text{"N/A"}), 0, 0.75 \cdot k_{\text{intact}}(T3) + 0.25 \cdot k_{\text{consolidate}}\left(\frac{t}{\text{yr}}, T3\right)]$$

$$k_{\text{intact}}(t, T4) := \text{if}[(k2 = \text{"N/A"}), 0, 0.75 \cdot k_{\text{intact}}(T4) + 0.25 \cdot k_{\text{consolidate}}\left(\frac{t}{\text{yr}}, T4\right)]$$

$$k_4[0\text{-yr}, (100 + 273.15)\text{-K}] = 3.619 \cdot \frac{\text{W}}{\text{m} \cdot \text{K}} \quad k_4[1\text{-yr}, (100 + 273.15)\text{-K}] = 3.578 \cdot \frac{\text{W}}{\text{m} \cdot \text{K}}$$

$$k_4[2\text{-yr}, (100 + 273.15)\text{-K}] = 3.542 \cdot \frac{\text{W}}{\text{m} \cdot \text{K}} \quad k_4[10\text{-yr}, (100 + 273.15)\text{-K}] = 3.372 \cdot \frac{\text{W}}{\text{m} \cdot \text{K}}$$

Define the total thermal resistance between the rock wall and the waste package surface based on a heat flux per unit area, it is then applied to a heat flux per unit length adjusting to area per unit length and q_L (W/m):

$$r_{WP} = 0.585 \text{ m} \quad r_4 = 1.406 \text{ m} \quad r_3 = 2.227 \text{ m} \quad r_2 = 3.048 \text{ m} \quad r_1 = 4 \text{ m} \quad r_{DW} = 4 \text{ m}$$

$$R_1(T) := \text{if} \left[\left[\text{thickness}_1 = 0 \vee (k_1 = \text{"N/A"}) \right], 0, \frac{r_{DW}}{k_1(T)} \cdot \ln \left(\frac{r_1}{r_2} \right) \right] \quad R_1[(100 + 273.15)\text{-K}] = 0.258 \frac{\text{m}^2 \cdot \text{K}}{\text{W}} \text{ Thermal resistance}$$

EBS_name₁ = "Salt Layer 4" EBS_material₁ = "Intact Salt 100°C"

$$R_2(t, t_{\text{operate}}, t_{\text{backfill}}, T_2) := \begin{cases} k_1 \leftarrow k_{\text{radiation}}(t, T_2) \cdot [t < (t_{\text{operate}} + t_{\text{backfill}})] + k_2(t, T_2) \cdot [t \geq (t_{\text{operate}} + t_{\text{backfill}})] \\ \text{return if} \left[\left[\text{thickness}_2 = 0 \vee (k_2 = 0) \right], 0, \frac{r_{DW}}{k_1} \cdot \ln \left(\frac{r_2}{r_3} \right) \right] \end{cases}$$

$$\frac{r_{DW}}{k_2[0\text{-yr}, (100 + 273.15)\text{-K}]} \cdot \ln \left(\frac{r_2}{r_3} \right) = 0.347 \frac{\text{m}^2 \cdot \text{K}}{\text{W}}$$

EBS_name₂ = "Salt Layer : EBS_material₂ = "75% Intact Salt at T2°C"

$$R_2(5\text{-yr}, 300\text{-yr}, 10\text{-yr}, 373.15\text{-K}) = 0.363 \frac{\text{m}^2 \cdot \text{K}}{\text{W}}$$

$$R_3(t, T_3) := \text{if} \left[\left[\text{thickness}_3 = 0 \vee (k_3 = \text{"N/A"}) \right], 0, \frac{r_{DW}}{k_3(t, T_3)} \cdot \ln \left(\frac{r_3}{r_4} \right) \right] \quad R_3(0\text{-yr}, 373.15\text{-K}) = 0.508 \frac{\text{m}^2 \cdot \text{K}}{\text{W}}$$

EBS_name₃ = "Salt Layer 2" EBS_material₃ = "75% Intact Salt at T3°C"

$$R_4(t, T_4) := \text{if} \left[\left[\text{thickness}_4 = 0 \vee (k_4 = \text{"N/A"}) \right], 0, \frac{r_{DW}}{k_4(t, T_4)} \cdot \ln \left(\frac{r_4}{r_{WP}} \right) \right] \quad R_4(0\text{-yr}, 373.15\text{-K}) = 0.969 \frac{\text{m}^2 \cdot \text{K}}{\text{W}}$$

EBS_name₄ = "Salt Layer 1" EBS_material₄ = "75% Intact Salt at T4°C"

$$R_{\text{Total}}(t, T_1, T_2, T_3, T_4) := R_1(T_1) + R_2(t, t_{\text{operate}}, t_{\text{backfill}}, T_2) + R_3(t, T_3) + R_4(t, T_4) \text{ Total thermal resistance between wall and waste package}$$

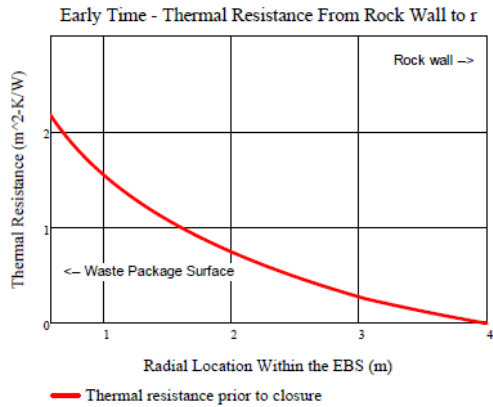
$$t_{\text{backfill}} = 0\text{-yr} \quad t_{\text{operate}} = 50\text{-yr}$$

```

R_continuous(t,r,T1,T2,T3,T4) :=
kk2 ← k_radiation(t,T2) [t < (t_operate + t_backfill)] + k2(t,T2) [t ≥ (t_operate + t_backfill)]
R ← R1(T1) + R2(t,t_operate,t_backfill,T2) + R3(t,T3) + if [(thickness4 = 0) ∨ (k4 = "N/A")], 0,  $\frac{r_{DW}}{k_4(t,T4)} \cdot \ln\left(\frac{r_4}{r}\right)$  if r ≤ r4 ∧ r ≥ rWP
R ← R1(T1) + R2(t,t_operate,t_backfill,T2) + if [(thickness3 = 0) ∨ (k3 = "N/A")], 0,  $\frac{r_{DW}}{k_3(t,T3)} \cdot \ln\left(\frac{r_3}{r}\right)$  if r ≤ r3 ∧ r > r4
R ← R1(T1) + if [(thickness2 = 0) ∨ (k2 = 0)], 0,  $\frac{r_{DW}}{k_2} \cdot \ln\left(\frac{r_2}{r}\right)$  if r ≤ r2 ∧ r ≥ r3
R ← if [(thickness1 = 0) ∨ (k1 = "N/A")], 0,  $\frac{r_{DW}}{k_1(T1)} \cdot \ln\left(\frac{r_1}{r}\right)$  if r ≤ rDW ∧ r ≥ r2
R ← "Invalid Radius" otherwise
return R
    
```

$$R_{\text{continuous}}(5\text{-yr}, r_{\text{WP}}, 373.15\text{-K}, 373.15\text{-K}, 373.15\text{-K}, 373.15\text{-K}) = 2.169 \frac{\text{m}^2 \cdot \text{K}}{\text{W}}$$

$$R_{\text{continuous}}(5\text{-yr}, r_{\text{WP}}, 473.15\text{-K}, 373.15\text{-K}, 373.15\text{-K}, 373.15\text{-K}) = 2.249 \frac{\text{m}^2 \cdot \text{K}}{\text{W}}$$



$$r_{\text{DW}} = 4 \text{ m}$$

$$r_1 = 4 \text{ m}$$

EBS_name₁ = "Salt Layer 4" EBS_material₁ = "Intact Salt 100°C"

$$r_2 = 3.048 \text{ m}$$

Note that for "open modes", the backfill hasn't been emplaced at early time, and EBS-2 is only radiation.

$$r_3 = 2.227 \text{ m}$$

EBS_name₃ = "Salt Layer 2" EBS_material₃ = "75% Intact Salt at T3°C"

$$r_4 = 1.406 \text{ m}$$

EBS_name₄ = "Salt Layer EBS_material₄ = "75% Intact Salt at T4°C"

$$r_{\text{WP}} = 0.585 \text{ m}$$

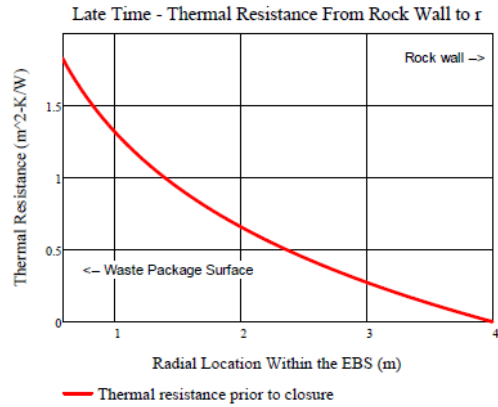
$$R_1(373.15\text{-K}) = 0.258 \frac{\text{m}^2 \cdot \text{K}}{\text{W}}$$

$$R_2(5\text{-yr}, t_{\text{operate}}, t_{\text{backfill}}, 373.15\text{-K}) = 0.363 \frac{\text{m}^2 \cdot \text{K}}{\text{W}}$$

$$R_3(5\text{-yr}, 373.15\text{-K}) = 0.532 \frac{\text{m}^2 \cdot \text{K}}{\text{W}}$$

$$R_4(5\text{-yr}, 373.15\text{-K}) = 1.015 \frac{\text{m}^2 \cdot \text{K}}{\text{W}}$$

$$R_{\text{Total}}(5\text{yr}, 373.15\text{-K}, 373.15\text{-K}, 373.15\text{-K}, 373.15\text{-K}) = 2.169 \frac{\text{m}^2 \cdot \text{K}}{\text{W}}$$



$$r_{DW} = 4 \text{ m}$$

$$r_1 = 4 \text{ m} \quad \text{EBS_name}_1 = \text{"Salt Layer 4"} \quad \text{EBS_material}_1 = \text{"Intact Salt 100°C"}$$

$$r_2 = 3.048 \text{ m} \quad \text{EBS_name}_2 = \text{"Salt Layer 3"} \quad \text{EBS_material}_2 = \text{"75\% Intact Salt at T2°C"}$$

$$r_3 = 2.227 \text{ m} \quad \text{EBS_name}_3 = \text{"Salt Layer 2"} \quad \text{EBS_material}_3 = \text{"75\% Intact Salt at T3°C"}$$

$$r_4 = 1.406 \text{ m} \quad \text{EBS_name}_4 = \text{"Salt Layer"} \quad \text{EBS_material}_4 = \text{"75\% Intact Salt at T4°C"}$$

$$r_{WP} = 0.585 \text{ m}$$

$$R_1(373.15\text{-K}) = 0.258 \frac{\text{m}^2 \cdot \text{K}}{\text{W}} \quad R_2(1000\text{-yr}, t_{\text{operate}}, t_{\text{backfill}}, 373.15\text{-K}) = 0.298 \frac{\text{m}^2 \cdot \text{K}}{\text{W}}$$

$$R_3(1000\text{-yr}, 373.15\text{-K}) = 0.437 \frac{\text{m}^2 \cdot \text{K}}{\text{W}} \quad R_4(1000\text{-yr}, 373.15\text{-K}) = 0.834 \frac{\text{m}^2 \cdot \text{K}}{\text{W}}$$

$$R_{\text{Total}}(1000\text{yr}, 373.15\text{-K}, 373.15\text{-K}, 373.15\text{-K}, 373.15\text{-K}) = 1.828 \frac{\text{m}^2 \cdot \text{K}}{\text{W}}$$

INPUT 6 = WASTE FORM DATA

Input_6 := READEXCEL(file, concat(sheet, "A35:B38"))

Input_6 = $\begin{pmatrix} \text{"Waste form short name"} & \text{"UOX-40"} \\ \text{"Waste form type"} & \text{"Assembly"} \\ \text{"Waste package capacity"} & 12 \\ \text{"Waste package length, m"} & 5 \end{pmatrix}$

WF_name := Input_6_{1,2} = "UOX-40"

WF_type := Input_6_{2,2} = "Assembly"

WP_cap := Input_6_{3,2} = 12

WP_length := Input_6_{4,2} = 5 m

Outside of the liner

$$A_1 := 2 \cdot \pi \cdot r_1 \cdot \text{WP_length} = 125.66 \text{ m}^2$$

$$A_{DW} := 2 \cdot \pi \cdot r_{DW} \cdot \text{WP_length} = 125.664 \text{ m}^2$$

Outside of the backfill

$$A_2 := 2 \cdot \pi \cdot r_2 \cdot \text{WP_length} = 95.76 \text{ m}^2$$

Outside of the envelope

$$A_3 := 2 \cdot \pi \cdot r_3 \cdot \text{WP_length} = 69.96 \text{ m}^2$$

Outside of the buffer

$$A_4 := 2 \cdot \pi \cdot r_4 \cdot \text{WP_length} = 44.17 \text{ m}^2$$

$$A_{WP} := 2 \cdot \pi \cdot r_{WP} \cdot \text{WP_length} = 18.378 \text{ m}^2$$

Stefan Boltzmann constant $\sigma := 5.670 \cdot 10^{-8} \frac{W}{m^2 \cdot K^4}$

The basis for the rock and waste package emissivity assumed is F. P. Incropera and D.P. DeWitt, *Fundamentals of Heat and Mass Transfer*, 4th Edition, 1996, Table A-11, which shows a range of 0.88 to 0.93 is adapted from hemispherical emissivity of rock at around 300 K. This range is corroborated by the "Heat Transmission" section of Perry's Chemical Engineers Handbook, 6th Edition, 1964 (Table 10-17, pages 10-51 to 10-52) for normal emissivity of rough silica and rough fused quartz, ranging from 0.8 to 0.93. The waste package surface is assumed to be covered with dust and dirt. The emissivity values to the left were specified in DSEF, and should be changed there if necessary.

Waste Package emissivity $\epsilon_{WP} = 0.6$

Rock wall or cementitious liner emissivity $\epsilon_{wall} = 0.9$

Reference for radiation heat transfer coefficient, h_{rad} , is from Incropera and DeWitt, Table 13.3 for concentric infinite cylinders (based on the inner surface as the heat source), and is also referenced in the YMP *Ventilation Model and Analysis Report*, ANL-EBS-MD-000030 REV 04, Oct. 2004, page 6-8.

$$h_{rad_infinite}(r_1, r_o, \epsilon_1, \epsilon_o) := \frac{\sigma}{\frac{1}{\epsilon_1} + \left(\frac{1 - \epsilon_o}{\epsilon_o}\right) \cdot \frac{r_1}{r_o}} \quad h_{rad_infinite}(r_{WP}, r_{DW}, \epsilon_{WP}, \epsilon_{wall}) = 3.369 \times 10^{-8} \frac{W}{m^2 \cdot K^4}$$

Usage is Q in watts = $h \cdot A \cdot (T_1^4 - T_o^4)$

For radiation between the liner and the envelope (both metal surfaces) use r_2 and r_3 , and assume the same emissivity for both surfaces.

$$Q_{rad_infinite}(r_1, r_o, \epsilon_1, \epsilon_o, L, T_{cold}, T_{hot}) := h_{rad_infinite}(r_1, r_o, \epsilon_1, \epsilon_o) \cdot (2 \cdot \pi \cdot r_1 \cdot L) \cdot (T_{hot}^4 - T_{cold}^4) \quad Q_{rad_infinite}(r_3, r_2, \epsilon_{WP}, \epsilon_{wall}, WP_length, 300\text{-K}, 600\text{-K}) = 2.758 \times 10^5 \text{ W}$$

$$Q_{L_rad_infinite}(r_1, r_o, \epsilon_1, \epsilon_o, T_{cold}, T_{hot}) := h_{rad_infinite}(r_1, r_o, \epsilon_1, \epsilon_o) \cdot (2 \cdot \pi \cdot r_1) \cdot (T_{hot}^4 - T_{cold}^4) \quad Q_{L_rad_infinite}(r_3, r_2, \epsilon_{WP}, \epsilon_{wall}, 300\text{-K}, 600\text{-K}) = 5.515 \times 10^4 \frac{W}{m}$$

Heat transfer by radiation from NIRAS/ONDRAF December 2005 Report: Eef Weetjens and Xavier Sillen; *Thermal analysis of the Supercontainer concept 2D axisymmetric heat transport calculations*, Section 6.4.3. Pg 34, equation 29.

$$Q_{L_infinite}(r_1, r_o, \epsilon_1, \epsilon_o, T_{cold}, T_{hot}) := \frac{2\pi\sigma(T_{hot}^4 - T_{cold}^4)}{\frac{1 - \epsilon_1}{\epsilon_1} + \frac{1}{r_1} + \frac{1 - \epsilon_o}{\epsilon_o} \cdot \frac{r_o}{r_1}} \quad Q_{L_infinite}(r_3, r_2, \epsilon_{WP}, \epsilon_{wall}, 300\text{-K}, 600\text{-K}) = 5.515 \times 10^4 \frac{W}{m}$$

This is the same as the Incropera and DeWitt result, $Q_{L_rad_infinite}$

INPUT 7 = PARAMETRIC STUDY VARIABLE INPUT DATA

Input_7 := READEXCEL(file, concat(sheet, "F29:F41"))

	1
1	1
2	"Single"
3	"None"
4	""
5	""
6	""
7	""
8	""
9	""
10	""
11	""
12	""
13	""

PARAMETRIC STUDIES OF "BACKFILL THERMAL CONDUCTIVITY" NOT ALLOWED FOR TEMPERATURE AND TIME-DEPENDENT THERMAL PROPERTY ANALYSES. THEREFORE, PARAMETER TYPE IS RESET TO "SINGLE",

Cases := $\begin{cases} \text{Input_7}_1 & \text{if Input_7}_2 \neq \text{"Backfill Thermal Conductivity"} \\ 1 & \text{otherwise} \end{cases}$

Parameter := $\begin{cases} \text{"Single"} & \text{if Input_7}_2 = \text{"Backfill Thermal Conductivity"} \\ \text{Input_7}_2 & \text{otherwise} \end{cases}$

Parameter_units := Input_7_3 = "None"

ij := 1 .. Cases

Parameter_data_{ij} := Input_7_{ij+3}

Parameter_description_{ij} := $\begin{cases} \text{"Single Base Case"} & \text{if Cases} = 1 \\ \text{concat}[\text{num2str}[\text{Input_7}_{(ij+3)}], ", ", \text{Input_7}_2] & \text{otherwise} \end{cases}$

Parameter_data = ("") Parameter_description = ("Single Base Case")

INPUT 8 = DECAY HEAT INPUT DATA PER UNIT SOURCE (ASSEMBLY OR CANISTER):

Input_8_size := READEXCEL(file, concat(sheet, "C43")) Input_8_size₁ = 58 Decay_heat_range := concat["A43:B", num2str((Input_8_size₁ + 42))] = "A43:B100"

Input_8 := READEXCEL(file, concat(sheet, Decay_heat_range))

Time_out_of_Reactor := Input_8⁽¹⁾.yr

Decay_Heat_per_Cut := Input_8⁽²⁾.W

Input_8 =

	1	2
1	5	1.028·10 ³
2	5.1	1.011·10 ³
3	5.5	949.125
4	5.75	916.671
5	6	887.984
6	8	742.948
7	10	670.028
8	11.5	634.239
9	15	576.929
10	20	...

Time_out_of_Reactor =

	1
1	5
2	5.1
3	5.5
4	5.75
5	6
6	8
7	10
8	11.5
9	15
10	...

.yr

Decay_Heat_per_Cut =

	1
1	1.028·10 ³
2	1.011·10 ³
3	949.125
4	916.671
5	887.984
6	742.948
7	670.028
8	634.239
9	576.929
10	...

W

$Q(t) := \text{interp}(\text{csp}(\text{Time_out_of_Reactor}, \text{Decay_Heat_per_Cnt}), \text{Time_out_of_Reactor}, \text{Decay_Heat_per_Cnt}, t)$

Ventilation efficiency for open systems is $V_{\text{eff}} = 0$ between t_{store} and t_{operate}

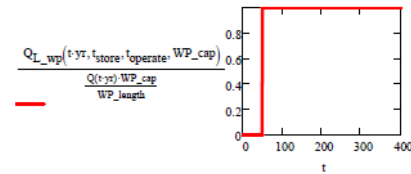
FUNCTION DEFINITION FOR ONE OUTPUT FILE

FORMULAS FOR CALCULATING THE TRANSIENT DRIFT WALL TEMPERATURE:

Central waste package:

$$Q_{L_wp}(t, t_{\text{store}}, t_{\text{operate}}, WP_cap) := \frac{Q(t) \cdot WP_cap}{WP_length} [1 - 1 \cdot (t \leq t_{\text{store}})] [1 - V_{\text{eff}}(t \leq t_{\text{operate}})]$$

$$Q_{L_wp}(55\text{-yr}, t_{\text{store}}, t_{\text{operate}}, 12) = 709.459 \frac{\text{W}}{\text{m}}$$



Note - added r_{DW} as a function parameter to allow calculations at additional compliance points inside the rock, where r_{DW} would be replaced with new radius value.

$$DW_T_finite_line(t, r_{\text{DW}}, y, t_{\text{store}}, t_{\text{operate}}, WP_cap, Kth, \alpha) := \left[\int_0^t \frac{Q_{L_wp}(\tau, t_{\text{store}}, t_{\text{operate}}, WP_cap)}{8 \cdot (\pi \cdot Kth) \cdot (t - \tau)} e^{-\frac{r_{\text{DW}}^2}{4 \cdot \alpha \cdot (t - \tau)}} \left[\text{erf} \left[\frac{1}{2} \frac{y + WP_length}{\sqrt{\alpha \cdot (t - \tau)}} \right] - \text{erf} \left[\frac{1}{2} \frac{y - WP_length}{\sqrt{\alpha \cdot (t - \tau)}} \right] \right] d\tau \right]$$

Adjacent drifts:

$$Q_{L_avg}(t, t_{store}, t_{operate}, WP_cap, WP_spacing) := \frac{Q(t) \cdot WP_cap}{WP_spacing} [1 - 1 \cdot (t \leq t_{store})] [1 - V_{eff}(t \leq t_{operate})]$$

Note - added r_{DW} as a function parameter to allow calculations at additional compliance points inside the rock, where r_{DW} would be replaced with new radius value.

$$DW_T_drifts(t, r_{DW}, t_{store}, t_{operate}, WP_cap, WP_spacing, Drift_spacing, Kth, \alpha) := 2 \left[\sum_{id=1}^{N_{drifts}} \int_0^t \frac{Q_{L_avg}(\tau, t_{store}, t_{operate}, WP_cap, WP_spacing)}{4 \cdot (\pi \cdot Kth) \cdot (t - \tau)} \cdot e^{-\frac{[(t_{DW})^2 + (id \cdot Drift_spacing)^2]}{4 \alpha \cdot (t - \tau)}} d\tau \right]$$

Adjacent waste packages:

$$Q_{wp}(t, t_{store}, t_{operate}, WP_cap) := Q(t) \cdot WP_cap [1 - 1 \cdot (t \leq t_{store})] [1 - V_{eff}(t \leq t_{operate})]$$

Note - added r_{DW} as a function parameter to allow calculations at additional compliance points inside the rock, where r_{DW} would be replaced with new radius value.

$$DW_T_adjacent_pkgs(t, r_{DW}, t_{store}, t_{operate}, WP_cap, WP_spacing, Kth, \alpha) := 2 \left[\sum_{ip=1}^{N_{adj}} \int_0^t \frac{Q_{wp}(\tau, t_{store}, t_{operate}, WP_cap)}{8 \cdot Kth \cdot \sqrt{\alpha} \cdot \pi^{1.5} \cdot (t - \tau)^{1.5}} \cdot e^{-\frac{[(t_{DW})^2 + (ip \cdot WP_spacing)^2]}{4 \alpha \cdot (t - \tau)}} d\tau \right]$$

This command specifies two rows of column headings for output parameter sensitivity runs

OutfileName := file = "DSEF R3.0C_2013Jul29_HRG-Salt_UOX-40_Enclosed mode variable kth_Case-Kth-1.xlsm"

Out_sheet := "Thermal-Analytical Output!"

This section specifies the column headings for output sensitivity studies

Cases := 1 Read in from Thermal-Analytical sheet in DSEF (Inputs_7)

i := 1..Cases

Parameter_vector_i := $\begin{cases} \text{"Base Case"} & \text{if Cases} = 1 \\ \text{concat(Parameter, " ", Parameter_description)} & \text{otherwise} \end{cases}$

outdata(t_{DW}, t_{CP2}, t_{store}, t_{operate}, WP_{cap}, WP_{spacing}, Drift_{spacing}, Kth, α)

jjj := 1..Cases Cases = 1

X_{jjj} := Parameter_data_{jjj} Parameter = "Single" PARAMETRIC STUDIES OF "BACKFILL THERMAL CONDUCTIVITY" NOT ALLOWED FOR TEMPERATURE AND TIME-DEPENDENT THERMAL PROPERTY ANALYSES. THEREFORE, PARAMETER TYPE IS RESET TO "SINGLE";

Temp_array_{jjj} := outdata(t_{DW}, t_{CP2}, t_{store}, t_{operate}, WP_{cap}, WP_{spacing}, Drift_{spacing}, Kth, α) if Parameter = "Single"
 outdata(t_{DW}, t_{CP2}, t_{store}, t_{operate}, WP_{cap}, WP_{spacing}, X_{jjj}, m, Kth, α) if Parameter = "Drift Spacing"
 outdata(t_{DW}, t_{CP2}, t_{store}, t_{operate}, WP_{cap}, X_{jjj}, m, Drift_{spacing}, Kth, α) if Parameter = "WP Spacing"
 outdata(t_{DW}, t_{CP2}, X_{jjj}, yr, t_{operate}, WP_{cap}, WP_{spacing}, Drift_{spacing}, Kth, α) if Parameter = "Storage Time"
 outdata(t_{DW}, t_{CP2}, t_{store}, t_{store} + X_{jjj}, yr, WP_{cap}, WP_{spacing}, Drift_{spacing}, Kth, α) if Parameter = "Ventilation Duration"
 outdata(t_{DW}, t_{CP2}, t_{store}, t_{operate}, WP_{cap}, WP_{spacing}, Drift_{spacing}, X_{jjj}, $\frac{W}{m \cdot K}$, α) if Parameter = "Rock Conductivity"
 "Undefined" otherwise

Temp_array₁ := outdata(t_{DW}, t_{CP2}, t_{store}, t_{operate}, WP_{cap}, WP_{spacing}, Drift_{spacing}, Kth, α)

File_array_{jjj} := stack(Title_array_{jjj}, Temp_array_{jjj})



File_array₁ =

	1	2	3	4	5	6
1	"Parameter value: Base Case"	---	---	---	---	---
2	"TooR (yr)"	"Wall ΔT Central Line Src"	"Wall ΔT Adj Drifts"	"Wall ΔT Adj Pkgs"	"Compliance Point 2, C"	"Rock Wall Temp, C"
3	50	0	0	0	27.5	27.5
4	55	10.991	7.223	3.07	45.86	48.785
5	60	10.687	12.867	4.27	52.544	55.323
6	65	10.188	16.843	4.835	56.761	59.367
7	70	9.666	19.727	5.112	59.55	62.005
8	75	9.166	21.846	5.232	61.43	63.745
9	80	8.695	23.415	5.259	62.685	64.868
10	85	8.263	24.576	5.229	63.499	65.568
11	90	7.871	25.432	5.163	63.997	65.966
12	95	7.505	26.048	5.082	64.261	66.134
13	100	7.171	26.493	4.977	64.355	66.141
14	105	6.864	26.797	4.872	64.327	66.033
15	110	6.584	26.984	4.759	64.193	65.827
16	115	6.328	27.091	4.652	64.021	...




```

OutfileName = "DSEF R3.0C_2013Jul29_HRG-Salt_UOX-40_Enclosed mode variable kth_Case-Kth-1.xlsm"
Write_file := Write_OK = "No"

write_the_peaks(Write_file) :=  $\begin{cases} \text{write\_it} \leftarrow \begin{cases} \text{WRITEEXCEL}(\text{Peak\_values}, \text{OutfileName}, \text{peaks\_write\_range}) & \text{if } (\text{Write\_file} = \text{"Yes"}) \vee (\text{Write\_file} = \text{"YES"}) \\ \text{"File written"} \end{cases} \\ \text{write\_it} \leftarrow \text{"No file written"} & \text{otherwise} \end{cases}$ 

write_the_peaks(Write_file) = "No file written"

write_the_transient_size(Write_file) :=  $\begin{cases} \text{write\_it} \leftarrow \begin{cases} \text{WRITEEXCEL}(\text{Transient\_size}, \text{OutfileName}, \text{Transient\_size\_range}) & \text{if } (\text{Write\_file} = \text{"Yes"}) \vee (\text{Write\_file} = \text{"YES"}) \\ \text{"File written"} \end{cases} \\ \text{write\_it} \leftarrow \text{"No file written"} & \text{otherwise} \end{cases}$ 

write_the_transient_size(Write_file) = "No file written"

Write_file = "No"
Cases = 1
iww := 1 .. Cases
NOTE - USE File_array to write to stand-alone Excel files, and Temp_array to write back to the DSEF Excel file.

write_the_transients(jj) :=  $\begin{cases} \text{write\_array} \leftarrow \text{Temp\_array}_{jj} \\ \text{write\_it} \leftarrow \begin{cases} \text{WRITEEXCEL}(\text{write\_array}, \text{OutfileName}, \text{transient\_write\_range}_{jj}) & \text{if } (\text{Write\_file} = \text{"Yes"}) \vee (\text{Write\_file} = \text{"YES"}) \\ \text{"File written"} \end{cases} \\ \text{write\_it} \leftarrow \text{"No file written"} & \text{otherwise} \end{cases}$ 

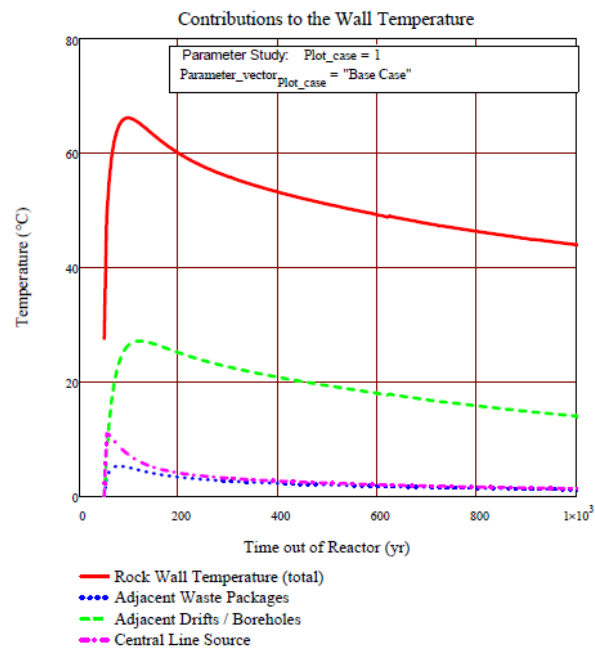
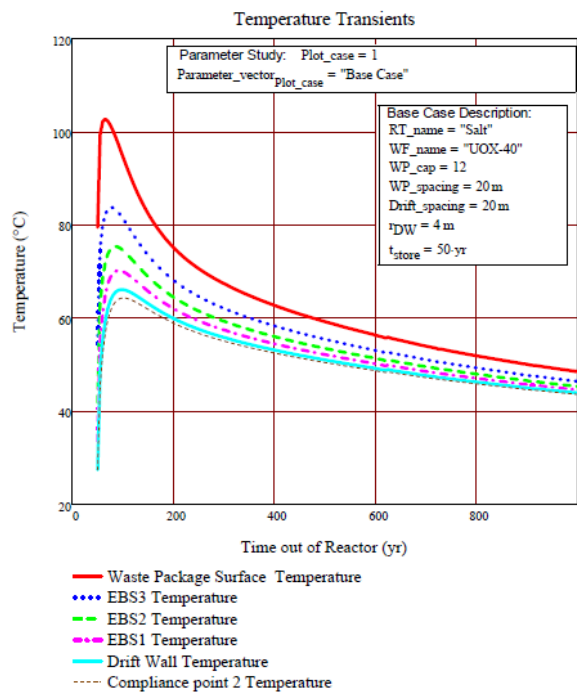
write_the_transients(iww) = ("No file written")

Plot_case := 1
Select parametric study case to plot (default plot is for case 1)

WP_plot :=  $\left[ (\text{Temp\_array}_{\text{plot\_case}})^{\langle 10 \rangle} \right]$ 
EBS3_T_plot :=  $\left[ (\text{Temp\_array}_{\text{plot\_case}})^{\langle 9 \rangle} \right]$ 
EBS2_T_plot :=  $\left[ (\text{Temp\_array}_{\text{plot\_case}})^{\langle 8 \rangle} \right]$ 
EBS1_T_plot :=  $\left[ (\text{Temp\_array}_{\text{plot\_case}})^{\langle 7 \rangle} \right]$ 
Wall_T_plot :=  $\left[ (\text{Temp\_array}_{\text{plot\_case}})^{\langle 6 \rangle} \right]$ 

CP2_plot :=  $\left[ (\text{Temp\_array}_{\text{plot\_case}})^{\langle 5 \rangle} \right]$ 
Delta_WP2_T_plot :=  $\left[ (\text{Temp\_array}_{\text{plot\_case}})^{\langle 4 \rangle} \right]$ 
Delta_drifts_T_plot :=  $\left[ (\text{Temp\_array}_{\text{plot\_case}})^{\langle 3 \rangle} \right]$ 
Delta_central_T_plot :=  $\left[ (\text{Temp\_array}_{\text{plot\_case}})^{\langle 2 \rangle} \right]$ 

```



$$tt_rw := [(Peak_values)^{Plot_case-2}]_2 = 100$$

$$CP2_T_at_tt_rw := \left[(Temp_array_{Plot_case})^{(5)} \right] \left(\frac{tt_rw - t_{store}}{yr} \right)_{+1}^{Step} = 64.355$$

$$Wall_T_at_tt_rw := [(Peak_values)^{Plot_case-2-1}]_2 = 66.141$$

$$EBS1_T_at_tt_rw := \left[(Temp_array_{Plot_case})^{(7)} \right] \left(\frac{tt_rw - t_{store}}{yr} \right)_{+1}^{Step} = 70.007$$

$$EBS2_T_at_tt_rw := \left[(Temp_array_{Plot_case})^{(8)} \right] \left(\frac{tt_rw - t_{store}}{yr} \right)_{+1}^{Step} = 74.59$$

$$EBS3_T_at_tt_rw := \left[(Temp_array_{Plot_case})^{(9)} \right] \left(\frac{tt_rw - t_{store}}{yr} \right)_{+1}^{Step} = 81.408$$

$$WP_T_at_tt_rw := \left[(Temp_array_{Plot_case})^{(10)} \right] \left(\frac{tt_rw - t_{store}}{yr} \right)_{+1}^{Step} = 94.699$$

$$r_array := \begin{pmatrix} r_{WP} \\ r_4 \\ r_3 \\ r_2 \\ r_1 \\ r_{CP2} \end{pmatrix} = \begin{pmatrix} 0.585 \\ 1.406 \\ 2.227 \\ 3.048 \\ 4 \\ 5.25 \end{pmatrix} \text{ m}$$

$$T_at_tt_rw := \begin{pmatrix} WP_T_at_tt_rw \\ EBS3_T_at_tt_rw \\ EBS2_T_at_tt_rw \\ EBS1_T_at_tt_rw \\ Wall_T_at_tt_rw \\ CP2_T_at_tt_rw \end{pmatrix} = \begin{pmatrix} 94.699 \\ 81.408 \\ 74.59 \\ 70.007 \\ 66.141 \\ 64.355 \end{pmatrix}$$

$$T_at_tt_wp := \begin{pmatrix} WP_T_at_tt_wp \\ EBS3_T_at_tt_wp \\ EBS2_T_at_tt_wp \\ EBS1_T_at_tt_wp \\ Wall_T_at_tt_wp \\ CP2_T_at_tt_wp \end{pmatrix} = \begin{pmatrix} 102.771 \\ 82.272 \\ 71.879 \\ 64.949 \\ 59.367 \\ 56.761 \end{pmatrix}$$

$$tt_wp := [(Peak_values)^{Plot_case-2}]_6 = 65$$

$$CP2_T_at_tt_wp := \left[(Temp_array_{Plot_case})^{(5)} \right] \left(\frac{tt_wp - t_{store}}{yr} \right)_{+1}^{Step} = 56.761$$

$$Wall_T_at_tt_wp := \left[(Temp_array_{Plot_case})^{(6)} \right] \left(\frac{tt_wp - t_{store}}{yr} \right)_{+1}^{Step} = 59.367$$

$$EBS1_T_at_tt_wp := \left[(Temp_array_{Plot_case})^{(7)} \right] \left(\frac{tt_wp - t_{store}}{yr} \right)_{+1}^{Step} = 64.949$$

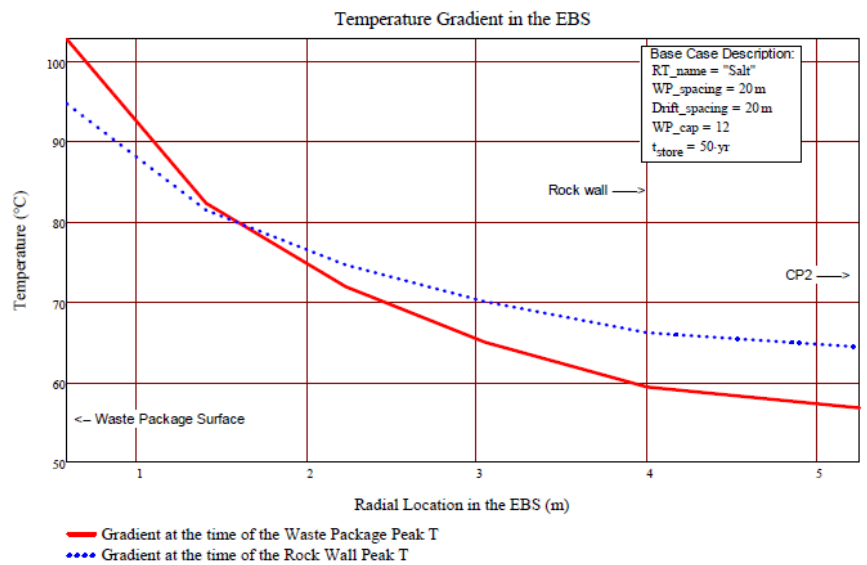
$$EBS2_T_at_tt_wp := \left[(Temp_array_{Plot_case})^{(8)} \right] \left(\frac{tt_wp - t_{store}}{yr} \right)_{+1}^{Step} = 71.879$$

$$EBS3_T_at_tt_wp := \left[(Temp_array_{Plot_case})^{(9)} \right] \left(\frac{tt_wp - t_{store}}{yr} \right)_{+1}^{Step} = 82.272$$

$$WP_T_at_tt_wp := [(Peak_values)^{Plot_case-2-1}]_6 = 102.771$$

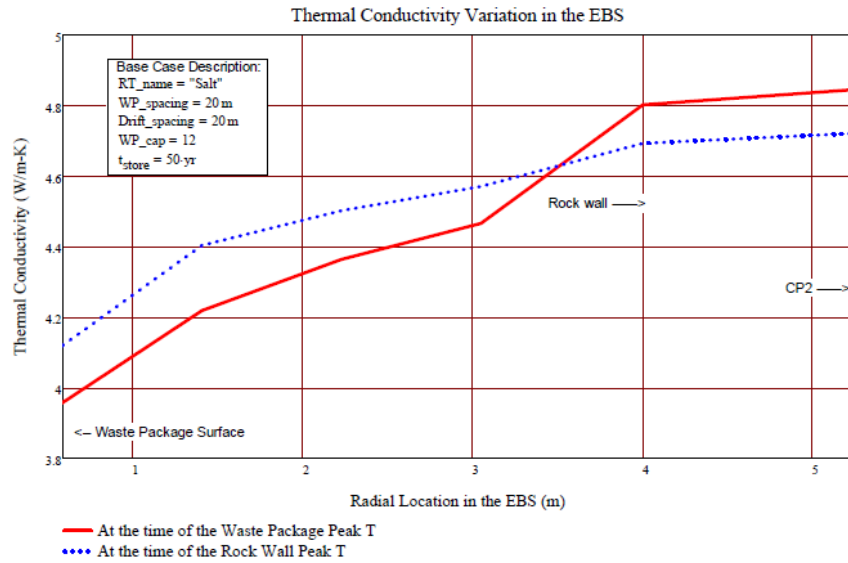
$$k_at_tt_wp := \begin{pmatrix} k_4[tt_wp-yr, (WP_T_at_tt_wp + 273.15)\cdot K] \\ k_3[tt_wp-yr, (EBS3_T_at_tt_wp + 273.15)\cdot K] \\ k_2[tt_wp-yr, (EBS2_T_at_tt_wp + 273.15)\cdot K] \\ k_2[tt_wp-yr, (EBS1_T_at_tt_wp + 273.15)\cdot K] \\ k_1[(Wall_T_at_tt_wp + 273.15)\cdot K] \\ k_1[(CP2_T_at_tt_wp + 273.15)\cdot K] \end{pmatrix} = \begin{pmatrix} 3.958 \\ 4.219 \\ 4.364 \\ 4.466 \\ 4.802 \\ 4.846 \end{pmatrix} \frac{W}{m\cdot K}$$

$$k_at_tt_rw := \begin{pmatrix} k_4[tt_rw-yr, (WP_T_at_tt_wp + 273.15)\cdot K] \\ k_3[tt_rw-yr, (EBS3_T_at_tt_rw + 273.15)\cdot K] \\ k_2[tt_rw-yr, (EBS2_T_at_tt_rw + 273.15)\cdot K] \\ k_2[tt_rw-yr, (EBS1_T_at_tt_rw + 273.15)\cdot K] \\ k_1[(Wall_T_at_tt_rw + 273.15)\cdot K] \\ k_1[(CP2_T_at_tt_rw + 273.15)\cdot K] \end{pmatrix} = \begin{pmatrix} 4.12 \\ 4.404 \\ 4.502 \\ 4.571 \\ 4.693 \\ 4.721 \end{pmatrix} \frac{W}{m\cdot K}$$



$$k_{at_tt_wp} := \begin{bmatrix} k_4[tt_wp_yr, (WP_T_at_tt_wp + 273.15)\text{-K}] \\ k_3[tt_wp_yr, (EBS3_T_at_tt_wp + 273.15)\text{-K}] \\ k_2[tt_wp_yr, (EBS2_T_at_tt_wp + 273.15)\text{-K}] \\ k_2[tt_wp_yr, (EBS1_T_at_tt_wp + 273.15)\text{-K}] \\ k_1[(Wall_T_at_tt_wp + 273.15)\text{-K}] \\ k_1[(CP2_T_at_tt_wp + 273.15)\text{-K}] \end{bmatrix} = \begin{pmatrix} 3.958 \\ 4.219 \\ 4.364 \\ 4.466 \\ 4.802 \\ 4.846 \end{pmatrix} \frac{\text{W}}{\text{m}\cdot\text{K}} \quad k_{at_tt_rw} := \begin{bmatrix} k_4[tt_rw_yr, (WP_T_at_tt_wp + 273.15)\text{-K}] \\ k_3[tt_rw_yr, (EBS3_T_at_tt_rw + 273.15)\text{-K}] \\ k_2[tt_rw_yr, (EBS2_T_at_tt_rw + 273.15)\text{-K}] \\ k_2[tt_rw_yr, (EBS1_T_at_tt_rw + 273.15)\text{-K}] \\ k_1[(Wall_T_at_tt_rw + 273.15)\text{-K}] \\ k_1[(CP2_T_at_tt_rw + 273.15)\text{-K}] \end{bmatrix} = \begin{pmatrix} 4.12 \\ 4.404 \\ 4.502 \\ 4.571 \\ 4.693 \\ 4.721 \end{pmatrix} \frac{\text{W}}{\text{m}\cdot\text{K}}$$

$$0.75 \cdot k_{intact}[(WP_T_at_tt_wp + 273.15)\text{-K}] + 0.25 \cdot k_{crushed}[Porosity(tt_wp), (WP_T_at_tt_wp + 273.15)\text{-K}] = 3.958 \cdot \frac{\text{W}}{\text{m}\cdot\text{K}}$$



$$0.75 \cdot k_{intact}[(WP_T_at_tt_wp + 273.15)\text{-K}] = 3.132 \cdot \frac{\text{W}}{\text{m}\cdot\text{K}}$$

$$Porosity(tt_wp) = 0.111$$

$$0.25 \cdot k_{crushed}[Porosity(tt_wp), (WP_T_at_tt_wp + 273.15)\text{-K}] = 0.826 \cdot \frac{\text{W}}{\text{m}\cdot\text{K}}$$

$$0.25 \cdot k_{consolidate}[tt_wp, (WP_T_at_tt_wp + 273.15)\text{-K}] = 0.826 \cdot \frac{\text{W}}{\text{m}\cdot\text{K}}$$

Previous analysis with constant salt thermal properties in the EBS assumed 75% surface contact with intact salt, and took no credit for conduction through the crushed salt.

$$0.75 \cdot k_{intact}[(100 + 273.15)\text{-K}] = 3.158 \cdot \frac{\text{W}}{\text{m}\cdot\text{K}}$$

$$0.75 \cdot k_{intact}[(200 + 273.15)\text{-K}] = 2.409 \cdot \frac{\text{W}}{\text{m}\cdot\text{K}}$$

$$k_{crushed}[Porosity(tt_wp), (WP_T_at_tt_wp + 273.15)\text{-K}] = 3.305 \cdot \frac{\text{W}}{\text{m}\cdot\text{K}}$$

$$k_{consolidate}[Porosity(tt_wp), (WP_T_at_tt_wp + 273.15)\text{-K}] = 1.809 \cdot \frac{\text{W}}{\text{m}\cdot\text{K}}$$

VERRIDE COUNTER AND STEP SIZE TO GET FINER CONVERGENCE ON THE ANSWER

```

t_vent = 0.yr
OPTIONALLY OVERRIDE VENTILATION TIME TO SHORTEN ITERATION CONVERGENCE
ITERATE_OK = "NO"
t_convergence = 1.yr

t_required_storage(t_operate, T_criteria, t_convergence) :=
timeOK ← t_operate - t_convergence
Peak_Wall_T_check ← (Peak_Wall_T + 273.15).K
timeOK ← t_operate if Peak_Wall_T_check ≤ T_criteria
while Peak_Wall_T_check > T_criteria
    timeOK ← timeOK + t_convergence
    calc_array ← outdata(t_DW, t_CP2, t_store, timeOK, WP_cap, WP_spacing, Drift_spacing, Kth, α)
    Peak_Wall_T_check ← (max(calc_array) + 273.15).K
return (
    (
        timeOK
        /
        yr
        *
        (
            Peak_Wall_T_check - 273.15K
            /
            K
        )
    )
    outdata(t_DW, t_CP2, t_store, timeOK, WP_cap, WP_spacing, Drift_spacing, Kth, α)
)

```

```

Final_array := (
    t_required_storage(t_operate, T_criteria, t_convergence) if ITERATE_OK = "YES"
    "No Iteration Performed" otherwise
)

```

```

t_operate_required := Final_array_1.yr + 1.yr

```

```

t_vent_required := t_operate_required - t_store = 1.yr
T_criteria = 100.°C

```

```

Peak_Wall_T_check := (Final_array_2 + 273.15).K = 1.°C

```

```

Result := stack(Title_array_1, Final_array_3)

```

Result = ■

```

Time_array := (Final_array3)(1)
Peak_Temp(n) := max[(Final_array3)(n)]      Peak_Temp(6) = ■
Peak_t(n) := lookup[Peak_Temp(n), (Final_array3)(n), Time_array]  Peak_t(6)1, yr = ■, yr
mn := 5..10  Peak_resultsmn-4, 1 := Peak_Temp(mn)  Peak_resultsmn-4, 2 := Peak_t(mn)1

CP2      , time of peak
Peak Wall T, time of peak
Peak EBS 1, time of peak
Peak EBS 2, time of peak
Peak EBS 3, time of peak
Waste Pkg T, time of peak

Peak_results = ■

Array_row_at_Wall_T_peak := match[Peak_Temp(6), (Final_array3)(6)]1 = ■
CP2_at_Wall_T_pk_t := [(Final_array3)(5)]Array_row_at_Wall_T_peak = ■
Central_WP_delta := [(Final_array3)(2)]Array_row_at_Wall_T_peak = ■
Adj_Drift_delta := [(Final_array3)(3)]Array_row_at_Wall_T_peak = ■
Adj_WP_delta := [(Final_array3)(4)]Array_row_at_Wall_T_peak = ■
    
```

$$\text{Result_Vector} := \left(\frac{\text{WP_spacing}}{m} \quad \text{TC} \quad \frac{\text{Drift_spacing}}{m} \quad \text{Peak_results}_{6,1} \quad \text{Peak_results}_{6,2} \quad \text{Peak_results}_{2,1} \quad \text{Peak_results}_{2,2} \quad \text{CP2_at_Wall_T_pk_t} \quad \frac{t_{\text{vent_required}}}{\text{yr}} \quad \text{Central_WP_delta} \quad \text{Adj_Drift_delta} \quad \text{Adj_WP_delta} \right)$$

Result_headings := ("WP Spacing" "Temp Criteria" "Drift Spacing" "Peak WP T" "Time of WP Peak" "Peak Wall T" "Time of Wall Peak" "Peak CP2 T" "Ventilation time" "Central WP delta" "Adj Drift delta" "Adj WP delta")

Result_Vector = ■

This is the result vector for transcription to the Excel case results tracking file

RV := augment(Result_headings^T, Result_Vector^T) T_ambient = 27.5 °C Contribution percentages at time of peak wall temperature

$$\text{Percent_central_WP_delta} := \frac{\text{Central_WP_delta}}{\text{Peak_Temp}(6) - \frac{(T_{\text{ambient}} - 273.15 \text{ K})}{K}} \cdot 100 = \blacksquare$$

$$\text{Percent_adj_Drift_delta} := \frac{\text{Adj_Drift_delta}}{\text{Peak_Temp}(6) - \frac{(T_{\text{ambient}} - 273.15 \text{ K})}{K}} \cdot 100 = \blacksquare$$

NOTE THAT THESE RESULTS WILL BE MISSING IF Iterate_OK = "No"

RV = ■

$$\text{Percent_adj_WP_delta} := \frac{\text{Adj_WP_delta}}{\text{Peak_Temp}(6) - \frac{(T_{\text{ambient}} - 273.15 \text{ K})}{K}} \cdot 100 = \blacksquare$$

$$\text{Percent_central_WP_delta} + \text{Percent_adj_WP_delta} + \text{Percent_adj_Drift_delta} = \blacksquare$$

